THEORETICAL STUDIES OF CHEMICAL REACTION DYNAMICS

Thesis by

Jack Alan Kaye

In Partial Fulfillment of the Requirements
for the Degree of
Doctor of Philosophy

California Institute of Technology
Pasadena, California

1982

(Submitted January 21, 1982)

To my parents.

ACKNOWLEDGMENTS

I would like to thank my advisor, Professor Aron Kuppermann, for his encouragement, advice, and help over the past few years. His interest in our work and his enthusiasm for science have been important factors in my development as a scientist. His knowledge of chemical physics and suggestions of a number of interesting and important problems on which to work have made my graduate career a challenging but always pleasurable one.

I acknowledge the help and friendship of my "theoretical" colleagues in the Kuppermann group: John Dwyer, Diane Hood, and post-docs Hank Suzukawa, Greg Parker, Vasil Babamov, Nancy Harvey, and Joe Wong. Our many discussions about technical and non-technical matters have made life in the sub-basement enjoyable. Much of the work reported in this thesis was begun by John Dwyer, and its successful achievement is due in a large part to his efforts.

The experimentalists in the Kuppermann group have also been a source of friendship, help, and diversion. In particular, Bob Frueholz, Jeff Sell, Mark Keil, Dave Moll, Jerry Winniczek, and Charlie Koerting have been good friends. I also enjoyed collaborating with Jim Garvey on a Chem 227 project turned research project.

I wish to thank a number of professors here for their interest in me and my work and for serving in their various roles as classroom teacher, teaching supervisor, and first baseman: William A. Goddard III, Vincent McKoy, Rudolph Marcus, John Baldeschwieler, Kenneth Janda, and Yuk Yung.

Adria McMillan, the group secretary, has been a good friend and a great help in the preparation of this thesis. She and Henriette Wymar deserve enormous thanks for typing the bulk of this thesis. I am also grateful to Pat Bullard, who as Chemistry Graduate Records Secretary takes care of so many little things that it is impossible to count them.

Financial support has come from the Institute in the form of an Earle C. Anthony Fellowship, tuition scholarships, and teaching and research assistantships. Most of the computations reported here would not have been possible were it not for a generous donation of computer time from Ambassador College. I thank the entire operations staff there for their cheerful assistance. I also acknowledge the receipt of a Dreyfus Traveling Fellowship.

My decision to pursue graduate work in chemistry was derived mainly from a sense of how enjoyable science can be which I got from the chemistry, physics, and mathematics departments at Adelphi University, especially from Professors Stanley Windwer, Frederick Bettelheim, Sung Moon, Anthony Lemos, Edward Burke, and Herbert Kurss, and also Rich Silvestri, my freshman calculus TA. Dr. Windwer gave me more good advice than he can ever imagine. I also thank Dr. Robert L. Strong at Rensselaer Polytechnic Institute for providing my first research experience.

One's ability to work efficiently requires the support of a strong network of friends. I have enormously enjoyed my interactions with many people from my three years in Keck Graduate House, notably Dan McIntyre, Glenn Greene, Neil Gehrels, Ellen Williams, Sati Sadhal, Ron Melton, and Bill Dow. Among my non-Keck friends, I especially thank Alex Gerwer, Maile Smith, Diane Hood, Brad Ng, and my apartment-mate for the last 2.5 years, Mike Casassa. Finally, it is a special pleasure to thank my friend Mark Dolson. Any intellectual and social growth I have achieved here is due largely to his efforts.

I thank my family - my brother Jim, my grandmother Jeanne Goldner, and my parents Gloria and Ira. The emotional support and encouragement which they have provided have made my graduate

career that much easier. This thesis is dedicated to my parents. Were it not for the self-discipline and the enthusiasm for learning which they encouraged me to develop, I never could have completed this work.

ABSTRACT

The collinear collision of an atom with a diatomic molecule has been studied within the frameworks of quantum and classical mechanics. Three major topics have been investigated.

In part I, the collinear collision of hydrogen atoms with hydrogen fluoride (and singly deuterium substituted variants of this system) have been studied in the exchange channel by coupled-channel quantum mechanical calculations using a realistic (high barrier) potential energy surface. We have also investigated the effect on the dynamics of varying the barrier height of the potential energy surface.

In part II, we consider the characterization of low energy resonances in the collinear $H + H_2$ and $F + H_2(HD, DH, D_2)$ systems. A variety of characterization techniques are used; the most useful proves to be the variation with energy of the eigenvalues of the collision lifetime matrix.

In part III, we develop the method of hyperspherical coordinates for the study of collinear reactive atom-diatomic molecule collisions. The method is tested for the $H + H_2$ system, and is applied to a model system above the threshhold for collision-induced dissociation and to reactions in which a light atom (hydrogen) is transferred between two heavy ones. Systems of this type studied include $I + HI$ and $Br + HCl$; we also consider some aspects of the dynamics in the $Cl + HCl$ system. We develop the formalism to extract the physical scattering wave function from the method and present preliminary results of probability densities and probability current densities on the $H + H_2$ system. We also consider the formulation of the method in the adiabatic representation and examine both numerically and analytically the behavior of the coupling matrices at large values of the propagation variable. Convergence properties of the method are investigated in detail for the H + H_2 and F + H_2 systems. Quasi-classical trajectory calculations have been used to help understand the results obtained and to determine the importance of quantum mechanical effects.

TABLE OF CONTENTS

PART I

Collinear Quantum Mechanical Study of the Reactions H + FH, D + FH, and H + FD

PART II

Characterization of Low Energy Resonances in the Collinear $H + H_2$ and $F + H_2$ Systems

PART III

Collinear Atom-Diatomic Molecule Collisions Studied by Hyperspherical Coordinates

PART I

COLLINEAR QUANTUM MECHANICAL STUDY OF THE REACTIONS H + FH, D + FH, and H + FD

INTRODUCTION

INTRODUCTION

In this section we present the results of quantum mechanical coupled-channel calculations on the collinear systems

$$H' + FH(v) \longrightarrow H'F(v') + H\ ,\ H' + FH(v')$$
$$D + FH(v) \longrightarrow DF(v') + H\ ,\ D + FH(v')$$
$$H + FD(v) \longrightarrow HF(v') + D\ ,\ H + FD(v')$$

Our interest in these systems is derived from two major considerations. First, it is now recognized that the barrier height in the exchange reaction in these systems is quite large (over 40 kcal/mole), whereas previous collinear quantum mechanical calculations assumed the barrier height to be much smaller (~1.2 kcal/mole). Thus, it is worthwhile to restudy these reactions on a realistic potential energy surface. We use a model surface with a 40 kcal/mole barrier to exchange. Second, these processes have been thought to be a possible mechanism for removal of population inversions in the HF/DF chemical laser system. Accurate knowledge of the kinetics and dynamics of the HF/DF laser system is important if one is to successfully understand (and model) its operation, and the calculations performed may shed some light on these kinetics.

There are three papers in this section. Paper I. 1 examines the D + FH(v=0, 1, 2) and H + FD(v=0, 1, 2, 3) reactions on a high barrier (40 kcal/mole) potential energy surface. We are particularly interested in the effectiveness of vibrational excitation in promoting reaction. We show that many aspects of the dynamics of these reactions can be understood quite easily in terms of a one-dimensional model.

Paper I. 2 presents results for both reactive and non-reactive processes on the 40 kcal/mole barrier surface for the H + FH(v) and D + FH(v) systems. A wide variety of dynamical properties of these systems, such as state-to-state transition probabilities, activation energies, and reaction product state distributions. Non-reactive processes are found to be the predominant ones, and we show that a number of aspects of the non-reactive dynamics are well understood in terms of the simple Landau-Teller model for vibrational-to-translational energy transfer.

Paper I.3 presents results for both reactive and non-reactive processes on six different potential energy surfaces, which have barrier heights to exchange of 1.5, 5, 10, 20, 30, and 40 kcal/mole for the H + FH(v) and D + FH(v) systems. Three main topics are considered: the relative rates and mechanisms of vibrational deactivation on the different surfaces, the effect of reagent vibrational excitation on probabilities for chemical reaction, in particular on the translational energy threshhold for reaction and the vibrational state distribution of the reaction product, as a function of the height of the barrier in the surface, and the relative importance of quantum mechanical resonances for the different potential energy surfaces and the two isotopic systems.

I.1 QUANTUM MECHANICAL COLLINEAR CALCULATION OF THE REACTIONS D + FH(v=0, 1, 2) $\longrightarrow$ DF(v') + H AND H + FD(v=0, 1, 2, 3) $\longrightarrow$ HF(v') + D ON A REALISTIC POTENTIAL ENERGY SURFACE

QUANTUM MECHANICAL COLLINEAR CALCULATION OF THE REACTIONS D + FH (v = 0, 1, 2) → DF (v′) + H AND H + FD (v = 0, 1, 2, 3) → HF (v′) + D ON A REALISTIC POTENTIAL ENERGY SURFACE*

Jack A. KAYE,** John P. DWYER,‡ and Aron KUPPERMANN

Arthur Amos Noyes Laboratory of Chemical Physics,‡‡
California Institute of Technology, Pasadena, California 91125, USA

Received

Collinear coupled channel quantum mechanical calculations have been performed on the title reactions on a potential energy surface with a 40 kcal/mole barrier to exchange. This barrier height is close to that predicted by ab initio calculations and suggested by experiments. The relative effectiveness of reagent vibrational and translational excitation to promote reaction is considered. A one-mathematical dimensional (1MD) model for these reactions is constructed and is shown to work very well for the D + FH reaction at high temperatures, and less well for that reaction at lower temperatures as well as for the H + FD reaction. Possible reasons for the breakdowns of the 1MD model are discussed.

---

[*] This work was supported in part by a contract (No. F49620-79-C-0187) from the Air Force Office of Scientific Research.

[**] Work performed in partial fulfillment of the requirements for the PhD degree in Chemistry at the California Institute of Technology.

[‡] Present address: Supreme Court of the United States, Washington, DC 20543, USA.

[‡‡] Contribution No.

1. Introduction

The exchange reactions between hydrogen or deuterium atoms and hydrogen halides

$$H'(D) + HX \rightarrow H'X(DX) + H \tag{1}$$

(X = F, Br, Cl, I) have been among the more studied simple chemical reactions [1]. These reactions compete with the H(D) atom abstraction process

$$H'(D) + HX \rightarrow HH'(HD) + X \, . \tag{2}$$

One of the goals of studies of these systems is the understanding of the relative importance of the exchange and abstraction channels.

Interest in reactions (1) and (2) has been heightened by the recognition of their possible importance in collisional deactivation of vibrationally excited HX in HX chemical lasers, especially when X = **F** [2]. State-to-state rate constants for processes of the type

$$H'[D] + HX(v) \rightarrow H'X(v' < v)\,[DX(v' < v)] + H \tag{3a}$$

$$\rightarrow H'H(v'')\,[HD(v'')] + X \tag{3b}$$

are necessary if one is to successfully model the kinetics of HX lasers.

The exchange reactions (1) have been extensively studied by classical trajectory calculations as well as collinear quantum mechanical calculations for X = F [3], Cl [4], and Br [5]. Interest has been greatest in the H(D) + FH and H(D) + ClH systems, which have the smallest number of electrons and are thus candidates for the calculation of accurate potential energy surfaces by ab initio techniques. Such calculations have been performed on the HFH and HClH systems, and the results suggest the existence of large barriers to exchange, in excess of

40 kcal/mole for HFH and 20 kcal/mole for HClH [6]. Recent experiments on these systems appear to confirm the existence of a high barrier to exchange [7].

Most of the early theoretical studies of these systems were carried out on potential energy surfaces with a small barrier to exchange, and therefore cannot be expected to give even qualitatively correct behavior for many important dynamical properties [8]. These surfaces were normally obtained by using global semi-empirical potential energy functions, such as the extended LEPS form [9], which were obtained by optimizing agreement between quasi-classical trajectory calculations and experiments on the reverse of reaction (2). In particular, in previous quantum mechanical studies of the HFH exchange reaction, both collinear [10] and coplanar [11], potential energy surfaces with barriers to exchange of 1.2 kcal/mole and 1.8 kcal/mole, respectively, were used.

In this work, we report the results of collinear quantum mechanical calculations of the reactions

$$D + FH(v) \rightarrow DF(v') + H \tag{4a}$$

$$H + FD(v) \rightarrow HF(v') + D \tag{4b}$$

on a potential energy surface with a barrier to exchange of 40 kcal/mole. We will be particularly concerned with the effects of reagent vibrational excitation on the rate of reactions (4a, b) as this is a quantity which is obtainable by experiment, and has been determined for reaction (4a) [7b]. The ability of a one-mathematical dimension (1MD) model to predict and explain the results will also be considered.

2. Potential Energy Surface and Computational Model

The potential energy surface used in these calculations is of the rotating Morse-cubic spline type, which has been described elsewhere [12]. In its application to this system, we have constrained the energy level at the bottom of the local Morse oscillator well as a function of the swing angle θ (defined in ref. [12]) to be a Gaussian, with a maximum at $\theta = \pi/4$ radians. The saddle point occurs at $R_{HF} = R_{FH} =$ 1.97 bohr. The values of $\beta(\theta)$ were determined by fitting to the exchange channel portion of the semi-empirical (extended LEPS form) Muckerman V FH_2 potential energy surface [13]. Thus, the position of the minimum energy path on this surface is identical to that on the Muckerman V surface. Note that the saddle point on this surface occurs at a shorter R_{HF} distance than that predicted by ab initio calculations. A fuller description of the potential energy surface will be given in a forthcoming paper [14]. This surface is plotted for the D + FH reaction in the mass-weighted Delves coordinate system [15] in fig. 1.

A vibrational correlation diagram [16] for this surface, also showing the potential along the minimum energy path, is shown in fig. 2. The potential energy $V_n(s)$ along each curve (except, of course, for that showing the minimum energy path) is the sum of the potential energy along the minimum energy path $V^{mep}(s)$ and the appropriate eigenvalue $E_v(s)$ of the potential formed by taking a cut perpendicular to the minimum energy path (in Delves coordinates)

$$V_v(s) = V^{mep}(s) + E_v(s) \quad , \tag{5}$$

where s is the distance along the minimum energy path measured from the saddle point, also measured in Delves coordinates. The eigenvalues $E_v(s)$ are determined numerically from the potential by a finite difference procedure [17].

The numerical calculations were performed using the coupled-channel method of Kuppermann, which has been described previously [18]. Between 20 and 24 basis functions were used in the calculations, and unitarity of the open part of the scattering matrix $\underset{=}{S}$ was obtained to within 3% for all energies used; for most energies it was obtained to better than 1%. Calculations were carried out to energies up to 2.45 eV above the isolated HF (v = 0) energy level. At the highest energies studied, there were six open HF states and eight open DF states. State-to-state rate constants were calculated from the reaction probabilities $P_{vv'}$, which are a function of the reagent translational energy E^{tr} by the expression

$$k_{vv'}(T) = (2\pi \mu_{a,bc} kT)^{-\frac{1}{2}} \int_0^\infty P_{vv'}(E^{tr}) e^{-E^{tr}/kT} dE^{tr} , \qquad (6)$$

where $\mu_{a,bc}$ is the reduced mass of the a, bc collision pair. The exact method of evaluating this integral has been discussed by Truhlar and Kuppermann [19].

Because of the large barrier to reaction, probabilities of reaction are extremely small ($< 10^{-12}$) at small values of E^{tr}. As the collinear reactive scattering program is written in single precision (for use on an IBM 370/158 computer), we do not entirely trust the exact magnitude of these very small probabilities. Hence, we restrict the temperature range of our rate constant calculations to those temperatures where the major contribution to the integral in eq. (6) comes from energy ranges where the reaction probabilities are larger and thus more reliable.

3. Results and Discussion

Reactions (4) only become probable in this system for fairly large values of the translational energy. In figs. 3 and 4, respectively, we plot as a function of E^{tr} the total reaction probability for reactions (4a) and (4b), respectively, for a few of the lowest reagent vibrational states. While there are some strong similarities between the two figures, such as the large threshold to reaction, the relative magnitude of the threshold lowering with vibrational excitation, and the approximately parallel nature of the probability versus energy curves in the region of greatest increase of probability with energy, there are some major differences, however.

In the immediate vicinity of and slightly above the threshold energy, there are major differences in figs. 3 and 4 for vibrationally excited reagents. For reaction (4a), for the D + FH ($v = 1, 2$) reaction, the probability of reaction rises smoothly and rapidly in an s-shaped curve from 0 to 1, while for reaction (4b), for the reaction H + FD ($v = 1, 2$), there exist broad shoulders in these curves. It can be seen by examining state-to-state reaction probability versus energy curves that the shoulders seen in fig. 4 are due to reactions of the type

$$H + FD(v) \rightarrow HF(v - 1) + D\,. \qquad (7)$$

This is shown graphically for the $v = 1$ case in fig. 5, where state-to-state reaction probabilities P^R_{10}, P^R_{11}, and P^R_{12} are shown as a function of E^{tr}. It is worth noting that at higher translational energies, P^R_{11} becomes substantially smaller than P^R_{10} and P^R_{12}.

One other difference observed between figs. 3 and 4 is that at high translational energies, the probability of reaction (4a) stays near unity, while that of reaction (4b) is smaller than unity and is highly irregular.

The vibrational correlation diagram in fig. 2 provides a useful way of looking at the DXH systems. A number of conclusions may be drawn from a quick examination of this diagram for the DFH system. First, because of the large barrier, there are no wells in the vibrationally adiabatic correlation diagram, at least for the first few levels. As wells in this diagram have been shown to be related to resonances in reaction probabilities [16], we can conclude that in the energy range considered here there should be no resonances, and, indeed, none has been observed in the dynamics. Second, because of the large difference between HF and DF vibrational frequencies, the highest point on the vibrationally adiabatic correlation diagram moves into the HF reagent channel, especially for vibrationally excited reagents. Thus, one may interpret, within a vibrationally adiabatic model, reaction (4a) as having its saddle point on the reagent side, while reaction (4b) has its on the product side. Third, the vibrational frequencies at and near the saddle point are fairly large; hence the magnitude of the vibrationally adiabatic barriers decreases with energy by an amount that is substantially smaller than the vibrational energy spacing of HF and DF. Thus, for example, the translational energy threshold for reactions (4a) should decrease by 0.21 eV on going from the ground to the first excited level of HF and 0.17 eV on going from the first to the second excited state of HF; the differences in vibrational energies between these levels are 0.49 and 0.46 eV, respectively. The lowering in threshold energies (defined as the energy at which the probability of reaction first reaches 0.02) for reaction (4a) are 0.22 and 0.17 eV, respectively. Thus, the simple one-dimensional vibrationally adiabatic picture provides a good model for the D + FH system at low translational energies.

For the H + FD reactions one can interpret the low energy non-adiabatic reaction as occurring due to a crossing from the DF(v) curve to the HF(v - 1) curve. If this crossing occurs on the DF side of the saddle point (as seems reasonable from examination of fig. 2), the apparent barrier to reaction should be much smaller than to vibrationally adiabatic reaction. This qualitatively explains the 0.25 eV separation in fig. 5 between the center of the P^R_{10} flat maximum and that of the P^R_{11} maximum.

Rate constants for reactions (4a) and (4b) are plotted in fig. 6 as a function of temperature in the form of an Arrhenius plot (log of the rate constant versus inverse temperature). Such plots are frequently linear, over a broad temperature range, and linearity or near-linearity is seen in all of the plots shown. In the usual way, Arrhenius pre-exponential parameters (A) and activation energies (E_a) are obtained for the linear region of these curves, and the resulting data are summarized in Table 1. The vibrational energy associated with each reagent level is also included in Table 1 for comparison.

The rate constants obtained are quite small in all cases; by comparison, the gas kinetic rate constant k_{gk} (that when every collision results in reaction) is given by the formula

$$
\begin{aligned}
k_{gk}(T) = \left(\frac{kT}{2\pi\mu}\right)^{\frac{1}{2}} &= 2.69 \times 10^{3}\, T^{\frac{1}{2}}\ \text{cm}\cdot\text{molec}^{-1}\ \text{sec}^{-1}\ (\text{D + FH}) \quad (6a) \\
&= 3.71 \times 10^{3}\, T^{\frac{1}{2}}\ \text{cm}\cdot\text{molec}^{-1}\ \text{sec}^{-1}\ (\text{H + FD}). \quad (6b)
\end{aligned}
$$

Even at the highest temperatures considered, the rate constants are five to seven orders of magnitude less than gas kinetic. Thus, the large barrier and the resulting large threshold for reaction produce small rate constants.

The activation energies E_a shown in Table 1 decrease as reagent vibrational excitation is increased. The lowering of the activation energy with reagent vibrational excitation is less than the amount of internal energy in the vibrationally excited reagents, however. Recall that a similar behavior was observed for the lowering of the threshold energy with reagent vibrational excitation. The decrease in activation energy with reagent vibrational excitations is, however, greater than the corresponding decrease in the vibrationally adiabatic barrier height. This difference can be explained by the dominance of vibrationally nonadiabatic reaction over vibrationally adiabatic reaction in the energy region where the reaction probabilities are small ($< 10^{-2}$). This energy region only makes a substantial contribution to the integral in eq. (5) at fairly low temperatures.

In order to further understand the applicability of the one-dimensional vibrationally adiabatic model, we have calculated transmission coefficients for the three lowest vibrationally adiabatic barriers for reaction (4a) as a function of translational energy. These calculations, involving a numerical solution of the one-dimensional Schrödinger equation, were performed with the method described by Truhlar and Kuppermann [20]. We then used these transmission coefficients (equivalent to reaction probabilities in the coupled-channel calculations) to calculate rate constants for the D + FH (v = 0, 1, 2) reactions, and the results (labeled 1MD for one mathematical dimension) at 500° K and 1000° K are given in Table 1, along with those obtained in the full two mathematical dimension (2MD) coupled-channel calculation. For comparison, the gas kinetic rate constants are also included.

At 1000° K, the results of the 1MD and 2MD calculations agree quite well (within 5%), while at 500° K, the agreement is less satisfactory, becoming worse as one goes from HF ($v = 0$) to HF ($v = 2$). This lack of agreement when the HF reagent is vibrationally excited is due to the above mentioned dominance of vibrationally nonadiabatic reactions at low translational energies.

The usefulness of the vibrationally adiabatic model for the DFH system makes it worthwhile to well characterize the potential energy surface in the region at the saddle point; in particular, accurate values of the local vibrational frequencies (i. e., the symmetric stretch at the saddle point) are important, as these, along with the actual barrier height itself, combine to give the vibrationally adiabatic correlation diagram shown in fig. 2 and found to be so useful.

A word of caution must be expressed concerning the applicability of a collinear model to reactions (4). Ab initio calculations by Wadt and Winter [6] suggest that the lowest barrier to exchange occurs not for a collinear H-F-H configuration, but rather for one with a 106° bond angle, and further that the barrier height is nearly independent of the bond angle. Thus, it appears that an accurate dynamical treatment of the exchange reaction would require three physical dimensions (3D). A 3D calculation on this system would have the advantage of allowing one to directly compare the importance of the abstraction and exchange channels. Such a calculation would require a good semi-empirical potential energy surface incorporating a large barrier to exchange. A method for constructing such a surface has been developed by Baer and Last [21], and has been applied to all XH_2 systems. Their FH_2 surface has a reasonably high barrier (33.5 kcal/mole), but has much stronger dependence of the barrier height on the H-X-H bond angle than that predicted by Wadt and Winter [6].

4. Conclusions

Reaction probabilities and rate constants for reactions (4a) and (4b) have been obtained on a realistic potential energy surface by a collinear quantum mechanical calculation. Reaction has been shown to set in at large values of the translational energy (≥ 1 eV) for reagents in their first three vibrational states. Vibrational excitation has been shown to promote the reaction, although the decrease in the activation energy is less than the internal energy added to the reagents on vibrational excitation. A number of aspects of the dynamics, such as the translational energy threshold for reaction and the importance of vibrationally nonadiabatic processes near the threshold region for reaction (4b), have been shown to be explained by use of vibrationally adiabatic correlation diagrams. The overall rate of reaction (4a) has been shown to be reproduced quite well at high temperatures by a 1MD model based on these vibrationally adiabatic correlation diagrams. The results obtained help demonstrate the importance of an accurate knowledge of the potential energy surface in the immediate vicinity of the saddle point.

Acknowledgements

We thank Ambassador College for the generous use of their computational facilities for the scattering calculations. Additional calculations were carried out at the Dreyfus-NSF Theoretical Chemistry Computer at Caltech, which is funded through grants from the Camille and Henry Dreyfus Foundation, the National Science Foundation (Grant No. CHE78-20235), and the Sloan Fund of the California Institute of Technology.

Table 1

Arrhenius parameters for rate constants for reactions (4a, b)

V	T (°K)	ℓn A (cm · molec^{-1} sec^{-1})	E_a (kcal/mole)	Internal Energy of Reagent (kcal/mole)
A. $D + FH(v) \rightarrow DF(v' = \text{all}) + H$				
0	500-950	11.8	36.8	5.8
1	450-700	9.3	28.3	17.0
2	450-600	4.8	18.0	27.7
B. $H + FD(v) \rightarrow HF(v' = \text{all}) + D$				
0	550-1000	11.9	38.6	4.2
1	450-800	9.4	30.3	12.4
2	450-700	6.8	22.8	20.4
3	450-700	4.5	16.5	28.1

Table 2

Rate constants for the reaction D + FH(v) → DF(v′ = all) in units cm · $\text{molec}^{-1}\text{sec}^{-1}$

T (°K)	v = 0	v = 1	v = 2
2MD			
500	1.16 (-11)	3.91 (-9)	8.42 (-7)
1000	1.29 (-3)	1.61 (-2)	1.07 (-1)
1MD			
500	9.80 (-12)	1.43 (-9)	8.28 (-8)
1000	1.23 (-3)	1.57 (-2)	1.07 (-1)
Gas Kinetic			
500	6.02 (4)	6.02 (4)	6.02 (4)
1000	8.51 (4)	8.51 (4)	8.51 (4)

References

[1] M. R. Levy, Progr. Reaction Kinetics **10** (1979) 1.

[2] N. Cohen and J. F. Bott, in Handbook of Chemical Lasers, eds. F. Gross and J. F. Bott (Wiley-Interscience, New York, 1976), pp 33-94.

[3] D. L. Thompson, J. Chem. Phys. 57 (1972) 4170; R. L. Wilkins, J. Chem. Phys. 58 (1973) 3039; R. L. Wilkins, Mol. Phys. 29 (1975) 555.

[4] I. W. M. Smith and P. M. Wood, Mol. Phys. 25 (1973) 441; D. L. Thompson, H. H. Suzukawa, Jr., and L. M. Raff, J. Chem. Phys. 62 (1975) 4727; R. L. Wilkins, J. Chem. Phys. 63 (1975) 534.

[5] J. M. White, J. Chem. Phys. 65 (1976) 3674; D. J. Malcolme-Lawes, J. Chem. Soc. Faraday Trans. 2 74 (1978) 182.

[6] C. F. Bender, B. J. Garrison, and H. F. Schaeffer III, J. Chem. Phys. 62 (1975) 1188; P. Botschwina and W. Meyer, Chem. Phys. 20 (1977) 43; W. R. Wadt and N. W. Winter, J. Chem. Phys. 67 (1977) 3068; A. F. Voter and W. A. Goddard III, J. Chem. Phys. 75 (1981) 3638; T. H. Dunning, Jr., J. Chem. Phys. 66 (1977) 2752.

[7] a) J. F. Bott, J. Chem. Phys. 65 (1976) 1976.

b) F. E. Bartoszek, D. M. Manos, and J. C. Polanyi, J. Chem. Phys. 69 (1978) 933.

c) W. Bauer, L. Y. Rusin, and J. P. Toennies, J. Chem. Phys. 68 (1978) 4490.

[8] H. F. Schaefer III, in Atom-Molecule Collision Theory, ed.

R. B. Bernstein (Plenum Press, New York, 1979), pp. 45-78.

[9] P. J. Kuntz, E. M. Nemeth, J. C. Polanyi, S. D. Rosner, and C. E. Young, J. Chem. Phys. 44 (1966) 1168.

[10] G. C. Schatz and A. Kuppermann, J. Chem. Phys. 72 (1980) 2737.

[11] M. Baer, J. Chem. Phys. 65 (1976) 493.

[12] J. M. Bowman and A. Kuppermann, Chem. Phys. Lett. 34 (1975) 523.

[13] G. C. Schatz, J. M. Bowman and A. Kuppermann, J. Chem. Phys. 63 (1975) 674; J. T. Muckerman, J. Chem. Phys. 56 (1972) 2997.

[14] J. A. Kaye, J. P. Dwyer, and A. Kuppermann, manuscript in preparation.

[15] L. M. Delves, Nucl. Phys. 9 (1959) 391; 20 (1960) 275.

[16] S. L. Latham, J. F. McNutt, R. E. Wyatt, and M. J. Redmon, J. Chem. Phys. 69 (1978) 3746; A. Kuppermann, J. Phys. Chem. 83 (1979) 171.

[17] D. G. Truhlar, J. Comp. Phys. 10 (1972) 123.

[18] A. Kuppermann, in Proceedings of the Conference on Potential Energy Surfaces in Chemistry, ed. W. A. Lester (University of California, Santa Cruz, 1979), pp. 121-124; in Proceedings of the 7th International Conference on the Physics of Electronic and Atomic Collisions (North-Holland, Amsterdam, 1971), pp. 3-5.

[19] D. G. Truhlar and A. Kuppermann, J. Chem. Phys. 56 (1972) 2232.

[20] D. G. Truhlar and A. Kuppermann, J. Am. Chem. Soc. 93 (1971) 1840.

[21] M. Baer and I. Last, in Potential Energy Surfaces and Dynamics Calculations, ed. D. G. Truhlar (Plenum, New York, 1981), pp. 519-534.

Figure Captions

Figure 1. Contour plot of the potential energy surface for the reaction D + FH → DF + H in Delves scaled coordinates. The solid curves are equipotential contours at the total energies measured with respect to the bottom of the HF (DF) wells. The dashed line is the minimum energy path. The cross indicates the location of the saddle point.

Figure 2. Vibrationally adiabatic correlation diagram for the reaction D + FH(v) → DF(V) + H, v = 0, 1, 2. The vertical scale is an energy scale. The lowest curve is the potential energy along the minimum energy path $V^{mep}(s)$ as a function of the distance s along the minimum energy path from the saddle point. Positive values of s take one towards separated D + FH, negative values of s towards DF + H. The higher curves are plots as a function of s of the potential $V_v(s)$ defined in eq. (5) of the text for v = 0, 1, 2.

Figure 3. Probabilities $P^R_{D+FH}(v)$ of the reactions D + FH(v) → DF(v′ = all) + H for v = 0, 1, 2 as a function of reagent translational energy E^{tr}. The solid line is for v = 0, the dashed line is for v = 1, and the dotted line is for v = 2.

Figure 4. Probabilities $P^R_{H+FD}(v)$ of the reactions H + FD(v) → HF(v′ = all) + D for v = 0, 1, 2, 3 as a function of reagent translational energy E^{tr}. The solid line is for v = 0, the dashed line is for v = 1, the dotted line is for v = 2, and the dashed line is for v = 3.

Figure 5. State-to-state reaction probabilities $P^R_{H+FD(1)\rightarrow HF(v')+D}$ of the reaction H + FD(v = 1) → HF(v′) + D for v′ = 0, 1, 2 as a function of reagent translational energy E^{tr}. The dashed line is for v′ = 0, the

solid line is for $v' = 1$, and the dotted line is for $v' = 2$. While the HF($v' = 3$) product channel is energetically accessible in this energy range, the probability of reacting into it is less than 1% in this energy range, and is not shown.

Figure 6. Arrhenius plot of rate constants for the reactions D + FH(v) → DF($v' =$ all) + H (dashed line) and H + FD(v) → HF($v' =$ all) + D (solid line) over a temperature range from 450 to 1500° K. Where the curves are not continued to the highest temperatures, the scattering calculations were not carried out to sufficiently high energy for the integrand in eq. (6) to become sufficiently small. (a) H + FD($v = 0$), (b) D + FH ($v = 0$), (c) H + FD ($v = 1$), (d) D + FH ($v = 1$), (e) H + FD ($v = 2$), (f) D + FH ($v = 2$), (g) H + FD ($v = 3$).

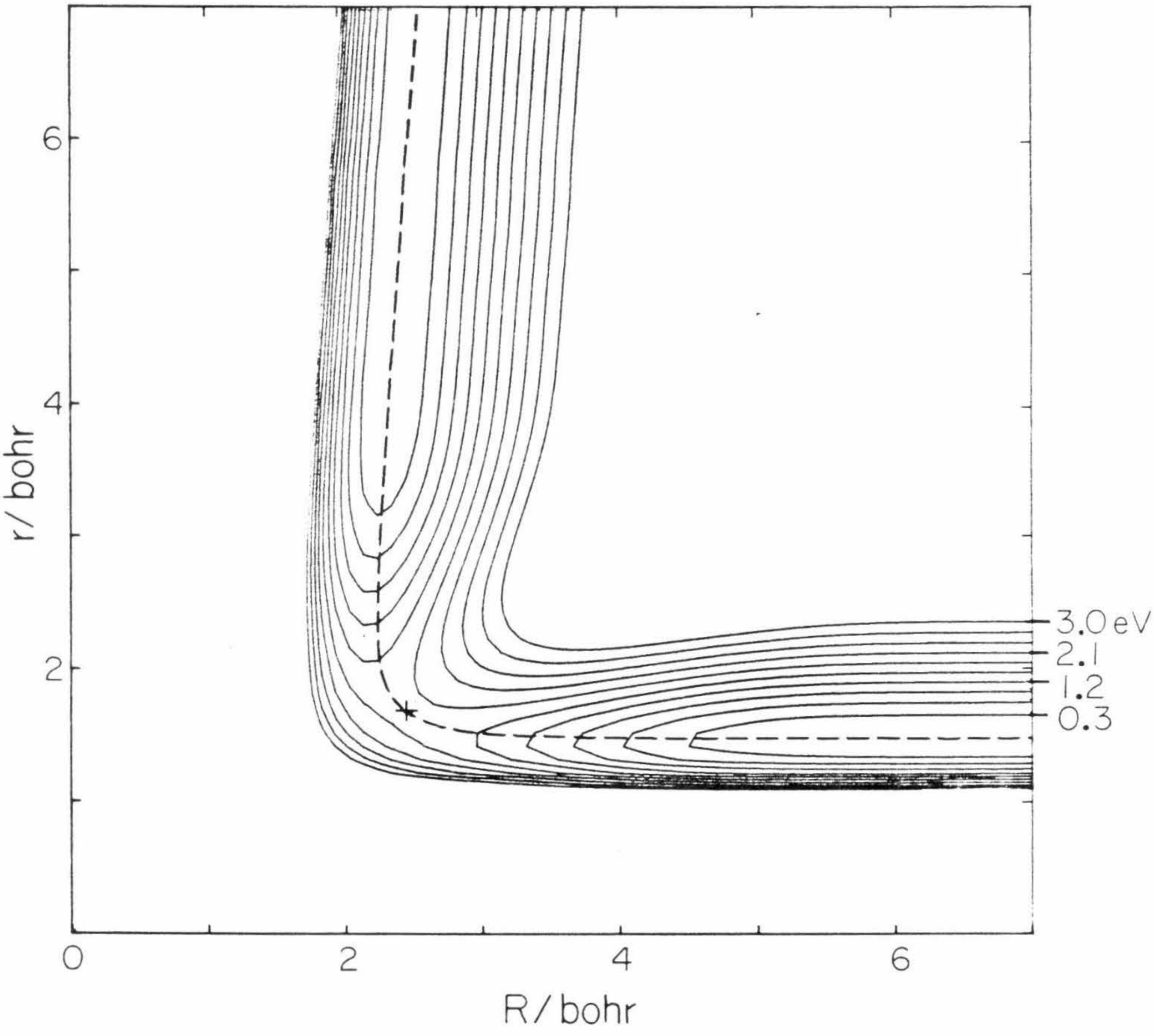

Figure 1

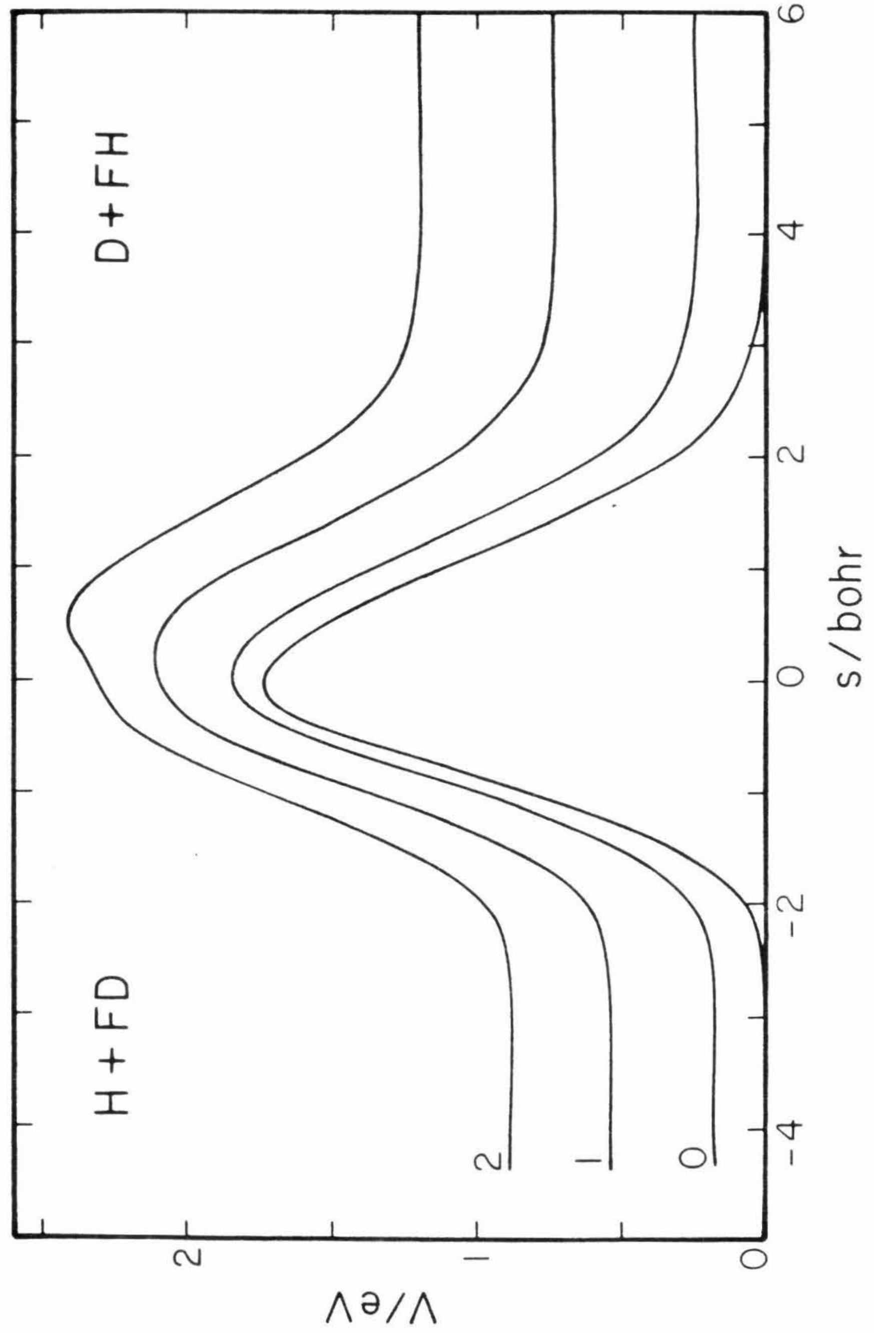

Figure 2

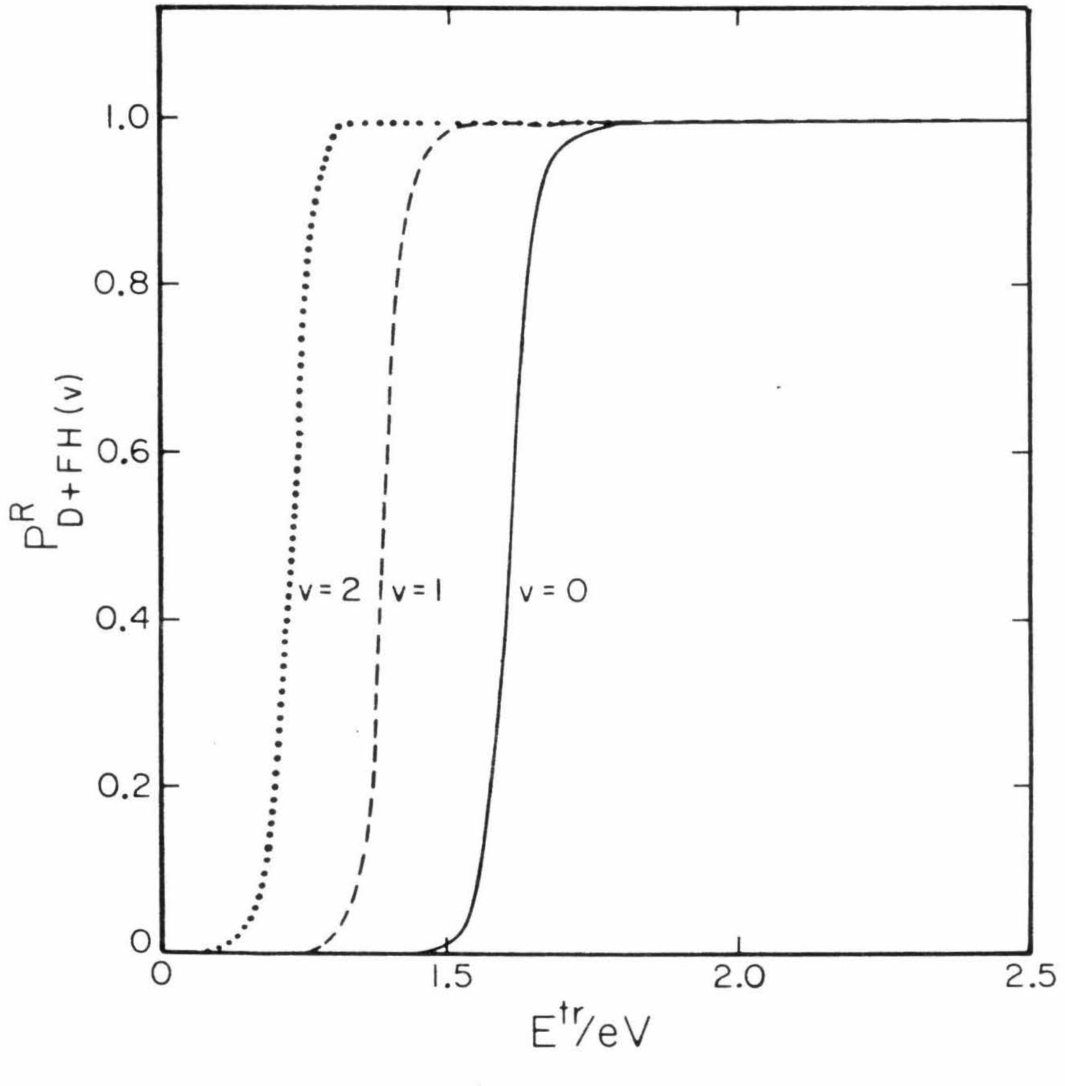

Figure 3

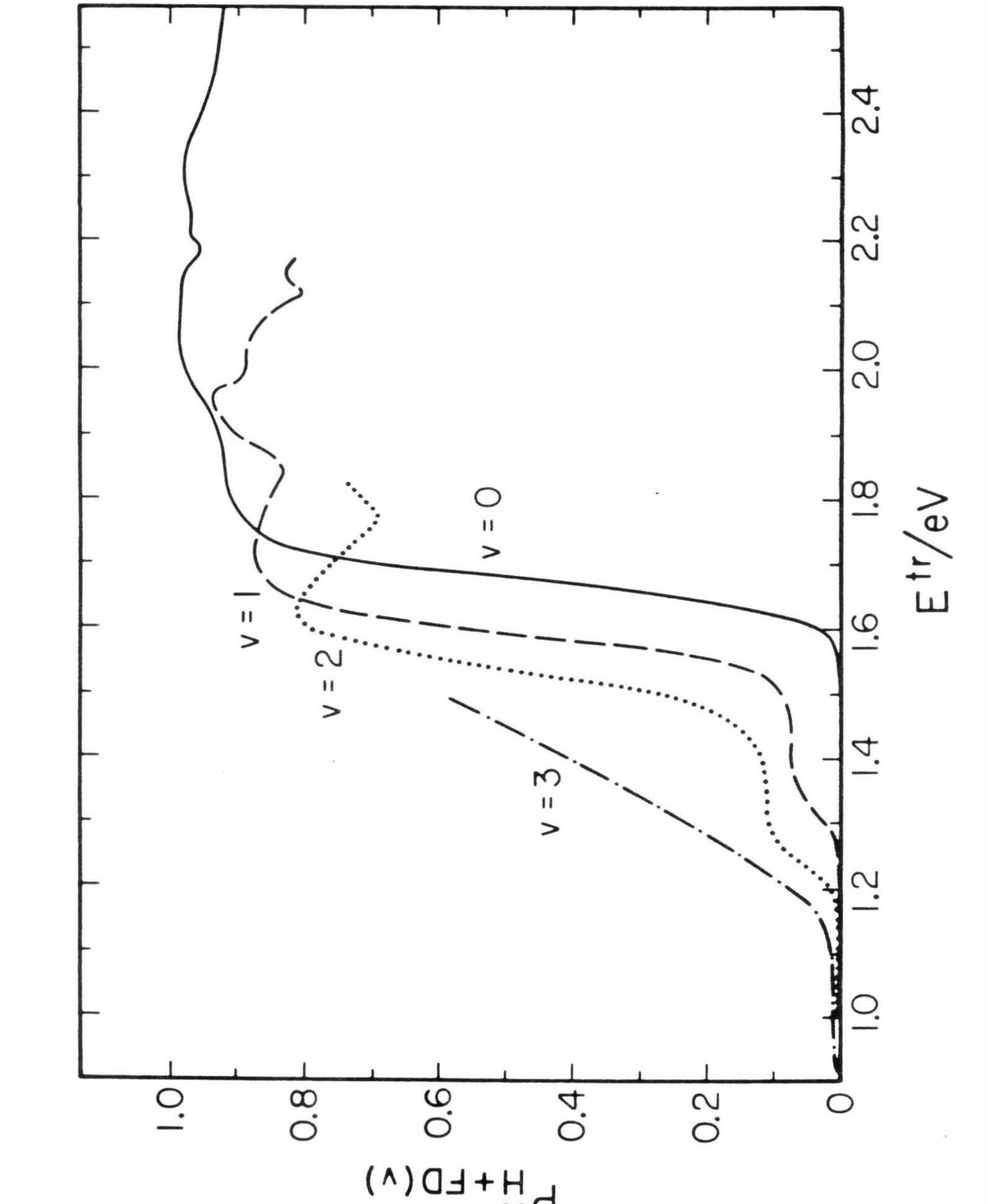

Figure 4

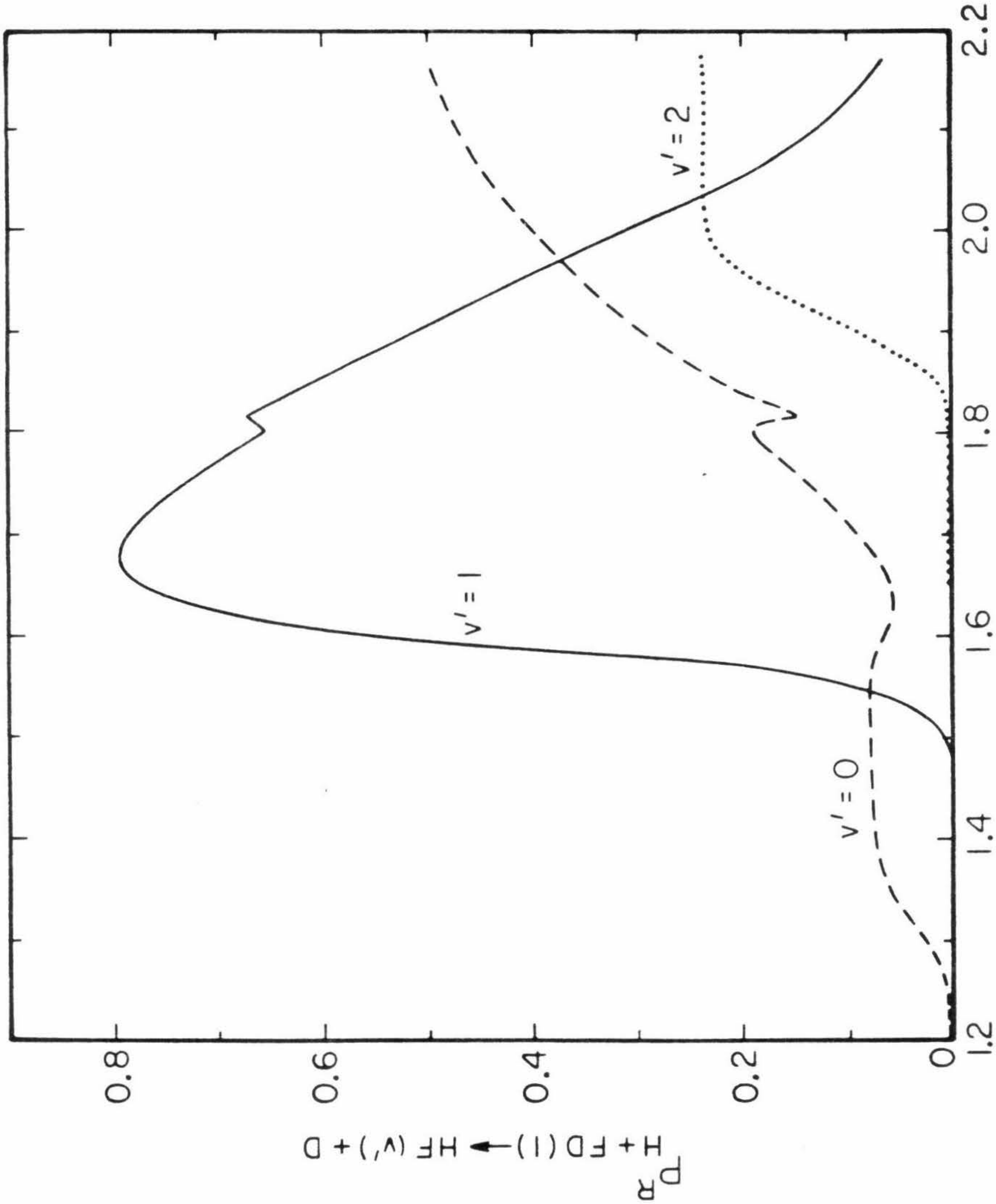
$P^{R}_{H+FD(1) \rightarrow HF(v')+D}$
0
0.2
0.4
0.6
0.8
1.2
1.4
1.6
1.8
2.0
2.2
E^{tr}/eV
v' = 0
v' = 1
v' = 2

Figure 5

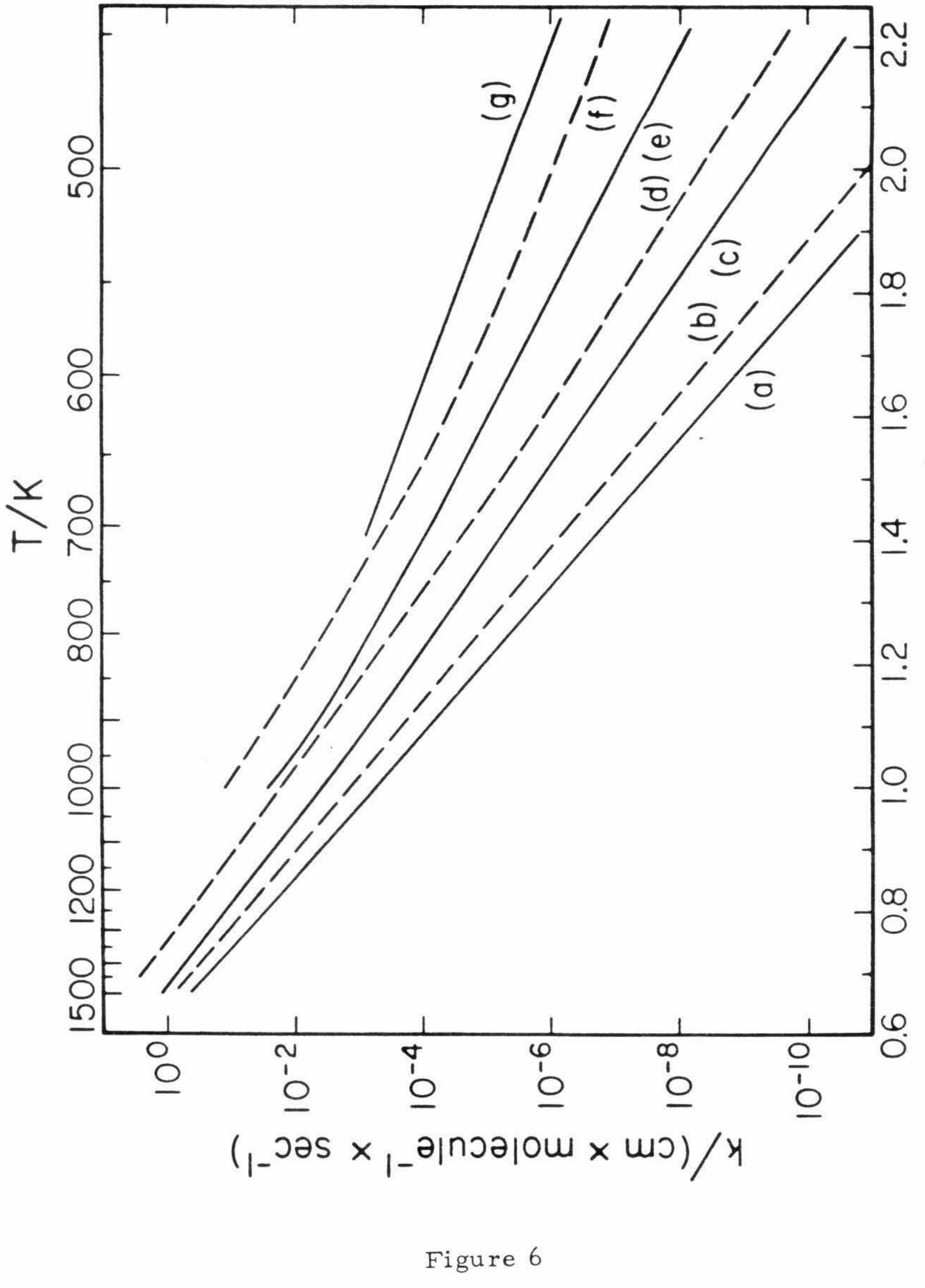
T/K
1500
1200
1000
800
700
600
500
1000 K/T
0.6
0.8
1.0
1.2
1.4
1.6
1.8
2.0
2.2
10^{0}
10^{-2}
10^{-4}
10^{-6}
10^{-8}
10^{-10}
k/(cm × molecule^{-1} × sec^{-1})
(a)
(b)
(c)
(d)
(e)
(f)
(g)

Figure 6

I.2 COLLINEAR QUANTUM MECHANICAL CALCULATIONS ON THE SYSTEMS HF(v) + H AND HF(v) + D ON A REALISTIC POTENTIAL ENERGY SURFACE

Collinear Quantum Mechanical Calculations on the Systems HF(v) + H and HF(v) + D on a Realistic Potential Energy Surface.[a)]

Jack A. Kaye[b)], John P. Dwyer[c)], and Aron Kuppermann
Arthur Amos Noyes Laboratory of Chemical Physics,[d)]
California Institute of Technology, Pasadena, California 91125

(Received)

The rates of the reactions HF(v) + H and HF(v) + D as well as those of processes resulting in vibrational deactivation of HF have been studied by collinear quantum mechanical calculations on a realistic potential energy surface. The surface used has a 40 kcal/mole barrier to exchange, far greater than those used in previous calculations and in the vicinity of that suggested by ab initio calculations and recent experiments. It is found that vibrational deactivation of HF in this exchange channel occurs almost entirely by non-reactive single-quantum processes, and the rate of which varies weakly with reagent vibrational state. The rate of chemical reaction, however, is enhanced dramatically by reagent vibrational excitation, although vibrational energy lowers the threshhold for reaction by far less than a vibrational quantum of energy. The relationship between vibrational and translational energy in promoting reaction will be discussed, as will the relationship of the results of these calculations to experimental data.

---

a) This work was supported in part by a contract (No. F49620-79-C-0187) from the Air Force Office of Scientific Research.

b) Work performed in partial fulfillment of the requirements for the Ph. D. degree in Chemistry at the California Institute of Technology.

c) Present Address: Supreme Court of the United States, Washington, D.C. 20543

[d] Contribution No.

I. INTRODUCTION

A knowledge of accurate rate constants for the reactions of vibrationally excited hydrogen fluoride (HF) molecules with those atoms and molecules present in the HF laser system (1) (F_2, H_2, HF, H, F) is important if one is to accurately model the system's behavior. In the HF laser system, vibrationally excited HF is produced by one of the highly exoergic reactions (2)

$$F + H_2 \longrightarrow HF(v \leq 3) + H \tag{1a}$$

$$H + F_2 \longrightarrow HF(v \leq 10) + F \tag{1b}$$

These pumping reactions have received a great deal of attention, both experimentally (3) and theoretically (4). Of the deactivating processes present in the HF laser, the best studied are those due to inelastic collisions of vibrationally excited HF with other diatomics (ground state HF and H_2) (5). Collisions of vibrationally excited HF and H or F atoms have received less attention. Among the few studies of these processes include the experiments of Bott and Heidner (6) and Bartoszek, et al. (7), and the quasi-classical trajectory calculations of Wilkins (8), Thompson (9), and Thommarson and Berend (10). Recently, Schatz and Kuppermann (11) have studied the HF + H system (and its D-substituted counterparts) via a collinear quantum-mechanical calculation, although the barrier to reaction in the potential energy surface used in these calculations is now known to be unreasonably low. Baer (12) has performed a coplanar quantum mechanical calculation on the HF + H reaction, also on a surface with an unreasonably low barrier.

In this paper, we report the results of collinear quantum mechanical calculations on the systems HF(v) + H and HF(v) + D. We consider those processes, both reactive and non-reactive, responsible for vibrational deactivation of HF, which may be represented by the reactions

$$HF(v) + H' \longrightarrow HF(v') + H' \tag{2a}$$

$$\longrightarrow H + FH'(v'') \tag{2b}$$

$$\mathrm{HF}(v) + \mathrm{D} \longrightarrow \mathrm{HF}(v') + \mathrm{D} \tag{3a}$$

$$\longrightarrow \mathrm{H} + \mathrm{FD}(v'') \tag{3b}$$

The potential energy surface used in these calculations has a barrier to exhange of 40 kcal/mole. This is in line with recent ab initio calculations (13) as well as the definitive experiments of Bartoszek, et al. (7).

No attention will be given to deactivating processes in the abstraction channel

$$\mathrm{H}' + \mathrm{HF}(v) \longrightarrow \mathrm{H}_2(v') + \mathrm{F} \tag{4a}$$

$$\longrightarrow \mathrm{H}' + \mathrm{HF}(v'') \tag{4b}$$

in this paper, although this channel is likely the one in which much of the deactivation of HF($v \leq 3$) occurs.

We focus in this work on the relative rates of vibrational deactivation as a function of the initial state of the HF reagent, the fraction of deactivation occurring by reaction (processes 2b and 3b, respectively in the HFH and DFH systems), the relative importance of single and multi-quantum deactivating processes, and the relative effectiveness of translational energy in promoting reaction.

A brief outline of this paper is as follows. In section 2, we consider the potential energy surface used in these calculations and the reasons for which we chose to use it. In section 3, we very briefly discuss some of the important aspects of the calculation. In section 4, we present our results, which will be discussed in section 5. In section 6 we summarize by reviewing their significance.

II. POTENTIAL ENERGY SURFACE

There has been a great deal of interest over the last decade in determining the nature of the potential energy surface for reactions 2b and 3b. A large number of semi-empirical global potential energy surfaces, mainly of the extended LEPS type (14), have been developed for reaction 1a (15). The parameters for these surfaces were normally chosen to maximize agreement between the results of quasi-classical trajectory calculations and experiments on reaction 1a (quantities compared are usually rate constants and distributions of product vibrational and rotational states). Since these surfaces are global, the form of the exchange channel is determined by this optimization procedure (which has taken place in the abstraction channel). Most of these surfaces have a very small barrier to exchange, for example 1.2 kcal/mole for the well-known Muckerman V surface (4d). Such low barrier surfaces have been used in most dynamical calculations performed so far on reactions 2 and 3. A notable exception is the calculation done by Thompson (9), in which a surface with a barrier to exchange of 28.6 kcal/mole was used.

Four high quality ab initio calculations on the potential energy surface of reactions 2b and 3b yielded barrier heights of 49.0 (13a), 44.9 (13b), 47.6 (13c), and 48.3 (13d) kcal/mole, however, and the experiments of Bartoszek, et al. (7) seem to securely resolve this question in favor of a high barrier to exchange. In this calculation, therefore, we use a potential energy surface with a barrier to exchange of 40 kcal/mole, which seems to be within the range of uncertainty of the ab initio calculations.

The potential energy surface used in these calculations is of the rotating Morse- cubic spline type (16), made slightly less general by requiring that the potential energy along the minimum energy path as a function of the angle θ in reference 16 to be given by a Gaussian:

$$D(\theta) = D(\theta=0) - (A + B*\exp(-C*(\pi/4 - \theta)^2)) \tag{5}$$

The parameters have values A = 0.01681 kcal/mole, B = 39.983 kcal/mole, and C = 33.879 radians^{-1}. $\beta(\theta)$ and $\ell_{eq}(\theta)$ are defined in reference 16, and are obtained by cubic spline interpolation between the values given for the supplied points listed in Table 1. The profile of the barrier height vs. reaction coordinate (distance along the minimum energy path from the saddle point as calculated in Delves mass-scaled coordinates (17)) for H + FH is shown in figure 1, along with the asymptotic eigenvalues for HF and DF. A contour plot of the potential energy surface for H + FH in Delves coordinates is shown in figure 2.

III. DETAILS OF THE CALCULATION

Numerical solution of the Schrödinger equation for these systems was performed using the coupled-channel method of Kuppermann (18), which has been described elsewhere. This technique has previously been applied to a number of systems, including $H + H_2$ and its isotopically substituted analogues (20), $F + H_2$ (4d), $F + D_2$ (21), H + FH (on a low barrier surface) (11), and Be + FH (22). 20 - 24 basis functions were used in the calculation, although no more than seven were open asymptotically at any of the energies studied.

Reactions 2a and 2b were studied in the energy range up to 2.94 eV above the zero-point energy of HF, while reactions 3a and 3b were studied up to 2.45 eV above the HF zero-point energy. The smaller range in the latter case was due to the smaller vibrational requency of DF, which results in more open channels at a given energy than in the HF system (energy levels of isolated HF and DF are shown in figure 1). In all calculations reported here, flux was conserved to better than 3%; for most energies it was conserved to better than 1%.

From the transition probabilities obtained in these calculations, state-to-state rate constants were calculated by evaluating the usual integral

$$k_{ij}(T) = (2\pi\mu_{a,bc}kT)^{-1/2}\int_0^\infty P_{ij}(E^{tr})\exp(-E^{tr}/kT)dE^{tr} \qquad (6)$$

where P_{ij} is the probability for the transition from state i to state j, E^{tr} is the relative translational energy of the collision, and $\mu_{a,bc}$ is the reduced mass of the a, bc collision pair.

IV. RESULTS

We have obtained information on many aspects of the dynamics of the collinear HFH and DFH systems and will try to present some of the most important features of our results in this section. In particular, we will consider in this section and the ensuing discussion section questions such as the following:

1) What are the relative rates of deactivation of the vibrationally excited HF, and how do they vary with initial reagent excitation?
2) What is the relative importance of reactive and non-reactive processes?
3) What is the relative importance of single and multi-quantum transitions?
4) How do all of these quantities vary with temperature?
5) How do the roles of translational and vibrational energy in promoting reaction compare?
6) How do the results obtained for non-reactive processes compare with those predicted from simple models, such as the Landau-Teller model (23)?
7) What is the nature and magnitude of the isotope effect on going from the HFH to the DFH system?

A. H + FH

Rates for state-to-state vibrational deactivation have been calculated for temperatures in the range 200 K $\leq$ T $\leq$ 1000 K. Values of the rate constants at three temperatures (300, 650, 1000 K) are contained in Table 2. For purposes of comparison, we also include in Table 2 the "gas kinetic" rates for the H + FH system at these three temperatures. This rate is that obtained if a transition occurred with unit probability at all energies; hence, it represents the sum of all possible state-to-state rate constants at a given temperature. It is seen that at all three temperatures, the total rates of deactivation are less that 1% of the gas kinetic rate. Thus, vibrational deactivation is a very unlikely process.

We display total rate constants for vibrational deactivation, both reactive and non-reactive, as a function of initial HF quantum number in figure 3. Three important features of the dynamics are clearly evident on this plot:

1) For all initial quantum states at all temperatures, non-reactive deactivating processes are much more likely than reactive processes, and account for, to a good degree of approximation, all the deactivating processes.
2) The variation of the rate of deactivation occurring by non-reactive processes with initial HF quantum number is far less than that of the reactive processes.
3) The variation of the rate of deactivation occurring by non-reactive processes with temperature is far less than that of the reactive processes.

An additional difference between the dynamics of deactivating processes in non-reactive collisions from those occurring in reactive ones may be seen in Table 2. Specifically, in non-reactive collisions, vibrational deactivation occurs overwhelmingly by single-quantum transitions, while in reactive collisions, deactivation by multi-quantum transitions is favored. Further, while the dominance of non-reactive deactivating processes by single-quantum transitions occurs over the whole temperature range considered, in reactive deactivating processes, as temperature increases, the single-quantum processes become more important than they are at lower temperatures. This may be seen graphically in figure 4, in which four state-to-state rate constants (k_{20}^{N}, k_{21}^{N}, k_{20}^{R}, k_{21}^{R}, where the superscripts N and R refer to non-reactive and reactive processes, respectively) are plotted vs. temperature as Arrhenius plots, that is, ln k vs. 1/T. We will consider in some detail the vibrational state distribution of the products of reactions 2b and 3b later on.

In considering the temperature dependence of the rate constants obtained, it is frequently useful to make Arrhenius plots (defined above) of the rate constants as a function of temperature. It is known that for a wide variety of chemical reactions, such plots yield straight lines, although curved Arrhenius plots are also common (24). In the systems studied, it is frequently seen that Arrhenius plots for state-to-state rate constants are linear at high temperatures ($\geq$700 K), but are non-linear at lower temperatures. Frequently, they have linear regions at high (700 - 1000 K) and low temperatures (200 - 400 K), but are curved in between.

Reactions yielding linear Arrhenius plots obey the relationship

$$k = A\exp(-E_a/k_bT) \tag{7}$$

where A is the Arrhenius pre-exponential factor, E_a is the activation energy for the reaction, and k_b is Boltzmann's constant. These quantities correspond to the y intercept and slope of the Arrhenius plots, respectively. For ground vibrational state reagents, the activation energy of a reaction is usually fairly close to the barrier height to the reaction in the potential energy surface; when the reagents are vibrationally excited, it is frequently less. We examine plots of activation energies vs. initial quantum states for n-quantum non-reactive and reactive deactivating processes in figures 5 and 6, respectively.

In figure 5, it is seen that there is no well-defined relationship between the activation energies for the non-reactive processes and reagent vibrational state. There does seem to be a clear difference in the magnitudes of the activation energies for deactivation from $v = 4$ and 5 and those from $v \leq 3$. Further, for deactivation from the higher vibrational state, the activation increases drastically for large multi-quantum transitions. Much more regular (and different) behavior is observed in figure 6, in which we consider activation energies for reactive deactivating processes. In this case, one may clearly see that the activation energies decrease substantially with reagent vibrational excitation, and in general, decrease as one goes from single-quantum to multi-quantum transitions. This is another example of differing dynamics between non-reactive and reactive collisions. This subject will be further explored later on.

Because of the large barrier to exchange (40 kcal/mole) in the potential energy surface used in these calculations, it is reasonable that reaction should only occur at high translational energies. This may be e easily seen in figure 7, in which the total probability of reaction P_v^R is plotted vs. translational energy for initial reagent vibrational states v = 0-3. Reaction becomes appreciable at successively smaller values of the translational energy as the vibrational level of the HF reagent is increased. The decrease in translational energy requirement for reaction threshhold is in the vicinity of 0.15 - 0.20 eV per vibrational quantum, which is substantially smaller than the vibrational quantum of 0.45 - 0.49 eV. This difference will be considered more fully later. It is also evident that as the initial HF vibrational state is increased, the probability for reaction vs. translational energy curve becomes more irregular, not increasing smoothly to one as the v = 0 curve does.

In studying the dynamics of the reactive processes in general, it is worthwhile to consider the distribution of product vibrational states, for deactivating, vibrationally adiabatic (involving no change in quantum number) and exciting (involving an increase in the quantum number) processes. We consider some of these distributions for the HF reagent in its v = 1 and v = 2 states at differing translational energies in figures 8 and 9, respectively. In these figures, the product state distribution is given in terms of $F_{vv'}^R$, the fraction of reaction products going into the product state v'

$$F_{vv'}^R = \frac{P^R_{vv'}}{\sum_{v'=0}^{v_{max}} P^R_{vv'}} \qquad (8)$$

where v_{max} is the maximum quantum number permitted by energy conservation. It is seen that at lower translational energies (but high enough for a large probability for reaction), vibrationally adiabatic reaction is far more likely to occur than either deactivating or exciting reaction. This preference for vibrational adiabaticity decreases as translational energy increases. At the highest translational energies considered, the distribution of product states is fairly flat for v = 2 reagent and shows some evidence of bimodality for v = 1 reagent.

One good measure of the distribution of product states is the average fraction of available energy going into product vibration, which is defined by the formula

$$\langle f_v^R \rangle = \frac{\sum_{v'=0}^{v_{max}} P_{vv'}^R E_{v'}}{(E^{tr} + E_v)\sum_{v'=0}^{v_{max}} P_{vv'}^R} \tag{9}$$

where energies are measured with respect to the bottom of the product well. This quantity is displayed in figure 10 for the H + FH($v \leq 3$) reactions. No data are presented for the v= 4 and 5 initial reagent states because the calculations were not carried out to sufficiently high energy for there to be appreciable reaction. Lines are drawn to represent the value this quantity would have if all reactions proceeded adiabatically (with no change of quantum number). For v = 0 and v = 1 reagents, at low translational energies (but still high eneough for appreciable reaction), this quantity is fairly close to that expected if all reaction proceeded adiabatically, but at higher translational energies, it increases. Thus, at high translational energies, vibrational excitation is more likely than deactivation in reactive collisions. For v = 2 and v = 3 reagents, the calculated points lie below the lines; hence, in the energy range considered, the net effect of the reactive collisions is a deactivating one.

B. D + FH

In considering the deactivation processes in this system, we have elected to look mainly at the processes which represent deactivation in an "absolute quantum number" sense, that is, for reactive deactivating processes, only those of the type

$$D + FH(v) \longrightarrow DF(v' < v) + H \qquad (10)$$

Due to the smaller vibrational energy spacing in DF than in HF, it is possible, as may be seen from figure 1, for some DF(v) levels to actually have less internal energy than some HF(v-n) level, where n is an integer that is 0 for v = 0, 1, 2, 3, 1 for v = 4, and which increases irregularly with v thereafter. Further, since all vibrationally adiabatic reactions of the type 3b (where $v'' = v$) have the DF product containing less internal energy than the reagent HF, they might be defined as deactivating processes in the "strict energetic" sense.

State-to-state rate constants for the deactivating processes 4a and 4b are given in Table 3, at 300, 650, and 1000 K along with the corresponding gas kinetic rate constants. Again, the overwhelming dominance of non-reactive processes (and single-quantum deactivating ones) is seen. A few reactive processes not satisfying the strict quantum number definition for deactivation are also included in Table 3. These processes become more important relative to the total set of reactive deactivating processes as temperature increases. As in the H + FH case, the net contribution of reactive processes to the total deactivation of vibrationally excited HF may be neglected.

On the whole, the deactivation rates for HF by collisions with D is smaller than that for deactivation by H. Some of this difference is to be expected by consideration of the gas kinetic rate constants, which are related by the expression

$$k^{GK}_{D+FH} = 0.724 k^{GK}_{H+FH} \qquad (11)$$

(the superscript GK refers to gas kinetic); the magnitude of the difference observed is greater than this, however.

Because of the similarity between the dynamics of the non-reactive deactivating processes in the H + FH and D + FH systems, we will focus our attention on the reactive ones, particularly because these are most easily amenable to experimental study. We first consider the total probability for reaction as a function of translational energy for initial HF states v = 0, 1, 2. This is plotted in figure 11 in a manner analogous to that used in figure 7 for the H + FH system. We see large tresholds, very similar in magnitude to those observed in the H + FH case. The spacings between the curves are on the order of 0.15 and 0.22 eV between the v = 1 and 2 and the v = 0 and 1 curves. This is very close to the 0.15 - 0.20 eV spacings observed in the H + FH system. One difference between the two systems is that the reaction probabilities seem to rise more smoothly to one (and to stay there) for reagent states v = 1 and 2 in D + FH(v) collisions than in the corresponding H + FH ones.

We have also examined the distribution of product (DF) vibrational states for initial reagent states HF(v = 1, 2) at a few translational energies, some of which were the same as in the corresponding H + FH cases. These are shown in figures 12 and 13 for v = 1 and 2, respectively. It is observed that there is slightly less tendency towards vibrational adiabaticity than in H + FH. As in the H + FH case, the product distribution broadens as one goes to higher translational energies, and there is some evidence for bimodality in the distribution at high energies.

Finally, we have calculated the average fraction of product energy going into vibration. This is displayed in figure 14 for HF initial states v = 0, 1, 2 (this is analogous to figure 10 for H + FH). Again, lines are drawn through the points representing the value of $\langle f_v \rangle$ if the reaction proceeded adiabatically. Since the DF vibrational spacing is smaller than that of HF, $\langle f_v \rangle$ for the D + FH reaction should be smaller than for the H + FH one. By comparing figures 10 and 14, it can be seen that this is indeed the case.

V. DISCUSSION

The overwhelming dominance of non-reactive processes in accounting for vibrational deactivation of HF in collisions with H and D atoms in the exchange channel makes it useful to discuss the non-reactive processes separately from the reactive ones. Also, we have shown that the dynamics of the reactive and non-reactive processes are very different (for example in their preference for single or multi-quantum transitions, and in their activation energies). We will consider first the non-reactive deactivating processes, focusing on the variation of the deactivation rate with reagent vibrational state and the degree to which the calculated deactivation rates obey predictions of the approximate Landau-Teller theory. We will then consider the reactive processes, particularly the relative ability of translational and vibrational energy to promote reaction. We will also examine the results of our calculations in the light of experimental studies of the vibrational deactivation of HF by H and D atoms to show that deactivation of HF(v=1, 2, 3) must be dominated by processes occurring in the abstraction channel 4.

A. NON-REACTIVE PROCESSES

The calculations show that, in general, the rate of vibrational deactivation increases as reagent vibrational excitation increases. This is true for HF(v=1, 2, 3) + H and D. In the HF(v=4, 5) + H cases one does see lower deactivation rates than for HF(v=3) + H, although the decrease becomes smaller at higher temperatures. Because of the large barrier to exchange present in the potential energy surface, it may be reasonable to consider whether the key features in the results obtained here might have been obtained by a model based on a purely non-reactive system, i.e. one in which reactions 2b and 3b cannot occur.

Such a model is the Landau-Teller model (described in reference 23) for energy transfer in non-reactive collisions. The chief predictions of this model (that of a collision of a particle with a harmonic oscillator governed by a repulsive exponential potential) are as follows:

1) All deactivations occur by single quantum transitions.

2) The rate constants for deactivating processes between different vibrational levels are related to the $1 \longrightarrow 0$ deactivation rates by the expression

$$k^N_{v,v-1} = vk^N_{1,0} \tag{12}$$

3) The rate constant for the deactivating process is related to the temperature T by the expression:

$$\ln k^N_{v,v-1} = A - BT^{1/3} \tag{13}$$

where

$$B = 3\left(\frac{2\pi^4\mu\nu^2}{\alpha^2 k_b}\right)^{1/3} \tag{14}$$

where μ is the reduced mass of the collision partners, ν is the vibrational frequency of the harmonic oscillator, and α is related to the steepness of the assumed exponential interaction potential

$$V(r) = V_o \exp(-\alpha r) \tag{15}$$

where r is the distance from the center of mass of the harmonic oscillator to that of the second particle.

Landau-Teller plots (plots of $\ln k^N_{v,v-1}$ vs. $T^{-1/3}$) for H + FH and D + FH are shown in figures 15 and 16, respectively. The plots are all reasonably linear (meaning equation 13 is approximately obeyed by the data), especially at lower temperatures. Further, the slopes of the v = 1, 2, 3 curves for H + FH are all roughly the same, as are those for the v = 4 and 5 curves for HF and those for v = 1, 2, 3 for D + FH. The major deviation in behavior from that predicted by Landau-Teller theory, then, is the smaller value of the rate constants for deactivation from v = 4 and 5 in H + FH(v) collisions, and the different slope from the v = 1, 2, 3 curves (notice that according to eq. 13 the slope of the Landau-Teller plot should be independent of the initial vibrational state).

The effect of substituting D for H as one of the collision partners may also be examined in light of the predictions of the Landau-Teller model. From equation 13, one sees that the slope of the Landau-Teller plot should be proportional to the one-third power of the reduced mass of the collision. Since this mass for D + FH is roughly twice its value for H + FH, the slopes for D + FH deactivations should be greater than for H + FH deactivations by a factor of $2^{1/3}$ or roughly 5/4. It is difficult to calculate exact ratios of slopes due to the non-linearity in the Landau-Teller plots in figures 15 and 16 at high temperature. Using crude estimates, however, one can find that the slopes are indeed greater for the D + FH deactivations than for H + FH by a number that varies between 20% and 45%. Thus, the Landau-Teller model does predict the general behavior and magnitude of the effect of isotopic substitution on the temperature dependence of the single-quantum non-reactive deactivating processes.

The main failing of the Landau-Teller theory, then, is its inability to predict the difference in the temperature dependence and thus the magnitude of the rate constants k^N_{43} and k^N_{54}. It is tempting to attribute this failing to the fact that the total vibrational energy associated with the v = 4 and 5 levels is greater than the 40 kcal/mole barrier. Since there is always sufficient energy in collisions involving these states to overcome the classical barrier, one might expect different dynamics than in cases (i.e. $v \leq 3$) where a substantial amount of translational energy is needed. There is no strong evidence for this interpretation, however.

One might be able to verify such a hypothesis by reducing the barrier height of the surface somewhat such that it is between the v = 2 and v = 3 levels. In that case, one might expect different dynamics in collisions involving HF(v = 2) and HF(v = 3). We have carried out scattering calculations for this reaction on a variety of surfaces with reduced barriers (25) but otherwise identical to that used here (the parameters A, B, and C defined in eq. 5 giving the energy along the minimum energy path as a function of the angle θ differ; the functions $l_{eq}(\theta)$ and $\beta(\theta)$ as defined in ref. 16 are identical), and will conduct similar Landau-Teller analyses of the dynamics on those surfaces.

A dynamical reason for this difference might be observable in collinear quasi-classical trajectory calculations. However, the small fraction of collisions resulting in vibrational deactivation might make such a study difficult.

B. REACTIVE PROCESSES

As has been mentioned repeatedly, the net contribution of reactive processes to vibrational deactivation is essentially negligible over the temperature range studied. Thus, the interest in reactive processes centers around the effect of reagent vibrational excitation on reaction rate and the distribution of product vibrational states. For reaction 3b both of these quantities should be fairly easily accessible to experimental study (the experiments of Bartoszek, et al. (7) included a study of the former).

From table 2 and figure 3, the enhancement in the rate of reaction with vibrational excitation for reaction 2b is clear; table 3 similarly shows the effect for reaction 3b. For reaction 2b at 300 K, for example, the relative rates of reaction for v = 1, 2, 3, 4, 5 are approximately $1:10^4:10^{11}:10^{13}:10^{15}$. In spite of this large vibrational enhancement, we can show that the efficiency of vibrational excitation in promoting reaction is quite small. This can be seen in a variety of ways. First, one may consider the threshold energy for reaction. We define this quantity as the translational energy at which the probability for vibrationally adiabatic reaction first reaches 0.01. This quantity is plotted as a function of vibrational energy in figure 17 for both reactions 2b (for v = 0, 1, 2, 3, 4) and 3b (for v = 0, 1, 2, 3). If vibrational energy and translational energy were equally effective in promoting reaction, the lines in figure 17 would have slopes of -1, as the total energy threshold for reaction would be independent of reagent vibrational state. Instead, the curves are non-linear, although they can be fairly well approximated by straight lines whose slopes are approximatley -0.31 for reaction 2b and -0.36 for reaction 3b. Thus, only some 1/3 of the vibrational energy goes towards promoting reaction. This fact can also be seen in the plots of total reaction probability vs. translational energy for reactions 2b and 3b (figures 7 and 11, respectively) in which it is seen that each quantum of reagent excitation lowers the region of rapid increase of probability with translational energy by only 0.15 - 0.20 eV, less than half the vibrational spacing of HF of 0.45 - 0.50 eV. This inefficiency of vibrational energy is also seen in figure 6, in which even in the $v = 5$ state, where the reagent has some 2.4 eV of vibrational energy above the zero-point energy, the activation energies for reaction 2b may be as high as 13 kcal/mole. Since this amount of vibrational energy is far in excess of the 40 kcal/mole classical barrier height, one can see that vibrational energy is not entirely useful in promoting reaction.

In comparing threshold energies for different reagent vibrational states, it is important not to neglect the contributions of the vibrational energies for the H--F--H configuration occurring at the saddle point $(R^{\ddagger}, r^{\ddagger})$ on the potential energy surface. Because the surface does not appreciably widen near the saddle point region these energies will be fairly large, and thus the vibrationally adiabatic barrier height $\Delta V_v^{\ddagger}$, defined by the expression

$$\Delta V_v^{\ddagger} = E_v(R^{\ddagger}, r^{\ddagger}) - E_v(R = \infty) \tag{15}$$

will decrease only gradually with increasing v.

We have calculated the $\Delta V_v^{\ddagger}$ for reaction 2b, and plotted the reaction threshold vs. them in figure 18. The resulting plot is approximately linear with a slope of 0.8. Thus, as the reagent vibrational state is increased (decreasing $\Delta V_v^{\ddagger}$), the reaction threshold does not decrease as quickly as $\Delta V_v^{\ddagger}$, although the two decreases are fairly close in magnitude. Thus, much of the inefficiency of vibrational excitation in producing reaction is due to the persistence of a large vibrationally adiabatic barrier height to large quantum numbers. Because the vibrationally adiabatic barrier heights can be expected to be slightly smaller for reaction 3b than for 2b due to the heavier D atom being substituted for one of the H atoms at the saddle point, vibrational energy should be slightly more effective at promoting reaction 3b than 2b. This is observed in figure 15, where the slope of the threshold energy vs. vibrational energy curve is some 10% higher for reaction 3b than for 2b.

This feature of the dynamics might be particularly sensitive to the exact nature of the potential energy surface near the saddle point, as a smaller vibrational frequency at the saddle point would decrease $\Delta V_v^{\ddagger}$, thus increasing the efficiency of vibrational energy in promoting reaction. Similarly, increased curvature in the minimum energy path produced, for example, by moving the saddle point to large values of R_{HF}, might better couple translational and vibrational energy, thus leading to increased efficiency of reagent vibrational excitation.

C. RELATIONSHIP TO EXPERIMENT

In analyzing the vibrational deactivation of HF by H and D, one must be careful in relating the results of collinear quantum mechanical calculations to experiment. The calculations reported here do not include the abstraction channel, which may be where most of the deactivation occurs, and include only the collinear portion of the exchange channel, possibly eliminating important non-collinear reactions of the overall potential energy surface. We will attempt in what follows to deal with these two limitations.

The experiments most relevant to the study of HF vibrational deactivation by H and D atoms are those of Bartoszek, et al. (7) and of Bott and Heidner (6). Additional experiments have been performed by Quigley and Wolga (26). Bartoszek, et al. (7) showed that DF formation via the reaction 3b only becomes appreciable when the initial vibrational state of HF was five or greater. They also showed that disappearance of HF(v = 3, 4) was due to the abstraction reaction (the D analogue of reaction 4a). In their kinetic work, Bott and Heidner (6) found relative rate constants for removal of HF(V = 1, 2, 3) by collision with H atoms of1:4:400, and determined that the abstraction reaction 4a can contribute only some 20% of the observed removal rate of HF(v = 3) at 295 K. This latter result seems to contradict that of Bartoszek, et al. (7), who relate the increase in deactivation of HF(v = 3) by D atoms to the opening up of the abstraction channel.

In our calculations in the exchange channel, we see nothing remotely resembling the 1:4:400 ratio for deactivation of HF(v = 1, 2, 3) by H atoms observed by Bott and Heidner (6). Instead, as mentioned earlier, the deactivation rate increases nearly linearly with reagent vibrational state for $v \leq 3$. Unless these results were to change drastically on going to a full three-dimensional calculation, it seems reasonable to attribute the results of Bott and Heidner (6) to deactivating processes occurring in the abstraction channel. Our rate constants for reactions 2b and 3b do show a very dramatic increase with reagent vibrational excitation, and support the interpretation of Bartoszek, et al. (7) that the barrier to exchange for reactions 2b and 3b must be large (over 40 kcal/mole).

The usefulness of the calculations for reactions 2b and 3b depends to some extent on the accuracy of the potential energy surface, and in particular, the requirement of collinearity implicit in these calculations. While it has long been assumed that the transition states for the exchange reactions 2b and 3b are collinear, ab initio calculations (13c) suggest that the transition state should instead have an HFH angle of 106°, although the height of the barrier should be relatively insensitive to that angle, increasing from 47.1 kcal/mole at 106° to 47.6 kcal/mole at 180°. Including these non-collinear configurations could easily influence the observed dynamics of the exchange reactions.

Further, the exact form of the potential energy surface used here was chosen mainly for its flexibility. There is no reason to believe that the appearance of the minimum energy path is exactly that shown in figures 1 and 2; in fact, it is quite possible that the 40 kcal/mole barrier is a few kcal/mole less than the correct one, and that the position of the saddle point used (R_{HF} = 1.975 bohr) is smaller than the correct value (for example, Bender, Garrison, and Schaefer (13a) calculated it to occur at 2.15 bohr). Thus, the results obtained for the exchange reactions should not be taken to be more than qualitatively correct.

VI. CONCLUSIONS

We have studied on a realistic (high barrier) potential energy surface the dynamics of vibrational deactivation of HF in collision with H and D atoms in the exchange channel and also the dynamics of the H + FH and HF + D exchange reactions. The important features of the dynamics are as follows:

1) Vibrational deactivation in the exchange channel occurs almost entirely by single-quantum, non-reactive processes. The rate of this deactivation varies only weakly with temperature, and, in general, increases weakly with reagent vibrational excitation. The overall dynamics of the deactivation processes are in line with the predictions of Landau-Teller theory.

2) The rate of the exchange reactions is increased dramatically by reagent vibrational excitation, although the effective lowering of the threshold to reaction is less than half the extra energy associated with each vibrational quantum. Rates of exchange reactions are characterized by large temperature dependences, and at high translational energies, broad product state distributions. The relative inefficiency of vibrational energy in promoting reaction can be related to the large symmetric stretch vibrational frequency at the H--F--H saddle point, resulting in a vibrationally adiabatic barrier height which decreases only weakly with an increase in the reagent vibrational quantum number.

3) The relationship of the calculated results to experimental ones on these systems is complicated because of the collinear nature of the theory; nevertheless, the results do support interpretations that the deactivation of HF($v \leq 3$) by H atoms must be occurring by processes in the abstraction channel and also support interpretations of experimental results that the barrier to exchange is quite high ($\geq$ 40 kcal/mole).

A fuller understanding of the dynamics in this system awaits a study of the dynamics of the abstraction channel (preliminary work on the H + HF system has been performed (27)) and the relation of the results of the two channels by some technique (i.e. information theoretic one dimensional to three dimensional transformation (28)). Finally, additional information from *ab initio* calculations on the potential energy surface for the exchange calculation would be useful in insuring a more accurate description of the saddle point region.

ACKNOWLEDGMENTS

We thank Ambassador College for the generous use of its computational facilities for most of the calculations reported here. Additional calculations were performed on the Dreyfus-NSF Theoretical Chemistry Computer (VAX 11/780) at Caltech, which was funded through grants from the Camille and Henry Dreyfus Foundation, the National Science Foundation (Grant No. CHE78-20235), and the Sloan Fund of the California Institute of Technology. One of us (JAK) would like to thank Dr. Nancy M. Harvey for helpful comments on an earlier version of this manuscript.

REFERENCES

1. N. Cohen and J. F. Bott, in: Handbook of Chemical Lasers, ed. R. W F. Gross and J. F. Bott (Wiley-Interscience, York, 1976), Ch. 2

2. The F + H_2 reaction has been reviewed in J. B. Anderson, Adv. Chem. Phys. 41, 229 (1980); an extensive review of all work on the F + H_2 and H + F_2 reactions may be found in M. R. Levy, Prog. React. Kin. 10, 1, (1979).

3. Recent references include, for F + H_2:
E. Wurzberg and P. L. Houston, J. Chem. Phys. 72, 4811 (1980), R. F. Heidner III, J. F. Bott, C. E. Gardner, and J. E. Melzer, J. Chem. Phys. 72, 4815 (1980); R. K. Sparks, C. C. Hayden, K. Shobatake, D. M. Neumark, and Y. T. Lee, in : Horizons of Quantum Chemistry, ed. K. Fukui and B. Pullman (D. Reidel, Boston, 1980), pp. 91 - 105.

4. For example, for F + H_2:
a) S. H. Suck, Chem. Phys. Lett. 77, 390 (1981);
b) M. J. Redmon and R. E. Wyatt, Chem. Phys. Lett. 63, 209 (1979); c) J. N. L. Connor, W Jakubetz, and J. Manz, Mol. Phys. 35, 1301 (1978); d) G. C. Schatz, J. M. Bowman, and A. Kuppermann, J. Chem. Phys. 63, 674 (1975).
for H + F_2:
e) D. C. Clary and J. N. L. Connor, Chem. Phys. Lett. 66, 493 (1979); f) W Jakubetz, Chem. Phys. 35, 129 (1978).

5. See, for example: a) G. M. Jurisch and F. F. Crim, J. Chem. Phys. 74, 4455 (1981); b) R. L. Wilkins and M. A. Kwok, J. Chem. Phys. 73, 3198 (1980); c) R. L. Wilkins, J. Chem. Phys. 70, 2700 (1979); d) M. E. Coltrin and R. A. Marcus, J. Chem. Phys. 73, 4390 (1980).

6. a) J. F. Bott and R. F. Heidner III, J. Chem. Phys. 68, 1708

(1978); b) R. F. Heidner III and J. F. Bott, Ber. Bunsen. Gesellschaft 81, 128 (1977); c) J. F. Bott and R. F. Heidner III, J. Chem. Phys. 66, 2878 (1977); d) R. F. Heidner III and J. F. Bott, J. Chem. Phys. 63, 1810 (1975).

7. F. E. Bartoszek, D. M. Manos, and J. C. Polanyi, J. Chem. Phys. 69, 933 (1978).

8. R. L. Wilkins, J. Chem. Phys. 58, 3038 (1975); Mol. Phys. 29, 555 (1975).

9. D. L. Thompson, J. Chem. Phys. 57, 4~64, 4~75 (1972).

10. R. L. Thommarson and G. C. Berend, Int. J. Chem. Kin. 6, 597 (1974).

11. G. C. Schatz and A. Kuppermann, J. Chem. Phys. 72, 2737 (1980).

12. M. Baer, J. Chem. Phys. 65, 493 (1976).

13. a) C. F. Bender, B. J. Garrison, and H. F. Schaefer III, J. Chem. Phys. 62, 1188 (1975); b) P. Botschwina and W. Meyer, Chem. Phys. 20, 43 (1977); c) W. R. Wadt and N. W. Winter, J. Chem. Phys. 67, 3068 (1977); d) A. F. Voter and W. A. Goddard III, J. Chem. Phys. 75, 3638 (1981).

14. P. J. Kuntz, E. M. Nemeth, J. C. Polanyi, S. D. Rosner, and C. E. Young, J. Chem. Phys. 44, 1168 (1966).

15. H. F. Schaefer III, in: Atom-Molecule Collision Theory, ed. R. B. Bernstein (Plenum Press, New York, 1979), pp. 45-78.

16. J. M. Bowman and A. Kuppermann, Chem. Phys. Lett. 34, 523 (1975).

17. L. N. Delves, Nucl. Phys. 9, 391 (1959); 20, 275 (1960).

18. A. Kuppermann, in: Potential Energy Surfaces in Chemistry, ed. W. A. Lester (U. Calif. Santa Cruz, 1970), pp. 121-129; in: Abstracts of Papers VII, ICPEAC, (North-Holland, Amsterdam, 1971), pp. 3-5.

19. G. C. Schatz, J. M. Bowman, and A. Kuppermann, J. Chem. Phys. 63, 685 (1975).

20. J. P. Dwyer, Ph. D. Thesis, California Institute of Technology, 1977; A. Kuppermann and J. P. Dwyer, Abstracts of Papers XI, ICPEA C, (Society for Atomic Collision Research, Japan, 1979), pp. 888-889.

21. G. C. Schatz and A. Kuppermann, J. Chem. Phys. 59, 964 (1973).

22. J. F. Garvey, J. A. Kaye, and A. Kuppermann, in Abstracts of Papers, 1979 Pacific Conference on Chemistry and Spectroscopy, Pasadena, Ca., p. 39.

23. See, for example J. D. Lambert, Vibrational and Rotational Relaxation in Gases (Clarendon Press, Oxford, 1977).

24. W. C. Gardiner, Jr., Acc. Chem. Res. 10, 327 (1977).

25. J. A. Kaye, J. P. Dwyer, and A. Kuppermann, manuscript in preparation; a preliminary account of this work was presented at the 1979 Pacific Conference on Chemistry and Spectroscopy, Pasadena, Ca.

26. G. P. Quigley and G. J. Wolga, Chem. Phys. Lett. 27, 276 (1974).

27. J. A. Kaye and A. Kuppermann, unpublished results.

28. R. B. Bernstein and R. D. Levine, Chem. Phys. Lett. 29, 314 (1974); J. N. L. Connor, W. Jakubetz, J. Manz, and J. C. Whitehead, Chem. Phys. 39, 395 (1979).

Table 1. Parameters for Rotating Morse cubic spline surface for $H + FH \longrightarrow HF + H$

$R_{10} = R_{20} = 7.0$ bohr

θ (deg)	$l_{eq}(\theta)$ (bohr)	$\beta(\theta)$ (bohr^{-1})
0	5.267	1.163
6	5.296	1.149
15	5.453	1.122
30	6.079	1.012
39	6.742	0.9022
45	7.106	0.8194
51	6.742	0.9022
60	6.079	1.012
75	5.453	1.122
84	5.296	1.149
90	5.267	1.163

Table 2. Selected State-to-State and Summed Deactivation Rate Constants for the Processes HF(v) + H' ⟶ HF(v' < v) + H' (NR) and HF(v) + H' ⟶ H + FH'(v' < v) (R)

All rate constants* are in units of cm*molecule^{-1}*sec^{-1}

	T = 300 K		T = 650 K		T = 1000 K	
v--v'	NR	R	NR	R	NR	R
1 0	1.185(2)	4.120(-16)	2.065(2)	1.821(-7)	2.782(2)	3.768(-4)
2 0	2.854(0)	5.172(-10)	4.192(0)	5.392(-5)	5.437(0)	5.097(-3)
2 1	1.189(2)	7.983(-13)	2.657(2)	2.108(-5)	3.780(2)	1.640(-2)
3 0	1.082(-1)	1.195(-4)	1.741(-1)	3.198(-3)	2.210(-1)	2.501(-2)
3 1	6.322(0)	3.548(-7)	1.098(1)	1.957(-3)	1.549(1)	9.502(-2)
3 2	3.992(2)	8.586(-9)	5.552(2)	5.454(-4)	7.412(2)	1.706(-1)
4 0	1.546(-3)	3.705(-3)	5.533(-3)	1.522(-2)	2.516(-2)	8.998(-2)
4 1	1.849(-1)	1.649(-2)	4.567(-1)	1.226(-1)	8.098(-1)	4.982(-1)
4 2	5.746(0)	8.555(-5)	1.612(1)	3.034(-2)	2.595(1)	7.082(-1)
4 3	6.039(1)	2.946(-6)	2.621(2)	4.648(-3)	5.269(2)	6.205(-1)
5 0	6.393(-4)	1.625(-2)	5.211(-3)	7.784(-2)	3.764(-2)	3.378(-1)
5 1	1.727(-2)	1.045(-1)	6.570(-2)	3.626(-1)	2.498(-1)	1.280(0)
5 2	4.121(-1)	3.043(-1)	1.345(0)	1.103(0)	3.083(0)	3.054(0)
5 3	1.151(1)	2.854(-3)	3.588(1)	4.064(-1)	5.840(1)	3.595(0)
5 4	1.098(2)	1.043(-4)	4.465(2)	1.528(-2)	7.919(2)	4.774(-1)
1 all	1.185(2)	4.120(-16)	2.065(2)	1.821(-7)	2.782(2)	3.768(-4)
2 all	1.197(2)	5.180(-10)	2.699(2)	7.500(-5)	3.834(2)	2.150(-2)
3 all	4.056(2)	1.199(-4)	5.664(2)	5.701(-3)	7.569(2)	2.906(-1)
4 all	6.605(1)	2.028(-2)	2.786(2)	1.728(-1)	5.537(2)	1.917(0)
5 all	1.217(2)	4.279(-1)	4.838(2)	1.965(0)	8.537(2)	8.744(0)
gas kin.	6.433(4)		9.469(4)		1.174(5)	

* Numbers in parentheses represent powers of 10 by which the written number should be multiplied.

Table 3. Selected State-to-State Rate Constants for the Processes

$$\mathrm{HF}(v) + \mathrm{D} \longrightarrow \mathrm{HF}(v' < v) + \mathrm{D} \qquad (\mathrm{NR})$$

$$\mathrm{HF}(v) + \mathrm{D} \longrightarrow \mathrm{H} + \mathrm{FD}(v') \qquad (\mathrm{R})$$

All rate constants* are in units of cm*molecule^{-1}*sec^{-1}

v→v'	NR	R	NR	R	NR	R
1 0	3.421(1)	1.265(-14)	6.267(1)	5.584(-7)	8.425(1)	1.266(-3)
2 0	9.141(-1)	6.015(-12)	1.812(0)	6.574(-6)	2.537(0)	4.635(-3)
2 1	6.476(1)	3.548(-13)	1.123(2)	1.454(-5)	1.556(2)	1.437(-2)
3 0	6.875(-2)	4.113(-5)	1.149(-1)	1.041(-3)	1.439(-1)	7.812(-3)
3 1	7.950(0)	3.514(-6)	1.044(1)	7.205(-4)	1.178(1)	1.997(-2)
3 2	9.057(1)	1.441(-7)	1.592(2)	1.944(-4)	2.106(2)	1.950(-2)
3 3		2.837(-9)		6.343(-5)		1.705(-2)
3 4		1.356(-10)		1.426(-5)		5.357(-3)
gas kin.	4.656(4)		6.855(4)		8.499(4)	

* Numbers in parentheses represent powers of 10 by which the written number should be multiplied.

FIGURE CAPTIONS

Figure 1. Plot of the potential energy V along the minimum energy path as a function of the reaction coordinate s for the reaction H' + FH $\longrightarrow$ H'F + H. s = 0 at the barrier (along the H--F--H symmetric stretch line). The energy levels of the isolated HF reagent molecule are shown on the left side of the plot. For comparison purposes, those of the isolated DF molecule are shown at the right.

Figure 2. Contour plot of the potential energy surface for the reaction H' + FH $\longrightarrow$ H'F + H in the Delves coordinate system. Equipotentials are drawn every 0.3 eV. The origin of energy is the bottom of the isolated HF well. A cross is drawn at the saddle point, and the minimum energy path is indicated by a dashed line.

Figure 3. Plot of rate constants $k_{v \rightarrow v' < v}$ for total reactive (R) and non-reactive (N) deactivation in the collision H + FH(v) $\longrightarrow$ H + FH(v' < v) at T = 300, 650, and 1000 K as a function of the vibrational state v of the reagent molecule. All curves for reactive collisions are indicated by solid lines; those for non-reactive ones are indicated by dashed, dotted, and dashed-dotted lines, respectively, for T = 300, 650, and 1000 K.

Figure 4. Arrhenius plot of state-to-state rate constants $k_{vv'}$ for the reactive (superscript R) and non-reactive (superscript N) collisions H + FH(v = 2) $\longrightarrow$ H + FH(v'=0, 1). Curves for non-reactive transitions are indicated by solid lines; those for reactive ones are indicated by dashed lines.

Figure 5. Plot of high temperature (700 - 1000 K) Arrhenius activation energies $E_a^N(v \rightarrow v-n)$ for n-quantum non-reactive deactivating collisions HF(v=1-5) + H' $\longrightarrow$ HF(v-n) + H' as a function of the internal energy E_{int} of the HF(v) reagent. The quantum number of each reagent state is indicated on the upper abscissa. Different line types are used to connect each of the data points: n=1 - solid line; n=2 - dashed line; n=3 - dotted line; n=4 - dashed-dotted line. For n=5, only one data point exists; it

is marked by a plus sign.

Figure 6. Plot of high temperature (700-1000 K) Arrhenius activation energies $E_a^R(v \rightarrow v-n)$ for n-quantum reactive deactivating collisions $HF(v=1-5) + H' \longrightarrow H + FH'(v-n)$ as a function of the internal energy E_{int} of the HF(v) reagent. All line types and markings are as in figure 5.

Figure 7. Plot of the probability $P^R_{HF(v) + H}$ of the reaction $HF(v) + H' \longrightarrow H + FH'$ as a function of the initial translational energy of the reagents E^{tr} for $v = 0, 1, 2, 3$.

Figure 8. Histogram plot of the fraction of reaction product $F^R_{vv'}$ for all possible product states v' for the reaction $HF(v=1) + H' \longrightarrow H + FH'(v')$ at three values of the initial reagent translational energy E^{tr}. Bars marked a, b, and c are for $E^{tr} = 1.5361$ eV, 1.9443 eV, and 2.4068 eV, respectively.

Figure 9. Histogram plot of the fraction of reaction product $F^R_{vv'}$ for all possible product states v' for the reaction $HF(v=2) + H' \longrightarrow H + FH'(v')$ at three values of the initial reagent translational energy E^{tr}. Bars marked a, b, and c are for $E^{tr} = 1.3161$ eV, 1.6154, eV, and 1.9964 eV, respectively.

Figure 10. Plot of the average fraction of product energy going into vibration $\langle f^R_v \rangle$ as a function of the initial reagent translational energy E^{tr} for $v = 0, 1, 2, 3$. Results for different values of v are indicated by different symbols: v=0 - open circles; v=1 - open squares; v=2 - open triangles; v=3 - filled circles. Lines correspond to the value expected if the reaction were vibrationally adiabatic. Results are shown only for energies where the probability of reaction is significantly greater than zero.

Figure 11. Plot of the probability $P^R_{D + FH(v)}$ of the reaction $HF(v) + D \longrightarrow DF + H$ as a function of the initial reagent translational energy E^{tr} for $v = 0, 1, 2$. The solid line is for $v = 0$; the dashed line is for $v = 1$; and the dotted line is for $v = 2$.

Figure 12. Histogram plot of the fraction of reaction product $F^R_{vv'}$ for all possible product states v' for the reaction $HF(v=1) + D \longrightarrow H + FD(v')$ at three values of the initial reagent translational energy E^{tr}. Bars marked a, b, and c are for $E^{tr} = 1.5361$ eV, 1.7538 eV, and 1.9443 eV, respectively.

Figure 13. Histogram plot of the fraction of reaction product $F^R_{vv'}$ for all possible product states v' of the reaction $HF(v=2) + D \longrightarrow H + FD(v')$ at two values of the initial reagent translational energy E^{tr}. Bars marked by a and b are for $E^{tr} = 1.3161$ eV and 1.5066 eV, respectively.

Figure 14. Plot of the average fraction of product energy going into vibration f^R_v as a function of the initial reagent translational energy E^{tr} for v = 0, 1, 2. Symbols and lines have their same meaning as in figure 10.

Figure 15. Landau-Teller plot of rate constants $k^N_{v,v-1}(HF + H')$ for single-quantum non-reactive deactivating collisions $HF(v) + H' \longrightarrow HF(v-1) + H'$ for v=1-5. The temperature is indicated on the upper abscissa. Different line types are used for each v: v=1 - solid line; v=2 - dashed line (large dashed); v=3 - dotted line; v=4 - dashed-dotted line; v=5 - dashed line (small dashes).

Figure 16. Landau-Teller plot of rate constants $k^N_{v,v-1}(HF + D)$ for single-quantum non-reactive deactivating collisions $HF(v) + D \longrightarrow HF(v-1) + D$ for v = 1, 2, 3. The temperature is indicated on the upper abscissa. Different line types are used for each v: v=1 - solid line; v=2 - dashed line; v=3 - dotted line.

Figure 17. Plot of the threshhold energy E^{th}_v for the vibrationally adiabatic reactions $HF(v) + H' \longrightarrow H + FH'(v)$ (solid line) and $HF(v) + D \longrightarrow H + FD(v)$ (dashed line) as a function of the internal energy E^{int} of the reagent HF molecule. Open circles and squares, respectively, are used to plot the original data points for the HF + H' and HF + D systems,

respectively. The quantum number of the reagent HF state is indicated on the upper abscissa.

Figure 18. Plot of the threshhold energy E^{th} for the vibrationally adiabatic reaction $HF(v) + H' \longrightarrow H + FH'(v)$ as a function of the vibrationally adiabatic barrier height $\Delta V_v^{\ddagger}$, defined in eq. 15 of the text for v = 0-4. The open circles mark the actual data points. The values of v are indicated on the upper abscissa.

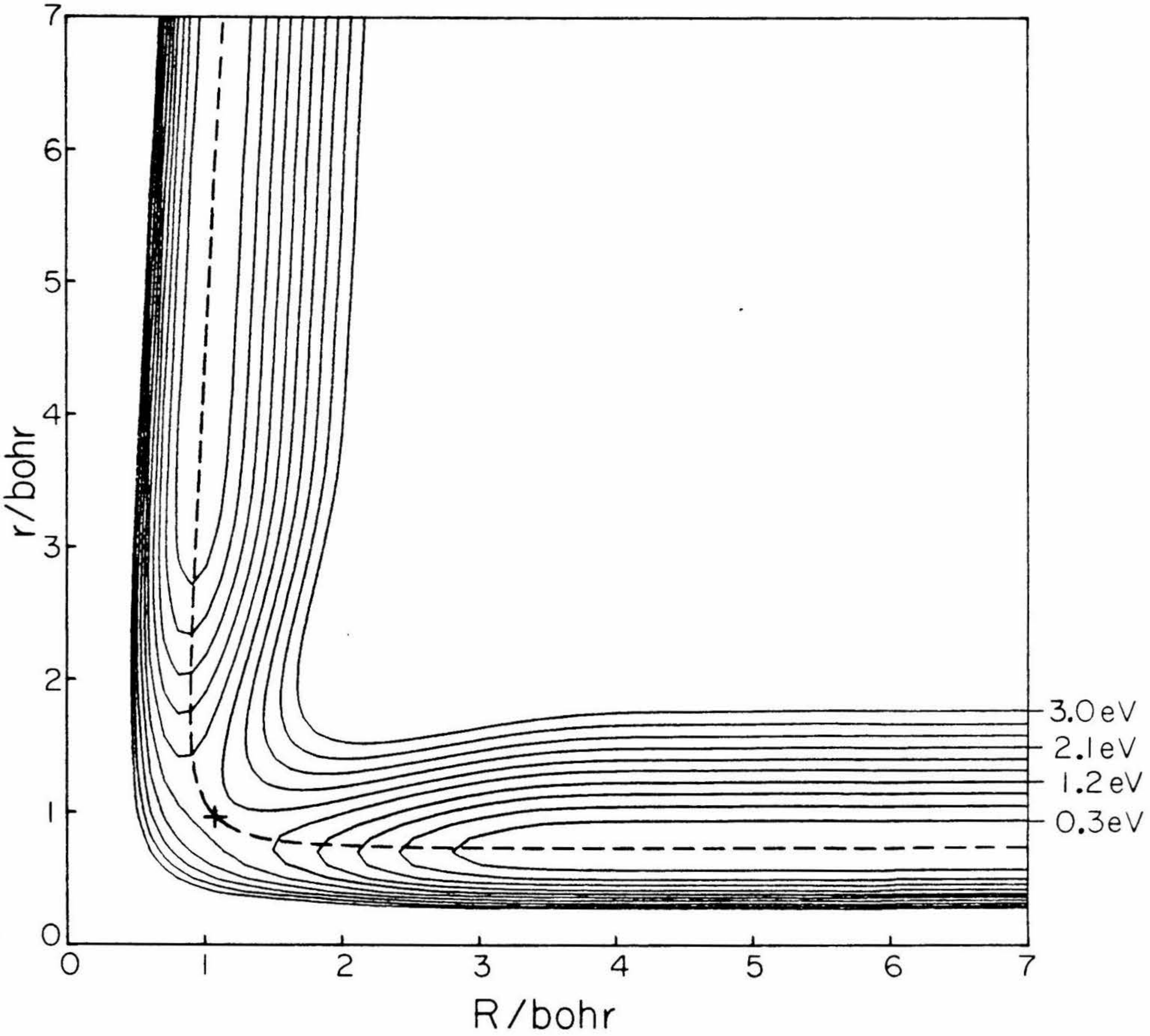

Figure 1

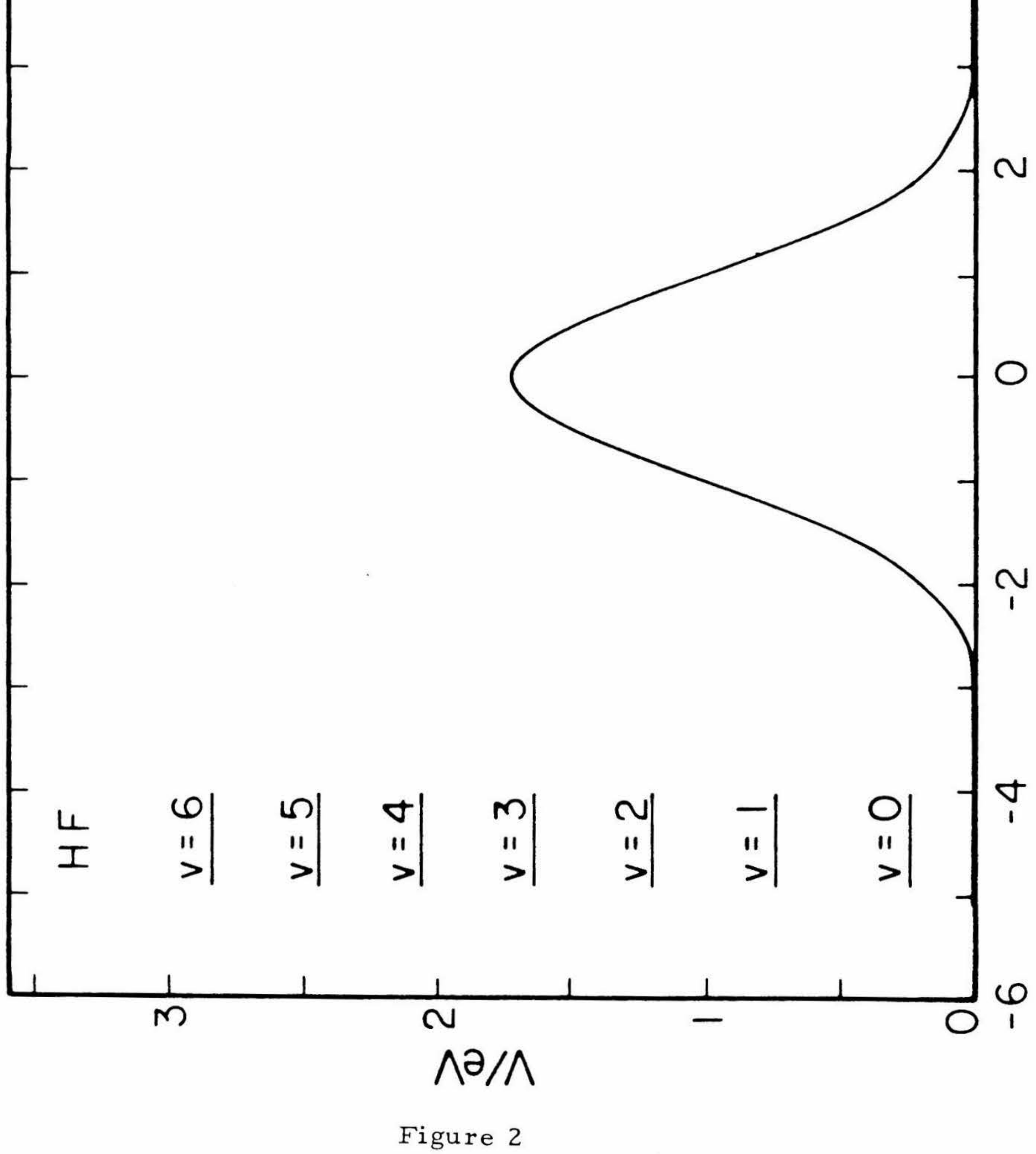
V/eV
0
1
2
3
s/bohr
-6
-4
-2
0
2
4
6
HF
v = 0
v = 1
v = 2
v = 3
v = 4
v = 5
v = 6
DF
v = 0
v = 1
v = 2
v = 3
v = 4
v = 5
v = 6
v = 7
v = 8
v = 9

Figure 2

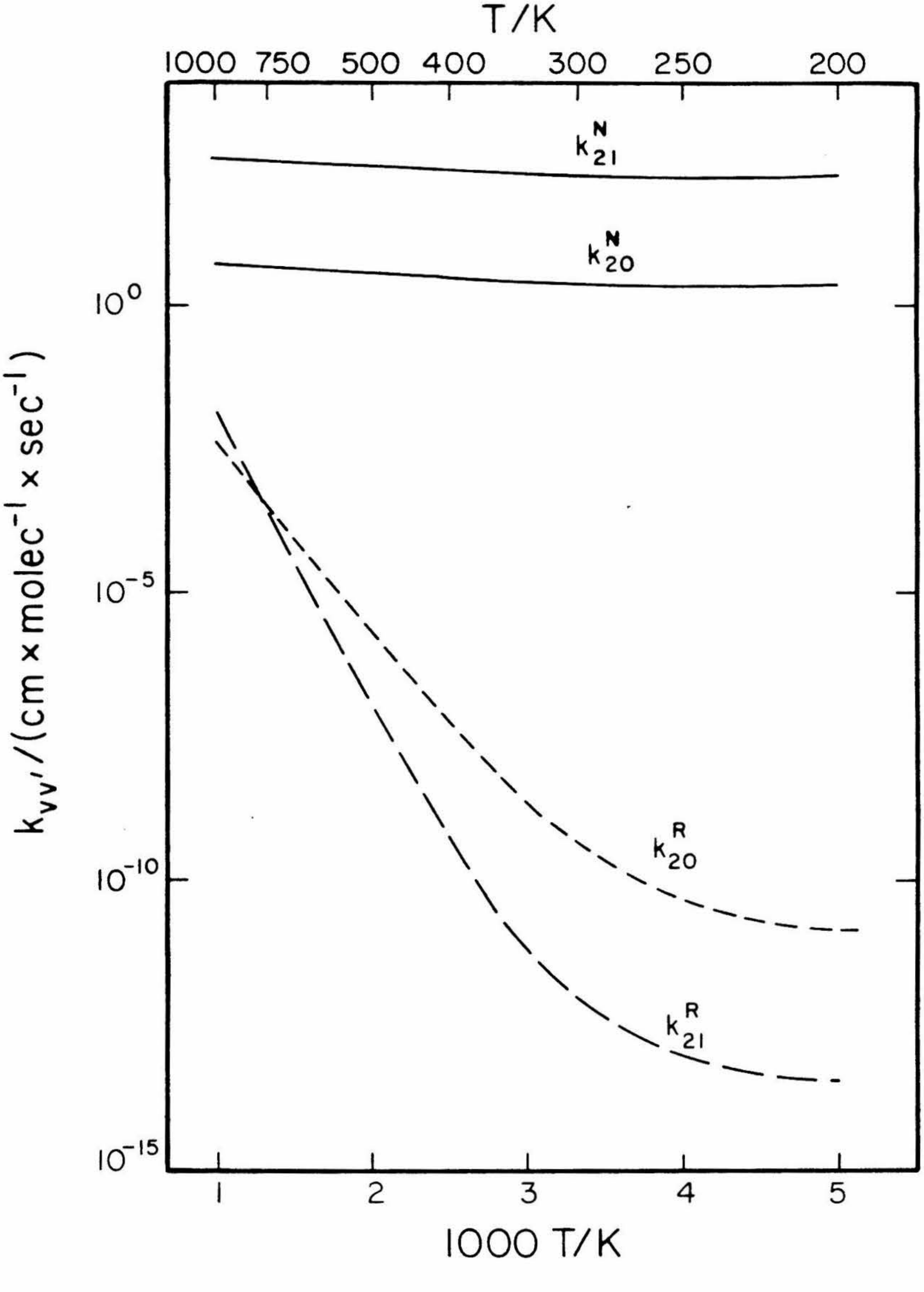
T/K
1000
750
500
400
300
250
200
k_{21}^{N}
k_{20}^{N}
10^{0}
10^{-5}
10^{-10}
10^{-15}
$k_{vv'}/(\mathrm{cm} \times \mathrm{molec}^{-1} \times \mathrm{sec}^{-1})$
k_{20}^{R}
k_{21}^{R}
1
2
3
4
5
1000 T/K

Figure 3

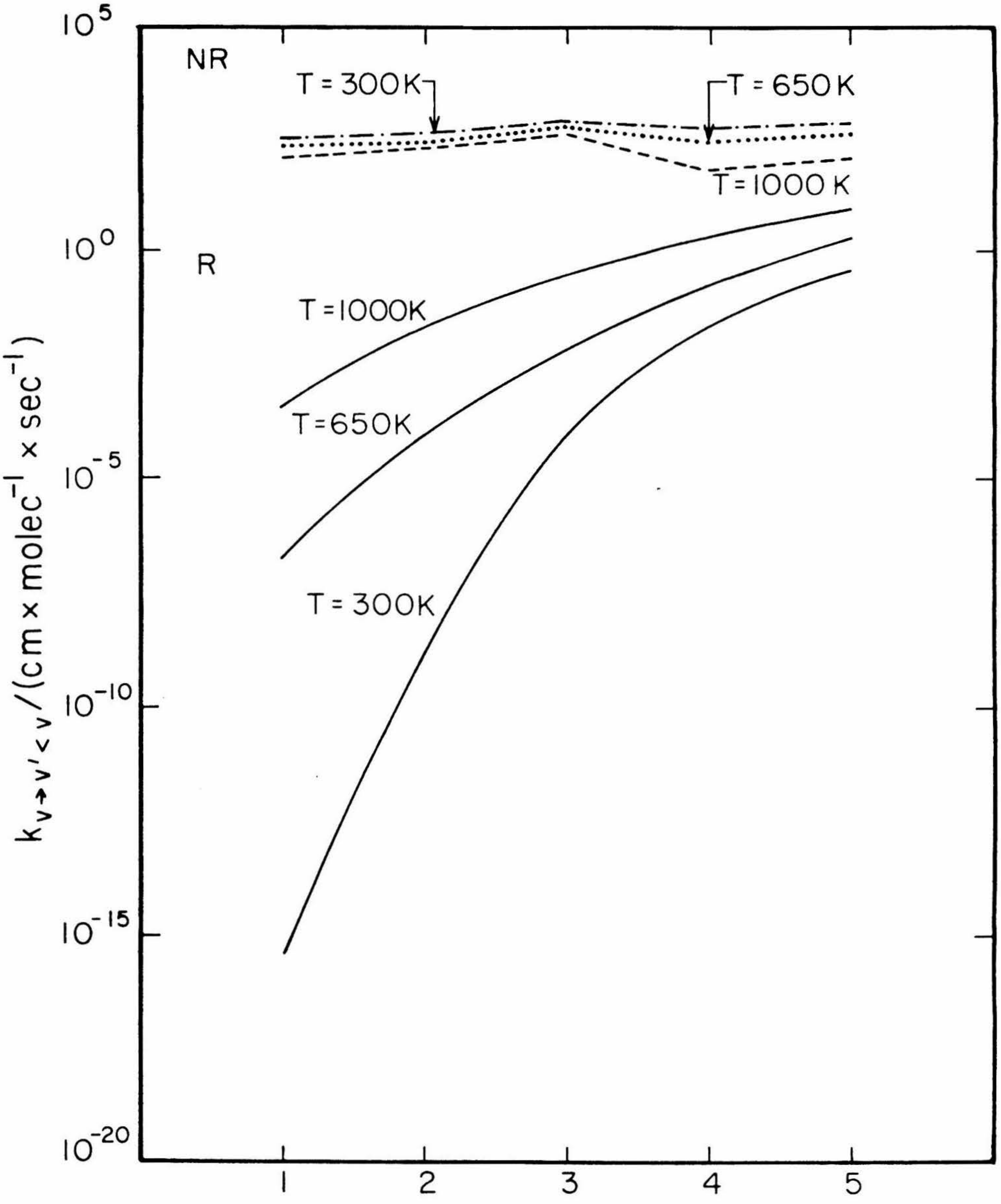

10^5
10^0
10^{-5}
10^{-10}
10^{-15}
10^{-20}
NR
R
T = 300K
T = 650K
T = 1000K
T = 1000K
T = 650K
T = 300K
$k_{v \to v' < v}$/(cm × molec^{-1} × sec^{-1})
1
2
3
4
5
v

Figure 4

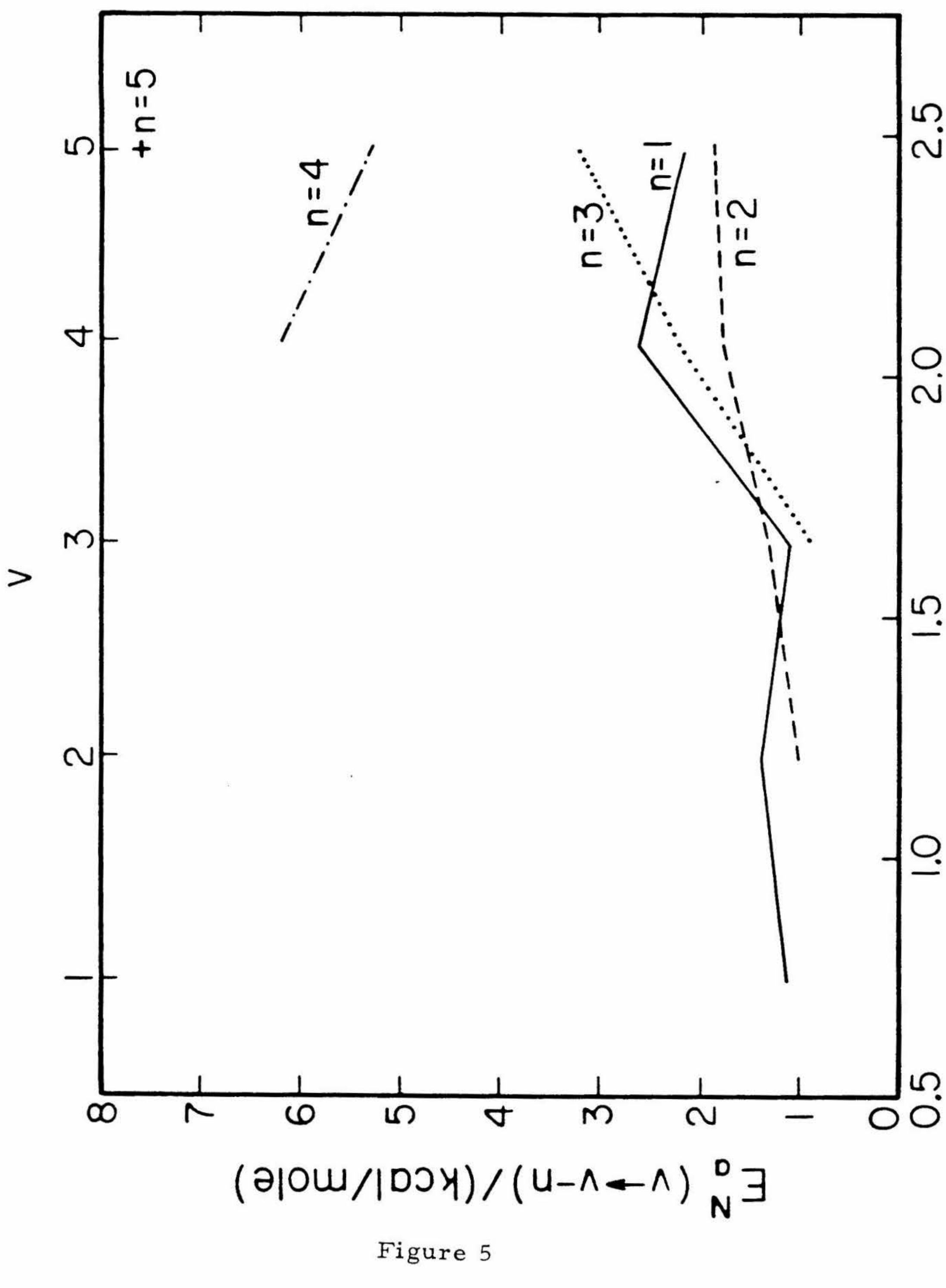
v
1
2
3
4
5
0.5
1.0
1.5
2.0
2.5
E_{int} /eV
0
1
2
3
4
5
6
7
8
E_a^z (v→v−n)/(kcal/mole)
n=1
n=2
n=3
n=4
+n=5

Figure 5

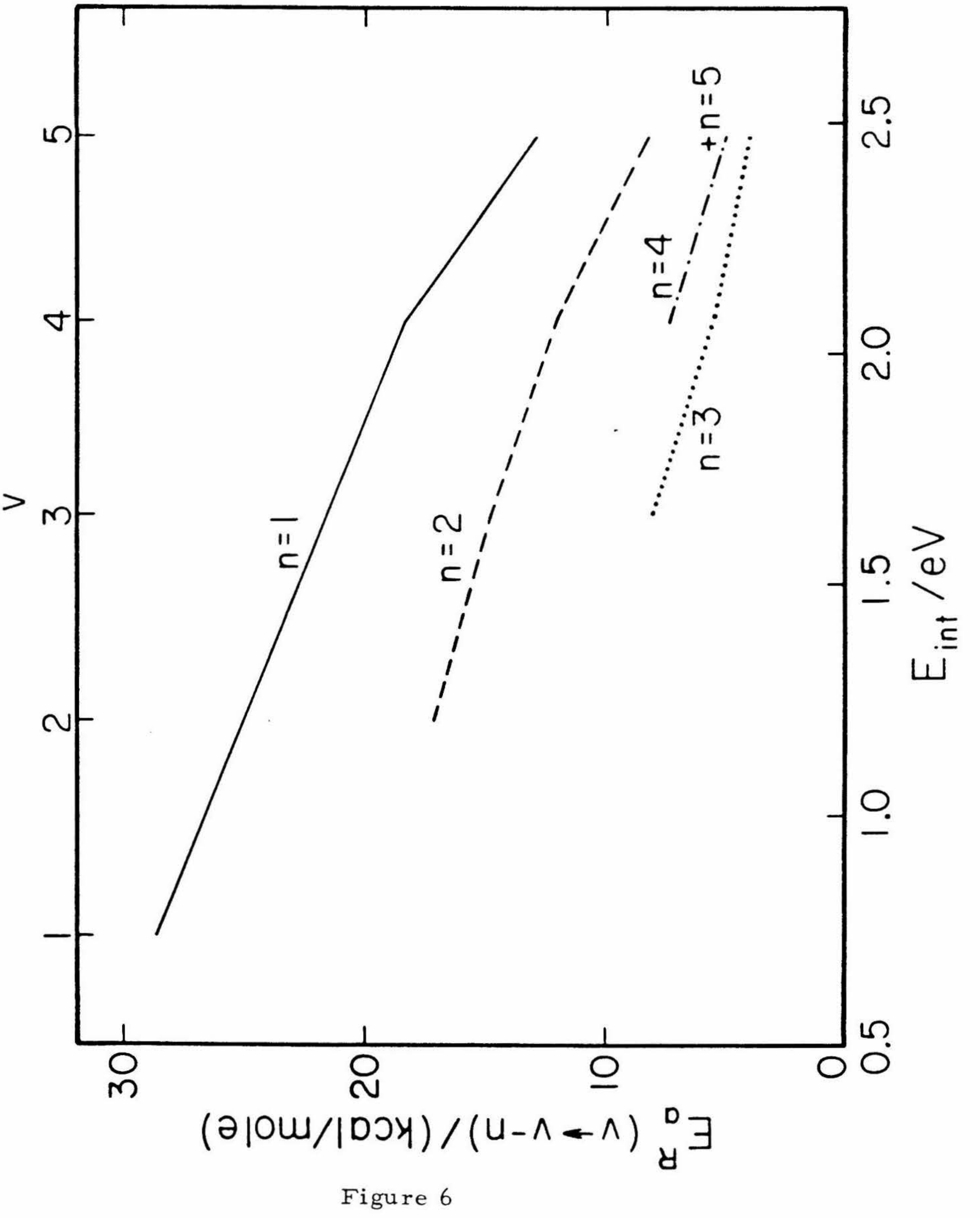
E_a^R (v→v-n)/(kcal/mole)
0
10
20
30
v
1
2
3
4
5
E_{int} /eV
0.5
1.0
1.5
2.0
2.5
n=1
n=2
n=3
n=4
n=5

Figure 6

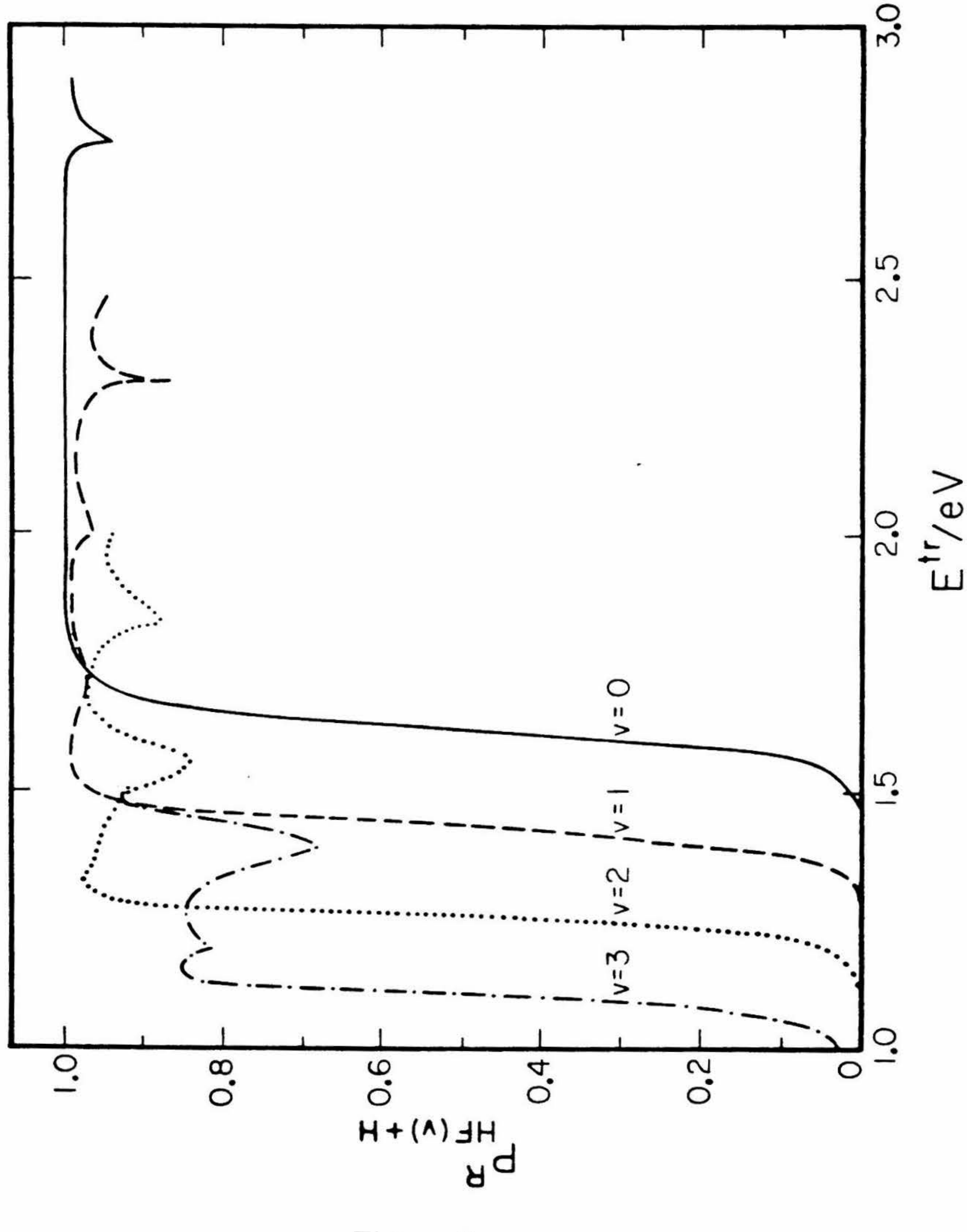

Figure 7

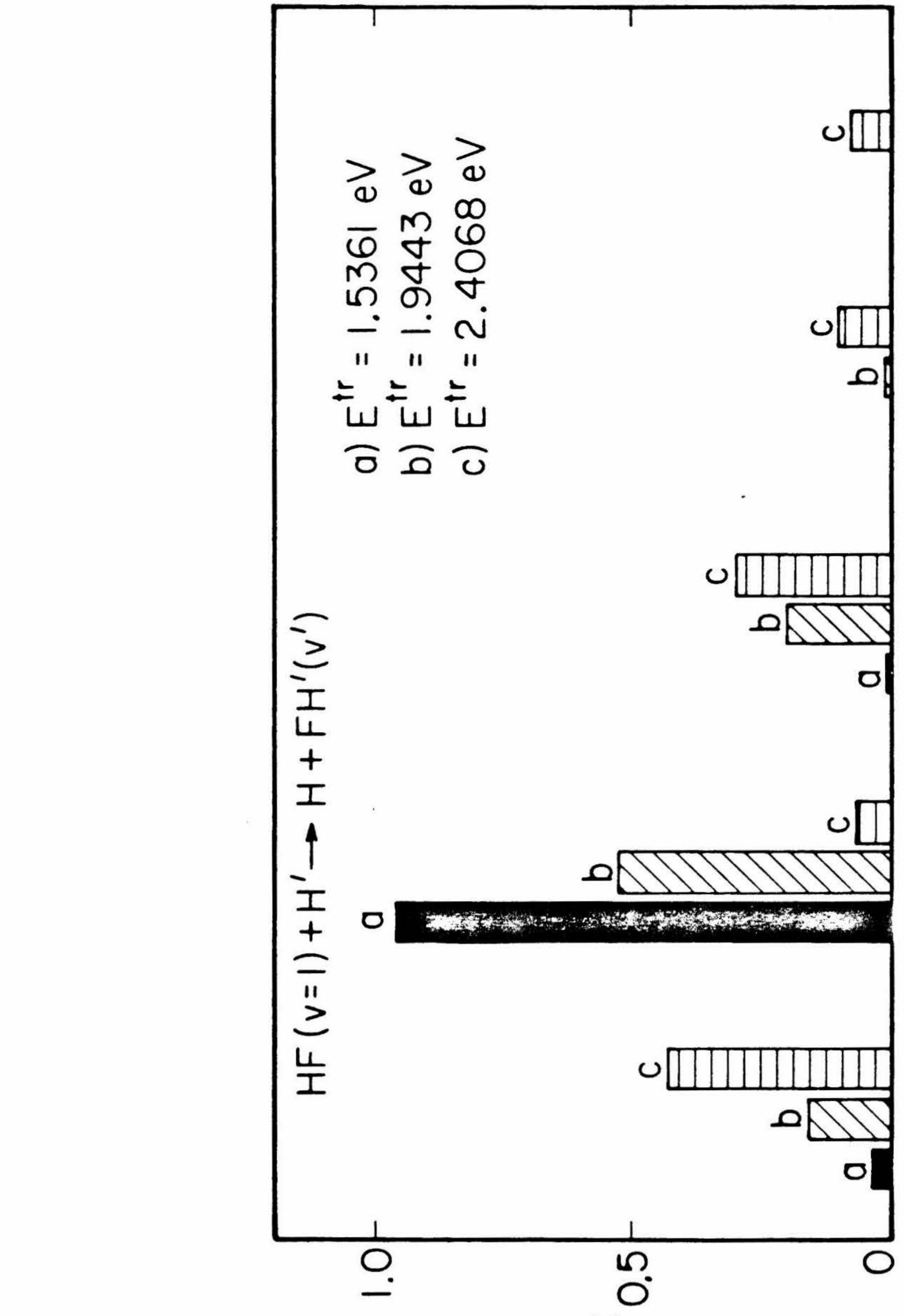
HF (v=1) + H' ⟶ H + FH'(v')
a) E^{tr} = 1.5361 eV
b) E^{tr} = 1.9443 eV
c) E^{tr} = 2.4068 eV
$F^{R}_{v,v'}$
1.0
0.5
0
v'
0
1
2
3
4
a
b
c

Figure 8

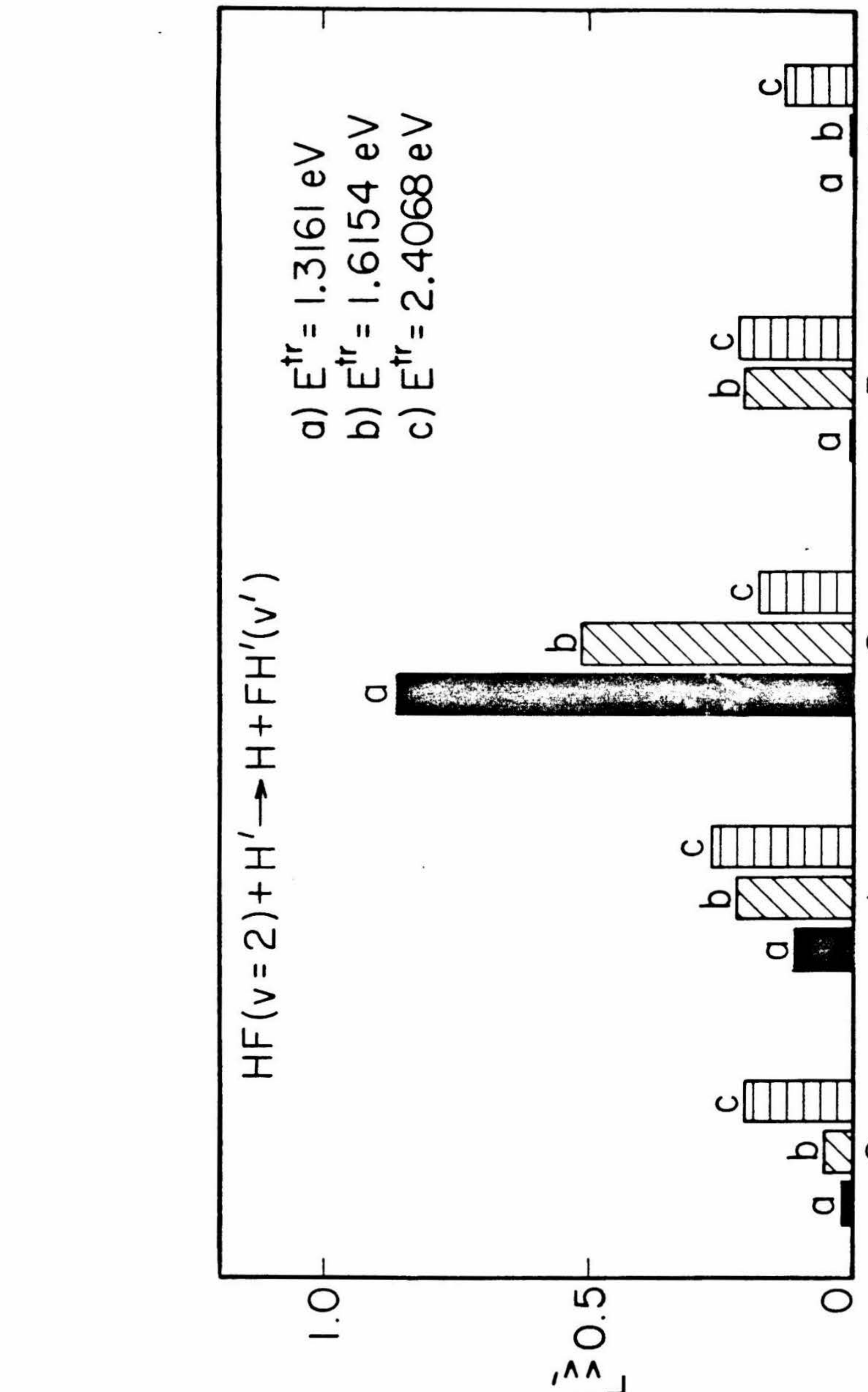
HF(v=2)+H'⟶H+FH'(v')
a) E^tr = 1.3161 eV
b) E^tr = 1.6154 eV
c) E^tr = 2.4068 eV
F_R^vv'
0
0.5
1.0
v'
0
1
2
3
4
a
b
c

Figure 9

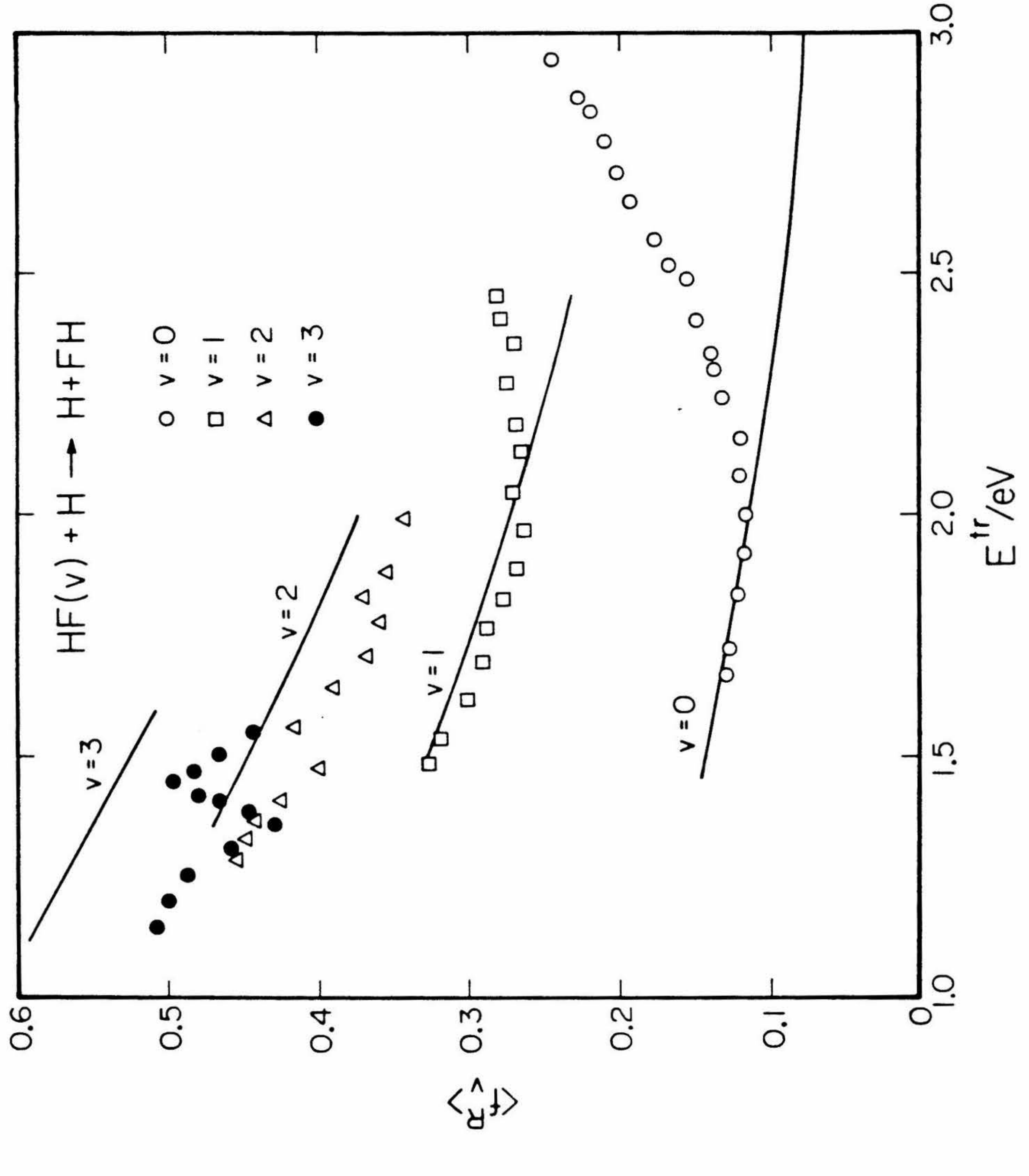
HF(v) + H → H+FH
○ v = 0
□ v = 1
△ v = 2
● v = 3
v = 3
v = 2
v = 1
v = 0
0
0.1
0.2
0.3
0.4
0.5
0.6
1.0
1.5
2.0
2.5
3.0
E^{tr}/eV
$\langle f_R \rangle$

Figure 10

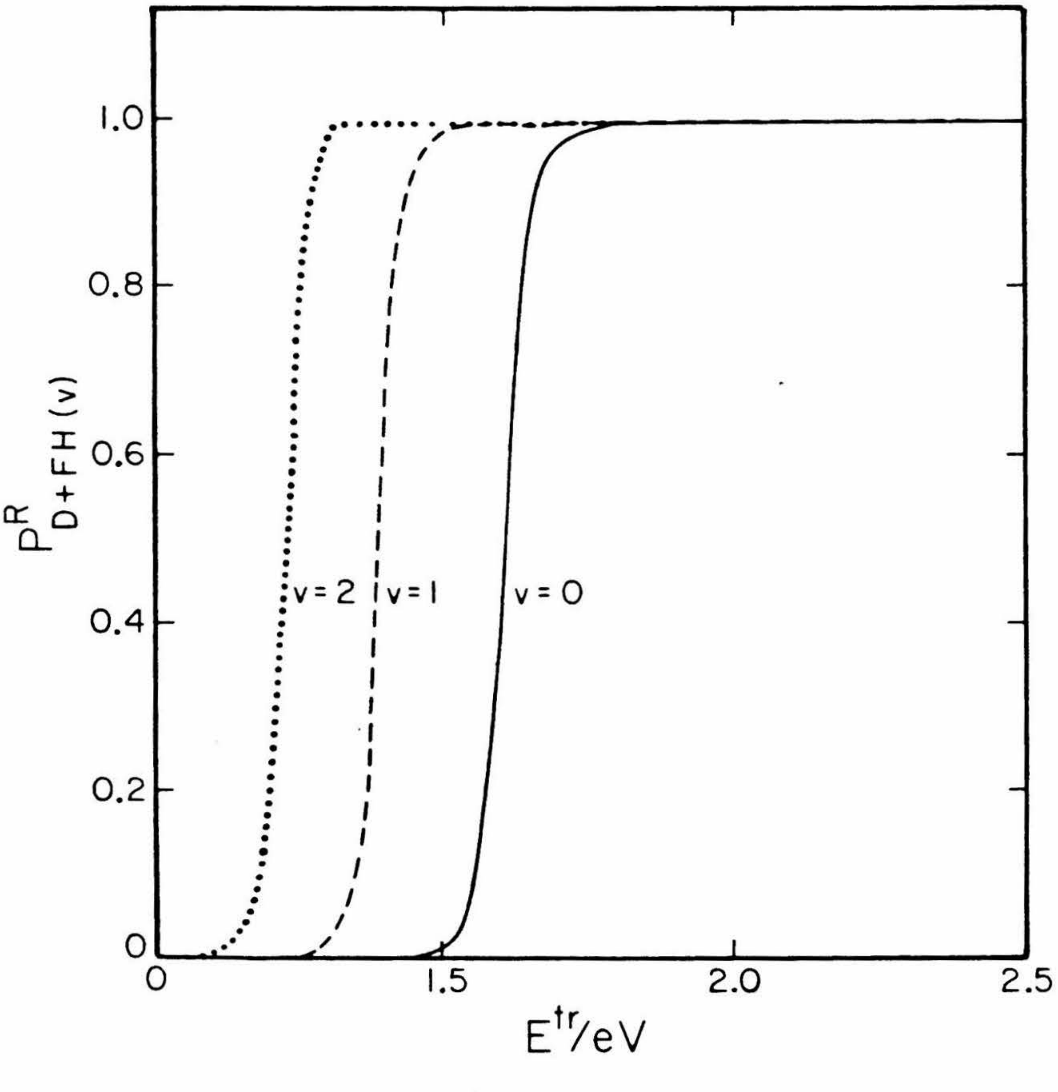

Figure 11

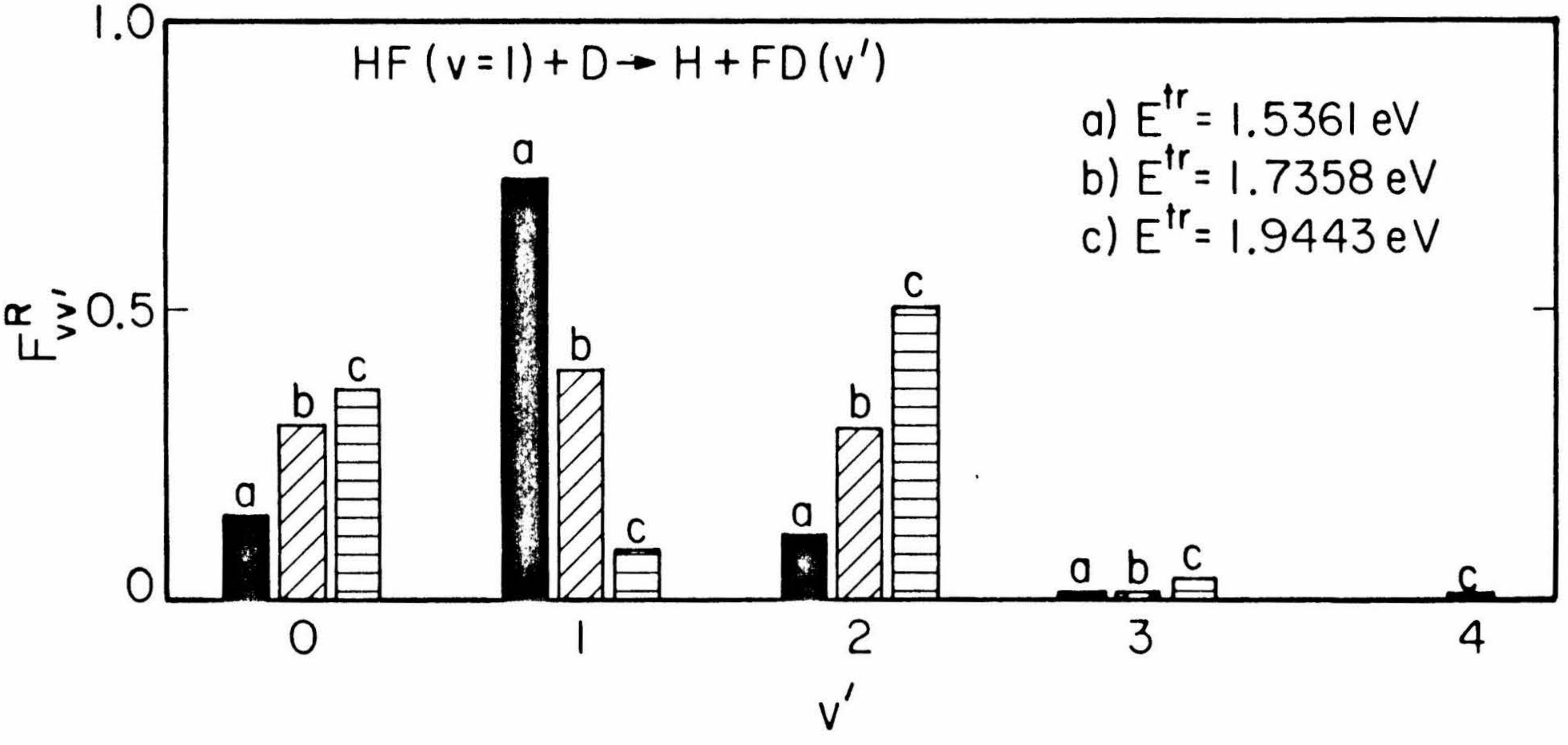
HF (v=1) + D → H + FD (v′)
a) E^{tr} = 1.5361 eV
b) E^{tr} = 1.7358 eV
c) E^{tr} = 1.9443 eV
$F^{R}_{vv'}$
1.0
0.5
0
a
b
c
0
1
2
3
4
v′

Figure 12

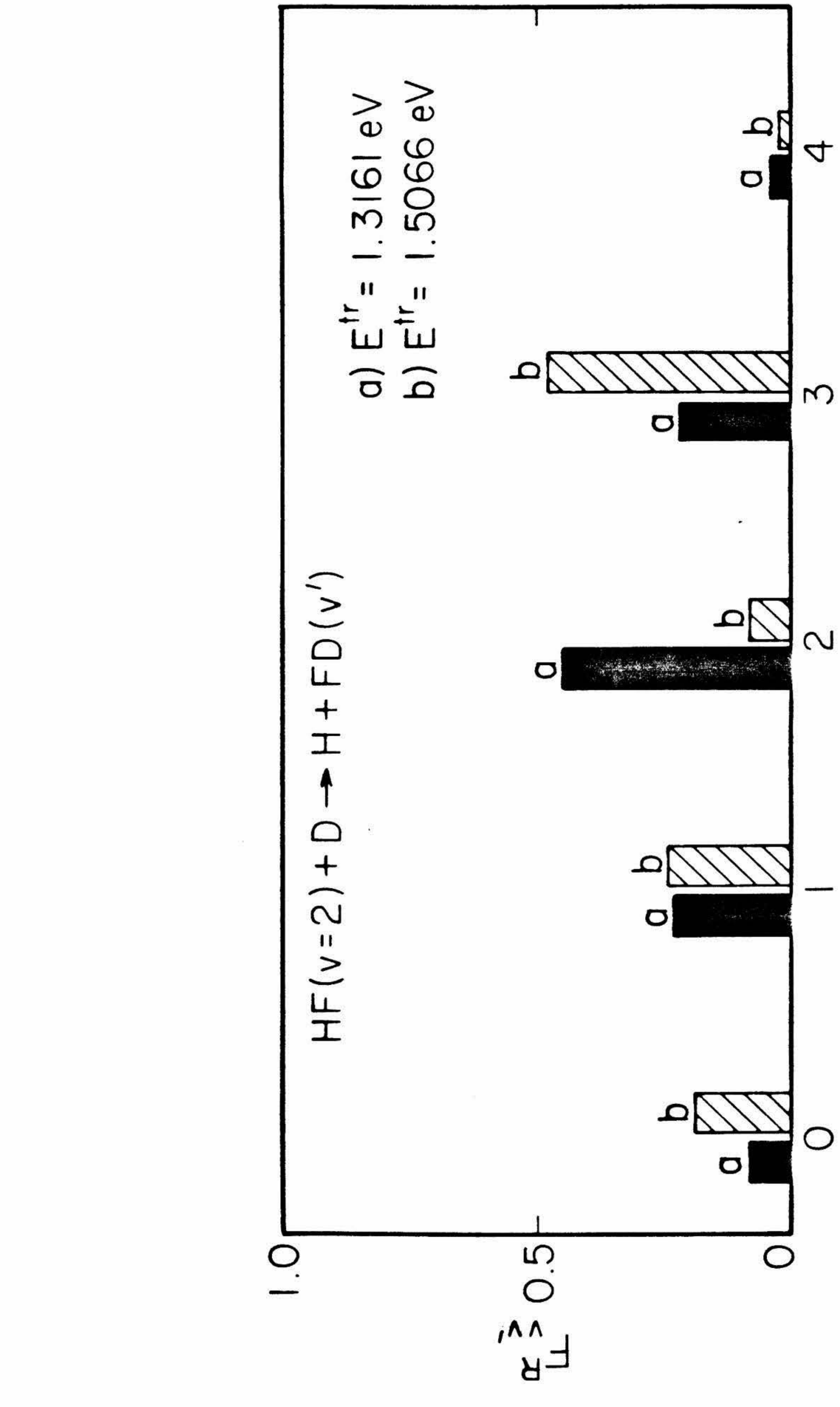

Figure 13

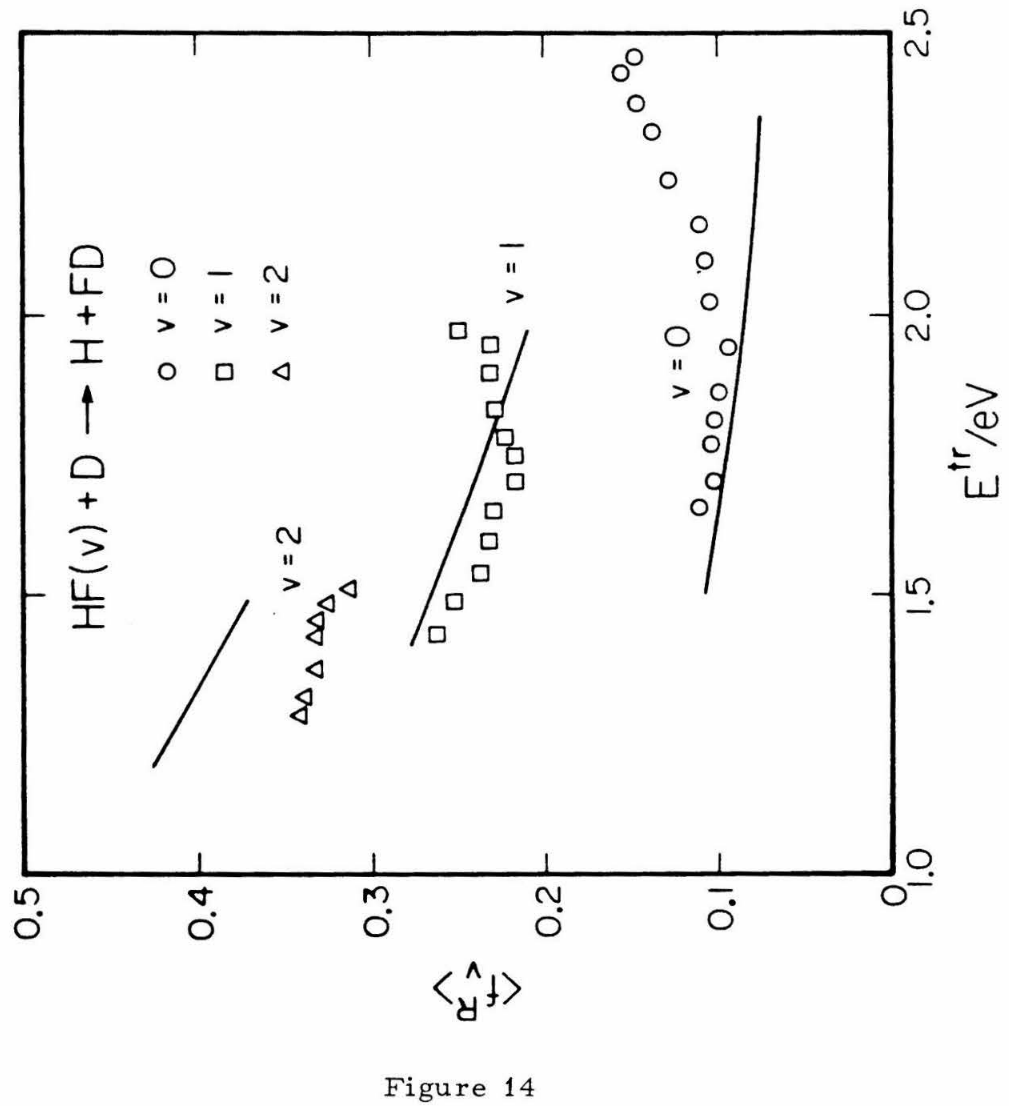

Figure 14

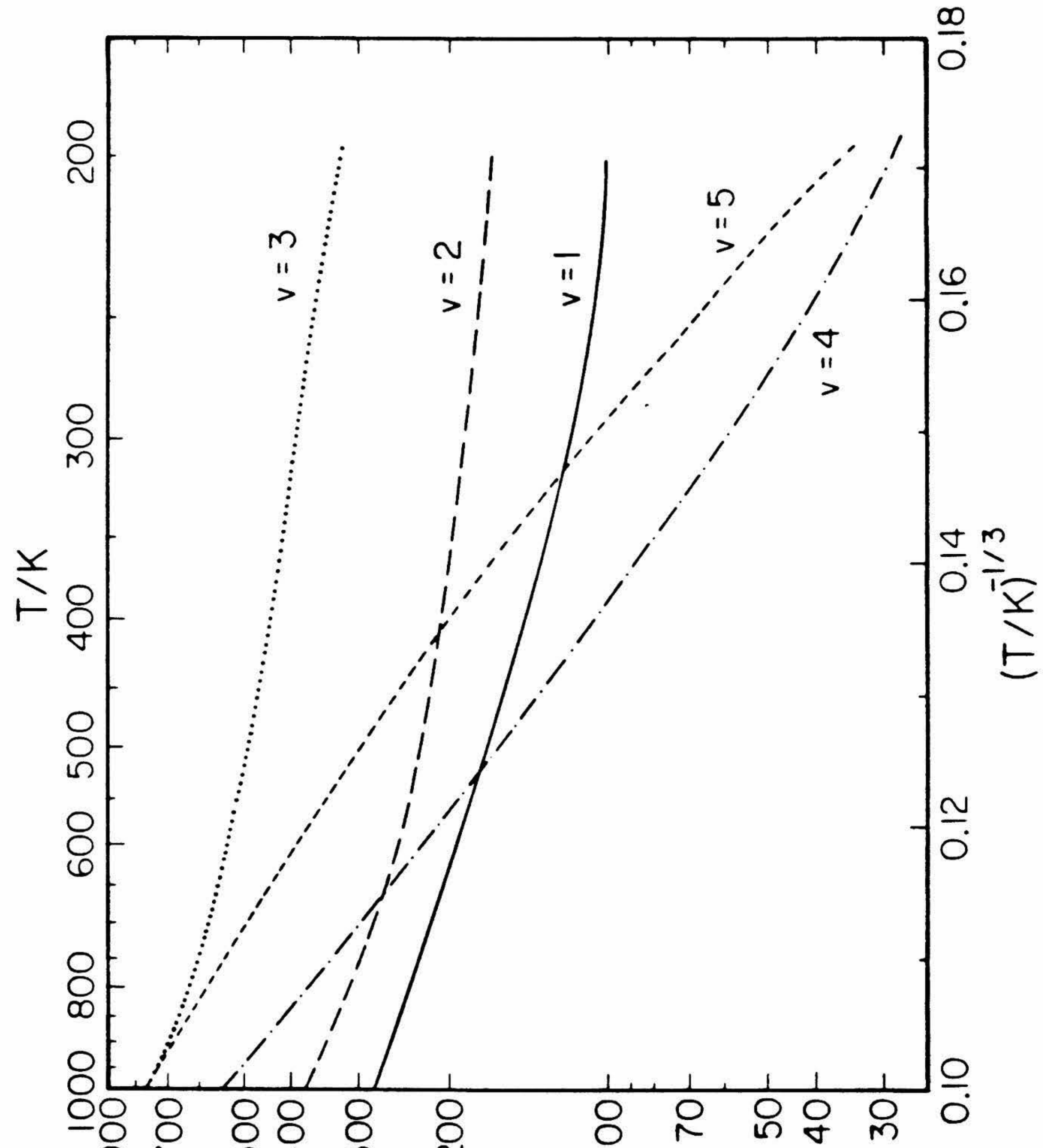
T/K
200
300
400
500
600
800
1000
$k^Z_{v,v-1}(HF + H')/(cm \times molec^{-1} \times sec^{-1})$
1000
900
700
500
400
300
200
100
70
50
40
30
0.10
0.12
0.14
0.16
0.18
$(T/K)^{-1/3}$
v = 3
v = 2
v = 1
v = 5
v = 4

Figure 15

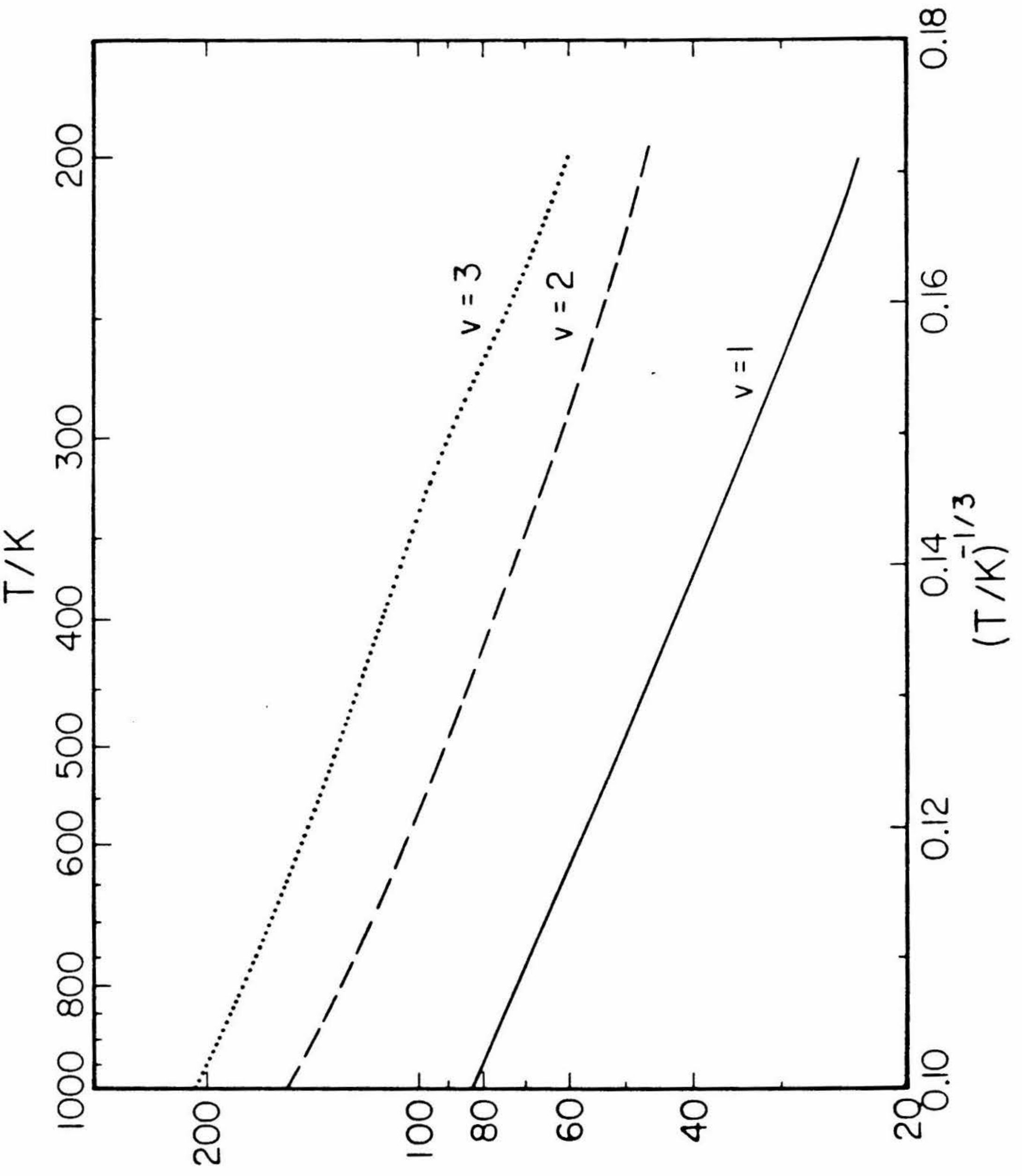
T/K
1000
800
600
500
400
300
200
$k^{N}_{v,v-1}(HF + D)/(cm \times molec^{-1} \times sec^{-1})$
200
100
80
60
40
20
v = 3
v = 2
v = 1
0.10
0.12
0.14
0.16
0.18
$(T/K)^{-1/3}$

Figure 16

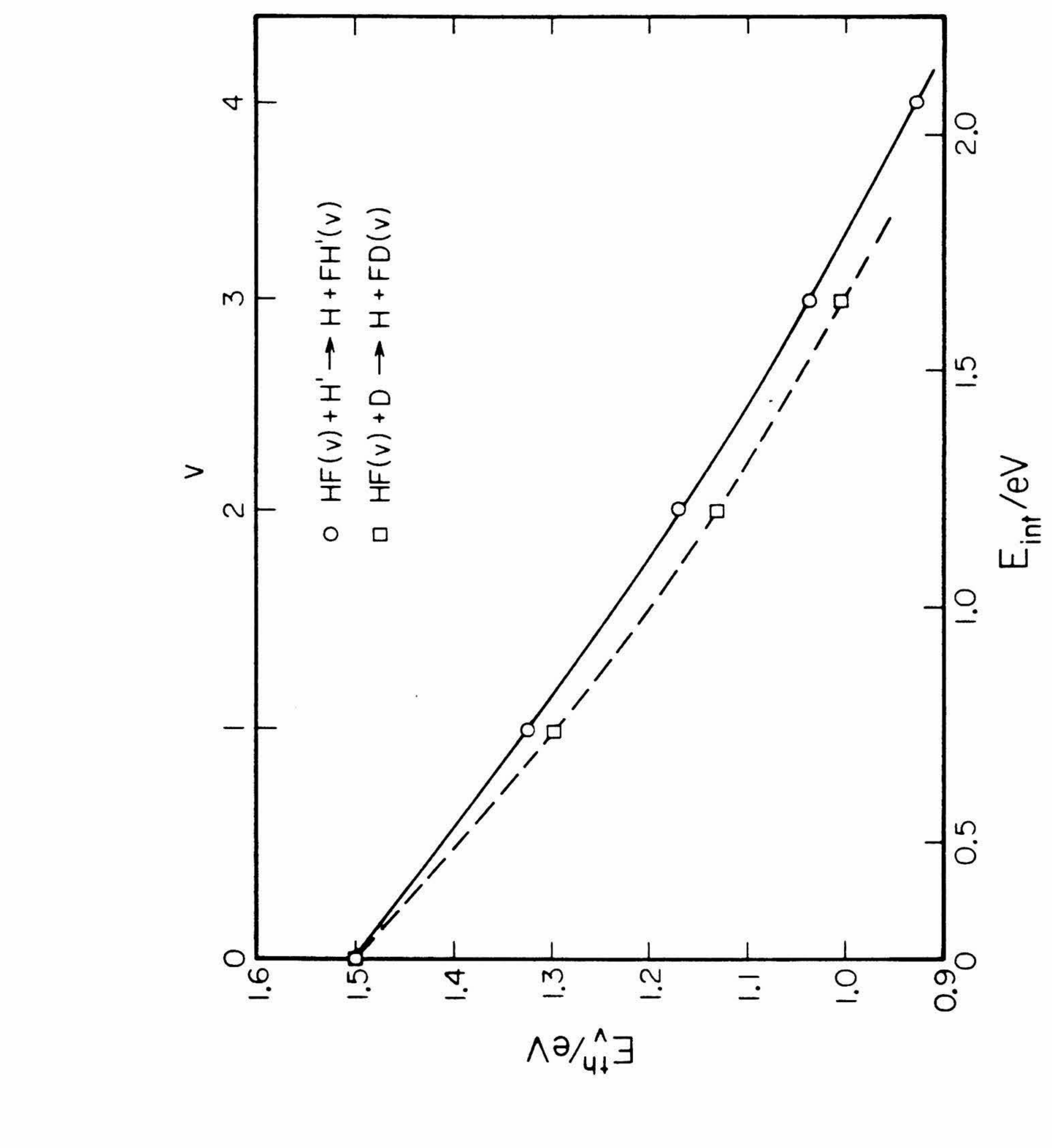
v
0
1
2
3
4
E_{th}^{v}/eV
1.6
1.5
1.4
1.3
1.2
1.1
1.0
0.9
E_{int}/eV
0
0.5
1.0
1.5
2.0
○ HF(v) + H' → H + FH'(v)
□ HF(v) + D → H + FD(v)

Figure 17

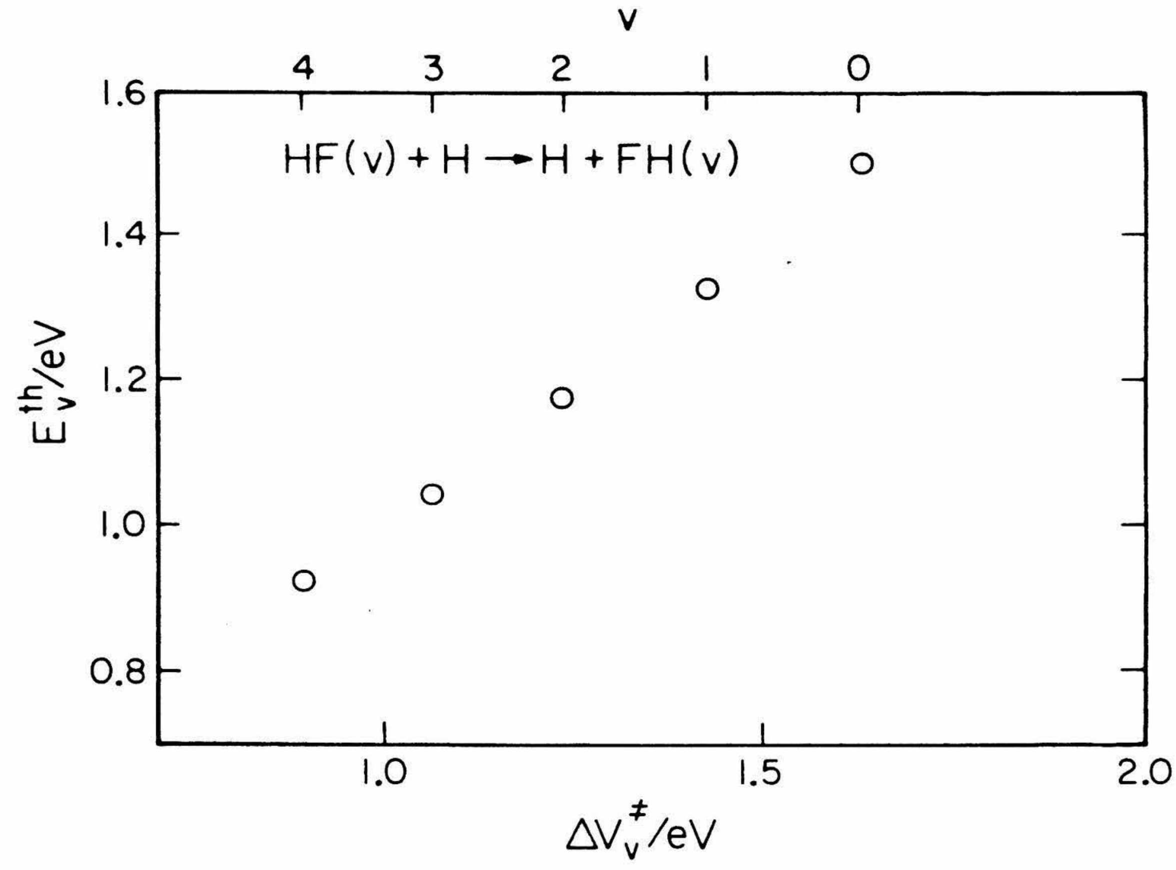

Figure 18

I.3 BARRIER HEIGHT DEPENDENCE OF DYNAMICS IN THE COLLINEAR H + FH(v) AND D + FH(v) SYSTEMS

Barrier Height Dependence of Dynamics in the Collinear H + FH(v) and D + FH(v) Systems.[a)]

Jack A. Kaye[b)], John P. Dwyer[c)], and Aron Kuppermann
Arthur Amos Noyes Laboratory of Chemical Physics[d)]
California Institute of Technology, Pasadena, California 91125

(Received)

Collinear coupled-channel quantum mechanical calculations have been performed on the title systems on potential energy surfaces with barriers to reaction of 1.5, 5, 10, 20, 30, and 40 kcal/mole. We have examined the differences in the dynamics on the different surfaces, emphasizing the rate and mechanism of vibrational deactivation of HF in H + FH(v) collisions and the influence of reagent vibrational excitation on reaction probabilities and product state distributions in the D + FH(v) reaction. The rate of vibrational deactivation decreases as the barrier height is increased for low barrier height surfaces, but becomes relatively insensitive to barrier height at higher barrier heights at the temperatures studied. On the lower barrier surfaces vibrational deactivation occurs mainly in multi-quantum reactive transitions, while for higher barrier surfaces it occurs in single-quantum non-reactive transitions. In the D + FH(v) reaction, reagent vibrational excitation reduces the translational energy threshhold by an amount smaller than the vibrational quantum and can lead to different product state distributions depending on the potential energy surface. Quantum mechanical resonances observed on the low barrier surfaces can be understood by reference to vibrationally adiabatic correlation diagrams.

---

[a] This work was supported in part by a contract (No. F49620-79-C-0187) from the Air Force Office of Scientific Research.

[b] Work performed in partial fulfillment of the requirements for the Ph.D. degree in Chemistry at the California Institute of Technology.

[c] Present Address: Supreme Court of the United States, Washington, D. C. 20543

[d] Contribution No.

I. INTRODUCTION

The dependence of the dynamics of chemical reactions on the potential energy surface governing the motion of the nuclei has been the subject of substantial attention. In a pioneering series of papers, Polanyi and collaborators used the classical trajectory technique to study how the dynamics of the general class of reactions

$$A + BC(v, J) \longrightarrow AB(v', J') + C \tag{1}$$

varied with changes in the potential energy surface (1). Features of particular interest have been how the disposal of energy in exoergic reactions or the usefulness of various forms of internal energy in endoergic reactions depends on the position of the saddle point on the surface. Other workers have also explored the relationship between the potential energy surface and the dynamics obtained from classical mechanical calculations for both reactive and non-reactive processes (2).

For quantum mechanical calculations, such studies have been far fewer in number. As new potential energy surfaces are developed over the years, dynamical calculations are frequently performed, providing information on the sensitivity of dynamics to surface parameters. For example, for the $H + H_2$ system and its D substituted analogs, in exact and approximate quantum calculations (in one, two, and/or three dimensions) (3), surfaces studied include the scaled SSMK(4), the Porter-Karplus (5), and the SLTH (6) ones, among others. For the $F + H_2$ system, a variety of potential energy surfaces, both semi-empirical (7) and ab initio (8) have been used in collinear quantum mechanical calculations (7b, 9). Similar studies have been carried out on the $I + H_2$ (10), $O + H_2$ (11), and $I + HI$ (12) systems, among others.

In most of this work, attention has been focused on the dynamics of chemically reactive processes. If one is to understand the full dynamics of potentially reactive chemical systems, however, one must also understand how the dynamics of non-reactive processes depend on the nature of the assumed potential energy surface. For example, in studying the dynamics of the collisional deactivation of a vibrationally excited molecule (such as that present in a chemical laser system), the quantities most of interest are the rates of vibrational deactivation and the number of quanta transferred . Rabitz and co-workers (13) have studied the sensitivity of energy transfer processes to the nature of the assumed potential energy surface in non-reactive collisions.

In this work we study the dynamics of the collinear systems

$$HF(v) + H' \longrightarrow HF(v') + H' \tag{2a}$$

$$H + FH'(v'') \tag{2b}$$

$$HF(v) + D \longrightarrow HF(v') + D \tag{3a}$$

$$H + FD(v'') \tag{3b}$$

by coupled-channel quantum mechanical calculations on six related potential energy surfaces. These surfaces are identical except for their profile along the minimum energy path, and have barriers of 1.5, 5, 10, 20, 30, and 40 kcal/mole. The first is close to the barrier of the Muckerman V surface (7b) used in a previous collinear quantum mechanical study of these systems (14); the last is closest to the barrier heights indicated by the most recent experiments (15) and also by ab initio calculations (16). The results of the calculation on this surface have been presented separately (17).

In our calculations we will examine the effects of the change of barrier height on various features of the H or D atom induced collisional deactivation of HF(v), including the overall rate of deactivation, the fraction of deactivation occurring by reactive and non-reactive processes, the relative importance of single and multi-quantum transitions, and the temperature dependence of these quantities. We will also consider the general class of reactive processes (2b and 3b) and the role of quantum mechanical resonances on the different surfaces.

The outline of this paper is as follows. In section 2 we discuss potential energy surfaces used in the calculations, and in section 3 we briefly review some important aspects of the calculations performed. The results obtained will be presented in section 4, and their significance will be discussed in section 5. Finally, in section 6 we will summarize the results and conclusions obtained.

II. POTENTIAL ENERGY SURFACES

The potential energy surfaces used in this study are all of the highly flexible rotating Morse-cubic spline form (18), in which the potential energy as a function of the internuclear coordinates R_{AB} and R_{BC} is given by the expression

$$V(R_{AB}, R_{BC}) = D(\theta)((1 - \exp(-\beta(\theta)(\ell_{eq}(\theta) - \ell)))^2 - 1) + D(\theta=0) \quad (4)$$

where

$$\theta = \tan^{-1}((R_{AB} - R_{AB}^{o})/(R_{BC} - R_{BC}^{o})) \quad (5)$$

and

$$\ell = ((R_{AB} - R_{AB}^{o})^2 + (R_{BC} - R_{BC}^{o})^2)^{1/2} \quad (6)$$

(R_{AB}^{o}, R_{BC}^{o}) is the point from which one swings the Morse oscillator, whose parameters are thus functions of the angle ; when $R_{AB} > R_{AB}^{o}$ or when $R_{BC} > R_{BC}^{o}$, the potential is just that of a Morse oscillator. Normally, the point (R_{AB}^{o}, R_{BC}^{o}) is far up the dissociative plateau, that is, both R_{AB}^{o} and R_{BC}^{o} are large. The coordinate system and definition of terms are indicated schematically in figure 1.

The Morse parameters $\ell_{eq}(\theta)$ and $\beta(\theta)$ are given at a small number of values of the swing angle , and a cubic spline interpolation is then performed. A similar interpolation could be performed for $D(\theta)$; however, in this case we assume it to be given by a Gaussian

$$D(\theta) = D(\theta=0) - (A + B\exp(-C(\pi/4 - \theta)^2)) \quad (7)$$

Values of the constants A, B, and C for each of the surfaces used are given in Table 1; values of $\ell_{eq}(\theta)$ and $\beta(\theta)$ have been presented elsewhere (17).

The values of $\ell_{eq}(\theta)$ and $\beta(\theta)$ were obtained by numerically finding their values on the Muckerman V surface (7b) in the exchange channel and then splining together; the values for A, B, and C were first obtained from the Muckerman V surface at 3 values of θ (0°, 22°, and 45°). To increase the barrier height, only parameters B and C in eq. 7 were changed.

For $R_{AB} > R_{AB}^{o}$ (R_{BC} small) or $R_{BC} > R_{BC}^{o}$ (R_{AB} small), the potential energy was taken to be independent of R_{AB} and R_{BC}, respectively. This produced a slight upward shift (~0.0168 kcal/mole) in the bottom of the HF diatomic well relative to its dissociation energy. For use in the calculations reported here, we have constructed surfaces with barrier heights of 1.5, 5, 10, 20, 30, and 40 kcal/mole. We have plotted the 40 kcal/mole barrier surface in the Delves mass scaled coordinate system (19) for the HFH system in figure 2. In figure 3 we display the vibrational energy levels of HF and DF along with the energies of the barriers on the six surfaces used.

III. NUMERICAL ASPECTS

Numerical solution of the Schrödinger equation has been performed by the coupled-channel method of Kuppermann (20). 20 - 24 basis functions were used in these calculations, and unitarity of the scattering matrix was obtained to better than 3% at nearly all energies studied; at most it was obtained to better than 1%. For those calculations where unitarity was not obtained to 3%, we do not include the results in our analysis.

Reactions 2a and 2b were studied in the energy range up to 2.94 eV above the zero-point energy of HF, while reactions 3a and 3b were studied up to 2.45 eV above the HF zero-point energy. The smaller range in the latter calculation was due to the smaller vibrational energy spacing of DF (see figure 3) than HF, which gives rise to more open channels at a given total energy than at the same total energy in the HF + H system.

State-to-state rate constants have been calculated from the transition probabilities obtained in the scattering calculations by the relationship

$$k_{ij}(T) = (2\pi\mu_{a,bc}k_bT)^{-1/2} \int_0^\infty P_{ij}(E^{tr})\exp(-E^{tr}/k_bT)dE^{tr} \tag{8}$$

where P_{ij} is the probability for the transition from state i to state j, E^{tr} is the initial reagent relative translational energy of the collision, $\mu_{a,bc}$ is the reduced mass of the a, bc collision pair, and k_b is Boltzmann's constant.

IV. RESULTS

We have studied a number of aspects of the dynamics of the collinear HFH and DFH systems on six different, but related, potential energy surfaces, and will try to present some of the most important features of our results in this section. We will consider the following questions:

1) What are the relative rates of collisional deactivation of vibrationally excited HF and how do they depend on the surface used and on the reagent vibrational state?

2) How do deactivating processes occur (single vs. multi-quantum, reactive vs. non-reactive) on the different surfaces?

3) How do these quantities vary with temperature?

4) How do the dynamics of the reactive processes (energy thresholds, product vibrational state distribution, effect of reagent vibrational excitation) depend on the surface?

5) What is the nature and magnitude of the isotope effect on going from the HFH to the DFH system?

6) How important are quantum mechanical resonances on the different surfaces, and how do their position and strength vary as the barrier height is increased?

A. VIBRATIONAL DEACTIVATION

The rate of vibrational deactivation varies significantly as the barrier height of the potential energy surface varies. This may be seen in figures 4 and 5, in which the overall rate of vibrational deactivation in the H + FH(v) system is plotted as a function of the barrier height of the surface for v = 1 -5 at 300 and 650 K, respectively. There are three important features of these figures. First, for low barrier height surfaces, the rate of deactivation decreases rapidly as the barrier height of the surface increases. For example, in figure 4 one sees that as the barrier height increases from 1.5 to

10 kcal/mole, the overall deactivation rates decrease by nearly two orders of magnitude. As the barrier height is further increased beyond 10 kcal/mole, however, the deactivation rates no longer continue to decrease; instead, they remain relatively constant. Second, the variation in the deactivation rates with reagent vibrational excitation differs on the low and high barrier surfaces. In the former region, the deactivation rate in general increases as the reagent HF molecule excitation is increased, while in the latter region there appears to be no clear correlation between reagent excitation and deactivation rate. Third, the barrier height at which the transition between low barrier and high barrier behavior occurs is temperature dependent. In comparing figures 4 and 5, for example, we can see that at 300 K the division seems to occur at 10 kcal/mole; at 650 K it occurs at 20 kcal/ mole.

This behavior is also seen to be independent of isotopic substitution. In figure 6 we present a plot of deactivation rates in the HF(v) + D system at 300 K. In this figure we only include FD states whose quantum number v'' is smaller than that of the reagent HF(v) molecule.

We next consider the details of the deactivation process (those features mentioned in item 2 above) in the HF(v) + H system. Plots of the fraction $f_v^{(1)}$ of deactivation occurring by single-quantum transitions as a function of the barrier height of the surface are shown in figure 7 for v = 2-5(for v=1 all deactivation occurs by single quantum transitions) at 300 K. Clearly this quantity varies substantially as the barrier height is increased although when the barrier is above 20 kcal/mole, the fraction for v=2 and 3 is close to unity and thus nearly independent of the barrier height. In general, as the barrier height increases, the importance of single-quantum deactivation increases substantially till on the 40 kcal/mole surface, it accounts for more than 80% of the deactivation, even in collisions of v = 4 and 5.

In figure 8 we plot the fraction f_v^R of deactivation occurring by reactive processes (that is, those of the type 2b rather than 2a defined above) as a function of the barrier height for v = 1 to 5 at 300K. At low barrier heights, reactive deactivation is clearly the rule, as for all initial states considered, over 75% of the deactivation rate on the 1.5 kcal/mole barrier surface occurs by reaction. On high barrier surfaces, the deactivation occurs totally by non-reactive processes. From the arrows in figure 8 showing the vibrational energy of the isolated HF(v) molecule, one can see that the v = 4 and 5 levels of HF already have sufficient energy to overcome any of the barriers studied here. Thus, the absence of reactive deactivation here indicates one of two things: either translational and vibrational energy are so weakly coupled that the latter is not useful in promoting reaction, or that reaction is possible but that it occurs overwhelmingly by a vibrationally adiabatic proces. Examination of state-to-state reaction probabilities indicates that the former explanation must be the correct one, as at all but very high translational energies the vibrationally adiabatic reaction probability is smaller than the deactivating ones. For example, on the 40 kcal/mole surface, just above the opening of the HF(v=4) level, the state-to-state reaction probabilities P_{40}^R and P_{41}^R are over 10^5 times greater than P_{44}^R; at some 0.4 eV above the opening, P_{42}^R is nearly 10^4 times greater than P_{44}^R. Only at translational energies above 1.0 eV does P_{44}^R become the greatest of the reactive probabilities.

While figure 7 gives some feeling as to the importance of multi-quantum transitions, it does not provide an indication of the relative importance of the different possible multi-quantum transitions. To aid in assessing their importance, in figure 9 we plot the average number $\langle \Delta n_v \rangle_{de}$ of vibrational quanta lost in deactivating collisions, both reactive and non-reactive, as a function of the barrier height for v = 2 - 5 at both 300 K (solid lines) and 1000 K (dashed lines). This quantity is given by the formula

$$\langle \Delta n_v \rangle_{de} = \frac{\sum_{v'=0}^{v-1} (v - v')k_{vv'}^{T}}{\sum_{v'=0}^{v-1} k_{vv'}^{T}} \tag{9}$$

where $k_{vv'}^{T}$ is the total (sum of reactive and non-reactive) deactivation rate constant for the $v \longrightarrow v'$ transition. Since the rate constants vary with temperature, so will $\langle \Delta n_v \rangle_{de}$. For a given reagent vibrational level v, the maximum value this quantity may have is also v, as would be the case when all deactivation occurred by a v-quantum process, in which only ground state molecules were formed.

From figure 9 we see four main features. First, this average number of quanta lost is always less than its maximum value, by an amount ranging from almost 4 quanta for v = 5 on the 40 kcal/mole barrier surface to 1/2 quanta for v = 2 on the 1.5 kcal/mole barrier surface. Second, this quantity decreases as the barrier height of the surface increases, till it is very close to 1 for all reagent states on the 30 kcal/mole barrier surface. Third, this quantity is strongly temperature dependent, with the temperature dependence in the 300 - 1000 K range having its greatest value for the intermediate (10 - 20 kcal/mole) barrier surfaces. Fourth, this quantity increases with v. Thus, we see that on low barrier surfaces, not only are multi-quantum transitions likely, but those multi-quantum transitions which transfer more than 2 quanta of vibrational energy are quite likely.

Finally, we wish to consider the temperature dependence of the rate constants for single-quantum deactivation as a function of the reagent vibrational state and the barrier height of the potential energy surface. To show this temperature dependence, we calculate

Arrhenius activation energies ($E_a^{v,v-1}$) for these rate constants in the high temperature (700 - 1000 K) and plot them as a function of reagent internal energy in figure 10. These are the slopes of the corresponding Arrhenius plots (logarithm of rate constant vs. inverse temperature), which have been found normally to be reasonably linear in the low (200 - 400 K) and high (700 - 1000 K) temperature regions, but curved in between. The activation energies calculated increase as the barrier height of the potential energy surface increases and, in general, decrease as the vibrational excitation of the reagent increases. This decrease is far less than the increase in internal energy, however. For example, the activation energy on the 40 kcal/mole barrier surface decreases only by some 16 kcal/mole as one adds over 40 kcal/mole of internal energy. This is another manifestation of the relative inefficiency of vibrational energy in promoting reaction.

B. REACTIVE PROCESSES

In this section we will examine a few aspects of the dynamics of reactive processes in the HF(v) + D system. This system is a better one for experimental study than the HF(v) + H system, as the reactive and non-reactive processes can be easily differentiated. In fact, experiments on this system taking advantage of the mass difference between the H and D atoms have already been performed (15). The aspects of the dynamics of the reactive processes which we will mainly consider are the gross features of the reaction probability and the vibrational state distribution of the DF product formed in the reaction.

We examine the threshold region of the total reaction probability for reaction of ground state HF with D atoms on the six surfaces in figure 11. In this figure, we plot the reaction probability vs. energy curves only in the threshold region, in which the probability increases rapidly and smoothly from zero to one. We also indicate in the figure the translational energy equal to the classical barrier height of the six surfaces studied. Note that this quantity is measured with respect to the bottom of the HF well, while the translational energy is measured with respect to the HF zero-point energy. The important points to be learned from the figure are as follows. First, for all surfaces the reaction probability does rise smoothly from zero to one over a fairly narrow range of energy. Second, the threshold energy (the energy at which the probability of reaction first becomes large, say 0.02) is always smaller than the classical barrier height by an amount which increases as the barrier height increases (some 0.04 eV for the 1.5 kcal/mole barrier surface to some 0.23 eV for the 40 kcal/mole barrier surface). Third, the width of the threshold region also increases as the barrier height increases (from some 0.03 eV for the 1.5 kcal/mole barrier surface to some 0.25 eV for the 40 kcal/mole barrier surface).

In figure 12 we plot the total reaction probability for reaction of HF(v=1) with D atoms vs. energy in the threshold region on the six surfaces. While this plot is fairly similar to that in figure 11, there are two major differences. First, the probability vs. energy curves have shifted to lower energy. This is reasonable, as the vibrational energy should be at least partially effective in reducing the translational energy threshold for reaction. One sees that its effectiveness is limited, however, as the translational energy threshold has been reduced by no more than 0.2 eV on vibrational excitation, even though the vibrational quantum is 0.49 eV. Second, the behavior of the probability vs. energy curves at the high energy end of the threshold region is different than it is in figure 11 for the lower barrier (1.5, 5, 10 kcal/mole) surfaces. In these cases, we see that the reaction probabilities do not stay near unity as they do in figure 11; instead, they reach a maximum somewhat less than unity and then decrease with increasing energy. On the higher barrier surfaces, behavior is similar to that in figure 11. We will discuss later possible explanations for the more complicated nature of the dynamics on the low barrier surfaces.

The next aspect of the reactive processes which we will consider is the vibrational state distribution of the DF formed in the reaction, and how it varies with the barrier height of the potential energy surface and with reagent vibrational excitation. The quantity which we will frequently consider in order to avoid having to look at the entire product state distribution is the average fraction $\langle f_v \rangle$ of product energy going into product vibration

$$\langle f_v \rangle = \frac{\sum_{v'=0}^{v_{max}} E_{v'} P_{vv'}^{R}}{\sum_{v'=0}^{v_{max}} P_{vv'}^{R}} \tag{10}$$

In figure 13 we plot for energies at which the reaction probability is appreciable (more than 60%) this quantity for reactions of ground state HF on the 1.5, 20, and 40 kcal/mole barrier surfaces. From this figure we see that the barrier height of the surface has a major influence not only on the translational energy threshhold for reaction, but also on the product state distribution. As the barrier height increases, there is less vibrational excitation of the DF product. We also note that $\langle f_v \rangle$ is a much smoother function of the energy for the higher barrier surfaces (20, 40 kcal/mole) than it is for the low (1.5 kcal/mole) barrier surface. Some of the lack of smoothness in the plot for that surface can be attributed to at most very small translational energy thresholds for vibrational excitation into newly opened states. The arrows on the abscissa of figure 13 indicate the energies at which DF product states become open, and we see that the curve for the 1.5 kcal/mole barrier surface rises rapidly at almost identically those energies. This is particularly true at the energies where the DF(v=1, 2, and 3) state become open. No such rapid increases are seen for $\langle f_v \rangle$ on the high barrier surfaces, suggesting that reaction to higher vibrational energy product states occurs with a large translational energy threshold.

To determine how reagent vibrational excitation influences the vibrational state distribution of the DF product, we examine $\langle f_v \rangle$ for v = 0-4 at a variety of energies on the different potential energy surfaces. The values obtained are given in Table 2. In this table we only consider those combinations of potential energy surface, energy, and reagent vibrational state for which the reaction probability has gone through its initial rise; on the high barrier surfaces we will only be able to examine the few lowest reagent vibrational states, as the translational energy thresholds for reaction are too great for reaction to occur in the energy range studied.

From the data in table 2, we can see that the influence of reagent vibrational excitation on the product state distribution depends strongly on the total energy and on the barrier height of the potential surface.

On high barrier surfaces, reagent vibrational excitation leads to a higher fraction of the product energy going into vibration, whereas on low barrier surfaces, it leads to no particular behavior. In a number of cases one actually sees less product vibrational excitation in collisions of vibrationally excited reagents (see for example the 2.410 eV results on the 1.5 kcal/mole barrier surface and the 2.002 eV results on the 5 kcal/mole barrier surface). On the intermediate barrier surfaces, one can see both types of behavior. For example, on the 10 kcal/mole barrier surface, reaction of vibrationally excited HF leads to a more highly excited DF distribution than does that of ground state HF at low energy (1.186 eV), but leads to a less highly excited one at higher energy (2.410 eV).

We can also obtain additional information about how the product state distribution depends on the potential energy surface from the data in table 2, especially for reactions of vibrationally excited molecules (in figure 13 we considered only reaction of ground state species). It appears that this dependence is itself energy dependent. At the lowest energy considered (1.186 eV), while $\langle f_0 \rangle$ decreases as the barrier height is increased, $\langle f_1 \rangle$ increases. At most other combinations of energy and reagent vibrational state, $\langle f_v \rangle$ is essentially independent of the barrier height (or more precisely, depends on the barrier height in no easily recognizable way) on low barrier height surfaces, but decreases substantially as the barrier height further increases.

The distribution of the DF product states for reaction from HF(v= 0, 1, and 2) at a total energy of 2.410 eV is shown in figure 14 in the form of histogram plots. In these plots, the height of the bar is proportional to the reaction probability to the indicated product state. We note here the most important features of these plots. For the ground reagent state, as the barrier height increases, the product state distribution as a whole shifts to lower vibrational states, until on the 40 kcal/mole barrier surface, 75% of the reaction occurs by a vibrationally adiabatic process. On the low barrier surfaces the product state distribution is quite broad, being spread out over 3-5 product states. For the v=1 reagent state, the product distribution also shifts to lower vibrational states as the barrier height increases, but the shift is not as dramatic as for ground state reactions. This is true for two reasons. First, on the 40 kcal/mole barrier surface the reaction is primarily vibrationally adiabatic; hence the distribution for that surface is peaked about v=1 and not about v=0 as in the ground state reaction. Second, the product state distributions on the low barrier surfaces are wider than for ground state reaction, so that there is appreciable population of the DF(v'=2) state on all surfaces. An interesting feature is that at this energy, the probability of vibrationally adiabatic reaction on the 30 kcal/mole surface is significantly smaller than the probability for reaction with an increase or decrease of one in the vibrational quantum number. Thus, one cannot simply assume that the reaction is vibrationally adiabatic on high barrier surfaces at all energies. The product state distributions in reactions of HF(v=2) are even broader than those for reactions of HF(v=1), and are also somewhat irregular (they are not smoothly peaked about one quantum state). We note that some of the state-to-state reaction probabilities on the low barrier surfaces vary fairly rapidly with energy at high energy; it is this variation that gives rise to the irregular structure of the plot of $\langle f_0 \rangle$ in figure 13.

C. QUANTUM MECHANICAL RESONANCES

The existence of low energy resonances in the collinear HFH system (Muckerman V surface) has been noted previously (14), and here we consider some aspects of the resonance structure on the surfaces used. We are particularly interested in how the resonances change in position and intensity as the barrier height is raised. In figures 15-18 we present plots of state-to-state probabilities of reaction 3b on the 1.5, 5, 10, and 20 kcal/mole barrier surfaces, respectively, in the region of energy containing the threshold for reaction from v = 0 and continuing up some 0.4 eV above that. The plots strongly suggest the existence of a resonance in these systems. The resonance is strongest on the 1.5 kcal/mole barrier surface, and is substantially weaker on the 10 kcal/mole barrier surface. On the 20 kcal/mole barrier surface it has almost totally disappeared; it is seen only by the formation of a small shoulder in the P_{00}^{R} and P_{01}^{R}

curves. There is no minimum in P_{00}^{R} as there is on each of the lower barrier surfaces. It is also interesting to consider the effect of isotopic substitution on the strength of the resonance. To do this, we plot state-to-state probabilities for reaction 2b on the 10 kcal/mole barrier surface in figure 19. It is quite clear that the resonance is much stronger in this system than it is in the D substituted system. There are two other interesting features of figure 19. First, there is a small dip in the reaction probability shortly after it first reaches unity. At higher energies the probability does return to one, and stays there until the resonance. Second, the resonance occurs at a translational energy of 0.735 eV, which is some 0.1 eV greater than the energy of the weaker and broader resonance in the D + FH system. We will discuss these features of the dynamics in the ensuing discussion section.

V. DISCUSSION

The dynamics of the collinear HFH and DFH systems are shown to depend substantially on the barrier height of the potential energy surface used. As the barrier height is increased a number of important changes in the dynamics take place. In collisions of vibrationally excited HF molecules, the overall rate of vibrational deactivation of the HF decreases for a while as the barrier height increases; further increase of the barrier height makes little change in the deactivation rate. The value of the barrier height at which this takes place is a function of temperature (increasing as the temperature is increased). On low barrier surfaces, the bulk of the deactivation occurs by reactive (and multi-quantum) processes; on high barrier surfaces, it occurs by non-reactive (and single-quantum) processes. On the lowest barrier surfaces (1.5 and 5 kcal/mole), what non-reactive deactivation there is occurs from both single and multi-quantum transitions at 300 K; the higher the reagent vibrational state, the greater the contribution of multi-quantum non-reactive deactivation processes. On the highest barrier surfaces (30 - 40 kcal/mole), reactive deactivation occurs mainly by multi-quantum transitions at 300 K, for example two quantum processes in collisions of HF(v=3) with H and 3 and 4 quantum ones in collisions of HF(v=5) + H. We have shown elsewhere (17) that as the temperature increases, the relative importance of single quantum reactive deactivating processes increases. On the highest barrier surface studied (40 kcal/mole) the deactivation of vibrationally excited HF can be thought of, to a good approximation, as occurring entirely in single-quantum non-reactive processes.

On this class of surfaces, vibrational energy is not spectacularly effective at promoting reaction. This is seen in two ways: the fairly small decrease (0.10 to 0.22 eV) in translational thresholds for reaction on the moderate and high barrier surfaces to the vibrational quantum (0.49 eV), and the calculation of large activation energies for reactive single-quantum deactivation processes at high temperatures (700 - 1000 K). Elsewhere, we have shown that this partial effectiveness of vibrational energy can be explained on the 40 kcal/mole surface by a vibrationally adiabatic model (17). The feature of the potential energy surface which is greatly responsible for this partial effectiveness is the relative narrowness of the reaction channel in the saddle point region (see figure 2). This narrowness produces a large vibrational frequency for symmetric stretch motion at the saddle point, meaning that the vibrationally adiabatic barriers will be fairly large, even when there are a few quanta of vibrational excitation.

For the surfaces with low or only moderate barriers, a vibrationally adiabatic model provides useful insight into the dynamics of the reaction. In figure 20 we plot a vibrationally adiabatic correlation diagram for the DFH reaction on the 1.5 kcal/mole surface. In this figure, the energy $V_n(s)$ of the vibrational state n everywhere along the reaction coordinate s is plotted. We also plot the energy $V^{mep}(s)$ along the minimum energy path. In this case, one can see that there are wells in the vibrationally adiabatic correlation diagram for all reagent states, and the wells become deeper as the vibrational state increases. Since it is known that wells in the vibrationally adiabatic correlation diagram can lead to reactive scattering resonances (21), the existence of resonances in this system is not unexpected. Indeed, in figure 15 we see a very strong resonance in the reaction probability P_{00}^R at $E_0 = 0.3$ eV. We indicate this energy on figure 20 with a dotted line. The correlation between resonances and bound states of the wells in the vibrationally adiabatic correlation diagram is obvious. For higher vibrational states the wells are quite deep and wide, suggesting that large numbers of bound states of the curves might exist, producing numerous resonances and hence quite complicated dynamics. We also note that the curves for the different states come quite close to each other, suggesting that crossing from one to another should occur fairly easily, especially between states with n greater than 1.

If this picture is correct, it must explain both the decrease in resonance intensity as the barrier height is increased and the greater strength and higher energy of the resonance in the 10 kcal/mole barrier surface for H + FH than for D + FH. In figure 21 we present the vibrationally adiabatic correlation diagram for the DFH system on the 10 kcal/mole barrier surface. The main differences between this figure and figure 20 are the absence of the small well in the n=0 curve and the much smaller depth of the well in the n=1 curve. Because of this small well depth, the resonance is expected to be substantially broadened. The vibrationally adiabatic correlation diagram for the HFH system on the 10 kcal/mole barrier surface is shown in figure 22. As in figure 20, the energy of the resonance is indicated by a dotted line. We note two major differences between figures 21 and 22. First, in the HFH system, the well in the v=1 curve is fairly deep (~0.1 eV); the resonance energy is seen to lie about halfway between the bottom and top of the well. Second, the vibrationally adiabatic correlation diagram curves for HFH are symmetric about s = 0. Thus, the formation of a flat shoulder-like area on the curves, such as that seen for n = 1 in figure 21, cannot occur in the HFH case; any well must be symmetric about the saddle point. The greater depth of the well in the HFH case than for the DFH one is responsible for the greater strength and smaller width of the resonance in the former system. Because the vibrational frequencies near the saddle point are greater for HFH than they are for DFH, the curves in the vibrationally adiabatic correlation diagram for HFH will be at higher energy in the saddle point region than are those for DFH. Thus, the vibrationally adiabatic correlation diagrams produce the correct dependence of the resonance strength and energy on isotopic substitution.

VI. CONCLUSIONS

On the basis of the scattering calculations performed, we are able to answer the questions posed at the beginning of section 4 about the dynamics of the collinear HFH and DFH systems and how those dynamics depend on the barrier height of the potential energy surface used. We briefly summarize what we have learned in regard to each question.

1) The relative rates of collisional deactivation of vibrationally excited HF decrease substantially with increasing barrier height for small barrier height surfaces; on larger barrier surfaces they are relatively independent of the barrier height. The barrier height at which this transition occurs increases with temperature.

2) On low barrier surfaces vibrational deactivation occurs primarily by reactive multi-quantum processes, while on high barrier surfaces it occurs primarily by non-reactive single-quantum processes.

3) Vibrational deactivation rates increase with temperature. On the high barrier surfaces the rate of reactive deactivation increases with temperature much more rapidly than that of non-reactive deactivation. As the temperature increases, multi-quantum deactivations increase in importance.

4) As the barrier height of the surface increases, both the translational energy threshold for reaction increases and the average fraction of energy going into product vibration decreases. On the high barrier surfaces reagent vibrational excitation leads to a higher fraction of energy going into product vibration; on the low-barrier surfaces this is not always true.

5) The gross features of the non-reactive dynamics are not affected by isotopic substitution; the reactive dynamics differ substantially in their resonance behavior. This difference may be under-

stood in terms of the vibrationally adiabatic correlation diagram for the HFH and DFH systems.

6) Quantum mechanical resonances are strongest on the low barrier surfaces and significantly weaker or absent on the higher barrier ones. They move to higher energy as the barrier height of the surface increases. Consideration of the vibrationally adiabatic correlation diagram helps one understand this dependence.

ACKNOWLEDGMENTS

The calculations reported here were performed on the IBM 370/158 computer of Ambassador College, Pasadena, California, for which we express our appreciation. Additional calculations were performed on the Dreyfus-NSF Theoretical Chemistry Computer at Caltech, which was funded through grants from the Camille and Henry Dreyfus Foundation, the National Science Foundation (Grant No. CHE78-20235), and the Sloan Fund of the California Institute of Technology.

REFERENCES

1. J. C. Polanyi and J. L. Schreiber, in: Kinetics of Gas Reactions (Vol. VIA, Physical Chemistry, an Advanced Treatise), ed. W. Jost (Academic Press, New York, 1974) pp. 383-487 and references therein.
2. J. T. Muckerman, in: Theoretical Chemistry, Advances and Perspectives, Vol. 6A, ed. D. Henderson (Academic Press, New York, 1981), pp. 1-77.
3. D. G. Truhlar and R. E. Wyatt, Ann. Rev. Phys. Chem. 27, 1 (1976); E. B. Stechel, R. B. Walker, and J. C. Light, in: Proceedings of the CECAM Reactive Scattering Workshop, Orsay, France 1977; R. B. Walker, E. B. Stechel, and J. C. Light, J. Chem. Phys. 69, 2922 (1978); M. Baer, V. Khare, and D. J. Kouri, Chem. Phys. Lett. 68, 378 (1979); J. M. Bowman and K. T. Lee, Chem. Phys. Lett. 64, 291 (1979); J. Chem. Phys. 72 , 5071 (1980); D. C. Clary and J. N. L. Connor, Chem. Phys. 48, 175 (1980); Y. Y. Yung, B. H. Choi, and K. T. Tang, J. Chem. Phys. 72, 621 (1980); J. C. Sun, B. H. Choi, R. T. Poe, and K. T. Tang, J. Chem. Phys. 73, 6095 (1980); A. Kuppermann, J. A. Kaye, and J. P. Dwyer, Chem. Phys. Lett. 74, 257 (1980); J. Römelt, Chem. Phys. Lett. 74, 263 (1980).
4. I. Shavitt, R. M. Stevens, F. L. Minn, and M. Karplus, J. Chem. Phys. 48, 2700 (1968); a simple fit to this potential energy surface has been outlined in D. G. Truhlar and A. Kuppermann, J. Chem. Phys. 56, 2232 (1972).
5. R. N. Porter and M. Karplus, J. Chem. Phys. 40, 1105 (1964).
6. P. Siegbahn and B. Liu, J. Chem. Phys. 68, 2457 (1978); D. G. Truhlar and C. J. Horowitz, J. Chem. Phys. 68, 2466 (1978).

7. a) J. T. Muckerman, J. Chem. Phys. 56, 2997 (1972); b) G. C. Schatz, J. M. Bowman, and A. Kuppermann, J. Chem. Phys. 63, 674 (1975).

8. C. F. Bender, P. K. Pearson, S. V. O'Neil, and H. F. Schaefer III, J. Chem. Phys. 56, 4626 (1972).

9. J. N. L. Connor, W Jakubetz, and J. Manz, Mol. Phys. 35, 1301 (1978); G. C. Schatz, J. M. Bowman, and A. Kuppermann, J. Chem. Phys. 58, 4023 (1973).

10. J. C. Gray, D. G. Truhlar, L. Clemens, J. W Duff, F. M. Chapman, Jr., G. O. Morrell, and E. F. Hayes, J. Chem. Phys. 69, 240 (1977).

11. D. C. Clary, J. N. L. Connor, and C. J. Edge, Chem. Phys. Lett. 68, 154 (1979).

12. J. A. Kaye and A. Kuppermann, Chem. Phys. Lett. 77, 573 (1981); J. Manz and J. Römelt, Chem. Phys. Lett. 81, 179 (1981).

13. J.-T. Hwang and H. Rabitz, J. Chem. Phys. 70, 4609 (1979); L. Eno and H. Rabitz, J. Chem. Phys. 72, 2314 (1980); L. A. Eslava, L. Eno, and H. Rabitz, J. Chem. Phys. 73, 4998 (1980).

14. G. C. Schatz and A. Kuppermann, J. Chem. Phys. 72, 2737 (1980).

15. F. E. Bartoszek, D. M. Manos, and J. C. Polanyi, J. Chem. Phys. 69, 933 (1978).

16. C. F. Bender, B. J. Garrison, and H. F. Schaefer III, J. Chem. Phys. 62, 1188 (1975); P. Botschwina and W. Meyer, Chem. Phys. 20, 43 (1977); W. R. Wadt and N. W. Winter, J. Chem. Phys. 67, 3068 (1977); A. F. Voter and W. A. Goddard III, J. Chem. Phys. 75, 3638 (1981).

17. J. A. Kaye, J. P. Dwyer, and A. Kuppermann, manuscript in preparation.

18. J. M. Bowman and A. Kuppermann, Chem. Phys. Lett. 34, 523 (1975).

19. L. M. Delves, Nucl. Phys. 9, 391 (1959); 20, 275 (1960).

20. A. Kuppermann, in: Potential Energy Surfaces in Chemistry, ed. W. A. Lester, (U. Calif., Santa Cruz, August 1970), pp. 121-9; in: Abstracts of Papers VII International Conference on the Physics of Electronic and Atomic Collisions (North-Holland, Amsterdam, 1971), pp. 3-5; in: Theoretical Chemistry, Advances and Perspectives, Vol. 6a, ed. D. Henderson, (Academic Press, New York, 1981), pp. 79-164.

21. S. Latham, J. F. McNutt, R. E. Wyatt, and M. Redmon, J. Chem. Phys. 69, 3746 (1978).

Table 1. Parameters for Minimum Energy Path (Eq. 7)

Surface Barrier kcal/mole	A kcal/mole	B kcal/mole	C radians^{-1}
1.5	0.01681	1.4832	1.3434
5	0.01681	4.9832	20.955
10	0.01681	9.9832	25.268
20	0.01681	19.983	29.575
30	0.01681	29.983	32.093
40	0.01681	39.983	33.879

Table 2. $\langle f_v \rangle$ for Different Energies, Reagent Vibrational States, and Potential Energy Surfaces

		E/eV				
Surface[a]	v[b]	1.186	1.594	2.002	2.410	2.655
1.5	0	0.555	0.652	0.716	0.692	0.705
	1	0.259	0.532	0.583	0.549	0.530
	2	-[c]	0.637	0.461	0.511	0.552
	3	-	-	0.501	0.460	0.554
	4	-	-	-	0.394	0.480
	5	-	-	-	-	0.585
5	0	0.494	0.543	0.627	0.647	NA[d]
	1	0.350	0.378	0.504	0.513	NA
	2	-	0.415	0.457	0.488	NA
	3	-	-	0.447	0.475	NA
	4	-	-	-	0.604	NA
10	0	0.357	0.473	0.508	0.620	0.648
	1	0.508	0.433	0.377	0.507	0.528
	2	-	0.399	0.381	0.477	0.492
	3	-	-	0.465	0.455	0.485
	4	-	-	-	-	0.521
	5	-	-	-	-	0.621
20	0	0.159	0.222	0.330	0.412	0.456
	1	-	0.348	0.344	0.422	0.448
	2	-	-	0.335	0.401	0.444
	3	-	-	-	0.434	0.427
	4	-	-	-	-	0.522
30	0	-	0.116	0.149	0.233	NA
	1	-	-	0.267	0.300	NA
	2	-	-	-	0.379	NA
40	0	-	-	0.107	0.112	0.143
	1	-	-	-	0.230	0.240
	2	-	-	-	-	0.332

a) Number indicated is the barrier height of the potential energy surface in kcal/mole

b) Reagent Vibrational State

c) There is insufficient (below ~ 60%) reaction for this combination of potential energy surface, reagent vibrational state and total energy

d) Calculations performed on this potential energy surface for this energy gave scattering matrices which were not unitary to within 3% so we did not use the results (NA = not available)

FIGURE CAPTIONS

Figure 1. Schematic diagram of coordinate system for rotating Morse-cubic spline potential energy surface.

Figure 2. Potential energy surface for the collinear H + FH system on the 40 kcal/mole barrier surface in the mass-scaled Delves coordinate system. Equipotentials are drawn every 0.3 eV from 0.3 eV with respect to the bottom of the HF well up to a maximum of 3.0 eV. The minimum energy path is indicated by a dashed line; the saddle point is marked by an "x".

Figure 3. Energy level diagram of the energy V of the various HF(right) and DF (left) states and the barrier heights of the surfaces (center).

Figure 4. Plot of the total rate constant (sum of reactive and non-reactive) k_v^{de} for deactivation in the collision $H + FH(v) \longrightarrow H + FH(v' < v)$ at 300 K for v = 1-5 as a function of the barrier height E_{barr} of the potential energy surface. Arrows mark the internal energies of the four lowest HF states. Line types are as follows: v=1 : solid line; v=2 : dashed line; v=3 : dashed-dotted line; v=4 : dotted line; v=5 : dashed-triple-dotted line.

Figure 5. Plot of the total rate constant for deactivation k_v^{de} in the collision $H + FH(v) \longrightarrow H + FH(v' < v)$ at 650 K for v = 1-5 as a function of the barrier height E_{barr} of the potential energy surface. Arrows and line types are as in figure 4.

Figure 6. Plot of the total rate constant for deactivation k_v^{de} in the collision $D + FH(v) \longrightarrow D + FH(v' < v)$, $DF(v'' < v) + H$ at 300 K for v = 1-3 as a function of the barrier height E_{barr} of the potential energy surface. Arrows and line types are as in figure 4.

Figure 7. Plot of the fraction $f_v^{(1)}$ of deactivation occurring by single quantum transitions in the collision $H + FH(v) \longrightarrow H + FH(v-1)$ (both reactive and non-reactive) at 300 K for v = 2-5 as a function of the barrier height E_{barr} of the potential energy surface. Arrows and line types are as in figure 4.

Figure 8. Plot of the fraction f_v^R of deactivation occurring by reaction in the collision $H + FH(v) \longrightarrow HF(v' < v) + H$ at 300 K for v = 1-5 as a function of the barrier height E_{barr} of the potential energy surface. Arrows and line types are as in figure 4.

Figure 9. Plot of the average number $\langle \Delta n_v \rangle_{de}$ of vibrational quanta lost in deactivating collisions in $H + FH(v) \longrightarrow H + FH(v' < v)$ (both reactive and non-reactive) at 300 K (solid line) and 1000 K (dashed line) for v = 2-5. Arrows are used as in figure 4. Symbols used are as follows: v = 2 : circles; v = 3 : squares; v = 4 : triangles; v = 5 : diamonds. Where no line is shown, $\langle \Delta n_v \rangle_{de}$ may be taken as being one.

Figure 10. Plot of Arrhenius activation energies $E_a^{v,v-1}$ for the single-quantum deactivation reactions $H + FH(v) \longrightarrow HF(v-1) + H$ for v = 1-5 as a function of the internal energy E_{int} of the HF(v) reagent state on the six potential energy surfaces studied. The barrier height E_{barr} of these surfaces is indicated on the right side of the plot. Internal energies of the v = 2-5 states are indicated by arrows.

Figure 11. Plot of probability $P^R_{D+FH(0)}$ of the reaction $D + FH(0) \longrightarrow DF + H$ as a function of the reagent translational energy E_0 in the threshold region on the six potential energy surfaces studied, the barrier heights of which are indicated. The arrows indicate the energies corresponding to the heights of the barriers.

Figure 12. Plot of probability $P^R_{D+FH(1)}$ of the reaction D + FH(1) $\longrightarrow$ DF + H as a function of the reagent translational energy E_1 in the threshold region on the six potential energy surfaces studied. All labeling is as in figure 11. The arrows on the abscissa indicate the energies of the surface barrier heights.

Figure 13. Plot of the average fraction of available energy $\langle f_0 \rangle$ going into product vibration in the reaction D + FH(0) $\longrightarrow$ DF + H as a function of the reagent translational energy E_0 on the 1.5 (triangles), 20 (squares) and 40 (circles) kcal/mole barrier surfaces. Energies of the various DF product states are indicated on the abscissa.

Figure 14. Histogram plot showing product state distributions for the reaction D + FH(v) $\longrightarrow$ DF(v') + H at a total energy of 2.410 eV for v' up to and including 6 on the 6 potential energy surfaces, the barrier height of which is indicated in the upper right corner of each strip. The height of the bar is proportional to the magnitude of the state-to-state reaction probability $P_{D+FH(v) \longrightarrow DF(v')+H}$. a) v=0; b) v=1; c) v=2.

Figure 15. Plot of the state-to-state reaction probability $P_{D+FH(0) \longrightarrow DF(v')+H}$ for the reaction D + FH(v=0) $\longrightarrow$ DF(v') + H as a function of the reagent translational energy E_0 on the 1.5 kcal/mole barrier surface. The arrow marks the energy at which the DF (v=1) state becomes accessible. A solid line is used for the v'=0 transition; a dashed one is used for the v'=1 transition.

Figure 16. Plot of the state-to-state reaction probability $P_{D+FH(0) \longrightarrow DF(v')+H}$ defined for fig. 15 as a function of the reagent translational energy E_0 on the 5 kcal/mole barrier surface. Arrows mark the energies at which the indicated states become accessible. Line types are as in figure 15.

Figure 17. Plot of the state-to-state reaction probability $P_{D+FH(0) \longrightarrow DF(v')+H}$ defined for figure 15 as a function of the reagent translational energy E_0 on the 10 kcal/mole barrier surface. Arrows and line types are as in figure 16.

Figure 18. Plot of the state-to-state reaction probability $P_{D+FH(0) \longrightarrow DF(v')+H}$ defined for figure 15 as a function of the reagent translational energy E_0 on the 20 kcal/mole barrier surface. Arrows and line types are as in figure 16.

Figure 19. Plot of the state-to-state reaction probability $P_{H+FH(0) \longrightarrow HF(v') + H}$ for the reaction H + FH(v=0) ⟶ HF(v') + H as a function of the reagent translational energy E_0 on the 10 kcal/mole barrier surface. Arrows and line types are as in figure 16.

Figure 20. Vibrationally adiabatic correlation diagram showing the energy V along the minimum energy path (MEP) and of the n^{th} local vibrational state as a function of the reaction coordinate s measured along the minimum energy path for the 1.5 kcal/mole barrier surface for the D + FH reaction. The dotted line marks the energy at which the resonance seen in figure 15 is observed.

Figure 21. Vibrationally adiabatic correlation diagram for the 10 kcal/mole barrier surface for the D + FH reaction.

Figure 22. Vibrationally adiabatic correlation diagram for the 10 kcal/mole barrier surface for the H + FH reaction.

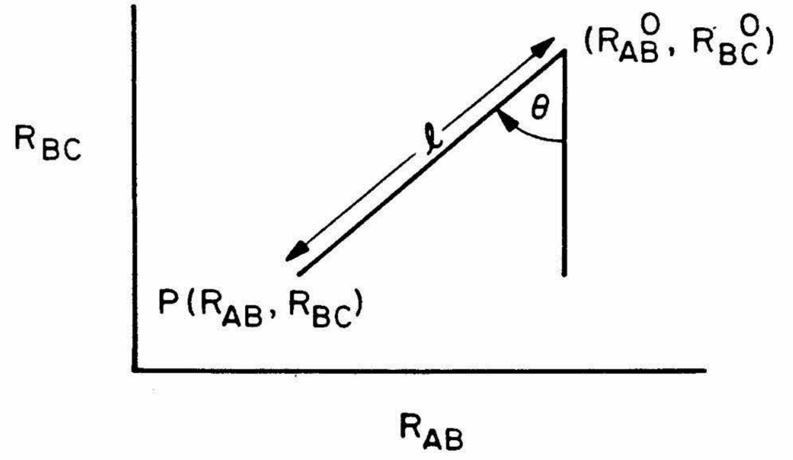

Figure 1

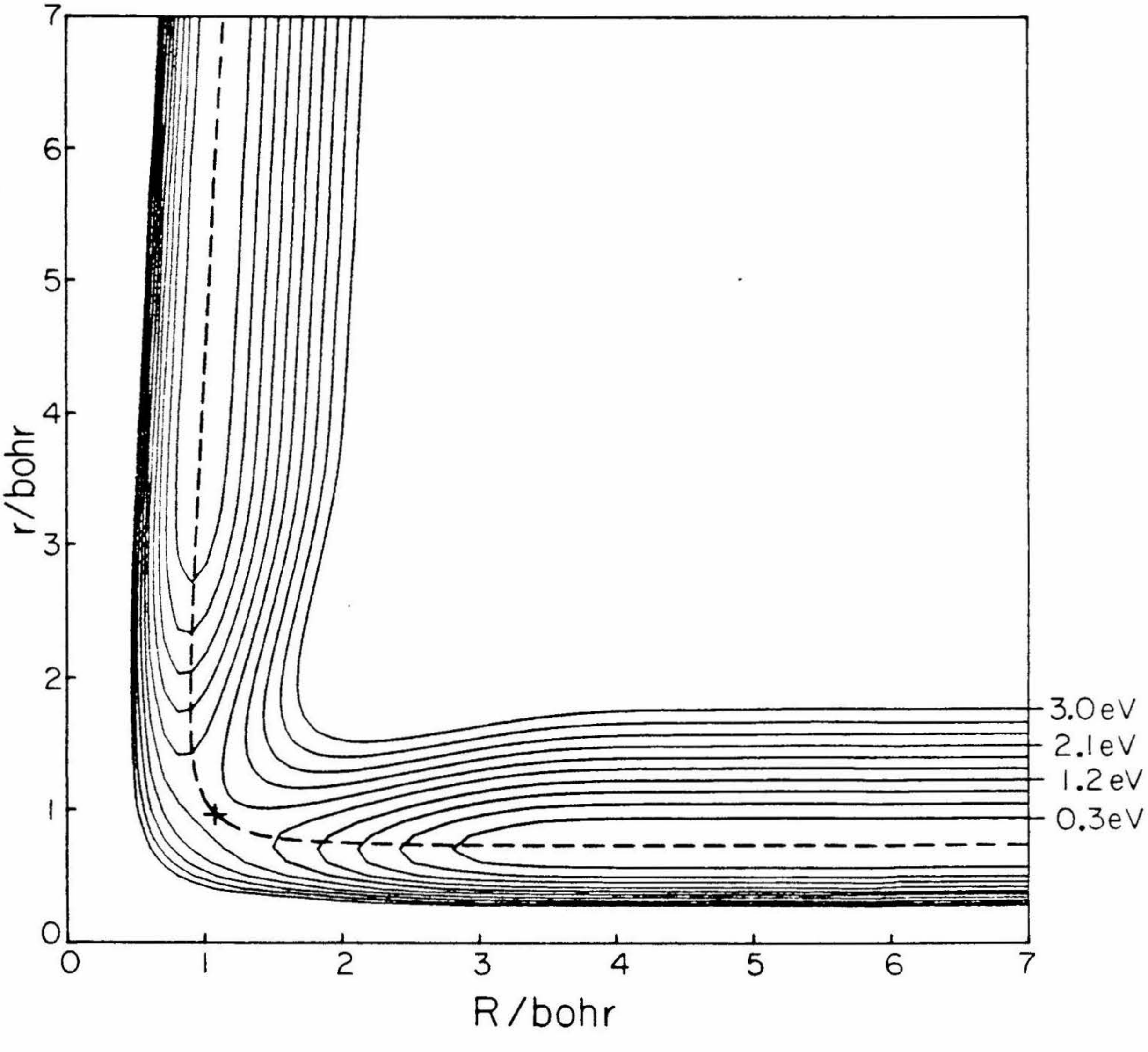

Figure 2

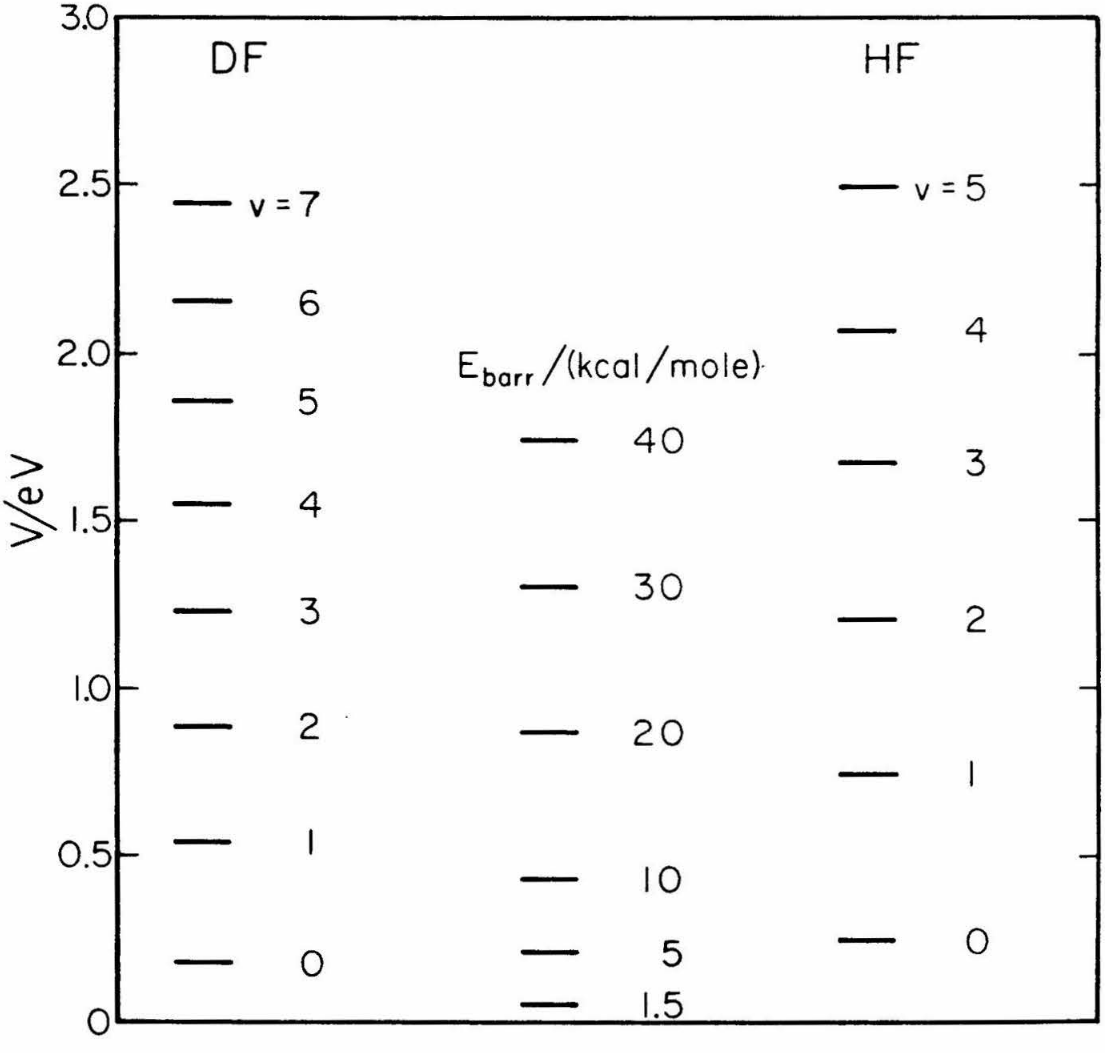
3.0
2.5
2.0
1.5
1.0
0.5
0
V/eV
DF
v = 7
6
5
4
3
2
1
0
Ebarr /(kcal/mole)
40
30
20
10
5
1.5
HF
v = 5
4
3
2
1
0

Figure 3

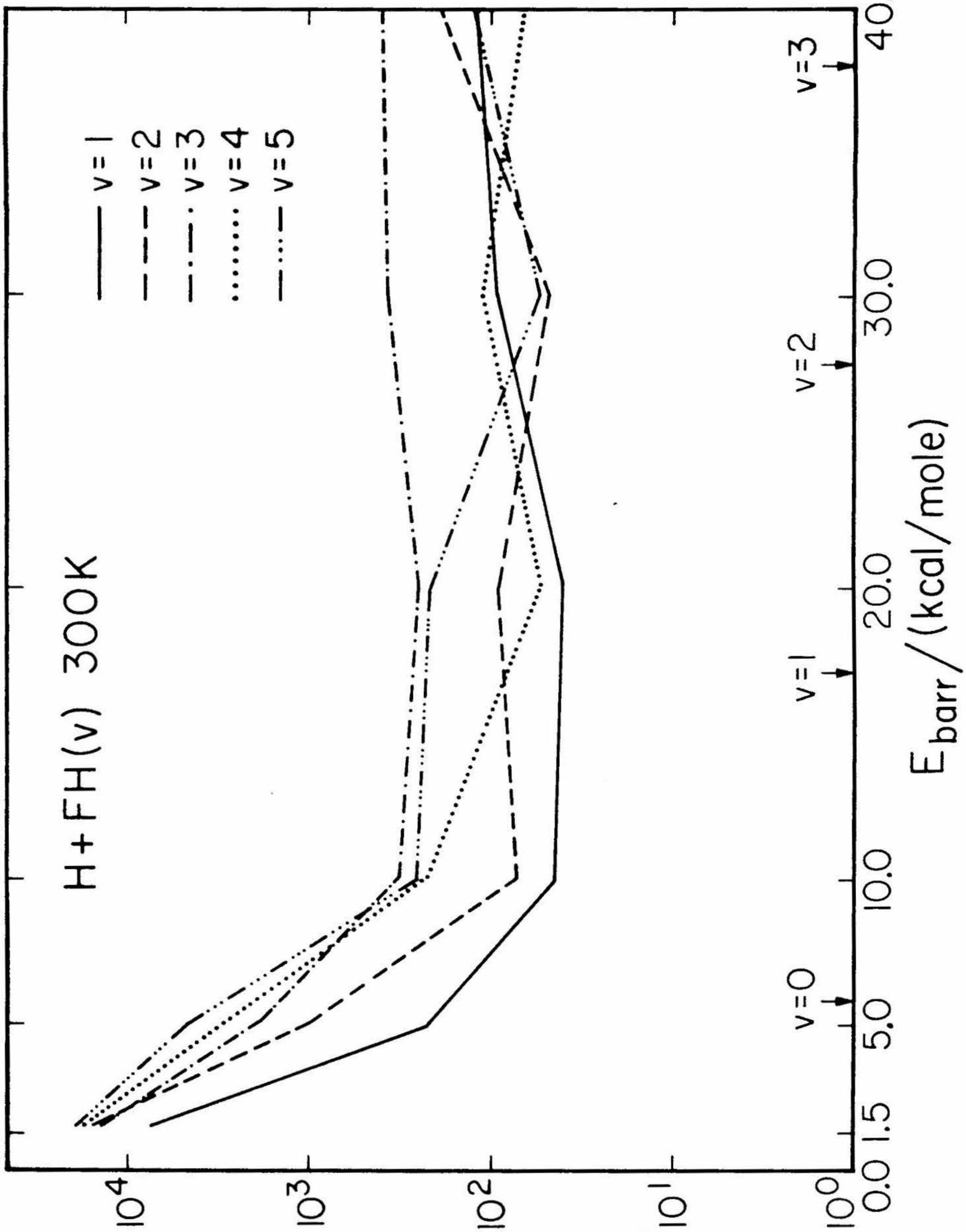
H + FH(v) 300K
v = 1
v = 2
v = 3
v = 4
v = 5
10^0
10^1
10^2
10^3
10^4
k^v_{de}/(cm · molecule^{-1} sec^{-1})
0.0
1.5
5.0
10.0
20.0
30.0
40.0
v=0
v=1
v=2
v=3
E_{barr}/(kcal/mole)

Figure 4

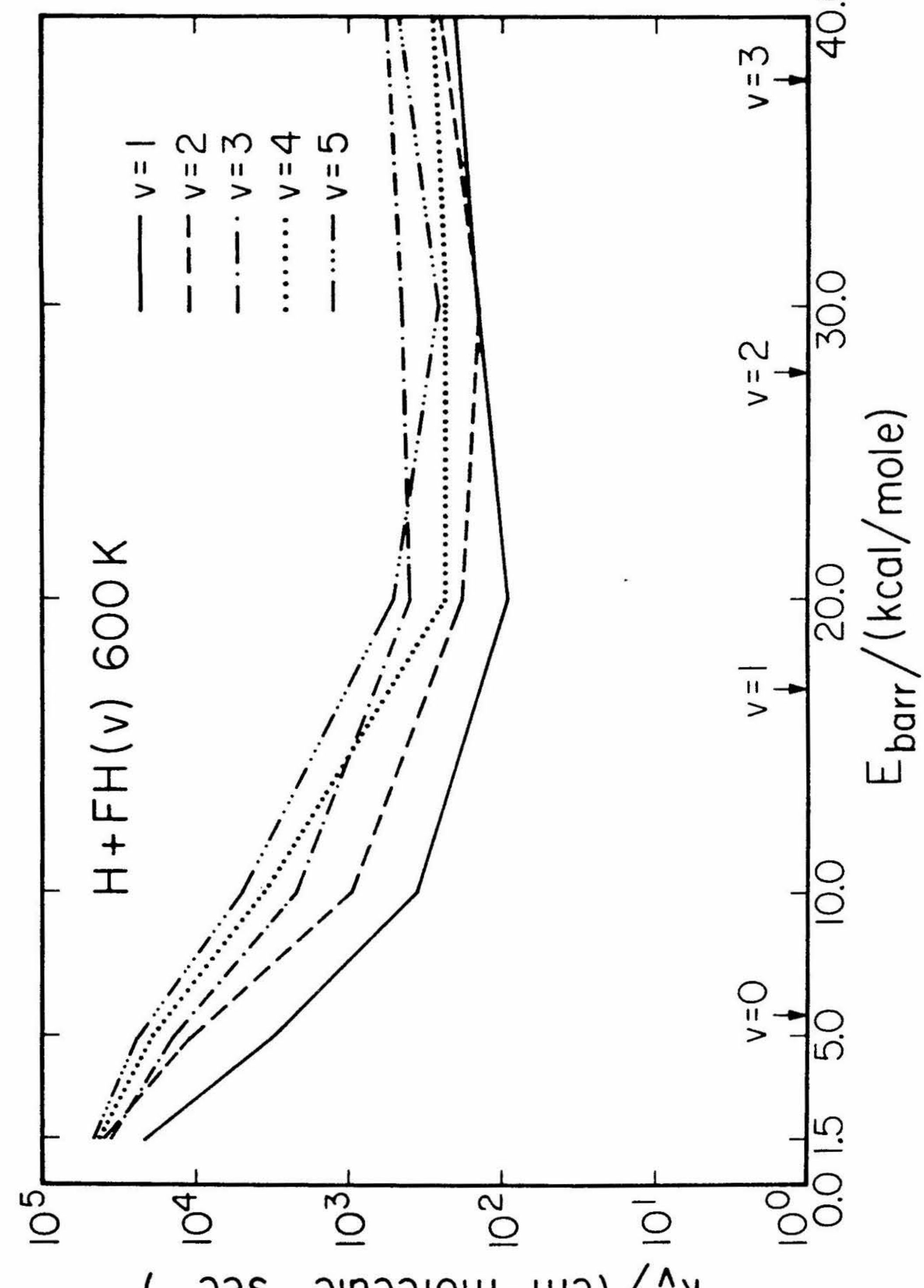
H + FH(v) 600 K
v = 1
v = 2
v = 3
v = 4
v = 5
k^{v}_{de}/(cm · molecule^{-1} sec^{-1})
10^0
10^1
10^2
10^3
10^4
10^5
E_{barr}/(kcal/mole)
0.0
1.5
5.0
10.0
20.0
30.0
40.0
v=0
v=1
v=2
v=3

Figure 5

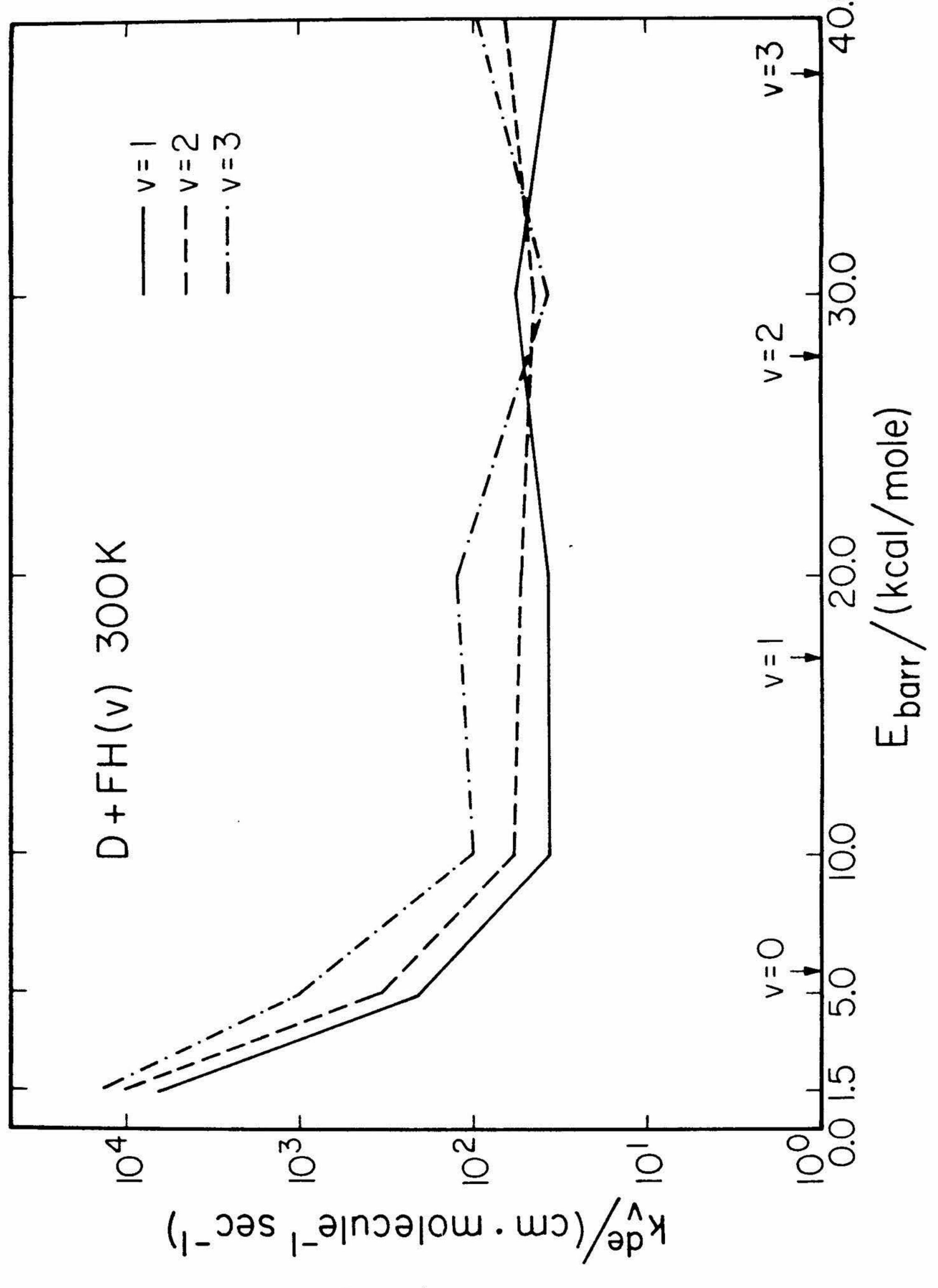
D + FH(v) 300K
v = 1
v = 2
v = 3
v=0
v=1
v=2
v=3
0.0
1.5
5.0
10.0
20.0
30.0
40.0
E_{barr}/(kcal/mole)
10^0
10^1
10^2
10^3
10^4
k_{de}^{v}/(cm · molecule^{-1} sec^{-1})

Figure 6

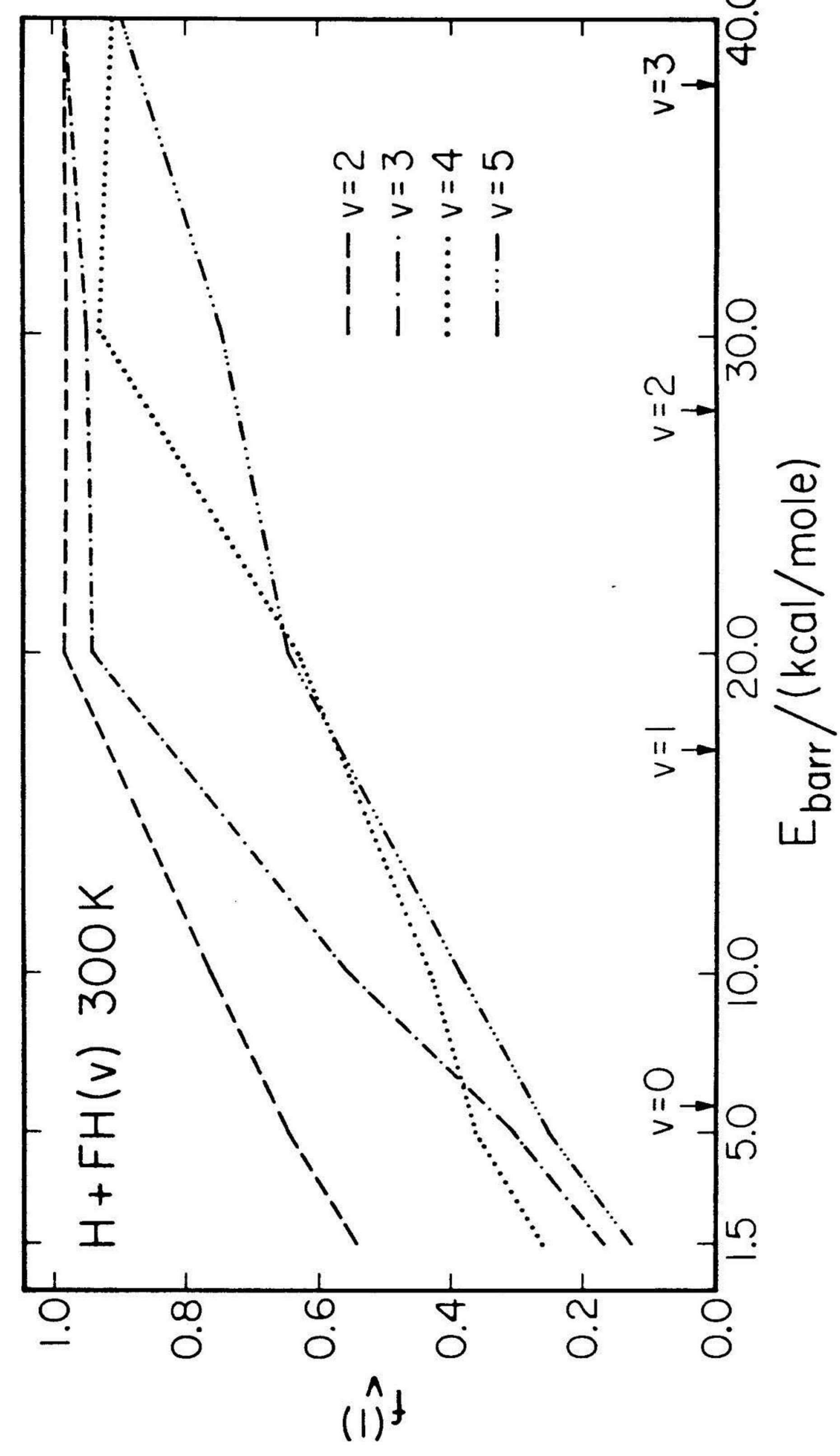
H + FH(v) 300 K
v = 2
v = 3
v = 4
v = 5
$\hat{f}^{(1)}$
0.0
0.2
0.4
0.6
0.8
1.0
1.5
5.0
10.0
20.0
30.0
40.0
v=0
v=1
v=2
v=3
E_{barr}/(kcal/mole)

Figure 7

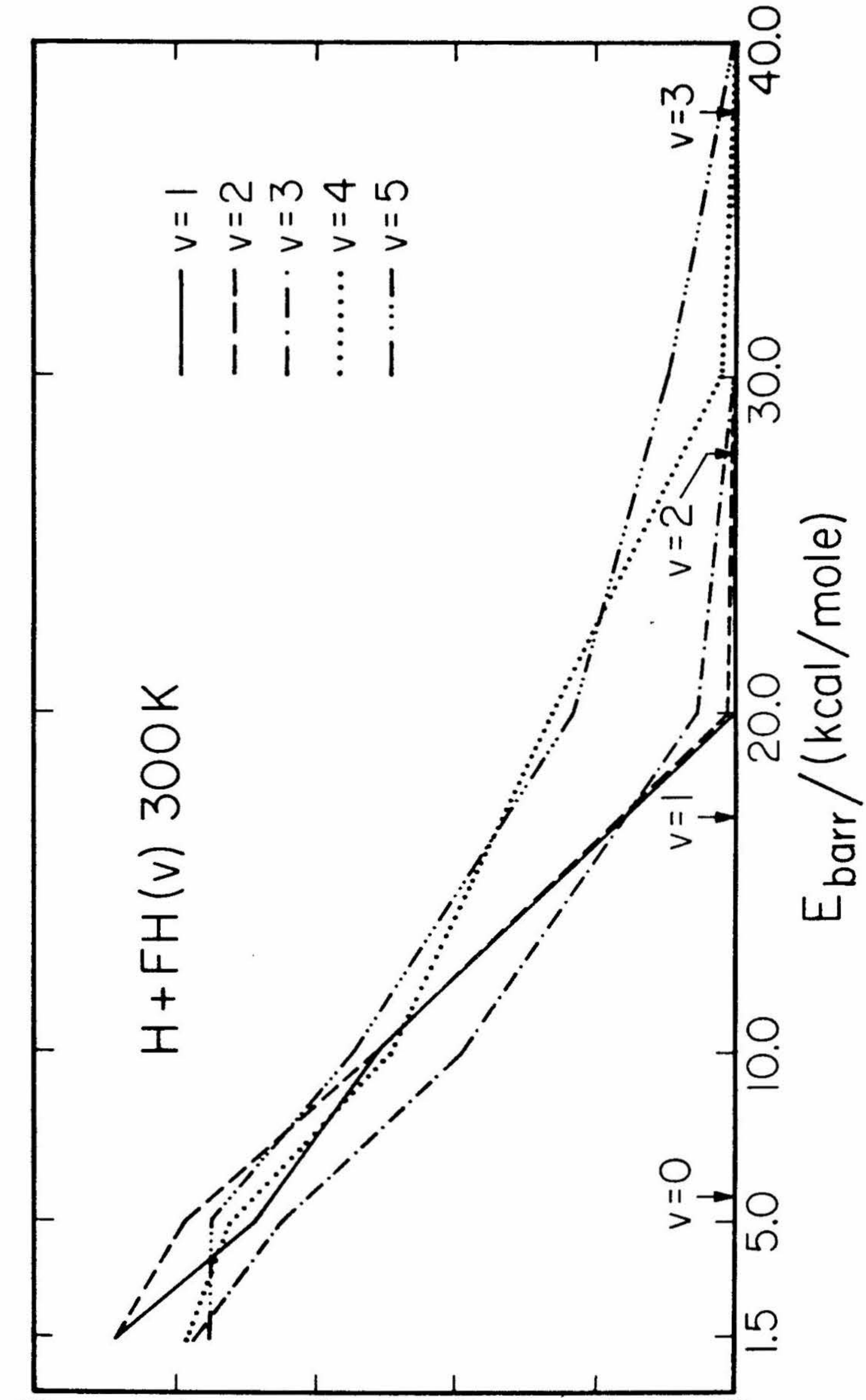
H+FH(v) 300K
v=1
v=2
v=3
v=4
v=5
$\langle f_R \rangle$
1.0
0.8
0.6
0.4
0.2
0.0
1.5
5.0
10.0
20.0
30.0
40.0
E_{barr}/(kcal/mole)
v=0
v=1
v=2
v=3

Figure 8

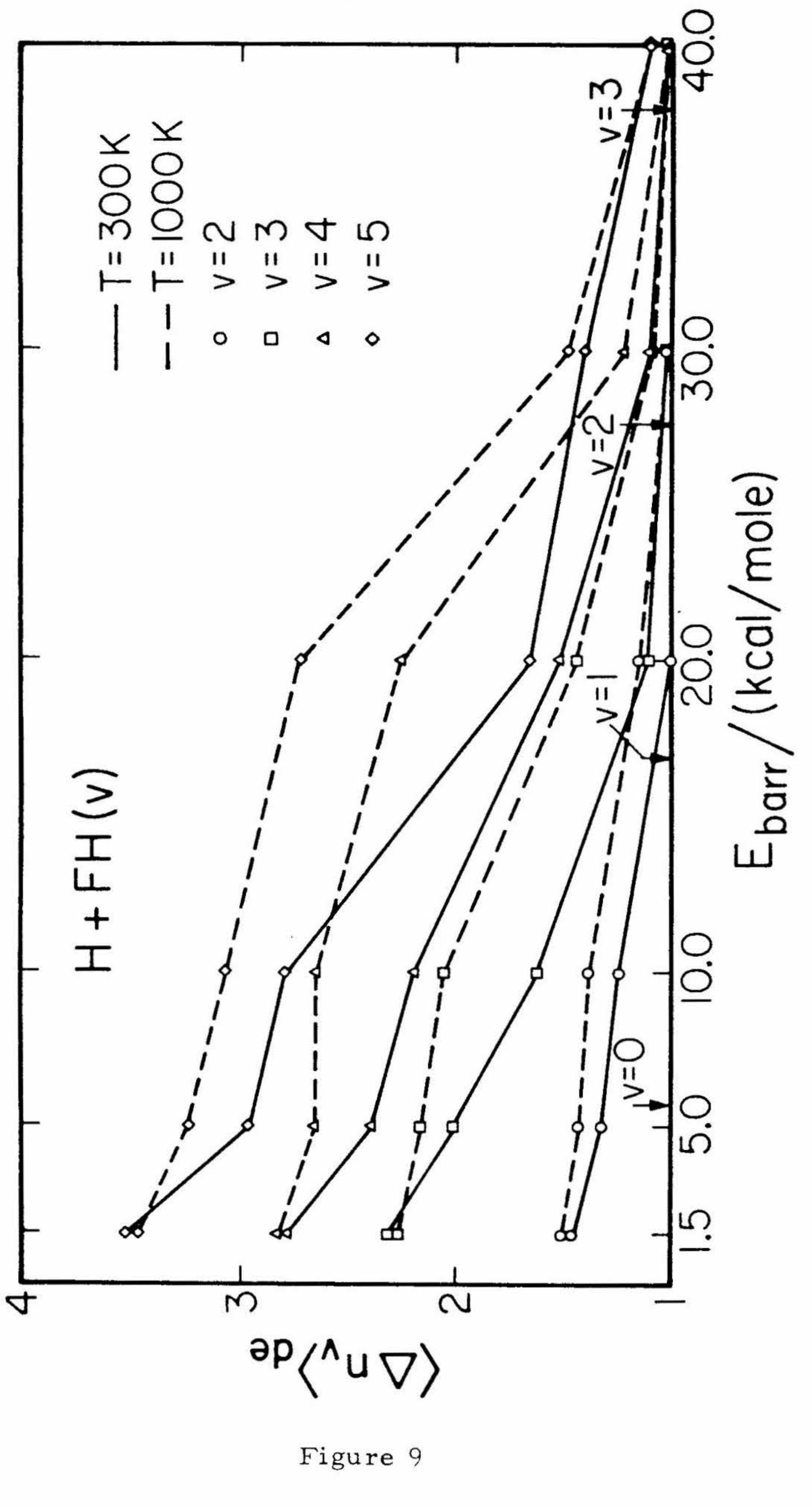
H + FH(v)
— T=300K
– – T=1000K
○ v=2
□ v=3
△ v=4
◇ v=5
v=0
v=1
v=2
v=3
1.5
5.0
10.0
20.0
30.0
40.0
1
2
3
4
E_barr /(kcal/mole)
⟨Δn_v⟩_de

Figure 9

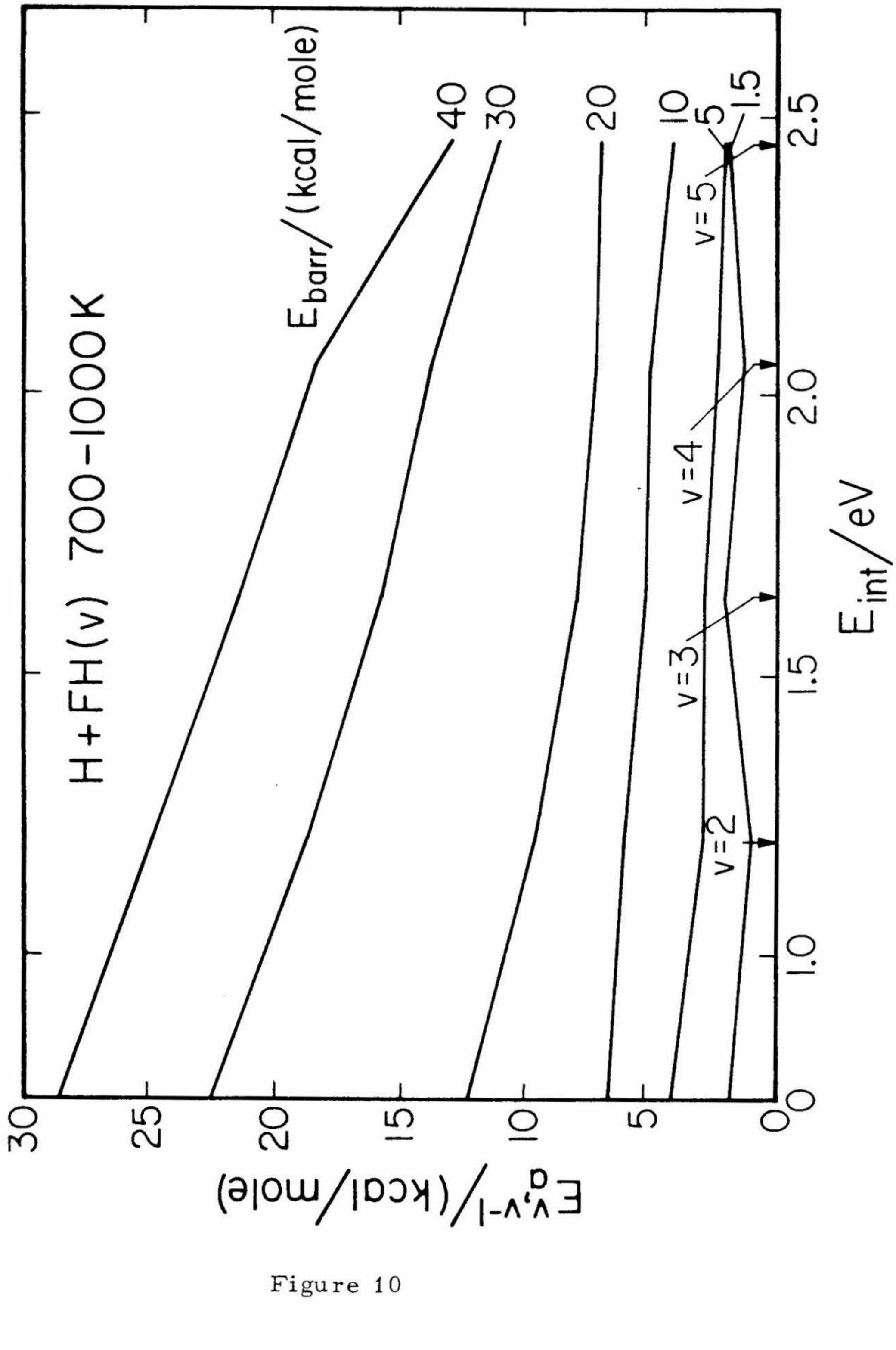
H + FH(v) 700-1000 K
E_{barr}/(kcal/mole)
40
30
20
10
5
1.5
v=2
v=3
v=4
v=5
E_{int}/eV
0
1.0
1.5
2.0
2.5
$E^{a}_{v,v-1}$/(kcal/mole)
0
5
10
15
20
25
30

Figure 10

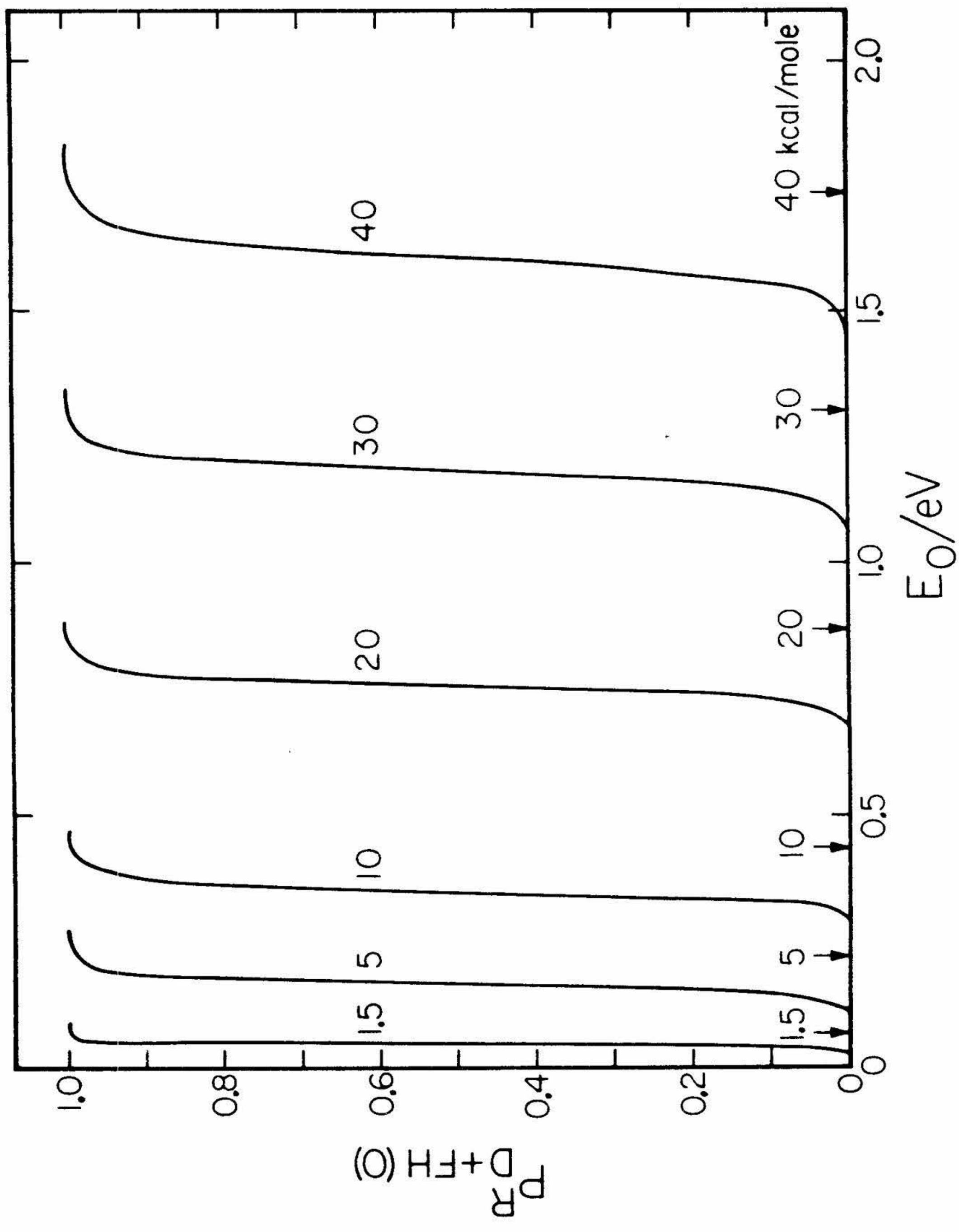
$P^R_{D+FH}(0)$
1.0
0.8
0.6
0.4
0.2
0
0
0.5
1.0
1.5
2.0
E_0/eV
1.5
5
10
20
30
40
1.5
5
10
20
30
40 kcal/mole

Figure 11

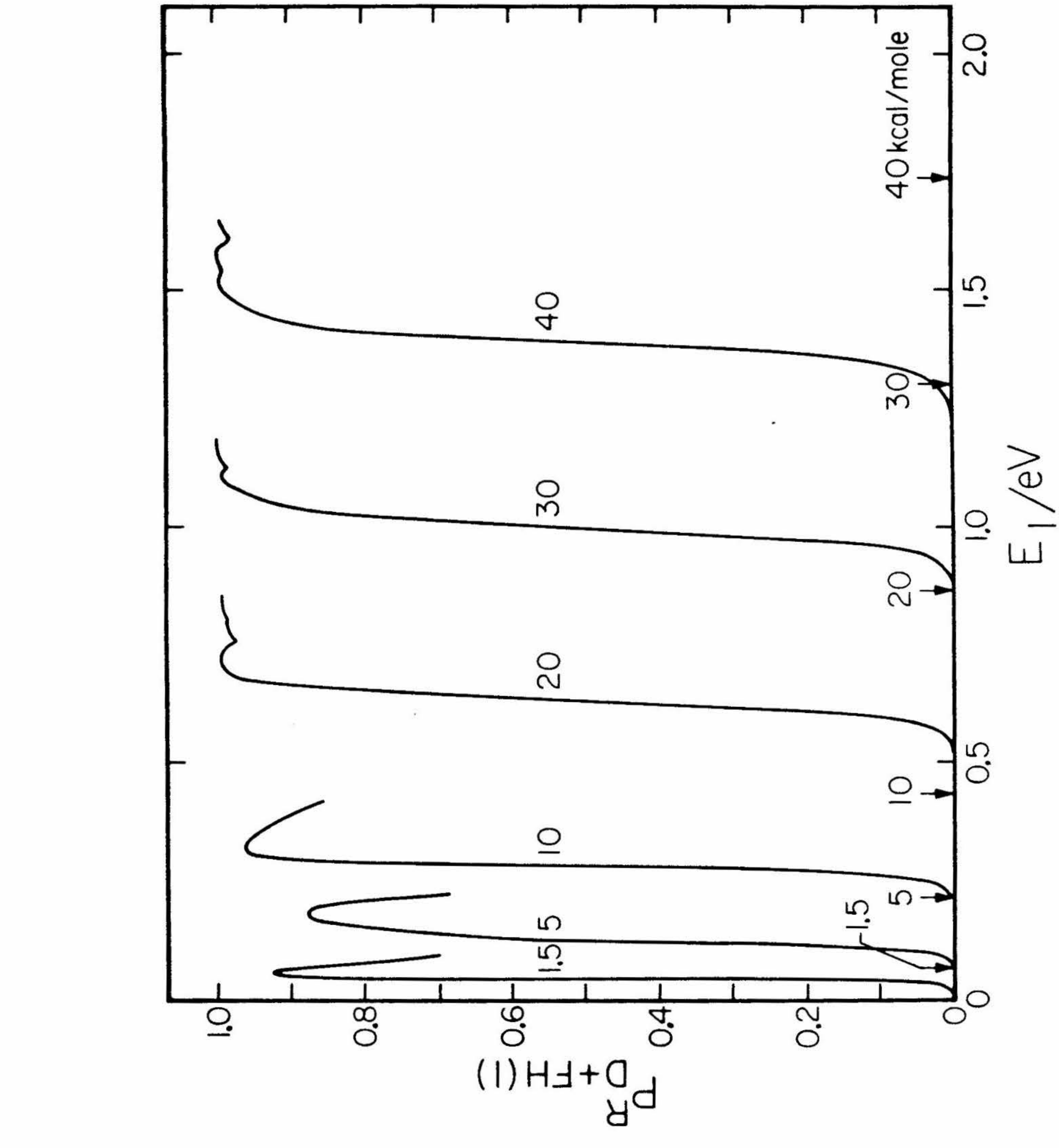
$P^R_{D+FH(1)}$
0
0.2
0.4
0.6
0.8
1.0
E_1/eV
0
0.5
1.0
1.5
2.0
1.5
5
10
20
30
40
1.5
5
10
20
30
40 kcal/mole

Figure 12

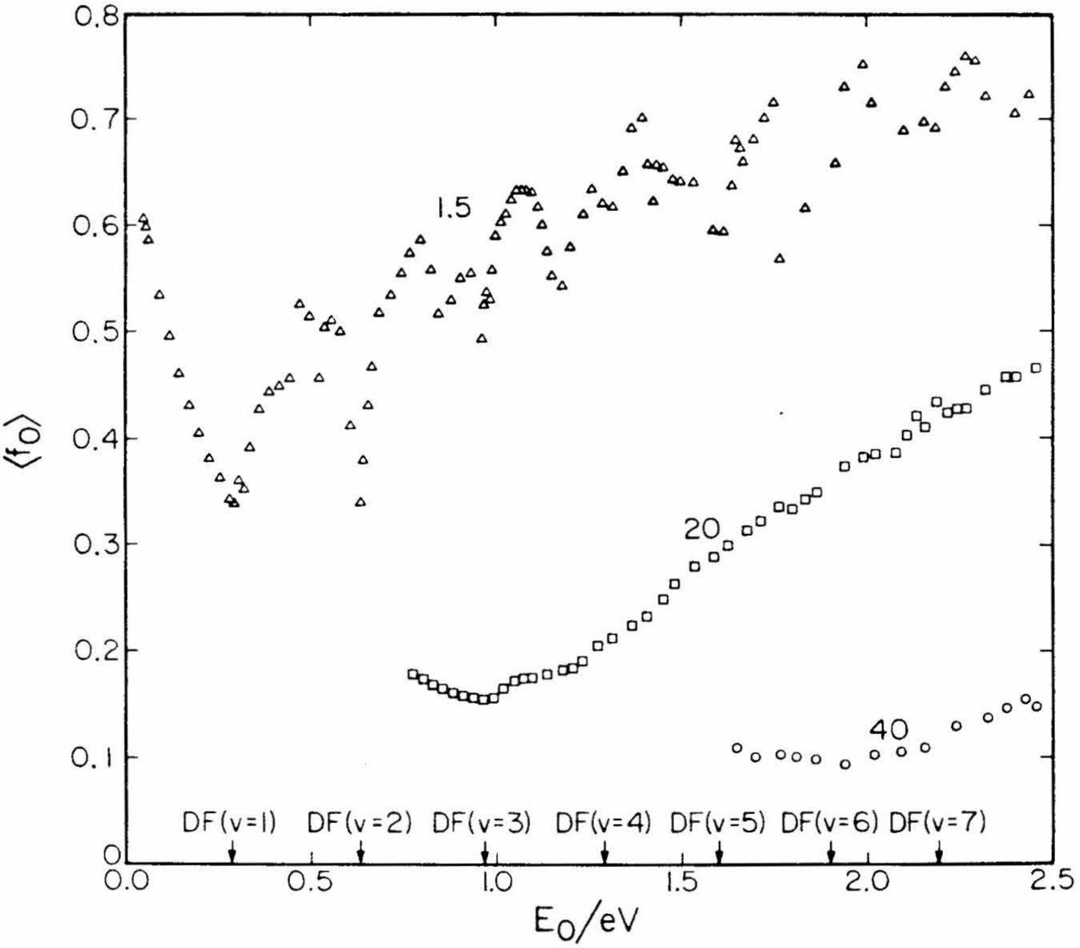
0.8
0.7
0.6
0.5
0.4
0.3
0.2
0.1
0
⟨f_0⟩
1.5
20
40
DF(v=1)
DF(v=2)
DF(v=3)
DF(v=4)
DF(v=5)
DF(v=6)
DF(v=7)
0.0
0.5
1.0
1.5
2.0
2.5
E_0/eV

Figure 13

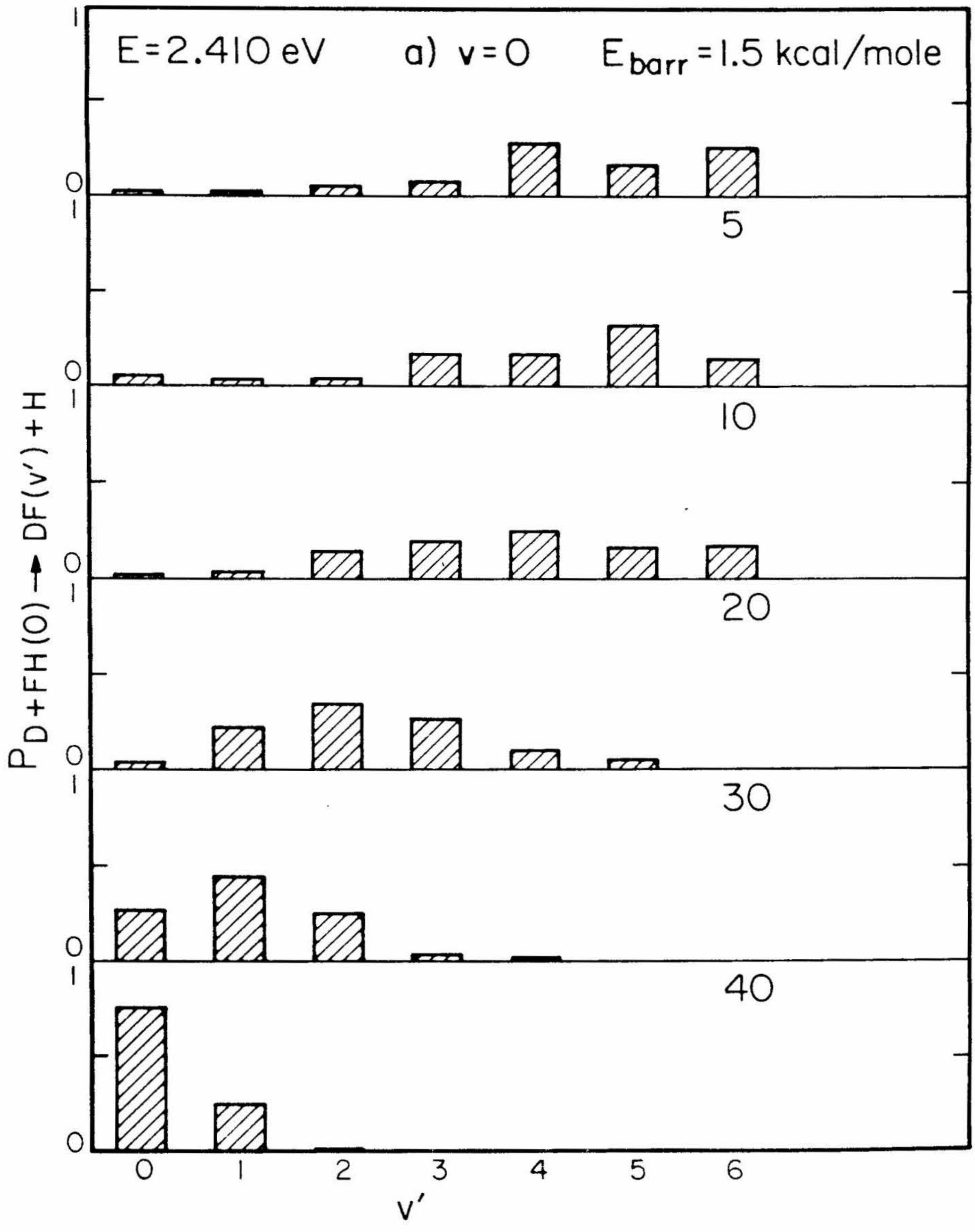
E=2.410 eV
a) v=0
E_{barr}=1.5 kcal/mole
5
10
20
30
40
1
0
$P_{D+FH(0) \rightarrow DF(v')+H}$
0
1
2
3
4
5
6
v'

Figure 14a

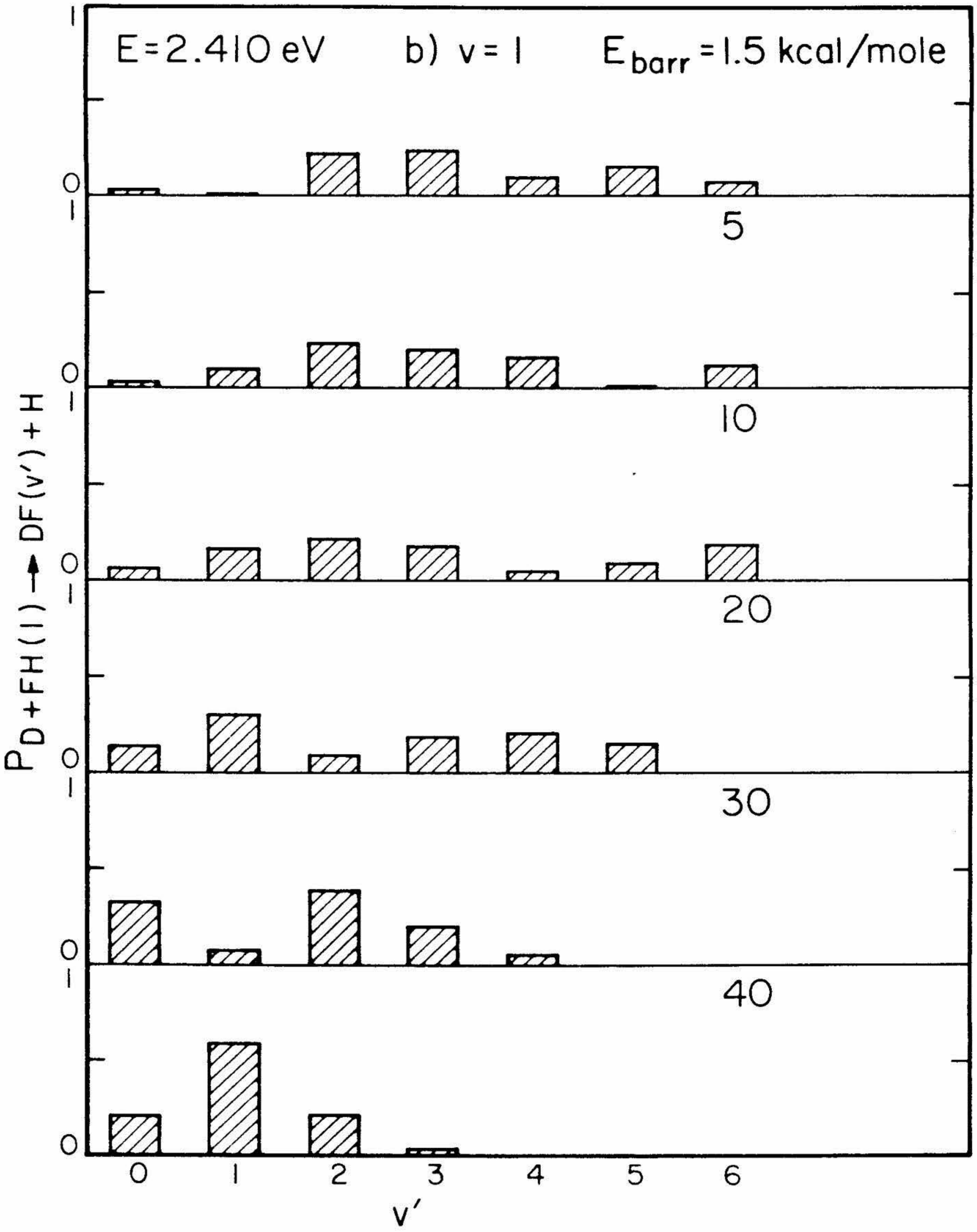
E=2.410 eV
b) v = 1
E_{barr} = 1.5 kcal/mole
5
10
20
30
40
1
0
$P_{D+FH(1)\rightarrow DF(v')+H}$
0
1
2
3
4
5
6
v′

Figure 14b

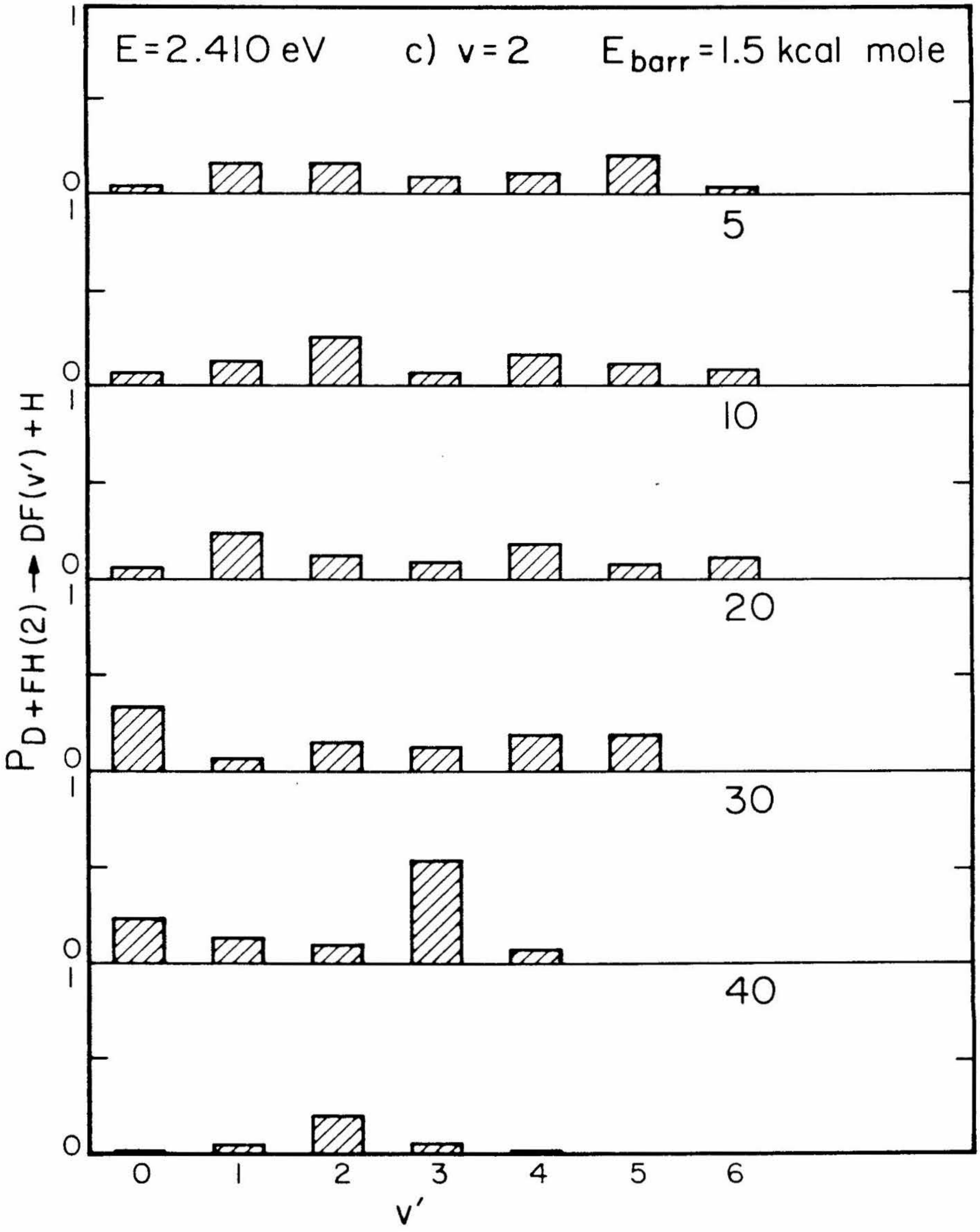
E=2.410 eV
c) v=2
E_{barr}=1.5 kcal mole
5
10
20
30
40
1
0
$P_{D+FH(2) \rightarrow DF(v')+H}$
0
1
2
3
4
5
6
v'

Figure 14c

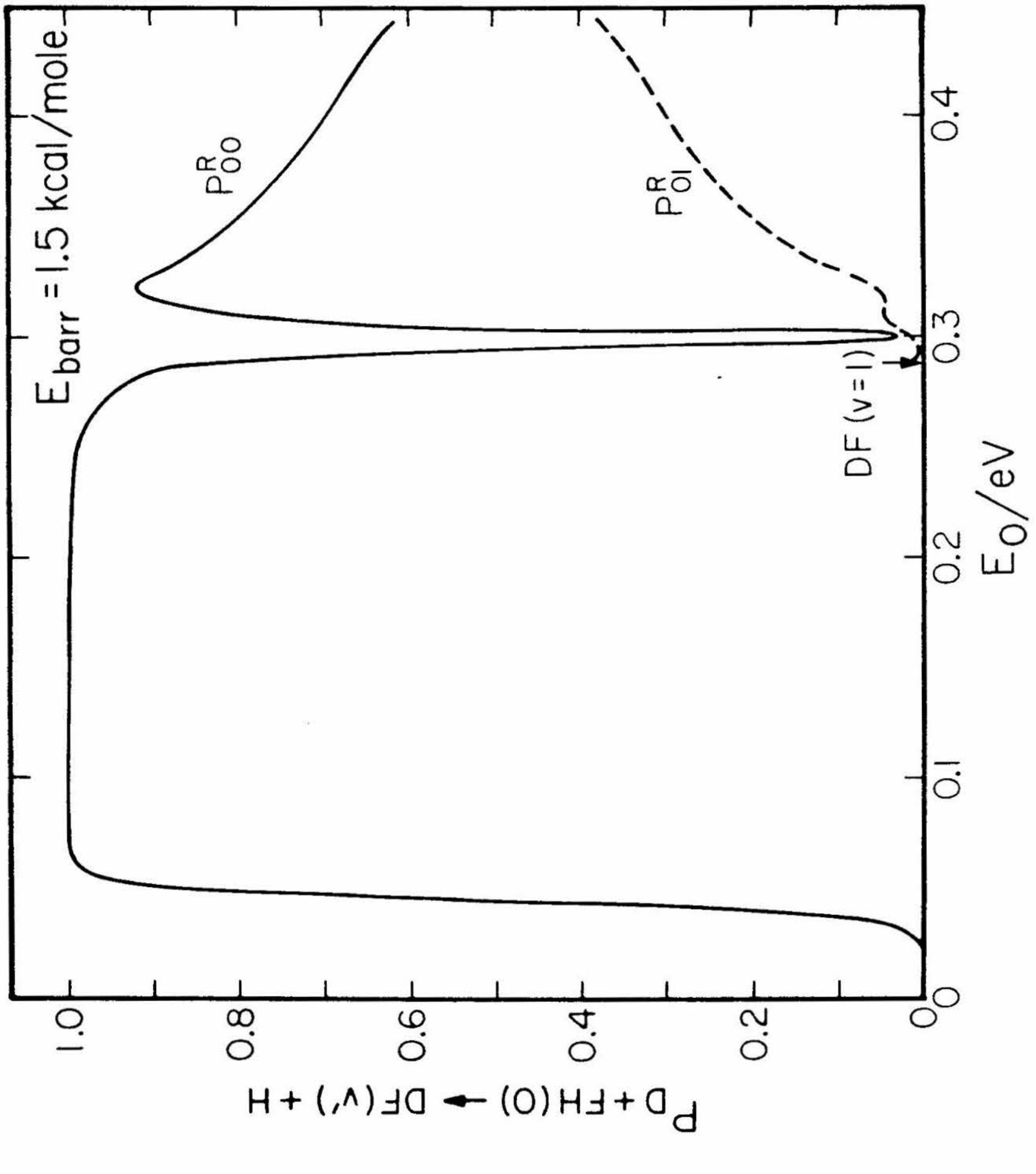
E_{barr} = 1.5 kcal/mole
P^R_{00}
P^R_{01}
DF (v=1)
0.0
0.1
0.2
0.3
0.4
E_0/eV
1.0
0.8
0.6
0.4
0.2
0.0
$P_{D+FH(0) \rightarrow DF(v')+H}$

Figure 15

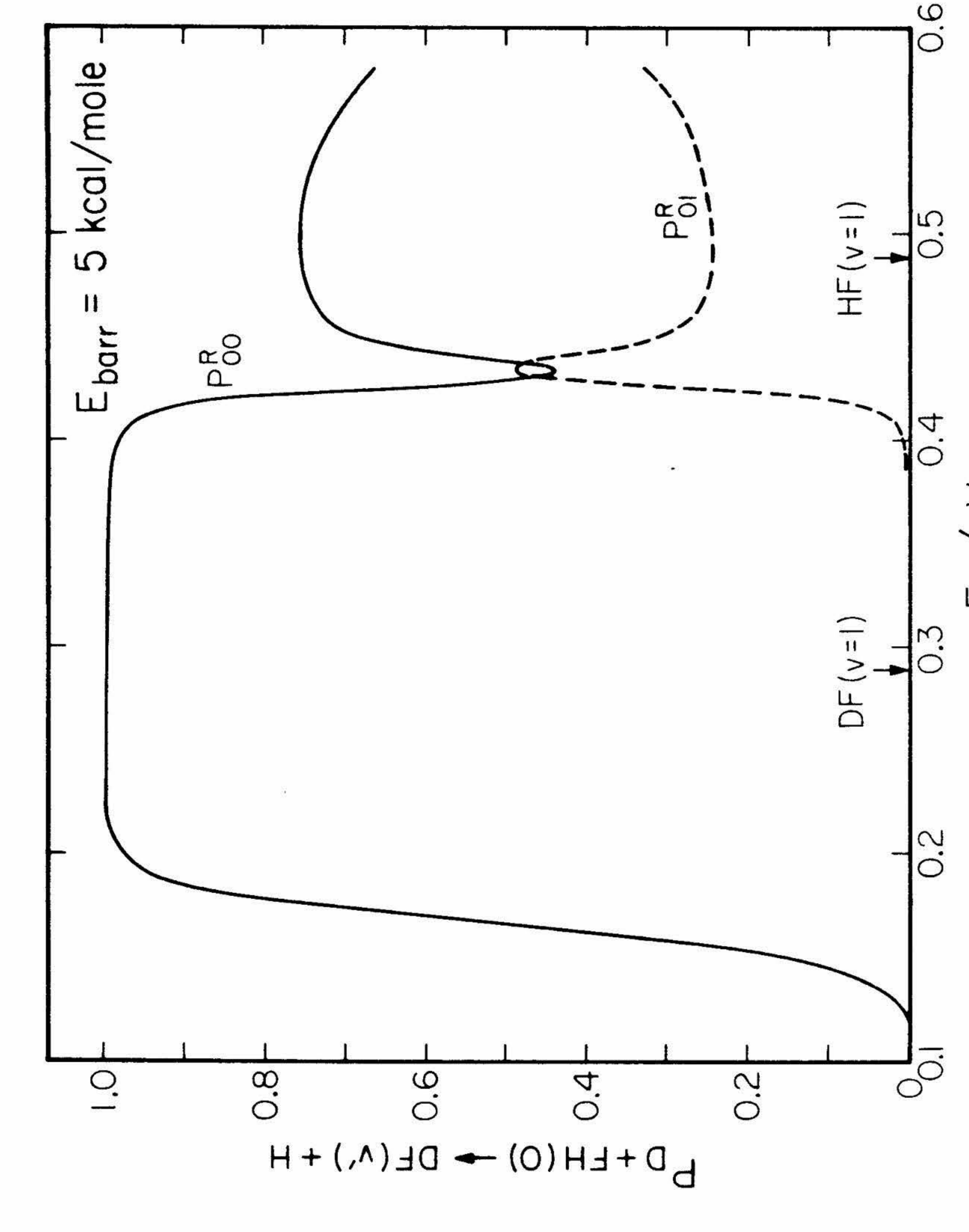
E_{barr} = 5 kcal/mole
P^R_{00}
P^R_{01}
HF(v=1)
DF(v=1)
E_0/eV
0.1
0.2
0.3
0.4
0.5
0.6
0
0.2
0.4
0.6
0.8
1.0
$P_{D+FH(0) \rightarrow DF(v')+H}$

Figure 16

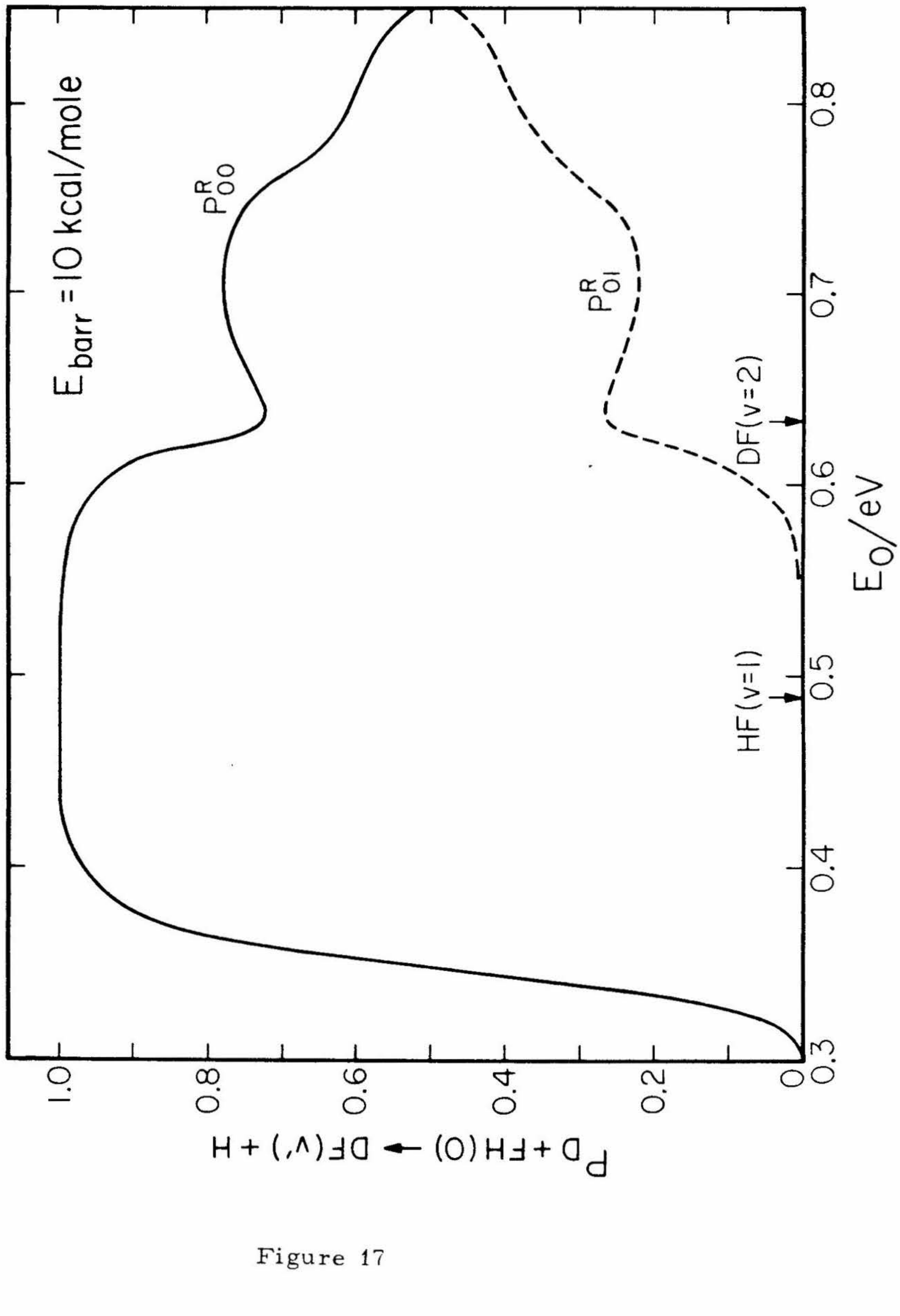
E_{barr} = 10 kcal/mole
P^R_{00}
P^R_{01}
DF(v=2)
HF(v=1)
0.3
0.4
0.5
0.6
0.7
0.8
E_0/eV
0
0.2
0.4
0.6
0.8
1.0
$P_{D+FH(0) \rightarrow DF(v')+H}$

Figure 17

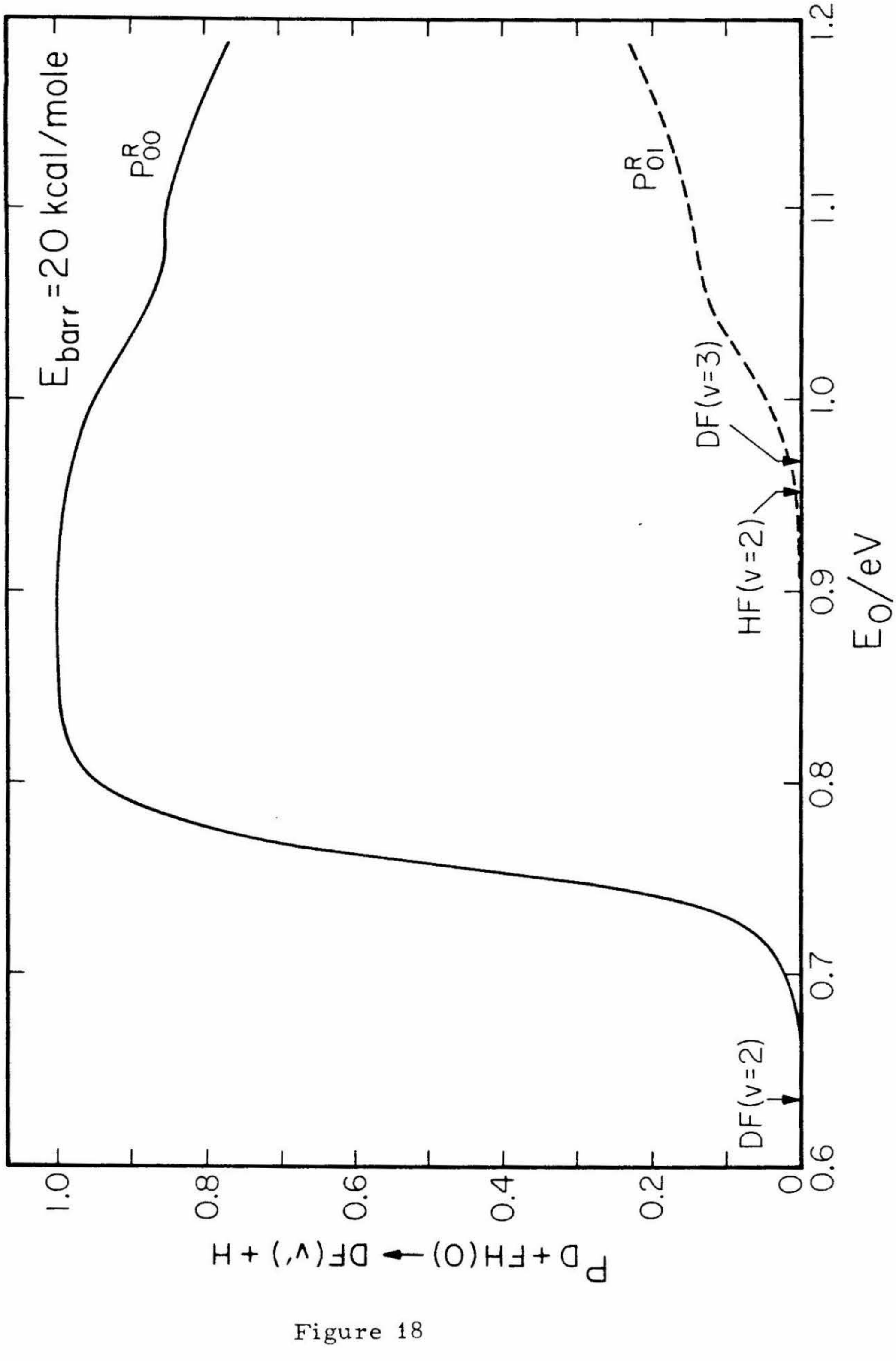
E_{barr} = 20 kcal/mole
P^R_{00}
P^R_{01}
DF(v=3)
HF(v=2)
DF(v=2)
E_0/eV
0.6
0.7
0.8
0.9
1.0
1.1
1.2
0
0.2
0.4
0.6
0.8
1.0
$P_{D+FH(0) \rightarrow DF(v') + H}$

Figure 18

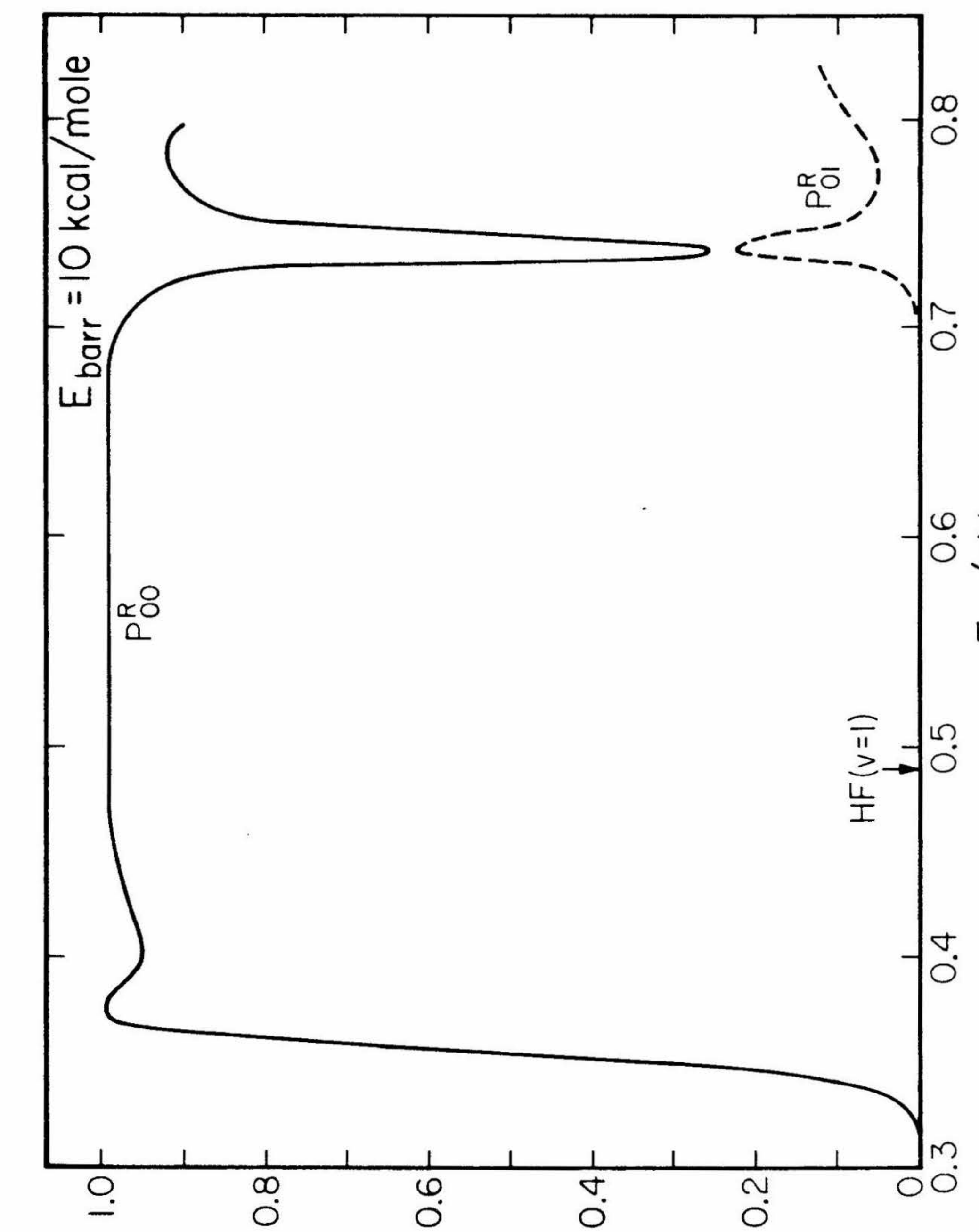
E_{barr} = 10 kcal/mole
P^R_{00}
P^R_{01}
HF(v=1)
$P_{H+FH(0)\rightarrow HF(v')+H}$
E_0/eV
0
0.2
0.4
0.6
0.8
1.0
0.3
0.4
0.5
0.6
0.7
0.8

Figure 19

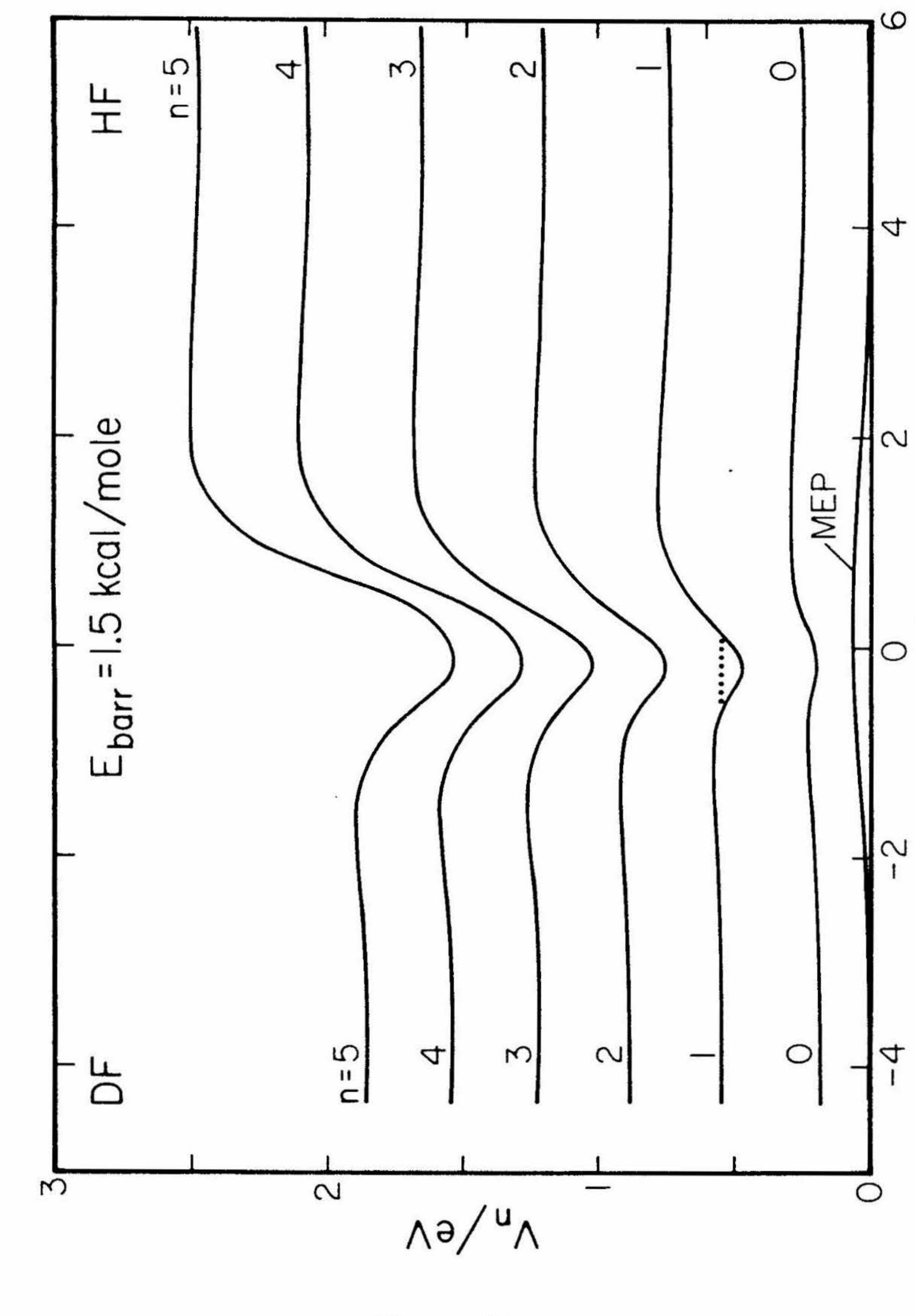

E_{barr} = 1.5 kcal/mole
DF
HF
n=5
4
3
2
1
0
n=5
4
3
2
1
0
MEP
s/bohr
V_n/eV
-4
-2
0
2
4
6
0
1
2
3

Figure 20

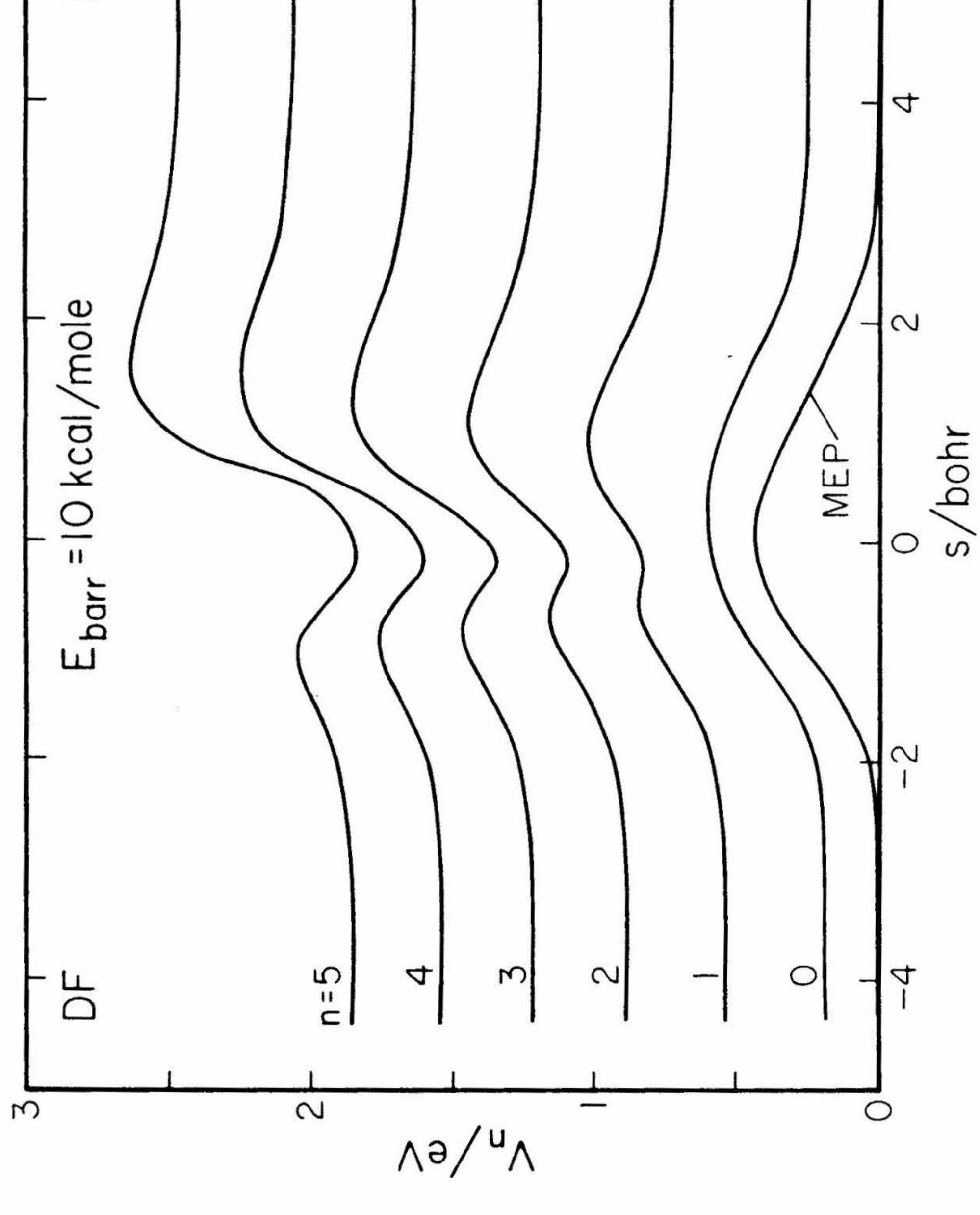
DF
E_{barr} =10 kcal/mole
HF
n=5
4
3
2
1
0
n=5
4
3
2
1
0
MEP
s/bohr
-4
-2
0
2
4
6
V_n/eV
0
1
2
3

Figure 21

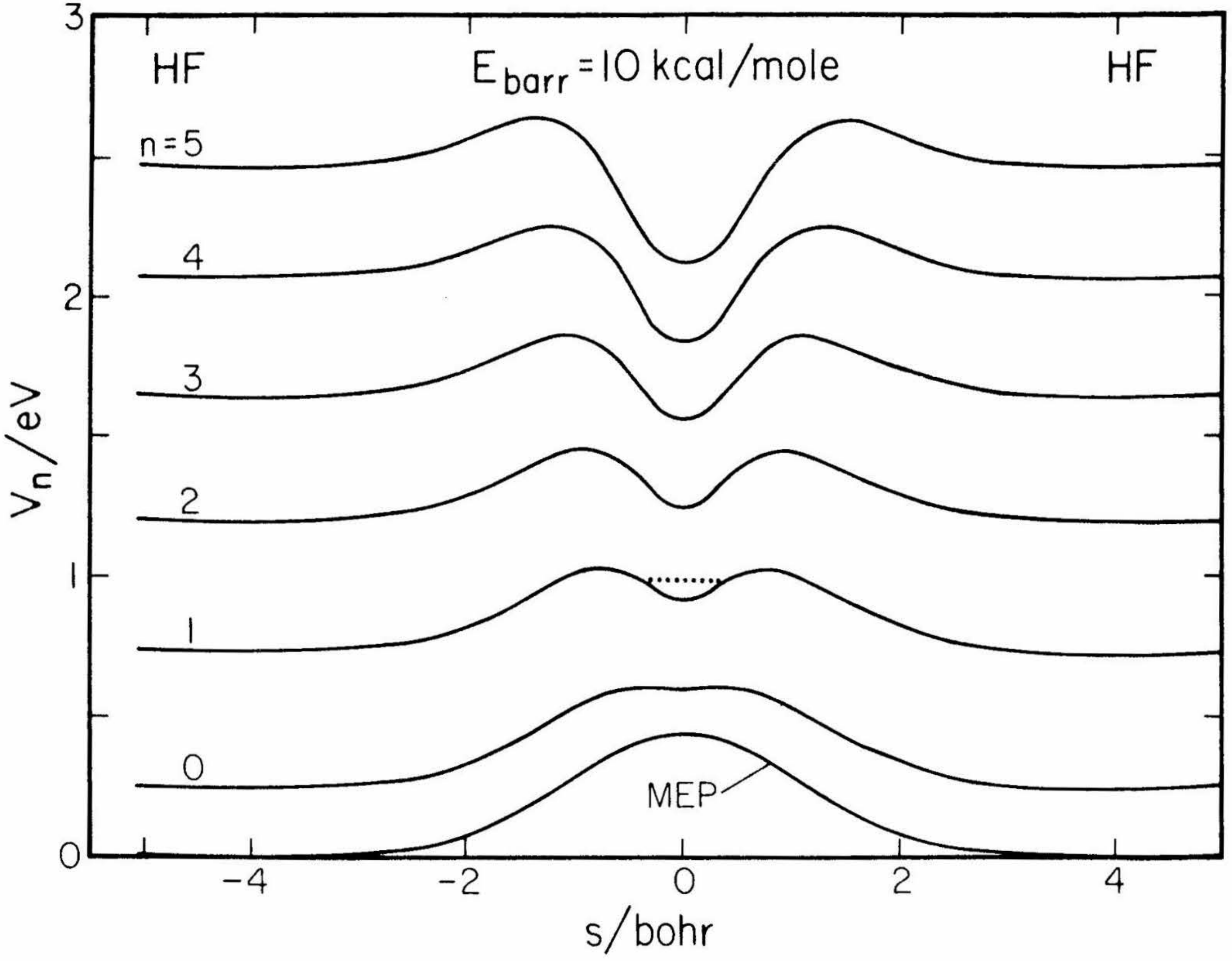

Figure 22

PART II

CHARACTERIZATION OF LOW ENERGY RESONANCES IN THE COLLINEAR $H + H_2$ AND $F + H_2$ SYSTEMS

INTRODUCTION

INTRODUCTION

Dynamical resonances have been found to be one of the most interesting results of collinear quantum mechanical calculations on the dynamics of atom-diatomic molecule reactions. Knowledge of the features of the potential energy surfaces responsible for their existence is important if one is to be able to understand their dependence on the potential energy surface, reagent vibrational excitation, and isotopic substitution. Similarly, it is important that one be able to adequately recognize and characterize dynamical resonances, especially when they are partially masked by direct processes occurring in the same energy region.

In this section we consider various characterization techniques for the recognition and characterization of dynamical resonances for two different systems: the collinear $H + H_2$ and the collinear $F + H_2$ (HD, DH, D_2) ones. Characterization techniques include studies of the variation with energy of the state-to-state reaction probabilities, scattering matrix element phases and their energy derivatives, eigenphase shifts, and diagonal elements, eigenvalues, and eigenvectors of the collision lifetime matrix of Smith.

Paper II.1 presents results of a collision lifetime matrix analysis of the low energy resonances in the collinear $F + H_2(HD, DH, D_2)$ systems. The strength of the resonances is shown to decrease in the order $FHD \gg FH_2 > FD_2 > FDH$. Because the collision lifetime matrix localizes the resonance into a single eigenchannel, it allows one to determine the resonance position, width, and lifetime with a minimum of ambiguity. The peak in the reaction probability vs. energy curve for each system is shown to occur at higher energy than the peak in the eigenvalue of the collision lifetime matrix vs. energy curve for the same system, with the energy difference increasing as the resonance weakens.

Paper II.2 consists of a detailed study of the two lowest energy resonances in the collinear H + H_2 system on the Porter-Karplus potential energy surface. All of the characterization techniques mentioned above are utilized. The resonances are found to be reflected in all of these methods, most notable the eigenvalues of the collision lifetime matrix. Again, the resonances are almost entirely localized in a single eigenchannel of this matrix. The effect of the symmetry of the system in the results of the characterization procedures is discussed. There appear to be substantial differences between the two resonances as seen by the eigenvectors of the collision lifetime matrix near the resonance energies.

Paper II.3 includes a detailed study of the resonances studied in paper II.1. As in paper II.2, all of the above mentioned characterization techniques are utilized. The degree to which the resonances are reflected by the different techniques in each of the systems is discussed.

II. 1 COLLISION LIFETIME MATRIX ANALYSIS OF THE FIRST RESONANCE IN THE COLLINEAR F + H_2 REACTION AND ITS ISOTOPICALLY SUBSTITUTED ANALOGS*

---

*This paper appeared in Journal of Physical Chemistry <u>85</u>, 1969 (1981).

Collision Lifetime Matrix Analysis of the First Resonance in the Collinear $F + H_2$ Reaction and Its Isotopically Substituted Analogs*

Aron Kuppermann and Jack A. Kaye**

Arthur Amos Noyes Laboratory of Chemical Physics,[†]
California Institute of Technology, Pasadena, California 91125

(Received)

A collision-lifetime matrix analysis of the first resonance in the collinear $F + H_2$ reaction and its D-substituted analogs shows that near the resonance only one of its eigenvalues is positive and displays a maximum. This indicates that the resonance is associated with a single lifetime eigenchannel. The observed lifetime order is FHD $\gg$ $FH_2 > FD_2 >$ FDH.

---

* This work was supported in part by a grant (No. CHE77-26515) from the National Science Foundation.

** Work performed in partial fulfillment of the requirements for the Ph. D. degree in Chemistry at the California Institute of Technology.

[†] Contribution No. 6420.

1. Introduction

Among the most important results to come from quantum mechanical calculations of the probabilities of chemical reactions are the existence and significance of resonant processes. Reactive scattering resonances were first found in collinear calculations on the $H + H_2$ system[1,2] and have been observed in a variety of other collinear atom-diatom calculations, including those on the $F + H_2$, HD, D_2,[3,4] $Cl + H_2$,[5] $I + H_2$,[6] $Ba + N_2O$,[7] I + HI,[8] and Cl + HCl[9] systems. The $F + H_2$ system and its isotopically substituted counterparts are of particular interest because of their simplicity and relative ease of study by both theoretical and experimental techniques. It has recently been proposed that these systems are prime candidates for experimental observation of resonances.

Approximate j_z-conserving three-dimensional calculations on the $F + H_2$ system have been performed, and they suggest that the resonance found in the collinear calculations exists in the three-dimensional world.[10] Molecular beam experiments also provide indications of a resonance in this system.[11]

Resonances have been observed in a wide variety of scattering processes and are known to be associated with the existence of long-lived metastable states.[12] Once a resonance is known to exist in a chemically reactive system, one desires to know what features of the potential energy surface are responsible for its existence and what its lifetime is. The latter is especially important in determining what systems are the most suitable for the experimental detection of resonances.

Babamov and Kuppermann have recently developed a model that gives a physical interpretation and predicts the location of the lowest energy resonance in the collinear $F + H_2$ and isotopically substituted systems.[13] Hayes and Walker have also recently developed simple models for the lowest collinear $F + H_2$ resonance.[14] Here we consider the lifetime of the metastable state using the formalism of the collision lifetime matrix developed by Smith.[15] This approach was previously applied to the second resonance in the collinear $H + H_2$ reaction.[16]

In section 2 we briefly review Smith's collision lifetime matrix approach; in section 3 we present results obtained for the collinear $F + H_2$, HD, DH, and D_2 systems; and in section 4 we discuss their significance.

2. Theory

The definition of a lifetime of a metastable state in a quantum mechanical molecular scattering problem is not unique. For scattering in one dimension, it is well known[17] that the delay time τ of a particle due to the existence of a potential is associated with the phase shift η of the transmitted wave according to

$$\tau = \frac{\hbar}{v} \frac{\partial \eta}{\partial p} = \hbar \frac{\partial \eta}{\partial E} \quad , \tag{1}$$

where v, p, and E are, respectively, the initial velocity, momentum, and energy of the particle.

In the multichannel case, such as reactive scattering, there exists a set of quantum numbers, j, which describes the internal states of both colliding partners. Smith, in a seminal paper,[15] has shown that the corresponding delay times are given by the diagonal elements Q_{jj} of the hermitian collision lifetime matrix $\underline{\underline{Q}}$ defined by

$$\underline{\underline{Q}} = i\hbar \underline{\underline{S}} \frac{d\underline{\underline{S}}^{\dagger}}{dE} \quad , \tag{2}$$

where $\underline{\underline{S}}$ is the scattering matrix for the system. A resonance picture of the scattering process in collision channel j is useful when the inequality

$$\frac{2E_jQ_{jj}}{\hbar} \gg 1 \qquad (3)$$

holds, where E_j is the initial relative translational energy in that channel. In those cases, one may diagonalize the $\underline{\underline{Q}}$ matrix and associate the eigenvalues q_n (which are real because $\underline{\underline{Q}}$ is hermitian), when large and positive, with the exponential decay times of long-lived metastable states. Further, the wavefunction describing this state, called a lifetime-eigenchannel state, may be obtained from the n^th^ eigenvector, $\hat{U}_n$, of $\underline{\underline{Q}}$. In general, $\underline{\underline{Q}}$, its eigenvalues, and eigenvectors are a function of the energy.

The exact connection between the lifetime t_n of the metastable state and the eigenvalue q_n is not obvious because away from resonances, q_n may be negative. In the rest of this paper we will determine the nature of the variation of q_n with energy across a resonance for the collinear F + HD, F + H_2, F + D_2, and F + DH systems and suggest a definition t_n.

3. Results

The coupled-channel calculations performed to generate the $\underline{\underline{S}}$ matrices use the method of Kuppermann[18] and are additions to the calculations performed on these systems by Schatz, Bowman, and Kuppermann.[3,4] They were performed at a sufficiently dense energy grid to obtain the energy derivative of the $\underline{\underline{S}}$ matrix by a three-point finite difference method. As a result of this three-point approximation, the $\underline{\underline{Q}}$ matrix was almost but not precisely hermitian. To avoid complex eigenvalues, $\underset{\approx}{Q}$ was then forced to be hermitian by replacing it by the average of it and its hermitian conjugate. Diagonalization of the resulting matrix was performed by a standard EISPACK routine.[19] Its eigenvalues were calculated as a function of energy and were associated with a given lifetime-eigenchannel by requiring that its eigenvectors, which vary slowly with energy, be continuous within the accuracy of the calculations.

Plots of the eigenvalues q_n versus the total energy E of the system (measured with respect to the bottom of the hydrogenic molecule well) are presented in figure 1. Three main features of the curves are worthy of notice. First, in each of the four isotopic systems, only one of the curves displays a positive maximum, and for only this curve does q acquire positive values. Second, at values of E sufficiently above the resonant energy, all eigenvalues q are negative and nearly independent of energy. Third, there is usually at least one curve substantially removed from the others (the bottom one or two curves in the FH_2, FD_2, and FDH panels of figure 1), and examination of the corresponding eigenvectors indicates that these are usually due to higher energy HF or DF states that do not contribute significantly to the reaction dynamics in the energy range considered.

We conclude from these properties that the resonance is associated with a single eigenchannel $\bar{n}$ of the collision lifetime matrix; namely, the one for which the corresponding $q_{\bar{n}}(E)$ curve has a positive maximum. In view of the bell-shaped nature of this curve, we choose to define the lifetime $t_{\bar{n}}$ of a collision associated with the resonance lifetime eigenchannel $\bar{n}$ by the expression

$$t_{\bar{n}}(E) = q_{\bar{n}}(E) - q_{\bar{n}}^{as} , \qquad (4)$$

where $q_{\bar{n}}^{as}$ is the value of $q_{\bar{n}}$ at an asymptotic energy sufficiently large with respect to the resonance energy for $q_{\bar{n}}$ to have become essentially independent of energy. The values of $t_{\bar{n}}$ for the resonance lifetime-eigenchannels of the systems being considered are given by the right-hand-side ordinates of fig. 1. This definition has the convenient property that it makes $t_{\bar{n}}(E)$ be greater than or equal to zero for all energies considered. We define the resonance lifetime $t_{\bar{n}}^{res}$ as the maximum value of $t_{\bar{n}}$ and the energy at which it occurs the resonance energy $E_{\bar{n}}^{res}$. Although for long-lived resonances, such as the FHD one, the difference between $t_{\bar{n}}^{res}$ and $q_{\bar{n}}(E_{\bar{n}}^{res})$ is rather small; for short-lived ones, such as for FDH, $t_{\bar{n}}^{res}$ can be significantly larger than $q_{\bar{n}}(E_{\bar{n}}^{res})$. The shape of the $q_{\bar{n}}(E)$ curve, for each of the four isotopic systems, is approximately Lorentzian over a 1 to 2 FWHM energy range. We define that FWHM as the resonance width $\Delta E_{res}^{\bar{n}}$.

As can be seen from fig. 1, the resonance lifetimes clearly decrease in the order FHD $\gg$ FH_2 > FD_2 > FDH. This is to be expected on examination of the width of the peaks in the plots of reaction probability versus energy for these systems given in fig. 2. However, even weak resonances, such as those in the FD_2 and FDH systems, which do not show up as clearly resolved peaks in the probability versus energy plots, do exhibit distinct resonant behavior in the plots of fig. 1. This is particularly important since in those two systems direct processes contribute in a major way to the probability versus energy curves.

For each value of E, the components $U_{n'n}$ of the eigenvector $\underset{\sim}{U}_n$ of $\underline{\underline{Q}}$ furnish the contribution to the eigenchannel wavefunction ψ_n of each of the reagent or product molecule eigenstates. Those change significantly with energy across a resonance eigenchannel and will be discussed elsewhere.

4. Discussion and Conclusions

The $q(E)$ and $t(E)$ curves of fig. 1 clearly demonstrate the usefulness of the eigenvalues of Smith's collision lifetime matrix[15] for the recognition and lifetime characterization of reactive scattering resonances. Of particular interest is the fact that in the four isotopic systems considered, the presence of the resonance manifests itself in only one of the lifetime eigenchannels, in contrast to an eigenphase shift analysis, in which several of the scattering matrix eigenchannels are affected by the resonance.[20] Thus, this kind of analysis seems specially well suited for separating resonance processes, even very weak ones, from direct reaction mechanisms, even when the latter are dominant, as seems to be the case for the FD_2 and FDH systems.

The localization of the resonance in a single lifetime eigenchannel implies that a single linear combination of reagent and product asymptotic states, at the resonance energy, leads to an effective trapping of the energy in internal degrees of freedom of the compound system. This eigenchannel should play an important role in modeling resonances. Whether or not resonances are normally confined to a single lifetime eigenchannel is not clear at the present time, and further work is required to elucidate this point.

A comparison of figs. 1 and 2 indicates that the resonance energy E^{res}, as defined in section 3, is always lower than the energy E^{P}_{max} at which the reaction probability curves of fig. 2 achieve a maximum. The vertical arrows in the latter figure indicate the corresponding E^{res} positions. This shift appears to be at least in part due to the concomitant occurrence of a direct mechanism. Table I furnishes several quantities of interest for the systems being considered. From the last column in that table we see that the shift between E^{res} and E^{P}_{max}, in units of the resonance width ΔE^{res}, increases in the order FHD, FH_2, FD_2, FDH. We conclude that for weak resonances superimposed on direct processes the identification of the resonance energy with the energy at which a transition probability has a maximum may be inappropriate.

Other techniques used for the characterization of resonances, such as Argand diagrams,[21] the derivative of the phases of the $\underline{\underline{S}}$ matrix elements with respect to energy,[21] or the energy-dependence of its eigenphase shifts mentioned above, all manifest the presence of the resonance to some degree, but not as clearly as the collision lifetime matrix eigenvalues. This is particularly true in the FDH and FD_2 systems for which this resonance is quite weak.

The results in the sixth column of Table I and in Fig. 1 show that the FHD resonance is about 75 times longer-lived than the FDH one. This gives an indication of the dynamic range of the lifetime matrix analysis technique. These results lend further support to the recent suggestion[18c, 20] that the F + HD system is a particularly promising one for the experimental detection of resonances. In that system, the F + HD ($v = 0$) → HF ($v' = 2$) + D channel should show sharp resonant behavior, whereas the F + DH ($v = 0$) → DF ($v' = 3, 4$) + H channels should show little, if any, such behavior. A further discussion of these resonances will be presented in a future publication.

Acknowledgments

The calculations reported here were performed on the Dreyfus-NSF Theoretical Chemistry Computer (VAX 11/780) which was funded through grants from the Camille and Henry Dreyfus Foundation, the National Science Foundation (Grant No. CHE78-20235), and the Sloan Fund of the California Institute of Technology, and on the IBM 370/158 computer of Ambassador College, Pasadena, California, for which we express our appreciation. We would like to thank Dr. V. K. Babamov for useful discussions.

References

(1) Truhlar, D. G.; Kuppermann, A. J. Chem. Phys. 1970, 52, 3841; 1972, 56, 2232.

(2) Wu, S.-F.; Levine, R. D. Mol. Phys. 1972, 22, 882; Chem. Phys. Lett. 1971, 11, 557.

(3) Schatz, G. C.; Bowman, J. M.; Kuppermann, A. J. Chem. Phys. 1973, 58, 4023; 1975, 63, 674.

(4) Schatz, G. C.; Bowman, J. M.; Kuppermann, A. J. Chem. Phys. 1975, 63, 685.

(5) Baer, M. Mol. Phys. 1976, 27, 1429.

(6) Chapman, F. N., Jr.; Hayes, E. F. J. Chem. Phys. 1977, 66, 2554.

(7) Bowman, J. M.; Leasure, S. C.; Kuppermann, A. Chem. Phys. Lett. 1976, 43, 374.

(8) Kaye, J. A.; Kuppermann, A. Chem. Phys. Lett. 1981, 77, 573.

(9) Kaye, J. A.; Kuppermann, A., manuscript in preparation.

(10) Redmon, M. J.; Wyatt, R. E. Chem. Phys. Lett. 1979, 63, 209.

(11) Sparks, R. K.; Hayden, C. C.; Shobatake, K.; Neumark, D. N.; Lee, Y. T. In "Horizons in Quantum Chemistry", Fukui, K.; Pullman, B.; Eds.; D. Reidel: Boston, 1980; pp. 91-105.

(12) Goldberger, M. L.; Watson, K. M. "Collision Theory"; Krieger: Huntington, New York, 1975; pp. 424-509.

(13) Babamov, V. K.; Kuppermann, A. J. Chem. Phys., A Physical Interpretation of the Collinear Reactive Scattering Resonances in the F + HD, H_2, and D_2 Systems, J. Chem. Phys., submitted.

(14) Hayes, E. F.; Walker, R. B. Theoretical Analysis of the Reaction $F + H_2\ (v = 0) \rightarrow FH\ (v = 0, 1, 2, 3) + H$, forthcoming.

(15) Smith, F. T. Phys. Rev. 1960, 118, 349.

(16) Schatz, G. C.; Kuppermann, A., manuscript in preparation; Schatz, G. C. Ph. D. Thesis, California Institute of Technology (1975).

(17) Bohm, D. "Quantum Theory"; Prentice-Hall, Inc.: New York, 1951; pp. 257-262.

(18) Kuppermann, A. In (a) "Proceedings of the Conference on Potential Energy Surfaces in Chemistry"; Lester, W. A., Ed.; University of California, Santa Cruz, 1970; pp. 121-124; (b) "Proceedings of the 7th International Conference on the Physics of Electronic and Atomic Collisions"; North-Holland Publishing Co.: Amsterdam, 1971; pp. 3-5; (c) "Theory of Scattering: Papers in Honor of Henry Eyring"; Vol. 6A of "Theoretical Chemistry: Advances and Perspectives"; Henderson, D; Eyring, H.; Eds.; Academic Press, Inc.: New York, 1981; pp. 79-162.

(19) Smith, B. T.; Boyle, J. M.; Dongarra, J. J.; Farbow, B. S.; Ikebe, Y.; Klema, V. C.; Moler, C. B. In "Matrix Eigensystem Routines - EISPACK Guide, Lecture Notes in Computer Science"; Goos, G; Hartmanis, J., Eds; Springer-Verlag: Berlin, 1976.

(20) Kuppermann, A. In "Potential Energy Surfaces and Dynamics Calculations"; Truhlar, D. G., Ed.; Plenum Press: New York, 1981; pp. 375-420.

(21) Schatz, G. C.; Kuppermann, A. J. Chem. Phys. 1973, 59, 964; and references cited therein.

Table I. Resonance Characteristics.

System	E_0/meV[a]	E^{P}_{max}/meV[b]	E^{res}/meV[c]	t^{res}/psec[d]	ΔE^{res}/ meV[e]	$\frac{t^{res}\Delta E^{res}}{2\hbar}$	$\frac{E^{P}_{res}-E^{res}}{\Delta E_{res}}$
FHD	232.9	244.94	244.92	4.8	0.52	1.82	0.04
FH_2	268.4	283.5	281.6	0.33	7.2	1.81	0.26
FD_2	190.6	220.0	214.6	0.15	11.4	1.30	0.47
FDH	232.9	280[f]	253.3	0.064	21.2	1.03	1.3

[a] Zero point energy of isolated hydrogenic molecule.

[b] Total energy at which reaction probability of fig. 2 has a maximum.

[c] Total energy at which the resonance eigenvalue of fig. 1 has a maximum.

[d] Peak value of t(E) for resonance eigenchannel curves of fig. 2.

[e] Full width at half maximum of t(E) resonance eigenchannel curves of fig. 2.

[f] Observation of plots of the probability versus energy curves over a wider energy range[3,4,13] than that used in fig. 2 suggests that this maximum is probably related to a direct mechanism which occurs at higher energies than the resonance energy rather than to the resonance process of fig. 1.

Figure Captions

Fig. 1. Eigenvalues q of the collision lifetime matrix $\underset{=}{Q}$ and collision lifetime t as a function of energy for the collinear FHD, FH_2, FD_2, and FDH systems. The bottom abscissa in each panel (E) denotes the total energy with respect to the bottom of the isolated hydrogenic molecule well, whereas the top common abscissa (E_0) denotes the energy measured with respect to the zero point energy of that molecule. The left ordinate scale in each panel refers to all the curves in that panel, whereas the right one refers only to the corresponding bell-shaped curve. The dashed portion of the lowest curve of the FHD panel indicates a region of numerical noise associated with the sharp peak of the top curve. The horizontal straight line of that panel represents the eigenvalue curves for two distinct eigenchannels. These curves coincide within the plotting accuracy of the figure but are distinguishable on an expanded scale. The divisor in the three lower panels indicates the number by which the ordinate of the neighboring curve was divided before plotting.

Fig. 2. Probabilities of the collinear reactions $F + HD\ (v = 0) \rightarrow FH\ (v' = 2) + D$, $F + H_2\ (v = 0) \rightarrow FH\ (v' = 0) + H$, $F + D_2\ (v = 0) \rightarrow FD\ (v' = 3) + D$, and $F + DH\ (v = 0) \rightarrow FD\ (v' = 3) + H$ as a function of total energy E with respect to the bottom of the isolated hydrogenic molecule well and of the initial reagent relative translational energy E_0. The vertical arrows indicate the energies at which the resonance collision lifetime eigenvalues of fig. 1 achieve a maximum.

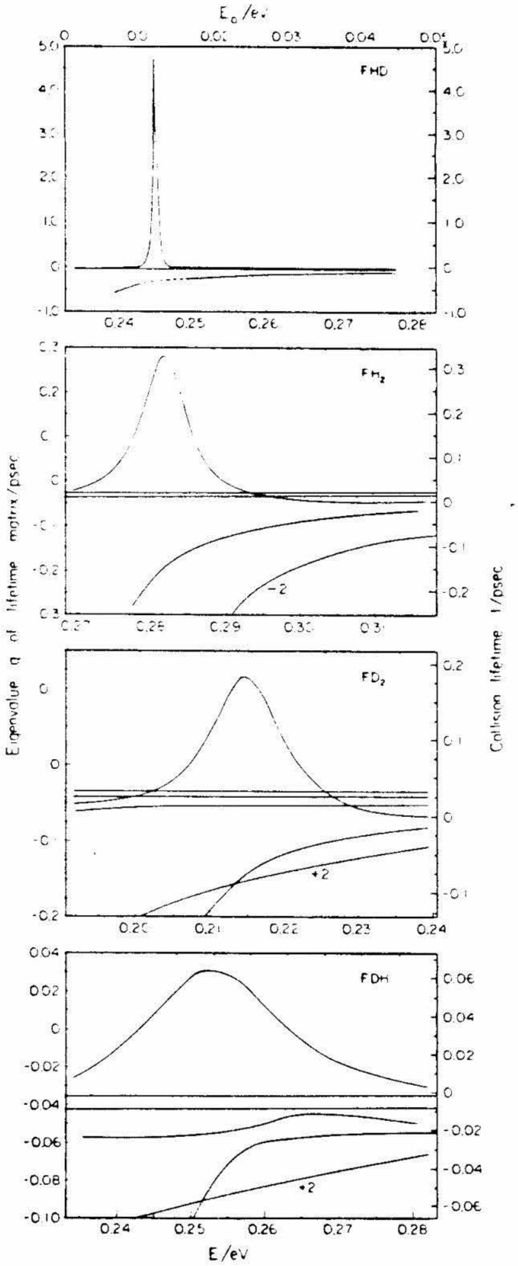
E₀ /eV
0
0.01
0.02
0.03
0.04
0.05
FHD
5.0
4.0
3.0
2.0
1.0
0
-1.0
0.24
0.25
0.26
0.27
0.28
FH₂
0.3
0.2
0.1
0
-0.1
-0.2
-0.3
0.27
0.28
0.29
0.30
0.31
-2
FD₂
0.2
0.1
0
-0.1
-0.2
0.20
0.21
0.22
0.23
0.24
+2
FDH
0.04
0.02
0
-0.02
-0.04
-0.06
-0.08
-0.10
0.06
0.04
0.02
0
-0.02
-0.04
-0.06
0.24
0.25
0.26
0.27
0.28
+2
E /eV
Eigenvalue q of lifetime matrix /psec
Collision lifetime 1/psec

Figure 1.

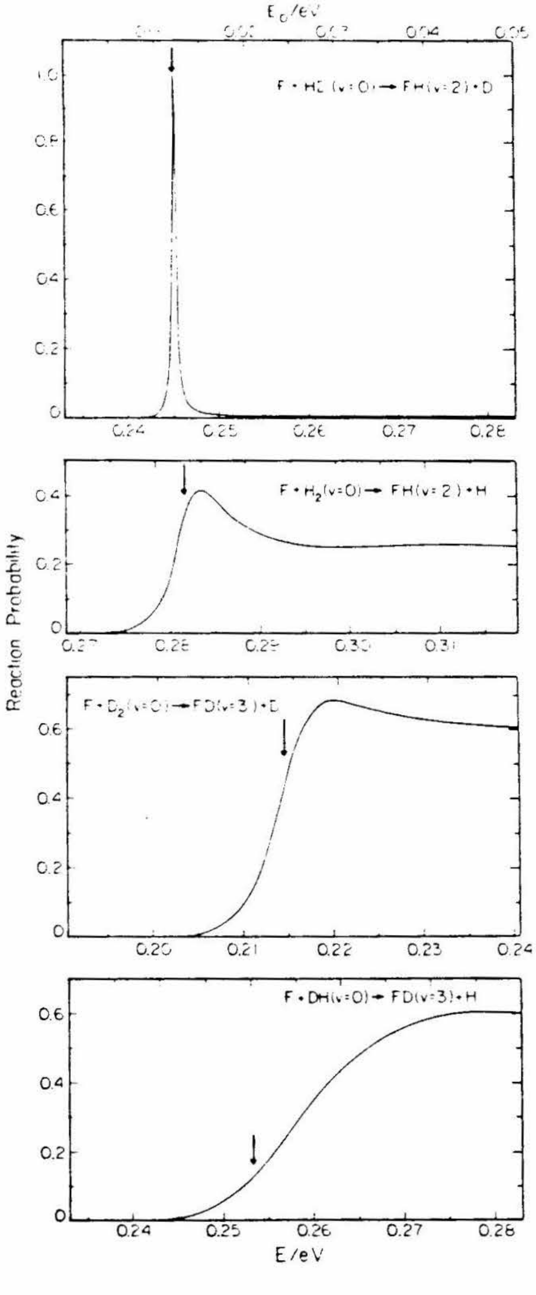
E_0/eV
0.01
0.02
0.03
0.04
0.05
F + HD (v=0) → FH(v=2) + D
1.0
0.8
0.6
0.4
0.2
0
0.24
0.25
0.26
0.27
0.28
F + H_2(v=0) → FH(v=2) + H
0.4
0.2
0
0.27
0.28
0.29
0.30
0.31
Reaction Probability
F + D_2(v=0) → FD(v=3) + D
0.6
0.4
0.2
0
0.20
0.21
0.22
0.23
0.24
F + DH(v=0) → FD(v=3) + H
0.6
0.4
0.2
0
0.24
0.25
0.26
0.27
0.28
E/eV

Figure 2.

II.2 CHARACTERIZATION OF THE TWO LOWEST ENERGY RESONANCES IN THE COLLINEAR $H + H_2$ SYSTEM

Characterization of the Two Lowest Energy Resonances in the Collinear H + H_2 System.[a)]

Jack A. Kaye[b)] and Aron Kuppermann

Arthur Amos Noyes Laboratory of Chemical Physics.[c)]

California Institute of Technology, Pasadena, California 91125

(Received)

We have performed quantum mechanical scattering calculations on the collinear H + H_2 reaction on the Porter-Karplus surface at energies in the vicinity of the two lowest energy resonances. We have examined the effect of the resonances on the energy dependence of the state-to-state reaction probabilities, individual $\underline{\underline{S}}$ matrix element phases and their energy derivatives, eigenphase shifts, and diagonal elements, eigenvalues, and eigenvectors of Smith's collision lifetime matrix. The eigenvalues of the collision lifetime matrix provide the most unambiguous means for characterizing the resonances and allow one to obtain the resonance position and width, as well as the lifetime of the long-lived metastable state associated with the resonance. The two resonances, located at 0.875 eV and 1.310 eV total energy, have widths (FWHM) of 0.021 eV and 0.028 eV and lifetimes of 0.091 psec and 0.085 psec, respectively. While both resonances are shown to be associated with symmetric collision lifetime eigenchannels, the two resonances differ markedly in the fractional compositions of the eigenvectors of the collision lifetime matrix. The limitations and advantages of each of the characterization techniques used was discussed. The eigenvalues of the collision lifetime matrix are compared to the results of a classical theory for the time delay.

---

[a] This work was supported in part by a grant (No. CHE77-26515) from the National Science Foundation.

[b] Work performed in partial fulfillment of the requirements for the Ph.D. degree in Chemistry at the California Institute of Technology.

[c] Contribution No.

I. INTRODUCTION

The reaction of atomic hydrogen with molecular hydrogen

$$H + H_2 \longrightarrow H_2 + H \tag{1}$$

has been the object of numerous theoretical studies, particularly in the last twenty years when the existence of large computers has made numerical calculations on this reaction feasible (1). The extensive study of this reaction is due mainly to its simplicity: the small number of electrons and nuclei makes the calculation of a chemically accurate potential energy surface possible, the absence of low-lying excited electronic states makes a single-surface calculation satisfactory, and the small masses and large spectroscopic constants of H_2 make quantum mechanical calculations of this reaction simpler (and less expensive) than those of reactions involving heavier atoms.

Although a large number of three-dimensional classical trajectory calculations have been performed on reaction 1 at energies below and above dissociation, where the reaction

$$H + H_2 \longrightarrow H + H + H \tag{2}$$

becomes energetically allowed (1, 2), the number of exact three dimensional quantum mechanical calculations is much smaller and has been restricted to energies well below dissociation. Most of the exact quantum mechanical calculations on reaction 1 have been restricted to collinear geometries, in which the three hydrogen atoms are restricted to forever lie on a straight line (4).

One of the crucial results to come out of the collinear calculations on reaction 1 is the presence of dynamical resonances in this system (4). These resonances may be seen as rapid changes in the state-to-state reaction probabilities with energy, although other results from the calculation (such as the phase of an $\underline{\underline{S}}$ matrix element) also change rapidly with energy near a resonance. The three-dimensional exact quantum mechanical calculations that have been performed already suggest that these resonances carry over, albeit broadened and diminished somewhat in intensity, to the three-dimensional world (5).

An understanding of what features of the potential energy surface are responsible for the observed resonances is important, especially if one is to use reactive scattering resonances as a "spectroscopy" of potential energy surfaces. Since it is known that a resonance in a scattering problem usually implies the existence of some long-lived metastable state (6), one wants to know what its nature is (i.e. does it involve excitation to a higher state in some internal degree of freedom). Finally, one wants to know the lifetime of this metastable state. If this lifetime is sufficiently large that, after allowing for the expected decrease on going from one dimension to three dimensions, it is significantly greater than the rotational period of the molecule, it is reasonable to expect that the resonance might make itself visible in the variation of the differential cross section for the reaction with energy (given an experiment of sufficient resolution).

In this paper, we attempt to characterize the first two resonances for the collinear $H + H_2$ reaction (on the Porter-Karplus surface) (7). We consider various ways in which the resonance manifests itself, including changes in probability and $\underline{\underline{S}}$ matrix element phase with energy. To help determine the lifetime of these resonant states, we calculate Smith's collision lifetime matrix (8), positive eigenvalues of which correspond roughly to the lifetimes of the resonant state. By considering the variation of the eigenvectors of the matrix with energy, we help determine the nature of the two resonances and show that the first two resonances are quite different from each other.

The outline of this paper is as follows: In section II we review the definitions and origins of the various quantities we have studied, including Smith's (8) collision lifetime matrix. We then briefly describe the numerical procedures employed in these calculations. In section

III, we present as a series of plots the results obtained. These are discussed in section IV. In section V we offer conclusions.

II. THEORY AND NUMERICAL PARAMETERS

The direct result of the collinear quantum mechanical calculations is the scattering matrix $\underline{\underline{S}}$ that relates the incoming and outgoing wave states associated with isolated reagents and products. A detailed description of the theory behind $\underline{\underline{S}}$ and how one goes about calculating it is presented elsewhere (9). $\underline{\underline{S}}$ should be unitary and symmetric (10); deviations from these conditions reflect inaccuracies in the scattering calculation. Henceforth, we shall consider $\underline{\underline{S}}$ to be both unitary and symmetric. The probability for reaction from state i to state j is just the absolute magnitude of the corresponding $\underline{\underline{S}}$ matrix element (9, 10):

$$P_{ij} = |S_{ij}|^2 \tag{3}$$

Because $\underline{\underline{S}}$ is symmetric, $S_{ij} = S_{ji}$ so $P_{ji} = P_{ij}$, as must be true to satisfy microscopic reversibility. Since $\underline{\underline{S}}$ is unitary,

$$\sum_{j=1}^{N} |S_{ij}|^2 = 1 \tag{4}$$

which must be true if probabilities are to be normalized to one. The amplitude and phase of the elements of $\underline{\underline{S}}$ are both functions of the energy. The variation of these quantities with energy will be the initial indicator of the presence of absence of resonances.

$\underline{\underline{S}}$ is related to the reactance matrix $\underline{\underline{R}}$, which is symmetric (9, 10) by the relationship

$$\underline{\underline{S}} = (\underline{\underline{I}} + i\underline{\underline{R}})(\underline{\underline{I}} - i\underline{\underline{R}})^{-1} \tag{5}$$

The eigenphase shifts (11) are defined as the angles whose tangents are the eigenvalues of $\underline{\underline{R}}$(which are real, due to the symmetry of $\underline{\underline{R}}$). These eigenphase shifts lie in the range from $-\pi/2$ to $\pi/2$; hence integral multiples of π may be added to or subtracted from the eigenphase shifts to insure continuity of eigenphase shift vs. energy curves. The eigenphase shifts have been shown to have unusual energy dependence in the region of a resonance (11-14). They may be thought of as being a generalization of the phase shift in single particle scattering.

The definition of the lifetime is not so clear, however. In single particle, one dimensional scattering, the delay time τ of a particle (the time spent by the particle in some region of space in excess of the time it would have spent there if there were no potential) is related to the phase shift η of the transmitted wave (15):

$$\tau = \frac{\hbar}{v}\frac{\partial \eta}{\partial p} = \hbar \frac{\partial \eta}{\partial E} \tag{6}$$

where v, p, and E are the initial velocity, momentum, and energy of the particle, respectively.

In the multi-channel case, instead of having a single equation (and thus a single phase shift and a single delay time), there is a set of equations, each of which may be thought to be related to an initial state j of the colliding particles. Smith (8) has shown that in this multi-channel case, the corresponding delay times of these states are given by the diagonal elements Q_{jj} of the collision lifetime matrix $\underline{\underline{Q}}$, which is defined by

$$\underline{\underline{Q}} = i\hbar \underline{\underline{S}} \frac{d\underline{\underline{S}}^{\dagger}}{dE} \tag{7}$$

Since $\underline{\underline{S}}$ is unitary, $\underline{\underline{Q}}$ will be hermitian.

A positive value for Q_{jj}, then, suggests a positive time delay. If Q_{jj} is sufficiently positive, a resonance picture of the scattering process is appropriate. Smith (8) has shown that a good definition of "sufficiently positive" is when the inequality

$$2E_j Q_{jj}/\hbar \gg 1 \tag{8}$$

is satisfied, where E_j is the initial relative translational energy for channel j (the total energy minus the internal energies of the colliding particles in internal state j).

When inequality 8 is satisfied, $\underline{\underline{Q}}$ may be diagonalized (since $\underline{\underline{Q}}$ is hermitian, its eigenvalues must be real), and any positive eigenvalues may be interpreted as the lifetime of the long-lived metastable states.

The wave function describing these states, known as a lifetime eigenchannel state, may be obtained from the corresponding eigenvector of $\underline{\underline{Q}}$. In general, $\underline{\underline{Q}}$, its eigenvalues, and its eigenvectors are a function of the energy.

As a rule, for an N channel scattering problem, all the matrices ($\underline{\underline{P}}$, $\underline{\underline{Q}}$, $\underline{\underline{R}}$, $\underline{\underline{S}}$) will be N x N, and there will be N independent quantities, such as the diagonal elements Q_{jj}. In the case of symmetric systems, that is, those of the type

$$A + BA \longrightarrow AB + A \tag{9}$$

there are only N/2 different diagonal elements Q_{jj}. This is due to the symmetric block structure of $\underline{\underline{S}}$ in the symmetric collision case:

$$\underline{\underline{S}} = \begin{pmatrix} \underline{\underline{S}}^N & \underline{\underline{S}}^R \\ \underline{\underline{S}}^R & \underline{\underline{S}}^N \end{pmatrix} \tag{10}$$

where the superscripts N and R refer to the non-reactive and reactive blocks of the $\underline{\underline{S}}$ matrix, respectively. In this symmetric case, the eigenvectors and eigvenvalues of $\underline{\underline{Q}}$ may be broken up into two classes: symmetric and anti-symmetric, as is shown in appendix A. The eigenvalues and eigenvectors of $\underline{\underline{R}}$ (and thus the eigenphase shifts) may be similarly categorized.

The coupled channel calculations from which the $\underline{\underline{R}}$, $\underline{\underline{S}}$, and $\underline{\underline{P}}$ matrices were obtained were performed using the method of Kuppermann (16), and are additions to the calculations performed previously on this system (5). Thirteen basis functions were used in all calculations. Calculations were performed at a sufficiently dense energy grid so that the energy derivative of $\underline{\underline{S}}$ needed in the construction of $\underline{\underline{Q}}$ could be approximated by a three-point finite difference procedure. For example, near the resonances, scattering calculations were performed every 2.5 meV. Because of the approximate nature of the differentiation, the $\underline{\underline{Q}}$ obtained was only nearly hermitian. For the sake of simplicity, this approximate $\underline{\underline{Q}}$ was replaced by the average of it and its hermitian conjugate. The resulting matrix was diagonalized by a standard EISPACK routine (17). The eigenvalues were calculated as a function of energy and were associated with a particular lifetime eigenchannel by requiring that the corresponding eigenvectors, which vary only slowly with energy, be continuous within the accuracy of the calculations. A similar procedure is used to associated the eigenphase shifts with a particular eigenstate of $\underline{\underline{R}}$. The assignment of collision lifetime matrix eigenvalues to their corresponding eigenvectors is simplified in symmetric systems because of the aforementioned separation of the eigenvectors and eigenvalues of $\underline{\underline{Q}}$ into symmetric and anti-symmetric sets.

III. RESULTS

The reaction probabilities in the vicinity of the first and second resonances are plotted as a function of energy in figures 1 and 2, respectively. A better feel for how the resonances fit in with the overall dynamics in the H + H_2 system may be obtained by examining figure 5 of reference 18, in which the reaction probabilities (for vibrationally adiabatic reaction, that is, that occurring with no change in vibrational state) are shown over a broad energy range (up to 3.0 eV). The resonances are seen as rapid changes in the reaction probabilities vs. energy. P_{00}^R and, to a lesser extent, P_{01}^R at the first resonance (figure 1) and P_{00}^R, P_{01}^R, and P_{11}^R at the second resonance (figure 2a) show such variation. Reactions involving the $v = 2$ state are unlikely near the resonance and show no rapid variation with energy (figure 2b), although the energy dependence of the probabilities of non-adiabatic reaction is somewhat unusual.

Next, we wish to consider the phases of those elements of $\underline{\underline{S}}$ mentioned above, which vary rapidly with energy and thus are most indicative of the existence of a resonance. In figure 3, we display Argand diagrams (19) for the S_{00}^R and S_{01}^R matrix elements. In the Argand diagram, the matrix element is plotted in the complex plane. Points at successive energies are connected and a curve tracing out the motion of the element in the complex plane is generated. Away from a resonance, the diagram usually consists of a smooth clockwise curve. Near a resonance, however, the curve frequently shifts to a counterclockwise direction, possibly "turning over" on itself to form a loop, as has been seen in the F + H_2, F + HD (14), I + HI (13), and H + H_2 (19) (second resonance on the scaled SSMK surface) systems. In cases where resonant and direct processes are both important, the curve may just cut across a region of the complex plane rather than smoothly following a circular or spiral-shaped curve, as has been seen in the F + D_2 case (14).

The Argand diagrams for these two transitions near the first resonance are quite different. The Argand diagram for S_{00}^R shows no loop formation; the curve does acquire a "half-moon" shape with a distinct region of counterclockwise direction running from approximately 0.86 to 0.89 eV (all energies given are total energies, that is, with respect to the bottom of the isolated H_2 well). The diagram for S_{01}^R does show loop formation, also in the region from 0.86 to 0.89 eV.

In figure 4 we display Argand diagrams for the S_{00}^R, S_{01}^R, and S_{11}^R matrix elements near the second resonance. Again, two kinds of behavior can be seen. S_{00}^R (figure 4a) and S_{11}^R (figure 4c) show loop formation, where the loop formed in the S_{00}^R diagram is much larger than that in the S_{11}^R diagram. S_{01}^R, on the other hand, shows half-moon formation. In the S_{00}^R curve, the loop occurs in the energy range from 1.28 to 1.32 eV, while in the S_{11}^R courve it is from 1.30 to 1.34 eV. The half-moon formation in the S_{01}^R curve is from 1.28 to 1.33 eV. The slight shift to higher energy of the S_{11}^R resonance as determined from the Argand diagram is consistent with a similar shift in the probability vs. energy curves (figure 2a), where the maximum in P_{11}^R occurs at about 0.01 eV higher energy than the maximum in P_{01}^R or the minimum on P_{01}^R.

Because the Argand diagram depends both on the phase and the amplitude (probability) of the element of $\underline{\underline{S}}$, it is worthwhile to focus just on the phase. The variation of the phase of the $\underline{\underline{S}}$ matrix element has been previously found to be a useful quantity for pinpointing the location of a resonance (19). Away from a resonance, the phase decreases monotonically with energy; this decrease is clearly related to the normal clockwise sense of the Argand diagram. Near a resonance, however, this steady monotonic decrease may be replaced by a less steep decrease (associated with straight cut formation in the Argand diagram), an increase (associated with loop formation), or a small area of rapid decrease followed by a return to the earlier slope, perhaps with the formation of a brief region of increasing phase separating them (associated with half-moon formation). $\underline{\underline{S}}$ matrix element phase vs. energy diagrams are presented in figures 5 (S_{00}^R, S_{01}^R near the first resonance) and 6 (S_{00}^R, S_{01}^R, and S_{11}^R near the second resonance). The smooth nature of these curves, along with the steady decrease in phase with energy away from the resonance suggests that a good way of examining solely the resonant processes would be to subtract out the background behavior, which would be associated with direct processes. Such an analysis has been performed previously (19).

The near energy independence of the slopes of the phase vs. energy curves away from the resonance suggests that the energy derivative of the $\underline{\underline{S}}$ matrix element phase is also a useful quantity. Away from the resonance, this quantity should be nearly independent of energy, allowing any effect of the resonance to clearly be seen. The energy derivative of the $\underline{\underline{S}}$ matrix element phase is also of interest because if one substitutes this quantity for the energy derivative of the phase shift in eq. 6, one obtains an expression for a delay time. When positive, this should provide some information as to the lifetime of the resonant state. In figures 7 and 8 we present plots of the delay time τ_{ij} given by

$$\tau_{ij} = \hbar \frac{d\phi^R_{ij}}{dE} = h\mathrm{Re}(-ih\,(S_{ij})^{-1}\, dS_{ij}/dE) \qquad (11)$$

for the transitions considered above at the first and second resonances, respectively.

At the first resonance, τ_{00} is always negative, while τ_{01} becomes positive, with a maximum value $\bar{\tau}_{01}$, of 0.016 psec. The peak location is slightly below that of the maximum in the P_{01}^R vs. energy curve (figure 1). At the second resonance, all three curves (figure 8) show positive maxima, with values of 0.018, 0.009, and 0.005 psec for $\mathcal{T}_{00}$, $\mathcal{T}_{01}$, and $\mathcal{T}_{11}$, respectively. The large negative dip in $\mathcal{T}_{01}$ at the second resonance (and also for $\mathcal{T}_{00}$ at the first resonance) is due to half-moon formation in the Argand diagram. Because the phase may change rapidly with energy over a fairly broad energy region, and plots of $\mathcal{T}_{ij}$ as a function of energy may have both minima and maxima, it is somewhat difficult to try to assign a resonance position from figures 7 and 8.

Eigenphase shifts have also been shown to be useful in the characterization of resonances (11-14). In figures 9 and 10 we present plots of the eigenphase shifts as a function of energy near the first and second resonances, respectively. The eigenphase shifts decouple into symmetric and anti-symmetric sets. There are four main features of these plots. First, the resonances are manifested as rapid changes of the eigenphase shift with energy; there are, in fact, increases in two of them for each resonance. Second, the resonance is seen in the symmetric eigenphase shifts only. This feature has been observed in other systems and has been explained previously (11-14). Third, there are a number of avoided crossings involving the anti-symmetric curves (at 0.855 eV near the first resonance and 1.365 eV near the second resonance). Avoided crossings have been seen before in eigenphase shift analyses of the F + H_2 and F + HD systems (14), and seem to imply the existence of some sort of non-crossing rule. In other cases however, (such as near the second resonance at 1.324 eV, and also in the F + H_2 system) (14), the curves do appear to cross. Finally, just above the opening of a new vibrational state, the symmetric and anti-symmetric eigenphase shifts are the same and they decrease extremely rapidly with energy (the lowest portions of these curves are not shown in the figures).

Next, we wish to consider Smith's collision lifetime matrix (8) $\underline{\underline{Q}}$. We are interested in three features of this matrix. First, we want to know whether any diagonal elements are anywhere positive, and if so, whether they are sufficiently positive that inequality 8 is satisfied. We expect an affirmative answer to these questions, as all that can be gathered from the probabilities, $\underline{\underline{S}}$ matrix element phases, and eigenphase shifts indicates that a resonant picture of the scattering is an appropriate one.

In figures 11 and 12 we present plots of the diagonal elements Q_{nn} in the region of the first and second resonances, respectively. As discussed previously (and shown in appendix A), each diagonal element in $\underline{\underline{Q}}$ appears twice; hence there are only one or two independent diagonal elements near the first resonance, and only two or three near the second resonance. For both resonances, Q_{11} becomes positive; Q_{22} becomes positive near the second resonance, and has a definite maximum near the first resonance. Near the opening of the $v = 1$ and $v = 2$ states, Q_{22} and Q_{33} have large negative values, increasing rapidly with energy. Near the second resonance Q_{33} does not have a maximum, as does Q_{22} near the first resonance.

The peak in Q_{11} near the first resonance occurs at an energy of 0.870 eV (corresponding to a reagent translational energy of 0.596 eV) and has a value of 0.0075 psec. The left hand side of eq. 8 has a value of 13.6, which is substantially greater than one. Thus, a resonant picture of the scattering in this region of energy is justified. Near the second resonance, the appropriate values for the left hand side of eq. 8 are 36.2 for Q_{11} and 2.2 for Q_{22}. Thus, the use of a resonant picture of the scattering at this higher energy is also justified. One cannot use these data to suggest the existence of two resonances at this higher energy, however. As one moves away from the resonance, the change in Q_{nn} with energy becomes small. This has been predicted by Smith (8) for high translational energy collisions.

It should be noted that the largest positive diagonal element of $\underline{\underline{Q}}$

is fairly similar in magnitude to the largest τ_{ij} determined from the energy derivative of the elements of $\underline{\underline{S}}$. The largest positive value of Q_{11} of 0.0075 psec at the first resonance is almost within a factor of two of the largest τ_{ij} of 0.016 psec. Similarly, at the second resonance, the maximum value of Q_{11}, 0.0115 psec, is close to the 0.0175 psec maximum of ${}_{00}$.

More important than the diagonal elements Q_{nn} are the eigenvalues of $\underline{\underline{Q}}$, q_n (note that there is no direct relationship between the n in Q_{nn} and the n in q_n; the same symbol is simply used for convenience). It has been seen earlier for the F + H_2, HD, DH, and D_2 systems (20) and for the H + H_2 system (11, 12) on the scaled SSMK surface (at the second resonance) that there will be only one positive eigenvalue; this eigenvalue and its corresponding eigenvector may then be unambiguously taken as those belonging to the long-lived metastable state. Similar behavior is seen for this system in figures 13 and 14 (first and second resonances, respectively). In both figures, only one eigenvalue becomes positive; the curves are labeled to show that the positive eigenvalues belong to symmetric lifetime eigenchannels. Near the first resonance (figure 13) a small maximum does develop in the curve of the second symmetric eigenvalue, but the maximum is small and has a peak value which is negative. As we have done previously for the F + H_2, HD, DH, and D_2 systems (20), we define the lifetime as being the difference between the eigenvalue in the curve containing the positive maximum and its asymptotic value q_π^{as}, to which it settles at high energy:

$$t_\pi(E) = q_\pi(E) - q_\pi^{as} \tag{12}$$

where the definition of the lifetime t(E) only applies to the eigenchannel π containing the maximum. These lifetime scales are shown on the right hand ordinates of figures 13 and 14. Since we have not performed scattering calculations at a sufficiently dense grid of energies for reliable $\underline{\underline{Q}}$ matrices to be calculated above 1.35 eV, we have visually estimated the q_π^{as}.

The maximum values $q_{\overline{n}}$ obtained, 0.076 psec for the first resonance and 0.074 psec for the second resonance, corresponding to lifetimes of 0.091 psec and 0.085 psec, respectively, are substantially greater than those lifetimes estimated from either the energy derivative of the $\underline{\underline{S}}$ matrix or the diagonal elements Q_{nn}. Above the opening of the new channel, but below the resonance, the two lowest eigenvalues (one each of symmetric and anti-symmetric) of $\underline{\underline{Q}}$ are very close to the corresponding diagonal element Q_{nn}.

Finally, we wish to consider the eigenvectors of the $\underline{\underline{Q}}$ matrix, which are complex. Since examination of the behavior of the phase of individual components showed no unusual variation near the resonance, we will restrict our attention to the amplitudes of the components, which do show interesting behavior. We will express these values as "fractional compositions of the eigenvectors", which are defined as the sum of the squares of the real and imaginary parts of the n^{th} component of the m^{th} eigenvector of $\underline{\underline{Q}}$. Thus, if an eigenvector of $\underline{\underline{Q}}$ has fractional compositions as follows:

$$\begin{pmatrix} 0.30 \\ 0.15 \\ 0.05 \\ 0.30 \\ 0.15 \\ 0.05 \end{pmatrix}$$

it will be considered to be 60% v=0, 30% v=1, and 10% v=2. Because of the symmetric or anti-symmetric nature of the eigenvectors, the amplitudes in rows 4, 5, and 6 will alway be the same as those in rows 1, 2, and 3, respectively at energies above the opening of the v = 2 state. Below that, a similar relationship holds with only two states (below the opening of v = 1) or four states present.

The orthogonality of the eigenvectors and the symmetric/anti-symmetric nature of the eigenvectors combine to reduce the number of independent eigenvectors. Near the first resonance but above the opening of the v = 1 level, there are only two independent eigenvectors - one symmetric and one anti-symmetric. The other one of each type is determined by the orthogonality condition. Thus, we will look only at one eigenvector of each symmetry type in this energy region. The fractional compositions of the other pair of eigenvectors is just the reverse of that of the first pair. Near the second resonance but above the opening of the v = 2 level, there are two independent eigenstates of each symmetry type. Since the fractional compositions of the third eigenvector of each type are not immediately obvious from those of the first two (although their calculation is simple), we will examine all the eigenvectors in this energy region.

We present one pair of eigenvectors near the first resonance in the form of plots of fractional composition vs. energy plots in figure 15. In figure 16 we show similar plots of the symmetric eigenvectors near the second resonance, and in figure 17 we do the same for the anti-symmetric eigenvectors. Our notation for a given component is $nm^{\pm}$, where $m^{\pm}$ gives the eigenvector number and symmetry type, and corresponds to the similarly labeled eigenvalue in figures 13 and 14. n is the number of the component.

Two major features are apparent from figure 15. First, near the first resonance the symmetric eigenvectors undergo a substantial change with energy. Symmetric eigenvectors which are purely v = 0 and v = 1 away from the resonance but above the opening of the v = 1 channel become nearly 50% of each at the center of the resonance (0.875 eV), and at higher energies revert back to being substantially, but not entirely, as they were before the resonance. Second, the anti-symmetric eigenvectors vary only slightly in the region of the resonance, mixing only about 2% of the v = 1 state into the predominantly v = 0 eigenvector and vice versa. These results are consistent with the eigenvalue vs. energy plots (figure 13) in which only the eigenvalues associated with the symmetric states have maxima.

The eigenvectors near the second resonance show both similarities and differences from those near the first resonance. The similarity is that the anti-symmetric eigenvectors are much closer to pure states than the symmetric ones. For example, eigenvector 1^- contains at most 7% v = 1, while eigenvector 1^+ contains as much as 53% v = 1. There are two major differences between these eigenvalues and those near the first resonance. First, the fractional compositions of the symmetric eigenvectors show no major variation with energy in the resonance region. The crossovers between the v = 0 and v = 1 fractional compositions are at energies substantially below the resonance location of 1.310 eV as determined from the peak in the q_{π} vs. energy curve (figure 14). Second, little v = 2 mixes into the symmetric eigenvectors (no more than 10% into the 1^+ and 4% into the 2^+ eigenvectors). This is substantially less than the 46% of the v = 1 that mixes into the 1^+ eigenvector at the first resonance.

IV. DISCUSSION

The existence of resonances in the dynamics of the collinear $H + H_2$ system on the Porter-Karplus surface has been conclusively demonstrated by examination of reaction probabilities, phases of individual $\underline{\underline{S}}$ matrix elements and their energy derivatives, eigenphase shifts, and the collision lifetime matrix and its eigenvalues and eigenvectors. On the basis of the eigenvalues of the collision lifetime matrix, these resonances are located at 0.877 eV and 1.310 eV total energy. There are a number of similarities and differences between the two resonances, and we will discuss these here. We will close this section with some general statements concerning the utility of the various quantities used for the characterization of the resonances.

The similarities between the two resonances are fairly obvious. For both, rapid variations with energy in all of the above mentioned quantities are observed. Two different types of Argand diagrams (half-moon and loop) are observed for the various $\underline{\underline{S}}$ matrix elements affected by both resonances. For those $\underline{\underline{S}}$ matrix elements which give rise to loop Argand diagrams, a positive delay time, as defined by eq. 11, is observed. These values (0.016 psec for τ_{01} at the first resonance and 0.0175, 0.009, and 0.005 psec for τ_{00}, τ_{01}, τ_{11} at the second resonance) are fairly similar in magnitude.

The eigenphase shift vs. energy curves near the resonances are also similar in their overall structure. In both, the resonance, as seen by regions of increasing eigenphase shift with energy, is restricted to those eigenvalues related to symmetric eigenvectors of $\underline{\underline{R}}$. The eigenphase shifts related to anti-symmetric eigenvectors of $\underline{\underline{R}}$ vary smoothly with energy, varying at most by avoided crossings with other anti-symmetric eigenvalue curves. Just above the opening of a new state, a degenerate pair of eigenphase shifts (one symmetric and one anti-symmetric) occurs. The eigenvectors associated with these eigenphase shifts show that they are related to the newly opened state.

At sufficiently higher energy for both resonances, the two curves become separated, and the symmetric one of the pair goes through the above mentioned increase with energy.

Additional similarities are seen in the plots of the diagonal elements Q_{nn} as a function of energy. Near both resonances, the one related to the newly opened state (Q_{22} where v = 1 opens and Q_{33} where v = 2 opens) is large and negative and increases rapidly with energy. Q_{11} has a single positive maximum in both cases, and the maximum is sufficiently positive that inequality 8 is satisfied, indicating that a resonance picture of the scattering is appropriate. In both cases Q_{22} achieves a local maximum also. The eigenvalues q_n behave fairly similarly in both cases. One (and only one) related to a symmetric eigenvector of $\underline{Q}$ becomes positive at both resonances, while those related to anti-symmetric eigenvalues vary very smoothly with energy. The lifetimes associated with both peaks, 0.091 psec and 0.086 psec for the first and second resonance, respectively, are quite similar, as are the widths (FWHM), 0.021 eV and 0.028 eV.

The differences between the resonances are related mainly in the extent of participation of the newly opened state in the dynamics. Near the first resonance, the participation of the v = 1 state is shown both by the appreciable reaction probabilities to and from that state (P_{01}^R gets as high as 0.28 near the resonance) and the sizable fractional contribution of the v = 1 level to both symmetric eigenvectors of $\underline{Q}$. In contrast, the v = 2 level contributes almost entirely to only one symmetric eigenvector of $\underline{\underline{Q}}$ near the second resonance.

A fundamental difference between the first two resonances is not unexpected in the light of various attempts over the years to model them. Kuppermann (14) has recently discussed the physical interpretation of these resonances, and has concluded that the first resonance is due mainly to the trapping of the system's energy in a motion corresponding to an asymmetric stretch of the saddle point region in the second symmetric eigenstate. The second resonance, while being shown to have some of this longitudinal character, has energy trapped in the third ($v = 2$) state of the internal motion along the symmetric stretch line.

In collinear calculations on this system carried out to higher energy (18) (up to 3.0 eV), it is seen that the resonance structure in the vibrationally adiabatic reaction probabilities P_{nn}^{R} for $n = 1, 2, 3, 4$ is quite similar. This suggests that whatever physical mechanism is responsible for the second resonance will be similar in nature to those of all higher resonances. Since the resonance can be seen to some extent or other in all vibrationally non-adiabatic reaction probabilities $P_{nn'}^{R}$ ($n \neq n'$) (21), it seems reasonable to expect that there will be some contribution of all states (except perhaps the most recently opened one) to the eigenvectors of $\underline{\underline{Q}}$.

The localization of the resonance to symmetric states (those with symmetric eigenvectors of $\underline{\underline{R}}$ and $\underline{\underline{Q}}$) has been observed previously for the H + FH reaction on an unrealistic potential energy surface (11, 12, 14) and for the I + HI (13) reaction. In both those systems, however, the resonance occurs at an energy below the opening of the $v = 1$ state. In those cases, the $\underline{\underline{R}}$, $\underline{\underline{S}}$, $\underline{\underline{P}}$, and $\underline{\underline{Q}}$ matrices are all 2×2; there are only two eigenphase shifts, one symmetric (δ_S) and one anti-symmetric (δ_A), and the eigenvectors of $\underline{\underline{R}}$ are independent of energy. It is found for these systems that a more useful quantity than the two eigenphase shifts δ_S and δ_A is their difference $\delta_S - \delta_A$ (11, 12, 14). This difference rises fairly sharply from near zero to some value less than π near the resonance energy. The closeness of the jump in $\delta_S - \delta_A$ to π is related to the relative importance of resonant and direct processes near the resonance energy. An increase of exactly π implies that there are no direct processes at all; the smaller the increase, the greater their contribution.

Such an analysis will not work for the two H + H_2 resonances, however, as they occur at energies at which more than one vibrational state of H_2 is open and there is more than one eigenphase shift of each symmetry type. A result of this is that the eigenvectors of $\underline{\underline{R}}$ need not be independent of energy; this is indeed the case here. A similar model might work for resonances in the vibrationally adiabatic reaction probabilities for reactions of vibrationally excited reagents in symmetric heavy-light-heavy collisions, where vibrationally non-adiabatic processes are known to occur with exceptionally low probability (22). In that case the eigenvectors of $\underline{\underline{R}}$ are essentially independent of energy: the symmetric and anti-symmetric linear combinations of each individual open vibrational state, with no mixing from the other states (21). A similar analysis would apply to the eigenvectors of $\underline{\underline{Q}}$ in this case.

At energies below the resonance but above the opening of the new vibrational level, the two eigenphase shifts most closely associated with the new state are degenerate. As one moves to higher energy and the symmetric and anti-symmetric curves separate, the appropriate linear combination to take is not $\delta_S - \delta_A$ but is rather some other one that would allow one to go smoothly from one of the affected symmetric curves to the other without any avoided crossing. This linear combination would be energy dependent. A similar conclusion, namely that some energy dependent linear combination of eigenphase shifts is needed to obtain maximum information from the eigenphase shift vs. energy curves was obtained for the F + H_2 and F + HD systems (14).

At this point we wish to consider the relative advantages and disadvantages of the various quantities examined here in the characterization of these resonances. The eigenvalues of the collision lifetime matrix appear to give the most unambiguous information about the resonances.

Let us first consider the simple matter of the position of the resonances. These are not uniquely defined by the probability vs. energy curves. This is best evidenced by the 0.012 eV difference between the maxima in P_{00}^R and P_{11}^R near the second resonance. A specification of the exact resonance energy does not come from the Argand diagrams; these show the resonance spread out over a region of the complex plane. Any definition of the resonance energy from the Argand diagram would, therefore, have to be fairly arbitrary. A better definition of the resonance energy might be obtained from the individual $\underline{\underline{S}}$ matrix element time delay plots (figures 5 and 6). However, even in this case one must decide in the case of half-moon Argand diagrams whether to choose the resonance location as the position of the minimum in the time delay plot or that of one of the adjacent maxima.

The eigenphase shifts also do not provide a clear definition (they might if there were a clear avoided crossing). The diagonal elements Q_{nn} provide a good indication, but for both resonances studied the two peaks occur at slightly different energies. It is only for the eigenvalues of $\underline{\underline{Q}}$ where there is one clearly dominant peak that a unique assignment of the resonance energy can be made. The width can also be determined, due to the nature of the peak in the eigenvalue vs. energy curve. Determinations of the resonance position and width were also made in the F + H_2, HD, DH, and D_2 systems by means of the collision lifetime matrix eigenvalues (20).

The main usefulness of the Argand diagrams appears to be confirmatory in nature. Loop or half-moon formation indicates the existence of a fairly strong resonance (weaker resonances will be reflected by straight cut formation). The exact nature of the diagram (loop or half-moon) varies from transition to transition and from resonance to resonance and thus seems to be of no particular importance.

The time derivative of individual $\underline{\underline{S}}$ matrix elements does seem to provide order of magnitude information about the time delay in collisions of particles with well defined internal states, as these are close in magnitude to the largest diagonal element Q_{nn}. However, different transitions have different values of τ_{ij}, so one cannot calculate a unique lifetime associated with the resonance from them (and one is not guaranteed that a given transition will have a positive τ_{ij}). An advantage of using these individual delay times rather than the diagonal elements or eigenvalues of $\underline{\underline{Q}}$ is that in the latter cases one must use the entire $\underline{\underline{S}}$ matrix (and its energy derivative) rather than a single element as in the former case. As in the location of the resonance, the eigenvalues Q_{nn} appear to be the only quantity which gives the lifetime uniquely, and it turns out that this lifetime is substantially greater than the diagonal elements Q_{nn}.

The eigenphase shifts also provide confirmatory evidence of the resonance, and do show that it is related to symmetric eigenvectors of $\underline{\underline{R}}$. However, some qualitatively different behavior of the eigenphase shifts and the eigenvalues q_n has been observed. For example, the symmetric eigenphase shifts most closely associated with the newly opened vibrational state are clearly affected by the resonance, but the corresponding eigenvalues of $\underline{\underline{Q}}$ do so only slightly (2^+ in figure 13) or not at all (3^+ in figure 14). Additional information could be obtained from the eigenphase shifts if one could relate them and their corresponding eigenvectors in order to construct modified curves in which the increase in eigenphase shift with energy is restricted to one curve. Such a procedure has not yet been developed, however.

The existence of positive eigenvalues of $\underline{\underline{Q}}$, corresponding to positive time delays in the bimolecular $H + H_2$ collisions, is a manifestation of quantum mechanical resonance effects. Away from the resonance, all eigenvalues are negative. A classical theory, by which the *lifetime* of a bimolecular collision may be calculated, has been developed by Brumer, *et al.* (23) and applied to the collinear H + H_2 system on the Porter-Karplus surface. In the energy range from 0 to 4.0 eV, they found the time delay to be everywhere negative, decreasing with increasing energy. At a total energy of 1.0 eV they calculated a time delay of approximately -0.06 psec (23), which is fairly close to the two lowest eigenvalues of $\underline{\underline{Q}}$ near this energy (-0.033 psec). The significance of this comparison is not at all apparent, however. At energies just above the opening of vibrationally excited H_2 levels, such a comparison would lead to drastic disagreement, as the lowest eigenvalues of $\underline{\underline{Q}}$ are quite large and negative and they increase with energy, unlike the classical time delay, which becomes more negative with increasing energy. Calculation of the eigenvalues of $\underline{\underline{Q}}$ at higher energy at non-resonance energies might provide sufficient information for a valid comparison between the classical and quantum theories.

V. CONCLUSIONS

We have performed quantum mechanical scattering calculations on the collinear H + H_2 system at energies near the first two resonances and have analyzed and characterized these resonances by a variety of techniques. These techniques consist of the examination of the energy dependence of various state-to-state reaction probabilities, $\underline{\underline{S}}$ matrix element phases and their energy derivatives, eigenphase shifts, and diagonal elements, eigenvalues, and eigenvectors of Smith's collision lifetime matrix. The resonances are shown to be reflected in all quantities to some extent or other; the one best suited for the unique determination of the position and width of the resonances is the eigenvalue of the collision lifetime matrix. This is due to that fact that only one eigenvalue of this matrix becomes positive, and, to a good approximation, is the only one to achieve a local maximum. The lifetime of the long-lived metastable state associated with the resonance may be obtained from the eigenvalues of the collision lifetime matrix; values of 0.091 and 0.085 psec were obtained for the first and second resonances, respectively.

As a result of our analyses, we have shown that both resonances are associated with states which are symmetric combinations of the initial H_2 states. The resonances differ in some ways, notably the absence of contribution of the v = 2 state to the eigenvector of $\underline{\underline{Q}}$ associated with the second resonance as opposed to the near 50% contribution of the v = 1 state to the eigenvector of $\underline{\underline{Q}}$ associated with the first resonance. Differences between the two resonances are reasonable in the light of various studies which suggest that the first and second resonance are associated with energy trapped primarily in asymmetric and symmetric stretching motions, respectively.

The eigenvalues q_n obtained have been compared to values for the delay time in this system calculated by a classical theory, and are shown to be substantially different.

ACKNOWLEDGMENTS

The calculations reported here were performed on the Dreyfus-NSF Theoretical Chemistry Computer (VAX 11/780) at Caltech, which was funded through grants from the Camille and Henry Dreyfus Foundation, the National Science Foundation (Grant No. CHE-78-20235), and the Sloan Fund of the California Institute of Technology, and on the IBM 370/158 computer of Ambassador College, Pasadena, California, for which we express our appreciation.

APPENDIX A : SYMMETRY CONSIDERATIONS IN SYMMETRIC COLLISIONS

In this appendix we demonstrate that the eigenvalues and eigenvectors of $\underline{\underline{Q}}$ for symmetric collisions may be broken up into symmetric and antisymmetric components.

Starting from eq. 10, we construct the 2 x 2 block $\underline{\underline{Q}}$ matrix in terms of $\underline{\underline{S}}^N$, $\underline{\underline{S}}^R$, and their energy derivatives (which will be represented by $\underline{\underline{S}}^{N\prime}$ and $\underline{\underline{S}}^{R\prime}$, respectively.

$$\underline{\underline{Q}}^{\mathrm{sym}} = i\hbar \begin{pmatrix} A & B \\ B & A \end{pmatrix}$$

where

$$\underline{\underline{A}} = \underline{\underline{S}}^N \underline{\underline{S}}^{\dagger N\prime} + \underline{\underline{S}}^R \underline{\underline{S}}^{\dagger R\prime}$$

$$\underline{\underline{B}} = \underline{\underline{S}}^N \underline{\underline{S}}^{\dagger R\prime} + \underline{\underline{S}}^R \underline{\underline{S}}^{\dagger N\prime}$$

From the unitarity of $\underline{S}$, we can show that A and B are skew-hermitian:

$$\underline{\underline{A}} = -\underline{\underline{A}}^\dagger$$

$$\underline{\underline{B}} = -\underline{\underline{B}}^\dagger$$

so

$$(i\hbar\underline{\underline{A}}) = -i\hbar\underline{\underline{A}}^\dagger = i\hbar\underline{\underline{A}}$$

$$(i\hbar\underline{\underline{B}}) = -i\hbar\underline{\underline{B}}^\dagger = i\hbar\underline{\underline{B}}$$

hence $(i\hbar A)$ and $(i\hbar B)$ are hermitian.

Defining

$$\bar{\underline{\underline{A}}} = i\hbar\underline{\underline{A}}$$

$$\bar{\underline{\underline{B}}} = i\hbar\underline{\underline{B}}$$

we need only to prove that the matrix $\underline{\underline{Q}}$ can be diagonalized by one pair of symmetric and anti-symmetric eigenvectors, or, mathematically, to show that there exists some matrix T, consisting of equal numbers of symmetric and anti-symmetric vectors, which diagonalizes $\underline{\underline{Q}}$

$$\underline{\underline{\Lambda}} = \underline{\underline{T}}^{-1}\underline{\underline{Q}}\,\underline{\underline{T}}$$

where

$$\underline{\underline{T}} = \begin{pmatrix} \underline{\underline{J}} & \underline{\underline{K}} \\ -\underline{\underline{J}} & \underline{\underline{K}} \end{pmatrix} = \begin{pmatrix} \underline{\underline{1}} & \underline{\underline{1}} \\ -\underline{\underline{1}} & \underline{\underline{1}} \end{pmatrix} \begin{pmatrix} \underline{\underline{J}} & \underline{\underline{0}} \\ \underline{\underline{0}} & \underline{\underline{K}} \end{pmatrix}$$

and

$$\underline{\underline{T}}^{-1} = \frac{1}{2} \begin{pmatrix} \underline{\underline{J}}^{-1} & \underline{\underline{0}} \\ \underline{\underline{0}} & \underline{\underline{K}}^{-1} \end{pmatrix} \begin{pmatrix} \underline{\underline{1}} & -\underline{\underline{1}} \\ \underline{\underline{1}} & \underline{\underline{1}} \end{pmatrix}$$

so

$$\begin{pmatrix} \underline{\underline{\Lambda}}_1 & \underline{\underline{0}} \\ \underline{\underline{0}} & \underline{\underline{\Lambda}}_2 \end{pmatrix} = \frac{1}{2} \begin{pmatrix} \underline{\underline{J}}^{-1} & \underline{\underline{0}} \\ \underline{\underline{0}} & \underline{\underline{K}}^{-1} \end{pmatrix} \begin{pmatrix} \underline{\underline{1}} & -\underline{\underline{1}} \\ \underline{\underline{1}} & \underline{\underline{1}} \end{pmatrix} \begin{pmatrix} \underline{\underline{\bar{A}}} & \underline{\underline{\bar{B}}} \\ \underline{\underline{\bar{B}}} & \underline{\underline{\bar{A}}} \end{pmatrix} \begin{pmatrix} \underline{\underline{1}} & \underline{\underline{1}} \\ -\underline{\underline{1}} & \underline{\underline{1}} \end{pmatrix} \begin{pmatrix} \underline{\underline{J}} & \underline{\underline{0}} \\ \underline{\underline{0}} & \underline{\underline{K}} \end{pmatrix}$$

$$= \begin{pmatrix} \underline{\underline{J}}^{-1} & \underline{\underline{0}} \\ \underline{\underline{0}} & \underline{\underline{K}}^{-1} \end{pmatrix} \begin{pmatrix} (\underline{\underline{\bar{A}}} - \underline{\underline{\bar{B}}}) & \underline{\underline{0}} \\ \underline{\underline{0}} & (\underline{\underline{\bar{A}}} + \underline{\underline{\bar{B}}}) \end{pmatrix} \begin{pmatrix} \underline{\underline{J}} & \underline{\underline{0}} \\ \underline{\underline{0}} & \underline{\underline{K}} \end{pmatrix}$$

$$= \begin{pmatrix} \underline{\underline{J}}^{-1} (\underline{\underline{\bar{A}}} - \underline{\underline{\bar{B}}}) \underline{\underline{J}} & \underline{\underline{0}} \\ \underline{\underline{0}} & \underline{\underline{K}}^{-1} (\underline{\underline{\bar{A}}} + \underline{\underline{\bar{B}}}) \underline{\underline{K}} \end{pmatrix}$$

Since $\underline{\underline{\bar{A}}}$ and $\underline{\underline{\bar{B}}}$ are hermitian, $\underline{\underline{\bar{A}}} - \underline{\underline{\bar{B}}}$ and $\underline{\underline{\bar{A}}} + \underline{\underline{\bar{B}}}$ must also be hermitian. Thus, there exist matrices $\underline{\underline{J}}$ and $\underline{\underline{K}}$ which diagonalize $(\underline{\underline{\bar{A}}} - \underline{\underline{\bar{B}}})$ and $(\underline{\underline{\bar{A}}} + \underline{\underline{\bar{B}}})$ respectively, and thus in the symmetric case, $\underline{\underline{Q}}$ can be diagonalized by a matrix containing only symmetric and antisymmetric eigenvectors.

REFERENCES

1. D. G. Truhlar and R. E. Wyatt, Ann. Rev. Phys. Chem. 27, 1 (1976); Adv. Chem. Phys. 36, 141 (1977).
2. N. C. Blais and D. G. Truhlar, in: Potential Energy Surfaces and Dynamics Calculations, ed. D. G. Truhlar (Plenum Press, New York, 1981), pp. 431-473; A. Jones and J. L. Rosenfeld, Proc. Roy. Soc. Lond. A 333, 419 (1973); D. J. Malcolme-Lawes, J. Chem. Soc. Far. Trans. II 71, 1183 (1975).
3. A. Kuppermann and G. C. Schatz, J. Chem. Phys. 62, 2502 (1975); G. C. Schatz and A. Kuppermann, J. Chem. Phys. 65, 4668 (1976); A. B. Elkowitz and R. E. Wyatt, J. Chem. Phys. 62, 2504 (1975); 63, 702 (1975); R. B. Walker, E. B. Stechel, and J. C. Light, J. Chem. Phys. 69, 2922 (1978).
4. D. G. Truhlar and A. Kuppermann, J. Chem. Phys. 52, 3841 (1970); 56, 2232 (1972); S. F. Wu, Mol. Phys. 22, 881 (1971); D. J. Diestler, J. Chem. Phys. 54, 4547 (1971); B. R. Johnson, Chem. Phys. Lett. 13, 172 (1972); G. C. Schatz and A. Kuppermann, J. Chem. Phys. 59, 964 (1973).
5. G. C. Schatz and A. Kuppermann, Phys. Rev. Lett. 35, 1266 (1975).
6. M. L. Goldberger and K. M. Watson, Collision Theory (Krieger, Huntington, N.Y., 1975), pp. 424 - 509.
7. R. N. Porter and M. Karplus, J. Chem. Phys. 40, 1105 (1964).
8. F. T. Smith, Phys. Rev. 118, 349 (1960).
9. A. Kuppermann, in: Theoretical Chemistry: Advances and Perspectives, Vol. 6A, ed. D. Henderson (Academic Press, New York, 1981), pp. 79 - 164.
10. A. M. Lane and R. G. Thomas, Rev. Mod. Phys. 30, 257 (1958).
11. G. C. Schatz, Ph. D. Thesis, California Institute of Technology, 1975.

12. G. C. Schatz and A. Kuppermann, Manuscript in Preparation.

13. J. A. Kaye and A. Kuppermann, Chem. Phys. Lett. 77, 573 (1981).

14. A. Kuppermann, in: Potential Energy Surfaces and Dynamics Calculations, ed. D. G. Truhlar (Plenum Press, New York, 1981), pp. 375 - 420.

15. D. Bohm, Quantum Theory (Prentice-Hall, New York, 1951), pp. 257 - 262.

16. A. Kuppermann, in: Proceedings of the Conference on Potential Energy Surfaces in Chemistry, ed. W. A. Lester (U. California, Santa Cruz, 1970), pp. 121-134; in: Proceedings of the 7th International Conference on the Physics of Electronic and Atomic Collisions (North-Holland, Amsterdam, 1971), pp. 3-5.

17. B. T. Smith, J. M. Boyle, J. J. Dongarra, B. S. Farbow, Y. Ikebe, V. C. Klema, and C. B. Moler, Matrix Eigensystem Routines - EISPACK Guide, Lecture Notes in Computer Science, ed. G. Goos and J. Hartmanis (Springer-Verlag, Berlin, 1976).

18. A. Kuppermann, J. A. Kaye, and J. P. Dwyer, Chem. Phys. Lett. 74, 257 (1980).

19. G. C. Schatz and A. Kuppermann, J. Chem. Phys. 59, 964 (1973) and references therein.

20. A. Kuppermann and J. A. Kaye, J. Phys. Chem. 85, 1969 (1981).

21. J. A. Kaye and A. Kuppermann, to be published.

22. J. Manz and J. Römelt, Chem. Phys. Lett. 81, 179 (1981).

23. P. Brumer, D. E. Fitz, and D. Wardlaw, J. Chem. Phys. 72, 386 (1980).

FIGURE CAPTIONS

Figure 1. Probability $P_{nn'}^R$ for the reaction $H + H_2(n) \longrightarrow H_2(n') + H$ as a function of energy in the vicinity of the first resonance. Translational energy scales for both the ground (E_0) and first excited (E_1) states are shown on the lower abscissa; the total energy (E) is shown on the upper abscissa. The arrow marks the energy at which the $v = 1$ state becomes open. Transitions are indicated by different line types: P_{00}^R : solid line; P_{01}^R : dashed line; P_{11}^R : dashed-dotted line.

Figure 2. Probability $P_{nn'}^R$ as a function of energy in the vicinity of the second resonance. The total energy scale is shown on the upper abscissa; the appropriate translational scales are shown on the lower abscissas. (a) P_{00}^R : dashed line; P_{01}^R : solid line; P_{11}^R : dashed-dotted line; (b) P_{20}^R : dashed line; P_{21}^R : dashed-dotted line; P_{22}^R : solid line. The values of P_{20}^R and P_{21}^R shown have been multiplied by 4 before plotting. In both figures, the arrow marks the energy at which the $v = 2$ state becomes open.

Figure 3. Argand diagram of Im $S_{nn'}^R$ vs. Re $S_{nn'}^R$ near the first resonance with the total energy E (measured with respect to the bottom of the H_2 well) as a parameter. The markers are placed every 0.01 eV. The arrows indicate the sense of the curve. (a) S_{00}^R. The shift from a clockwise to a counterclockwise back to a clockwise sense indicates a resonance. This Argand diagram is of the "half-moon" type. (b) S_{01}^R. In this figure the resonance is shown by loop formation.

Figure 4. Argand diagrams of Im $S_{nn'}$ vs. Re $S_{nn'}$ near the second resonance with the total energy E as a parameter. The symbols mark every 0.01 ev and the arrows indicate the sense of the curve.
(a) S_{00}^R; (b) S_{01}^R; (c) S_{11}^R.

Figure 5. Phase $\phi_{nn'}^R$ of the scattering matrix element $S_{nn'}^R$ as a function of the total energy E (upper abscissa) and the translational energy E_0 (lower abscissa) near the first resonance. (a) S_{00}^R (the arrow marks the opening of the v = 1 state); (b) : S_{01}^R.

Figure 6. Phase $\phi_{nn'}^R$ of the scattering matrix element $S_{nn'}^R$ as a function of the total energy E (upper abscissa) and the translational energy E_0 or E_1 (lower abscissa) near the second resonance. The arrow marks the opening of the v = 2 state. (a) S_{00}^R; (b) S_{01}^R; (c) S_{11}^R.

Figure 7. Delay time $\tau_{nn'}^R$ as a function of the total energy E (upper abscissa) and the translational energy E_0 (lower abscissa) near the first resonance. The arrow marks the opening of the v = 1 state. (a) τ_{00}^R; (b) τ_{01}^R.

Figure 8. Delay time $\tau_{nn'}^R$ as a function of the total energy E (upper abscissa) and the translational energy E_0 or E_1 (lower abscissa) near the second resonance. The arrow marks the opening of the v = 2 state. (a) τ_{00}^R; (b) τ_{01}^R; (c) τ_{11}^R.

Figure 9. Eigenphase shifts as a function of the total energy E near the first resonance. Those belonging to symmetric eigenvectors of $\underline{\underline{R}}$ are drawn with solid lines, those to anti-symmetric eigenvectors are drawn with dashed lines. The lowest energy portion of the two curves most closely associated with the v = 1 state is not shown; it is just a smooth curve which decreases rapidly with increasing energy. Below approximately 0.845 eV, those two curves lie on top of each other. The arrow marks the opening of the v = 1 state. Note that integral multiples of π have been added to or subtracted from the computed eigenphase shifts in order to generate smooth curves; the absolute values of the eigenphase shifts were chosen to show the avoided crossings and for convenience.

Figure 10. Eigenphase shifts as a function of the total energy E near the second resonance. All markings are as in figure 9. The lowest energy portion of the two curves most closely associated with the v = 2 state is not shown; its behavior is similar to that described for the v = 1 state in figure 9.

Figure 11. The diagonal elements Q_{nn} of Smith's collision lifetime matrix as a function of the total energy E near the first resonance. The lowest energy portion of the Q_{22} curve is not shown; it is just a smooth curve which increases rapidly with increasing energy. The Q_{22} curve has been divided by two prior to plotting. The arrow marks the opening of the v = 1 state.

Figure 12. The diagonal elements Q_{nn} as a function of the total energy E near the second resonance. Q_{33} has been divided by two prior to plotting; its lowest energy portion is not shown. The arrow marks the opening of the v = 2 state.

Figure 13. The eigenvalues q_n of the collision lifetime matrix $\underline{\underline{Q}}$ as a function of the total energy E near the first resonance. The numbers mark the eigenvector to which the eigenvalue belongs. The notation is discussed in the text. The eigenvalue of $\underline{\underline{Q}}$ is given on the left ordinate of the figure. The lifetime of the long-lived metastable state associated with the resonance, as defined by eq. 11, is shown on the right ordinate. The lowest energy portion of the curves marked 2^+ and 2^- is not shown; these portions are essentially superimposable down to the opening of the v = 1 state, which is marked by an arrow.

Figure 14. The eigenvalues q_n of the collision lifetime matrix $\underline{\underline{Q}}$ as a function of the total energy E near the second resonance. The numbering and axis labeling are as in figure 13. The 3^+ and 3^- curves have been divided by two before plotting. The arrow marks the energy at which the v = 2 state opens.

Figure 15. Fractional contribution to eigenvectors of $\underline{\underline{Q}}$ as a function of the total energy E near the first resonance. The numbering scheme is described in the text. Lines are drawn as follows: 11^+ : dashed line; 21^+ : solid line; 11^- : dashed-dotted line (short dashes); 21^- : dashed-dotted line (long dashes). The 21^- curve has been multiplied by twenty before plotting. The remaining two eigenvectors 2^+ and 2^- are not shown because their fractional contributions can be easily inferred from those shown. This is discussed fully in the text. The arrow marks the opening of the $v = 1$ state.

Figure 16. Fractional contributions to the symmetric eigenvectors of $\underline{\underline{Q}}$ as a function of the total energy near the second resonance. The numbering scheme is described in the text. Factors in parentheses indicate the values by which the fractional contributions have been multiplied prior to plotting. The arrows mark the energy at which the $v = 2$ state opens. For all plots, the $v = 0$ component (1) is indicated by a solid line; the $v = 1$ component (2) is indicated by a dashed line; the $v = 2$ component (3) is indicated by a dashed-dotted line. (a) Eigenvector 1^+; (b) 2^+; (c) 3^+.

Figure 17. Fractional contributions to the anti-symmetric eigenvectors of $\underline{\underline{Q}}$ as a function of the total energy near the second resonance. All symbols and line types are as in figure 16. (a) Eigenvector 1^-; (b) 2^-; (c) 3^-.

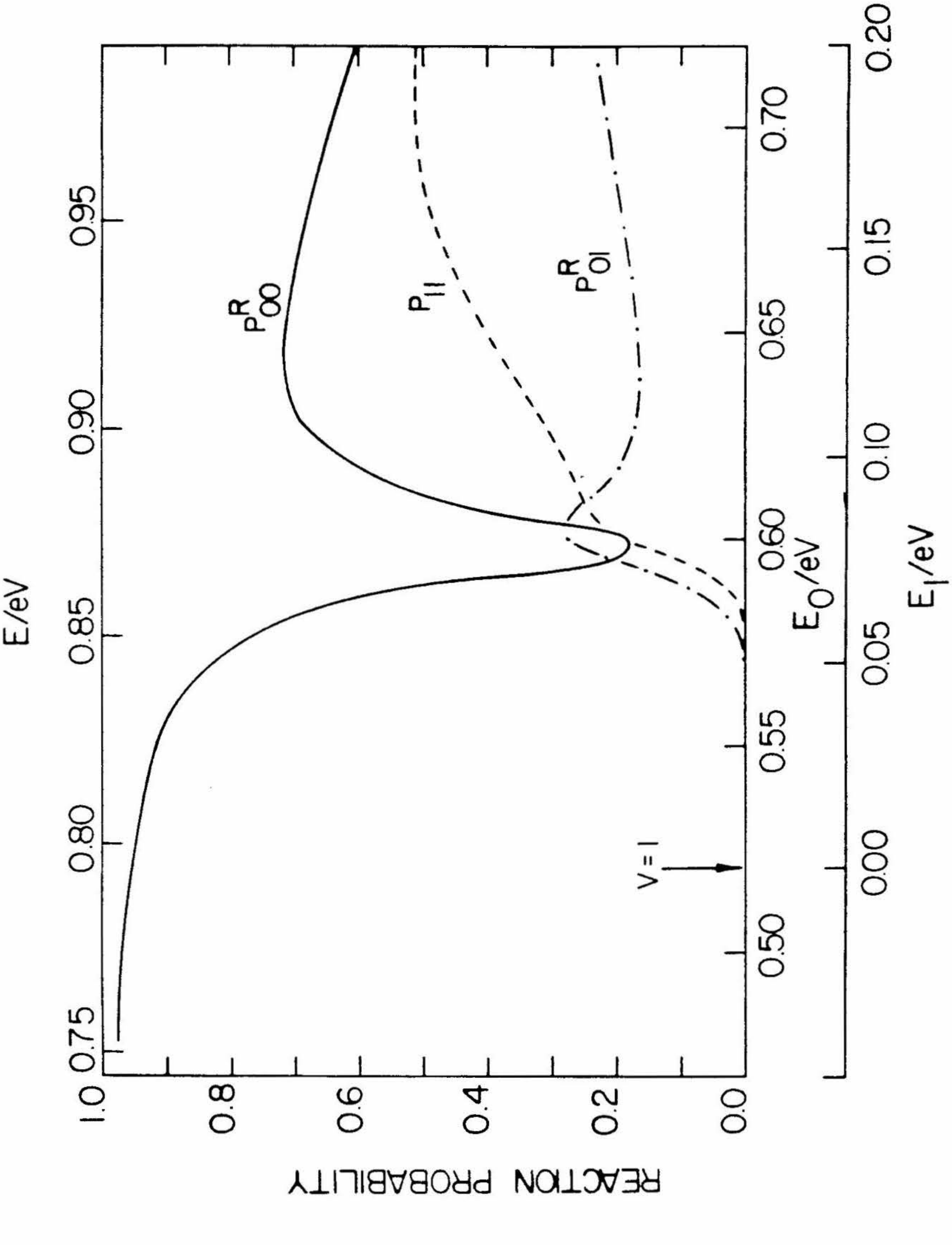
E/eV
0.75
0.80
0.85
0.90
0.95
E_0/eV
0.50
0.55
0.60
0.65
0.70
E_1/eV
0.00
0.05
0.10
0.15
0.20
REACTION PROBABILITY
1.0
0.8
0.6
0.4
0.2
0.0
P^R_{00}
P_{11}
P^R_{01}
V=1

Figure 1

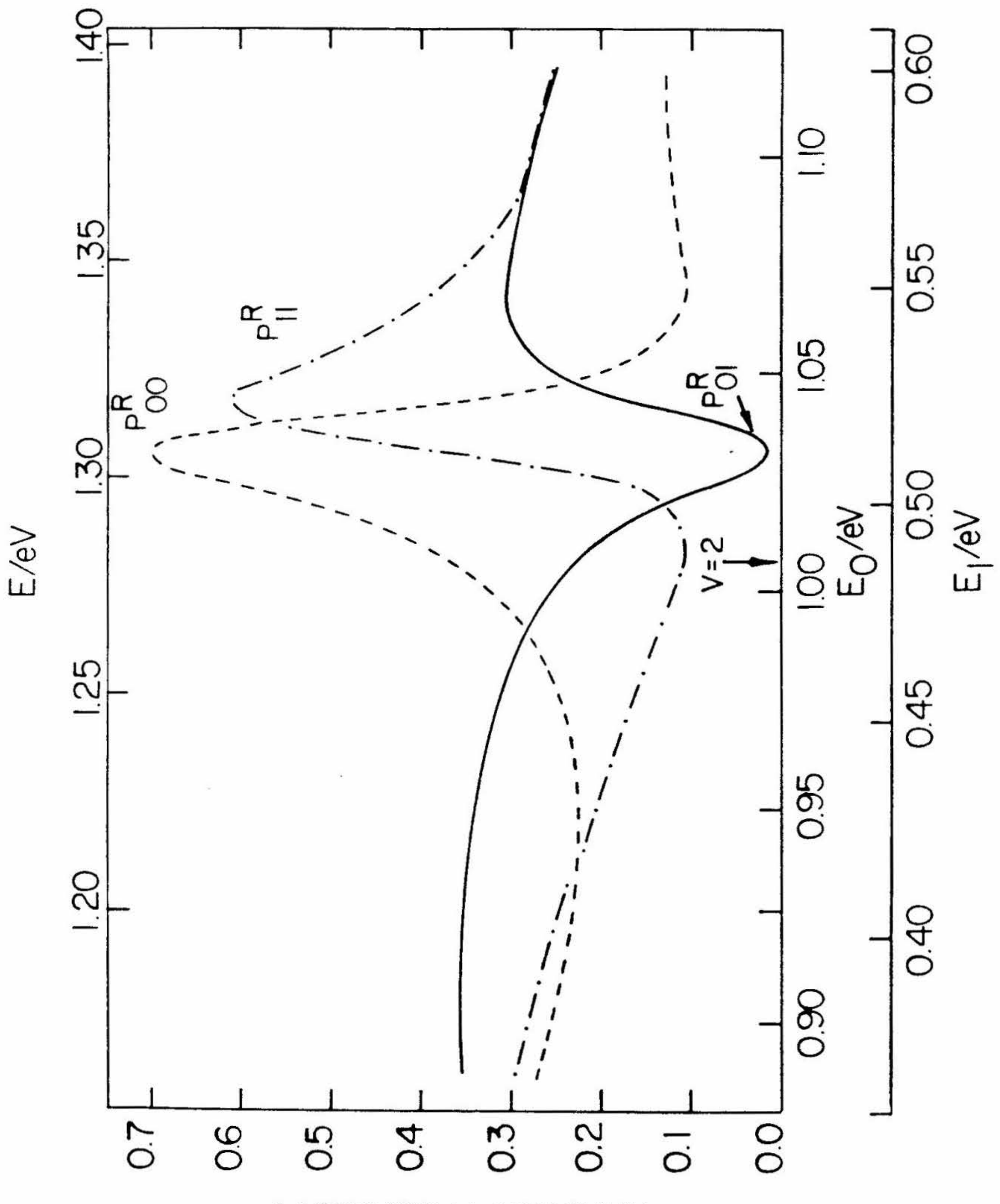
E/eV
1.20
1.25
1.30
1.35
1.40
REACTION PROBABILITY
0.0
0.1
0.2
0.3
0.4
0.5
0.6
0.7
P^R_{00}
P^R_{11}
P^R_{01}
V=2
0.90
0.95
1.00
1.05
1.10
E_0/eV
0.40
0.45
0.50
0.55
0.60
E_1/eV

Figure 2a

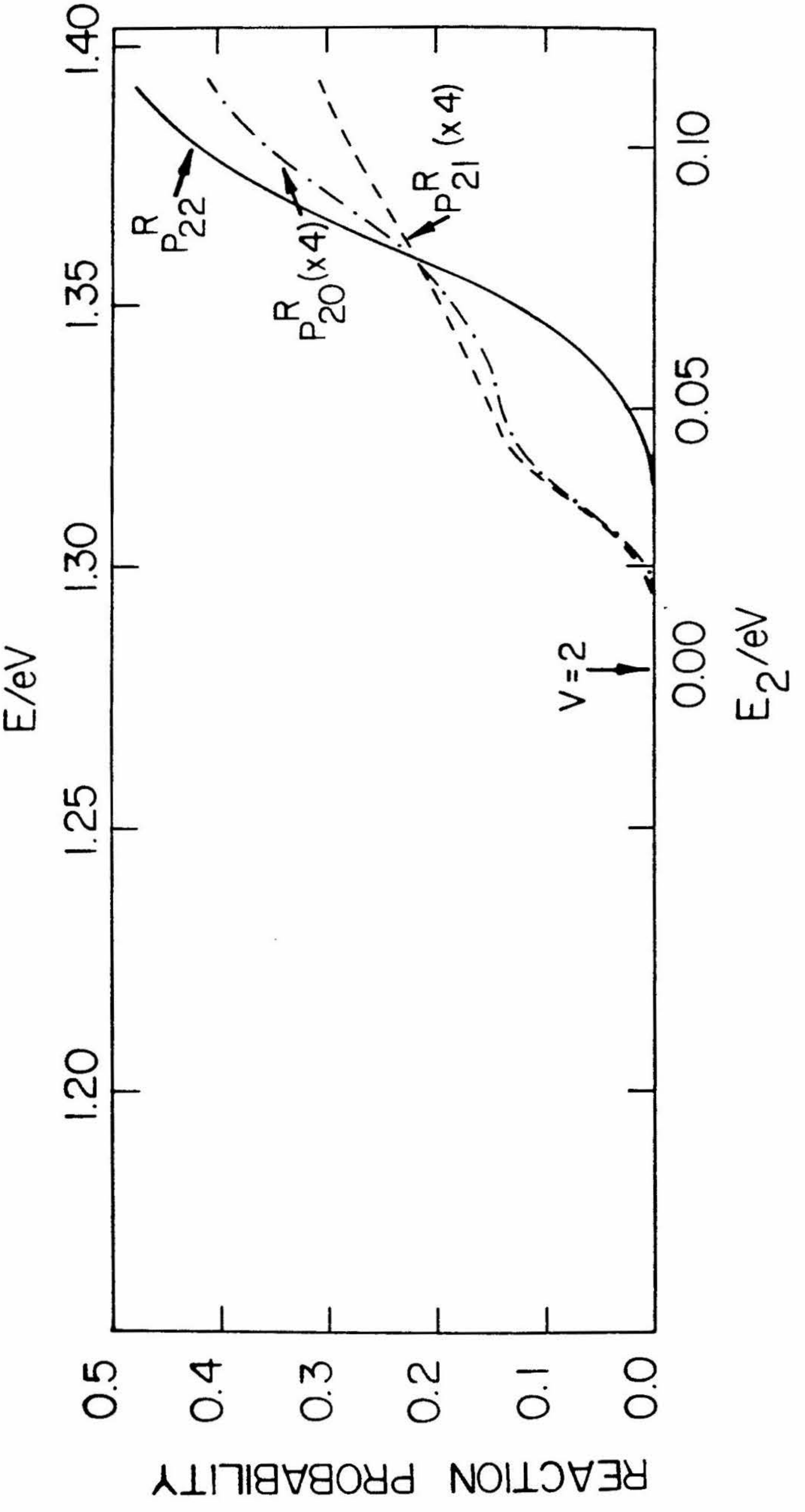
E/eV
1.20
1.25
1.30
1.35
1.40
REACTION PROBABILITY
0.0
0.1
0.2
0.3
0.4
0.5
P^R_{22}
P^R_{20}(x4)
P^R_{21} (x4)
V=2
0.00
0.05
0.10
E_2/eV

Figure 2b

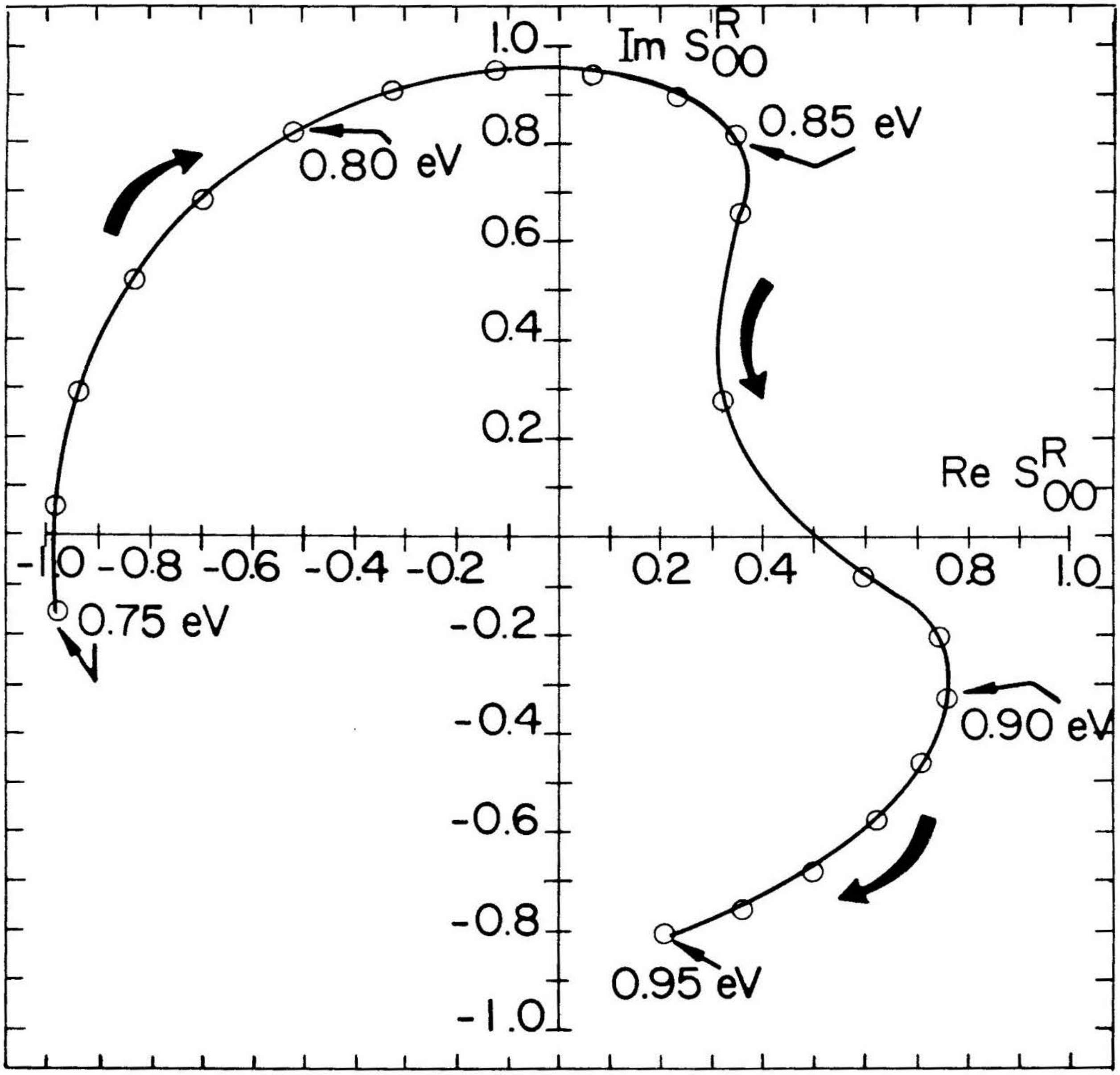
Im S^R_{00}
Re S^R_{00}
1.0
0.8
0.6
0.4
0.2
-0.2
-0.4
-0.6
-0.8
-1.0
-1.0
-0.8
-0.6
-0.4
-0.2
0.2
0.4
0.8
1.0
0.75 eV
0.80 eV
0.85 eV
0.90 eV
0.95 eV

Figure 3a

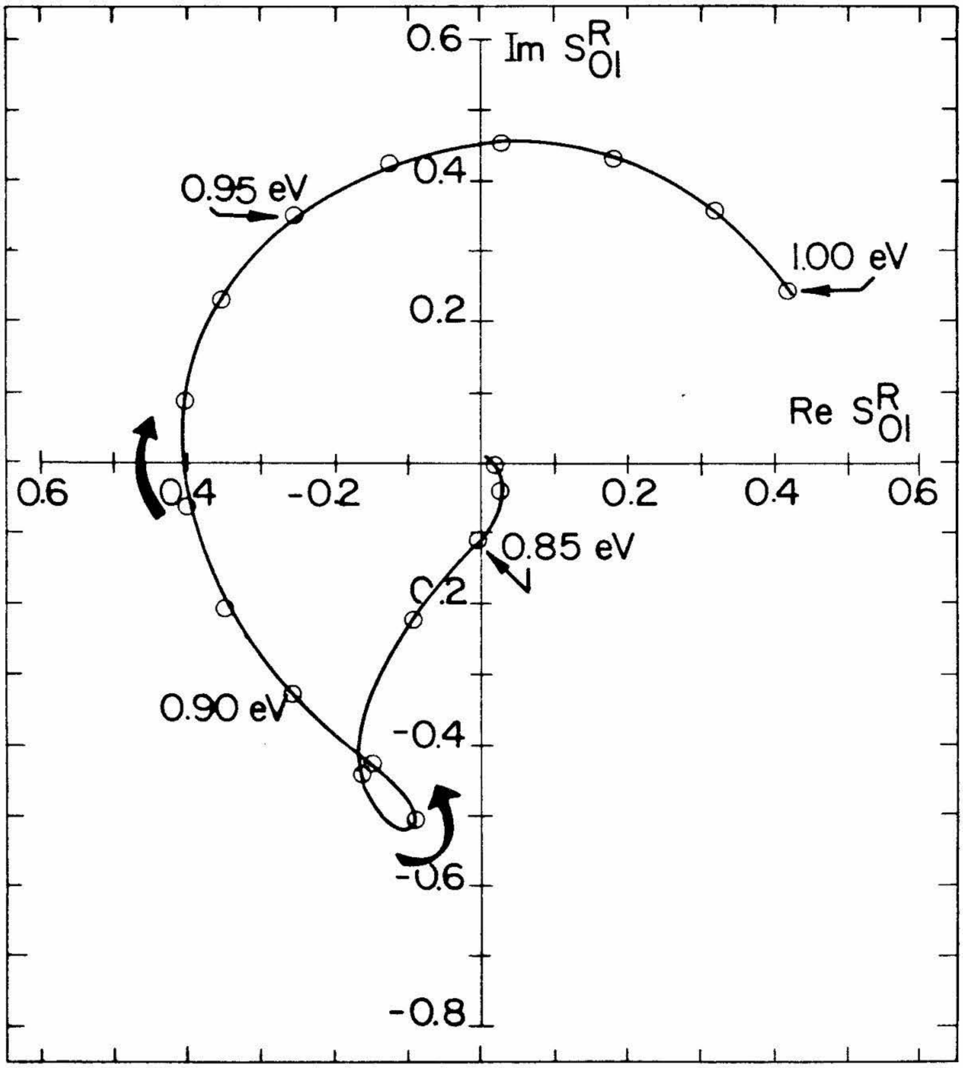
Im S^R_{01}
Re S^R_{01}
0.6
0.4
0.2
-0.2
-0.4
-0.6
-0.8
0.6
0.4
-0.2
0.2
0.4
0.6
0.95 eV
1.00 eV
0.85 eV
0.90 eV

Figure 3b

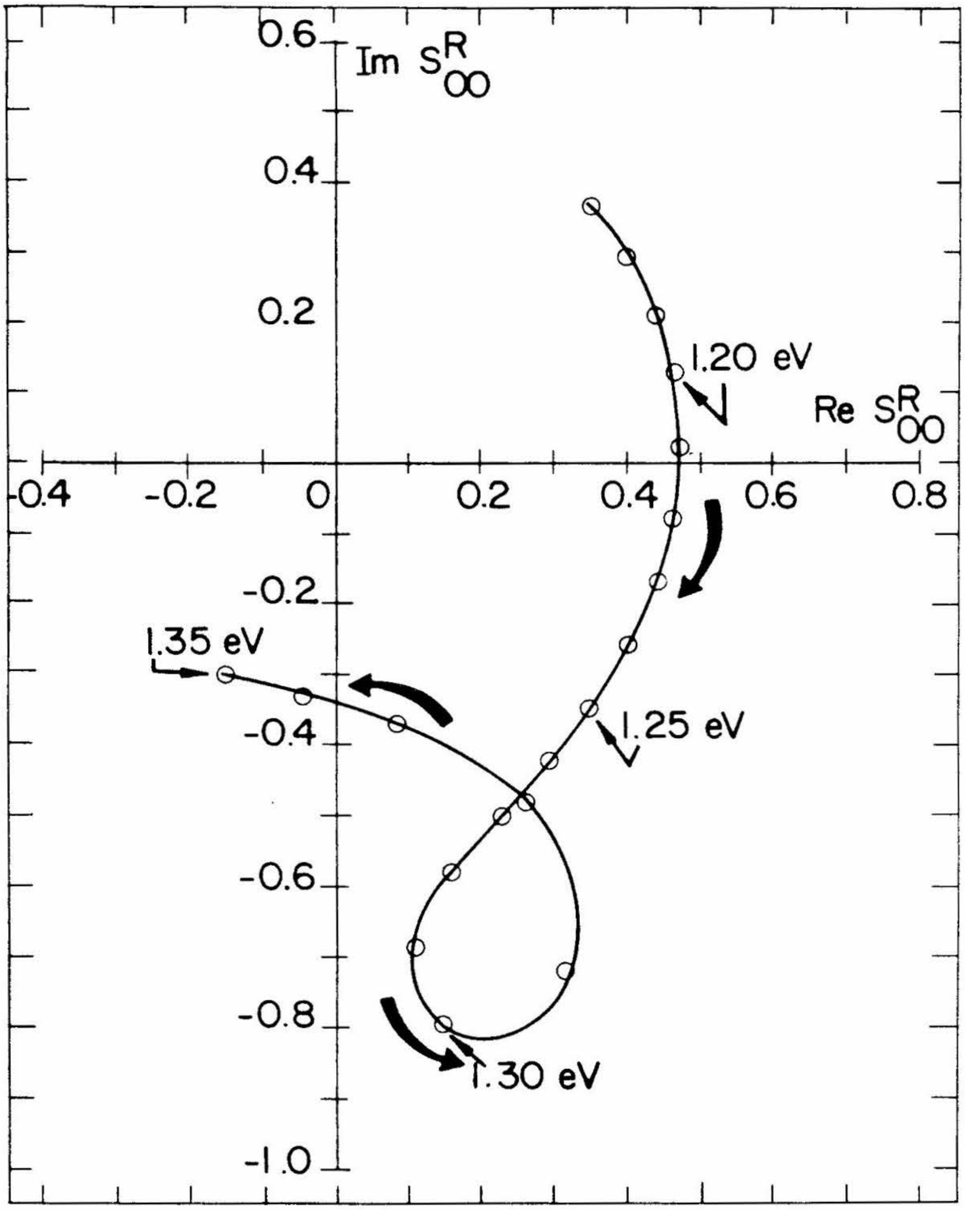
0.6
Im S^R_00
0.4
0.2
1.20 eV
Re S^R_00
-0.4
-0.2
0
0.2
0.4
0.6
0.8
-0.2
1.35 eV
-0.4
1.25 eV
-0.6
-0.8
1.30 eV
-1.0

Figure 4a

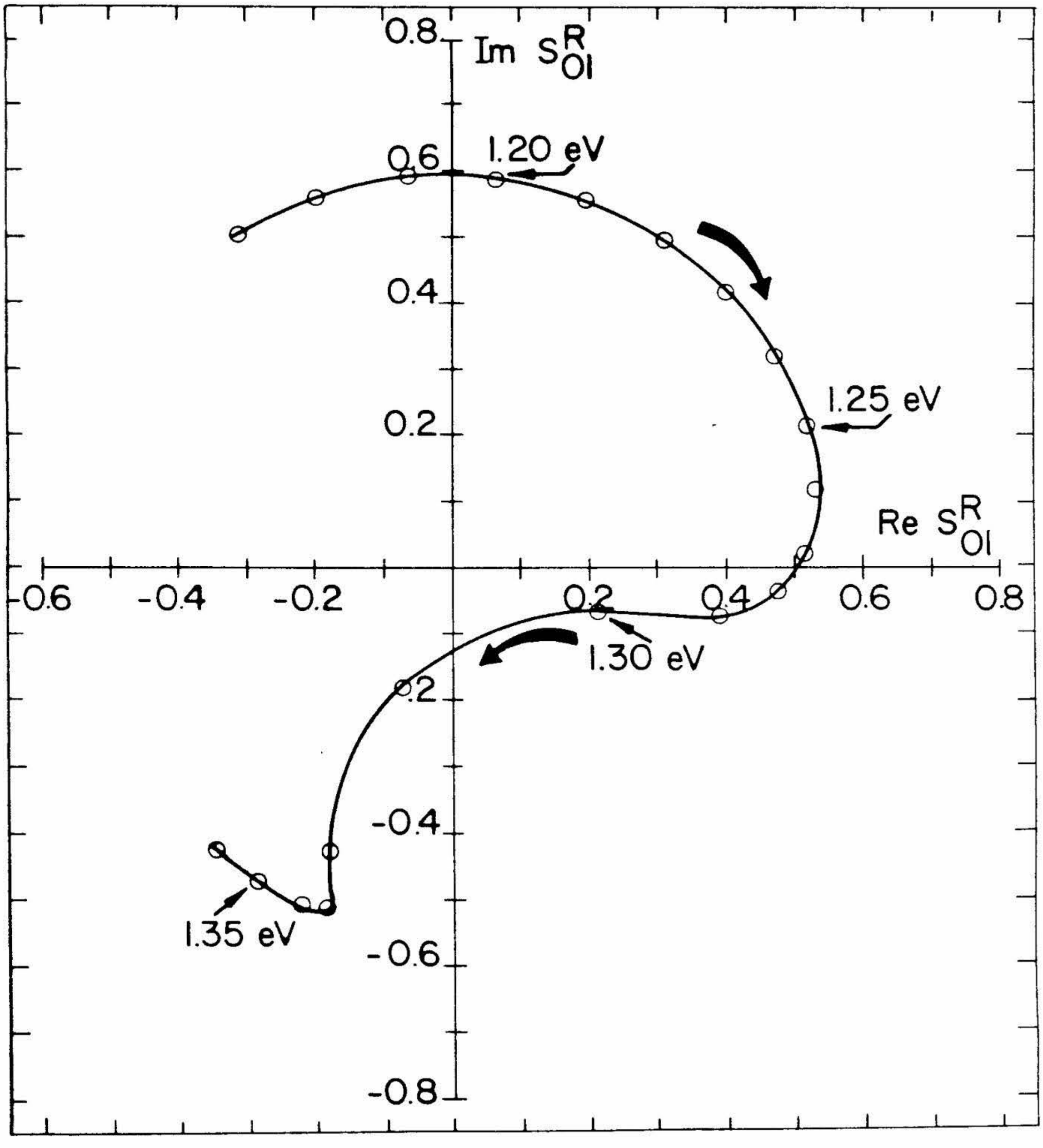
Im S_{01}^{R}
Re S_{01}^{R}
0.8
0.6
0.4
0.2
-0.2
-0.4
-0.6
-0.8
-0.6
-0.4
-0.2
0.2
0.4
0.6
0.8
1.20 eV
1.25 eV
1.30 eV
1.35 eV

Figure 4b

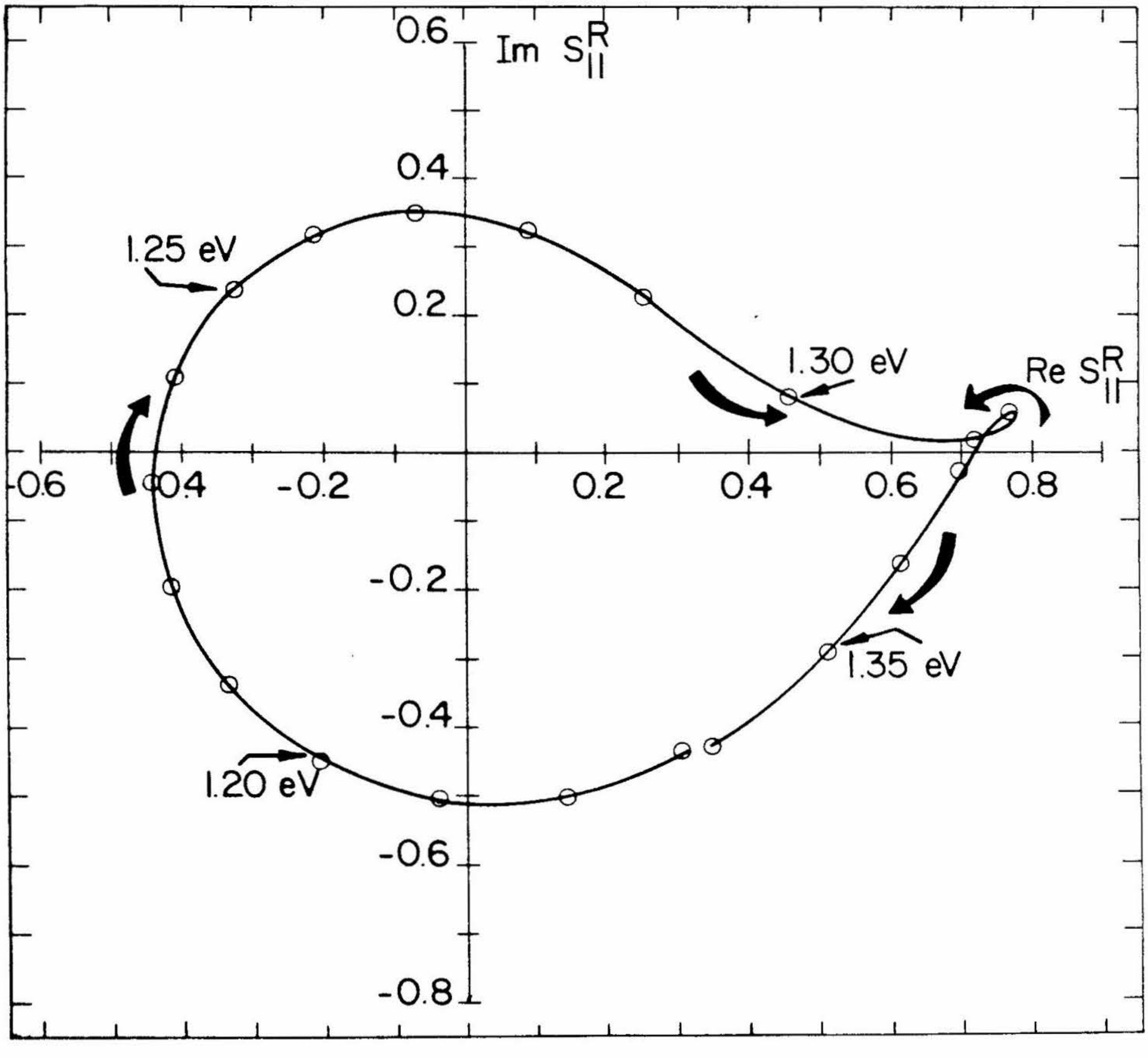
0.6
Im S_{11}^{R}
0.4
0.2
-0.2
-0.4
-0.6
-0.8
-0.6
-0.4
-0.2
0.2
0.4
0.6
0.8
Re S_{11}^{R}
1.25 eV
1.30 eV
1.35 eV
1.20 eV

Figure 4c

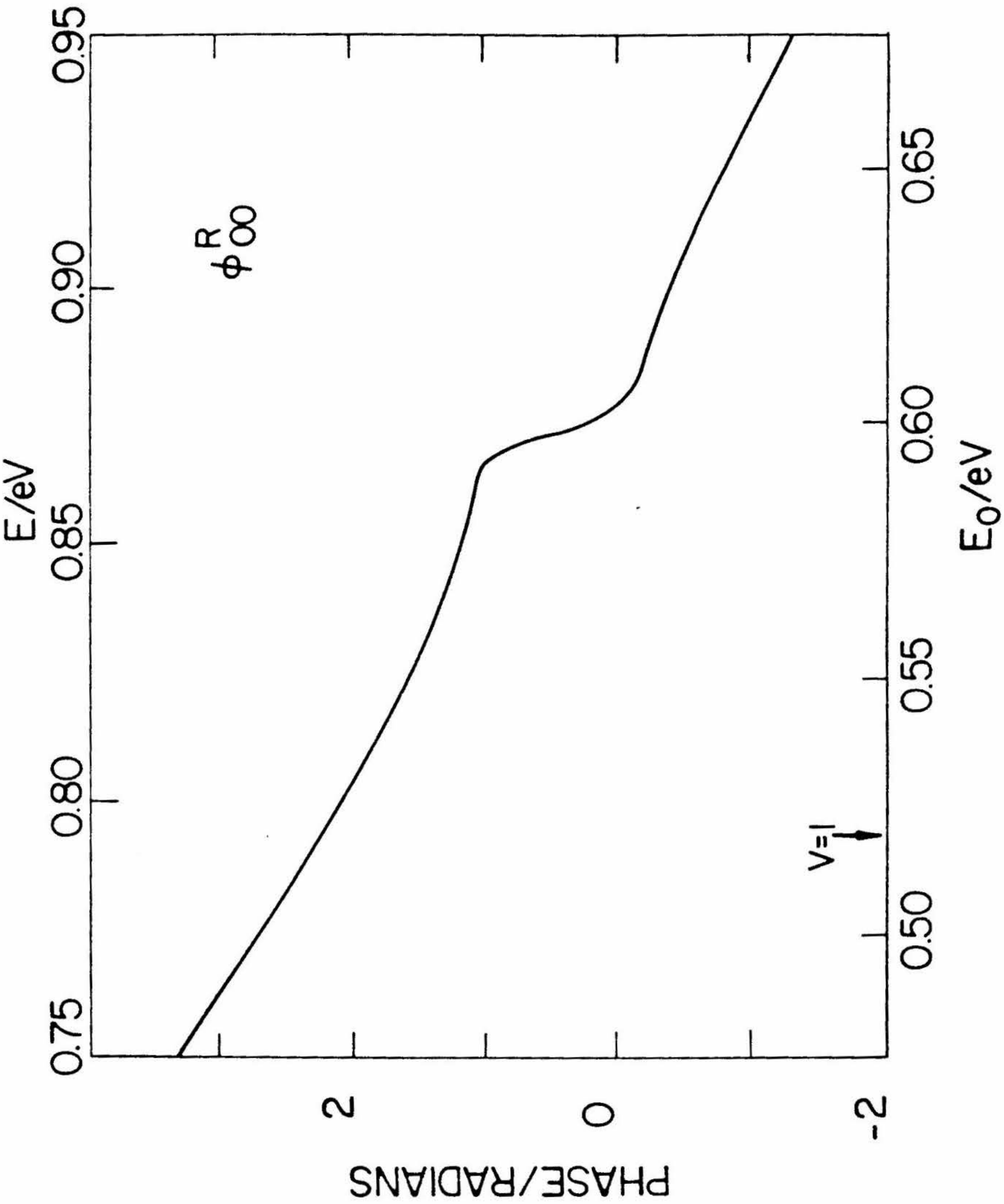
E/eV
0.75
0.80
0.85
0.90
0.95
E_0/eV
0.50
0.55
0.60
0.65
PHASE/RADIANS
2
0
-2
ϕ^R_{00}
v=1

Figure 5a

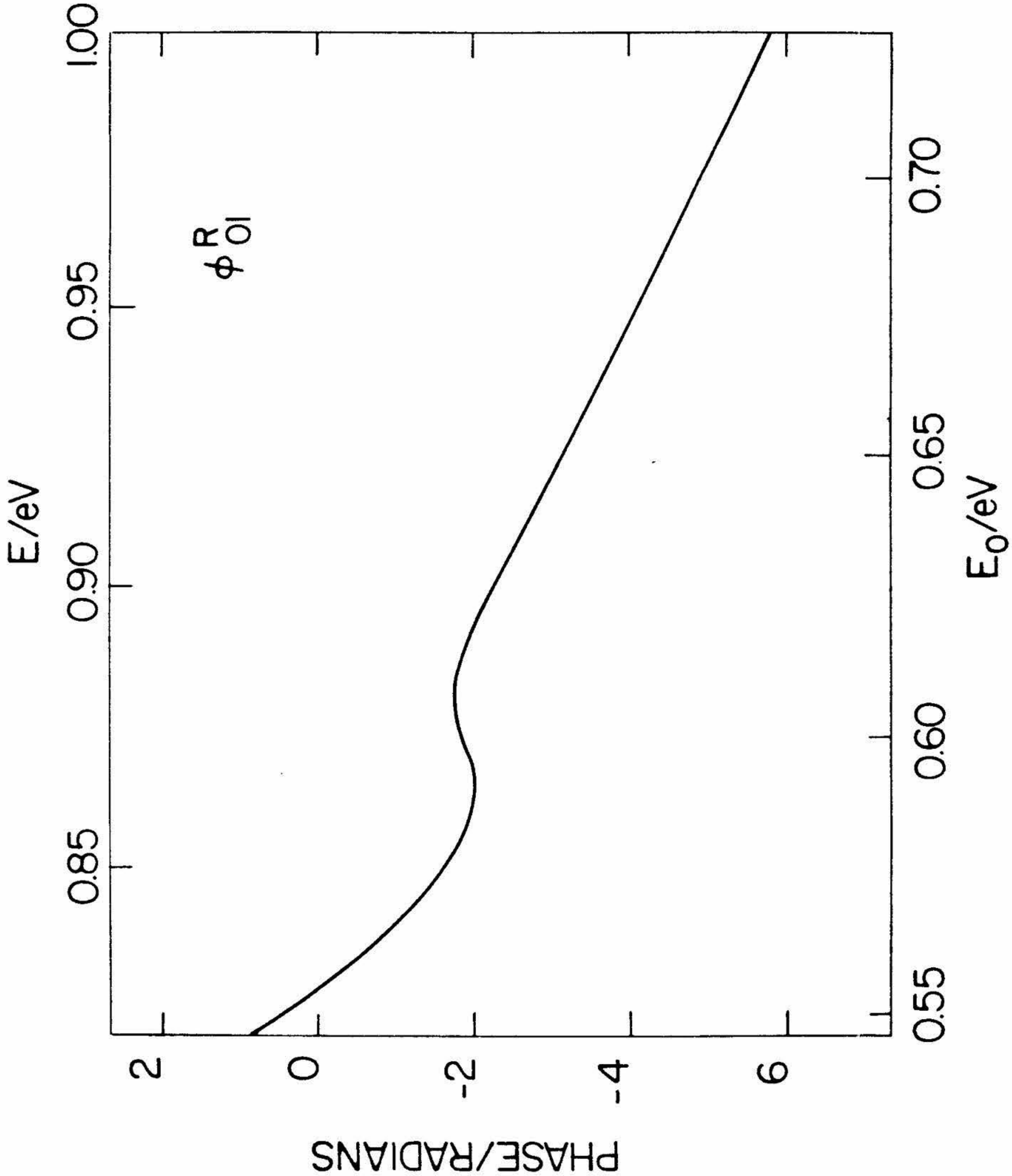
E/eV
0.85
0.90
0.95
1.00
ϕ^{R}_{01}
E_0/eV
0.55
0.60
0.65
0.70
PHASE/RADIANS
2
0
-2
-4
6

Figure 5b

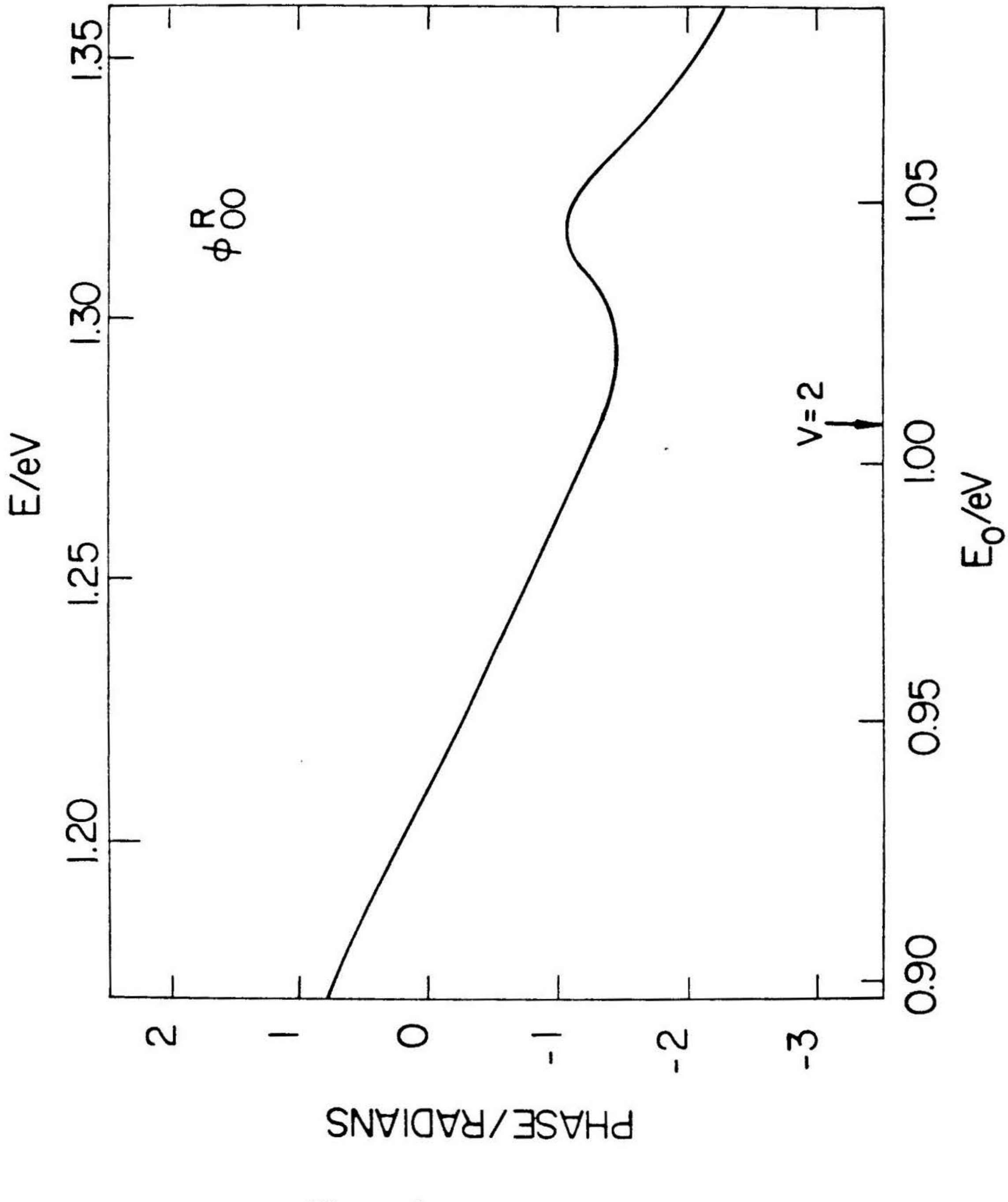
E/eV
1.20
1.25
1.30
1.35
ϕ^{R}_{00}
V=2
E_0/eV
0.90
0.95
1.00
1.05
PHASE/RADIANS
2
1
0
-1
-2
-3

Figure 6a

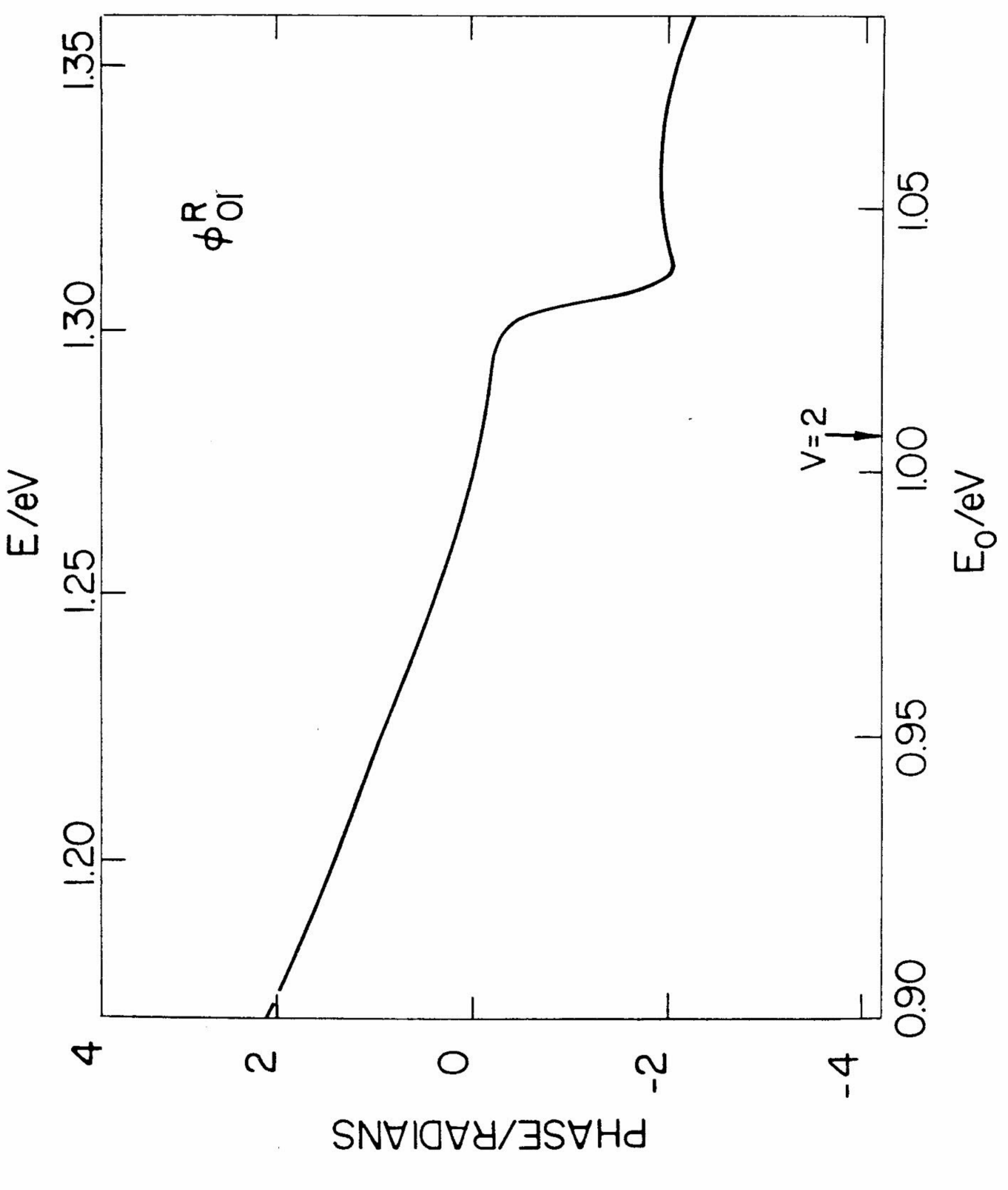
E/eV
1.20
1.25
1.30
1.35
ϕ^R_{01}
V=2
E_0/eV
0.90
0.95
1.00
1.05
PHASE/RADIANS
4
2
0
-2
-4

Figure 6b

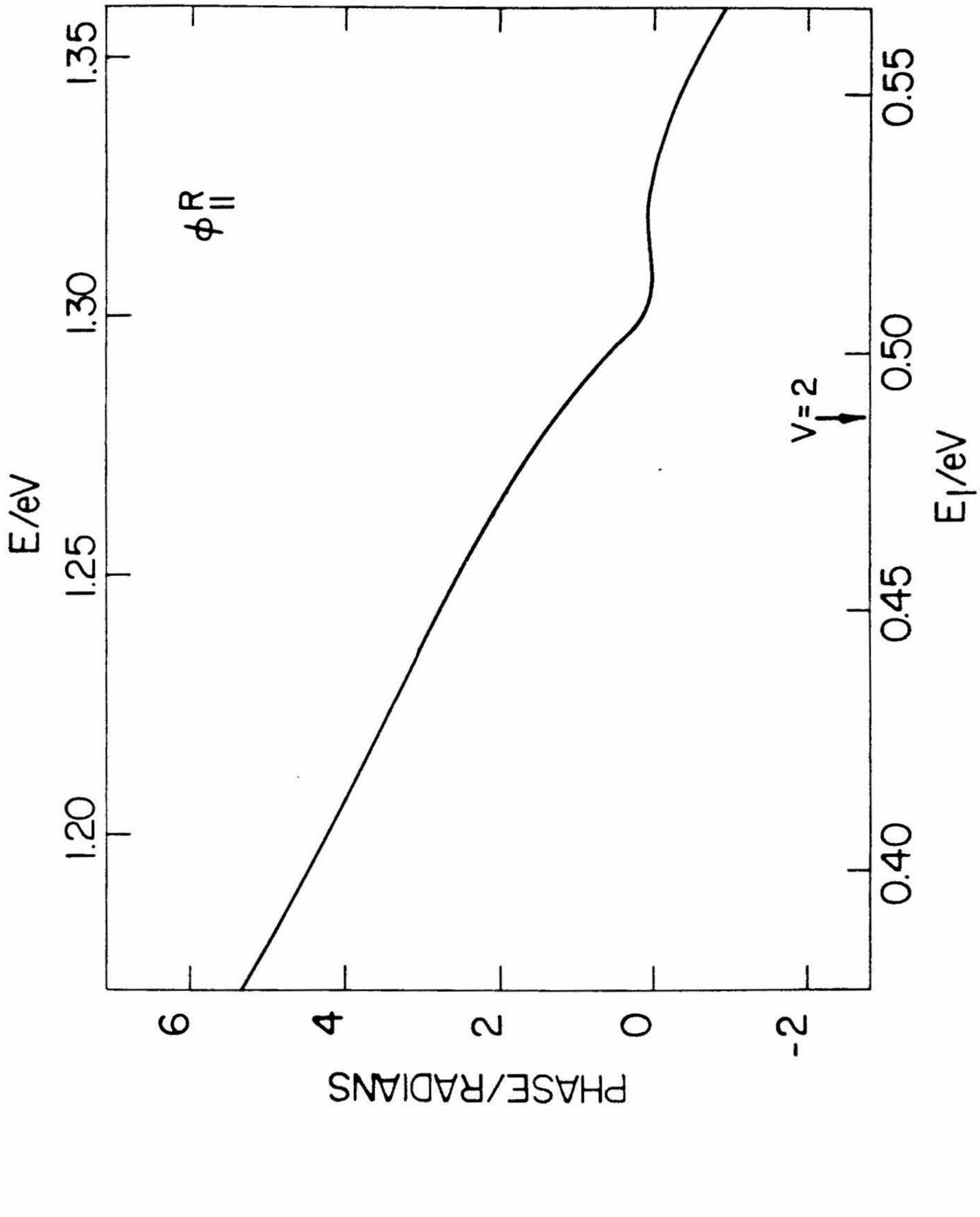
E/eV
1.20
1.25
1.30
1.35
PHASE/RADIANS
6
4
2
0
-2
$\phi_{\parallel}^{R}$
V=2
E_1/eV
0.40
0.45
0.50
0.55

Figure 6c

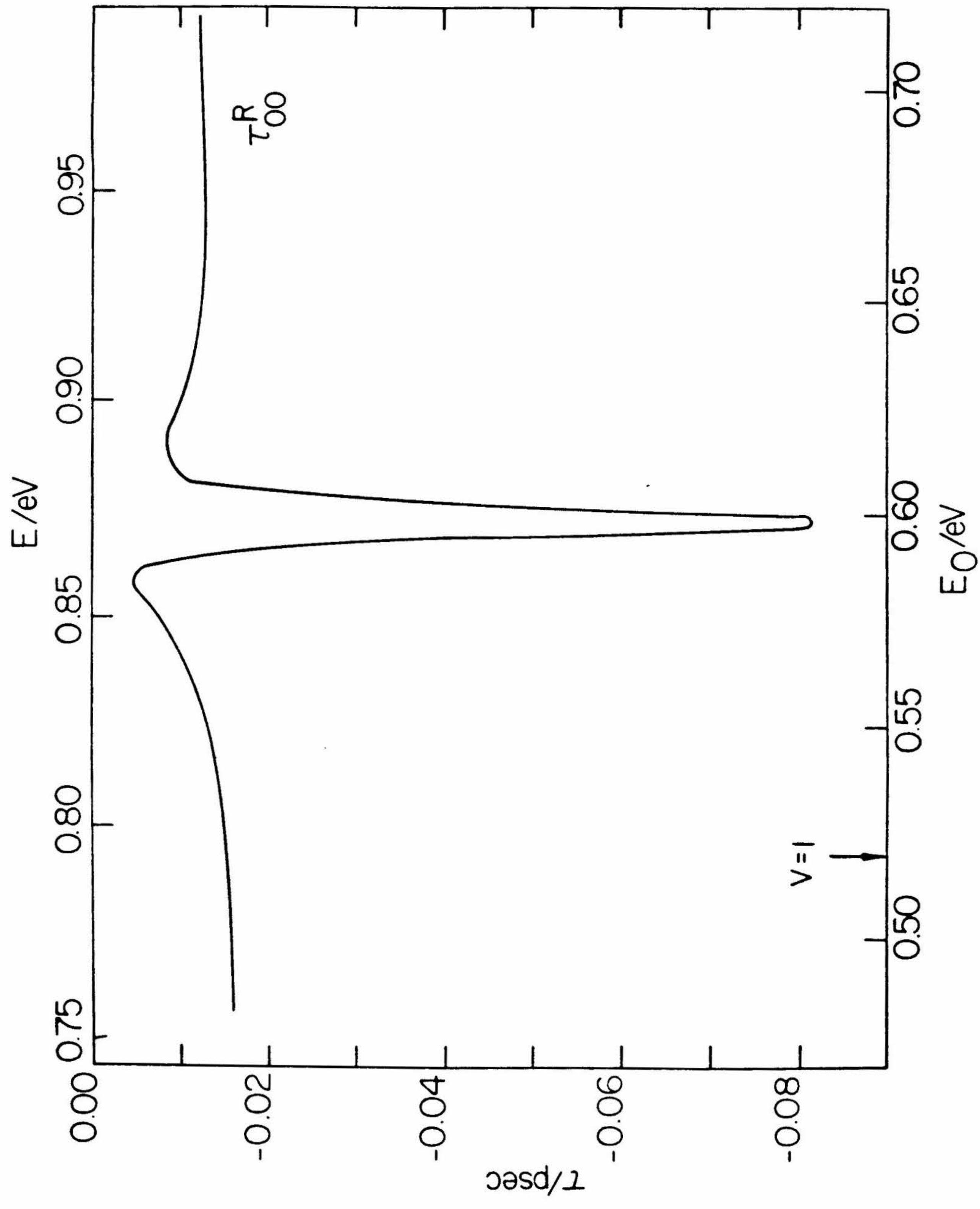
E /eV
0.75
0.80
0.85
0.90
0.95
E_0/eV
0.50
0.55
0.60
0.65
0.70
τ/psec
0.00
-0.02
-0.04
-0.06
-0.08
τ^R_{00}
V=1

Figure 7a

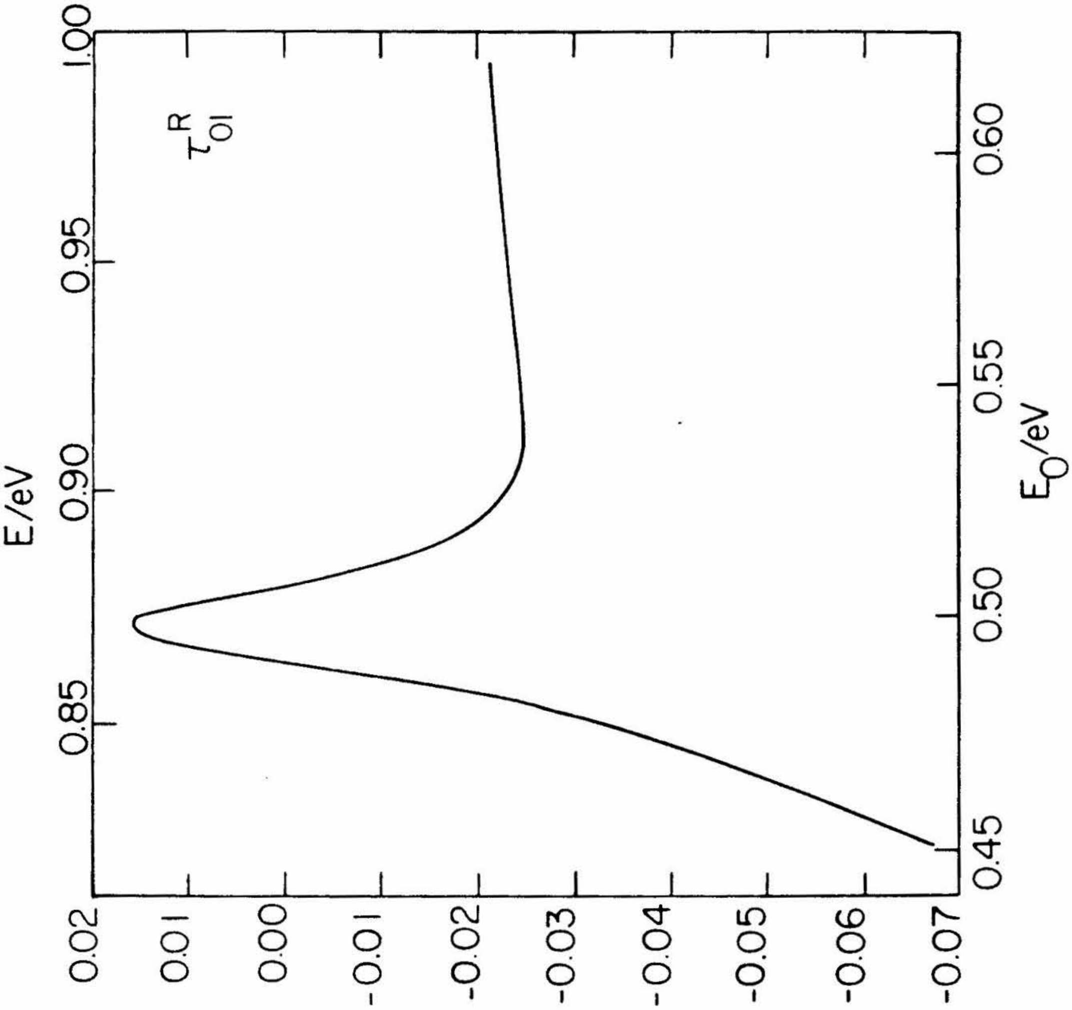
E/eV
0.85
0.90
0.95
1.00
E_0/eV
0.45
0.50
0.55
0.60
τ/psec
0.02
0.01
0.00
-0.01
-0.02
-0.03
-0.04
-0.05
-0.06
-0.07
τ_{01}^{R}

Figure 7b

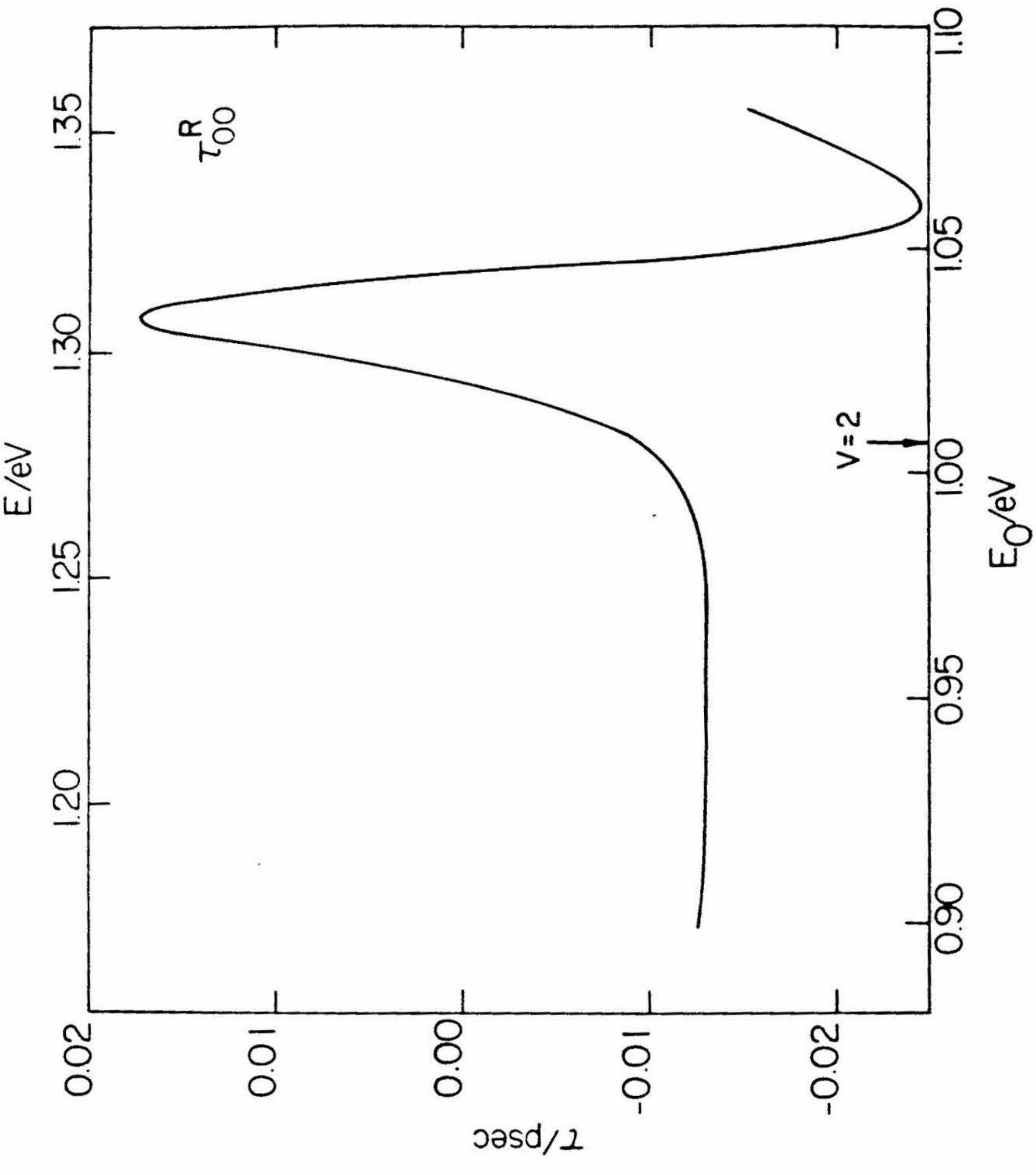
E/eV
1.20
1.25
1.30
1.35
τ^R_{00}
V=2
E_0/eV
0.90
0.95
1.00
1.05
1.10
τ/psec
0.02
0.01
0.00
-0.01
-0.02

Figure 8a

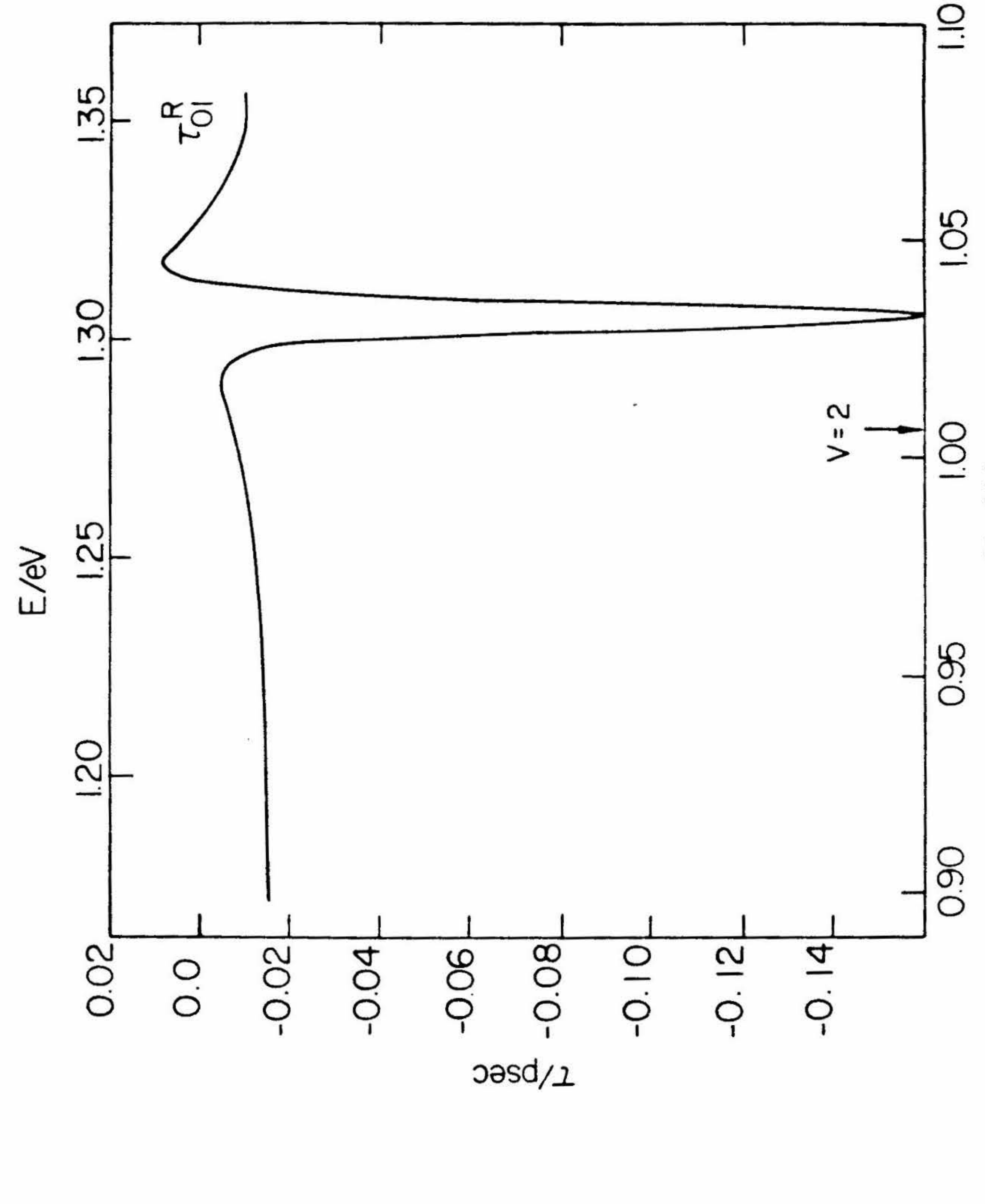
E/eV
1.20
1.25
1.30
1.35
τ_{01}^{R}
V = 2
0.90
0.95
1.00
1.05
1.10
E_0/eV
0.02
0.0
-0.02
-0.04
-0.06
-0.08
-0.10
-0.12
-0.14
τ/psec

Figure 8b

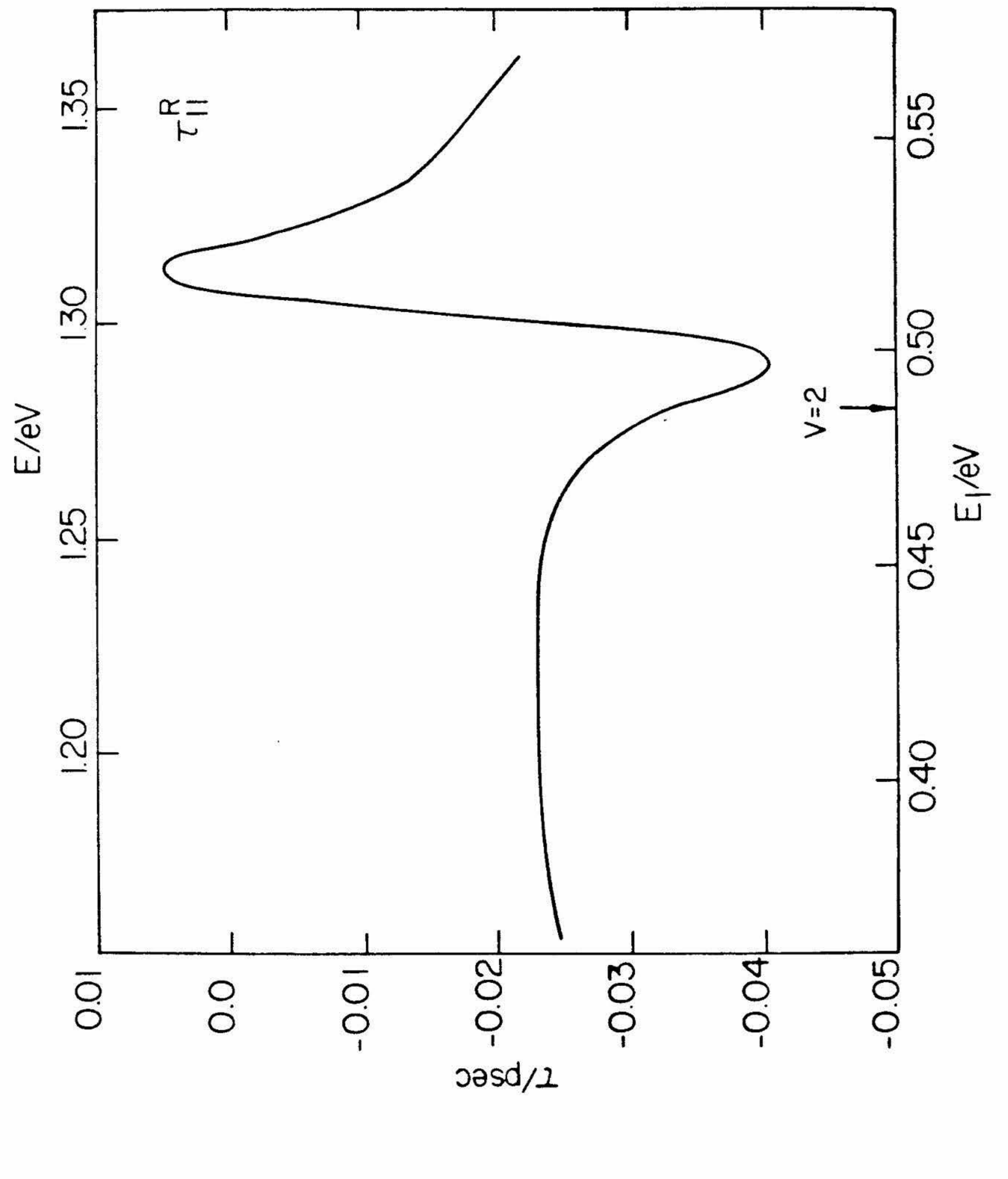
E/eV
1.20
1.25
1.30
1.35
τ_{11}^{R}
V=2
E_1/eV
0.40
0.45
0.50
0.55
τ/psec
0.01
0.0
-0.01
-0.02
-0.03
-0.04
-0.05

Figure 8c

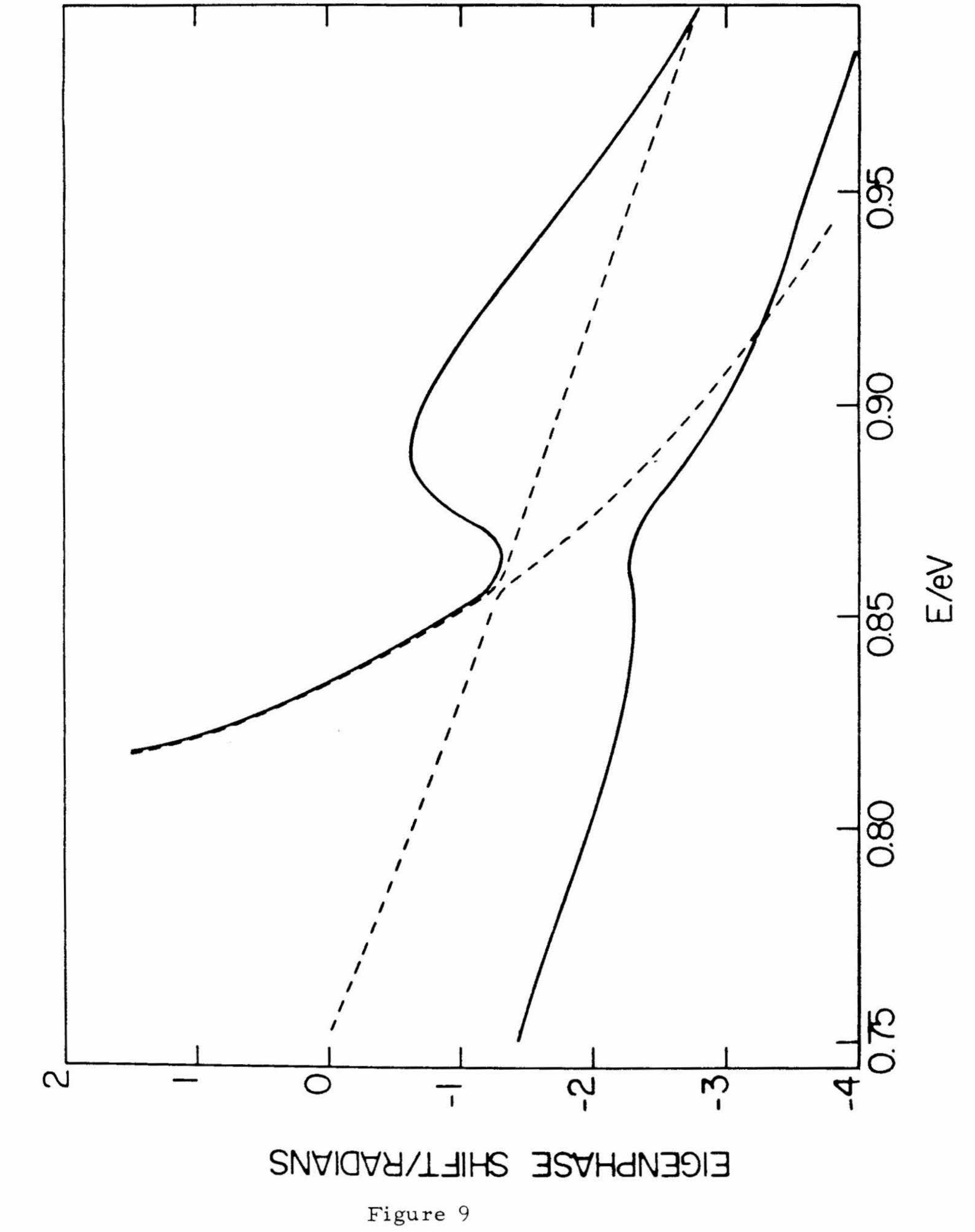

Figure 9

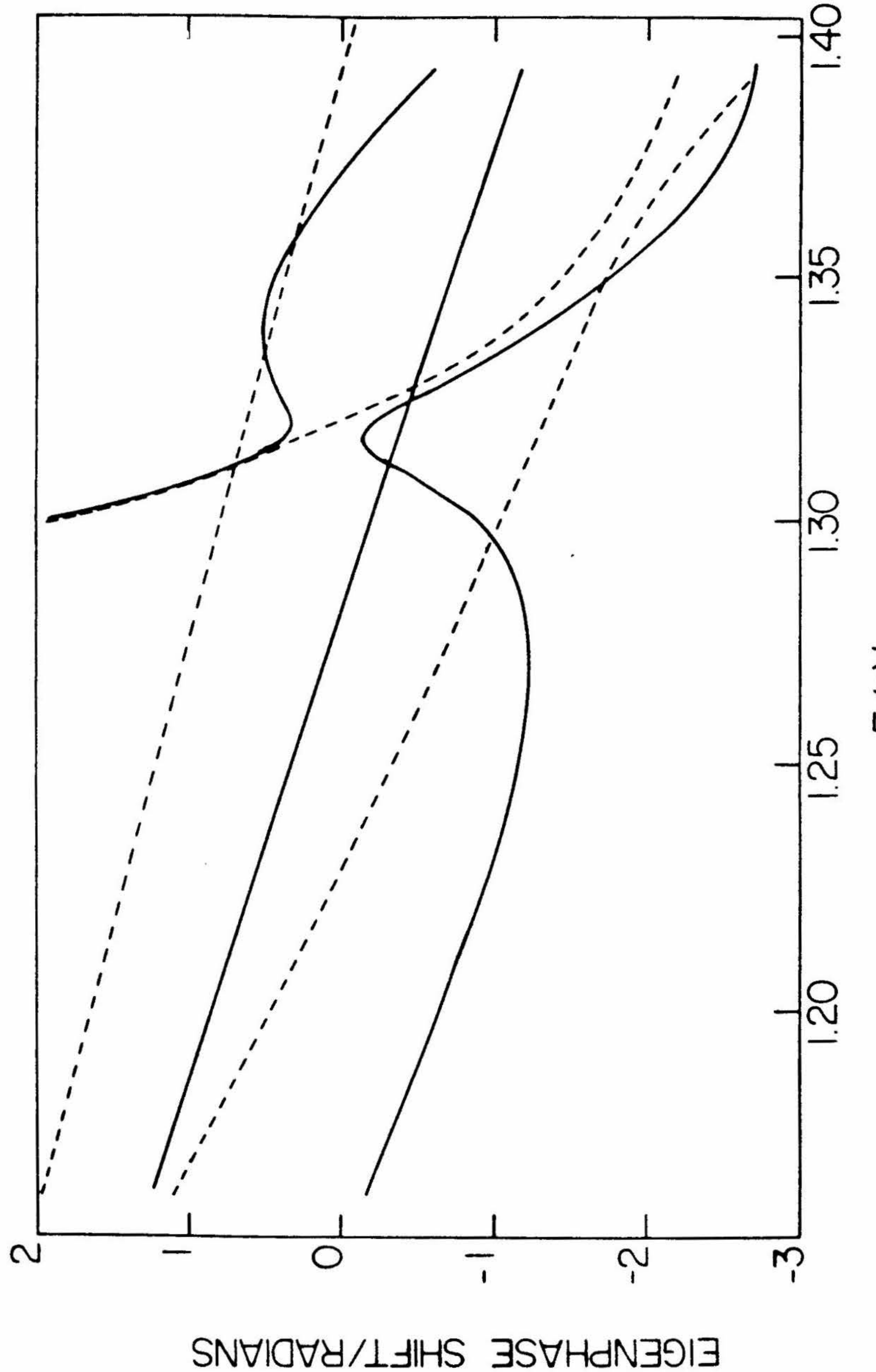

Figure 10

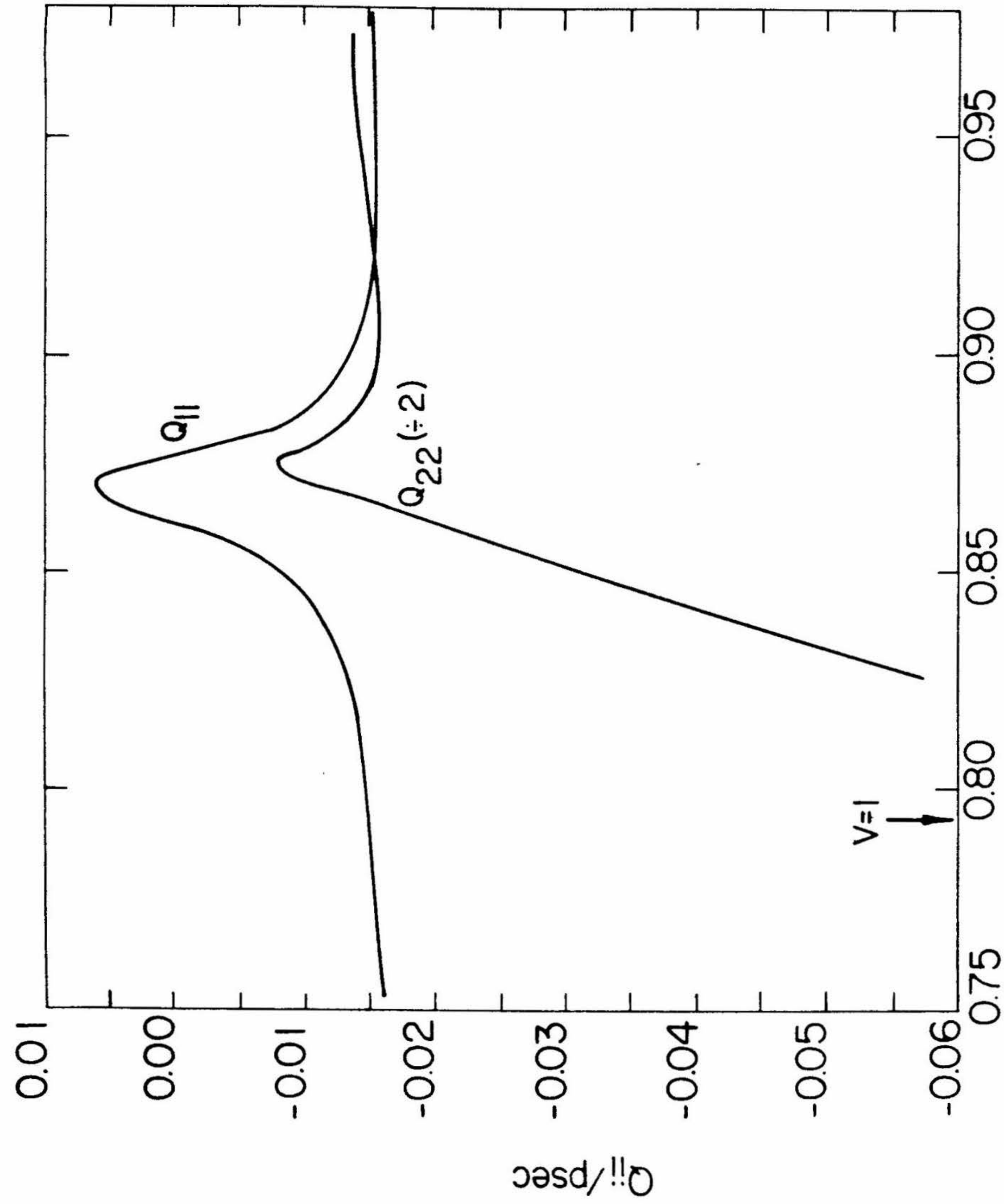
Q11
Q22(÷2)
V=1
E/eV
Qii/psec
0.75
0.80
0.85
0.90
0.95
0.01
0.00
-0.01
-0.02
-0.03
-0.04
-0.05
-0.06

Figure 11

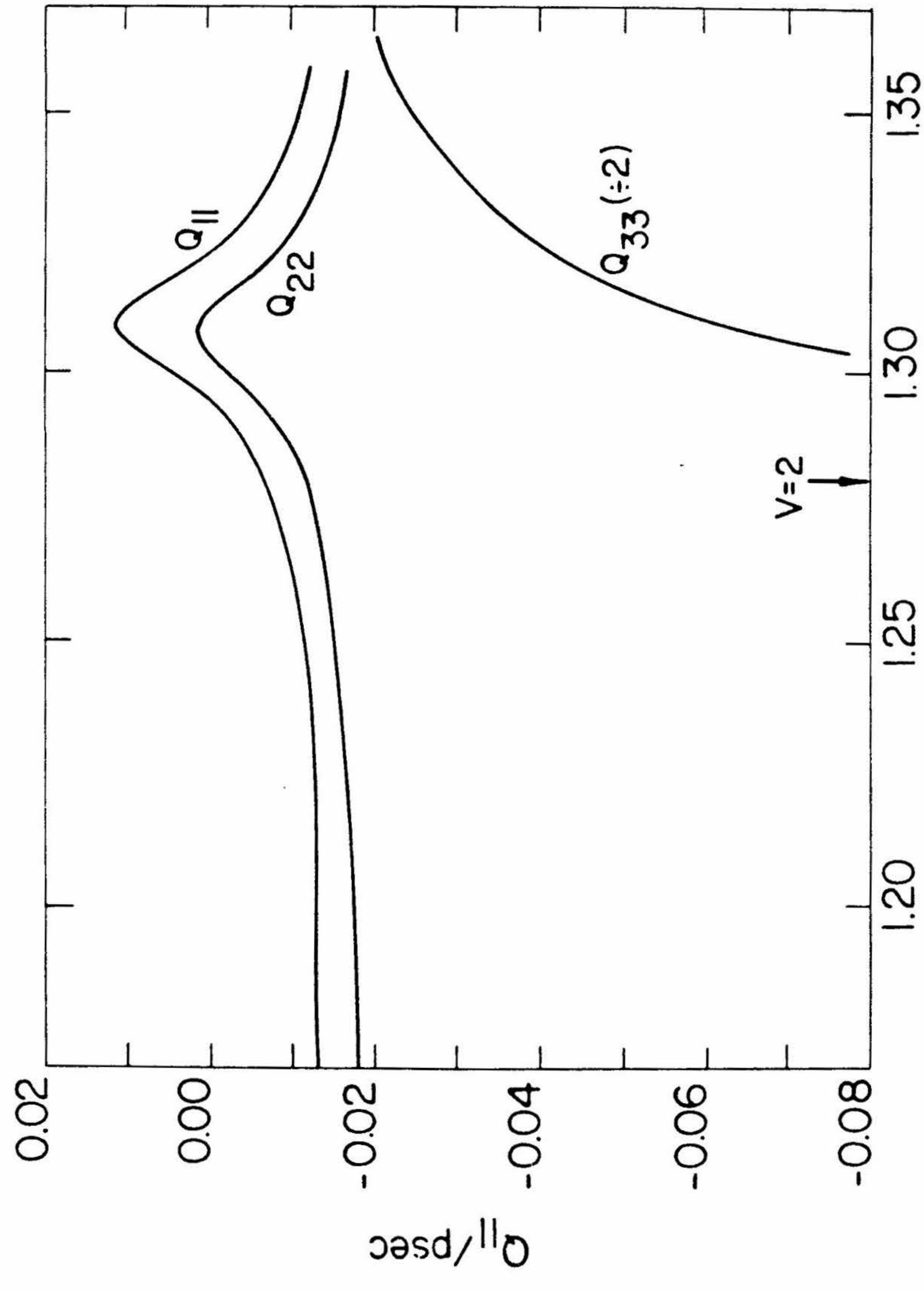
Q11
Q22
Q33(÷2)
V=2
E/eV
1.20
1.25
1.30
1.35
0.02
0.00
-0.02
-0.04
-0.06
-0.08
Q11/psec

Figure 12

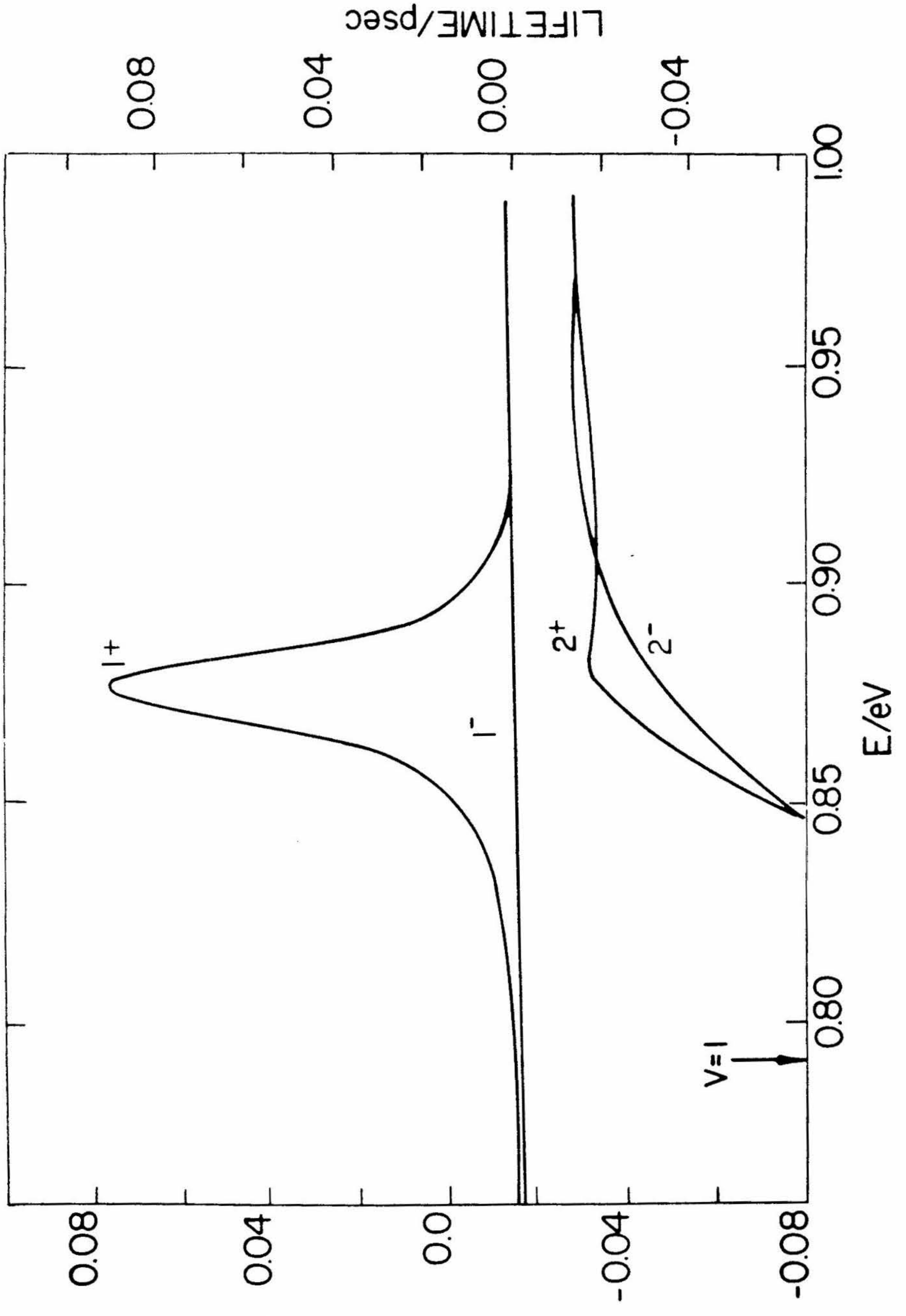
EIGENVALUE OF Q/psec
0.08
0.04
0.0
-0.04
-0.08
LIFETIME/psec
0.08
0.04
0.00
-0.04
E/eV
0.80
0.85
0.90
0.95
1.00
1+
1-
2+
2-
V=1

Figure 13

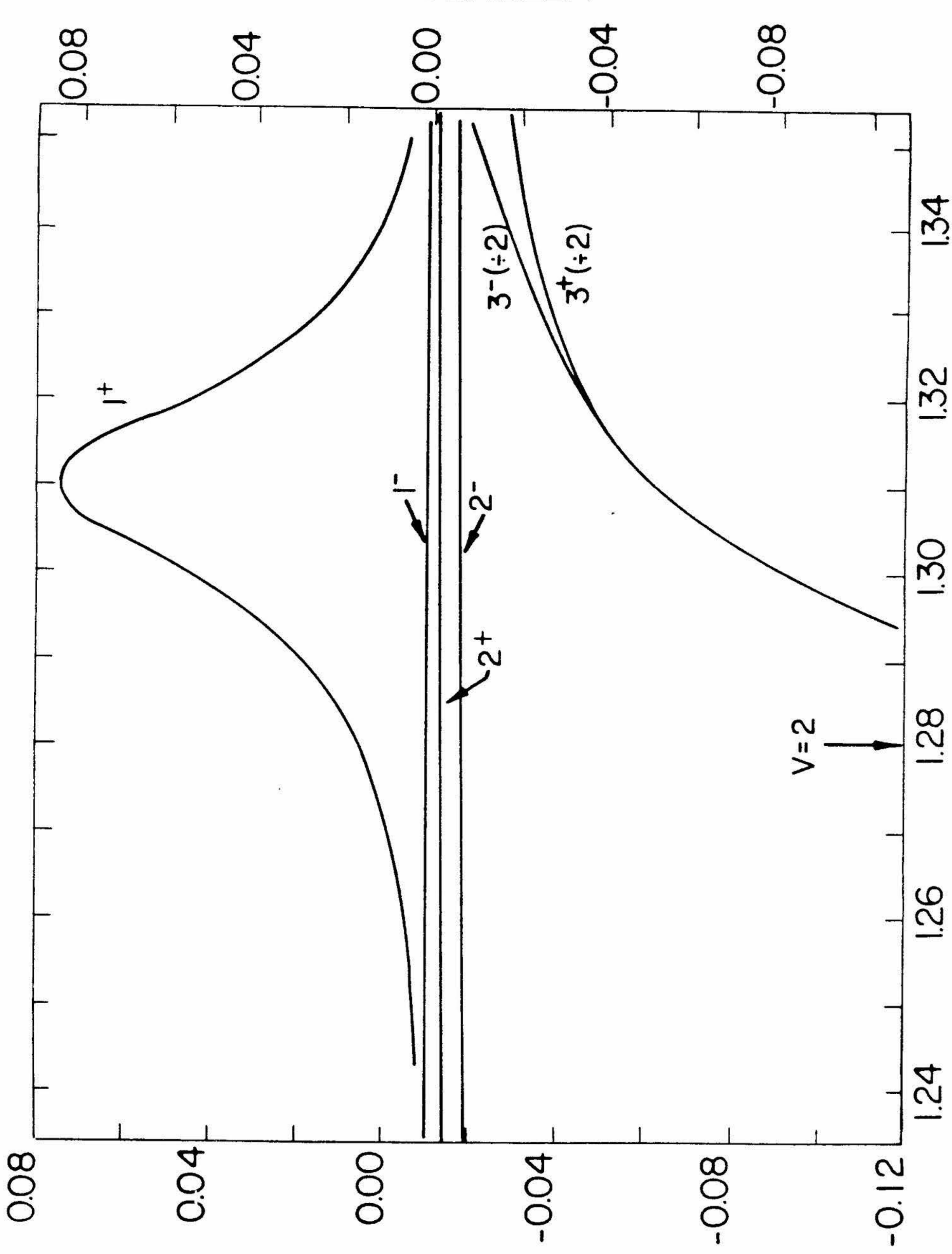
EIGENVALUE OF Q/psec
LIFETIME/psec
E/eV
0.08
0.04
0.00
-0.04
-0.08
-0.12
1.24
1.26
1.28
1.30
1.32
1.34
1$^+$
1$^-$
2$^-$
2$^+$
3$^-$(÷2)
3$^+$(÷2)
V=2

Figure 14

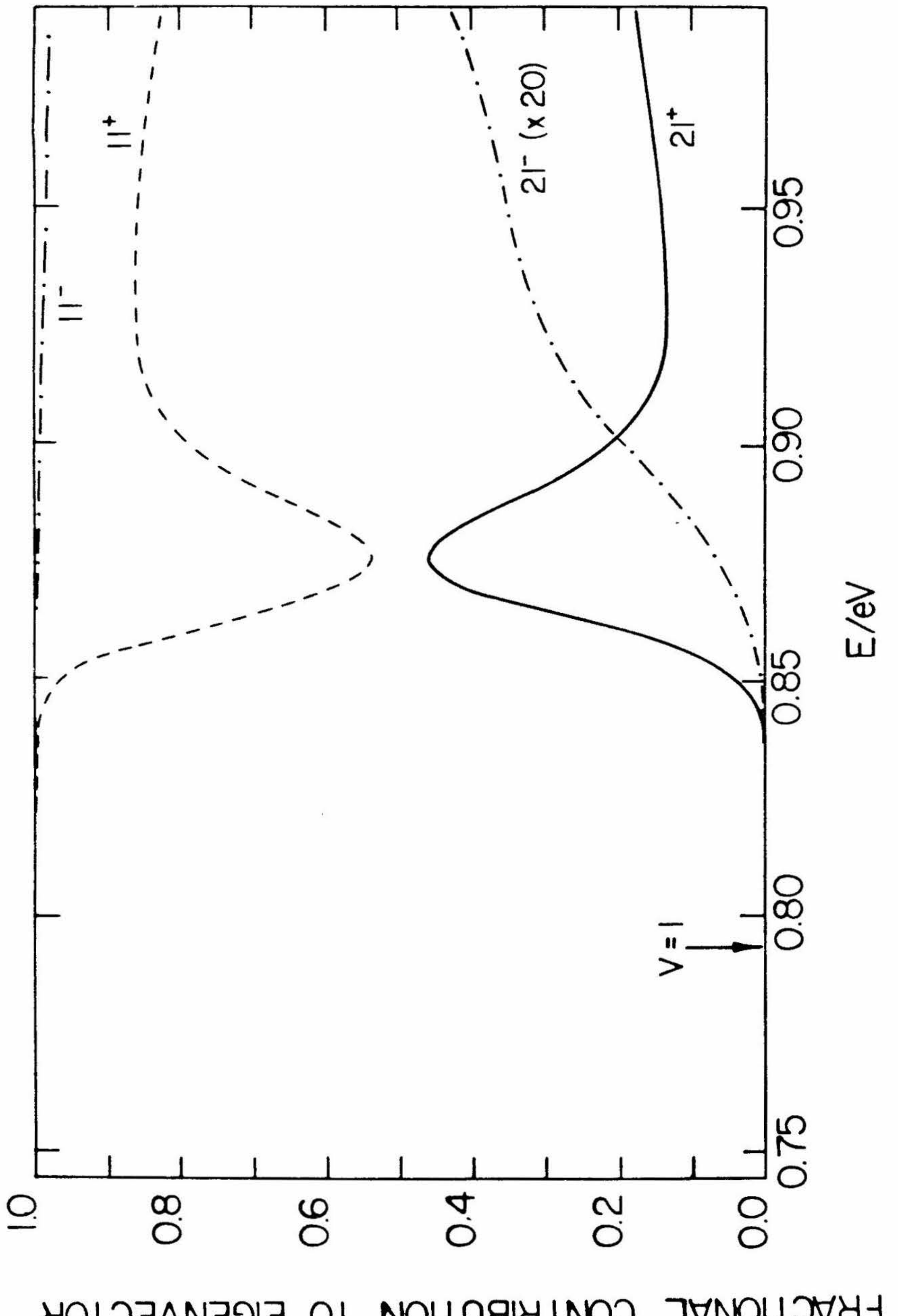
1.0
0.8
0.6
0.4
0.2
0.0
FRACTIONAL CONTRIBUTION TO EIGENVECTOR
0.75
0.80
0.85
0.90
0.95
E/eV
V = 1
$1l^-$
$1l^+$
$2l^-$ (x 20)
$2l^+$

Figure 15

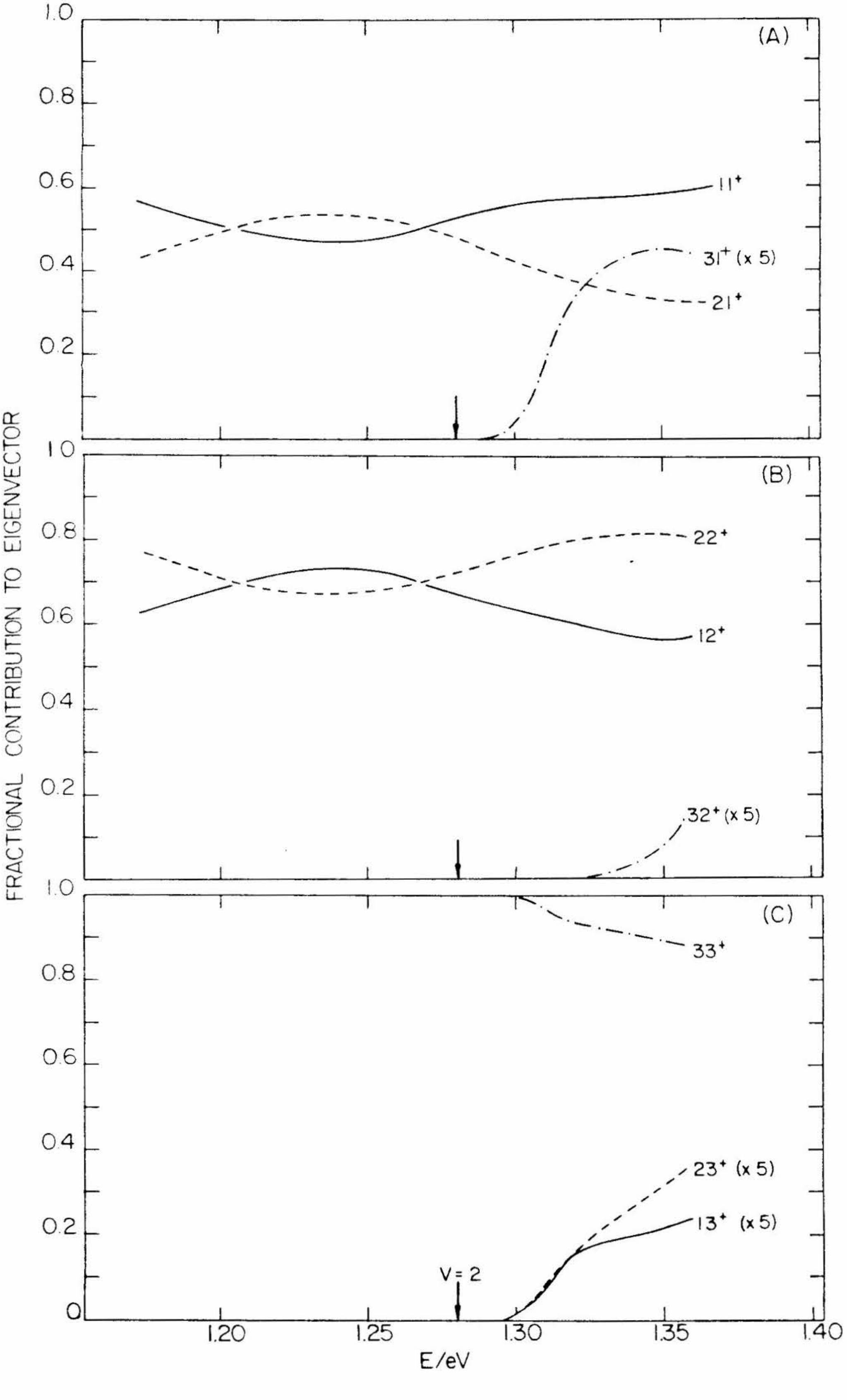
FRACTIONAL CONTRIBUTION TO EIGENVECTOR
(A)
11⁺
31⁺ (x 5)
21⁺
(B)
22⁺
12⁺
32⁺ (x 5)
(C)
33⁺
23⁺ (x 5)
13⁺ (x 5)
V = 2
0
0.2
0.4
0.6
0.8
1.0
1.20
1.25
1.30
1.35
1.40
E/eV

Figure 16

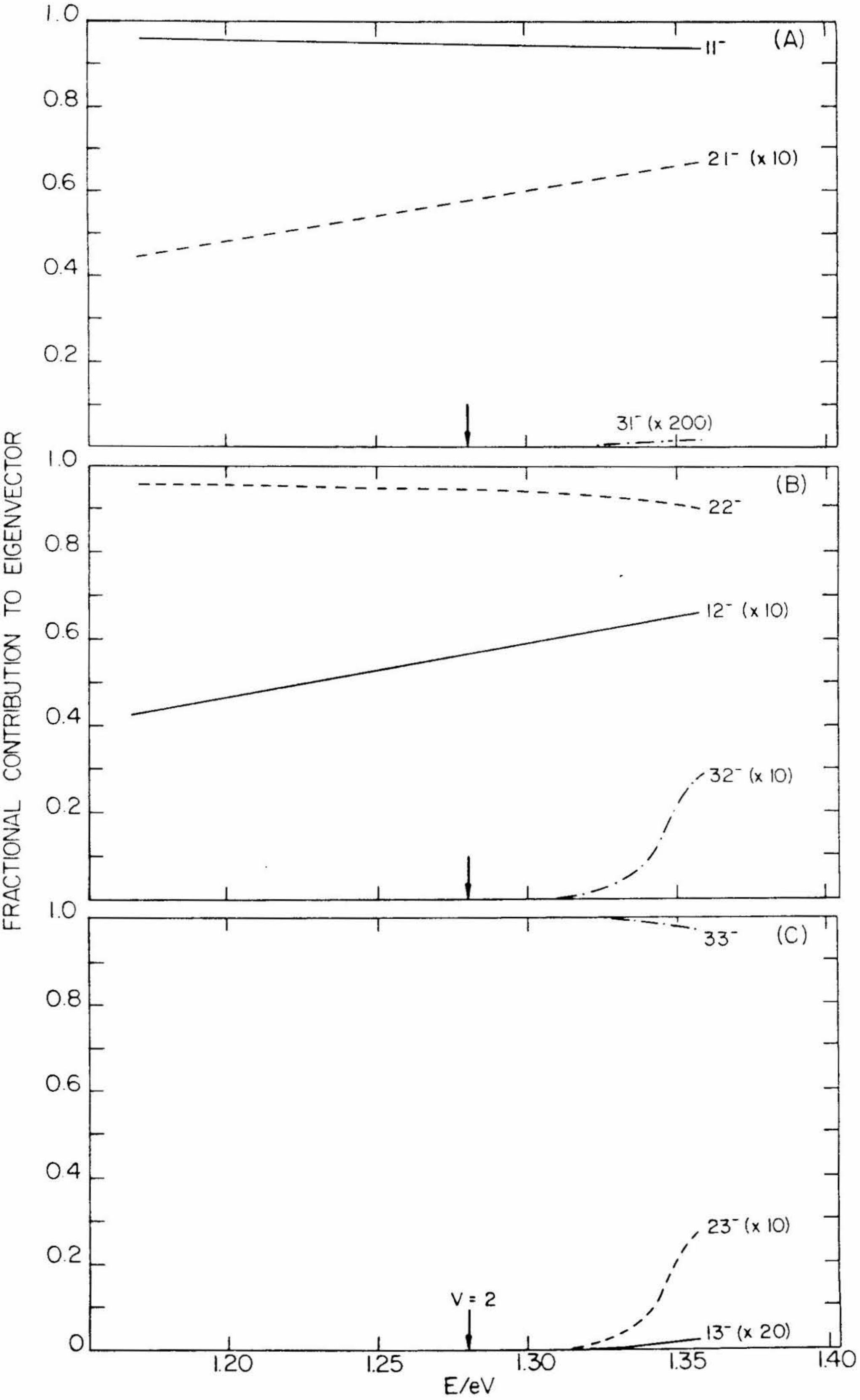
1.0
0.8
0.6
0.4
0.2
0
(A)
11⁻
21⁻ (x 10)
31⁻ (x 200)
(B)
22⁻
12⁻ (x 10)
32⁻ (x 10)
(C)
33⁻
23⁻ (x 10)
13⁻ (x 20)
V = 2
1.20
1.25
1.30
1.35
1.40
E/eV
FRACTIONAL CONTRIBUTION TO EIGENVECTOR

Figure 17

II.3 CHARACTERIZATION OF THE LOWEST ENERGY RESONANCES IN THE COLLINEAR F + H_2 SYSTEM AND ITS ISOTOPIC ANALOGUES

Characterization of the Lowest Energy Resonances in the Collinear $F + H_2$ System and its Isotopic Analogues.[a]

Jack A. Kaye[b] and Aron Kuppermann
Arthur Amos Noyes Laboratory of Chemical Physics,[c]
California Institute of Technology, Pasadena, California 91125

(Received)

Collinear quantum mechanical scattering calculations on the collinear $F + H_2$, HD, DH, and D_2 systems have been performed at energies near the lowest energy resonance. We have examined the effect of the resonance on reaction probabilities, individual scattering matrix element phases and their energy derivatives, eigenphase shifts, and diagonal elements, eigenvalues, and eigenvectors of Smith's collision lifetime matrix. The eigenvalues of the collision lifetime matrix provide the most sensitive means for characterizing these resonances, and are particularly useful in that they localize the resonance into a single eigenchannel. The lifetimes calculated for the FHD, FH_2, FD_2, and FDH systems are 4.8, 0.33, 0.15, and 0.064 psec, respectively. The eigenvectors associated with the eigenvalues containing the resonances consist mainly of the highest participating HF-like state (v=2 for HF formation, v=3 for DF formation) and smaller contributions from the hydrogenic molecule, and, in the FD_2 and FDH systems, a lower (v=2) state of DF. The limitations and advantages of each of the characterization techniques used were discussed. The differences and similarities between the effects of the resonance in the $F + H_2$ type systems and in the $H + H_2$ system are discussed.

---

[a] This work was supported in part by a grant (No. CHE77-26515) from the National Science Foundation.

[b] Work performed in partial fulfillment of the requirements for the Ph.D. degree in Chemistry at the California Institute of Technology.

[c] Contribution No.

I. INTRODUCTION

The reaction of fluorine atoms with hydrogen molecules and their various deuterium substituted counterparts

$$F + H_2(HD, D_2) \longrightarrow HF(DF) + H(D) \qquad (1)$$

is one of the best studied reactions in chemistry (1). Numerous experimental studies have been performed on the kinetics and dynamics of this system (1, 2). Theoretical treatments have utilized nearly all possible methods, including quasi-classical trajectory calculations (3), exact quantum mechanical calculations (4, 5) (assuming a collinear model for the reaction), and approximate three-dimensional quantum mechanical calculations (6), as well as other methods based on detailed consideration of the properties of the potential energy surface for the reaction (7). Interest in this system has also been sparked by the existence of low-lying excited electronic potential energy surfaces for the FH_2 triatomic system due to the small energy gap (404 cm^{-1}) between the ground ($^2P_{3/2}$) and excited ($^2P_{1/2}$) states of the fluorine atom (8). Because of the small number of electrons (11) in the FH_2 system, it is expected that by ab initio methods a chemically accurate potential energy surface should be obtainable and thus give confidence that the results of dynamical treatments of the FH_2 system are correct (9).

Among the most important results to come from the collinear quantum mechanical treatments of this reaction are the existence and importance of a low energy dynamical resonance (4, 5). This resonance is found for all possible H and D substituted analogues (FH_2, FHD, FDH, FD_2), although the strength of the resonance has been shown to vary dramatically with isotopic substitution (4, 10). The influence of changes in the potential energy surface on the reaction probabilities has been explored by Connor, et al. (5a).

Attempts have been made to understand what regions and features of the potential energy surface are most responsible for the existence of the low energy resonance. In particular, Babamov and Kuppermann (11) have developed a model which accurately predicts the location and strength of the lowest energy resonance in the collinear F + H_2 (HD) reactions and allows for a simple interpretation of the resonance. Hayes and Walker have also developed a simple model for these resonances (12). The calculations of Wyatt and co-workers (5b, 6b), in which probability density and probability current density are examined have provided additional insight into these reactions.

The approximate (j_z-conserving) three dimensional quantum mechanical calculations performed on this system suggest that the strong resonances observed in the collinear quantum mechanical calculations carry over into the real three dimensional world (6a). Indeed, the molecular beam experiments of Sparks, et al. (13) suggest experimental evidence for the existence of the resonance. Because of the greater strength of the resonance for the reaction

$$F + HD \longrightarrow FH + D \tag{2}$$

as predicted by the collinear quantum mechanical calculations, it has been suggested that that system is most likely to display a strong resonance in the three dimensional world (14).

In order to fully understand these resonances, it is necessary to examine more than just the reaction probabilities. Near a resonance, the phase of certain scattering matrix elements and their energy derivatives, the eigenphase shifts (arc tangents of the eigenvalues of the reactance matrix), and the eigenvalues of Smith's (15) collision lifetime matrix all may undergo rapid and unusual changes with energy (14, 16, 17). The latter quantity has been shown to be an especially useful indicator of resonances, as it isolates the resonance in a single channel, allowing for simple observation and characterization of the resonance (10). After suitable and simple modification, the eigenvalues of the collision lifetime matrix are directly related to the lifetime of the long-lived metastable state associated with the resonance. The eigenvector associated with the eigenvalue of the collision lifetime matrix which contains the resonance should also provide some insight as to the nature of the long-lived state.

In this work we characterize the lowest energy resonance in the collinear F + H_2, HD, DH, and D_2 systems by considering the variation with energy of various quantities obtained in and from the scattering calculation - reaction probabilities, scattering matrix element phases and their energy derivatives, eigenphase shifts, and diagonal elements, eigenvalues, and eigenvectors of the collision lifetime matrix. This paper is similar in spirit to the previous paper (18), in which we use the same quantities to characterize the two lowest energy resonances in the collinear H + H_2 system on the Porter-Karplus surface (19). We will consider at some length the differences between the H_3 and FH_2 systems as seen with the various characterization techniques applied.

The outline of this paper is as follows. In section 2 we briefly discuss the numerical methods used in the scattering calculations and in subsequent analysis (for a full discussion of the techniques used to characterize the resonance, the reader is referred to the previous paper (18)). In section 3 we present as a series of plots the results obtained. In section 4 we discuss them, and in section 5 we offer conclusions.

II. METHOD OF CALCULATION

The coupled channel calculations from which the reactance ($\underline{\underline{R}}$), scattering ($\underline{\underline{S}}$), and probability ($\underline{\underline{P}}$) matrices were obtained were performed using the method of Kuppermann (20). These calculations are extensions of those reported previously by Schatz, Bowman, and Kuppermann (4). Calculations were performed at a sufficiently dense energy grid near the resonances that the energy derivative of the $\underline{\underline{S}}$ matrix needed in the calculation of the collision lifetime matrix $\underline{\underline{Q}}$, where

$$\underline{\underline{Q}} = i\hbar \underline{\underline{S}}(d\underline{\underline{S}}^{\ddagger}/dE) \tag{3}$$

can be approximated by a three-point finite difference method. The same approximation was also used to calculate the energy derivative of the phases of individual $\underline{\underline{S}}$ matrix elements. As a result of this approximation, $\underline{\underline{Q}}$ was not precisely hermitian (given a unitary $\underline{\underline{S}}$ and the exact derivative $d\underline{\underline{S}}/dE$, it can be shown that $\underline{\underline{Q}}$ must be hermitian). To avoid complex eigenvalues, $\underline{\underline{Q}}$ was forced to be hermitian by taking the average of it and its hermitian conjugate.

In constructing plots of the eigenphase shifts and the eigenvalues of $\underline{\underline{Q}}$ as a function of energy, the eigenvalues were assigned to their respective eigenchannels by requiring that the eigenvectors, which vary slowly with energy (except in certain cases in which two of more eigenvalues are nearly degenerate) vary continuously. At certain of the energies near where degeneracies occur, the assignment of a given eigenvalue to its eigenchannel is difficult due to the inaccuracies in the calculations and the use of a finite energy spacing between adjacent calculations. This is particularly true in examining the eigenphase shifts in FD_2 and FDH (see below). In those cases, we have made what seems to be the best possible choice, but recognize the ambiguity and subjectivity inherent in such a process. In order to make a truly unambiguous assignment, one might require a much finer grid of energies than is necessary to adequately describe any of the other properties of interest, and we therefore made no further effort to remove this ambiguity. We will comment on this matter further when we show plots of certain eigenvectors of $\underline{\underline{Q}}$ for the FHD and FH_2 systems.

The potential energy surface used in the calculations reported here is the Muckerman V surface (3d, 4), which is in the form of an extended LEPS (21) surface. Plots of the potential energy surfaces for the reactions F + HD, F + H_2, F + D_2, and F + DH in the appropriate mass-scaled Delves (22) coordinate system are drawn in figure 1 (the reason for this ordering of the systems will become obvious later on). In these plots, equipotentials are drawn every 0.3 eV. The zero of energy is the bottom of the hydrogenic well. The saddle point for each surface is indicated by an "X", and the minimum energy path is indicated by a dashed line. The effect of isotopic substitution is seen mainly by consideration of the skew angle in each of the systems. These angles are 37.29°, 46.44°, 47.75°, and 56.69° for the FHD, FH_2, FD_2, and FDH systems, respectively. An energy level diagram for the lowest states of the molecules considered here (HF, DF, H_2, HD, D_2) is shown in figure 2, along with a plot of the minimum energy path for the F + H_2 reaction.

III. RESULTS

The reaction probabilities for the four systems studied here at energies near the first resonance are shown in figure 3. We display the three largest reaction probabilities for each system. Different energy regions are used in each of the figures in order to allow for sufficient bracketing of the resonance region such that at the high energy end of each plot, the dynamics should be almost entirely due to direct (as opposed to resonant) processes. Both total energies (E) and translational energies (E_0) are indicated in the plots. The resonant nature of these collisions at the low energies examined here is clearly suggested by the figures, most strongly so in the F + HD and least so in the F + DH systems. Besides the existence of rapid variations of reaction probability with energy, two features on these plots stand out. First, the resonance is reflected similarly in more than one state-to-state reaction probability in each system. Nearest the resonance there is one product state whose formation is most probable ($v = 2$ in F + HD and F + H_2 collisions, $v = 3$ in F + D_2 and F + DH collisions; note from figure 2 that these molecular states are nearly degenerate), but the product state with its quantum number reduced by one from the most probable product state is also appreciably populated. Second, with the exception of F + HD, in all systems studied, in the low energy region examined, the probability of formation of the product state whose quantum number is one greater than that populated predominantly at the resonance becomes appreciable.

Argand diagrams (14, 16) for certain of the $\underline{\underline{S}}$ matrix elements for these systems are shown in figures 4-7. In these diagrams, the $\underline{\underline{S}}$ matrix element is plotted in the complex plane. Elements at adjacent energies are connected, so that a single continuous curve is generated for each matrix element. Away from a resonance, these figures are normally clockwise circles or spirals. Near a resonance, this characteristic shape is not observed; the exact appearance of the diagram varies from resonance to resonance. Possible appearances of these diagrams near a resonance and their classification have been discussed in the previous paper (18). In the limit of an extremely strong resonance, the Argand diagram is a counterclockwise circle.

In figure 4 we present Argand diagrams for S_{02}^{R} and S_{01}^{R} for the F + HD reaction. The strength of the resonance in this system is seen by the form of the Argand diagam, which is almost precisely that of a counterclockwise circle. The similarity between the two Argand diagrams is obvious. The Argand diagram for S_{02}^{R} for the F + H_2 reaction is shown in figure 5. In this case, the resonance is substantially weaker, as evidenced by the formation of only a small counterclockwise loop instead of the large counterclockwise circle seen in the F + HD reaction. Argand diagrams for S_{03}^{R} and S_{02}^{R} for the F + D_2 reaction are shown in figure 6. The relative weakness of the resonance in this system is seen in that no region of counterclockwise sense is seen. Instead, the resonance is reflected by the region from 0.208 eV to 0.216 eV (measured with respect to the bottom of the hydrogenic well), in which the Argand diagram is essentially linear. In the weakest resonance studied, that in the F + DH reaction, the Argand diagram for S_{03}^{R} (figure 7a) has a clockwise sense everywhere. In the absence of the resonance, one might expect the Argand diagram to have much more the form of a spiral, such as that seen for S_{04}^{R} in figure 7b. Recall from figure 3d that the probability of reaction to form DF(v=4) increases monotonically with energy, and can thus be taken as a transition showing no effects of the resonance.

In order to allow us to focus solely on the phases (and not be distracted by the probabilities, as one might be in considering the Argand diagrams), we plot the phase $\Phi_{0v'}^{R}$ of the matrix element $S_{0v'}^{R}$ as a function of energy in figure 8 (v' is the quantum number of the HF or DF molecule formed in the reaction). In this plot, and in most of those that follow, we will restrict our attention to energies no more than 50 meV above the zero-point energy of the hydrogenic molecule. This energy is sufficiently large that the resonance can be considered to be entirely contained within it. The phase of an $\underline{\underline{S}}$ matrix element is only determined to within an additive constant of 2π, and hence integer multiples of 2π can be added to or subtracted from a given $\Phi_{0v'}^{R}$ to insure continuity of the phase vs. energy curve. The zero of phase in each of these plots is arbitrary, chosen only for simplicity of plotting.

The phase vs. energy curves show quite clearly the effect of the resonance in more than one product state. In fact, the similarity between these curves for a given system for all but the highest product state is quite remarkable, especially when one considers that the probabilities of populating the various product states may differ by a substantial factor. The highest product state, DF(v = 4), shown for the F + D_2 and F + DH systems, has an appreciably different phase vs. energy curve than that for the other product states. Similar behavior was seen in the probability vs. energy curves (figure 3).

As discussed in the previous paper, a simple estimate of the lifetime of the long-lived metastable state which must be associated with the resonance is the delay time

$$\tau_{0v'}^{R} = h(d\Phi_{0v'}^{R}/dE) \tag{4}$$

In the single channel case, the delay time of a particle due to the existence of a potential is given by a similar expression with the phase shift replacing the phase of the $\underline{\underline{S}}$ matrix element. Because of the similarity of the phase vs. energy curves shown in figure 8, it is expected that each of the appropriate delay times for a given system should be essentially the same. We plot these delay times in figure 9 only for those transitions having the largest probability at the resonance. We do also plot the delay time τ_{04}^{R} for the F + DH system to show how the delay times will differ when the dynamics are affected (τ_{03}^{R}) and

and unaffected (τ_{04}^{R}) by the resonance.

Two features are evident in these plots. First, all delay times shown, except τ_{04}^{R} for the F + DH system, have maxima. The maximum is largest and narrowest for F + HD, and is smallest and broadest for F + DH. The delay time becomes positive only for F + HD and F + H_2. Since it is just proportional to the energy derivative of the phase of the corresponding $\underline{\underline{S}}$ matrix element, it is clear that it can be positive only when the phase vs. energy curve has a positive slope, as was seen only in the F + HD and F + H_2 systems in figure 8. Second, at energies sufficiently past the resonance (measured by the maximum in the delay time vs. energy curve), the delay time is essentially independent of energy. This suggests that an improved value for the delay time, $\overline{\tau}_{0v'}^{R}$, may be calculated by subtracting its value at the right hand (asymptotic) end of the plot ($\tau_{0v'}^{as}$) from its maximum value ($\tau_{0v'}^{max}$)

$$\overline{\tau}_{0v'}^{R} = \tau_{0v'}^{max} - \tau_{0v'}^{as} \tag{5}$$

Results of this subtraction are given in Table 1. The improved delay times $\overline{\tau}_{0v'}^{R}$ are seen to decrease in the order FHD $\gg$ FH_2 $>$ FD_2 $>$ FDH, with an overall range of a factor of 100. This does provide a reasonable estimate for the lifetime of the metastable state associated with the resonance. We will consider the question of the lifetime again when we examine the eigenvalues of the collision lifetime matrix.

We next examine the eigenphase shifts as a function of energy, and these are plotted in figure 10. Away from resonances, the eigenphase shifts should decrease monotonically with increasing energy; near a resonance, they may either increase with energy or just decrease with energy less rapidly than would otherwise be expected. As the eigenphase shifts are determined to within an additive value of π, integer multiples of π may be added to or subtracted from the eigenphase shifts to generate smooth eigenphase shift vs. energy curves. The eigenphase shift origins (each has its own) were chosen both to most clearly display the largest possible number of avoided crossings and for convenience in plotting.

The resonance is seen to be reflected in the eigenphase shifts for all systems. For FHD, FH_2, and FD_2, regions in which the eigenphase shifts increase with energy are seen. These regions are not limited to a single eigenvalue as determined by the method outlined in section 2. Two other features of these figures merit attention. First, at low energies one or more of the eigenphase shifts vary unusually rapidly with energy. From consideration of the eigenvectors, one can show that these are associated with the states whose energies are closest to the energy shown. Hence, one of these curves belongs to the hydrogenic molecule; when another such curve exists, as in FH_2 and FD_2, it is shown to belong to the highest energy HF or DF state. Second, the eigenphase shift vs. energy curves display a number of crossings and/or avoided crossings. The difficulty sometimes involved in determining whether there is a real or an avoided crossing has been discussed earlier. An important fact is that these avoided crossings can occur at fairly large energies, where the resonance is essentially over. Thus, the avoided crossings need not be a manifestation of the resonance.

We next turn our attention to various properties (diagonal elements, eigenvalues, and eigenvectors) of the collision lifetime matrix $\underline{\underline{Q}}$. In figure 11, we plot the diagonal elements Q_{jj} as a function of energy. These may be thought of as being the average delay time in a collision described by the wave function of the state associated with the j^{th} column of the $\underline{\underline{S}}$ matrix. When Q_{jj} is positive and sufficiently large that the inequality

$$2E_jQ_{jj}/\hbar \gg 1 \tag{6}$$

is satisfied, where E_j is the initial relative translational energy in the j^{th} channel, the scattering process may be thought of as being resonant.

In all but the FDH system, at least one Q_{jj} becomes positive (three become positive for the FHD case). In the FDH case one of the Q_{jj} gets very close to zero, and the fact that its value at the high energy end of the graph is substantially smaller than zero suggests that some subtraction such as that performed in eq. 5 could be performed here to define an improved Q_{jj}. We will defer such a subtraction till later, when we consider the eigenvalues q_n of $\underline{\underline{Q}}$. In Table 2, we list the largest value of Q_{jj}, called Q_{jj}^{max}, obtained for each system and its associated energy in order to calculate the left hand side of the inequality in (6). From the data in table 2, it is clear that the inequality in eq. 6 is satisfied for the FHD, FH_2, and FD_2 collisions. For the FDH system, the inequality obviously cannot be satisfied because Q_{jj}^{max} is negative; nevertheless, the closeness of the left hand side of the inequality in 6 to zero suggests that although a resonant picture of the scattering is not entirely appropriate, it may not be overly inappropriate, either. Hence, in our analysis of the eigenvalues and eigenvectors of $\underline{\underline{Q}}$, we will examine all four isotopic systems.

We next examine the eigenvalues q_n of $\underline{\underline{Q}}$, plotting them as a function of energy. For all four systems, one and only one eigenvalue is seen to become positive. The maximum value this eigenvalue q_π takes is seen to be substantially greater than the Q_{jj}^{max} indicated in table 2 for the FHD, FD_2, and FDH systems. For the FH_2 system, the values are fairly close. As in the case of the delay times $\tau_{0v'}^{R}$, at energies sufficiently larger than that of the center of the resonance (again measured by the position of the peak in the eigenvalue vs. energy curve), the eigenvalue q_π is nearly independent of energy (π will be used to indicate only the eigenvalue containing the resonance). Thus, we define the lifetime t_π by the expression

$$t_\pi(E) = q_\pi(E) - q_\pi^{as} \tag{7}$$

where q_π^{as} is the asymptotic value of q_π. This lifetime is indicated in the right hand ordinates of figure 12. The maximum value of $t_{\pi}(E)$ is called t^{res}. In the ensuing discussion, we will tabulate the lifetimes and the resonance positions and widths, as well as comment on the relationship between the eigenvalues q_n and the diagonal elements Q_{jj}.

Finally, we consider the orthonormal eigenvectors $\underline{U}_n$ of $\underline{\underline{Q}}$. They are complex, but we will only be concerned with the square of the absolute values of their components $|U_{in}|^2$. These absolute values will be referred to as the "fractional compositions" of the eigenvectors. We will represent these eigenvectors by plotting as a function of energy the coefficients $|U_{in}|^2$ associated with the n^{th} eigenvector and the molecular state i. In Table 3 we give the correspondence between the values of i and the molecular states for each of the four systems considered. We will restrict our attention primarily to the eigenvectors associated with the eigenvalue q_{π} which contains the resonance. Other eigenvectors will be examined when deemed appropriate.

The first of these is for q_{π} in the FHD system, which is shown in figure 13. This is a particularly complicated plot. Two points are worth mentioning. First, away from the resonance, the eigenvector is composed almost entirely of component 4, while at the center of the resonance it is composed of almost equal parts of component 1, with much smaller contributions from components 2 and 3. Second, at energies slightly above and below that at the center of the resonance, appreciable amounts of components 2 and 3 mix in to the eigenvector. Since the eigenvectors are normalized

$$\sum_{i=1}^{N} |U_{in}|^2 = 1 \tag{8}$$

the increase in the amount of components 2 and 3 is compensated for by a reduction in the amount of components 1 and 4. We will discuss the origin of this complicated behavior in the ensuing discussion section.

In figure 14 we plot two eigenvectors of $\underline{\underline{Q}}$ for the FH_2 system.

The first of these (upper panel), eigenvector 4, corresponds to the eigenvalue $q_{\overline{\pi}}$ containing the resonance. Near the resonance, the fractional compositions change only slightly with energy, as a small amount of component 1 mixes in to the eigenvector, which at lower energies was predominantly made up of component 4. At energies substantially past the resonance (more than 0.01 ev), there is a brief (~0.03 eV) energy region in which a large amount of component 3 mixes in to the eigenvector. No such complicated structure is observed in figure 14b, in which we plot the fractional components of the eigenvector which is made up principally of component 1. It is seen that near the resonance, a small contribution from component 1 is seen, and that at higher energies, the fractional compositions are essentially independent of energy. Of particular interest is the fact that there is no contribution from component 3, which couples strongly in to the eigenvector displayed in the upper panel of figure 14. We will comment on the significance of this later.

Fractional compositions of the eigenvector belonging to the eigenvalue $q_{\overline{n}}$ containing the resonance in the FD_2 system are shown in figure 15. Contributions from three components : 1, 4, and 5 are observed. At energies below the resonance, components 4 and 5 make up essentially all the eigenvector, while component 1 only becomes appreciable near the resonance energy. The shift in the relative contributions of components 4 and 5 at low energies appears to be unrelated to the resonance. Since it is this shift, combined with the increasing growth of component 1, which gives rise to the maximum in the contribution of component 5 below the resonance, this maximum is not a sole consequence of the resonance.

In figure 16 we show fractional compositions of three eigenvectors of $\underline{\underline{Q}}$ in the FDH system. The first of these (top panel in figure 16) is for the eigenvalue $q_{\overline{\pi}}$ containing the resonance; the others are for the second lowest (center panel) and third lowest (bottom panel) curves for

FDH in figure 12 . The lowest curve is the one marked as being divided by two and which is composed almost entirely of component 6. The most important feature of these plots is the smooth behavior of the fractional components with energy. At energies near where the resonance is centered, no unusual or strong dependence on energy of the fractional compositions occurs. At the lowest energies considered, the relative contributions of components 4 and 5 do vary with energy, but as in the FD_2 case, that need not be related to the resonance . More likely associated with the resonance is the growth of the contribution from component 1 into the eigenvector in figure 16a, as in other systems, the eigenvector belonging to the eigenvalue containing the resonance always mixes in some component 1 near the resonance.

Because of inaccuracies in the scattering calculations and the approximation of the energy derivative of $\underline{\underline{S}}$, the fractional compositions of the eigenvectors of $\underline{\underline{Q}}$ occasionally scatter somewhat; the curves drawn then represent a reasonable fit to the compositions determined.

IV. DISCUSSION

In this section we will do three things. First, we will discuss the differences between the resonance in each of the isotopic systems as seen from the results presented earlier, particularly the eigenvalues and eigenvectors of $\underline{\underline{Q}}$. Second, we will review the information obtained from the various characterization techniques and attempt to draw conclusions about their utility. Third, we will compare the way in which the first two resonances in the H + H_2 system on the Porter-Karplus surface (described in detail in the previous paper) and the resonances in the F + HD, H_2, D_2, and DH systems examined here manifest themselves in the different characterization techniques used.

A. COMPARISON OF THE RESONANCES IN THE ISOTOPIC SYSTEMS

From the different characterization techniques used, it is quite clear that the strength of the resonance decreases in the order FHD $\gg$ FH_2 $>$ FD_2 $>$ FDH. The best measure of the strength of the resonance appears to be the lifetime defined in eq. 7. Since this lifetime is obtained from the eigenvalues of the collision lifetime matrix $\underline{\underline{Q}}$, the importance of that quantity in allowing one to obtain a good description of the resonance is seen. In Table 4 we list a number of useful quantities about the resonance in the different systems, including the resonance position as determined from the maximum in the plot of the eigenvalues q_n vs. the energy, the lifetime t^{res}, the width (FWHM) of the peak in the plot of q_π vs. energy, and the maximum in the plot of the state-to-state reaction probability vs. energy (for the highest product state participating in the resonance: v = 2 for HF products, v = 3 for DF products).

There are a number of interesting points to be made about the data in table 4. First, the lifetimes t^{res} can vary substantially; that for FHD is some 75 times greater than that for FDH. This provides an estimate of the useful dynamic range of this quantity as an indicator of resonances. Assuming that the resonance in FHD is about as strong a resonance as one is likely to see, one could reasonably expect to be able to see resonances whose strengths differ by more than a factor of 100, as the FDH resonance does not appear to be at the lower limit of detection of the method. For analysis of weak resonances, however, caution must be used, lest small numerical inaccuracies in either the scattering calculations or the approximation of the derivatives dS_{ij}/dE produce noise which could obscure the small maximum.

Second, the positions of the maxima in the plots of q_n vs. E in figure 12 are not the same as those of the maxima in the plots of reaction probability as a function of the energy in figure 3. To make this point more clearly, in figure 17 we replot the state-to-state reaction probabilities into v = 2 for HF product and v = 3 for DF product in a manner similar to that in which the eigenvalues q_n were plotted in figure 12. The arrows in figure 17 point to the energy at which the resonance eigenvalue q_π has its maximum in figure 12. It is clear that as one moves in the direction of decreasing resonance strength, the energy difference between these two maxima increases. In table 4 we compare this energy difference to the resonance width. Both quantities increase as the resonance strength decreases, but the energy separation between the maxima increases more rapidly, so their ratio, listed in the last column of table 4, increases substantially as the resonance strength decreases. The value of this ratio for FDH should be examined noting that the position of the maximum in the probability plot for this system is probably determined not by the resonance but by a direct process occurring at higher energies than seen in figure 17 (a feeling for the dynamics at higher energies may be obtained from the probability vs. energy plot in figure 3).

We would next like to consider the structure of the plots of the eigenvalues q_n as a function of energy in figure 12. In particular, we are interested in the strong similarity between the figures for each of the systems. This similarity is seen in various ways : only one eigenvalue q_π becomes positive, there are always one (in FHD) or two (in

FH_2, FD_2, and FDH) eigenvalues which are substantially smaller than the others at low energies, but which increase rapidly with energy, and there are always two or more eigenvalues which are essentially independent of energy. Before considering this similarity, it is worthwhile to reexamine the plots of the diagonal elements Q_{jj} as a function of energy, as these allow us to clearly assign molecular states to each. In addition, any differences between the diagonal element Q_{jj} and the eigenvalues q_n must be due to the diagonalization and can thus be thought of as the effect of taking the right linear combination of molecular states to get a resonance eigenstate.

The greatest difference between diagonal elements Q_{jj} and eigenvalues q_n occurs for FHD. In figure 11, we see that two diagonal elements, Q_{11} and Q_{44}, become large and positive at the resonance, while a third, Q_{33}, becomes positive but stays quite small. Q_{22} is more or less independent of energy; it appears to have a small increase at the resonance energy, but the change is probably within the numerical noise associated with all the calculations performed. The differences between this plot and that of the eigenvalues q_n for this system suggest that the eigenvector associated with the resonance should contain substantial amounts of components 1 and 4 and a smaller amount of component 3, which is indeed what was seen in figure 13. We will return to a discussion of the origin of the large contributions from components 2 and 3 at energies above and below the resonance shortly.

The differences between the diagonal elements Q_{jj} and eigenvalues q_n are much smaller for FH_2. The major difference is the existence of a shoulder in the Q_{11} curve near 0.283 eV, while the similar curve in figure 12 for the eigenvalues increases monotonically. This, coupled with the energy independence of Q_{22} and Q_{33} and the monotonic increase of Q_{55} (and the fact that its value is substantially smaller than that of the other diagonal elements), suggests that at the resonance, components 1 and 4 should mix together. Again, this is precisely what was seen in figure 14. We will comment on the large contribution of component 3 to the resonance eigenvector shortly.

The FD_2 curves differ in a manner similar to that of the FH_2 curves. One additional difference is that Q_{44} has a small (~0.01 psec) local maximum which is absent in the eigenvalue plot. We would expect the resonance eigenvector to mix in some of component 1 and a smaller amount of component 4 at the resonance. From figure 15 we see that there is a small contribution of component 1 to the resonance eigenvector, but that component 4 has mixed in substantially to the eigenvector at energies below the resonance. The most reasonable explanation for this mixing is a large inelastic transition probability at low energies between the states DF(v = 2) and DF(v = 3), which correspond to components 4 and 5, respectively. This is indeed the case, as may be seen from figure 18, in which we plot the transition probability P_{32}^{V} of the process

$$D + DF(v = 3) \longrightarrow D + DF(v = 2) \tag{8}$$

as a function of energy in the energy region considered here. The fact that the inelastic probability P_{32}^{V} is more than a factor of ten greater than that of any other inelastic transition probability (multi-quantum probabilities are substantially smaller than the single quantum ones) suggests that away from the resonance no appreciable coupling between components 2, 3, and 6, which correspond to the molecular states DF(v = 0, 1, and 4) respectively, should be observed in the eigenvectors of $\underline{\underline{Q}}$, which is what is observed.

The FDH curves also differ from each other similarly to those of the FD_2 system, although the maxima in Q_{11} and Q_{44} become more pronounced than they do for FD_2. The appearance of the curves for Q_{11}, Q_{44}, and Q_{55} and the existence of only one large peak in the plots of the eigenvalues q_n suggest that the eigenvectors of $\underline{\underline{Q}}$ containing components 1, 4, and 5 should be strongly mixed (this is observed - see figure 16), while those containing components 2, 3, and 6 should consist predominantly of one component. Examination of the eigenvectors confirms this hypothesis. As in the FD_2 case, the mixing of components 4 and 5 in the eigenvectors of $\underline{\underline{Q}}$ shown can be thought of as being a consequence of the large and rapidly varying P_{32}^V in this energy region (0.211 at E = 0.2334 eV, 0.0003 at E = 0.2476 eV, and 0.303 at E = 0.2666 eV). P_{21}^V is also fairly large (~0.10), but changes only by a small amount in the energy range considered (0.106 at E = 0.2334 eV and 0.074 at E = 0.2829 eV). P_{10}^V is small (less than 0.001) in this energy range, while P_{43} becomes moderately large (~0.06).

We will now consider the origin of the rapid and somewhat irregular variation of the resonance eigenvectors in FHD and FH_2 seen in figures 13 and 14. The first thing to notice about this variation is that it occurs away from the center of the resonance. In FHD it occurs at 2 meV both above and below the center of the resonance, while in FH_2 it occurs some 12 meV above the center of the resonance. This variation can be correlated with the crossing of the eigenvalue curves in figure 12, as both the eigenvector crossings and eigenvector variation occur at the same energy. It is a bit difficult to discern this for FHD from figure 12 because in the scale of the figure it is impossible to resolve the three nearly identical separate eigenvalue curves away from the resonance (recall that the horizontal line in figure 12 represents two eigenvalues). It is not immediately clear why in the FD_2 case, no rapid variation is seen from the crossings near 0.225 eV or why in the FH_2 case only growth of component 3 is seen. It may be that when the different states are not directly coupled by inelastic processes, no incorporation of the component whose eigenvalue (or more precisely, its diagonal element) is being crossed takes place.

As mentioned in section 2, to obtain an adequate description of the eigenvectors of $\underline{\underline{Q}}$ (or of the $\underline{\underline{R}}$ matrix) near where the eigenvalues either cross or undergo an avoided crossing, one might need a substantially finer energy grid than one needs for an adequate description of the eigenvalues q_n. Since, in general, these regions of rapid variation usually occur away from the center of the resonance, they are not of fundamental importance. While further examination of these regions of rapid variation of the eigenfunctions of $\underline{\underline{Q}}$ might enable one to unambiguously assign eigenvectors to eigenvalues, it would appear to provide essentially no new information about the dynamics at the resonance.

B. COMPARISON OF DIFFERENT CHARACTERIZATION TECHNIQUES

The existence of a resonance in the low energy dynamics of these systems is seen in all of the characterization techniques employed. These techniques - plots of probabilities, scattering matrix element phases and their derivatives (delay times), eigenphase shifts, and eigenvalues of the collision lifetime matrix as a function of energy - all reflect the resonance in varying amounts. The quantities most sensitive to the resonance, the eigenvalues of the collision lifetime matrix, not only allow one to recognize weak resonances, but they localize the resonance almost completely into one channel, allowing for unambiguous determination of the resonance energy, width, strength (as measured by the lifetime t^{res}, which is a quantity of interest in its own right), and character (obtainable from the eigenvector $\underline{\underline{U}}_{\Pi}$ associated with the eigenvalue q_{Π} which contains the resonance).

In the cases of weak resonances, where indirect processes contribute substantially to the overall dynamics, the best characterization technique will be that which best subtracts the effects of the direct processes from the overall dynamics, leaving one only with the effects of the resonant processes. When these subtractions are successfully performed, the quantities of interest will either increase with energy (such as $\underline{\underline{S}}$ matrix element phases and eigenphase shifts) or become positive (such as delay times, diagonal elements and eigenvalues of $\underline{\underline{Q}}$). The success of the various characterization techniques is summarized in Table 5, in which we indicate whether a quantity does (represented ty the word "YES") or does not (represented by the word "NO") satisfy the above conditions. For the state-to-state quantities, the $\underline{\underline{S}}$ matrix element phases and the delay times, we consider only the transition to the highest participating state : v = 2 for HF formation, v = 3 for DF formation. Using the data in Table 5, we see that the sensitivity of the characterization techniques decreases in the order eigenvalues q_n > diagonal elements Q_{jj} > eigenphase shifts δ_n > delay times $\tau_{0v'}^{R}$ = $\underline{\underline{S}}$ matrix element phases $\phi_{0v'}^{R}$.

We would like to make comments concerning two of these characterization techniques. First, we do not recommend the use of the diagonal elements Q_{jj} for anything other than interpretive purposes. Once one has gone so far as to calculate $\underline{\underline{Q}}$, one may as well diagonalize it, and we have seen both here and in the previous paper that there may be appreciable differences between Q_{jj} and the eigenvalues q_n. We have shown here that consideration of the differences between plots of q_n and Q_{jj} as a function of energy can be a useful exercise. Second, we wish to point out that the eigenphase shifts, which are a reasonably sensitive detector of resonances (two eigenphase shifts for FD_2 do increase with energy near the resonance) are suggestive of some method by which different curves might be connected to give one "resonant eigenphase shift." This would involve taking some linear combination of the eigenvectors of $\underline{\underline{R}}$ and defining new pseudo-eigenvalues which cross from what is now one eigenphase shift curve to another, removing the avoided crossing in the process. If such a rearrangement were applied in the FHD case, the change in the eigenphase shift across the resonance would be roughly 2.8, which is fairly close to the maximum value of π which it might take.

C. COMPARISON WITH THE RESONANCES IN $H + H_2$

On the basis of our characterization of the resonances in the F +

HD, H_2, D_2, and DH systems and in the H + H_2 system in the previous paper (18), we can make some comments about the differences between these resonances. Differences between them are not unexpected, given the differences between the systems. F + H_2 and its isotopic counterparts are asymmetric systems (end atoms different), while H + H_2 is symmetric. This symmetry difference alone has important implications in that in H + H_2 the eigenvectors of the $\underline{\underline{R}}$ and the $\underline{\underline{Q}}$ matrices will be decomposed into symmetric and anti-symmetric sets. It is known that the resonance must be reflected in the symmetric eigenvectors.

A fundamental difference between the resonances may be seen solely by considering the reaction probabilities (figures 1 and 2 of the previous paper, figure 3 here). In H + H_2, at the resonance each of the state-to-state reaction probabilities is quite different. For example, at the second resonance P_{00}^R goes through a maximum, while P_{01}^R goes through a minimum. In the F + H_2 type collisions, the resonance is manifested similarly in nearly all reaction probabilities (except P_{03}^R in F + H_2 and P_{04}^R in F + D_2 and F + DH). These differences are manifested in the Argand diagrams also. Since each transition probability varies differently with energy near the resonance in the H + H_2 collision, the Argand diagrams must necessarily be different. Indeed, both loop and half-moon Argand diagrams may be seen at the two resonances. In the F + H_2 collisions, different Argand diagrams for transitions participating in the resonance appear quite similar (see figures 4 and 6).

The two collisions differ substantially in the appearance of their respective curves of the diagonal elements Q_{jj} as a function of energy. For H + H_2, two curves have substantial maxima at the resonance energy; at the second resonance, both Q_{11} and Q_{22} become positive. This is the only case observed so far in which more than one diagonal element of $\underline{\underline{Q}}$ becomes positive. The curves of the eigenvalues q_n vs. E are more similar, as there is only one eigenvalue which becomes positive in all cases. Also, there are two eigenvalues q_n which are much smaller than the others in all cases except for F + HD. In H + H_2 these are the symmetric and anti-symmetric linear combinations of the newly opened state, while in the F + H_2 type collisions they are the hydrogenic ground state and the highest state of HF or DF. The reason why only one such eigenvalue is seen in the FHD curve at low energies is that HF(v = 3) opens up at a slightly higher energy (0.2863 eV) than considered in figure 12.

The differences between the Q_{jj} plots and the similarity between the q_n plots for the H + H_2 and F + H_2 type collisions imply that the eigenvectors of $\underline{\underline{Q}}$, especially those associated with the resonance, must be different for the two types of collisions. This is particularly true for eigenvector 1^+ in the second resonance for the H + H_2 collision, in which there are nearly equal contributions from components 1 and 2 near the resonance. This is the only case in which a resonance eigenvector contains nearly equivalent amounts of two components all through the resonance.

Given the substantial differences between the H + H_2 and F + H_2 type systems, none of the sorts of differences observed in Argand diagrams, eigenphase shifts, and diagonal elements Q_{jj} and eigenvalues q_n is surprising. In fact, the collision lifetime matrix analysis suggests substantial differences between the first two resonances for H + H_2. A valuable point is to be learned from this however: resonances arising from seemingly different physical processes may be manifested in substantially different ways when viewed by an appropriate characterization technique, such as the variation of the eigenvalues and eigenvectors of $\underline{Q}$ with energy. Thus, it may prove possible later to establish a correlation between the characterization of resonances and their underlying dynamical features such that one might discern the latter from the former. Such a method would be complementary to the approach adopted by Babamov and Kuppermann (11) and Hayes and Walker (12) for $F + H_2$ type collisions and by Babamov and Marcus (23) for light atom transfer reactions. In this work, they are able to simply describe the resonance by viewing the dynamics in the right coordinate system wherein a simple property such as a one-dimensional eigenvalue or phase shift can provide the necessary information about the resonance.

V. CONCLUSIONS

We have performed detailed coupled-channel quantum mechanical reactive scattering calculations on the collinear F + HD, H_2, D_2, and DH reactions, and have characterized the low energy resonances by study of the variation of reaction probabilities, $\underline{\underline{S}}$ matrix element phases, delay times, eigenphase shifts, and diagonal elements, eigenvalues, and eigenvectors of the collision lifetime matrix. The resonance is seen to decrease in strength in the order FHD $\gg$ FH_2 $>$ FD_2 $>$ FDH. Using the most sensitive characterization technique, the variation of the eigenvalues of the collision lifetime matrix with energy, we have shown that the resonance energy is not the same as the energy at which the related probability vs. energy curves have their maxima. The difference between these energies increases as the resonance weakens, and this increase is more rapid than the increase in the width of the resonance as it weakens.

By considering the variation with energy of the eigenvector of $\underline{\underline{Q}}$ containing the resonance, we have shown that the wave function best describing the long-lived state associated with the resonance consists mainly of the highest participating HF or DF state, with a smaller contribution from the hydrogenic molecule. Lower energy DF states contribute in the F + D_2 and F + DH systems. The FHD system is the only one in which the eigenvector varies rapidly with energy through the resonances; in the other systems the change is more gradual. In two systems (F + HD, F + H_2) instances in which the fractional compositions of the eigenvector of $\underline{\underline{Q}}$ containing the resonance vary rapidly and irregularly with energy away from the resonance were observed. This variation is believed to occur when two eigenvalues of $\underline{\underline{Q}}$ become nearly degenerate and the eigenvalue vs. energy curves cross. We argue that such crossings have little dynamical significance.

The most sensitive quantities for use in detecting resonances are the eigenvalues q_n. The fact that only one eigenvalue q_n becomes positive means that this method localizes the resonance in a single channel. The importance of looking at the eigenvalue q_n rather than the diagonal elements Q_{jj} may be seen by considering the case of the F + DH collision, in which no Q_{jj} is positive, but one eigenvalue q_n is positive. The variation of the eigenphase shifts with energy is a useful quantity, as evidenced by its ability to clearly show the resonance in the F + D_2 system. This technique has the disadvantage of not localizing the resonance into a single channel, unlike the examination of the eigenvalues q_n. The delay time provides a useful feel for the lifetime of the resonance, and has the advantage of requiring the use of only a single scattering matrix element, rather than the whole matrix, as is needed for the evaluation of the collision lifetime matrix.

The resonance in the F + H_2 type systems is quite different from either of the first two resonances in the H + H_2 system. These differences are reflected in the various characterization techniques employed, and suggest that it might be possible to develop a method by which one could obtain information about the underlying dynamical features responsible for the resonance from the results of the characterization techniques used. We offer no suggestions as to what such a method might be.

ACKNOWLEDGMENTS

The calculations reported here were performed on the Dreyfus-NSF Theoretical Chemistry Computer (VAX 11/780) at Caltech which was funded through grants from the Camille and Henry Dreyfus Foundation, the National Science Foundation (Grant No. CHE78-20235), and the Sloan Fund of the California Institute of Technology, and on the IBM 370/158 computer of Ambassador College, Pasadena, California, for which we express our appreciation. We thank Dr. Vasil K. Babamov for many interesting discussions.

REFERENCES

1. J. B. Anderson, Adv. Chem. Phys. 41, 229 (1980) and references therein.
2. J. C. Polanyi and K. B. Woodall, J. Chem. Phys. 57, 1574 (1972) J. C. Polanyi and J. L. Schreiber, Faraday Disc. Chem. Soc. 62, 267 (1977); R. F. Heidner III, J. F. Bott, C. E. Gardner, and J. E. Melzer, J. Chem. Phys. 70, 4509 (1979); 72, 4815 (1980); E. Wurzberg and P. L. Houston, J. Chem. Phys. 72, 4811 (1980); S. Bittenson, D. C. Tardy, and J. Wanna, Chem. Phys. 58, 313 (1981).
3. (a) J. T. Muckerman, J. Chem. Phys. 54, 1155 (1971); 56, 2997 (1972); (b) N. C. Blais and D. G. Truhlar, J. Chem. Phys. 58, 1090 (1973); (c) P. A. Whitlock and J. T. Muckerman, J. Chem. Phys. 61, 4618 (1974); (d) J. T. Muckerman, in: Theoretical Chemistry: Advances and Perspectives, Vol. 6A, ed. D. Henderson (Academic Press, New York, 1981), pp. 1-77.
4. G. C. Schatz, J. M. Bowman, and A. Kuppermann, J. Chem. Phys. 58, 4023 (1973); 63, 674 (1975); 63, 685 (1975).
5. (a) J. N. L. Connor, W. Jakubetz, and J. Manz, Mol. Phys. 35, 1301 (1978); (b) S. L. Latham, J. F. McNutt, R. E. Wyatt, and M. J. Redmon, J. Chem. Phys. 69, 3746 (1978).
6. (a) M. J. Redmon and R. E. Wyatt, Chem. Phys. Lett. 63, 209 (1979); (b) J. F. McNutt and R. E. Wyatt, in: Potential Energy Surfaces and Dynamics Calculations, ed. D. G. Truhlar (Plenum Press, New York, 1981), pp. 495-517; (c) V. Khare, D. J. Kouri, J. Jellinek, and M. Baer, in: Potential Energy Surfaces and Dynamics Calculations, ed. D. G. Truhlar (Plenum Press, New York, 1981), pp. 475-493; (d) S. H. Suck, Chem. Phys. Lett. 77, 390 (1981).
7. E. Pollak and P. Pechukas, J. Chem. Phys. 69, 1218 (1978);

E. Pollak, J. Chem. Phys. 74, 5586 (1981); 75, 4435 (1981).

8. F. Rebentrost and W A. Lester, Jr. J. Chem. Phys. 67, 3367 (1977); A. Komornicki, K. Morokuma, and T. F. George, J. Chem. Phys. 67, 5012 (1977); F. Rebentrost, Chem. Phys. Lett. 58, 18 (1978); H.-D. Meyer and W. H. Miller, J. Chem. Phys. 71, 2156 (1979); I. H. Zimmerman, M. Baer, and T. F. George, J. Chem. Phys. 71, 4132 (1979); J. F. McNutt and R. E. Wyatt, Chem. Phys. 58, 423 (1981); D. E. Fitz and D. J. Kouri, J. Chem. Phys. 74, 3933 (1981).

9. H. F. Schaefer III, in: Atom-Molecule Collision Theory, ed. R. B. Bernstein (Plenum Press, New York, 1979), pp. 45-78 and references therein.

10. A. Kuppermann and J. A. Kaye, J. Phys. Chem. 85, 1969 (1981).

11. V. K. Babamov and A. Kuppermann, J. Chem. Phys., in press.

12. E. F. Hayes and R. B. Walker, J. Phys. Chem., in press.

13. R. K. Sparks, C. C. Hayden, K. Shobatake, D. N. Neumark, and Y. T. Lee, in: Horizons in Quantum Chemistry, ed. K. Fukui and B. Pullman (Reidel, Boston, 1980), pp. 91-105.

14. A. Kuppermann, in: Potential Energy Surfaces and Dynamics Calculations, ed. D. G. Truhlar (Plenum Press, New York, 1981), pp. 375-420.

15. F. T. Smith, Phys. Rev. 118, 349 (1960).

16. G. C. Schatz and A. Kuppermann, J. Chem. Phys. 59, 964 (1973).

17. G. C. Schatz, Ph.D. Thesis, California Institute of Technology, 1975.

18. J. A. Kaye and A. Kuppermann, manuscript in preparation.

19. R. N. Porter and M. Karplus, J. Chem. Phys. 40, 1105 (1964).

20. A. Kuppermann, in: Proceedings of the Conference on Potential Energy Surfaces in Chemistry, ed. W. A. Lester (U. California, Santa Cruz, 1970), pp. 121-134; in: Proceedings of the 7th

International Conference on the Physics of Electronic and Atomic Collisions (North-Holland, Amsterdam, 1971), pp. 3-5; in: Theoretical Chemistry: Advances and Perspectives, Vol. 6A, Ed. D. Henderson (Academic Press, New York, 1981), pp. 79-162.

21. P. J. Kuntz, E. M. Nemeth, J. C. Polanyi, S. D. Rosner, and C. E. Young, J. Chem. Phys. 44, 1168 (1966).

22. L. M. Delves, Nucl . Phys. 9, 391 (1959); 20, 275 (1960).

23. V. K. Babamov and R. A. Marcus, J. Chem. Phys. 74, 1790 (1981).

Table 1. Maximum, Asymptotic, and Improved Delay Times

System	Transition	$\tau_{0v'}^{\max}$ a)	$\tau_{0v'}^{as}$ b)	$\overline{\tau}_{0v'}^{R}$ c)
F + HD	$0 \longrightarrow 2$	2.23	-0.08	2.31
F + H_2	$0 \longrightarrow 2$	0.060	-0.060	0.120
F + D_2	$0 \longrightarrow 3$	-0.014	-0.077	0.063
F + DH	$0 \longrightarrow 3$	-0.018	-0.040	0.022

a) $\tau_{0v'}^{\max}$ is the maximum value of the delay time $\tau_{0v'}^{R}$ in psec

b) $\tau_{0v'}^{as}$ is the value of the delay time $\tau_{0v'}^{R}$ at an energy $E_0 = 50$ meV, and is in psec.

c) $\overline{\tau}_{0v'}^{R}$ is defined by eq. 5 in the text and is given in psec.

Table 2. Maximum diagonal elements Q_{jj} and related quantities.

System	j	Product State	Q_{jj}^{max}/psec	E_j^{max}/eV	L_j[a)]
FHD	4	HF(v=2)	2.34	0.4079	2894
FH_2	4	HF(v=2)	0.254	0.4432	342
FD_2	5	DF(v=3)	0.072	0.3590	78.6
FDH	5	DF(v=3)	-0.001	0.3965	-1.2

a) $L_j = 2E_j^{max} Q_{jj}^{max} / \hbar$

Table 3. Molecular State Labels

i	FHD	FH_2	FD_2	FDH
		System		
1	HD(v=0)	H_2(v=0)	D_2(v=0)	HD(v=0)
2	HF(v=0)	HF(v=0)	DF(v=0)	DF(v=0)
3	HF(v=1)	HF(v=1)	DF(v=1)	DF(v=1)
4	HF(v=2)	HF(v=2)	DF(v=2)	DF(v=2)
5	x a)	HF(v=3)	DF(v=3)	DF(v=3)
6	x a)	x a)	DF(v=4)	DF(v=4)

a) Energy of state is sufficiently high that it does not contribute to the dynamics at the energies of interest.

Table 4. Resonance Characteristics.

System	E_0/meV[a]	E^{P}_{max}/meV[b]	E^{res}/meV[c]	t^{res}/psec[d]	ΔE^{res}/meV[e]	$t^{res}\Delta E^{res}/2\hbar$	$(E^{P}-E^{res})/\Delta E^{res}$
FHD	232.9	244.94	244.92	4.8	0.52	1.82	0.04
FH_2	268.4	283.5	281.6	0.33	7.2	1.81	0.26
FD_2	190.6	220.0	214.6	0.15	11.4	1.30	0.47
FDH	232.9	280[f]	253.3	0.064	21.2	1.03	1.3

a) Zero-point energy of isolated hydrogenic molecule.

b) Total energy at which reaction probability of figure 17 has a maximum.

c) Total energy at which the resonance eigenvalue of figure 12 has a maximum.

d) Peak value of t(E) for resonance eigenchannel curves of figure 12.

e) Full-width at half-maximum (FWHM) of t(E) resonance eigenchannel curves of figure 12.

f) Observation of plots of the probability vs. energy curves over a wider range of energies than that used in figure 12 (see figure 3d) suggests that this maximum is probably related to a direct mechanism which occurs at higher energies than the resonance energy rather than to the resonance process of figure 12.

Table 5. Summary of Effectiveness of Characterization Techniques.

System	$\phi_{0v'}^{R}$ a)	$\tau_{0v'}^{R}$ b)	δ_j c)	Q_{jj} d)	q_n e)
FHD	YES	YES	YES	YES	YES
FH_2	YES	YES	YES	YES	YES
FD_2	NO	NO	YES	YES	YES
FDH	NO	NO	NO	NO	YES

a) phase of scattering matrix element; v' = 2 for HF formation, v' = 3 for DF formation.

b) delay time using above phase from previous column

c) eigenphase shift

d) diagonal element of $\underline{\underline{Q}}$

e) eigenvalue of $\underline{\underline{Q}}$

FIGURE CAPTIONS

Figure 1. Contour plot of the potential energy surfaces for the F + HD (a), F + H_2(b), F + D_2(c), and F + DH(d) reactions plotted in Delves mass-scaled coordinate system. Equipotentials are drawn every 0.3 eV. The zero of energy is at the bottom of the hydrogenic well. The saddle point is marked with an "x". The dashed line marks the minimum energy path.

Figure 2. Energy level diagram for the molecular states considered in this work. The zero of energy is at the bottom of the hydrogenic well. The energy levels are shown on either side of a plot of the potential energy V along the minimum energy path as a function of the reaction coordinate s (which has its zero at the saddle point and is measured along the minimum energy path) in the FH_2 system.

Figure 3. State-to-state reaction probabilities for various reactions as indicated. Numbers in parentheses preceded by a multiplication sign (x) indicate the values by which the reaction probabilities for that transition have been multiplied prior to plotting. Vertical arrows in the F + HD and F + H_2 plots mark the energies of the v = 3 state of HF. The lower abscissa shows the value of the translational energy E_0; the upper abscissa shows the value of the total energy E (sum of the translational energy and the zero-point energy of the hydrogenic molecule). a) F + HD; b) F + H_2; c) F + D_2; d) F + DH.

Figure 4. Argand diagrams for the matrix elements S_{02}^R (a) and S_{01}^R (b) for the collinear reaction F + HD $\longrightarrow$ FH + D with the total energy E as the indicated parameter. Arrows mark the sense of the curve.

Figure 5. Argand diagram for the matrix element S_{02}^R for the collinear reaction F + H_2 $\longrightarrow$ FH + H with the total energy E as the indicated parameter. Arrows indicate the direction of the curve with increasing energy.

Figure 6. Argand diagram for the matrix elements S_{03}^{R} (a) and S_{02}^{R} (b) for the collinear reaction $F + D_2 \longrightarrow FD + D$ with the total energy E as the indicated parameter. Arrows indicate the direction of the curve with increasing energy.

Figure 7. Argand diagram for the matrix elements S_{03}^{R} (a) and S_{04}^{R} (b) for the collinear reaction $F + DH \longrightarrow FD + H$ with the total energy E as the indicated parameter. Arrows indicate the direction of the curve with increasing energy.

Figure 8. Phases $\Phi_{0v'}^{R}$ of the scattering matrix elements $S_{0v'}^{R}$ for the collinear reactions $F + HD(v=0) \longrightarrow FH(v'=0, 1, 2) + D$, $F + H_2(v=0) \longrightarrow FH(v'=1, 2) + H$, $F + D_2(v=0) \longrightarrow FD(v'=2, 3, 4) + D$, and $F + DH(v=0) \longrightarrow FD(v'=2, 3, 4) + H$ as a function of the total energy E with respect to the bottom of the isolated hydrogenic molecule well (lower abscissa) and of the initial reagent relative translational energy E_0 (upper abscissa). Phases are determined only modulo 2π; the zero for each phase was chosen to give an ordinate for each plot reasonably symmetric about zero. Note that the upper abscissa is common to all panels in the figure.

Figure 9. Delay times $\tau_{0v'}^{R}$ for the collinear reactions $F + HD(v=0) \longrightarrow FH(v'=2) + D$, $F + H_2(v=0) \longrightarrow FH(v'=2) + H$, $F + D_2(v=0) \longrightarrow FD(v'=3) + D$, and $F + DH(v=0) \longrightarrow FD(v'=3, 4) + H$ as a function of the total energy E with respect to the bottom of the isolated hydrogenic molecule well (lower abscissas) and of the initial reagent relative translational energy E_0 (upper abscissas). Note that the upper abscissa is common to all panels. Because of small numerical inaccuracies in the scattering calculations, the actual values of the delay times are scattered a bit about the curve shown, which is a smooth curve drawn visually to reasonably well represent the data.

Figure 10. Eigenphase shifts for the collinear collisions F + HD(a), $F + H_2$(b), $F + D_2$(c), and F + DH(d) as a function of the total energy E

with respect to the bottom of the isolated hydrogenic molecule well. The arrow in figure b marks the energy of the v = 3 state of HF. The eigenphase shift represented by the short dashed line in figure b has been divided by five prior to plotting. Eigenphase shifts are determined only modulo π, and the zero for each one was chosen to give an ordinate for each plot reasonably symmetric about zero and to best show the avoided crossings. In figure d, the eigenphase shift curve represented by short dashes is drawn twice to point up all its avoided crossings.

Figure 11. Diagonal elements Q_{jj} of the collision lifetime matrix $\underline{\underline{Q}}$ for the collinear collisions F + HD, F + H_2, F + D_2, and F + DH as a function of the total energy E with respect to the bottom of the isolated hydrogenic moelcule well (lower abscissas) and of the initial reagent relative translational energy E_0 (upper abscissas), which is common to all panels. The numbers associated with each curve indicate the value of the index j for that curve.

Figure 12. Eigenvalues q_n of the collision lifetime matrix $\underline{\underline{Q}}$ for the collinear collisions F + HD, F + H_2, F + D_2, and F + DH as a function of the total energy E with respect to the bottom of the isolated hydrogenic molecule well (lower abscissas) and of the initial reagent relative translational energy E_0 (upper abscissas), which is common to all panels. The left ordinate scale in each panel refers to all the curves in that panel, whereas the right one refers only to the corresponding bell-shaped curve. The dashed portion of the lowest curve of the FHD panel indicates a region of numerical noise associated with the sharp peak of the top curve. The horizontal straight line of that panel represents the eigenvalue curves for two distinct eigenchannels. These curves coincide within the plotting accuracy of the figure, but are distinguishable on an expanded scale. The divisor in the three lower panels indicates the number by which the ordinate of the neighboring curve was divided before plotting. The numbers assigned to each curve

provide a label which will be used in figures 13-16, in which the corresponding eigenvectors are examined. The numbers used as labels were chosen to point up the similarities between these plots and those of the diagonal elements Q_{jj} in figure 11.

Figure 13. Fractional compositions $|U_{in}|^2$ of eigenvector 4 of the collision lifetime matrix $\underline{\underline{Q}}$ for the collinear collision F + HD as a function of the total energy E with respect to the bottom of the isolated hydrogenic molecule well (lower abscissa) and of the initial reagent relative translational energy E_0 (upper abscissa). The two digit numbers for each curve indicate the number of the component i (first digit) and the eigenvector n(second digit). The number of the eigenvector refers to the eigenvalue of the same number in the top panel of figure 12.

Figure 14. Fractional compositions $|U_{in}|^2$ of eigenvectors 4 (upper panel) and 1 (lower panel) of the collision lifetime matrix $\underline{\underline{Q}}$ for the collinear collision F + H_2. Energy scales and component labeling is as in figure 13.

Figure 15. Fractional compositions $|U_{in}|^2$ of eigenvector 5 of the collision lifetime matrix $\underline{\underline{Q}}$ for the collinear collision F + D_2. Energy scales and component labeling are as in figure 13.

Figure 16. Fractional compositions $|U_{in}|^2$ of eigenvectors 5 (top panel), 4 (center panel), and 1 (bottom panel) for the collinear collision F + DH. Energy scales and component labeling are as in figure 13.

Figure 17. Probabilities of the collinear reactions F + HD(v=0) ⟶ FH(v'=2) + D, F + H_2(v=0) ⟶ FH(v'=2) + H, F + D_2(v=0) ⟶ FD(v'=3) + D, and F + DH(v=0) ⟶ FD(v'=3) + H as a function of the total energy E with respect to the bottom of the isolated hydrogenic molecule well (lower abscissa) and of the initial reagent relative translational energy E_0 (upper abscissa), which is common to all panels. The vertical ar-

rows indicate the energies at which the resonance collision lifetime eigenvalues of figure 12 (4 for FHD and FH_2 systems, 5 for FD_2 and FDH systems) achieve a maximum.

Figure 18. Transition probabilities for the inelastic processes $D + DF(v) \longrightarrow D + DF(v-1)$ in the collinear collision of D with DF for $v = 1, 2, 3, 4$ as a function of the energy E with respect to the bottom of the isolated D_2 molecule well (lower abscissa) and of the initial reagent relative translational energy. Note that this translational energy scale is not the same as that used in previous figures. The numbers in parentheses are the values by which probabilities have been multiplied before plotting. For P_{32}^{V}, no multiplication factor is shown; these probabilities are plotted as calculated.

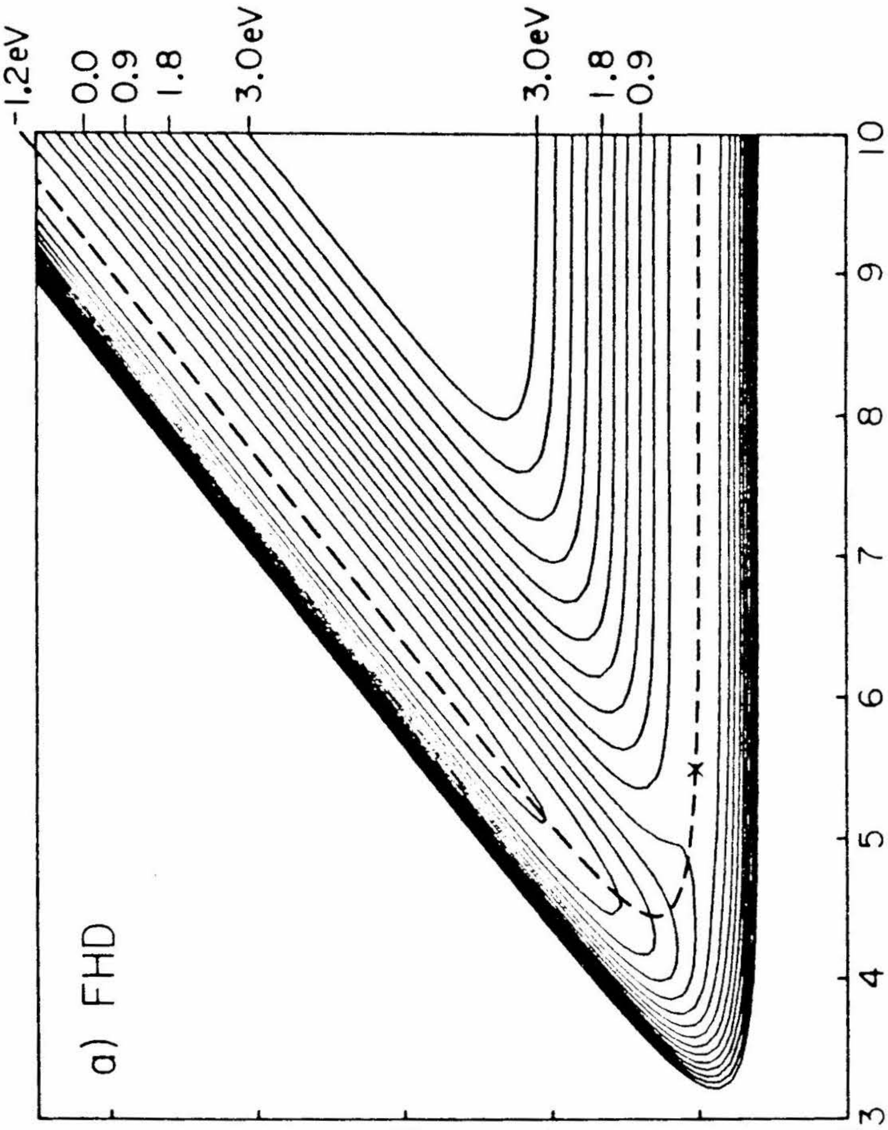
a) FHD
r/bohr
R/bohr
0
1
2
3
4
5
3
4
5
6
7
8
9
10
-1.2eV
0.0
0.9
1.8
3.0eV
3.0eV
1.8
0.9

Figure 1a

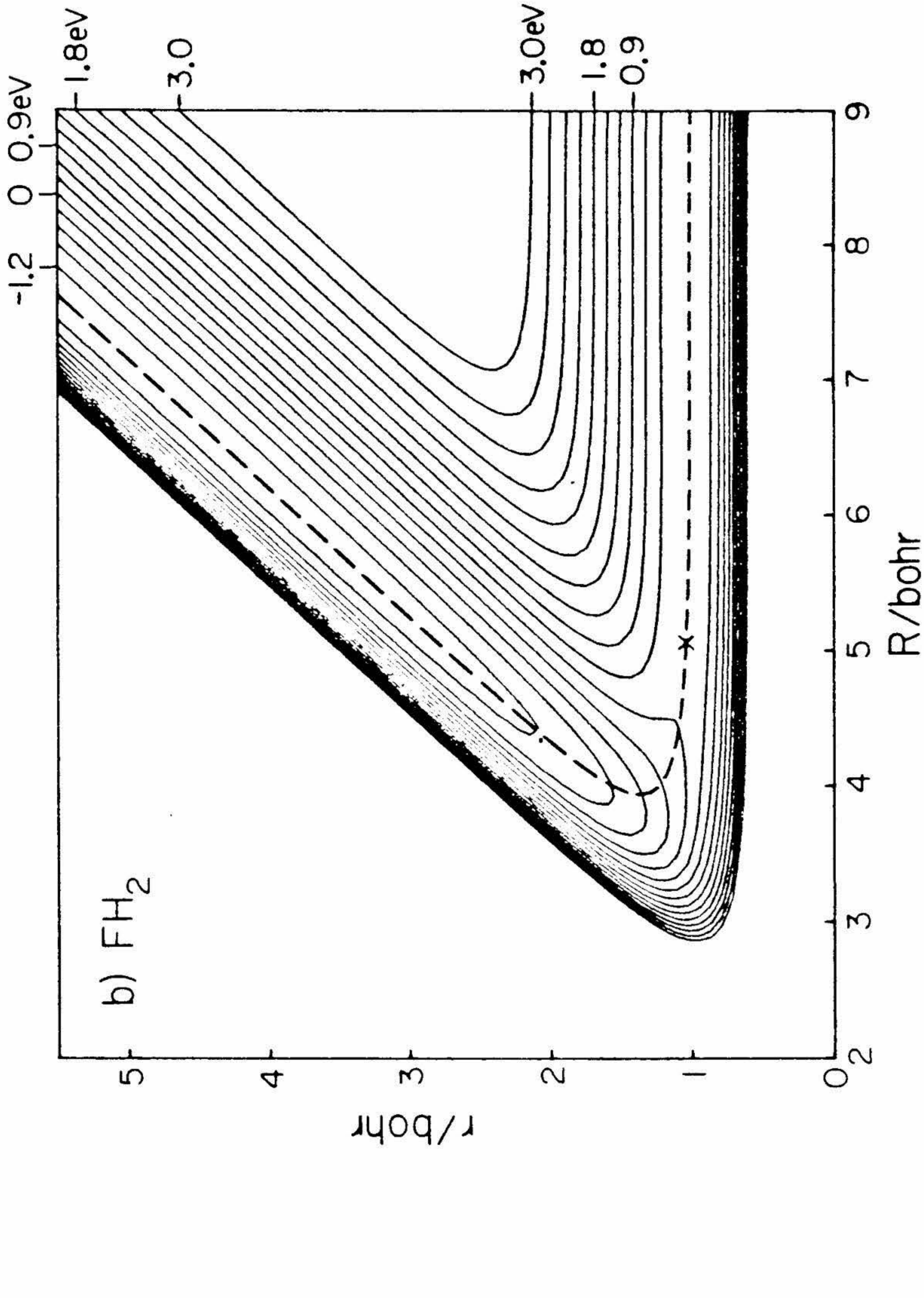

Figure 1b

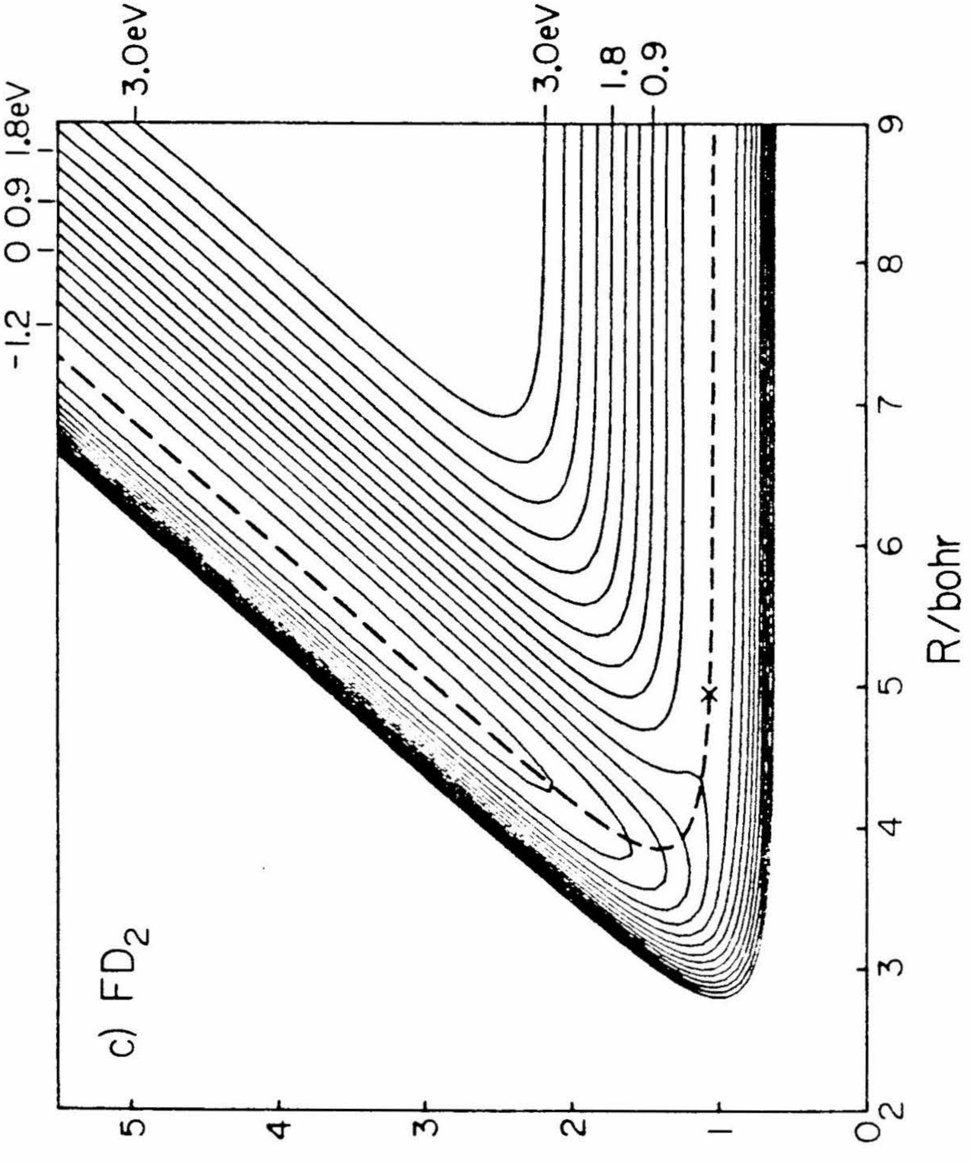

Figure 1c

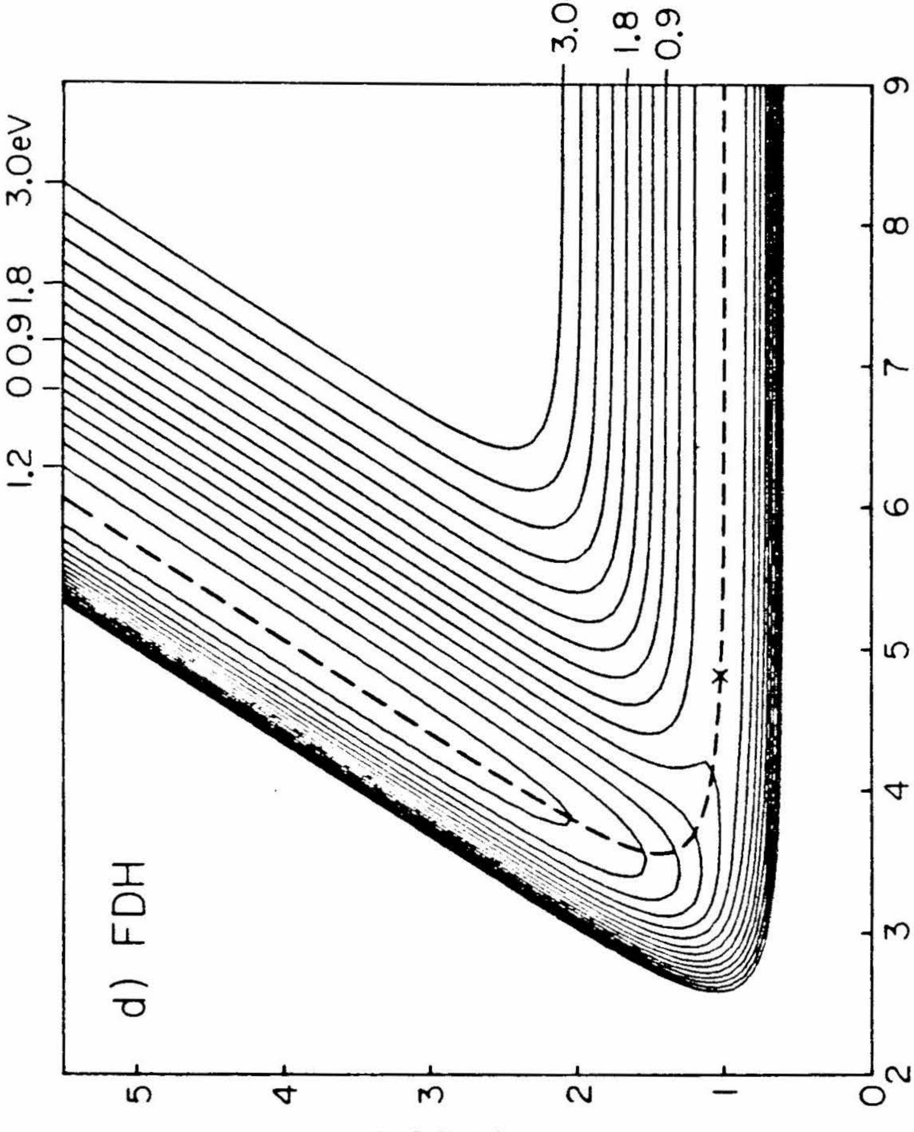

Figure 1d

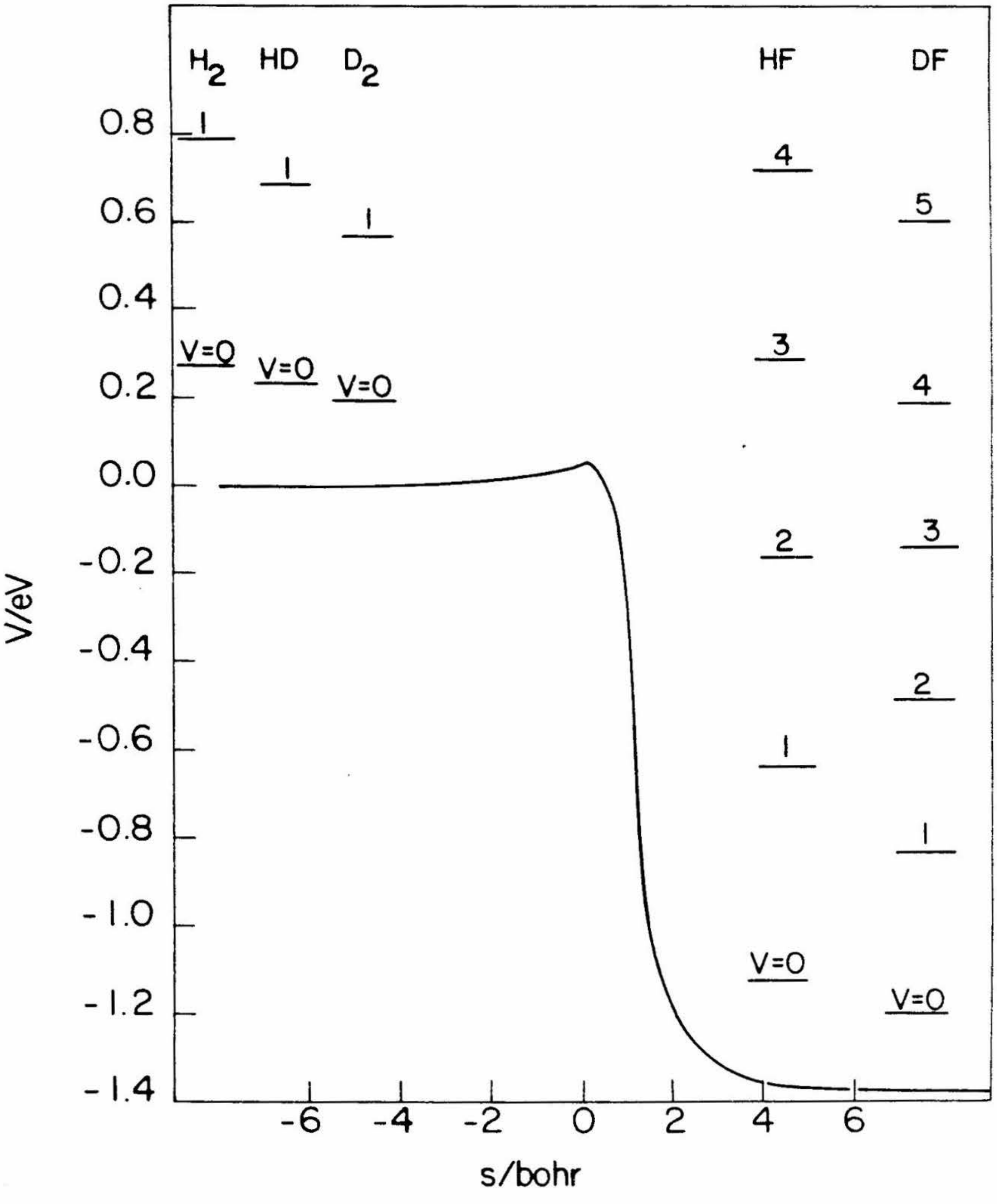
V/eV
0.8
0.6
0.4
0.2
0.0
-0.2
-0.4
-0.6
-0.8
-1.0
-1.2
-1.4
s/bohr
-6
-4
-2
0
2
4
6
H2
HD
D2
HF
DF
1
1
1
V=0
V=0
V=0
4
3
2
1
V=0
5
4
3
2
1
V=0

Figure 2

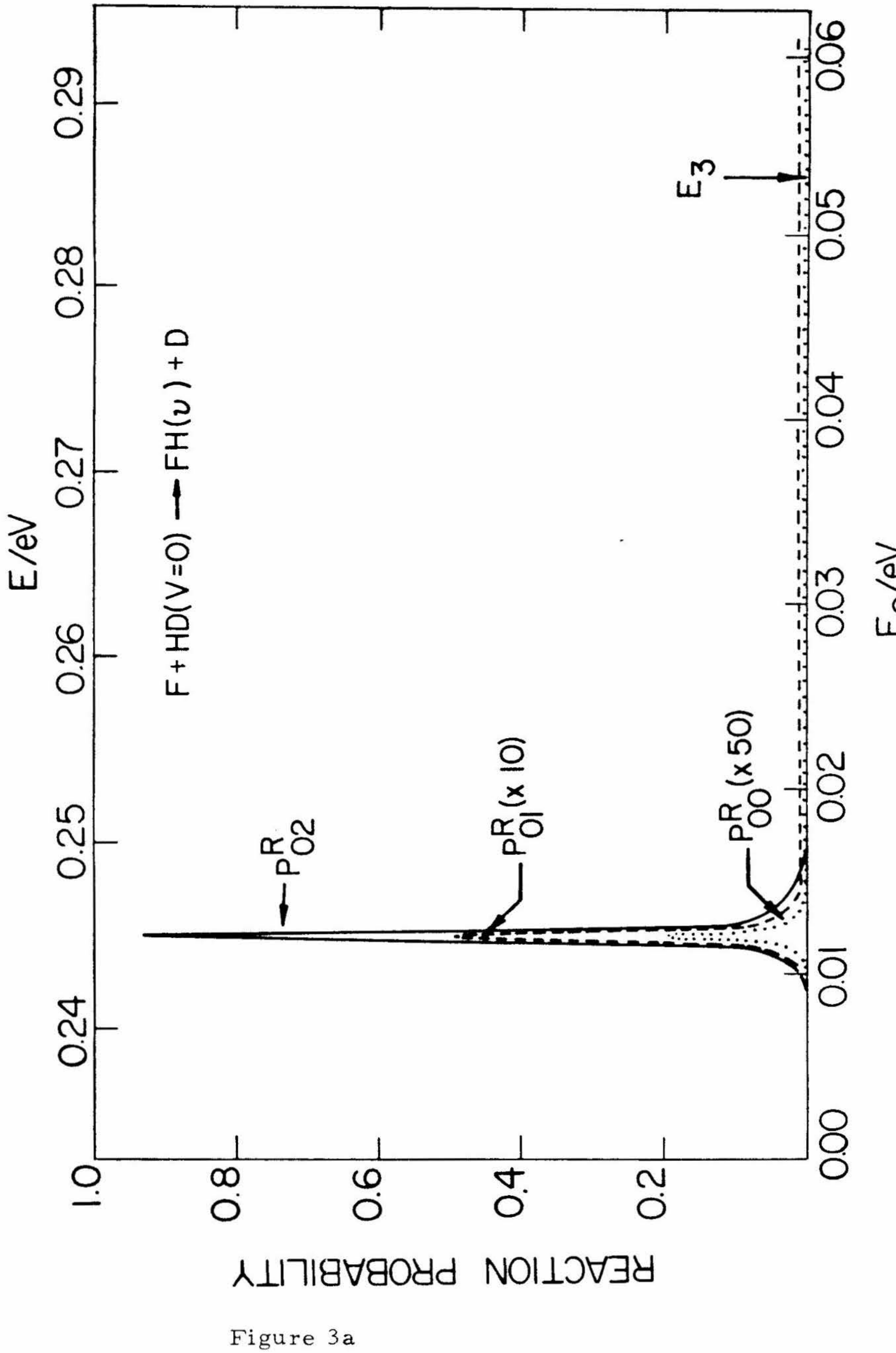
E/eV
0.24
0.25
0.26
0.27
0.28
0.29
F + HD(V=0) → FH(v) + D
P^R_{02}
P^R_{01} (x 10)
P^R_{00} (x 50)
E_3
REACTION PROBABILITY
1.0
0.8
0.6
0.4
0.2
0.00
0.01
0.02
0.03
0.04
0.05
0.06
E_0/eV

Figure 3a

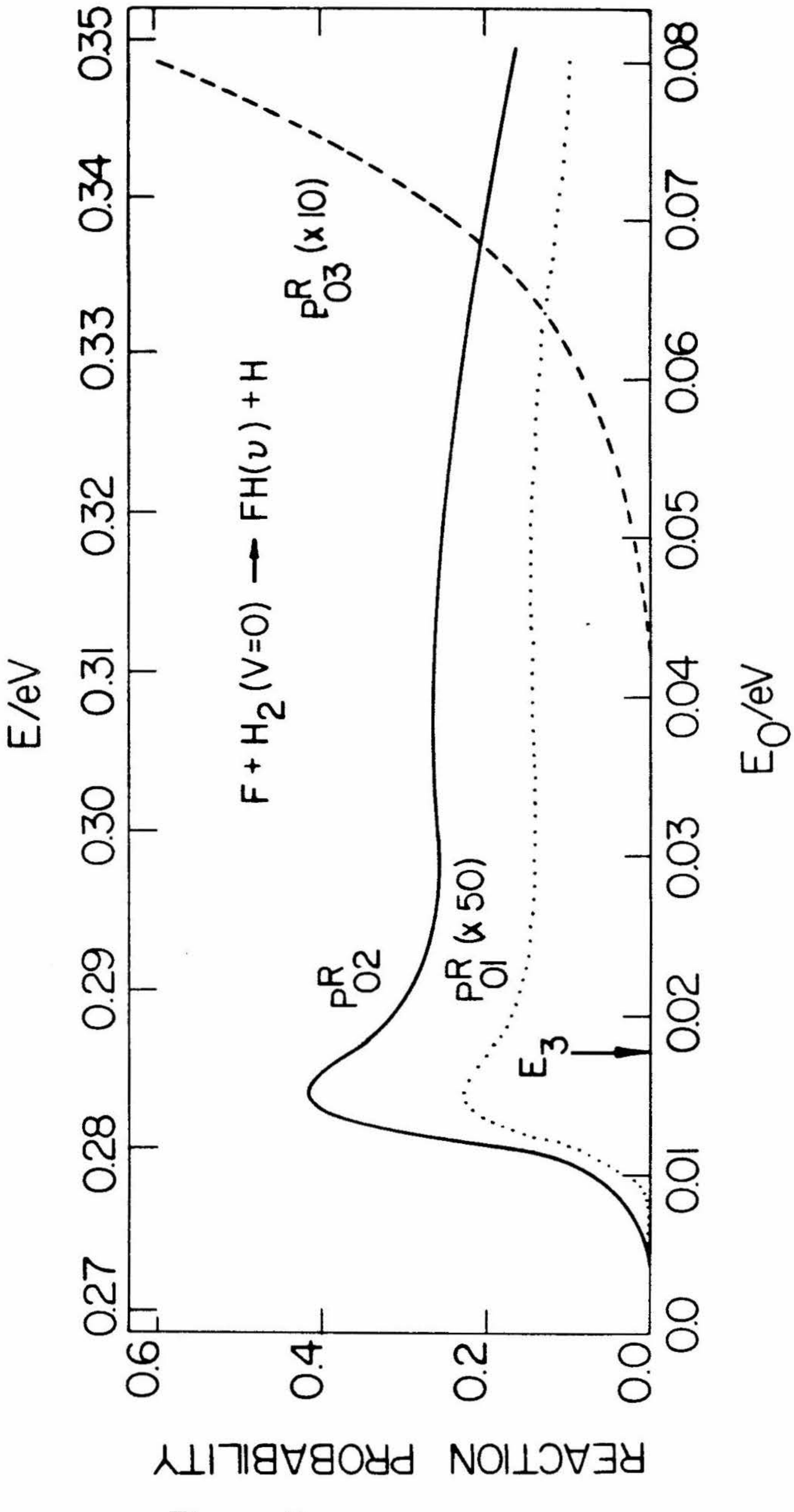
E/eV
0.27
0.28
0.29
0.30
0.31
0.32
0.33
0.34
0.35
E_0/eV
0.0
0.01
0.02
0.03
0.04
0.05
0.06
0.07
0.08
REACTION PROBABILITY
0.0
0.2
0.4
0.6
$F + H_2(V=0) \longrightarrow FH(\upsilon) + H$
P^R_{02}
P^R_{01} (x 50)
P^R_{03} (x 10)
E_3

Figure 3b

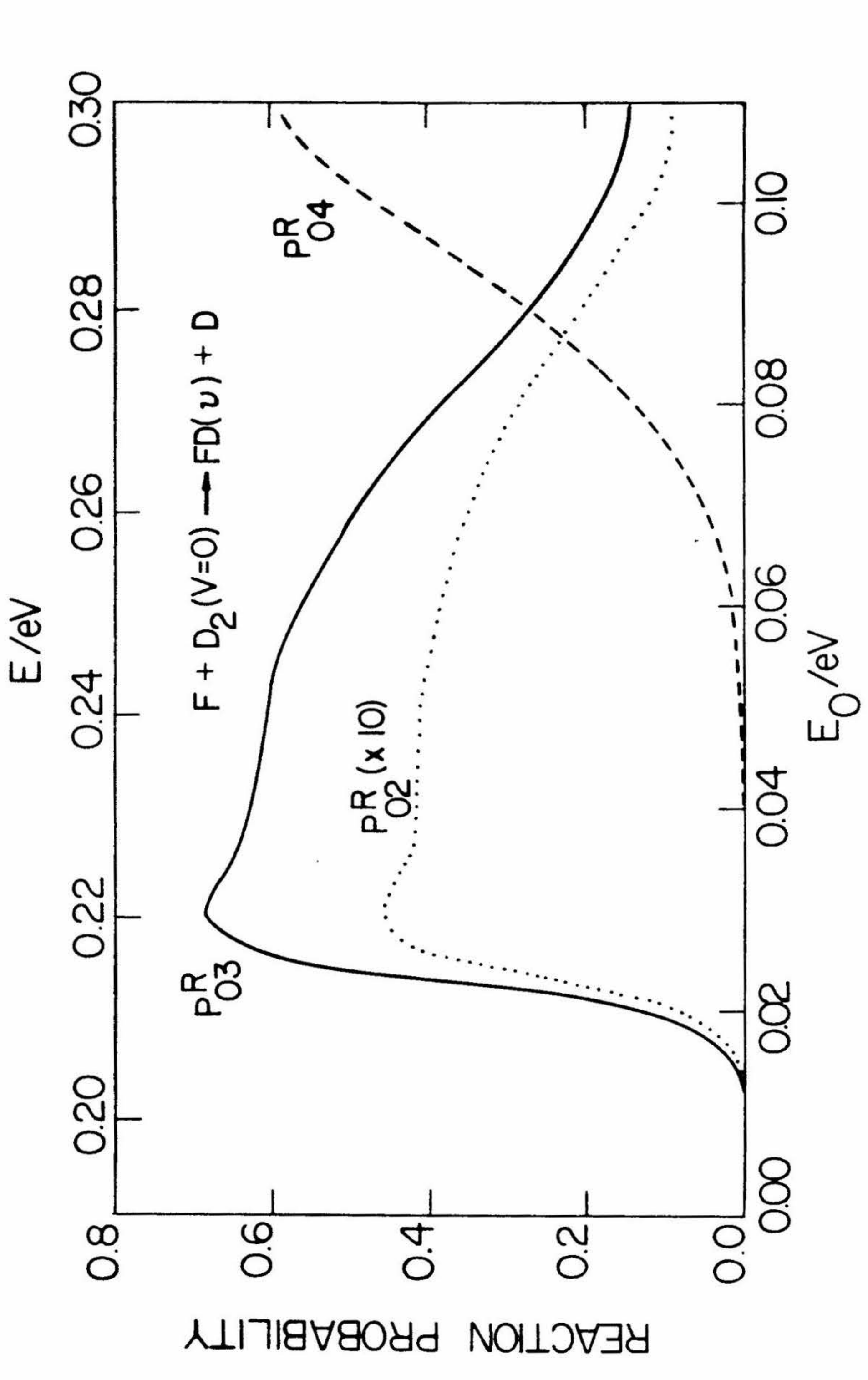
E/eV
0.20
0.22
0.24
0.26
0.28
0.30
$F + D_2(V=0) \longrightarrow FD(\nu) + D$
P^R_{03}
P^R_{02} (x 10)
P^R_{04}
E_0/eV
0.00
0.02
0.04
0.06
0.08
0.10
REACTION PROBABILITY
0.0
0.2
0.4
0.6
0.8

Figure 3c

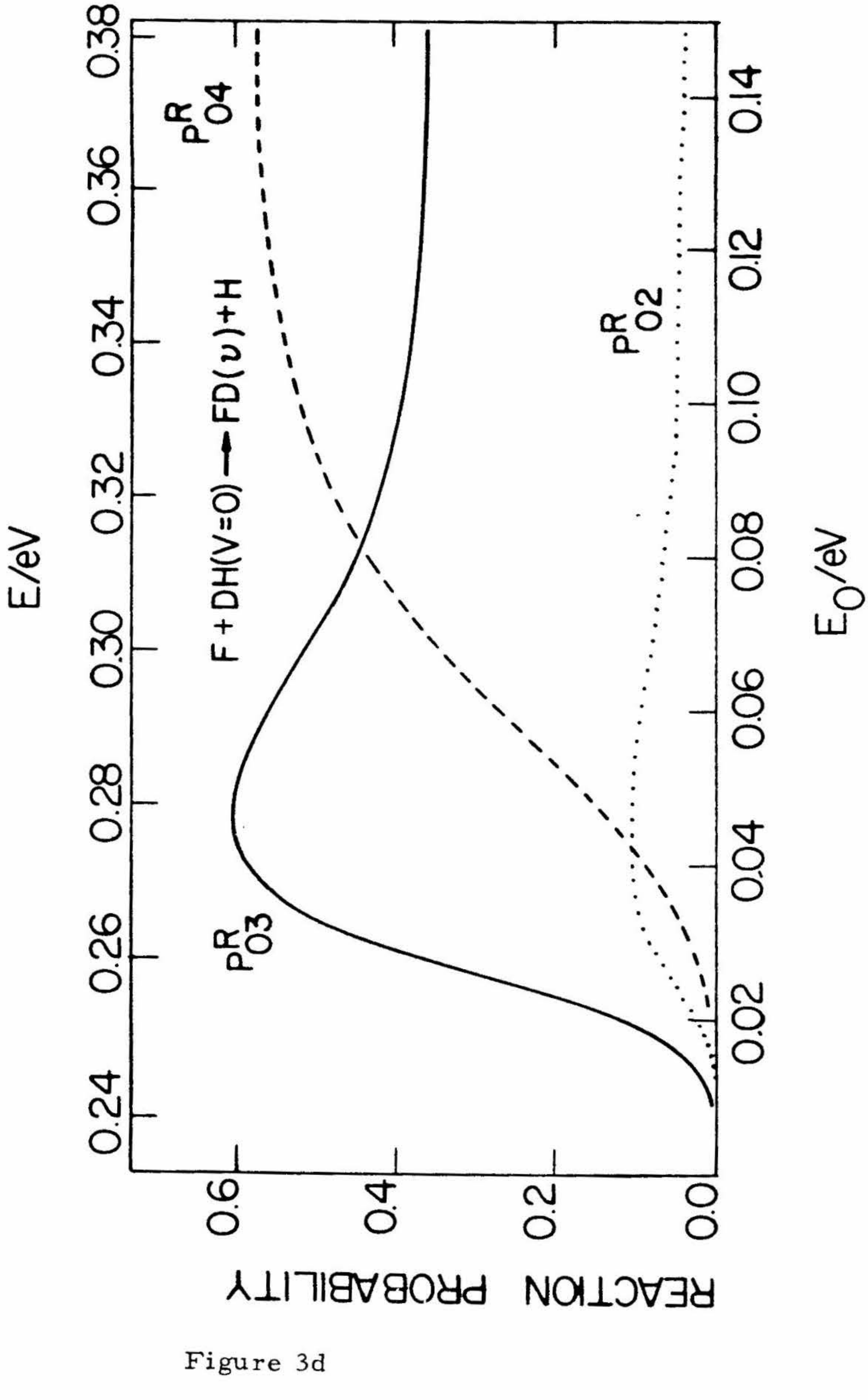
E/eV
0.24
0.26
0.28
0.30
0.32
0.34
0.36
0.38
E_0/eV
0.02
0.04
0.06
0.08
0.10
0.12
0.14
REACTION PROBABILITY
0.0
0.2
0.4
0.6
$F + DH(V=0) \longrightarrow FD(\upsilon)+H$
P^R_{03}
P^R_{04}
P^R_{02}

Figure 3d

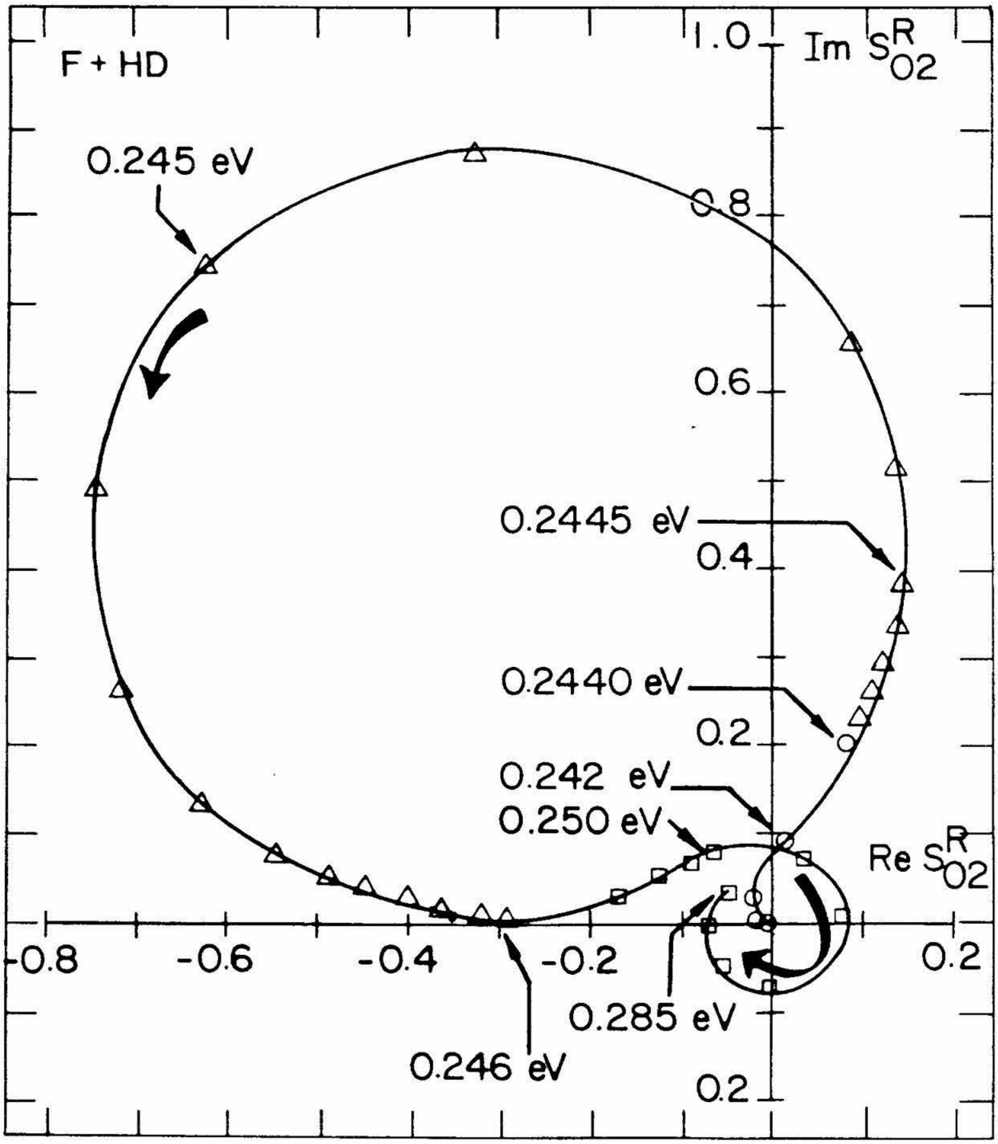
F + HD
$\mathrm{Im}\, S^R_{02}$
$\mathrm{Re}\, S^R_{02}$
1.0
0.8
0.6
0.4
0.2
0.2
-0.8
-0.6
-0.4
-0.2
0.2
0.245 eV
0.2445 eV
0.2440 eV
0.242 eV
0.250 eV
0.285 eV
0.246 eV

Figure 4a

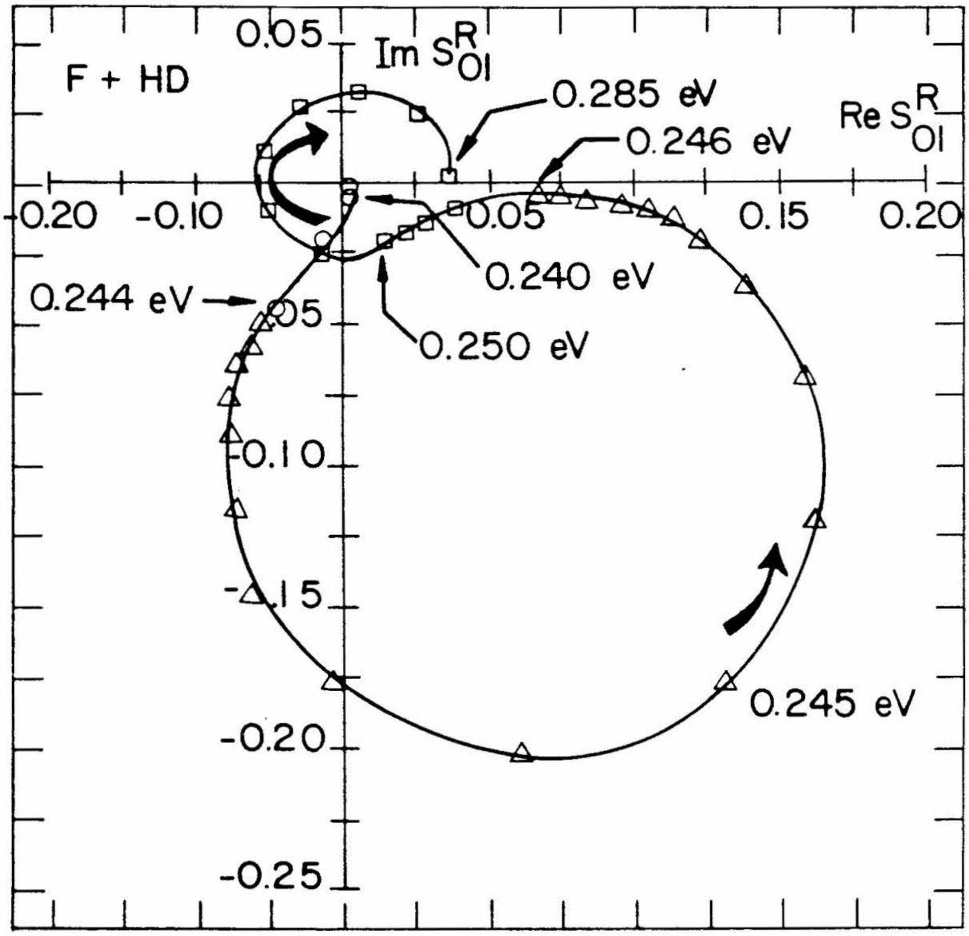
F + HD
Im S^R_{01}
Re S^R_{01}
0.05
-0.05
-0.10
-0.15
-0.20
-0.25
-0.20
-0.10
0.05
0.15
0.20
0.285 eV
0.246 eV
0.240 eV
0.244 eV
0.250 eV
0.245 eV

Figure 4b

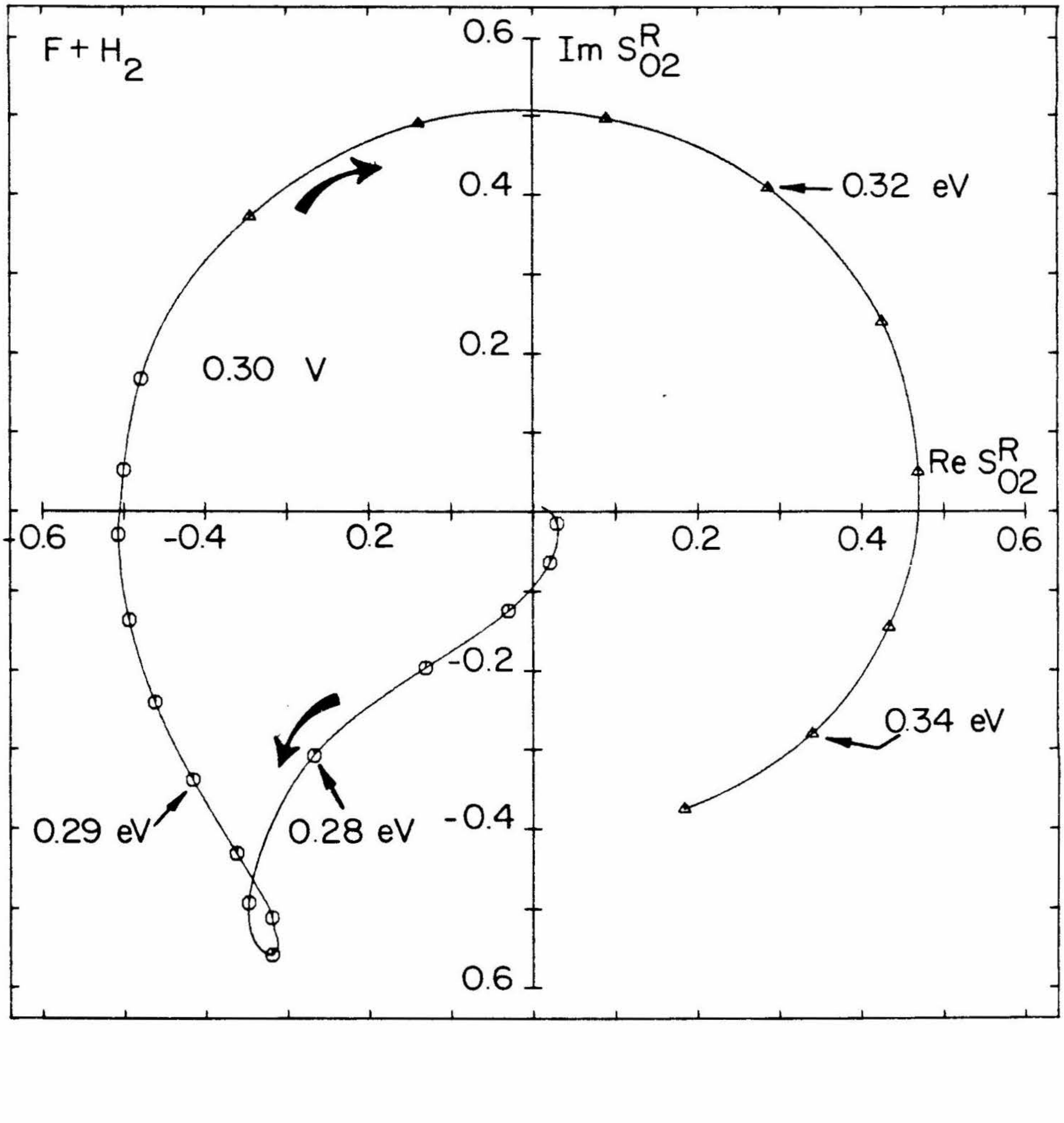
F + H$_2$
Im S_{02}^R
Re S_{02}^R
0.6
0.4
0.2
-0.2
-0.4
0.6
-0.6
-0.4
0.2
0.2
0.4
0.6
0.30 V
0.32 eV
0.34 eV
0.29 eV
0.28 eV

Figure 5

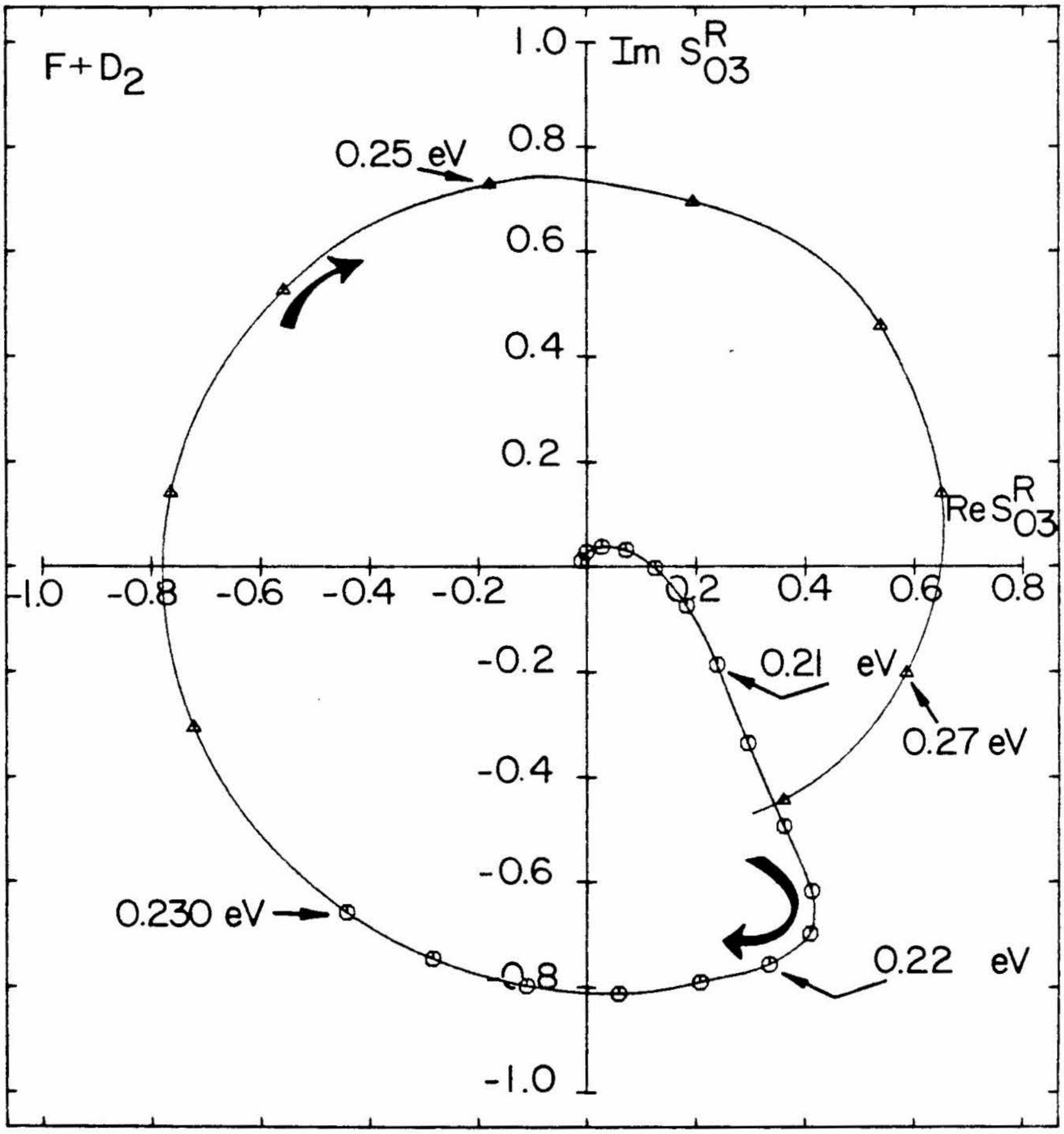
F + D_2
$\mathrm{Im}\, S^R_{03}$
$\mathrm{Re}\, S^R_{03}$
1.0
0.8
0.6
0.4
0.2
-0.2
-0.4
-0.6
-0.8
-1.0
-1.0
-0.8
-0.6
-0.4
-0.2
0.2
0.4
0.6
0.8
0.25 eV
0.21 eV
0.27 eV
0.230 eV
0.22 eV

Figure 6a

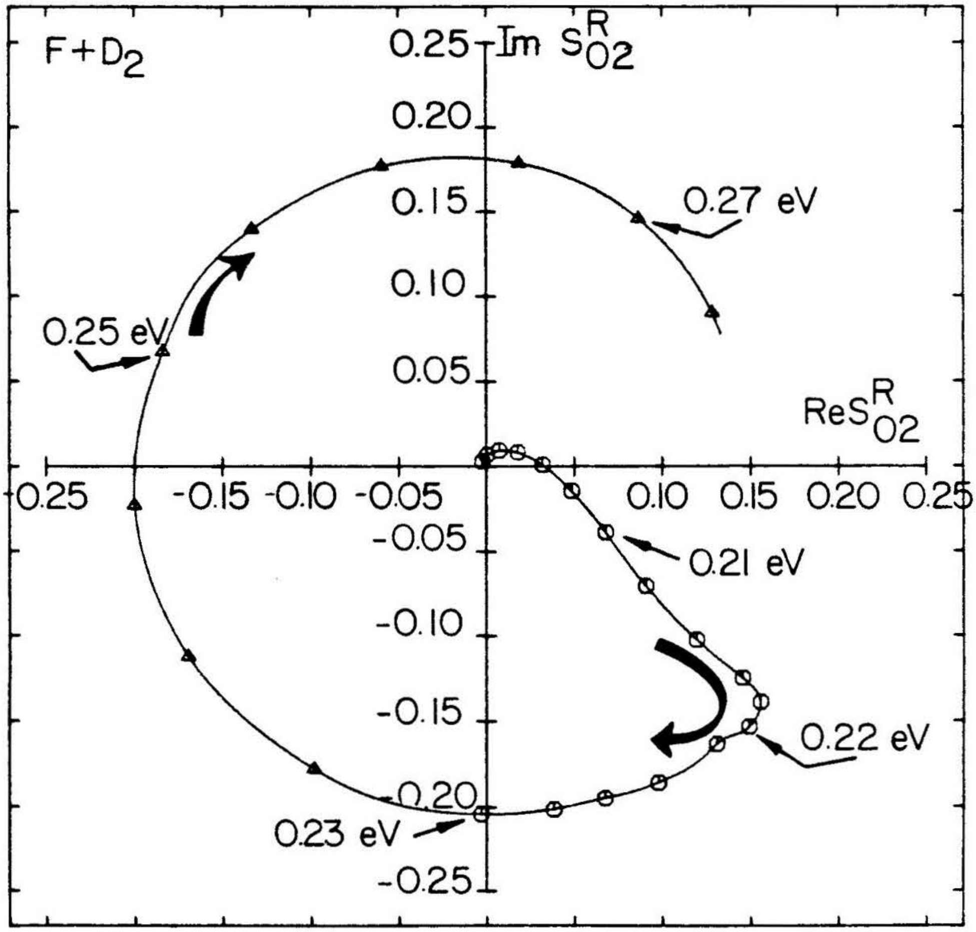
F+D$_2$
Im S$^R_{02}$
Re S$^R_{02}$
0.25
0.20
0.15
0.10
0.05
-0.05
-0.10
-0.15
-0.20
-0.25
0.25
-0.15
-0.10
-0.05
0.10
0.15
0.20
0.25
0.27 eV
0.25 eV
0.21 eV
0.22 eV
0.23 eV

Figure 6b

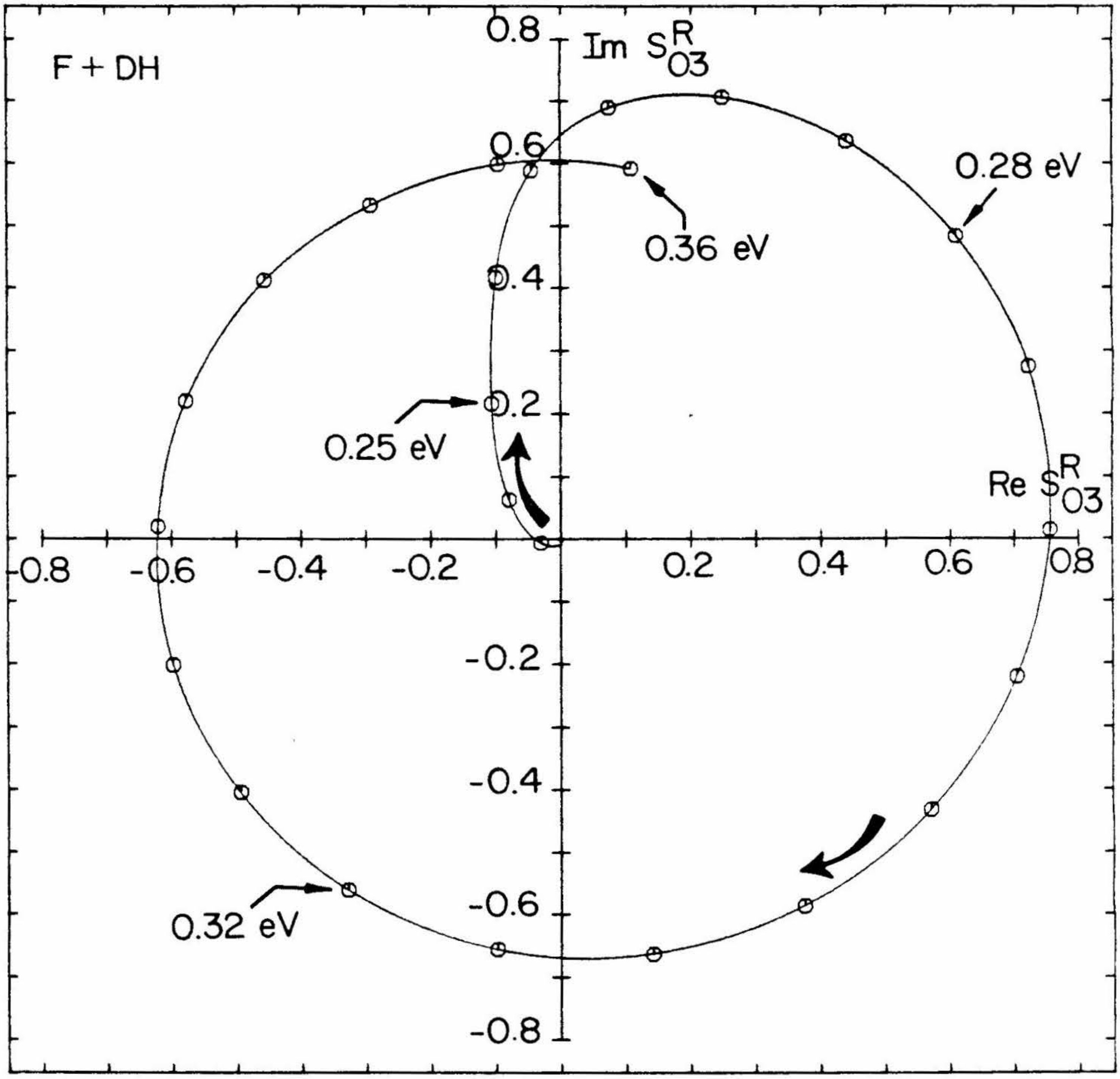
F + DH
Im S^R_{03}
Re S^R_{03}
0.28 eV
0.36 eV
0.25 eV
0.32 eV
0.8
0.6
0.4
0.2
-0.2
-0.4
-0.6
-0.8
-0.8
-0.6
-0.4
-0.2
0.2
0.4
0.6
0.8

Figure 7a

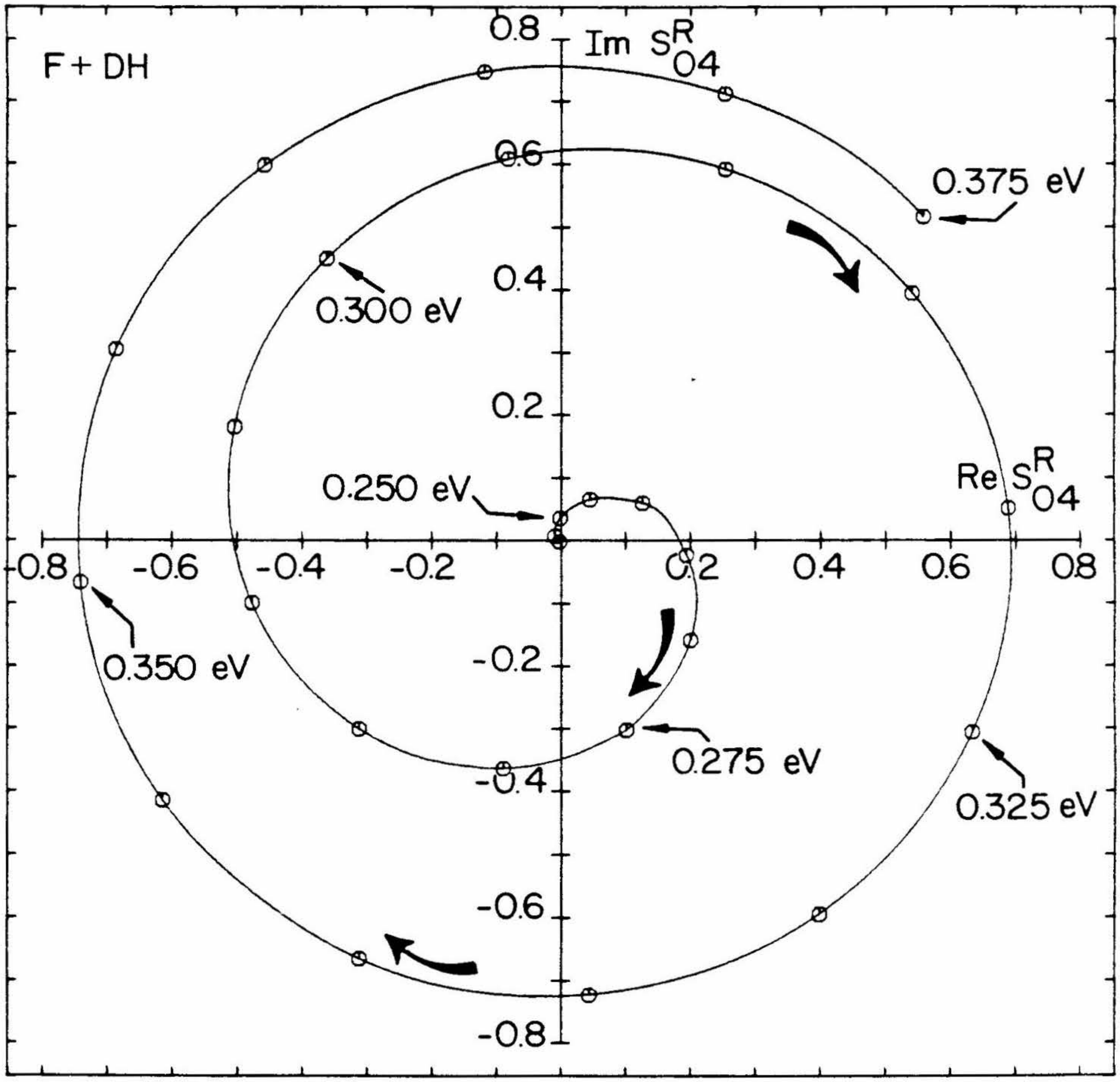
F + DH
Im S^R_{04}
Re S^R_{04}
0.375 eV
0.300 eV
0.250 eV
0.275 eV
0.350 eV
0.325 eV
0.8
0.6
0.4
0.2
-0.2
-0.4
-0.6
-0.8
-0.8
-0.6
-0.4
-0.2
0.2
0.4
0.6
0.8

Figure 7b

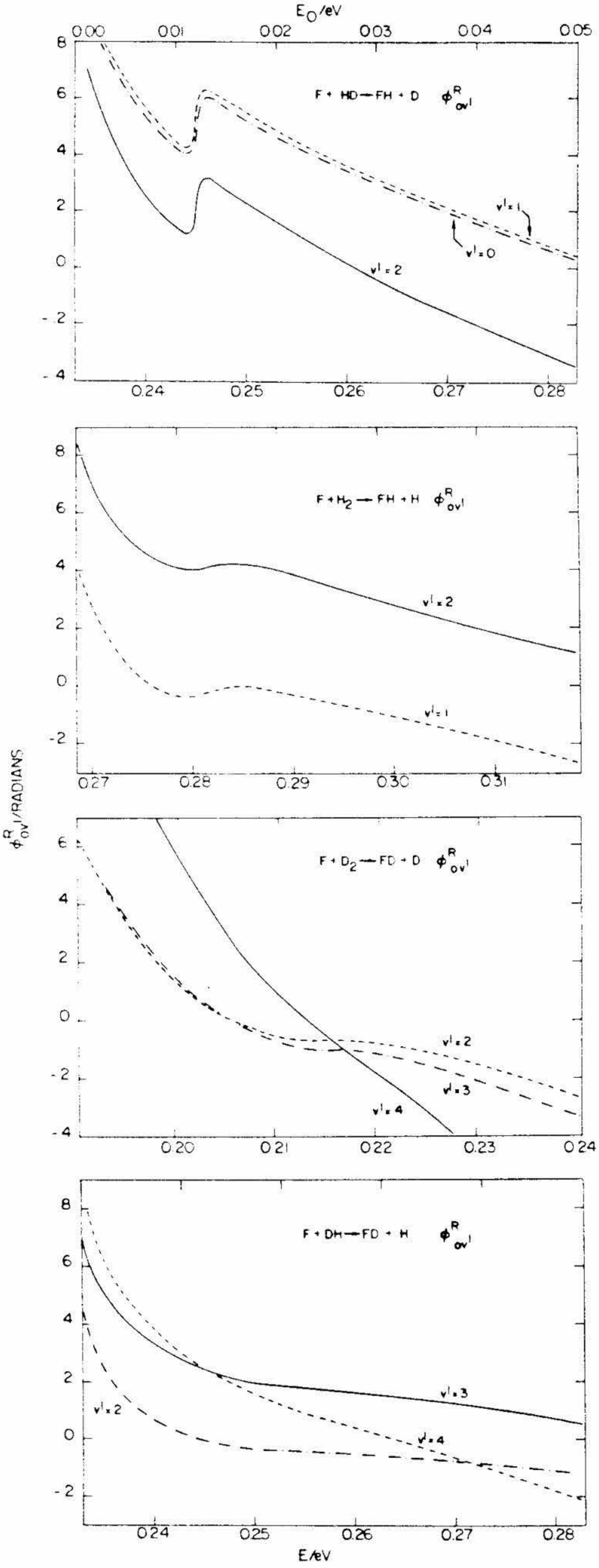
E0/eV
0.00
0.01
0.02
0.03
0.04
0.05
F + HD → FH + D φ^R_ov'
v' = 1
v' = 0
v' = 2
0.24
0.25
0.26
0.27
0.28
F + H2 → FH + H φ^R_ov'
v' = 2
v' = 1
0.27
0.28
0.29
0.30
0.31
φ^R_ov'/RADIANS
F + D2 → FD + D φ^R_ov'
v' = 2
v' = 3
v' = 4
0.20
0.21
0.22
0.23
0.24
F + DH → FD + H φ^R_ov'
v' = 3
v' = 2
v' = 4
0.24
0.25
0.26
0.27
0.28
E/eV
8
6
4
2
0
-2
-4

Figure 8

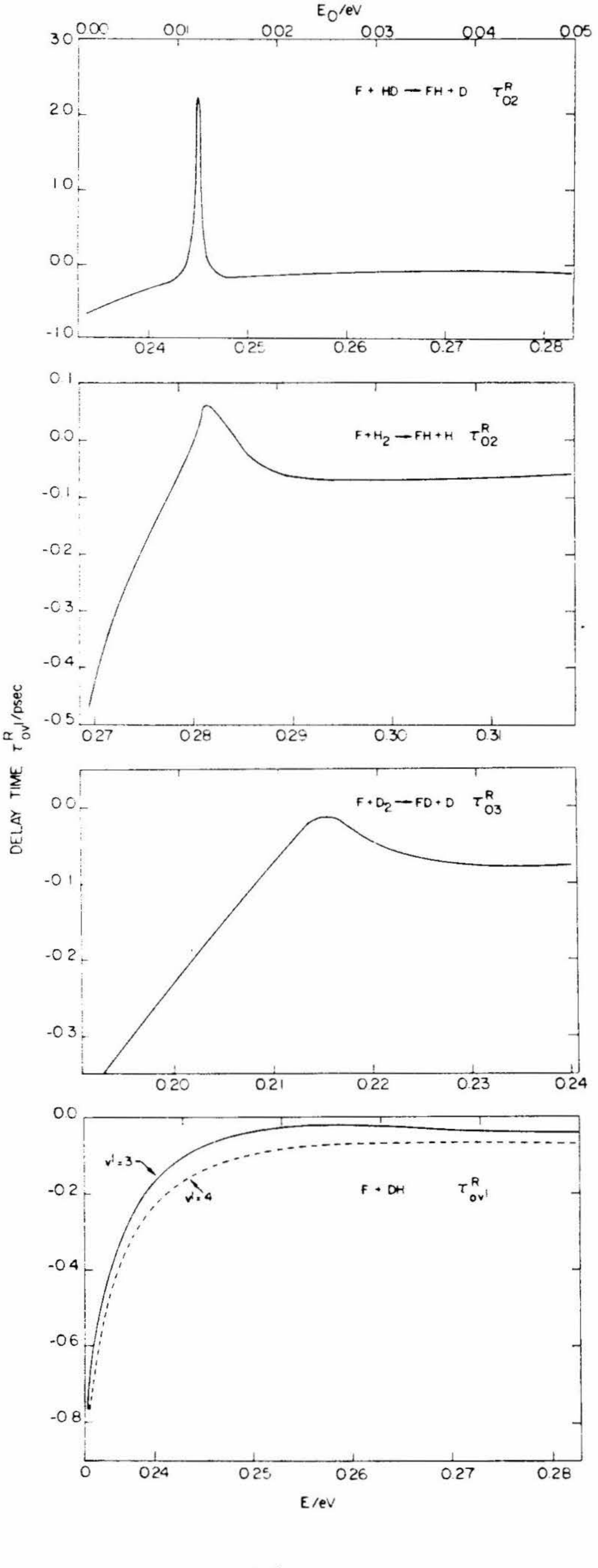
E$_0$/eV
0.00
0.01
0.02
0.03
0.04
0.05
3.0
2.0
1.0
0.0
-1.0
F + HD → FH + D τ^R_{02}
0.24
0.25
0.26
0.27
0.28
0.1
0.0
-0.1
-0.2
-0.3
-0.4
-0.5
F + H$_2$ → FH + H τ^R_{02}
0.27
0.28
0.29
0.30
0.31
DELAY TIME $\tau^R_{ov'}$/psec
0.0
-0.1
-0.2
-0.3
F + D$_2$ → FD + D τ^R_{03}
0.20
0.21
0.22
0.23
0.24
0.0
-0.2
-0.4
-0.6
-0.8
v' = 3
v' = 4
F + DH $\tau^R_{ov'}$
0
0.24
0.25
0.26
0.27
0.28
E/eV

Figure 9

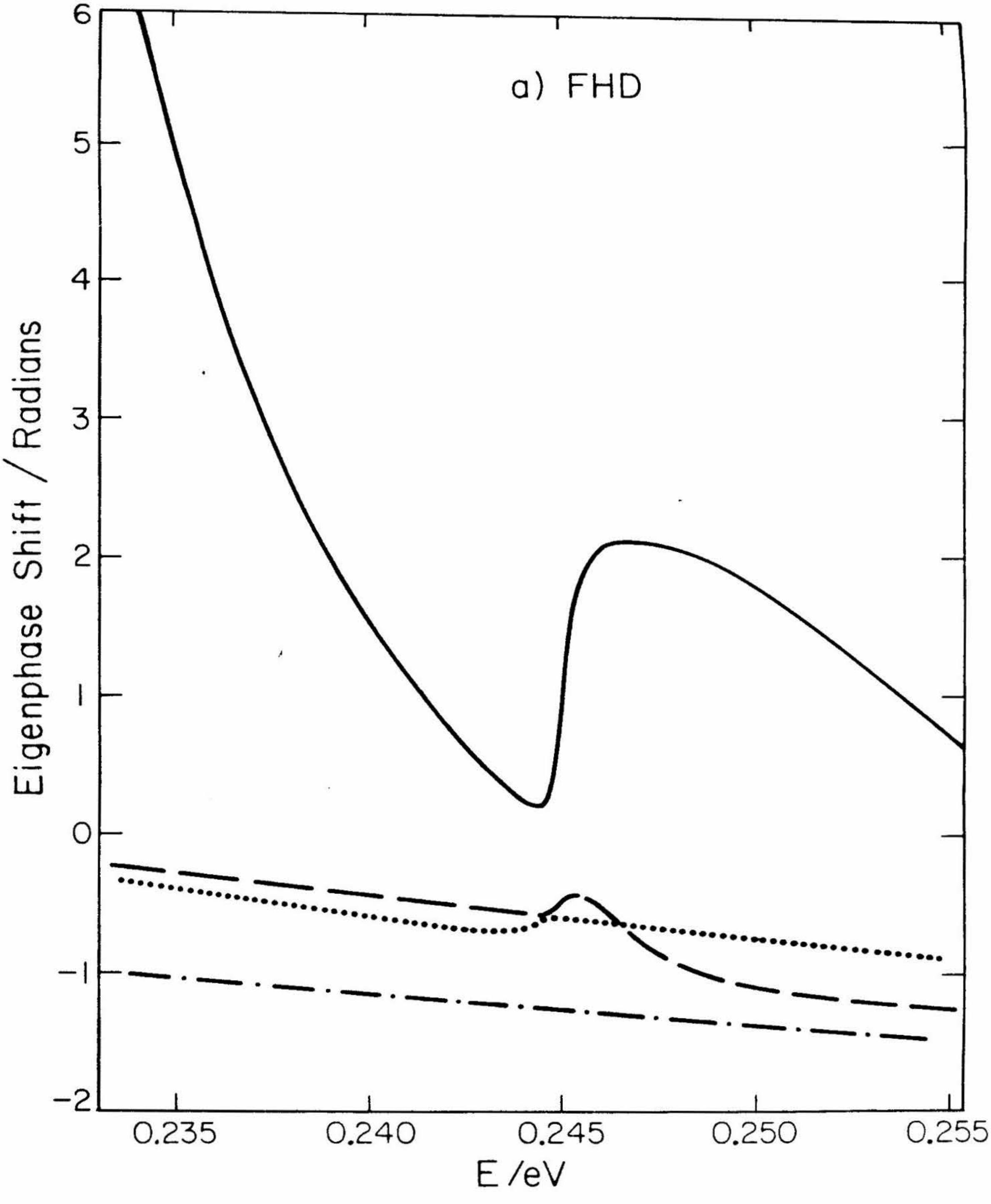
a) FHD
Eigenphase Shift / Radians
E /eV
6
5
4
3
2
1
0
−1
−2
0.235
0.240
0.245
0.250
0.255

Figure 10a

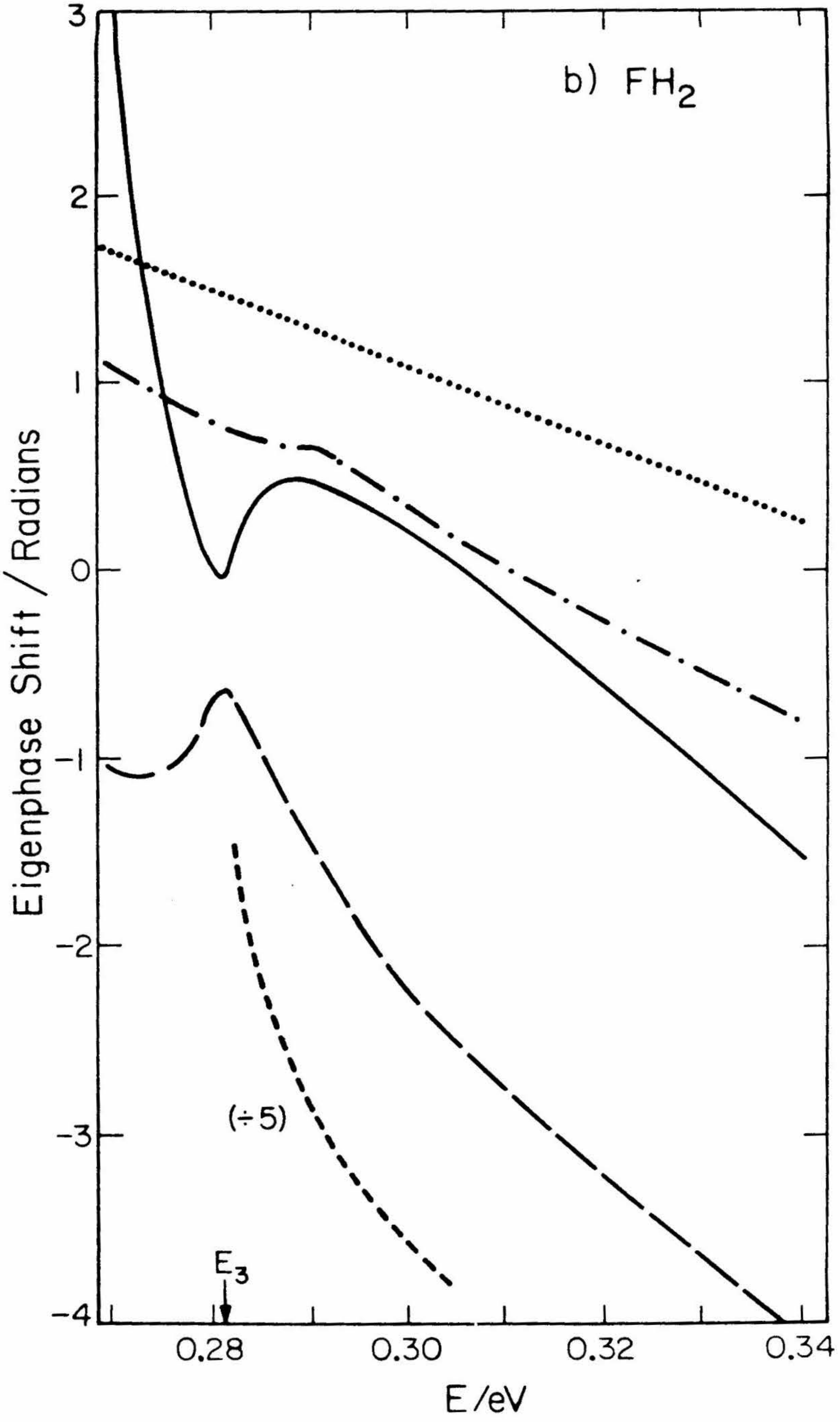
b) FH$_2$
Eigenphase Shift / Radians
3
2
1
0
−1
−2
−3
−4
(÷5)
E$_3$
0.28
0.30
0.32
0.34
E/eV

Figure 10b

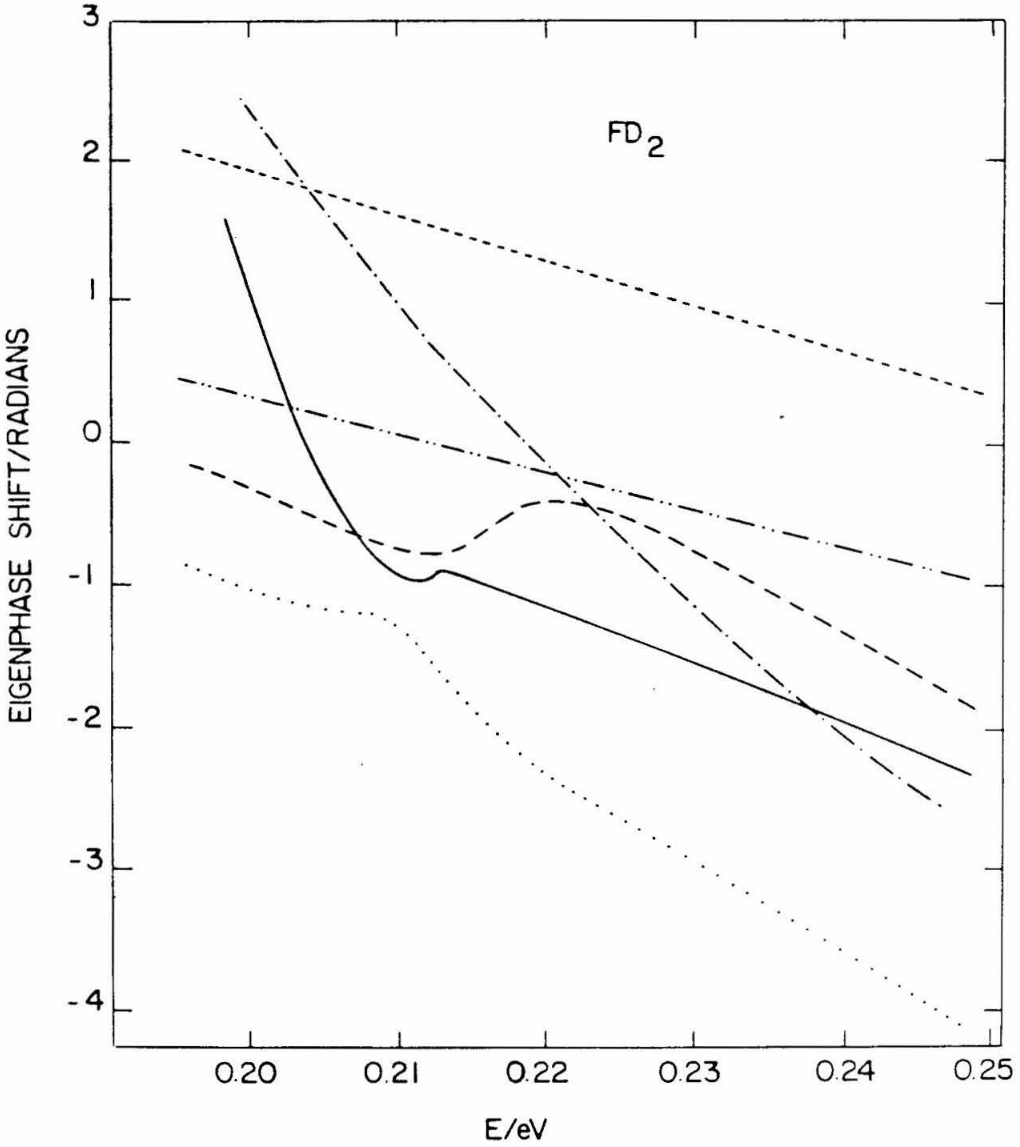
FD2
EIGENPHASE SHIFT/RADIANS
3
2
1
0
-1
-2
-3
-4
0.20
0.21
0.22
0.23
0.24
0.25
E/eV

Figure 10c

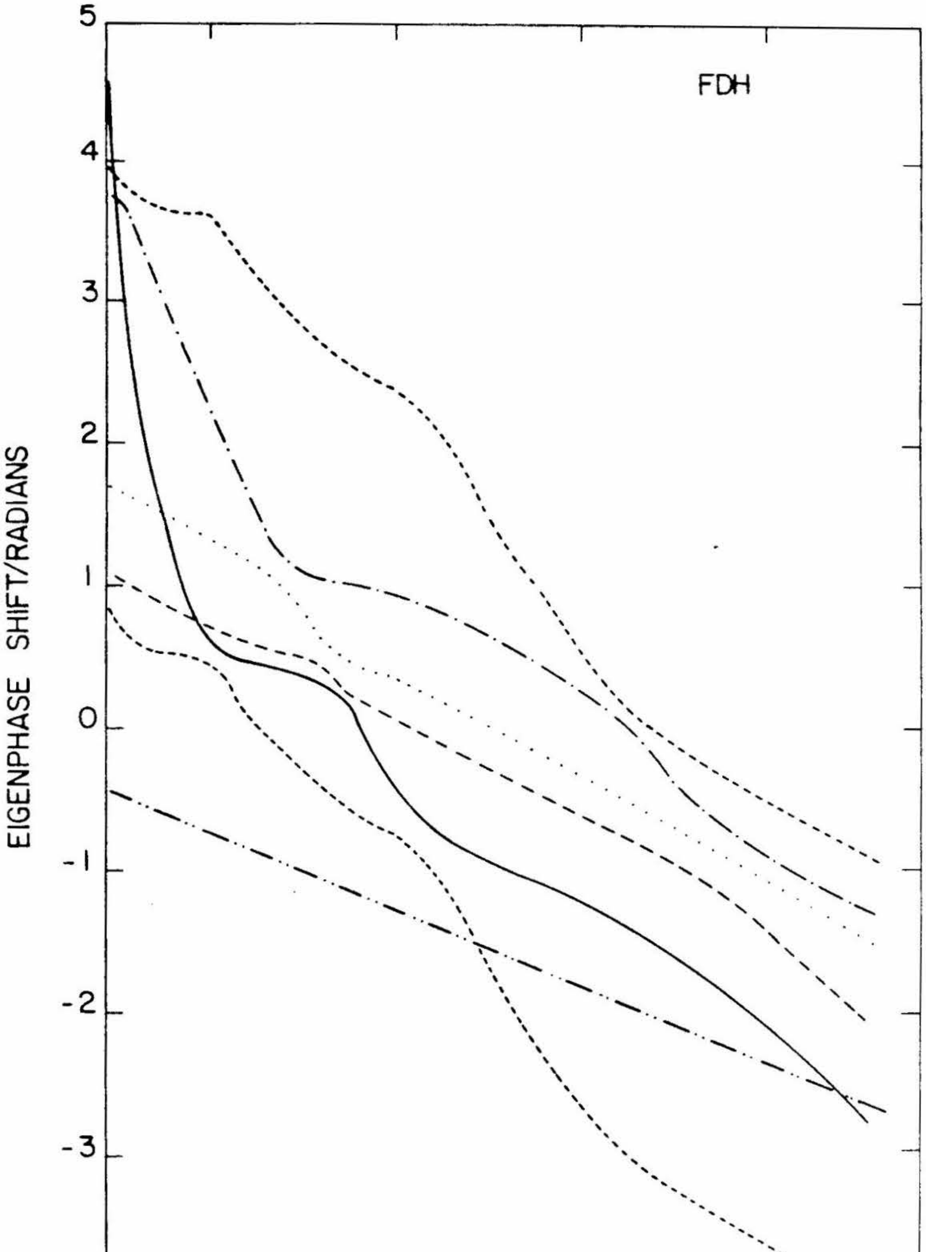
FDH
EIGENPHASE SHIFT/RADIANS
5
4
3
2
1
0
-1
-2
-3
-4
0.24
0.26
0.28
0.30
E/eV

Figure 10d

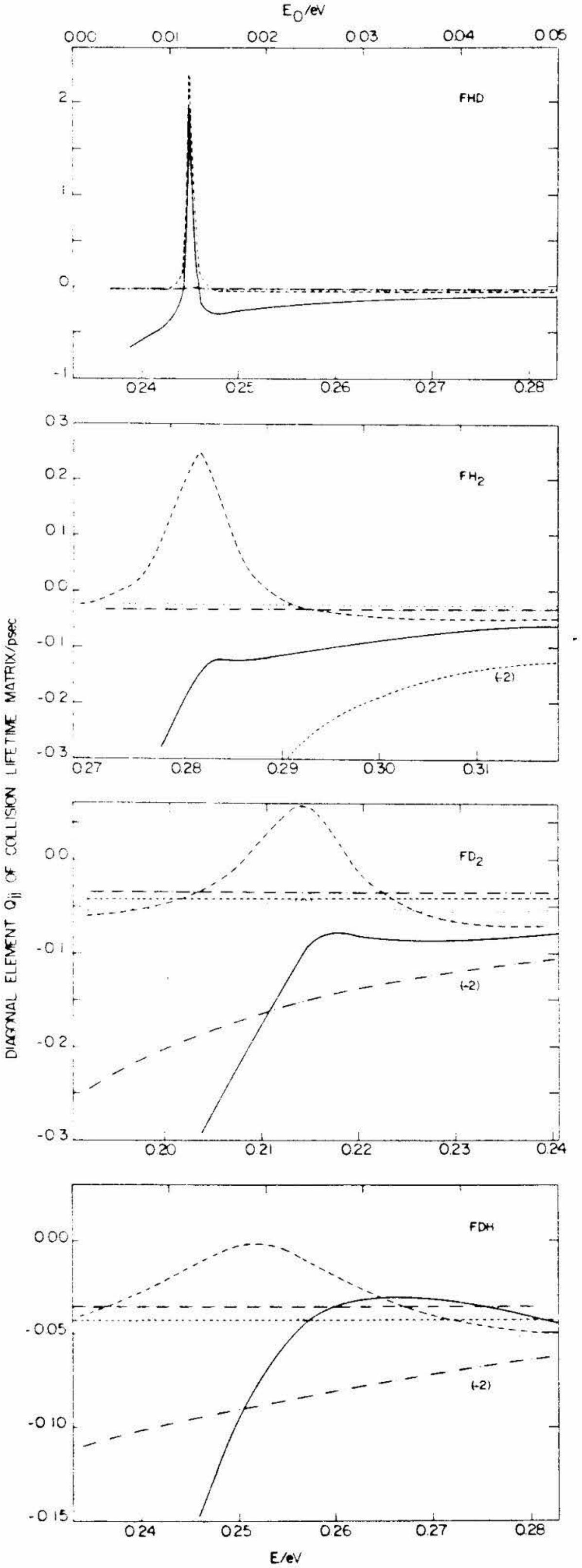
E_0/eV
0.00
0.01
0.02
0.03
0.04
0.05
FHD
2
1
0
-1
0.24
0.25
0.26
0.27
0.28
0.3
0.2
0.1
0.0
-0.1
-0.2
-0.3
FH2
(-2)
0.27
0.28
0.29
0.30
0.31
FD2
0.0
-0.1
-0.2
-0.3
(-2)
0.20
0.21
0.22
0.23
0.24
FDH
0.00
-0.05
-0.10
-0.15
(-2)
0.24
0.25
0.26
0.27
0.28
E/eV
DIAGONAL ELEMENT Q_ii OF COLLISION LIFETIME MATRIX/psec

Figure 11

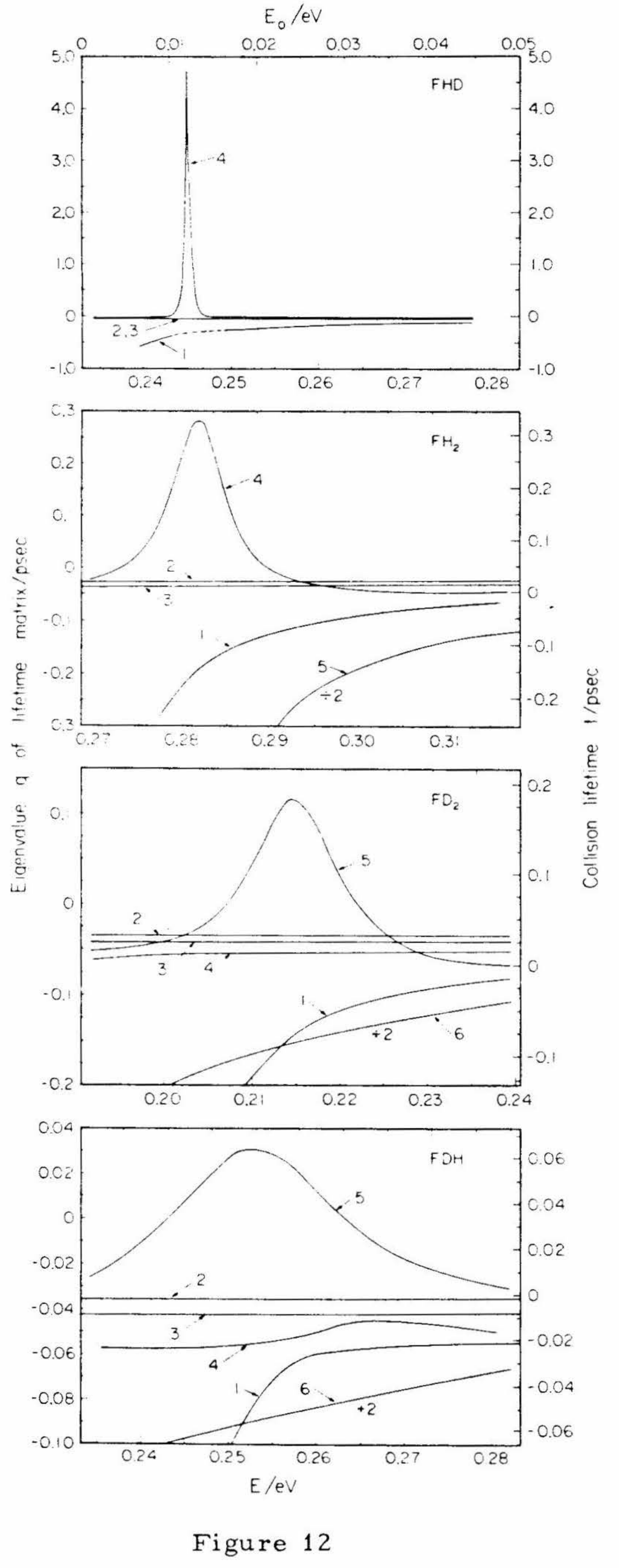
E$_o$ /eV
0
0.01
0.02
0.03
0.04
0.05
FHD
4
2,3
1
FH$_2$
4
2
3
1
5
÷2
FD$_2$
5
2
3
4
1
÷2
6
FDH
5
2
3
4
1
6
÷2
Eigenvalue q of lifetime matrix/psec
Collision lifetime t/psec
E/eV

Figure 12

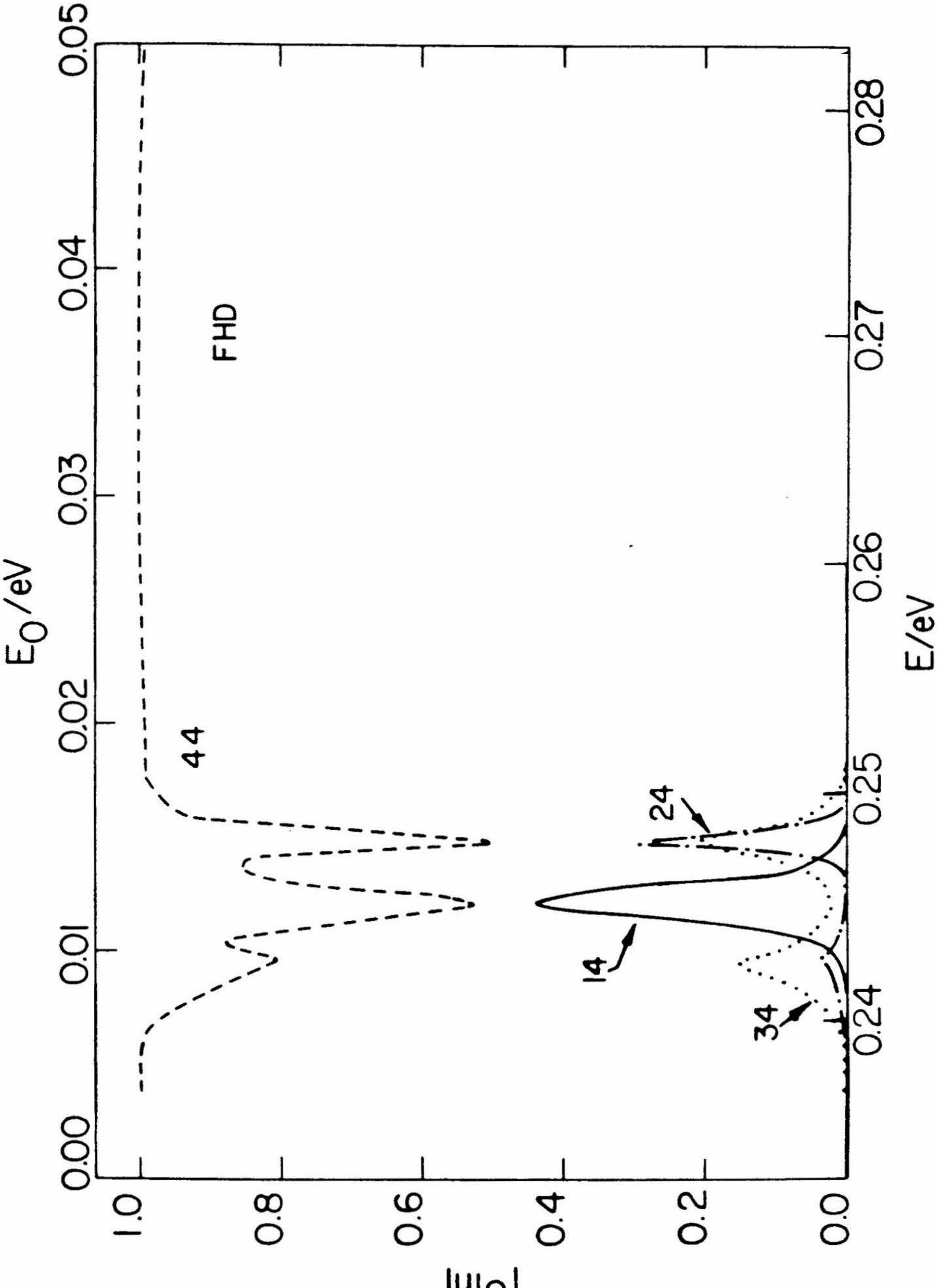
E_0/eV
0.00
0.01
0.02
0.03
0.04
0.05
E/eV
0.24
0.25
0.26
0.27
0.28
$|U_{in}|^2$
0.0
0.2
0.4
0.6
0.8
1.0
FHD
44
24
14
34

Figure 13

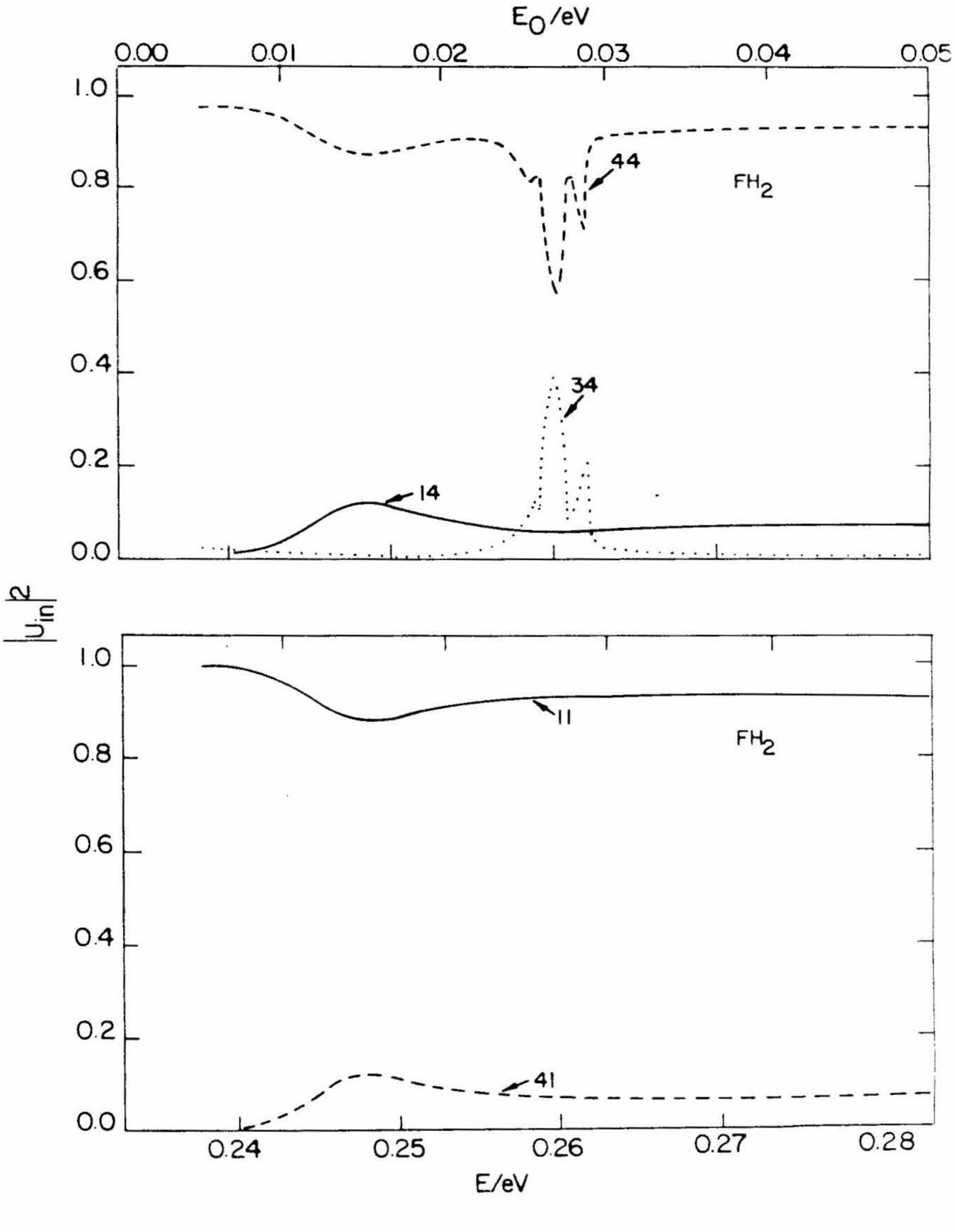
E$_0$/eV
0.00
0.01
0.02
0.03
0.04
0.05
1.0
0.8
0.6
0.4
0.2
0.0
44
FH$_2$
34
14
$|U_{in}|^2$
11
FH$_2$
41
0.24
0.25
0.26
0.27
0.28
E/eV

Figure 14

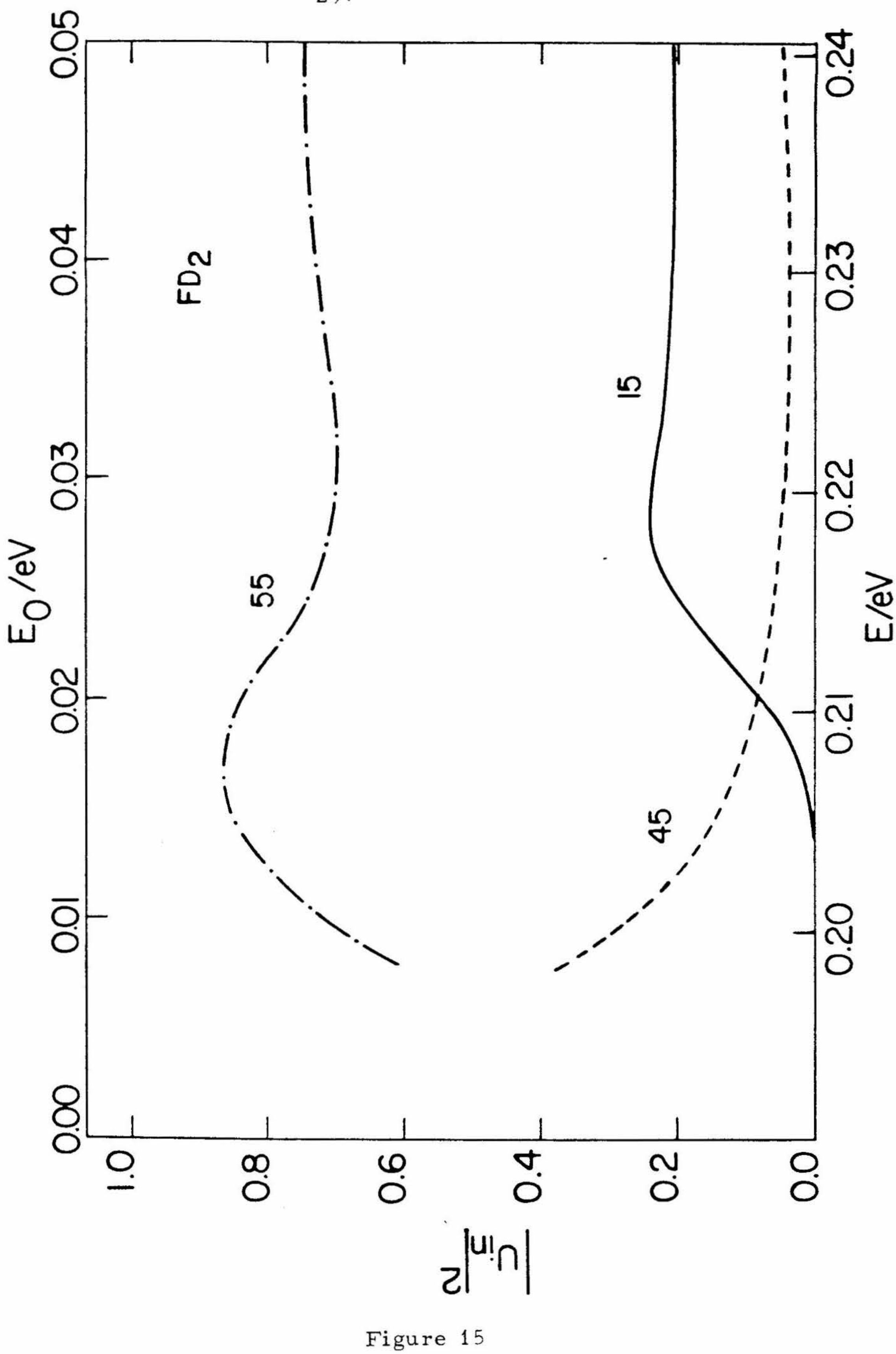
E_0/eV
0.00
0.01
0.02
0.03
0.04
0.05
E/eV
0.20
0.21
0.22
0.23
0.24
$|C_{in}|^2$
0.0
0.2
0.4
0.6
0.8
1.0
FD_2
55
15
45

Figure 15

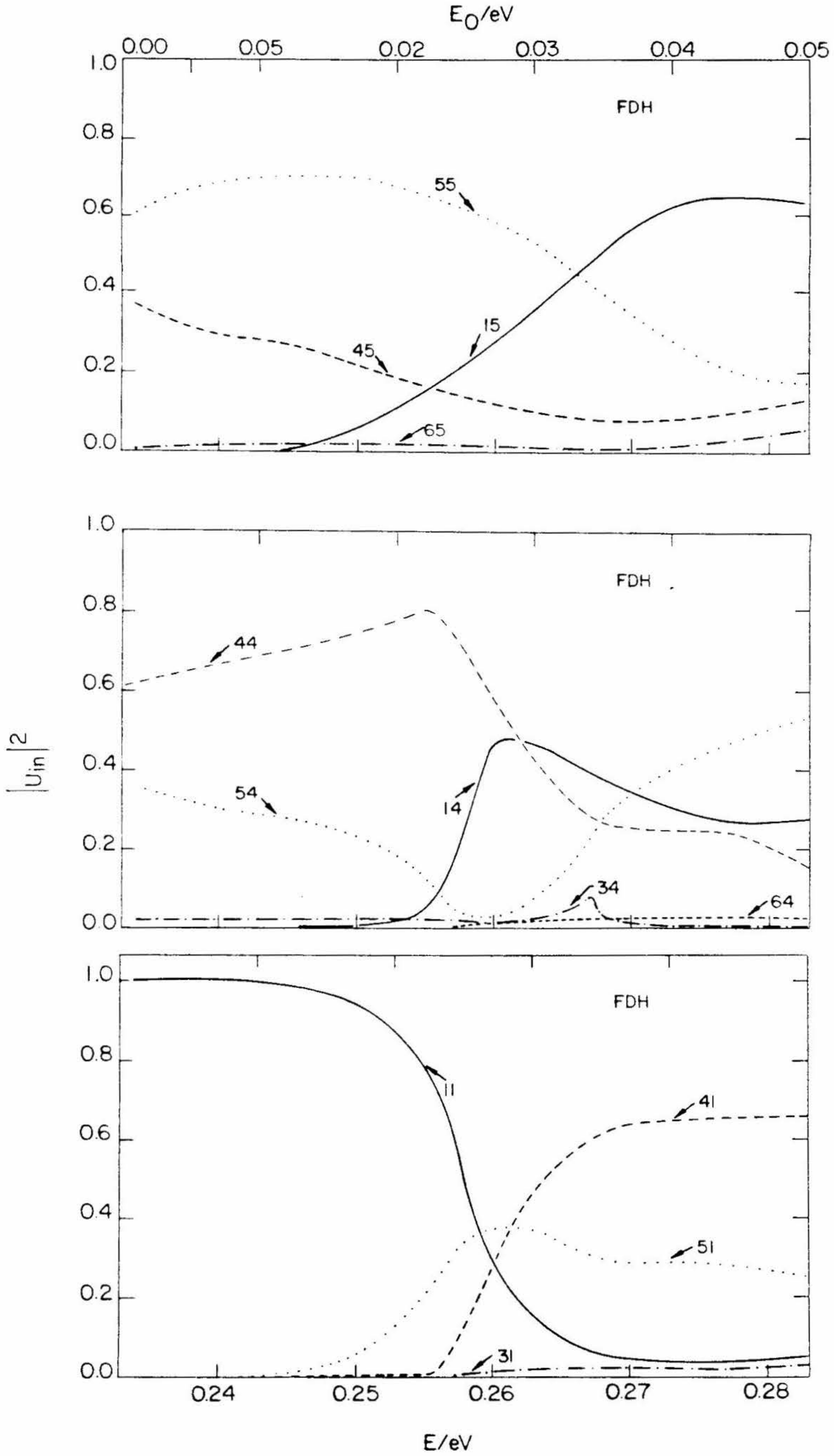
E_O/eV
0.00
0.05
0.02
0.03
0.04
0.05
FDH
55
15
45
65
FDH
44
54
14
34
64
FDH
11
41
51
31
$|U_{in}|^2$
1.0
0.8
0.6
0.4
0.2
0.0
0.24
0.25
0.26
0.27
0.28
E/eV

Figure 16

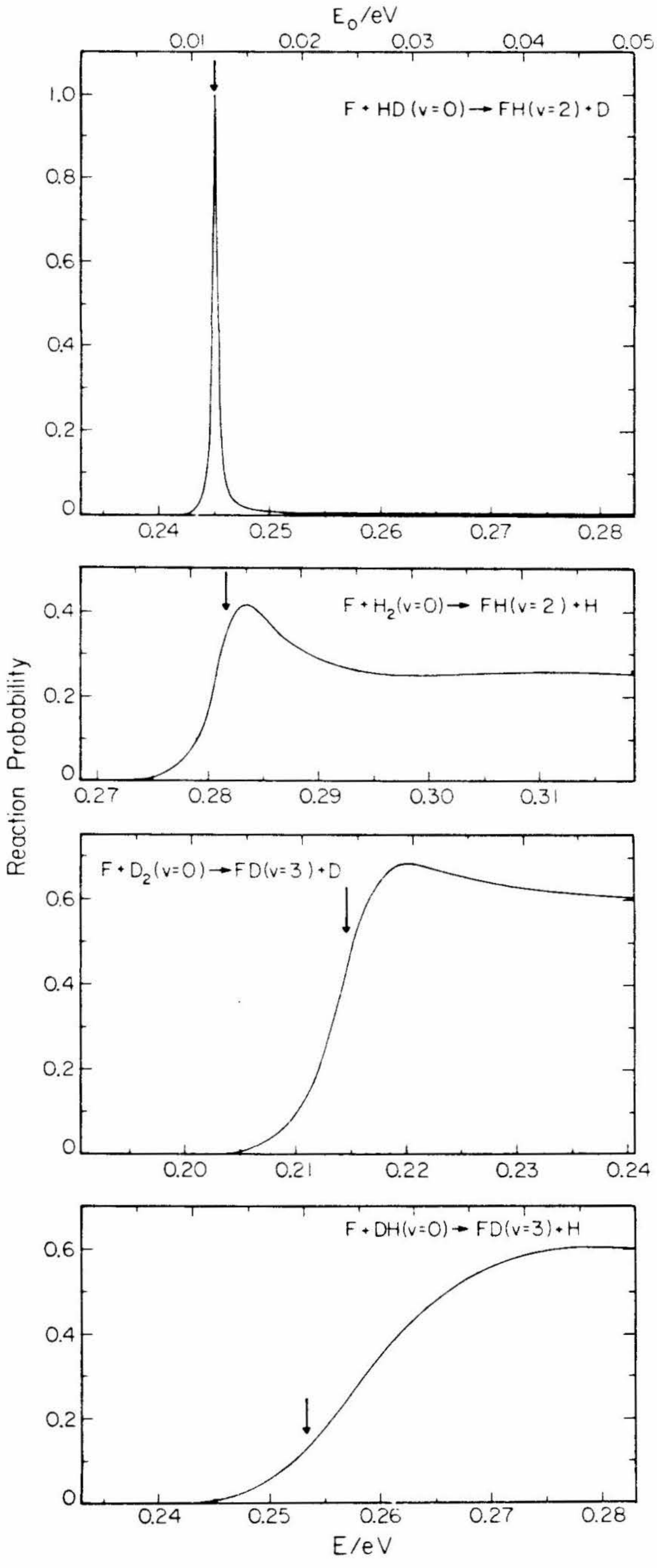

E_0/eV
0.01
0.02
0.03
0.04
0.05
1.0
0.8
0.6
0.4
0.2
0
F + HD (v=0) → FH(v=2) + D
0.24
0.25
0.26
0.27
0.28
0.4
0.2
0
F + H_2(v=0) → FH(v=2) + H
0.27
0.28
0.29
0.30
0.31
Reaction Probability
F + D_2(v=0) → FD(v=3) + D
0.6
0.4
0.2
0
0.20
0.21
0.22
0.23
0.24
F + DH(v=0) → FD(v=3) + H
0.6
0.4
0.2
0
0.24
0.25
0.26
0.27
0.28
E/eV

Figure 17

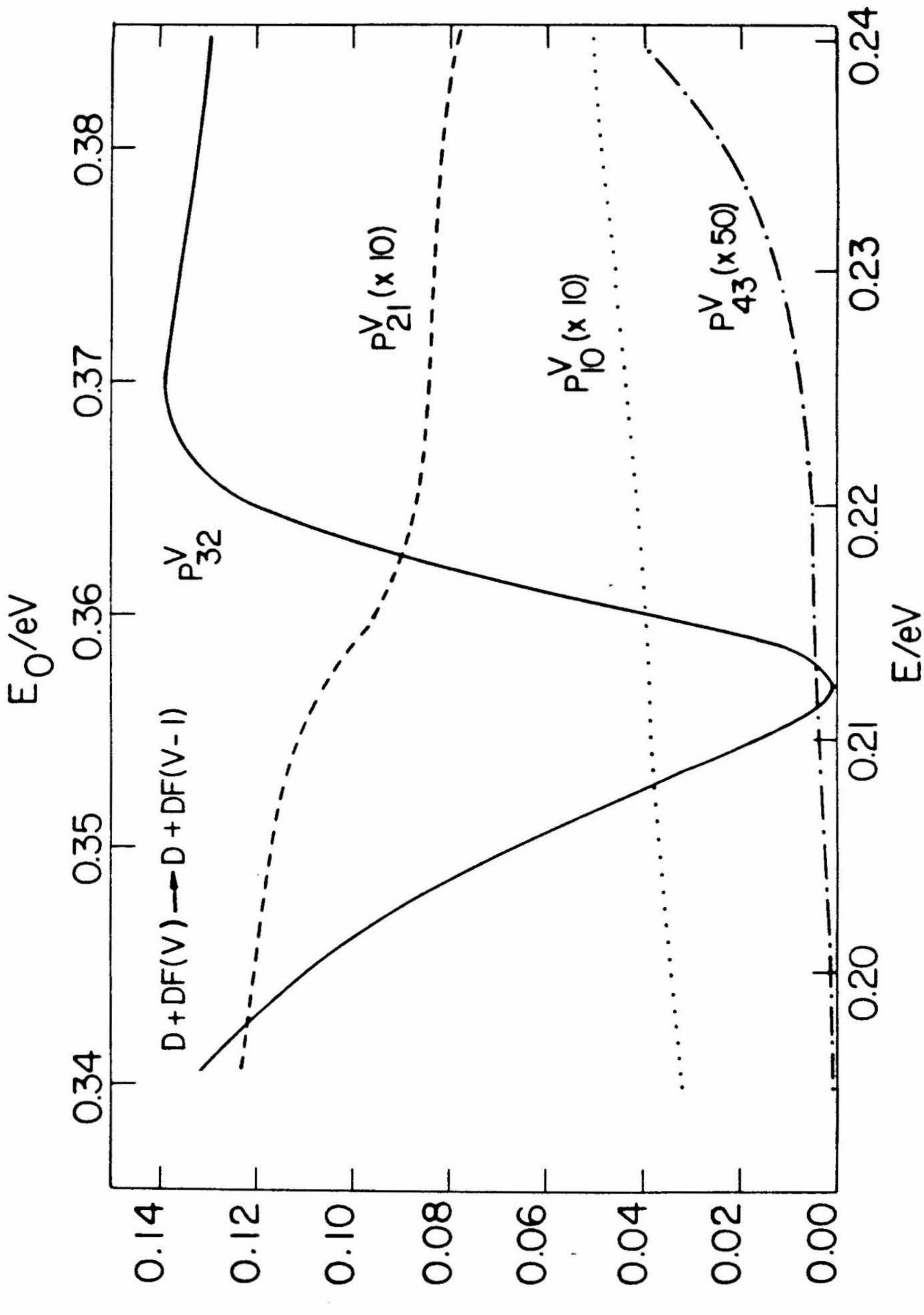
E$_0$/eV
0.34
0.35
0.36
0.37
0.38
D + DF(V) ⟶ D + DF(V−1)
P^V_{32}
P^V_{21}(x 10)
P^V_{10}(x 10)
P^V_{43}(x 50)
TRANSITION PROBABILITY
0.00
0.02
0.04
0.06
0.08
0.10
0.12
0.14
E/eV
0.20
0.21
0.22
0.23
0.24

Figure 18

PART III

COLLINEAR ATOM-DIATOMIC MOLECULE COLLISIONS STUDIED BY HYPERSPHERICAL COORDINATES

INTRODUCTION

INTRODUCTION

A variety of quantum mechanical methods have been developed for the study of collinear atom-diatomic molecule reactions. While these methods have achieved great success in studying a number of interesting systems, they have been unable to be used for two important classes of reactions: those in which a light atom is transferred between two heavy ones (the heavy-light-heavy, or H-L-H systems), and those above the threshold for collision-induced dissociation (CID). In this section we report on the development of a new method for quantum mechanically treating collinear atom-diatomic colecule reactions in a manner in which these two classes of reactions may be easily studied. This method, using hyperspherical coordinates, is applied to a number of these systems. Collinear quasi-classical trajectory calculations have been performed on a number of these systems to help understand the importance of quantum mechanical effects and the existence of classical mechanical explanations for some of the calculated behavior. We include the results of such quasi-classical trajectory calculations in this section, even though they of course do not use hyperspherical coordinates.

Paper III.1 presents the first results of the hyperspherical coordinate method. These are for the $H + H_2$ reaction, and they are shown to be in excellent agreement with results obtained previously. Quantum mechanical resonance effects are shown to persist to high energies and high reagent vibrational states.

Paper III.2 presents results for the I + HI reaction. This is an extreme case of the H-L-H mass combination mentioned above, and we show that in spite of the small skew angle (~7°) in this system when viewed in an appropriate mass scaled coordinate system, the hyperspherical coordinate treatment is quite simple. Reaction probabilities are seen to oscillate with energy, to show resonance effects which depend very strongly on the potential energy surface, and to be well reflected (except for the resonances) by quasi-classical trajectory calculations. The low energy resonance structure can be well represented by a method developed by Babamov and Marcus.

Paper III.3 presents results for a model CID system. Well converged dissociation probabilities can be obtained fairly easily. These probabilities are found to be fairly similar to those from quasi-classical trajectory calculations, in spite of the low masses and small molecular well depth used. CID was shown to be strongly vibrationally enhanced.

Paper III.4 presents in some detail the results of CID calculations for the model system considered in paper III.3. Three different mass combinations, corresponding to light-light-light (L-L-L), heavy-light-heavy (H-L-H), and light-heavy-light (L-H-L) ones, are studied. CID is shown to be greatest in the L-H-L system and least in the H-L-H one. Rate constants for CID and for chemical reaction are calculated and their temperature dependence is examined.

Paper III.5 presents some aspects of CID in a quasi-classical trajectory calculation of the model system studied in papers III.3 and III.4 (L-L-L mass combination). We report the formation of well defined reactivity bands for CID, and show that the absence of low energy CID in the ground vibrational state system can be understood in terms of the absence of the simplest possible dissociative trajectory, which does occur in the vibrationally excited system. Kinetic energy distributions of the atoms formed in CID are obtained, and they are shown to possess a number of interesting and unexpected features, the origin of which may be seen as a consequence of the existence of well-defined reactivity bands for CID.

Paper III.6 presents preliminary results of the calculation of the kinetic energy distributions of the atoms formed in CID determined by the hyperspherical coordinates method for the system and mass combination studied in the previous paper. The quantum mechanical distributions are shown to have a much less irregular structure than the quasi-classical ones.

Paper III.7 attempts to explain an interesting and unexpected feature of the dynamics of the collinear Cl + HCl(v) reaction obtained from a hyperspherical coordinates study. This feature is the near total equivalence of the probabilities and rates of reactive and non-reactive deactivating processes in collisions of vibrationally excited HCl. This explanation is obtained by considering quasi-classical trajectories for this system. It is found that most vibrational deactivation occurs near the boundary between regions of reactive and non-reactive trajectories, and the trajectories involved in these highly non-adiabatic collisions all more or less follow the symmetric stretch line for a period of time. It is believed that this equivalence of reactive and non-reactive deactivating processes will be a feature in any symmetric H-L-H system.

Paper III.8 consists of the presentation of probabilities and rate constants for the system

$$\begin{aligned} \mathrm{Br} + \mathrm{HCl}(v{=}2,3,4) &\longrightarrow \mathrm{BrH}(v') + \mathrm{Cl} \\ &\longrightarrow \mathrm{Br} + \mathrm{HCl}(v' \quad v) \end{aligned}$$

obtained by a hyperspherical coordinate calculation. Removal of vibrationally excited HCl is found to occur mainly by reaction to the nearly degenerate HBr state (v-2). In deactivating collisions, the probabilities of forming HCl(v') and HBr(v'-2) are nearly identical. Multi-quantum deactivations are found to be far less likely than those involving only a single quantum.

Paper III.9 consists of conceptual and numerical analyses of the implementation of the hyperspherical coordinates method in the adiabatic representation rather than the diabatic representation, in which it has previously been formulated. Two different basis sets are studied. One is the purely polar coordinate basis set used in all previous work; the other is a hybrid one which consists of both linear and circular portions. Analytic properties of the coupling matrix elements are determined, and these matrix elements are evaluated out to very large (5000 bohr) values of the propagation coordinate in order to help understand their asymptotic properties. The adiabatic equations are integrated for a very simple model case, and the results can be understood in terms of a simple (and analytically solvable) 2x2 model.

Paper III.10 considers the extraction of physical wave functions from the hyperspherical coordinate method, and their use in calculating probability densities, probability current densities, and tunneling fractions. Preliminary (unconverged) results for these quantities on the collinear $H + H_2$ reaction are presented. Various difficulties encountered in this work are discussed, and ideas for their remedy are discussed.

Paper III.11 presents a study of the convergence properties of the hyperspherical coordinate method. In particular, state-to-state reaction probabilities and scattering matrix element phases are examined as a function of the number of basis functions and the distance at which the wave function is projected from a hyperspherical (polar) coordinate basis set to one in Cartesian coordinates. Probabilities and phases are found to converge very rapidly with basis set for the $H + H_2$ reaction and less so for the $F + H_2$ reaction. Reaction probabilities converge fairly well with projection distance for $H + H_2$ and less so (but still adequately) for $F + H_2$. Scattering matrix element phases converge slowly with projection distance for $H + H_2$, becoming converged to within 1-2° at a projection distance of 12 bohr. The phases calculated agree well with those of previous calculations. In $F + H_2$, convergence is slower, and does not appear to be to the values obtained by a previous method.

III. 1 HYPERSPHERICAL COORDINATES IN QUANTUM MECHANICAL COLLINEAR REACTIVE SCATTERING*

---

*This paper appeared in Chemical Physics Letters 74, 257 (1980).

HYPERSPHERICAL COORDINATES IN QUANTUM MECHANICAL COLLINEAR REACTIVE SCATTERING*

Aron KUPPERMANN, Jack A. KAYE** and John P. DWYER[†]

Arthur Amos Noyes Laboratory of Chemical Physics,[‡]
California Institute of Technology, Pasadena, California 91125, USA

Received

A new hyperspherical coordinate method for performing atom-diatom quantum mechanical collinear reactive scattering calculations is described. The method is applicable at energies for which breakup channels are open. Comparison with previous results and new results at high energies for H + H_2 are given. The usefulness of this approach is discussed.

---

* This work was supported in part by a contract (No. F49620-79-C-0187) from the Air Force Office of Scientific Research.

** Work performed in partial fulfillment of the requirements for the Ph. D. degree in Chemistry at the California Institute of Technology.

[†] Present address: School of Law, Boalt Hall, University of California, Berkeley, CA 94720.

[‡] Contribution No. 6215.

1. INTRODUCTION

Triatomic exchange reactions of the type A + BC → AB + C, with A, B, and C representing atoms confined to move on a laboratory-fixed straight line, constitute the simplest reactive processes which present a basic characteristic of many chemical reactions: the dissolution of a chemical bond and the formation of a new one. The low mathematical dimensionality of the corresponding theory permits a straightforward analysis of this system, unencumbered by the mathematical complexities of molecular rotations. Such a collinear model is therefore useful for developing insight into the reaction process, especially for systems which are collinearly dominated, i.e., for which collinear configurations have energies considerably lower than corresponding bent ones. For these reasons, collinear reactions have been the subject of extensive theoretical studies over the last decade. Reviews of the methods developed for such studies have been published previously [1-3]. We consider in this paper electronically adiabatic reactions of this type, although the method described is also applicable, with straightforward generalizations, to electronically nonadiabatic reactions.

The methods previously developed for studying these collinear processes are restricted to energies significantly below that for which the A + BC → A + B + C process is possible. Such breakup collisions, particularly when occurring in competition with exchange processes, have been particularly resilient to accurate quantum mechanical treatment [4]. In addition, accurate results for systems in which the central atom B is significantly lighter than the end atoms, such as the I + HI → IH + I reaction, have not been obtained so far by those methods, for reasons inherent to their nature (see Section 4). The use of hyperspherical coordinates, as described in the present paper, was developed in an attempt to overcome these shortcomings. Extension of these ideas to three dimensions was also kept in mind.

2. THEORY

Let r'_α, R'_α be, respectively, the BC internuclear distance and the distance of A to the center of mass G_{BC} of the BC molecule. Let r'_γ, R'_γ be the corresponding distances with the roles of A and C interchanged, as indicated in Figure 1. We define the Delves scaled coordinates [5] R_λ, r_λ $(\lambda = \alpha,\gamma)$ by

$$R_\lambda = a_\lambda R'_\lambda \; ; \quad r_\lambda = a_\lambda^{-1} r'_\lambda \; ; \quad a_\lambda = (\mu_{\lambda,\nu\kappa}/\mu_{\nu\kappa})^{\frac{1}{4}} \; . \tag{1}$$

In these equations, $\lambda\nu\kappa$ is either $\alpha\beta\gamma$ or $\gamma\beta\alpha$, $\mu_{\nu\kappa}$ is the reduced mass of m_ν and m_κ, $\mu_{\lambda,\nu\kappa}$ is the reduced mass of m_λ and $(m_\nu + m_\kappa)$, and m_α, m_β, and m_γ are the masses of A, B, and C, respectively. In terms of R_λ, r_λ, the relative nuclear motion hamiltonian of the triatomic system is

$$H = -\frac{\hbar^2}{2\mu}\left(\frac{\partial^2}{\partial R_\lambda^2} + \frac{\partial^2}{\partial r_\lambda^2}\right) + V_\lambda(R_\lambda, r_\lambda) \qquad \lambda = \alpha,\gamma \; , \tag{2}$$

where

$$\mu = [m_\alpha m_\beta m_\gamma/(m_\alpha + m_\beta + m_\gamma)]^{\frac{1}{2}} \tag{3}$$

is a reduced mass of the system and is the same whether $\lambda = \alpha$ or γ, and $V_\lambda(R_\lambda, r_\lambda)$ is the electronically adiabatic potential energy surface being considered, in λ coordinates. According to Eq. (2), the internal collinear motion of the triatomic system is isomorphic with that of a single point P of mass μ in the two-mathematical-dimensional (2MD) R_λ, r_λ configuration space, subject to the potential V_λ. The corresponding Porter-Karplus (PK) ground state collinear potential energy surface for the $H + H_2$ system [6] is depicted in Figure 2.

The coupled-equations approach to solving the Schrödinger equation for the Hamiltonian of Eq. (2) consists in choosing an "internal" variable x and a "propagation" variable y (transverse to x) which may be different in different regions of configuration space. The wavefunction $\psi(x, y)$ is then expanded in a quasi-complete discrete pseudo-vibrational basis set $\{\phi_n(x)\}$ of variable x, and the resulting coupled equations in the coefficients $g_n(y)$ of this expansion are integrated. Enough linearly-independent solutions of this type are obtained to permit the calculation of the $\underline{\underline{R}}$ matrix, and from it the $\underline{\underline{S}}$ matrix and the transition probability matrix $\underline{\underline{P}}$ [1], and care is taken to ascertain their convergence with respect to the number of terms used in this expansion. In the method developed by Light and co-workers [7], x and y have been chosen to be natural collision coordinates, whereas in that of Kuppermann [1b, 8], they are r_α and R_α for the reagent region of configuration space; the circular polar coordinates r and φ (centered on a point P_0 deeply imbedded in the A + B + C dissociation plateau) for the strong interaction region; and r_γ and R_γ for the product region. In both these methods, the wavefunction is assumed to vanish outside a reaction gulley which excludes the dissociative regions of configuration space.

In the present method, we use for x, y the circular polar coordinates ρ, α (see Figure 2) around the origin 0 of the R_λ, r_λ configuration space (for which origin A, B, and C coincide). Similar coordinates have been previously used by Tang, Kleinman, and Karplus to study a piece-wise flat potential energy surface system [9]. In the generalization to three-dimensional collisions [5, 10], ρ is a hyperdistance in a 6MD configuration space. The range of α is 0 to $\alpha_{max} = \tan^{-1}(m_\beta M/m_\alpha m_\gamma)^{\frac{1}{2}}$, where $M = m_\alpha + m_\beta + m_\gamma$. At the extremes of this range (where B coincides with A or C, respectively) the potential function V becomes, for all chemical purposes, infinite and the wavefunction vanishes. The nuclear motion Hamiltonian in these coordinates is

$$H(\rho, \alpha) = -\frac{\hbar^2}{2\mu}\left[\frac{\partial^2}{\partial\rho^2} + \frac{1}{\rho}\frac{\partial}{\partial\rho} + \frac{1}{\rho^2}\frac{\partial^2}{\partial\alpha^2}\right] + V(\alpha, \rho) \quad . \tag{4}$$

In Figure 3 we depict V as a function α for various constant values $\bar{\rho}$ of ρ for the PK surface. It can be seen that, because of the divergence of V at $\alpha = 0$ and $\alpha = \alpha_{\max}$, the eigenfunctions of

$$h(\alpha;\bar{\rho}) = -\frac{\hbar^2}{2\mu\bar{\rho}^2}\frac{\partial^2}{\partial\alpha^2} + V(\alpha,\bar{\rho}) \tag{5}$$

form an infinite but discrete set $\{\phi_n(\alpha;\bar{\rho})\}$ which samples the entire range of α, including those values which, for large $\bar{\rho}$, correspond to dissociated A + B + C configurations. In Figure 4 we display the even (see end of section) eigenfunctions for the PK surface, for $\bar{\rho} = 6$ bohr and n = 0 through 24 (in steps of 2), as well as the corresponding eigenvalues $E_n(\bar{\rho})$. The highest of these is larger than the dissociation energy 4.75 eV of H_2. Since the H_2 Morse curve included in the PK surface supports 17 bound states, for large $\bar{\rho}$ (larger than 11 bohr, it turns out), $E_n(\bar{\rho})$ exceeds 4.75 eV for $n \geq 32$. The corresponding eigenfunctions sample the dissociated plateau region of configuration space, which thereby, in principle, is made accessible to the system. Whether or not the system samples that region depends on energetic and dynamic considerations, rather than it being excluded by a priori considerations. Expanding an eigenfunction $\psi^n(\rho,\alpha)$ of $H(\rho,\alpha)$ according to

$$\psi^n(\rho,\alpha) = \rho^{-\frac{1}{2}} \sum_{n'=0}^{N} g^n_{n'}(\rho;\bar{\rho})\phi_{n'}(\alpha;\bar{\rho}) \tag{6}$$

leads without much difficulty to the following differential equation in the matrix $\underset{\approx}{g}(\rho;\bar{\rho})$, whose n'^{th} row and n^{th} column element is $g^n_{n'}$:

$$-\frac{\hbar^2}{2\mu}\frac{d^2\underset{\approx}{g}(\rho;\bar{\rho})}{d\rho^2} + \underset{\approx}{W}(\rho;\bar{\rho})\underset{\approx}{g}(\rho;\bar{\rho}) = \underset{\approx}{E}(\rho;\bar{\rho})\underset{\approx}{g}(\rho;\bar{\rho}) \ . \tag{7}$$

$\underset{\approx}{W}$ and $\underset{\approx}{E}$ are interaction and energy matrices whose n′ row and n column elements are given by

$$W^{n}_{n'}(\rho;\bar{\rho}) = \langle n | V(\alpha,\rho) - \frac{\bar{\rho}^2}{\rho^2} V(\alpha,\bar{\rho}) | n' \rangle \tag{8}$$

$$E^{n}_{n'}(\rho;\bar{\rho}) = [E + \frac{\hbar^2}{8\mu\rho^2} - E_n(\bar{\rho})]\delta^{n}_{n'} \;, \tag{9}$$

where $|n'\rangle = \phi_{n'}(\alpha;\bar{\rho})$, the integration variable implied in Eq. (7) is α, E is the total energy of the system, and $\delta^{n'}_{n}$ the Kronecker symbol.

The reactive scattering problem is solved as follows. We choose a set of ρ_i ($i = 0, 1, \ldots, i_{max}$). In the range ρ_{i-1} to ρ_i we chose a $\bar{\rho}_i$ for which we calculate the $\phi_n(\alpha;\bar{\rho}_i)$ by a numerical method (such as a finite difference one [11]). We then integrate numerically the coupled equations (7) from ρ_{i-1} to ρ_i, setting $\underset{\approx}{g}(0;\bar{\rho}_0) = \underset{\approx}{0}$ and $\underset{\approx}{g}'(0;\bar{\rho}_0) = \underset{\approx}{I}$ and requiring continuity of $\psi_n(\rho,\alpha)$ and of its derivative with respect to ρ at the boundaries $\rho = \rho_i$ between the ρ_{i-1} to ρ_i and ρ_i to ρ_{i-1} regions. The integration method used in the present calculations was that of Gordon [12], together with the reorthogonalization procedure of Riley and Kuppermann [13]. In this manner we obtain the $\psi^n(\rho,\alpha)$ for $0 \le \alpha \le \alpha_{max}$ and $\rho_0 \le \rho \le \rho_{i_{max}}$. We then project numerically these ψ^n onto the bound state eigenfunctions of BC and AB at a large and constant value of R_λ, from which we get by standard methods [1b] the $\underset{\approx}{R}$, $\underset{\approx}{S}$, and $\underset{\approx}{P}$ matrices defined above for energies below the A + B + C dissociation limit. Their convergence with respect to i_{max}, ρ_0, $\rho_{i_{max}}$, and the number N of terms used in Eq. (6) is established empirically, as is the symmetry of the open channel part of $\underset{\approx}{R}$ and the unitarity of the open channel part of $\underset{\approx}{S}$. For energies above that dissociation limit, the procedure described for the three-dimensional case by Delves [5b] should be used.

For symmetric reactions of the type $A + BA \rightarrow AB + A$, the potential energy function $V(\alpha,\rho)$ is symmetric with respect to the $\alpha = \alpha_{max}/2$ line in configuration space, and the solutions which are even or odd for reflection through that line may be obtained separately, thereby decreasing the amount of numerical effort.

3. RESULTS

The results of accurate calculations for the $H + H_2 \rightarrow H_2 + H$ reaction on the PK surface, using the hyperspherical coordinate method just described, are given in Figure 5, together with those of previous calculations. We plot in that figure the vibrationally adiabatic distinguishable-atom reaction probabilities P^R_{nn} from the initial vibrational state n of the reagents to the same vibrational state of the reaction products. The points in that figure are some of the present results, which are converged and accurate to about 1% or better. They have been carried out so far up to total energies of 2.88 eV (about 60% of the H_2 dissociation energy), without any signs of quality deterioration. The dashed lines are cubic spline fits to these results (which include a larger number of points than those displayed) for total energies in excess of 1.75 eV for the P^R_{00} and P^R_{11} curves, and for $E_{tr} > 0$ for the others. For comparison, the solid lines are cubic spline fits to the results of Schatz and Kuppermann [14], which were carried out using one of the previous methods [8], up to total energies of 1.75 eV for P^R_{00} and P^R_{11}. These latter results [14] are essentially indistinguishable from those of Diestler [15], who performed accurate calculations on the same PK surface at total energies up to 1.21 eV. For total energies for which other calculations are available (≤ 1.75 eV), the present results agree with the previous ones within the computational accuracy of about 1%. This validates the hyperspherical coordinate method.

An additional useful characteristic of this new calculational procedure is that convergence with respect to the number of basis functions used is more rapid than for other methods. For example, for E_{tr} in the range 0.22 eV to 0.43 eV, and using only two channels (one open and one closed, asymptotically), the absolute error in P^R_{00} is less than 0.02 in the new method, whereas for a previous method [1b, 8] that error is as high as 0.23. If four channels are used, the hyperspherical coordinate method produces reliable values of P^R_{00}

(to within 0.02) up to translational energies of 1.03 eV, whereas that previous method requires seven or eight channels for equivalent convergence. This faster basis set convergence efficiency may make this method particularly well suited for three-dimensional calculations, for which high efficiency is required for calculational feasibility [18, 19].

It is interesting to note that the P^R_{nn} curves for $n \geq 1$ in Figure 5 are very similar to each other and are nearly identical when plotted as functions of the initial relative translational energy. This is strongly suggestive that an effective 1MD potential may be found which duplicates all of them. The P^R_{00} curve is also similar to the $n \geq 1$ P^R_{nn} ones if energies below that of its first resonance are neglected. This comparison suggests that the second resonance in P^R_{00} and the first one in the P^R_{nn} $(n \geq 1)$ have analogous dynamical origins.

4. DISCUSSION AND CONCLUSIONS

The hyperspherical coordinate method seems capable of tackling reactive scattering problems at fairly high energies. The present calculations are being extended to energies above the H_2 dissociation limit. The method can also be generalized to electronically nonadiabatic processes in a straightforward manner [18, 19].

The difficulty other methods [1b, 7, 8] have in tackling reactions with a light middle atom, such as I + HI → IH + I, is related to the very sharp and rapidly changing curvature of the minimum energy path of these systems, in the strong interaction region of configuration space. This in turn is due to the smallness of the corresponding skew angle, $\alpha_{max} = \tan^{-1}(m_\beta M/m_\alpha m_\gamma)^{\frac{1}{2}}$, which in that system is about 7°. The present method does not suffer from this difficulty, since the propagation coordinate ρ is not related to that curvature.

Finally, the hyperspherical coordinate approach seems particularly suitable to the study of 3D systems [10], since it greatly simplifies the A + BC bifurcation problem associated with the existence of two kinds of reactive products, AB + C and AC + B. The solution to this problem is contained in the nature of the ρ = constant basis sets, which are the 3D generalizations of the $\phi_n(\alpha;\bar{\rho})$ eigenfunctions used in the present method. Such calculations are currently being performed in our laboratory [20].

5. ACKNOWLEDGMENTS

The calculations reported in this paper were performed on the Dreyfus-NSF Theoretical Chemistry Computer (VAX 11/780) at Caltech and on the IBM 370/158 computer of Ambassador College, Pasadena, California, for which we express our appreciation. One of us (JAK) would like to thank Dr. Gregory A. Parker for helpful discussions.

References

[1] A. Kuppermann, (a) Progress in the Quantum Dynamics of Reactive Molecular Collisions, in The Physics of Electronic and Atomic Collisions (Invited Lectures, Review Papers and Progress Reports of the IXth International Conference on the Physics of Electronic and Atomic Collisions, Seattle, Washington, 24-30 July 1975), J. S. Risley and R. Geballe, Eds. (University of Washington Press, Seattle, 1976), pp. 259-274; (b) Theoretical Aspects of the Mechanism of Simple Chemical Reactions, in the Proceedings of the Summer School on Chemical Photophysics, Les Houches, France, 18-30 June 1979, P. Glorieux, D. Lecler, and R. Vetter, Eds. (Centre de la Recherche Scientifique, Paris, 1979), pp. 293-384.

[2] D. Micha, in Advances in Chemical Physics, K. P. Lawley, Ed. (J. Wiley and Sons, New York, 1975), Vol. 30, pp. 7-75.

[3] J. N. L. Connor, Comput. Phys. Commun. 17 (1979) 117.

[4] D. J. Diestler, Collision-Induced Dissociation. I. Quantal Treatment, in Atom-Molecule Collision Theory, R. B. Bernstein, Ed. (Plenum Press, New York, 1979), pp. 655-667.

[5] L. M. Delves, Nucl. Phys. (a) 9 (1959) 391; (b) 20 (1960) 275.

[6] R. N. Porter and M. Karplus, J. Chem. Phys. 40 (1964) 1105.

[7] (a) C. C. Rankin and J. C. Light, J. Chem. Phys. 51 (1969) 1701; (b) G. Miller and J. C. Light, ibid. 54 (1971) 1635, 1643.

[8] A. Kuppermann (a) in Proceedings of the Conference on Potential Energy Surfaces in Chemistry, W. A. Lester, Ed. (University of California, Santa Cruz, 1970), pp. 121-124; (b) in Proceedings of the VIIth International Conference on the Physics of Electronic and Atomic Collisions (North-Holland Publishing Co., Amsterdam, 1971), pp. 3-5.

[9] K. T. Tang, B. Kleinman and M. Karplus, J. Chem. Phys. 50 (1969) 1119.

[10] A. Kuppermann, Chem. Phys. Lett. 32 (1975) 374.

[11] D. G. Truhlar, J. Comp. Phys. 10 (1972) 123.

[12] R. Gordon, J. Chem. Phys. 51 (1969) 14.

[13] M. E. Riley and A. Kuppermann, Chem. Phys. Lett. 1 (1968) 537.

[14] G. C. Schatz and A. Kuppermann (a) Phys. Rev. Lett. 35 (1975) 1266; (b) unpublished calculations.

[15] D. J. Diestler, J. Chem. Phys. 54 (1971) 4547.

[16] G. C. Schatz and A. Kuppermann, J. Chem. Phys. (a) 62 (1975) 2502; (b) 65 (1976) 4668.

[17] A. B. Elkowitz and R. E. Wyatt, J. Chem. Phys. (a) 62 (1975) 2504; (b) 63 (1975) 702.

[18] J. M. Bowman, S. C. Leasure and A. Kuppermann, Chem. Phys. Lett. 44 (1976) 499.

[19] Z. H. Top and M. Baer, J. Chem. Phys. 66 (1977) 1363.

[20] (a) R. T. Ling and A. Kuppermann, in Electronic and Atomic Collisions (Abstracts of Papers of the IXth International Conference on the Physics of Electronic and Atomic Collisions, Seattle, Washington, 24-30 July 1975), J. S. Risley and R. Geballe, Eds. (University of Washington Press, Seattle, 1975), pp. 353-354.

(b) J. K. C. Wong and A. Kuppermann, in Abstracts of Papers, Pacific Conference on Chemistry and Spectroscopy, Pasadena, California, 10-12 October 1979), p. 39.

Figure Captions

Fig. 1. Distance coordinates for collinear triatomic system.

Fig. 2. Porter-Karplus potential energy surface V for the H + H_2 system in Delves scaled coordinates R_α, r_α. The solid curves are equipotential contours at the total energies (with respect to the bottom of the isolated H_2 well) indicated in the lower right side of the figure. The dashed line is the minimum energy path. The polar coordinates ρ, α of a general point P in this R_α, r_α configuration space are also indicated. The three arcs of circles at $\rho = 2.00$, 3.13, and 6.00 bohr are cuts along which V is displayed in Figure 3. The second of these passes through the saddle point, indicated by a cross in the figure.

Fig. 3. Potential energy function $V(\alpha, \bar{\rho})$ of Figure 2 as a function of α for the following four constant values $\bar{\rho}$ of ρ: 2.00, 3.13, 6.00, and 20.00 bohr. The first three of these values correspond to the arcs displayed in Figure 2. The fourth one is outside of that figure.

Fig. 4. Potential energy function, eigenfunctions, and eigenvalues of the one-dimensional hamiltonian of Eq. (5), for $\bar{\rho} = 6$ bohr. The double-well curve is the same as that in Figure 3. The horizontal lines represent the eigenvalues for the quantum numbers given (for every other eigenvalue) at the right of the figure, for the even eigenfunctions (i.e., those which are symmetric for reflection through the $\alpha = 30°$ line). The latter are the oscillatory curves around the eigenvalue lines, and have been scaled so as not to overlap each other. The corresponding relative scaling factors are 1.00, 1.12, 1.08, 1.15, 1.18, 1.28, 1.59, 1.69, 1.45, 1.18, 1.01, 0.90, and 0.87.

Fig. 5. Vibrationally adiabatic reaction probabilities P^R_{nn} for the H + $H_2(n) \rightarrow H_2(n)$ + H exchange reaction on the Porter-Karplus potential energy surface, as a function of initial relative translational energy E_{tr} and total energy E

(measured with respect to the bottom of the isolated H_2 well). The points are the results of the present calculations. The solid P^R_{00} and P^R_{11} curves are cubic spline fits to the previous results of Schatz and Kuppermann, which were performed up to E = 1.75 eV. The dashed curves are cubic spline fits to the present points, including some omitted from the plots for reasons of visibility.

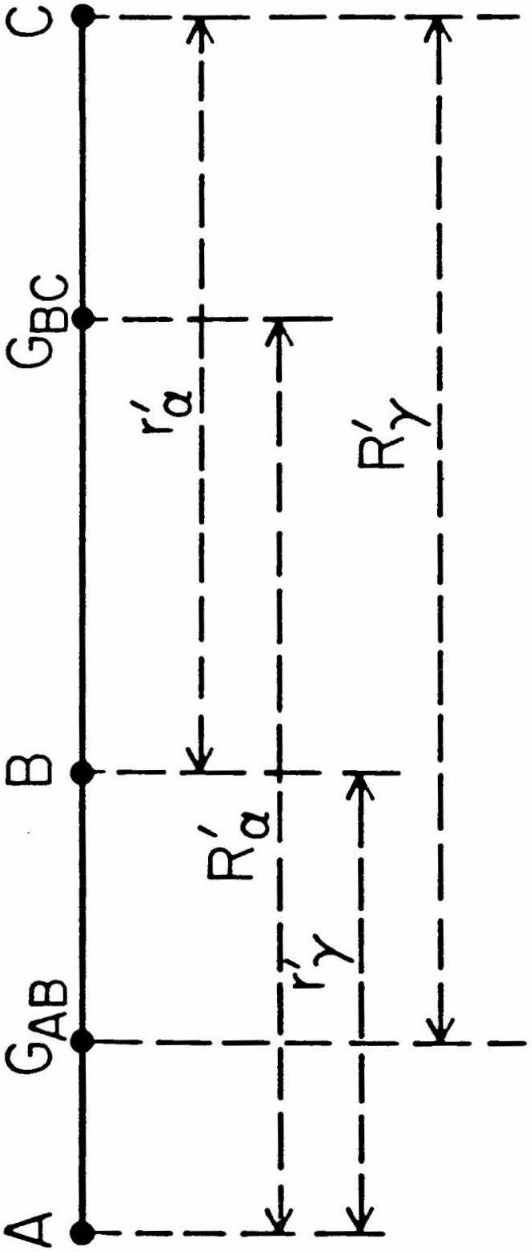

Figure 1.

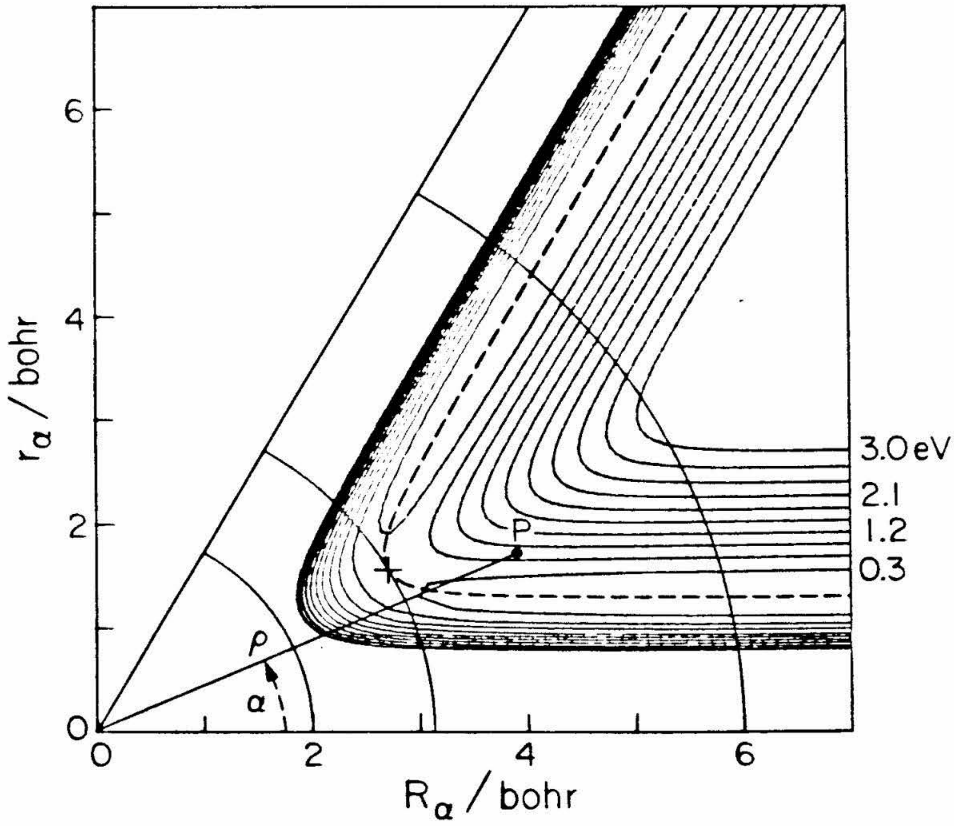

Figure 2.

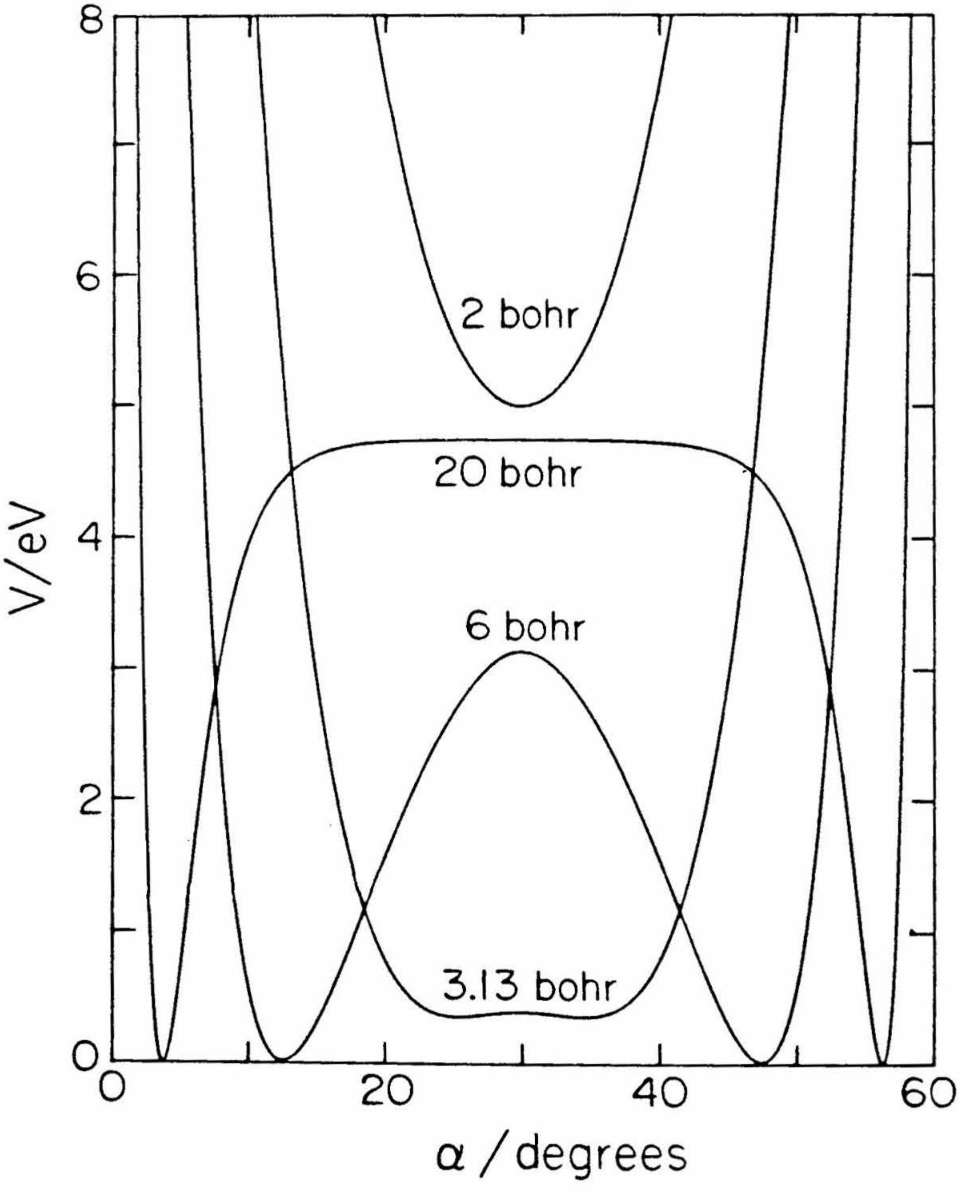

Figure 3.

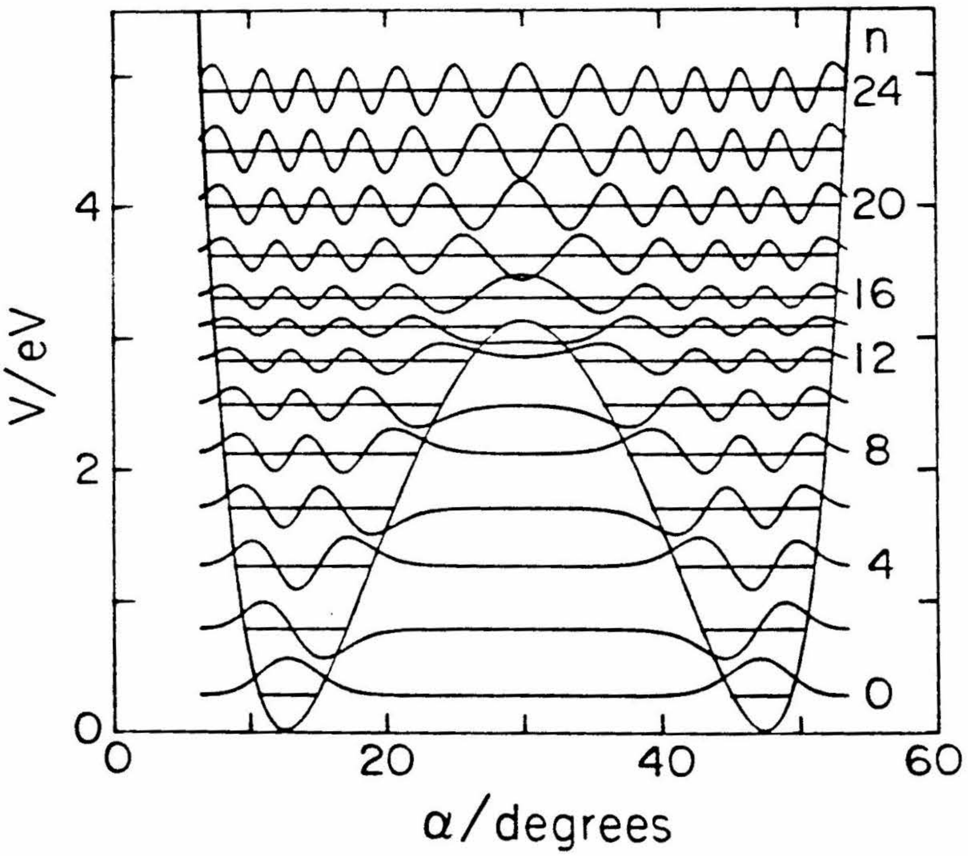

Figure 4.

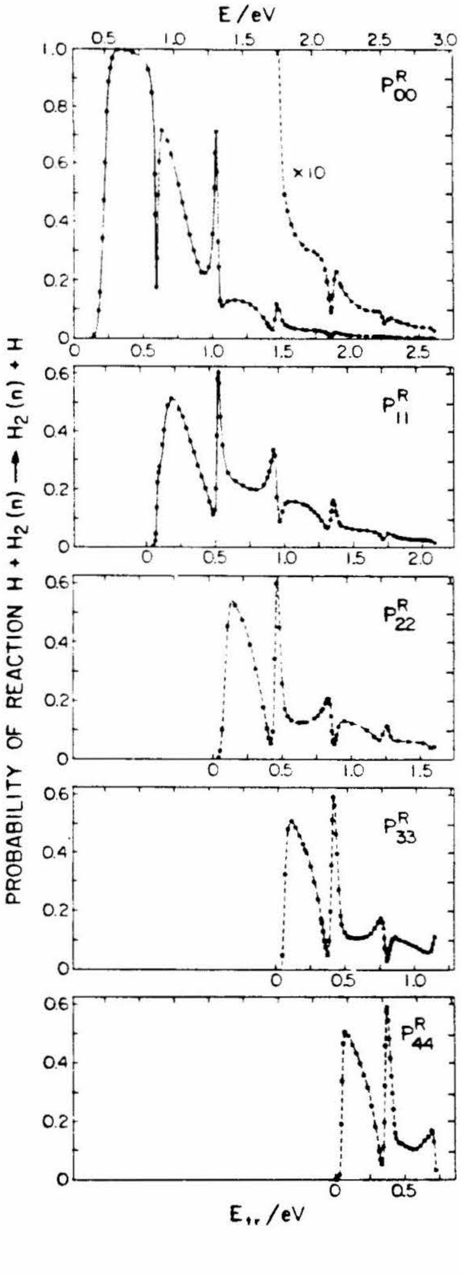
E / eV
0.5
1.0
1.5
2.0
2.5
3.0
1.0
0.8
0.6
0.4
0.2
0
P$^R_{00}$
×10
0
0.5
1.0
1.5
2.0
2.5
0.6
0.4
0.2
0
P$^R_{11}$
0
0.5
1.0
1.5
2.0
0.6
0.4
0.2
0
P$^R_{22}$
0
0.5
1.0
1.5
0.6
0.4
0.2
0
P$^R_{33}$
0
0.5
1.0
0.6
0.4
0.2
0
P$^R_{44}$
0
0.5
E$_{tr}$ /eV
PROBABILITY OF REACTION H + H$_2$(n) ⟶ H$_2$(n) + H

Figure 5.

III. 2 COLLINEAR QUANTUM MECHANICAL PROBABILITIES FOR THE I + HI $\longrightarrow$ IH + I REACTION USING HYPERSPHERICAL COORDINATES[*]

---

[*] This paper appeared in Chemical Physics Letters 77, 573 (1981).

COLLINEAR QUANTUM MECHANICAL PROBABILITIES FOR THE I + HI → IH + I REACTION USING HYPERSPHERICAL COORDINATES*

Jack A. KAYE** and Aron KUPPERMANN

Arthur Amos Noyes Laboratory of Chemical Physics,‡
California Institute of Technology, Pasadena, California 91125, USA

Received

Calculations of quantum mechanical probabilities for the I + HI → IH + I electronically adiabatic exchange reaction were performed using hyperspherical coordinates. In spite of the small skew angle of 7°, accurate results were obtained with a small number of channels. These results are compared with those of quasi-classical trajectory calculations.

---

* Research supported in part by the U. S. Air Force Office of Scientific Research (Contract No. F49620-79-C-0187).

** Work performed in partial fulfillment of the requirements for the PhD in Chemistry at the California Institute of Technology.

‡ Contribution No. 6056.

1. Introduction

Among the most important results to come from quantum mechanical calculations of the probabilities of chemical reactions are the existence and significance of resonant processes. Reactive scattering resonances were first found in collinear calculations on the H + H_2 system[1, 2] and have been observed in a variety of other collinear atom-diatom calculations, including those on the F + H_2, HD, D_2,[3, 4] Cl + H_2,[5] I + H_2,[6] Ba + N_2O,[7] I + HI,[8] and Cl + HCl[9] systems. The F + H_2 system and its isotopically substituted counterparts are of particular interest because of their simplicity and relative ease of study by both theoretical and experimental techniques. It has recently been proposed that these systems are prime candidates for experimental observation of resonances.

Approximate j_z-conserving three-dimensional calculations on the F + H_2 system have been performed, and they suggest that the resonance found in the collinear calculations exists in the three-dimensional world.[10] Molecular beam experiments also provide indications of a resonance in this system.[11]

Resonances have been observed in a wide variety of scattering processes and are known to be associated with the existence of long-lived metastable states.[12] Once a resonance is known to exist in a chemically reactive system, one desires to know what features of the potential energy surface are responsible for its existence and what its lifetime is. The latter is especially important in determining what systems are the most suitable for the experimental detection of resonances.

Babamov and Kuppermann have recently developed a model that gives a physical interpretation and predicts the location of the lowest energy resonance in the collinear F + H_2 and isotopically substituted far [13], 40 channels were required. The small skew angle permits certain dynamical approximations to be made, however, and a few approximate treatments of these H-L-H systems, both quantum mechanical and classical, have been developed [14].

In this paper we report the results of accurate coupled-channel electronically adiabatic quantum mechanical calculations for the collinear reaction,

$$\mathrm{I} + \mathrm{HI} \rightarrow \mathrm{IH} + \mathrm{I} \;, \tag{2}$$

using hyperspherical coordinates. Two slightly different potential energy surfaces were used. We also performed quasi-classical trajectory calculations on these surfaces. In Section 2 we describe the method and the surfaces, and in Section 3 we present and discuss the results.

2. Computational Method and Potential Energy Surfaces

The quantum mechanical method of hyperspherical coordinates developed previously [15] presents no particular difficulty when the skew angle is small, and in the calculations reported here, that method was used without change. Six even and six odd basis functions were used, and with them convergence of the transition probabilities to ± 0.005 and of flux to ± 0.0001 was usually achieved. Standard methods were used for the collinear quasi-classical trajectory calculations [16, 17].

The potential energy surfaces used were of the extended LEPS form [18] and their parameters and properties are listed in Table I. The Morse oscillator [19] parameters for one of the surfaces (surface B) were those used previously [20] for trajectory calculations on the $H + I_2$ system. However, we changed the Sato parameters from zero to 0.20 for HI and 0.125 for I_2 in order to decrease the barrier height from about 14.2 kcal/mole to about 1.5 kcal/mole. Although the barrier for the IHI system is not known, ab initio calculations on related systems (F + HF, Cl + HCl) suggest that a barrier of more than a few kcal/mole is unreasonably high [21]. The other surface (surface A) has the same LEPS parameters as surface B, except that the HI dissociation energy was increased by 3 kcal/mole. The main effect of this change is in the saddle point region, as can be seen by observing the 0.06 eV equipotential in the contour plots displayed in Figure 1.

3. Results and Discussion

Plots of the quantum probabilities of reaction (2) from the ground vibrational state of the reagents to the same state of the products, as a function of translational energy, are given in Figs. 2 and 3 for each of the two surfaces. For the low energy (0-15 meV) range covered by Figure 3, the curve for surface A displays a sharp peak followed by a second broader peak, whereas for surface B, the sharp feature is absent and the other one is much broader and less intense. In order to assess the nature of these features, we have made an Argand plot [22] of the corresponding scattering matrix element, S^R_{00}, for surface A in Figure 4. It can be seen that the sharp peak in Figure 3 is associated with a loop in Figure 4, along which a representative point moves counterclockwise with increasing energy, as indicated by the arrow in the upper part of the figure. This clearly demonstrates a scattering resonance. In the energy region corresponding to the second peak for surface A, the Argand diagram does not display such behavior, nor does that for surface B (not displayed), which has the appearance of a smooth clockwise spiral.

It has been shown [23] that for collinear symmetric atom-diatom systems of the form A + BA, at energies for which vibrationally excited channels of the BA molecule are closed, the difference, $\delta_S - \delta_A$, between the symmetric and antisymmetric eigenphase shifts increases by π across a narrow isolated resonance. In Figure 5 we display δ_S, δ_A, and their difference as a function of reagent translational energy for surface A. Over the energy range considered, only the $v = 0$ state of HI is accessible, and the open part of the $\underset{=}{R}$ matrix has dimensions 2×2. Its eigenvectors are independent of energy and correspond to symmetric and antisymmetric scattering states, and its eigenvalues are $\tan \delta_S$ and $\tan \delta_A$, respectively. It can be seen from Figure 5 that $\delta_S - \delta_A$

changes by approximately 2.6 radians ($\approx 0.85\ \pi$ radians) over the energy range associated with the narrow peak in Figure 3. This is slightly less than π radians because this resonance is not completely isolated, as is indicated by the fact that the reaction probability drops to 0.2 rather than zero after that peak, before starting to increase again. The time delay associated with this resonance,

$$\tau = 2\hbar\, d(\delta_S - \delta_A)/dE \ ,$$

has a maximum value of 2.04×10^{-11} sec, which is much larger than the symmetric stretch vibration period of 4.60×10^{-13} sec for the saddle point configuration of surface A. For comparison, across the broad peak in Figure 3 for surface B, $\delta_S - \delta_A$ increases by $0.14\ \pi$ radians only, and the corresponding maximum value of τ is 4.74×10^{-13} sec, compared with 4.64×10^{-13} sec for the saddle point symmetric stretch period of that surface. We conclude that the sharp peak in Figure 3 for surface A is associated with a strong, long-lived resonance, whereas for surface B, the broad peak in that figure is at most associated with a very weak resonance. This indicates once more [9a, 24] the great sensitivity that dynamic resonances on reactive systems can have to details of the saddle point region of potential energy surfaces. This sensitivity holds out the enticing possibility that the experimental measurement of such resonances may be useful in the determination of the characteristics of that region of potential energy surfaces.

An interpretation of this resonance can be obtained as follows. The hyperspherical coordinate method used in the present calculations [15] involves a radial distance ρ and a polar angle α associated with the Delves coordinates R_α, r_α of Figure 1. For fixed ρ, we can calculate the eigenvalues $E_n(\rho)$ of the α motion. A plot of the 12 lowest such eigenvalues versus ρ is given in Figure

6, and they show minima for the ones corresponding to symmetric eigenfunctions. Since motion from reagents to products across the strong interaction region of the surface involves a relatively small change in ρ and a relatively large fractional change in α, an α-adiabatic model of resonances was proposed recently [25]. This model consists of solving the Schrödinger equation for the quasi-bound one-dimensional ρ motion on each of the individual $E_n(\rho)$ curves, in analogy to the Born-Oppenheimer separation of electronic and nuclear motions. It was shown to work well for the first resonance in H + H_2 and its symmetric isotope counterparts. For the n = 0 curve of Figure 6, this model predicted the position and width of the surface A resonance indicated by "Model I" in Table II. The agreement with the exact values is satisfactory.

Babamov and Marcus [26] have recently shown that for H-L-H symmetric systems, below the opening of the first excited state, the P_{00}^R reaction probability is related to the phase shifts δ_S^{1D} and δ_A^{1D}, obtained from the one-dimensional ρ motion described above, by the expression

$$P_{00}^R = \sin^2(\delta_S^{1D} - \delta_A^{1D}).$$

Using this relation, we obtain the peak locations and widths given in the "Model II" column of Table II. The agreement with the accurate values is about the same as for Model I for the surface A resonance. However, it is better than Model I in that it also predicts quite well the position and height of the broad peak for surface B, which is not a resonance, whereas Model I is not applicable to features that are not resonances.

The difference in the dynamics of the reaction on the two surfaces at higher energies consists of a shift of the P_{00}^R curve by about 30 or 35 meV to the right on going from surface A to surface B. This shift is significantly higher than either the difference between the corresponding barrier heights

(7.5 meV) or between the reagent zero-point energies measured with respect to the corresponding barrier tops (10.3 meV). The reason for this may be that, since the reagent ground state energies are significantly greater than the saddle point energy, the sharp skew angle of the coordinate system makes "corner-cutting" quite likely. This suggests that the dominant region of the surface occurs at larger values of ρ than that of the saddle point. Additional information on this matter can be obtained from maps of quantum streamlines of probability current density or classical trajectories.

The oscillatory nature of the P_{∞}^{R} versus energy curves at translational energies above 10 meV is not of a quantum nature, as it is also present in the classical trajectory results displayed in Figure 2.

We wish to emphasize the ease with which the method of hyperspherical coordinates may be applied to collinear $\underset{\frown}{\underline{H}}$-$\underset{\frown}{\underline{L}}$-$\underset{\frown}{\underline{H}}$ systems. Applications of previous methods based on a propagation variable that scans the potential energy surface from the reagent region through the strong interaction region to the product region [8, 27, 28] are made very difficult by the smallness of the skew angle. Indeed, these methods involve expansions in eigenfunctions of cuts of the surface along a direction more or less transverse to the minimum energy path, and, as a result of that small angle, such cuts are very broad and support a large number of bound states.

Indeed, for the IHI system considered in this paper, the symmetric stretch cut through the surface A saddle point supports 50 bound states with energies below that of the v = 2 state of the isolated HI molecule, which is open at the highest energy considered in these calculations. In order to incorporate all such open local states and a sufficiently large number of closed states in that expansion so as to achieve reasonable convergence of the results would require an unreasonably large number of channels. By contrast, the present method requires only six even and six odd channels, as described in Section 2. The essential reason for the adequacy of such a small number of channels is that the hyperspherical coordinates avoid a proliferation of open-channel basis functions. Indeed, for these coordinates the number of open channels in the strong interaction region is about the same as it is in the separated reagent or separated product regions of the potential energy surface, as shown in Figure 6. This method is therefore to be preferred for the study of collinear H-L-H systems, whether symmetric or not.

Acknowledgments

We would like to thank Dr. Vasil Babamov for many helpful discussions. The calculations reported were performed on the Dreyfus-NSF Theoretical Chemistry Computer (VAX 11/780) which was funded through grants from the Camille and Henry Dreyfus Foundation, the National Science Foundation (Grant No. CHE78-20235), and the Sloan Fund of the California Institute of Technology, and on the IBM 370/158 computer of Ambassador College, Pasadena, California, for which we express our appreciation.

Table I

Parameters and properties of extended LEPS potential energy surfaces A and B

		HI	I_2
β (bohr^{-1})		0.9260	0.9843
R_e (bohr^{-1})		2.0236	5.0457
D_e (eV)	A)	3.3303	1.5567
	B)	3.2002	1.5567
Δ		0.2	0.125
Saddle Point Location (bohr)			
	A)	(3.366, 3.366)	
	B)	(3.370, 3.370)	
Barrier Height (kcal/mole)			
	A)	1.353	
	B)	1.526	
HI Zero-Point Energy (eV)			
	A)	0.14447	
	B)	0.14160	

Table II

Calculated and predicted properties of peaks of reaction probability versus energy curves

	Exact	Model I[a)]	Model II[b)]
Surface A			
Resonance Location (meV)	6.08	4.7	4.7
Resonance width (meV)			
FWHM	0.16	0.12	0.13
Surface B			
Peak Location (meV)	8.00	c)	8.2
Maximum reaction probability	0.187	c)	0.19

a) Ref. [25].

b) Ref. [26].

c) Not applicable, since this feature is not a resonance.

References

[1] For a recent review, see M. R. Levy, Prog. React. Kin. 10 (1979) 1.

[2] R. D. H. Brown, G. P. Glass and I. W. M. Smith, J. Chem. Soc. Faraday Trans. II 71 (1975) 1963; J. R. Grover, C. R. Iden and H. V. Lilenfeld, J. Chem. Phys. 64 (1976) 4657; M. Kneba and J. Wolfrum, J. Phys. Chem. 83 (1979) 69; C.-C. Mei and C. B. Moore, J. Chem. Phys. 70 (1979) 1759; E. Würzberg and P. L. Houston, ibid. 72 (1980) 5915.

[3] R. D. H. Brown and I. W. M. Smith, Int. J. Chem. Kin. 10 (1978) 1; R. G. Macdonald and C. B. Moore, J. Chem. Phys. 68 (1978) 513; J. E. Butler, J. W. Hudgens, M. C. Lin and G. K. Smith, Chem. Phys. Letters 58 (1978) 216.

[4] P. A. Andresen and A. C. Luntz, J. Chem. Phys. 72 (1978) 5842.

[5] A. T. Pritt, Jr. and R. D. Coombe, J. Chem. Phys. 65 (1976) 2096; J. R. Wiesenfeld and G. L. Wolk, ibid. 67 (1977) 509; A. J. Grimley and P. L. Houston, ibid. 68 (1978) 3366.

[6] I. W. M. Smith and P. M. Wood, Mol. Phys. 25 (1973) 441; I. W. M. Smith, J. Chem. Soc. Faraday Trans. II 71 (1975) 1970.

[7] C. A. Parr, J. C. Polanyi and W. H. Wong, J. Chem. Phys. 58 (1973) 5; H. E. Bass, L. S. Kenton and D. L. Thompson, Chem. Phys. Letters 44 (1976) 45.

[8] A. Kuppermann, in Proceedings of the Summer School on Chemical Photophysics, Les Houches, France, 18-30 June 1979, eds. P. Glorieux, D. Lecler and R. Vetter (Centre de la Recherche Scientifique, Paris, 1979), pp. 293-384; Theory of Scattering, Vol. VIII, Theoretical Chemistry: Advances and Perspectives, D. Henderson and H. Eyring,

eds. (Academic Press, Inc., New York, 1980), in press.

[9] a) A. Kuppermann, in The Physics of Electronic and Atomic Collisions, Invited Lectures, Review Papers and Progress Reports of the IXth International Conference on the Physics of Electronic and Atomic Collisions, Seattle, Washington, 24-30 June 1975, eds. J. S. Risley and R. Geballe (University of Washington Press, Seattle, 1976), pp. 259-274.
b) G. C. Schatz and A. Kuppermann, J. Chem. Phys. 65 (1976) 4652, 4668.
c) A. Kuppermann, in Proceedings of the IXth International Conference on the Few Body Problem, ed. M. Moravcsik, Nuclear Physics A (North-Holland Publishing Co., Amsterdam, 1980), in press.

[10] A. B. Elkowitz and R. E. Wyatt, J. Chem. Phys. 62 (1975) 2504; 63 (1975) 702.

[11] R. B. Walker, E. B. Stechel and J. C. Light, J. Chem. Phys. 69 (1978) 2992.

[12] For a review, see J. N. L. Connor, Comput. Phys. Commun. 17 (1979) 117.

[13] M. Baer, J. Chem. Phys. 62 (1975) 305.

[14] E. J. Shipsey, J. Chem. Phys. 58 (1973) 232; J. P. Simons and P. W. Tasker, J. Chem. Soc. Faraday Trans. II 70 (1974) 1496; T. Shirai, K. Igushi and T. Watanabe, J. Phys. Soc. Jpn. 49 (1976) 1137; M. Kimura, Chem. Phys. Letters 45 (1977) 489; M. Ya Ovchinnikova, Chem. Phys. 36 (1979) 85.

[15] A. Kuppermann, J. A. Kaye and J. P. Dwyer, Chem. Phys. Letters 74 (1980) 257; J. P. Dwyer, Quantum Mechanical Studies of Molecular Scattering, Ph.D. Thesis, California Institute of Technology (1977); R. T. Ling and A. Kuppermann, in Electronic and Atomic Collisions,

Abstracts of Papers of the IXth International Conference on the Physics of Electronic and Atomic Collisions, Seattle, Washington, 24-30 July 1975, eds., J. S. Risley and R. Geballe (University of Washington Press, Seattle, 1975), pp. 353-354. A related method, using the same coordinates but a different asymptotic analysis, has been developed by G. Hauke, J. Manz and J. Römelt, J. Chem. Phys., to be published, and used by J. Römelt, Chem. Phys. Letters 74 (1980) 263.

[16] M. Karplus, R. N. Porter and R. D. Sharma, J. Chem. Phys. 43 (1965) 3259.

[17] R. N. Porter and L. M. Raff, in Dynamics of Molecular Collisions, Part B, ed. W. H. Miller (Plenum Press, New York, 1976) pp. 1-52; D. G. Truhlar and J. T. Muckerman, in Atom-Molecule Collision Theory, ed. R. B. Bernstein (Plenum Press, New York, 1979), pp. 505-565.

[18] P. J. Kuntz, E. M. Nemeth, J. C. Polanyi, S. D. Rosner and C. E. Young, J. Chem. Phys. 44 (1966) 1168.

[19] H. Eyring, J. Walter and G. E. Kimball, Quantum Chemistry (John Wiley, New York, 1944), pp. 272-273.

[20] M. D. Pattengill and J. C. Polanyi, Chem. Phys. 3 (1974) 1; M. D. Pattengill, J. C. Polanyi and J. L. Schreiber, J. Chem. Soc. Faraday Trans. II 72 (1976) 897.

[21] S. V. O'Neil, H. F. Schaefer III and C. F. Bender, Proc. Nat. Acad. Sci. USA 71 (1974) 104; P. Botschwina and W. Meyer, Chem. Phys. Letters 44 (1976) 449.

[22] G. C. Schatz and A. Kuppermann, J. Chem. Phys. 59 (1973) 964, and references cited therein.

[23] G. C. Schatz, Ph.D. Thesis, California Institute of Technology (1975); G. C. Schatz and A. Kuppermann, manuscript in preparation.

[24] F. M. Chapman and E. F. Hayes, J. Chem. Phys. 62 (1975) 4400; 65 (1976) 1032.

[25] J. P. Dwyer, Ph.D. Thesis, California Institute of Technology (1977); A. Kuppermann and J. P. Dwyer, in Electronic and Atomic Collisions, Abstracts of Contributed Papers, XIth International Conference on the Physics of Electronic and Atomic Collisions (Society for Atomic Collision Research, Japan, 1979), pp. 888-889.

[26] V. K. Babamov and R. A. Marcus, J. Chem. Phys. 74 (1981) 0000.

[27] C. C. Rankin and J. C. Light, J. Chem. Phys. 51 (1969) 1701; G. M. Miller and J. C. Light, ibid. 54 (1971) 1635, 1643.

[28] A. Kuppermann, in Proceedings of the Conference on Potential Energy Surfaces in Chemistry, ed. W. A. Lester (University of California, Santa Cruz, 1970), pp. 121-124; in Electronic and Atomic Collisions, Abstracts of Papers, VIIth International Conference on the Physics of Electronic and Atomic Collisions (North-Holland Publishing Co., Amsterdam, 1971), pp. 3-5; G. C. Schatz, J. M. Bowman, and A. Kuppermann, J. Chem. Phys. 63 (1975) 674.

Figure Captions

Fig. 1. Equipotential contour plots for I + HI, surfaces A and B, in the region near the saddle points. The solid curves are the contours and are equally spaced in increments of 0.02 eV, from 0.04 eV to 0.20 eV. The zero of energy is the bottom of the HI well. The surfaces are plotted in Delves scaled coordinates [15]. The X's mark the saddle points, the dashed lines are the steepest ascent and descent paths as calculated in Delves scaled coordinates.

Fig. 2. Transition probability for the reaction $I + HI\ (v = 0) \rightarrow IH\ (v' = 0) + I$ as a function of reagent translational energy. Quantum mechanical results are indicated by the solid lines; the circles indicate surface A, the squares surface B. Classical trajectory results are given by the dashed line for surface A and the dashed-dotted line for surface B. The lowest energy portion of the quantum curve for surface A has been omitted for reasons of clarity.

Fig. 3. Quantum mechanical transition probabilities as in Figure 2 for the low translational energy range. No classical trajectory results are shown.

Fig. 4. Argand diagram [22] for the $\underline{\underline{S}}$ matrix element S^R_{00} corresponding to the exchange reaction $I + HI\ (v = 0) \rightarrow IH\ (v' = 0) + I$ on surface A. Circles represent points spaced by 0.05 meV; triangles represent points spaced by 0.1 meV. The energies indicated are reagent translational energies. Arrows parallel to the curve indicate direction of increasing energy.

Fig. 5. Symmetric (δ_S, dashed line) and antisymmetric (δ_A, dashed-dotted line) eigenphase shifts as a function of reagent translational energy calculated for surface A. The difference $\delta_S - \delta_A$ (solid line) is also shown (the right-hand ordinate scale is the appropriate one for this quantity).

Fig. 6. Eigenvalues $E_n(\rho)$ for surface A as a function of the propagation coordinate ρ. These curves are pairwise degenerate at large ρ, the symmetric one being always lower than the corresponding antisymmetric one at small ρ. Values of n for the symmetric curves are shown at the top of the figure. The dashed line in the $E_0(\rho)$ curve shows the position of the resonance and lies slightly above $E_0(\infty)$.

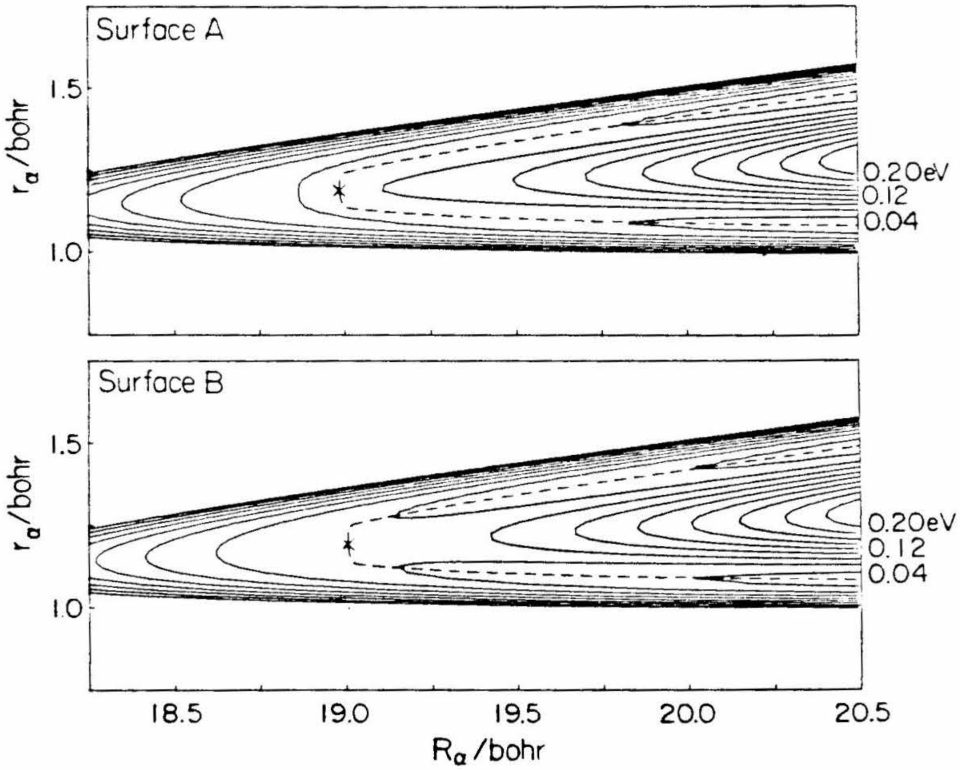
Surface A
Surface B
1.5
1.0
r_a/bohr
0.20eV
0.12
0.04
18.5
19.0
19.5
20.0
20.5
R_a/bohr

Figure 1.

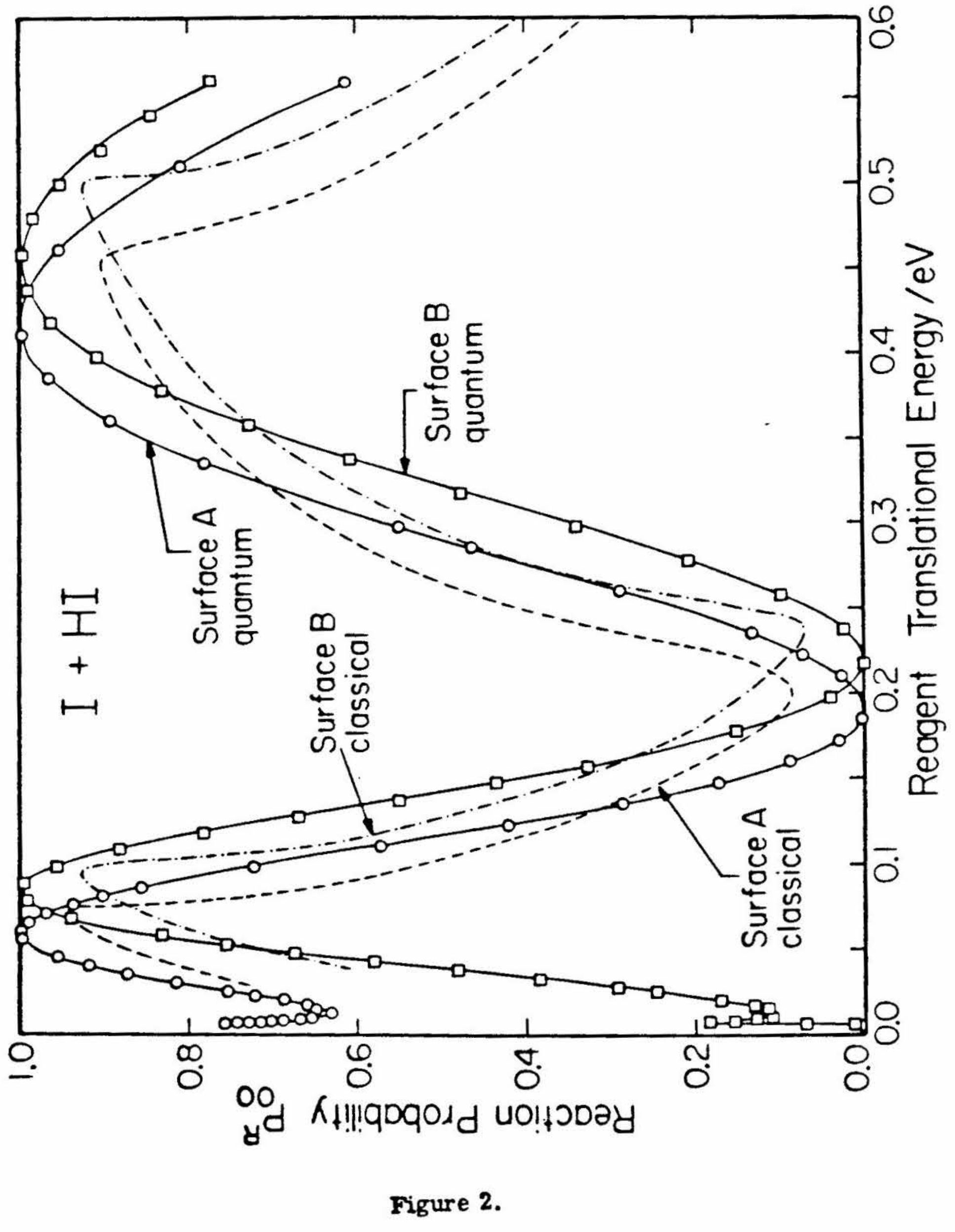
I + HI
Surface A quantum
Surface B quantum
Surface B classical
Surface A classical
Reaction Probability P^{00}_R
Reagent Translational Energy /eV
0.0
0.2
0.4
0.6
0.8
1.0
0.0
0.1
0.2
0.3
0.4
0.5
0.6

Figure 2.

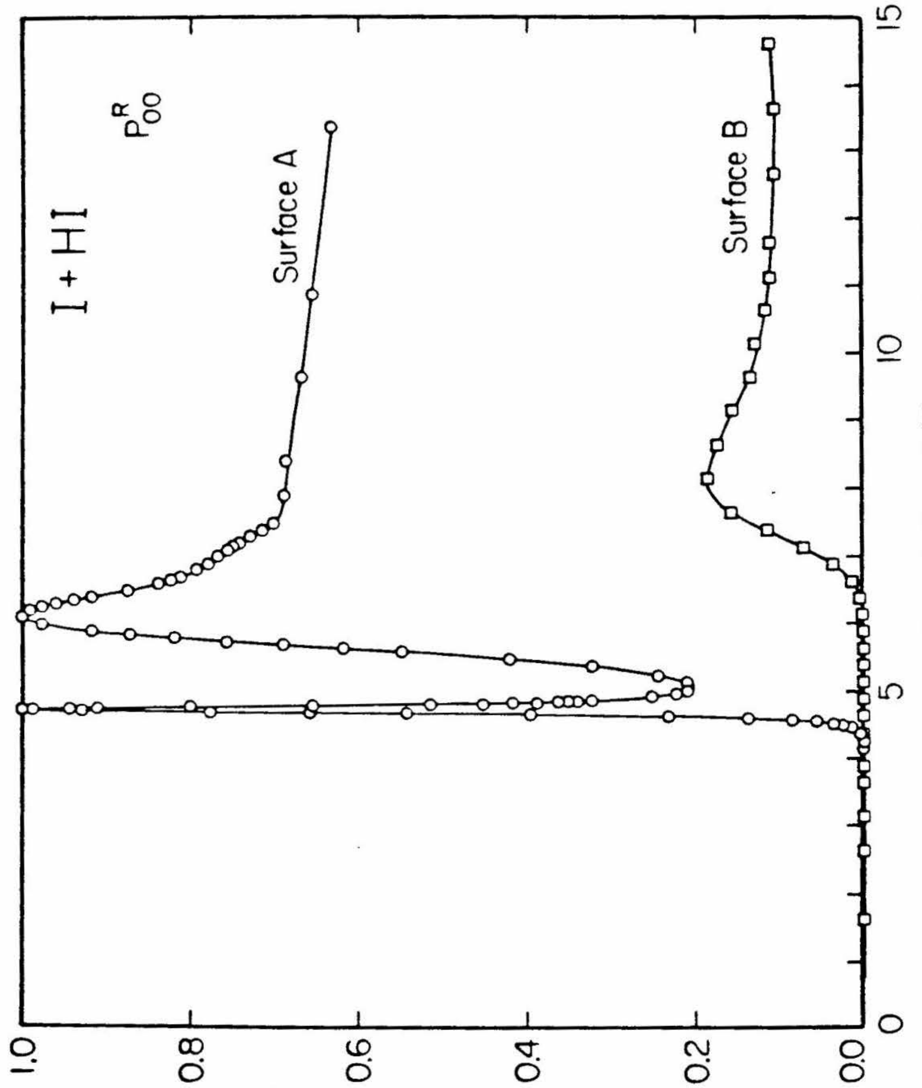
I + HI
P^R_{00}
Surface A
Surface B
Reaction Probability
0.0
0.2
0.4
0.6
0.8
1.0
Reagent Translational Energy /meV
0
5
10
15

Figure 3.

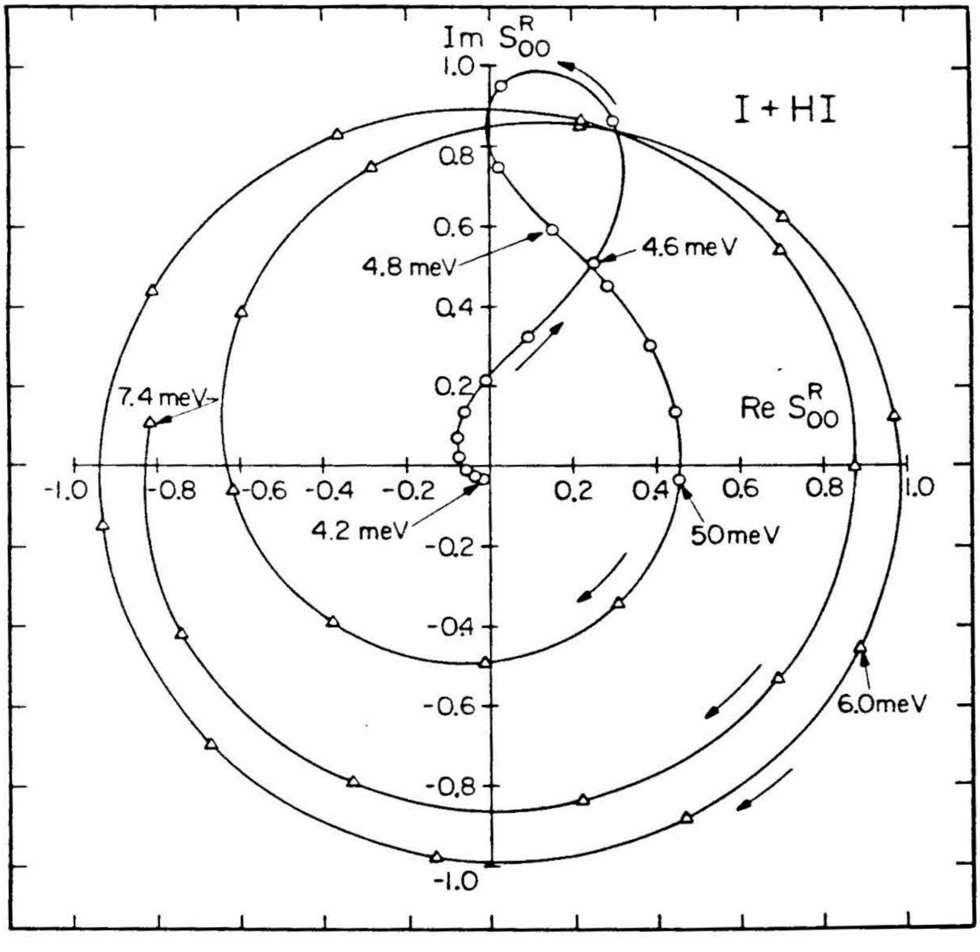
Im S_{00}^{R}
Re S_{00}^{R}
I + HI
1.0
0.8
0.6
0.4
0.2
-0.2
-0.4
-0.6
-0.8
-1.0
-1.0
-0.8
-0.6
-0.4
-0.2
0.2
0.4
0.6
0.8
1.0
4.8 meV
4.6 meV
7.4 meV
4.2 meV
5.0 meV
6.0 meV

Figure 4.

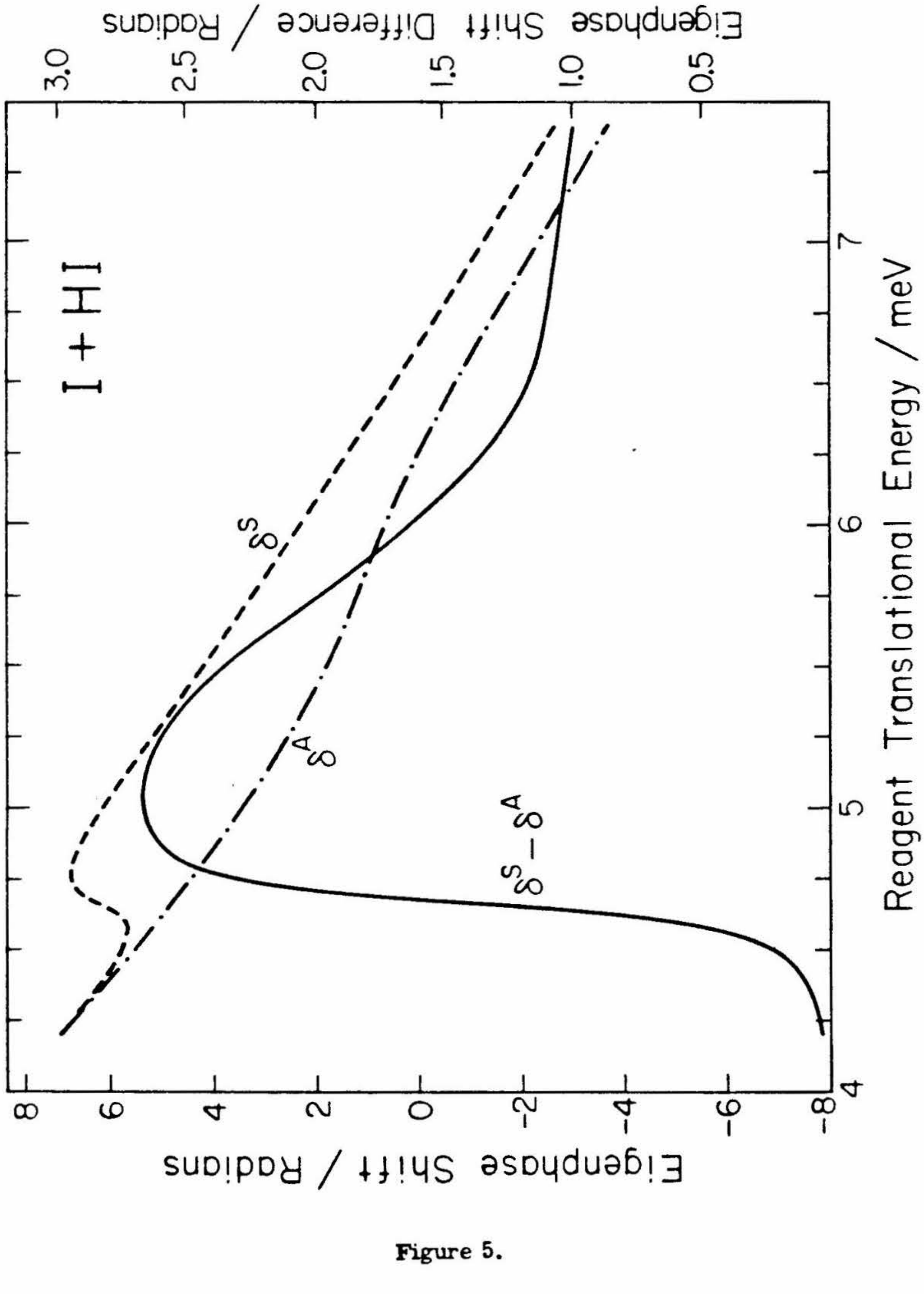
I + HI
δ^S
δ^A
δ^S – δ^A
Reagent Translational Energy / meV
4
5
6
7
Eigenphase Shift / Radians
8
6
4
2
0
-2
-4
-6
-8
Eigenphase Shift Difference / Radians
3.0
2.5
2.0
1.5
1.0
0.5

Figure 5.

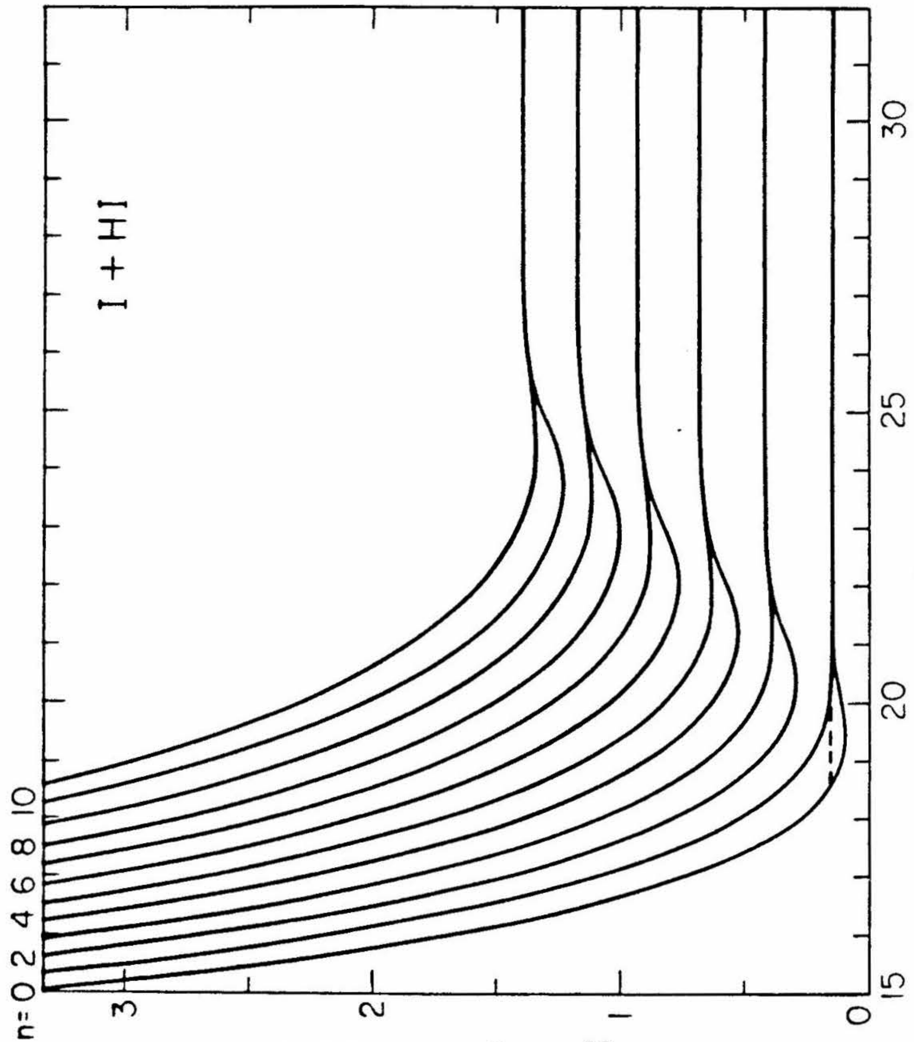

Figure 6.

III. 3 QUANTUM MECHANICAL COUPLED-CHANNEL COLLISION-INDUCED DISSOCIATION CALCULATIONS WITH HYPERSPHERICAL COORDINATES[*]

---

[*] This paper appeared in Chemical Physics Letters 78, 546 (1981).

QUANTUM MECHANICAL COUPLED-CHANNEL COLLISION-INDUCED DISSOCIATION CALCULATIONS WITH HYPERSPHERICAL COORDINATES[*]

Jack A. KAYE[**] and Aron KUPPERMANN

Arthur Amos Noyes Laboratory of Chemical Physics,[‡]
California Institute of Technology, Pasadena, California 91125, USA

Received

A time-independent coupled-channel method, using hyperspherical coordinates, has been developed for calculating quantum mechanical collision-induced dissociation probabilities for collinear atom-diatom systems in which the exchange reaction can also occur. The results for a model potential energy surface are compared with quasi-classical trajectory calculations and discussed.

---

[*] This work was supported in part by a Contract (No. F49620-79-C-0187) from the U. S. Air Force Office of Scientific Research.

[**] Work performed in partial fulfillment of the requirements for the PhD degree in Chemistry at the California Institute of Technology.

[‡] Contribution No. 6302.

1. Introduction

The collision-induced dissociation (CID) of diatomic molecules has been the subject of extensive experimental investigation [1-3]. In order to understand and to model this important process [4], it is necessary to obtain the bound-to-continuum transition probabilities as well as the usual bound-to-bound ones. Approximate classical [5], semi-classical [6], and quantum [7] techniques have been created for this purpose. However, the development of accurate quantum mechanical methods for systems in which CID competes with exchange processes has been hindered by the difficulty of representing the exchange product bound states in terms of the reagent bound and continuum states [7, 8]. As a result, systems in which the exchange channel is absent have mainly been considered in previous calculations [7, 9]. A method capable of taking such rearrangement channels into account, based on a multiple-collision expansion, has recently been applied for a potential that, however, does not support exchange products [10].

Kulander [11] has included exchange processes by solving numerically the time-dependent Schrödinger equation for cleverly chosen initial wave packets and obtained bound-to-continuum and bound-to-bound transition probabilities in collinear atom-diatom collisions. This conceptually elegant method is, however, computationally time-consuming and difficult to apply at energies close to the dissociation threshold.

In this paper we report the first successful time-independent treatment of CID in a collinear atom-diatom system in which the exchange process is present. This work uses the method of hyperspherical coordinates [12, 13] which has recently been applied to the collinear exchange reactions

$$H + H_2 \rightarrow H_2 + H$$

and [14]

$$I + HI \rightarrow IH + I$$

at energies below dissociation.

In Section 2 we briefly outline the nature and the method of hyperspherical coordinates, emphasizing those aspects of it which are crucial in the treatment of CID. The potential energy surface used in these calculations is discussed in Section 3, and the results obtained are presented, discussed, and compared with those from quasi-classical trajectory calculations in Section 4.

2. Theory

Let us consider the A + BC system, with A, B, and C representing distinguishable atoms confined to move on a laboratory-fixed straight line. Let r'_α and R'_α be, respectively, the BC internuclear distance and the distance of A to the center of mass of BC. Let r'_γ and R'_γ be the corresponding distances with the roles of A and C interchanged. The Delves scaled coordinates [12], R_λ and r_λ are defined as

$$R_\lambda = a_\lambda R'_\lambda \qquad r_\lambda = a_\lambda^{-1} r'_\lambda \qquad a_\lambda = (\mu_{\lambda,\nu\kappa}/\mu_{\nu\kappa})^{\frac{1}{4}} . \tag{1}$$

In these equations, $\lambda\nu\kappa$ is either $\alpha\beta\gamma$ or $\gamma\beta\alpha$, $\mu_{\nu\kappa}$ is the reduced mass of m_ν and m_κ, $\mu_{\lambda,\nu\kappa}$ is the reduced mass of m_λ and $(m_\nu + m_\kappa)$, and m_α, m_β, and m_γ are the masses of A, B, and C, respectively. The collinear hyperspherical coordinates are defined as

$$\rho = (R_\lambda^2 + r_\lambda^2)^{\frac{1}{2}} ; \quad \alpha = \tan^{-1}(r_\alpha/R_\alpha); \qquad 0 < \alpha < \frac{\pi}{2} \tag{2}$$

and are indicated in fig. 1. The Schrödinger equation for the internal motion of the ABC system is the same as that of a single particle P of mass $\mu = [m_\alpha m_\beta m_\gamma/(m_\alpha + m_\beta + m_\gamma)]^{\frac{1}{2}}$ moving in the two-dimensional ρ, α space and subject to the potential $V(\alpha,\rho)$ of the triatomic system. The motion of P on a circle of constant $\rho = \bar{\rho}$ is described by a set of energy eigenfunctions $\phi_n(\alpha;\bar{\rho})$ and eigenvalues $E_n(\bar{\rho})$. The former are called surface functions and constitute an infinite discrete set which, as $\bar{\rho} \to \infty$, spans the dissociation continuum. Expansion of the scattering wavefunction in the ϕ_n leads to a set of coupled-channel differential equations that have been derived and are integrated as described previously [13, 15] out to a sufficiently large value of ρ.

At energies at which no continuum states (those with positive eigenvalues with respect to the dissociated configuration A + B + C) need be included in the calculations, we reexpand, after that integration, the wavefunction ψ in R_α, r_α and R_γ, r_γ coordinates, using the numerically determined eigenfunctions $\phi_{\alpha n_\alpha}(r_\alpha)$ and $\phi_{\gamma n_\gamma}(r_\gamma)$ of the isolated reagent and product, respectively, as the new basis functions. In this manner, we obtain ψ and its R_λ derivative along lines of constant $R_\lambda = \bar{R}_\lambda$ ($\lambda = \alpha, \gamma$). We call this procedure a projection of ψ on the asymptotic reagent and product states. From the coefficients of this new expansion, the $\underline{\underline{R}}$, $\underline{\underline{S}}$, and $\underline{\underline{P}}$ matrices are calculated by standard techniques [13a, e]. For H + H_2, this procedure leads to results converged to 1% or better for values of $\bar{R}_\lambda$ of about 8 bohr or less [13a]. Alternatively, one can omit this projection altogether, since as $\bar{\rho} \to \infty$ the $\phi_n(\alpha;\bar{\rho})$ for negative eigenvalues become the separated reagent or product eigenstates (or their even and odd linear combinations for symmetric systems). However, this leads to a large amplitude oscillatory behavior of the reaction probabilities with ρ, as found by Rōmelt [15], which requires integration to appreciably larger values of ρ.

At total energies E for which dissociative channels must be included in the expansion to achieve convergence, as is the case for all collision energies above the dissociation limit, we have chosen to project the bound state channels as described above, and not to project the continuum ones at all. In the $\bar{\rho} \to \infty$

limit these results converge to the correct ones, while maintaining the rapid rate of convergence for the bound-to-bound transition probabilities. Other projection methods are possible and are being investigated.

The resulting scattering matrix $\underset{=}{S}$ is discrete, and the scattering wavefunction $\psi^{\alpha n_\alpha}$, corresponding to the system being initially in bound state n_α of the diatomic target BC, has the asymptotic form (for asymmetric systems, in which atoms A and C are different)

$$\psi^{\lambda n_\lambda} \underset{\rho\to\infty}{\sim} \sum_{\lambda' n'_{\lambda'}} [\exp(-ik_{\lambda' n'_{\lambda'}} R_{\lambda'})\delta^{\lambda n_\lambda}_{\lambda' n'_{\lambda'}} + \exp(ik_{\lambda' n'_{\lambda'}} R_{\lambda'}) \tag{3}$$
$$\times (v_{\lambda n_\lambda}/v_{\lambda' n'_{\lambda'}})^{\frac{1}{2}} S^{\lambda n_\lambda}_{\lambda' n'_{\lambda'}}]\phi_{\lambda' n'_{\lambda'}}(r_{\lambda'}) + \rho^{-\frac{1}{2}} \sum_n \exp(ik\rho)(v_{\lambda n_\lambda}/v)^{\frac{1}{2}} S_n^{\lambda n_\lambda} \phi_n(\alpha;\infty).$$

In this expression, the sum over $\lambda' n'_{\lambda'}$ extends over all bound states of BC and AB, whereas the sum over n extends over the continuum ($E_n > 0$) states. The several k and v represent, respectively, the appropriate channel wave numbers and velocities. In terms of the elements of the scattering matrix appearing in (3), the bound-to-bound and total bound-to-dissociated transition probabilities are given, respectively, by

$$P^{\lambda n_\lambda}_{\lambda' n'_{\lambda'}} = |S^{\lambda n_\lambda}_{\lambda' n'_{\lambda'}}|^2 \tag{4}$$

$$P_d^{\lambda n_\lambda} = \sum_n |S_n^{\lambda n_\lambda}|^2 . \tag{5}$$

The differential probability for producing dissociated products for which atom A has a center of mass energy E_A is given by

$$\sigma_d^{\lambda n_\lambda}(E_A) = \left|\frac{d\alpha}{dE_A}\right| \mathrm{Re}\,[\sum_{nn'} \phi_n^*(\alpha;\infty)\phi_{n'}(\alpha;\infty)(S_n^{\lambda n_\lambda})^* S_{n'}^{\lambda n_\lambda}] , \tag{6}$$

where α is related to E_A by

$$E_A = E_A^{\max}\cos^2\alpha \quad ; \qquad E_A^{\max} = [(m_\beta + m_\gamma)/(m_\alpha + m_\beta + m_\gamma)]E \,. \tag{7}$$

The total dissociation probability is related to the differential one by

$$P_d^{\lambda n_\lambda} = \int_0^{E_A^{\max}} \sigma_d^{\lambda n_\lambda}(E_A)dE_A \,. \tag{8}$$

For symmetric systems, the $\phi_n(\alpha;\infty)$ in Eqs. (3) and (6) must be replaced by appropriate linear combinations of the even and odd surface functions.

3. Potential Energy Surface

In order to test the method described above without excessive emphasis on bound states, we constructed a model collinear potential energy surface for which the isolated diatomic reagent or product potential energy curves supported only two such states, in analogy with weak van der Waals molecules. The mathematical form chosen for this surface was of the rotating Morse-cubic spline type [16]. The three atoms considered were identical but distinguishable (by virtue of their relative position on the line to which they were confined), and were assigned a mass equal to that of a hydrogen atom. The corresponding isolated diatomic molecules were chosen to have Morse parameters [17], $D_e = 0.22$ eV, $\beta = 1.6$ bohr^{-1}, and $r_e = 1.40083$ bohr. The energies of the two bound states supported by each of these Morse oscillators was 0.0817 and 0.1885 eV above the bottom of the diatom well. The saddle point occurred at internuclear distances $r'_{AB} = r'_{BC} = 1.6496$ bohr, and its height was 0.14 eV. In fig. 1 we display a contour plot of this potential energy function, and in fig. 2 we indicate schematically its features along the minimum energy path.

4. Results and Discussion

The results of these calculations as well as those of quasi-classical trajectory ones as a function of relative translational energy are given in figs. 3 and 4 for reagents in their ground and vibrationally excited states, respectively. Convergence of the transition probabilities to ± 0.02 or better was achieved with ten even and ten odd basis functions [13a]. The maximum value ρ_{max} of ρ needed to achieve this convergence was 64 bohr.

At the same translational energy, enhancement of the CID probabilities by reagent vibrational excitation is clearly observed, in agreement with a number of recent studies [10, 11, 18]. Up to translational energies of 0.10 eV for vibrationally excited reagents and 0.15 eV for ground state ones, the probability for the exchange reaction occurring without change of vibrational quantum number is significantly larger than the one with change in that number. Up to total energies of 0.32 eV the nonreactive inelastic process $0 \to 1$ (and $1 \to 0$) has probabilities smaller than 0.03 and is not shown in the figures.

The quasi-classical trajectory results display the same general features as the accurate quantum ones, giving confidence that classical mechanics furnishes an adequate qualitative description of the system's dynamics. However, errors of factors of two or greater are encountered in the quasi-classical probabilities when compared with the quantum ones.

We wish to emphasize the ease with which these calculations may be performed. The relatively large value of ρ_{max} required for good convergence of the transition probabilities does not increase the computation time excessively since in the large ρ region the integration step is quite large (> 0.1 bohr) and the calculation time increases only linearly with the number of integration steps. In addition, a more appropriate asymptotic analysis may permit a decrease in

ρ_{max}. The relatively small value of the number of $E_n > 0$ channels of each parity needed to provide an adequate discretized representation of the dissociation continuum, namely eight, for the energy range considered, is encouraging, since the computation time varies approximately as the cube of the number of coupled channels.

This hyperspherical coordinate approach has been shown recently to be very suitable for handling heavy-light-heavy collinear reactive systems [14]. The present work indicates that it is also suitable for collinear CID calculations. Extension of the method to encompass electronically nonadiabatic processes should be straightforward [19, 20]. The treatment of CID in atom-diatom collisions can, in principle, be extended to the three-dimensional physical world, since the corresponding generalization of the surface functions still forms an infinite discrete set [13c-e]. This extension is particularly important, since it has been observed in classical trajectory calculations [21] that a collinear model cannot adequately describe the dynamics of CID. However, the large number of channels involved in such three-dimensional systems will undoubtedly require the introduction of approximations in the calculation.

In summary, hyperspherical coordinates seem to provide a very useful language for the description and elucidation of the dynamical processes occurring in molecular collisions, including collision-induced dissociation and its reverse, three-body recombination.

Acknowledgements

The calculations reported were performed on the Dreyfus-NSF Theoretical Chemistry Computer which was funded through grants from the Camille and Henry Dreyfus Foundation, the National Science Foundation (Grant No. CHE78-20235), and the Sloan Fund of the California Institute of Technology, and on the

IBM 370/158 Computer of Ambassador College, Pasadena, California, for which we express our appreciation.

References

[1] R. L. Belford and R. A. Strehlow, Ann. Rev. Phys. Chem. 20 (1969) 247.

[2] E. K. Parks, N. J. Hansen and S. Wexler, J. Chem. Phys. 58 (1973) 5489; V. Havemann, V. Paca'k, Z. Herman, F. Schneider, Ch. Zuhrt and L. Zülicke, Chem. Phys. 28 (1978) 147.

[3] R. Huber and H. G. Weber, Chem. Phys. 35 (1978) 461.

[4] H. Johnston and J. Birks, Acc. Chem. Res. 5 (1972) 327; H. O. Pritchard, Spec. Period. Rep. React. Kin. 1 (1975) 243.

[5] P. J. Kuntz, in: Collision-Induced Dissociation. II. Trajectories and Models, in Atom-Molecule Collision Theory, ed. R. B. Bernstein (Plenum Press, New York, 1979) pp. 669-693 and references cited therein.

[6] I. Rusinek, J. Chem. Phys. 72 (1980) 4518; I. Rusinek and R. S. Roberts, ibid. 68 (1978) 1147; ibid. 65 (1976) 872.

[7] D. J. Diestler, in: Collision-Induced Dissociation. I. Quantal Treatment, in Atom-Molecule Collision Theory, ed. R. B. Bernstein (Plenum Press, New York, 1979) pp. 655-667 and references cited therein.

[8] G. Wolken, Jr., J. Chem. Phys. 63 (1975) 528.

[9] L. W. Ford, D. J. Diestler and A. F. Wagner, J. Chem. Phys. 63 (1975) 2019; E.-W. Knapp, D. J. Diestler and Y.-W. Lin, Chem. Phys. Lett. 49 (1977) 379; E.-W. Knapp and D. J. Diestler, J. Chem. Phys. 67 (1977) 4969.

[10] L. H. Beard and D. A. Micha, J. Chem. Phys. 73 (1980) 1193.

[11] K. C. Kulander, J. Chem. Phys. 69 (1978) 5064.

[12] L. N. Delves, Nucl. Phys. 9 (1959) 391; ibid. 20 (1960) 275.

[13] (a) A. Kuppermann, J. A. Kaye and J. P. Dwyer, Chem. Phys. Letters

74 (1980) 257; (b) J. P. Dwyer, Quantum Mechanical Studies of Molecular Scattering, Ph.D. Thesis, California Institute of Technology (1977); (c) R. T. Ling and A. Kuppermann, in: Electronic and Atomic Collisions (Abstracts of Papers of the IXth International Conference on the Physics of Electronic and Atomic Collisions, Seattle, Washington, 24-30 July 1975); eds. J. S. Risley and R. Geballe (University of Washington Press, Seattle, 1975) pp. 353-354; (d) J. K. C. Wong and A. Kuppermann, in: Abstracts of Papers of the Pacific Conference on Chemistry and Spectroscopy, Pasadena, California, 10-12 October 1979, p. 39; (e) A. Kuppermann, Theoretical Aspects of the Mechanism of Simple Chemical Reactions, in: Proceedings of the Summer School on Chemical Photophysics, Les Houches, France, 18-30 June 1979, eds. P. Glorieux, D. Lecler and R. Vetter (Centre National de la Recherche Scientifique, Paris, France, 1979) pp. 293-384.

[14] J. A. Kaye and A. Kuppermann, Collinear Quantum Mechanical Probabilities for the $I + HI \rightarrow IH + I$ Reaction Using Hyperspherical Coordinates, Chem. Phys. Letters, in press.

[15] A method similar to that of ref.[13a], using the same coordinates but a different asymptotic analysis, has been developed by G. Hauke, J. Manz, and J. Römelt, J. Chem. Phys., to be published, and used by J. Römelt, Chem. Phys. Letters 74 (1980) 263.

[16] J. M. Bowman and A. Kuppermann, Chem. Phys. Letters 34 (1975) 523.

[17] H. Eyring, J. Walter and G. Kimball, Quantum Chemistry (Wiley, New York, 1944) pp. 272-273.

[18] J. C. Gray, G. A. Fraser and D. G. Truhlar, Chem. Phys. Letters 68 (1979) 359; J. C. Gray, G. A. Fraser, D. G. Truhlar and K. C. Kulander, J. Chem. Phys., in press.

[19] J. M. Bowman, S. C. Leasure and A. Kuppermann, Chem. Phys. Letters 44 (1976) 499.

[20] Z. H. Top and M. Baer, J. Chem. Phys. 66 (1977) 1363.

[21] T. Lehr and J. W. Birks, J. Chem. Phys. 70 (1979) 4843.

Figure Captions

Fig. 1. Contour plot of the potential energy surface for a model collinear triatomic system in Delves scaled coordinates R_α, r_α. The solid curves are equipotential contours at the total energies (with respect to the dissociated system) indicated in the lower side of the figure. The dashed line is the minimum energy path. The polar coordinates ρ, α of a general point P in this R_α, r_α configuration space are also indicated.

Fig. 2. Schematic diagram of the potential energy function characteristics along the minimum energy path in Delves coordinate space. s is the distance along that path measured from the saddle point configuration, and V(s) the corresponding potential energy. The horizontal lines indicate the energy levels of the bound states ($v = 0$ and 1) of the isolated diatoms and of the dissociated configuration.

Fig. 3. Transition probabilities as a function of relative translational energy and total energy for ground state reagents. (a) Quantum mechanical (QM, solid line) and quasi-classical (CL, dashed line) total probabilities for reactive (R), nonreactive (N), and dissociative (D) processes. The arrows on the lower abscissa labelled E_1 and E_d indicate the energies of the first vibrationally excited state of the reagent and the reagent dissociation energy, respectively. (b) State-to-state quantum mechanical probabilities for vibrationally adiabatic (P_{00}^{R}, dotted line) and vibrationally nonadiabatic (P_{01}^{R}, dashed-dotted line) reactive processes. The dissociation probability curve ($P_0^{D\,QM}$, solid line) is included again for comparison purposes. Arrows in the abscissa have the same meaning as in (a).

Fig. 4. Transition probabilities as a function of relative translational energy and total energy for the diatom reagent in its first (and only) vibrationally excited state. Notation is the same as for fig. 3.

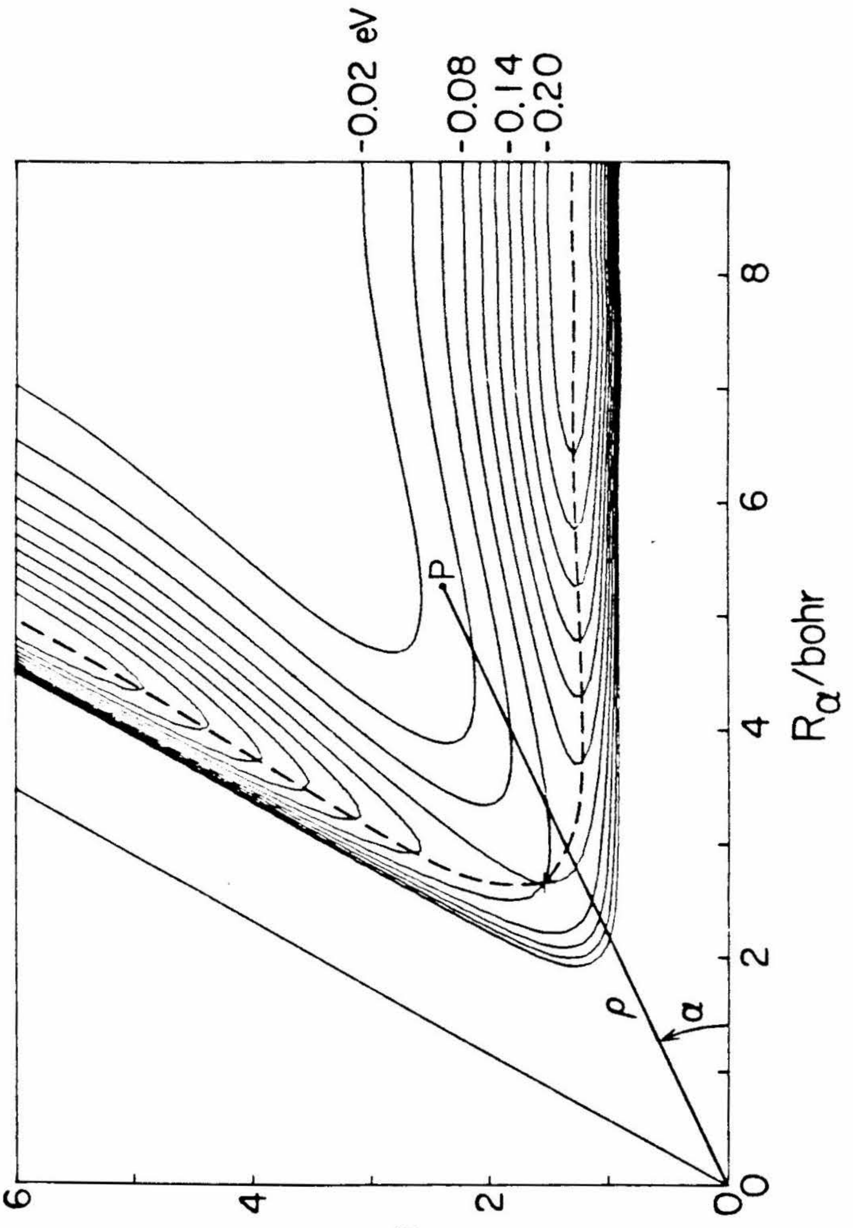

Figure 1.

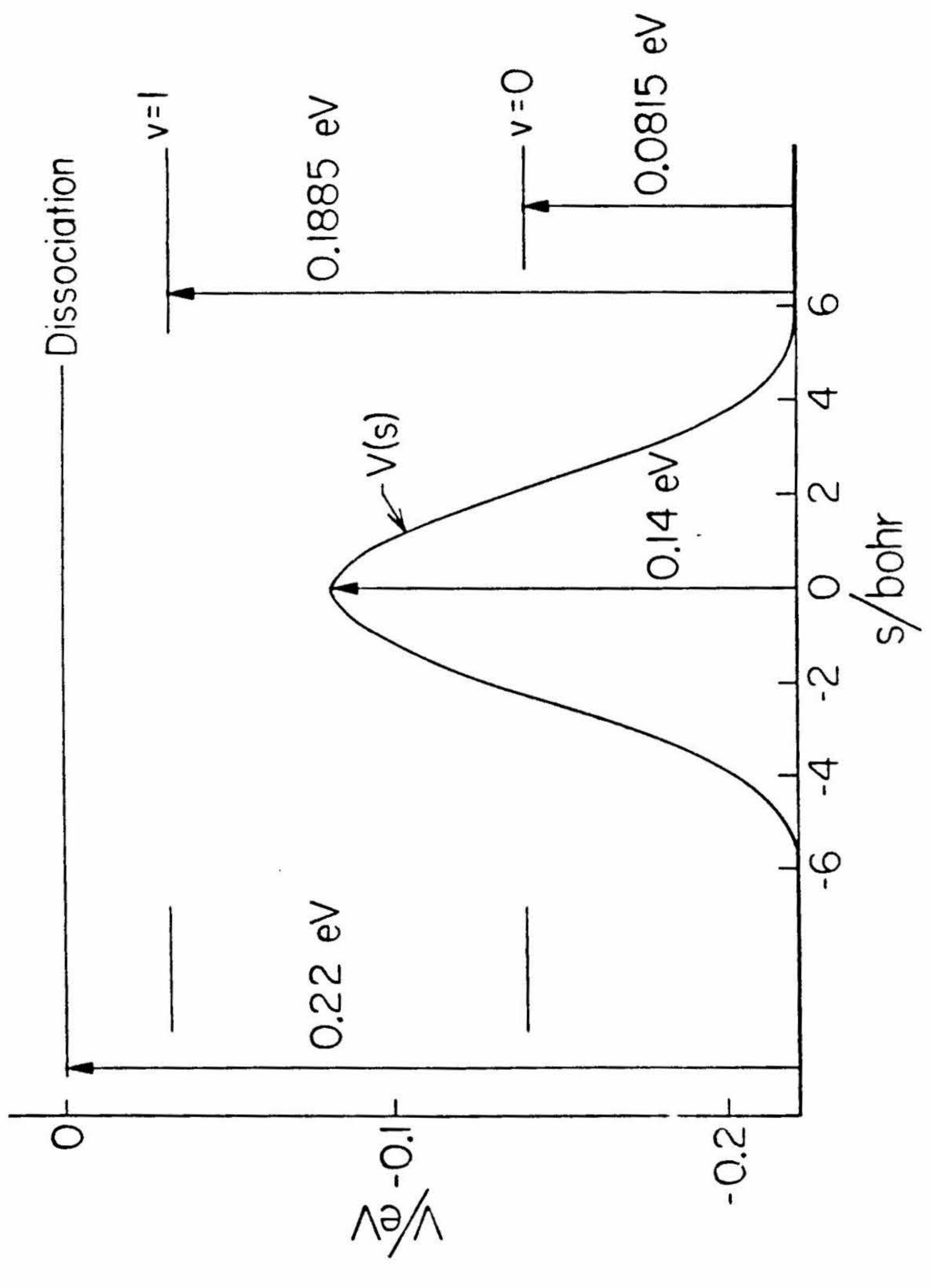
Dissociation
v=1
0.1885 eV
v=0
0.0815 eV
V(s)
0.14 eV
0.22 eV
-6
-4
-2
0
2
4
6
s/bohr
V/eV
0
-0.1
-0.2

Figure 2.

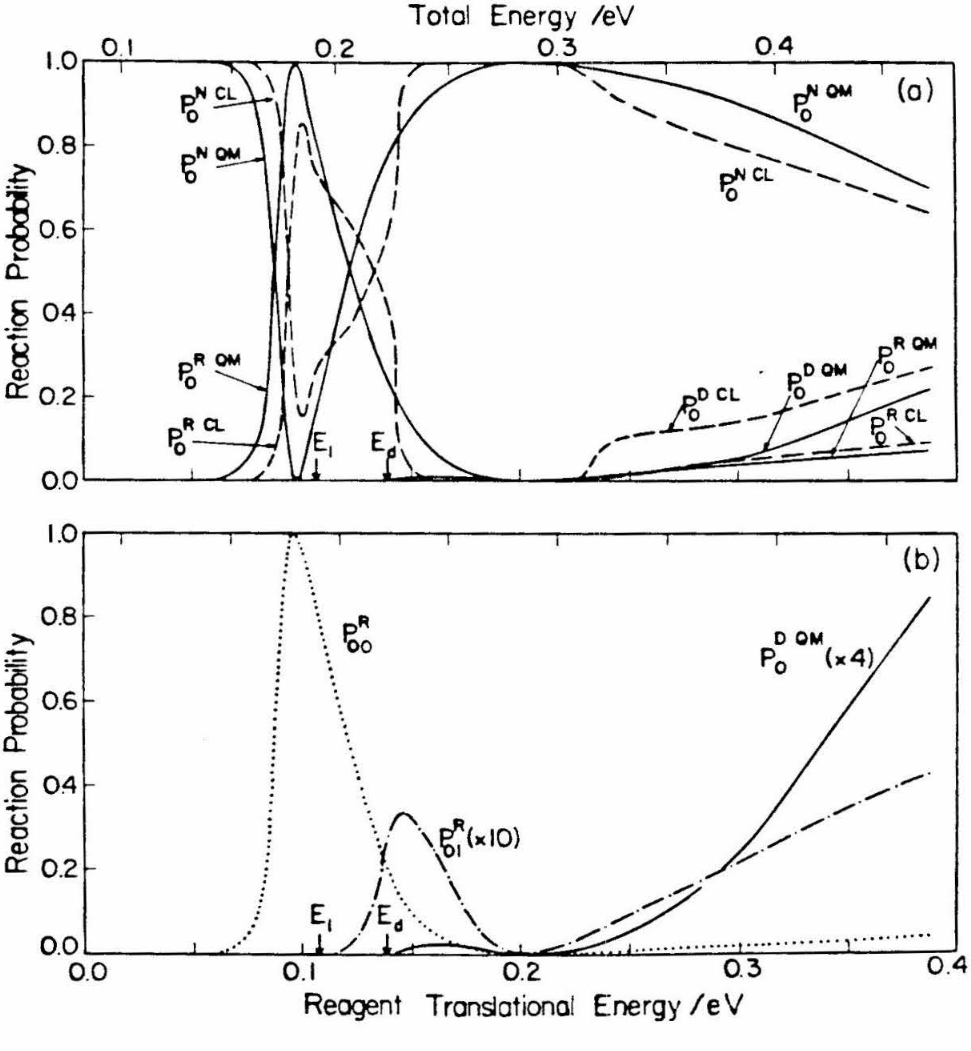
Total Energy /eV
0.1
0.2
0.3
0.4
(a)
Reaction Probability
1.0
0.8
0.6
0.4
0.2
0.0
$P_0^{N\ CL}$
$P_0^{N\ QM}$
$P_0^{R\ QM}$
$P_0^{R\ CL}$
E_1
E_d
$P_0^{N\ QM}$
$P_0^{N\ CL}$
$P_0^{D\ CL}$
$P_0^{D\ QM}$
$P_0^{R\ QM}$
$P_0^{R\ CL}$
(b)
Reaction Probability
1.0
0.8
0.6
0.4
0.2
0.0
P_{00}^{R}
$P_{01}^{R}(\times10)$
$P_0^{D\ QM}(\times4)$
E_1
E_d
0.0
0.1
0.2
0.3
0.4
Reagent Translational Energy /eV

Figure 3.

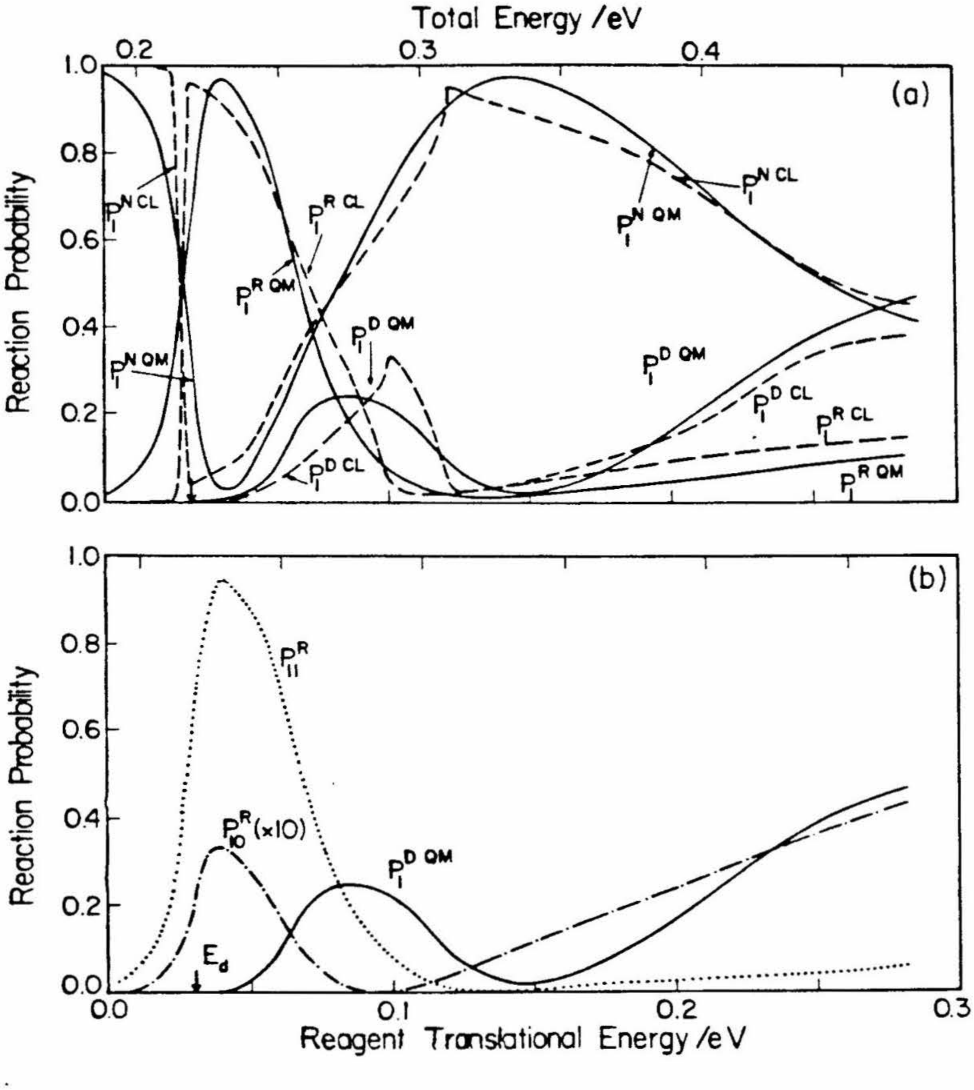
Total Energy /eV
0.2
0.3
0.4
1.0
0.8
0.6
0.4
0.2
0.0
Reaction Probability
(a)
$P_1^{N\,CL}$
$P_1^{N\,QM}$
$P_1^{R\,CL}$
$P_1^{R\,QM}$
$P_1^{D\,QM}$
$P_1^{D\,CL}$
$P_1^{N\,QM}$
$P_1^{N\,CL}$
$P_1^{D\,QM}$
$P_1^{D\,CL}$
$P_1^{R\,CL}$
$P_1^{R\,QM}$
(b)
P_{11}^{R}
$P_{10}^{R}(\times 10)$
$P_1^{D\,QM}$
E_d
0.0
0.1
0.2
0.3
Reagent Translational Energy /eV

Figure 4.

III.4 MASS EFFECT IN QUANTUM MECHANICAL COLLISION-INDUCED DISSOCIATION IN COLLINEAR REACTIVE ATOM-DIATOMIC MOLECULE COLLISIONS.

I. SYMMETRIC SYSTEMS.

Mass effect in quantum mechanical collision-induced dissociation in collinear reactive atom-diatomic molecule collisions.

I. Symmetric systems[a)]

Jack A. Kaye[b)] and Aron Kuppermann

Arthur Amos Noyes Laboratory of Chemical Physics,[c)]
California Institute of Technology, Pasadena, California 91125

(Received)

Quantum mechanical probabilities for collision-induced dissociation (CID) and chemical reactions have been obtained for a model triatomic collinear system,

$$A + BC(v) \rightarrow A + BC(v'),\ \ AB(v'') + C,\ \ A + B + C$$

using hyperspherical coordinates. Details of the methodology used for CID are presented. Calculations were performed for three different symmetric mass combinations ($m_A = m_B = m_C$, $m_A = m_C \neq m_B$) corresponding to light-light-light, heavy-light-heavy, and light-heavy-light systems. CID was found to be enhanced by reagent vibrational energy and to be most likely in the light-heavy-light system and least likely in the heavy-light-heavy system. Vibrationally nonadiabatic processes

---

a) This work was supported in part by a contract (No. F49620-79-C-0187) from the Air Force Office of Scientific Research.

b) Work performed in partial fulfillment of the requirements for the Ph. D. degree in Chemistry at the California Institute of Technology.

c) Contribution No.

were found to be of only secondary importance compared with either CID or vibrationally adiabatic ones. The activation energies for CID were found to be substantially in excess of the energetic threshold. The exchange reaction was found to be vibrationally enhanced, the reagent vibrational excitation being partly effective in lowering the activation energy of the reaction. Indication of a resonance in the heavy-light-heavy system has been found in spite of the large barrier to reaction. Quasi-classical trajectory calculations on the light-light-light system suggest that classical mechanics furnishes an adequate representation of the main features of the dynamics in these systems.

I. INTRODUCTION

The collision-induced dissociation (CID) of diatomic molecules

$$A + BC \rightarrow A + B + C \tag{1}$$

and its inverse process three-body recombination

$$A + B + C \rightarrow A + B \tag{2}$$

have been of great interest over the years to both experimentalists and theoreticians. To experimentalists, much of the interest has arisen from unusual temperature dependence of the rate of these reactions: the activation energy for CID is frequently less than the dissociation energy of the diatomic molecule,[1] and the rate of three-body recombination frequently decreases with increasing temperature.[2]

To theoreticians, however, the challenge has been to describe the dynamics of the collision process itself from first principles. Because of the double continuum of product states inherent in CID, this is far more complicated for this process than for the usual inelastic and/or reactive atom-diatomic molecule collision problem,

$$\begin{tikzcd}
A + BC(n) \arrow[r] \arrow[dr] & A + BC(n') & (3a) \\
 & AB(n'') + C \ , & (3b)
\end{tikzcd}$$

where n represents the set of all quantum numbers (electronic, vibrational, and rotational). Extension of the coupled-channel formulation to exact quantum mechanical calculations of CID, occurring in competition with exchange processes, has previously not been possible.[3]

Information about the CID process (and its inverse process three-body recombination) has been obtained from models based on kinematics,[4] from quasi-classical trajectory calculations,[5] from semi-classical calculations,[6] and from statistical models.[7] Quantum mechanical treatments have been limited mainly to studies of systems in which only CID and inelastic nonreactive processes [such as those represented by Eq. (3a)] occur.[3] Only recently have exact quantum mechanical methods for CID for systems in which chemical reactions [Eq. (3b)] may also occur been developed. These techniques consist of the time-dependent wave-packet approach developed by Kulander,[10] which has been applied to the collinear H + H_2 system above threshold, a multiple collision formalism developed by Beard and Micha (but so far applied only to nonreactive systems),[11] and the time-independent hyperspherical coordinate methods, developed independently by Kuppermann _et al._[12] and Manz _et al._[13]

The ability to study reactive systems is important, as experiments and quasi-classical trajectory calculations suggest that CID and its inverse process, three-body recombination, is much more rapid in reactive systems than in nonreactive ones.[8] In addition, the detailed nature of the dissociation or recombination processes may be different in reactive and nonreactive systems due to the greater diversity of types of collisions.[9]

As accurate quantum studies of CID are relatively new, it is important to perform studies that help to develop intuition about the effect on the CID process of changes in the potential energy surface and in the masses of the atoms involved. Most such studies have been limited to nonreactive systems, notably the quasi-classical trajectory calculations of Wong and Burns[14] on rare-gas plus bromine collisions and the collision-induced ion-pair experiments of Tully _et al._ on rare gas plus alkali halide systems[15] and of Parks _et al._ on rare gas plus thallium halide monomer and dimer systems.[16]

In this work we will discuss in detail the results of exact collinear quantum mechanical CID calculations on a model reactive potential energy surface for three different mass combinations: $m_A = m_B = m_C = 1$; $m_A = m_C = 10$, $m_B = 1$; and $m_A = m_C = 1$, $m_B = 35$, in units of the H-atom mass. Results for one of these mass combinations (and comparisons with collinear quasi-classical trajectory calculations) have been summarized previously.[12c] We will analyze and interpret the probability versus energy curves and temperature dependence of the corresponding CID and exchange reaction rate constants for the three cases studied.

In Sec. II we describe the potential energy surface and different mass combinations used in these calculations. In Sec. III we briefly review the application of the hyperspherical coordinate methods to CID. In Sec. IV we present the results obtained in these calculations, which are analyzed and discussed in Sec. V. Finally, in Sec. VI we summarize our results.

II. POTENTIAL ENERGY SURFACE

The potential energy surface V used in the calculations reported here is of the rotating Morse cubic spline type,[17] and has been briefly described previously.[12b] The three atoms are labeled A, B, and C, with B always occupying the middle position, and R_{AB} and R_{BC} representing the distance of the latter to A and C, respectively. For $R_{AB} >$ 7 bohr and $R_{BC} <$ 7 bohr, the potential energy function is that of a Morse oscillator

$$V(R_{AB}, R_{BC}) = D_e\{[e^{-\beta(R_{BC}-R_{eq})} - 1]^2 - 1\} , \tag{4}$$

where $D_e = 0.22$ eV, $\beta = 1.6$ bohr^{-1}, and $R_{eq} = 1.40083$ bohr. For $R_{BC} > 7$ bohr and $R_{AB} < 7$ bohr, an expression analogous to (4), with the roles of R_{AB} and R_{BC} interchanged, is used. For both R_{AB} and R_{BC} greater than 7 bohr, $V(R_{AB}, R_{BC}) = 0$. Finally, for R_{AB} and R_{BC} both smaller than 7 bohr, V is defined in Ref. 17. It has the form of a Morse curve,

$$V(R_{AB}, R_{BC}) = D(\theta)\{(1 - \exp[\beta(\theta)(\ell_{eq}(\theta) - \ell)]^2 - 1\} + D(\theta = 0).$$

In this expression, θ is the swing angle defined in Fig. 1 around the point S whose coordinates are $R_{AB} = R_{BC} = 7$ bohr, and ℓ is the distance of the point $P(R_{AB}, R_{BC})$ to S. θ varies from 0° to 90°, and the θ-dependent Morse parameters $D(\theta)$, $\ell_{eq}(\theta)$ and $\beta(\theta)$ are symmetric with respect to $\theta = 45°$ and are defined as follows. $D(\theta)$ is given by the Gaussian function

$$D(\theta) = D_e - b\{\exp[-c(\tfrac{\pi}{4} - \theta)^2] - \exp[-c(\tfrac{\pi}{4})^2]\} , \tag{5}$$

where $b = 0.14101$ eV and $c = 8.00876$ rad^{-1}, yielding a classical barrier height of 0.14 eV. The functions $\ell_{eq}(\theta)$ and $\beta(\theta)$ are given in Table I for eight values of θ in the range 0° to 45°. For intermediary values of θ, they are obtained by a cubic spline interpolation. For θ in the range of 45° to 90°, they are obtained by the symmetry condition with respect to $\theta = 45°$. A plot of the potential energy surface in Delves[18] mass scaled coordinates for the mass combination 1 - 1 - 1 is given in Fig. 2. As described previously, for this mass combination, asymptotically the Morse oscillator supports two ground states, with energy eigenvalues of 0.0817 and 0.1885 eV above the bottom of the isolated diatomic well.

In order to help elucidate the nature of the dependence of CID on masses, we considered, in addition, the mass combinations 10 - 1 - 10 and 1 - 35 - 1. These were chosen to broadly scan the possible range (0° to 90°) of skew angles in Delves[18] mass weighted coordinates, as it is known that this skew angle plays a major role in determining the dynamics of a reactive system independent of the nature of the forces between the atoms.[19] These mass combinations give skew angles of 24.62° and 88.41°, respectively, whereas the skew angle for the 1 - 1 - 1 combination is 60°. Various properties of the different mass combinations are summarized in Table II. Of particular note is the fact that for the 10 - 1 - 10 and 1 - 35 - 1 mass combinations, there are three bound states of the isolated diatomic molecules, as opposed to two for the 1 - 1 - 1 combination. Also, the two lowest eigenvalues of the isolated 1 - 10 and 35 - 1 diatomic molecules are quite similar, which suggests that differences in CID for these two systems cannot be attributed to differing amounts of reagent vibrational excitation energy.

III. THE HYPERSPHERICAL COORDINATE METHOD AND ITS APPLICATION TO CID

The hyperspherical coordinate method has been outlined previously[12a, 20] and we will not repeat the formalism in detail here. We have also indicated briefly how the method is applied to CID, and will expand upon that aspect of the treatment.

In the hyperspherical coordinate approach, the primitive wavefunctions $\psi_j(\rho, \alpha)$ are expanded in terms of a discrete set of basis functions,

$$\psi_j(\rho, \alpha) = \rho^{-\frac{1}{2}} \sum_{j=1}^{N} g_{ij}(\rho, \bar{\rho})\, \phi_i(\alpha; \bar{\rho}) \quad , \tag{6}$$

where ρ and α are, respectively, the distance and angle coordinates of a point in Delves' configuration space, and $\bar{\rho}$ is the value of ρ at which the diabatic basis functions ϕ_i are calculated. The use of a diabatic basis set gives rise to a parametric dependence of the expansion coefficients g_{ij} on $\bar{\rho}$. N is the number of channels included in the calculation.

As indicated previously,[12a] when ρ is sufficiently large and the A + BC and AB + C configurations are sufficiently separated from one another by the dissociative plateau, we may rewrite that portion ψ_j^b of the wavefunction that correlates asymptotically with the BC or AB by reexpanding it in terms of the eigenfunctions of the corresponding isolated diatomic molecule [in Delves [18] coordinates],

$$\psi_j^{b,\,A+BC}(\rho, \alpha) = \sum_{i=1}^{N_b^{BC}} h_{ij}^{A+BC}(R_A; \overline{R_A} = \infty)\, \chi_i^{A+BC}(r_A; \overline{R_A} = \infty), \tag{7}$$

a similar expression being used for ψ_j^{AB+C}. Using the orthogonality of the basis set $\chi^{A+BC}(r_A; \overline{R_A} = \infty)$, the h_{ij}^{A+BC} coefficients defined above can be calculated from

$$h_{ij}^{A+BC}(R_A;\overline{R_A}=\infty) = \int_{r_A(\min)}^{r_A(\max)} \chi_i^{A+BC}(r_A;\overline{R_A}=\infty) \times \psi_j^{b,\,A+BC}(\rho,\alpha)dr_A \quad , \tag{8}$$

where the integration limits are chosen so that contributions to the integral from outside their range are negligible. In this expression, ρ and α are functions of r_A and R_A through the relations $\rho = (r_A^2 + R_A^2)^{\frac{1}{2}}$ and $\alpha = \tan^{-1}(r_A/R_A)$. The derivative of the radial wavefunction matrix $\underline{\underline{h}}^{A+BC}$ with respect to R_A is obtained by differentiating Eq. (8) with respect to this variable.

In the symmetric systems studied here (where the mass combination is of the A + BC type), a projection onto the basis functions of the isolated AB diatomic need not be performed explicitly, as $\chi_i^{A+BC} = \chi_i^{AB+C}$ when A = C. In this case, we may obtain the corresponding radial wavefunction matrix elements from the relationship

$$h_{ij}^{AB+C}(R_C;\overline{R_C}=\infty) = \begin{cases} h_{ij}^{A+BC}(R_A;\overline{R_A}=\infty) \text{ if } \psi_j \text{ is symmetric} \\ -h_{ij}^{A+BC}(R_A;\overline{R_A}=\infty) \text{ if } \psi_j \text{ is antisymmetric ,} \end{cases}$$

where the symmetry of ψ_j is about the line $\alpha = \alpha_{\max}/2$. The derivatives $\underline{\underline{h}}'$ are similarly related.

The matrix $\underline{\underline{G}}$ of the coefficients used in the asymptotic ($\underline{\underline{R}}$ and $\underline{\underline{S}}$ matrix) analysis is given by

$$G = \begin{pmatrix} \underline{\underline{h}}^{A+BC} \\ \underline{\underline{h}}^{AB+C} \\ \rho_0^{-\frac{1}{2}} \underline{\underline{g}}^{un} \end{pmatrix} \tag{10}$$

where h^{A+BC} is evaluated at a large value of R_A, chosen arbitrarily, and h^{AB+C} is evaluated at $R_C = R_A$. The value of ρ at which the unprojected $\underline{\underline{g}}^{un}$ is evaluated can be chosen according to different criteria. One is to make it equal to R_A. Another is to make it equal to $[R_A^2 + r_A(\max)^2]^{\frac{1}{2}}$. Still another is to pick $[R_A^2 + r_A^{eq^2}(R_A)]^{\frac{1}{2}}$, where $r_A^{eq}(R_A)$ is the value of r_A for which $V(R_A, r_A)$ has a minimum for a given R_A. Alternate choices are obtained by interchanging the roles of A and C. In the limit as $R_A \sim \infty$, all of these should lead to the same result. In the calculations reported here, we selected the second criterion. The derivative $\underline{\underline{G}}'$ is defined by the expression

$$G' = \begin{pmatrix} \underline{\underline{h}}'^{A+BC} \\ \underline{\underline{h}}'^{AB+C} \\ \rho_0^{-\frac{1}{2}} \underline{\underline{g}}'^{un} - \frac{1}{2}\rho_0^{-\frac{3}{2}} \underline{\underline{g}}^{un} \end{pmatrix} \tag{11}$$

where $\underline{\underline{g}}'^{un}$ is also calculated at the same value of ρ as $\underline{\underline{g}}^{un}$.

In the asymptotic analysis,[21, 22] the eigenvalues of the bound states are precisely their asymptotic values due to the invariance of the potential beyond the R_{AB}, R_{BC} cutoff defined in the previous section. The eigenvalues of the continuum states decrease continuously with increasing $\bar{\rho}$, however, and the local wavenumber associated with each channel is nonzero and unique. At an infinite value of $\bar{\rho}$ and ρ, all continuum eigenvalues would be zero, however. Thus, stopping integration short of $\rho = \infty$ leads to approximations in the method, notably the assumption that the basis set $\{\chi^{A+BC}, \chi^{AB+C}, \phi(E > 0)\}$ is orthonormal, which is not true at finite $\bar{\rho}$.

As a result of this approximation, the convergence of state-to-state reaction probabilities with the stopping point of the integration ρ_{as} (where the asymptotic analysis is performed) is not nearly as rapid as in the bound-bound problem we have studied. For the 1-1-1 mass combination, plots of dissociation probability versus integration stopping point displayed what could best be described as damped oscillations. By carrying integration in that system to $\rho = 76$ bohr, all probabilities seem to be converged to ± 0.01; most probabilities, especially those involving the $v = 0$ state, should be even better converged. For the 10-1-10 and 1-35-1 mass combinations, integration was carried out to $\rho = 90$ and $\rho = 45$ bohr, which correspond to about the same value $R_{AB} = R_{BC} = 30$ bohr at which the 1-1-1 integration was stopped. The difference in these three values of ρ is due to the mass scaling inherent in the Delves coordinate systems. Ten even and ten odd channels were used in the integration of the coupled equations in the 1-1-1 system; 12 of each were used for the two others. Flux was conserved to better than 3% in the 1-1-1 calculations, 4.5% in the 10-1-10 calculations, and 12.5% in the 1-35-1 calculations. These limits were obtained at the highest energies; at lower energies, the flux conservation was far better. Since our interests here are mainly qualitative (i.e., to consider general dependence at CID on the initial reagent vibrational state and on the mass combination), we considered these calculations to be sufficiently accurate for analysis.

Rate constants were obtained from the calculated reaction probabilities by straightforward numerical integration, assuming an equilibrium (Boltzmann) distribution of relative kinetic energies. For the 1-1-1 system, rate constants were calculated using results obtained from scattering calculations in which the integration was stopped at $\rho = 32$ bohr, as calculations were performed for far more energies in these calculations than in those in which the integration was carried out to $\rho = 76$ bohr.

Arrhenius parameters (pre-exponential factors and activation energies) were obtained by a least-squares fit to the rate constant data over a region of temperature in which the Arrhenius plots (logarithm of rate constant versus inverse temperature) were linear.

IV. RESULTS

We have studied the dynamics of the model system described above for the mass combinations 1-1-1, 10-1-10, and 1-35-1 up to an energy 0.25 eV above the dissociation energy of the isolated diatomic molecules. Our attention has been focused on the probabilities of reaction and dissociation as a function of translational energy and of reagent vibrational excitation. We have looked at the amount of vibrational nonadiabaticity in the exchange reactions, and have calculated state-to-all and, in some cases, state-to-state rate constants (and their associated Arrhenius parameters).

Plots of state-to-state reaction probability versus reagent translational energy for the 1-1-1, 10-1-10, and 1-35-1 mass combinations are shown in Figs. 2, 3, and 4, respectively. The figures are constructed such that in any one figure, a vertical line always corresponds to the same total energy. Hence, the translational origins in each panel within a figure are shifted to account for the different internal energy in each reagent vibrational level. In Figs. 5, 6, and 7, similar plots are constructed for the total reactive, nonreactive, and dissociative probabilities. Reactive and dissociative rate constants in the temperature range 200°K < T < 650°K for the three mass combinations are given in the form of Arrhenius plots (in °K versus 1/T) in Figs. 8, 9, and 10. Finally, in Fig. 11, we present Arrhenius plots of state-to-state reactive (and dissociative) rate constants for the 1-35-1 mass combination, as that is the one with the greatest amount of vibrational nonadiabaticity and dissociation.

V. DISCUSSION

Two main features are evident in the results obtained from these calculations. First, there is substantial vibrational enhancement of CID as the reagent vibrational energy is increased, in all of the systems studied. Second, there is a major difference in the CID probability versus energy curves for the three different mass combinations. In addition, important information is contained in these results about the relative importance of CID, reaction, and nonreactive processes, the magnitude of vibrational nonadiabatic processes, and the possible importance of resonances in chemical reactions occurring in this model system. We now proceed to examine these points in greater detail.

The probabilities for reaction and for CID displayed in Figs. 3 to 7 clearly demonstrate the importance of vibrational enhancement of CID. While this is clearest in the 10-1-10 mass combination, it is still quite clear in the 1-1-1 mass combination, particularly in the region of the first peak in the CID versus energy probability curves, in which the probability for CID from the $v = 1$ state is some 40 times that from the $v = 0$ state. At higher energies, the enhancement is less pronounced. The vibrational enhancement is smallest for the 1-35-1 mass combination. In fact, up through about 0.08 eV above dissociation, the probability of CID from the $v = 0$ state is higher than that from the $v = 1$ state, although this is reversed at higher energies. The probability of CID from the $v = 2$ state is nearly always higher than that from the $v = 0$ and $v = 1$ states for this mass combination, except at the energy of the minimum in the $v = 2$ CID probability versus energy curve.

The vibrational enhancement of CID can also be seen by considering the rate constants for dissociation (k_i^D) shown in Figs. 8 to 10. There is a large increase in the rate constant with reagent vibrational excitation, much of which can be attributed simply to the decrease in the energetic threshold for CID with reagent vibrational excitation. An estimate of the magnitude of this effect can be obtained by consideration of the Arrhenius pre-exponential factors and activation energies associated with the Arrhenius plots in Figs. 8 to 10. Such an analysis for the dissociation curves is complicated by their nonlinearity, but the curvature is sufficiently small that we may obtain reasonably good fits to the calculated rate constants by assuming a linear Arrhenius plot in the temperature range from 350-650°K. Pre-exponential factors b and activation energies E_a for the exchange reaction and CID are given in Table III. Considering the CID Arrhenius parameters for the 1-1-1 and 10-1-10 mass combinations, the pre-exponential factors increase and the activation energies decrease with increasing reagent vibrational excitation, both effects contributing to an increase of the rates. For the 1-35-1 mass combination, the CID pre-exponential factors are all approximately equal, and the entire vibrational state dependence of the CID rate constant stems from decreases in the activation energy with increasing v.

In all cases the activation energy for CID is far greater than the corresponding classical energetic threshold for this process, the difference between these quantities lying in the range from 40-70 meV. This indicates that not all of the reagent vibrational energy is available to overcome the barrier to dissociation, resulting in an extra amount of translational energy to do so.

Vibrational enhancement of CID has been obtained in most previous calculations of the CID process; the present calculations further support that result.[10, 11, 22] In one previous study, CID had been found to be inhibited by reagent vibrational excitation, but this is now considered to be an artifact of the model used (impulsive force between the incident atom and the target atom of the diatomic molecule in a collinear collision.[23]

The state-to-all exchange reaction probabilities show less variation with reagent vibrational excitation than do the CID probabilities. This may be easily seen on examination of Figs. 5 to 7. The overall similarity of the P_i^R curves on each figure is striking. This particularly true for the 10-1-10 mass combination in which there are three peaks in each of the curves, with the energy spacing between the second and third peaks far greater than that between the first and second peaks. The vibrational enhancement of the rate of reaction is reflected in the rate constants for reaction plotted (using solid lines) in Figs. 8-10. The Arrhenius plots of these rate constants are linear over the entire 200-650°K temperature range, and this range was used in the calculation of the Arrhenius parameters, which are included in Table III. An examination of Table III shows that the pre-exponential factor is essentially independent of the reagent vibrational state. Thus, as in the case of CID for the 1-35-1 mass combination, reagent vibrational excitation only changes the activation energy for the exchange reaction. The decrease in activation energy with reagent vibrational excitation is substantially smaller than the added vibrational energy, however.

One especially noticeable feature of the exchange reaction probability curves is their different structure for the three different mass combinations. For the 1-1-1 case, these reaction probabilities reach their peaks and decrease to zero shortly above the opening of the dissociation channel and increase slowly at higher energies. For the 1-35-1 case, their decrease after the peak is much slower, and there is no further increase beyond the first maximum, up to the highest energies used in these calculations. For the 10-1-10 case, however, reaction probabilities vary substantially with reagent translational energy, even at the highest energies considered. It should be noted that oscillatory behavior in the reaction probability versus energy curves for heavy-light-heavy systems has been observed in the I-H-I[12b] and Cl-H-Cl[24] systems. Thus, this oscillatory behavior appears to be a feature common to systems with small skew angles.

It is interesting to consider the importance of vibrationally nonadiabatic processes, both reactive and nonreactive, as they are important in the collisional vibrational excitation or relaxation relevant to experimental studies of CID, especially shock-tube experiments. We will restrict our attention here to vibrationally nonadiabatic exchange reactive processes. In general, the probabilities of inelastic nonreactive processes of the type

$$A' + BA(v) \rightarrow A' + BA(v' \neq v)$$

have been found to be fairly similar— to those of the corresponding reactive processes[24]

$$A' + BA(v) \rightarrow A'B(v' \neq v) + A.$$

An examination of the relative importance of vibrationally nonadiabatic and CID probabilities is of interest since CID can be considered as an extreme case of vibrational excitation to a nonbound state.[1]

In general, nonadiabatic processes are seen from Figs. 2-4 to be of only secondary importance (as opposed to CID and vibrationally adiabatic processes). There is a correlation between the magnitude of CID and vibrationally nonadiabatic processes in that for the case where CID is the most likely (the 1-35-1 mass combination), the latter processes are also the most likely. On the other hand, vibrationally nonadiabatic processes are more likely for the 10-1-10 mass combination than they are in the 1-1-1 case, however, even though CID is more prevalent in the latter case than in the former.

To help elucidate the relative importance of the exchange reaction, both vibrationally adiabatic and nonadiabatic, and of CID, we have obtained Arrhenius plots of the state-to-state reaction and CID rate constants for the 1-35-1 case, and these are displayed in Fig. 11. It is clear that of all the above mentioned processes, vibrationally adiabatic reaction is the most likely. Further, it is not always true that CID rates are smaller than all the other bound-to-bound rate constants, as has been assumed in some models.[1]

Finally, we wish to consider the possible role of resonance processes in this model system. The large barrier to reaction in this system (relative to the dissociation energy) decreases the likelihood of resonances in the 1-35-1 and 1-1-1 mass combinations. The reason is that there will be no wells in the vibrationally adiabatic correlation diagrams, which are important mechanisms for the appearance of such resonances.[25,26] This picture is known to be less appropriate for heavy-light-heavy systems like the 10-1-10 mass combination being considered here,[12c, 26] which still leaves the possibility that there may be resonances in the 10-1-10 case, in spite of the large barrier.

In fact, the first peak in the P_{00}^{R} versus energy curve for this system can be shown to be associated with a resonance by construction of an Argand diagram,[26, 27] which is displayed in Fig. 12. The switch-over from a clockwise to counterclockwise sense near 0.15 eV total energy (as the diagram is traversed in the direction of increasing energies) makes the resonant nature of this process evident.[26, 27] The corresponding peak in the P_{11}^{R} versus energy curve does not appear to be associated with a resonant process on consideration of the appropriate Argand diagram (Fig. 13). The curve there has a clockwise sense over the entire range from 0.18 to 0.21 eV total energy, signifying that there is either no resonance at all or that if there is one, it is masked by a direct process and thus unobservable from an Argand diagram. An analysis via the collision lifetime matrix eigenvalue technique[28] would help elucidate this point.

We have performed quasi-classical trajectory calculations for the 1-1-1 mass combination and have found their results to be qualitatively similar to the quantum mechanical ones (the corresponding curves are plotted in Figs. 3 and 4 of Ref. 12b). The results are quantitatively sufficiently different, however, that rate constants for CID calculated using the quasi-classical probabilities were substantially different at times from those obtained from the quantum mechanical probabilities.

As mentioned in the Introduction, very little work has been done on the behavior of CID in reactive systems. Most of this work has been limited to quasi-classical trajectory calculations on the H + H_2 system and its isotopic counterparts, frequently including systems in which there is an incident tritium atom.[9, 29] This case corresponds closely to that studied in nuclear recoil experiments in which hot tritium atoms are used. Simple calculations using kinematic (i.e., hard sphere) models have also been performed, and have in general yielded satisfactory agreement with both experiment and quasi-classical trajectory calculations.[4]

That the masses of the colliding partners could have a major effect on the CID has been seen for some time in nonreactive systems. Fan[30] has performed collinear quasi-classical trajectory calculations on the $\mathrm{Xe} + \mathrm{CsBr} \rightarrow \mathrm{Xe} + \mathrm{Cs}^+ + \mathrm{Br}^-$ system, and found that dissociation is much more likely in collisions of Xe with Br than of Xe with Cs. A similar behavior was found both experimentally and in quasi-classical trajectory calculations by Tully et al.[15] Their results suggest that collisions leading to dissociative ion pair formation are near-collinear; that is, they occur with their relative velocity roughly parallel to the alkali halide axis, but with a small but non-zero impact parameter. Of particular interest is the fact that the scattering in the Xe-RbI and Xe-CsBr systems was very similar, which suggests that it is the masses of the atoms ($m_{\mathrm{Rb}} \sim m_{\mathrm{Br}}$, $m_{\mathrm{Cs}} \sim m_{\mathrm{I}}$) and not the details of the intermolecular forces that govern CID behavior. Further, in their experiments, Tully et al. found that CID rates were found to vary more with changes in the alkali halide molecule in Kr-MX collisions than in Xe-MX collisions.

Additional evidence of strong mass effects in CID was obtained by Shui et al.,[31] who found that a modified phase space theory, which *normally* predicts CID and three-body recombination rates fairly well for most systems, does not work in the case of HF and HCl dissociation in Ar. Their method involved the use of trajectories calculated for systems in which all the atoms and molecules had similar masses, and they attribute the inaccuracy for these systems to different dynamics than in most other cases.

In the results obtained here, we have also seen grossly different dynamics with changes in the atom masses. In particular, the dynamics of the heavy-light-heavy system are substantially different from those of the two others, lending support to the hypothesis of Shui et al.[31] described above. Because of our restriction to symmetric systems in the present calculations, we have been unable to consider the dependence of CID on orientation (i.e., A + BC versus A + CB), as was considered by Fan,[30] but we do hope to do so in the future.

VI. SUMMARY AND CONCLUSIONS

We have calculated probabilities for CID and exchange reaction for the collinear triatomic system A + BA on a model potential energy surface for three different mass combinations, using the hyperspherical coordinates coupled-channel technique. The mass combinations studied are of the light-light-light, light-heavy-light, and heavy-light-heavy types. Substantial vibrational enhancement of CID was seen, and in all three systems CID was found to be most important for the 1-35-1 mass combination and least so for the 10-1-10 mass combination. Arrhenius plots of rate constants for CID are reasonably but not precisely linear, and over the temperature range 350-600° K give rise to activation energies for CID which are substantially (normally 40-70 meV) greater than the energetic thresholds.

Probabilities for the exchange reaction, both vibrationally adiabatic and nonadiabatic, have also been obtained. In general, the shapes of the reaction probability versus energy curves vary only slightly with reagent vibrational excitation. There are substantial differences between the curves for the different mass combinations, however. Arrhenius plots of the rate constants for reaction are linear over the entire 200-650° K range. For each mass combination, the Arrhenius pre-exponential factors are approximately independent of reagent vibrational state; the activation energies do decrease with reagent vibrational excitation, but the magnitude of this decrease is substantially smaller than the added reagent vibrational energy. Vibrationally nonadiabatic processes are found to be less important than vibrationally adiabatic processes and CID. Rate constants for CID are usually smaller than those for the exchange reaction, but this is not always true, especially at the upper end of the range of temperatures considered.

We have shown that resonant processes can be important at energies not far from dissociation in this system for the heavy-light-heavy mass combination, although they do not necessarily occur for all reagent levels.

On the basis of quasi-classical trajectory calculations performed on the 1-1-1 mass combination, quantum effects, even for the weakly bound system studied here with the light masses used, are fairly small. Thus, classical mechanics should be able to give a reasonably good qualitative picture of the dynamics in these systems, although not necessarily a quantitative one.

We have recently modified the hyperspherical coordinate scattering program to allow for the study of asymmetric systems (i.e., three non-equivalent atoms), and hope to extend our studies of the CID process to them in the near future.

ACKNOWLEDGEMENTS

The calculations reported here were performed on the IBM 370/158 computer at Ambassador College in Pasadena, California, for which we express our appreciation. Additional calculations were performed on the Dreyfus-NSF Theoretical Chemistry Computer at Caltech which was funded through grants from the Camille and Henry Dreyfus Foundation, the National Science Foundation (Grant No. CHE78-20235), and the Sloan Fund of the California Institute of Technology.

REFERENCES

1. H. S. Johnston and J. Birks, Acc. Chem. Res. 5, 327 (1972); H. O. Pritchard, Specialist Periodical Reports, Reaction Kinetics, Vol. 1 (Chemical Society, London, 1975), p. 243.
2. H. O. Pritchard, Acc. Chem. Res. 9, 99 (1976).
3. D. J. Diestler, in Collision-Induced Dissociation. I. Quantal Treatment, in Atom-Molecule Collision Theory, R. B. Bernstein, Ed. (Plenum Press, New York, 1979), pp. 655-667, and references therein.
4. R. J. Suplinskas, J. Chem. Phys. 49, 5046 (1968); D. J. Malcolme-Lawes, ibid. 57, 5572 (1972).
5. P. J. Kuntz, in Collision-Induced Dissociation. II. Trajectories and Models, In Atom-Molecule Collision Theory, R. B. Bernstein, Ed. (Plenum Press, New York, 1979), pp. 669-692, and references therein; T. Lehr and J. W. Birks, J. Chem. Phys. 70, 4843 (1979).
6. C. S. Lin, Chem. Phys. 3, 125 (1974); I. Rusinek and R. E. Roberts, J. Chem. Phys. 65, 872 (1979); 68, 1147 (1978); I. Rusinek, ibid. 72, 4518 (1980).
7. W. B. Maier, J. Chem. Phys. 41, 2174 (1964); J. C. Keck, Adv. Chem. Phys. 13, 85 (1967); C. Rebick and R. D. Levine, J. Chem. Phys. 58, 3942 (1973); A. F. Wagner and E. K. Parks, ibid. 65, 4343 (1976).
8. R. T. V. Kung and J. B. Anderson, J. Chem. Phys. 60, 3732 (1974).
9. A. Jones and J. L. J. Rosenfeld, Proc. R. Soc. Lond. A 333,

419 (1973).

10. K. C. Kulander, J. Chem. Phys. 69, 5064 (1978); Nucl. Phys. A 353, 341c (1981).

11. L. H. Beard and D. A. Micha, J. Chem. Phys. 73, 1193 (1980).

12. (a) A. Kuppermann, J. A. Kaye, and J. P. Dwyer, Chem. Phys. Lett. 74, 257 (1980); (b) J. A. Kaye and A. Kuppermann, ibid. 77, 573 (1981); (c) 78, 546 (1981).

13. (a) G. Hauke, J. Manz, and J. Römelt, J. Chem. Phys. 73, 5040 (1980); (b) J. Römelt, Chem. Phys. Lett. 74, 263 (1980); (c) J. Manz and J. Römelt, ibid. 76, 337 (1980); (d) 77, 172 (1981).

14. W. H. Wong and G. Burns, J. Chem. Phys. 62, 1712 (1975).

15. (a) F. P. Tully, Y. T. Lee, and R. S. Berry, Chem. Phys. Lett. 9, 80 (1971); (b) F. P. Tully, N. H. Cheung, H. Haberland, and Y. T. Lee, J. Chem. Phys. 73, 4460 (1980).

16. E. K. Parks, N. J. Hansen, and S. Wexler, J. Chem. Phys. 58, 5489 (1973).

17. J. M. Bowman and A. Kuppermann, Chem. Phys. Lett. 34, 523 (1975).

18. L. N. Delves, Nucl. Phys. 9, 391 (1959); 20, 275 (1960).

19. J. C. Polanyi and J. L. Schreiber, in The Dynamics of Bimolecular Reactions, in Physical Chemistry, Advanced Treatise, Vol. 6A, Kinetics of Gas Reactions (Academic Press, New York, 1974), pp. 383-487.

20. J. P. Dwyer, Ph.D. Thesis, California Institute of Technology (1977).

21. A. M. Lane and R. G. Thomas, Rev. Mod. Phys. 30, 257 (1958);

A. Kuppermann, in Theoretical Chemistry: Advances and Perspectives, D. Henderson, Ed. (Academic Press, New York, 1981), Vol. 6A, pp. 79-164.

22. J. C. Gray, G. A. Fraser, and D. G. Truhlar, Chem. Phys. Lett. 68, 359 (1979); J. C. Gray, G. A. Fraser, D. G. Truhlar, and K. C. Kulander, J. Chem. Phys. 73, 5726 (1980); E. W. Knapp and D. J. Diestler, ibid. 67, 4969 (1977).

23. L. W. Ford, D. J. Diestler, and A. F. Wagner, J. Chem. Phys. 63, 2019 (1975).

24. J. A. Kaye and A. Kuppermann, manuscript in preparation.

25. S. L. Latham, J. F. McNutt, R. E. Wyatt, and M. J. Redmon, J. Chem. Phys. 69, 3746 (1978).

26. A. Kuppermann, in Potential Energy Surfaces and Dynamics Calculations, D. G. Truhlar, Ed. (Plenum Press, New York, 1981), pp. 375-420.

27. G. C. Schatz and A. Kuppermann, J. Chem. Phys. 59, 964 (1973), and references therein.

28. F. T. Smith, Phys. Rev. 118, 349 (1960); G. C. Schatz, Ph.D. Thesis, California Institute of Technology (1975); A. Kuppermann and J. A. Kaye, J. Phys. Chem. 85, 1969 (1981); G. C. Schatz and A. Kuppermann, manuscript in preparation.

29. M. Karplus, R. N. Porter, and R. D. Sharma, J. Chem. Phys. 45, 3871 (1976); D. J. Malcolme-Lawes, J. Chem. Soc. Faraday Trans. II 71, 1183 (1975).

30. H. Fan, J. Chem. Phys. 55, 4628 (1971).

31. V. H. Shui, J. P. Appleton, and J. C. Keck, in the Proceedings

of the 13th Symposium (International) on Combustion (The Combustion Institute, 1970), p. 21.

Table I. Parameters for rotating Morse cubic spline potential used (notation is as in Ref. 17).

θ (deg.)	$\ell_{eq}(\theta)$ (bohr)	$\beta(\theta)$ (bohr^{-1})
0	5.5993	1.600
15	5.7968	1.544
25	6.1774	1.458
30	6.4636	1.392
35	6.8284	1.321
40	7.2669	1.218
43	7.5047	1.142
45	7.5666	1.127

Table II. Properties of potential energy surfaces for different mass combinations.

Case	I	II	III
Masses[a]	1-1-1	10-1-10	1-35-1
Skew Angle	60°	24.62°	88.41°
Reduced Mass[a, b]	0.5774	2.1822	0.9726
Eigenvalues of Isolated Diatomic (eV)			
v = 0	0.0817	0.0625	0.0606
v = 1	0.1885	0.1561	0.1524
v = 2	c	0.2082	0.2055

[a] In units of the hydrogen atom mass.

[b] Defined as $\mu = [m_A m_B m_C / (m_A + m_B + m_C)]^{\frac{1}{2}}$.

[c] This system only supports two bound states.

Table III. Arrhenius parameters for rates of reaction and dissociation.[a]

Mass Combination[b]	v[c]	Exchange Reaction		Dissociation	
		ℓn b[d]	E_a[e]	ℓn b[d]	E_a[e]
1-1-1	0	11.1	0.086	8.5	0.213
	1	11.2	0.025	10.3	0.072
10-1-10	0	10.0	0.098	3.9	0.208
	1	10.1	0.046	5.7	0.104
	2	10.1	0.015	7.4	0.082
1-35-1	0	11.7	0.014	11.0	0.215
	1	11.6	0.063	10.9	0.133
	2	11.4	0.024	11.2	0.061

[a] From 200 to 650°K for the exchange reaction and 350 to 600°K for dissociation.

[b] In units of hydrogen atom masses.

[c] Reagent vibrational quantum number.

[d] In units of cm · $\text{molec}^{-1}\text{sec}^{-1}$.

[e] In eV.

FIGURE CAPTIONS

Figure 1. Schematic plot of the coordinate system (ℓ, θ) for the rotating Morse cubic spline surface. S is the swing point from which the Morse oscillator is rotated.

Figure 2. Contour plot of the potential energy surface for the model collinear triatomic system studied here (1-1-1 mass combination) in Delves scaled coordinates R_α, r_α. The solid curves are equipotential contours at the total energies (with respect to the dissociated system) indicated at the high side of the figure. The dashed line is the path of steepest descent from the saddle point. The polar coordinates ρ, α of a general point P in this R_α, r_α configuration space are also indicated.

Figure 3. State-to-state reaction and CID probabilities for the 1-1-1 mass combination as a function of relative translational energy and total energy for the reagent vibrational states v = 0 (top panel) and v = 1 (bottom panel). Total energy is indicated by the common horizontal scale (tic marks are on the top of each panel), while translational energy is indicated at the bottom of each panel. Curves are for vibrationally adiabatic reaction (solid line), vibrationally nonadiabatic reaction (dashed), and CID (dashed-dotted). Arrows are drawn at energies at which higher vibrational states and dissociation become energetically allowed, and are labeled on the top figure, e.g., E_1 for v = 1, E_2 for v = 2, and E_d for dissociation.

Figure 4. State-to-state reaction and CID probabilities for the 10-1-10 mass combination as a function of relative translational energy and total energy for the reagent vibrational states v = 0 (top panel), v = 1 (center

panel), and v = 2 (bottom panel). Energies and arrows are as indicated in Fig. 3. The solid curves always represent the vibrationally adiabatic reaction probability, the dashed-dotted curves always represent CID, and the dashed and dotted curves represent vibrationally nonadiabatic reaction probabilities as indicated in the figure.

Figure 5. State-to-state reaction and CID probabilities for the 1-35-1 mass combination as a function of relative translational energy and total energy for reagent vibrational states v = 0 (top), v = 1 (center), and v = 2 (bottom) panels. All markings are as in Fig. 4.

Figure 6. Probabilities for reactive (solid curve), dissociative (dotted curve), and nonreactive (dashed curve) processes as a function of relative translational energy and total energy for the 1-1-1 mass combination for vibrational states v = 0 (top) and v = 1 (bottom). Arrows and energies are as in Fig. 3.

Figure 7. Probabilities for reactive, dissociative, and nonreactive processes as a function of relative translational energy and total energy for the 10-1-10 mass combination for reagent vibrational states v = 0 (top), v = 1 (center), and v = 2 (bottom). Curves are as in Fig. 6; energies and arrows are as in Fig. 4.

Figure 8. Probabilities for reactive, dissociative, and nonreactive processes as a function of relative translational energy and total energy for the 1-35-1 mass combination for reagent vibrational states v = 0 (top), v = 1 (center), and v = 2 (bottom). Curves are as in Fig. 6; energies and arrows are as in Fig. 5.

Figure 9. Arrhenius plot of rate constant (in units of cm · $\text{molec}^{-1}\,\text{sec}^{-1}$)

versus inverse temperature for reactive and dissociative processes for the 1-1-1 mass combination. Solid lines are drawn for rate constants for reaction; dashed lines are used to indicate those for dissociation. Absolute temperature is indicated at the top of the graph.

Figure 10. Arrhenius plot of rates for reactive and dissociative processes for the 10-1-10 mass combination. Lines have the same meaning as in Fig. 9.

Figure 11. Arrhenius plot of rates for reactive and dissociative processes for the 1-35-1 mass combination. Lines have the same meaning as in Fig. 9.

Figure 12. Arrhenius plot of rates of state-to-state reactive and dissociative processes for the 1-35-1 mass combination, with the reagent in its $v = 0$ (top panel), $v = 1$ (center panel), and $v = 2$ (bottom panel). Lines have the same meaning as in Fig. 9.

Figure 13. Argand diagram for the transition $A + BC\ (v = 0) \rightarrow A^2B\ (v = 0) + C$ for the 10-1-10 mass combination. Energies are labeled every 10 meV and correspond to total energies. Points are marked with an X every 5 meV. Arrows are drawn to indicate the sense of the curve.

Figure 14. Argand diagram for the transition $A' + BA\ (v = 1) \rightarrow A'B\ (v = 1) + A$ for the 10-1-10 mass combination. All labeling is as in Fig. 13.

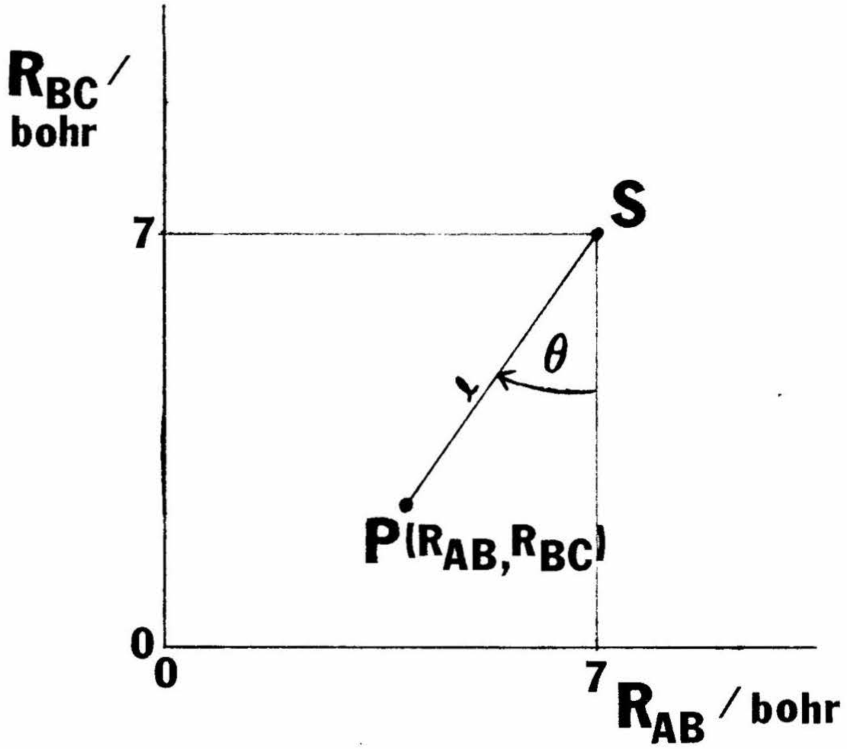

Figure 1

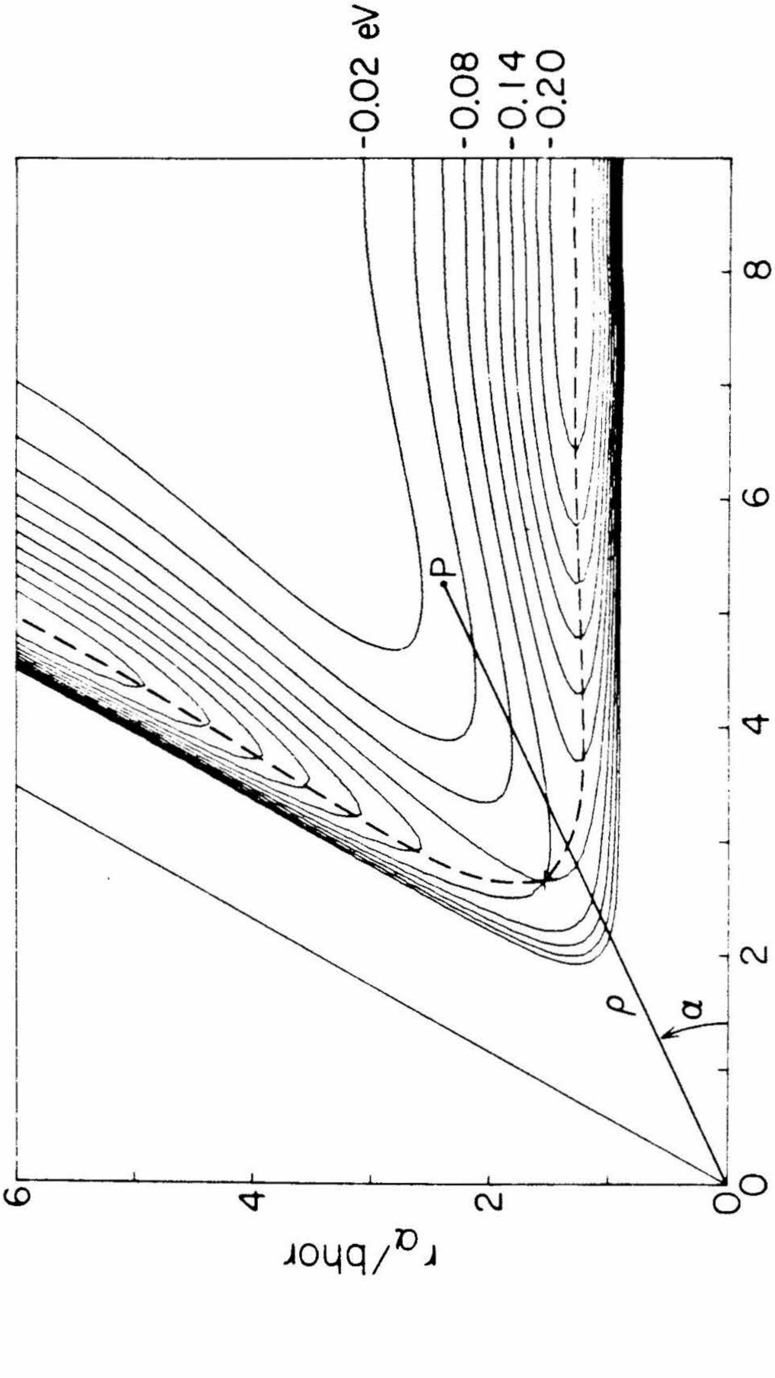
-0.02 eV
-0.08
-0.14
-0.20
R_α/bohr
r_α/bohr
0
2
4
6
8
0
2
4
6
P
ρ
α

Figure 2

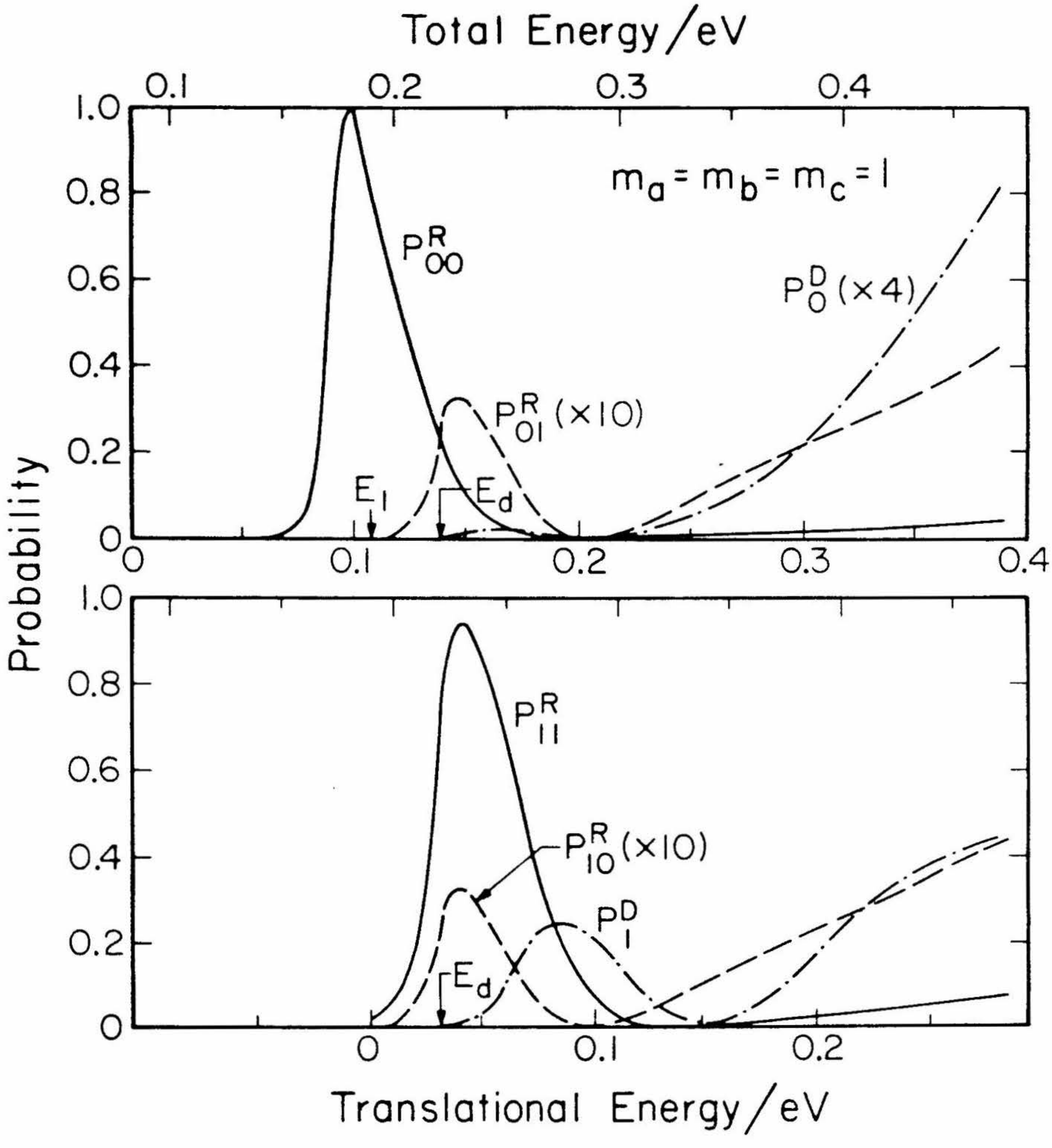
Total Energy/eV
0.1
0.2
0.3
0.4
1.0
0.8
0.6
0.4
0.2
0
$m_a = m_b = m_c = 1$
P^R_{00}
P^D_0 (×4)
P^R_{01} (×10)
E_1
E_d
0
0.1
0.2
0.3
0.4
Probability
1.0
0.8
0.6
0.4
0.2
0
P^R_{11}
P^R_{10} (×10)
P^D_1
E_d
0
0.1
0.2
Translational Energy/eV

Figure 3

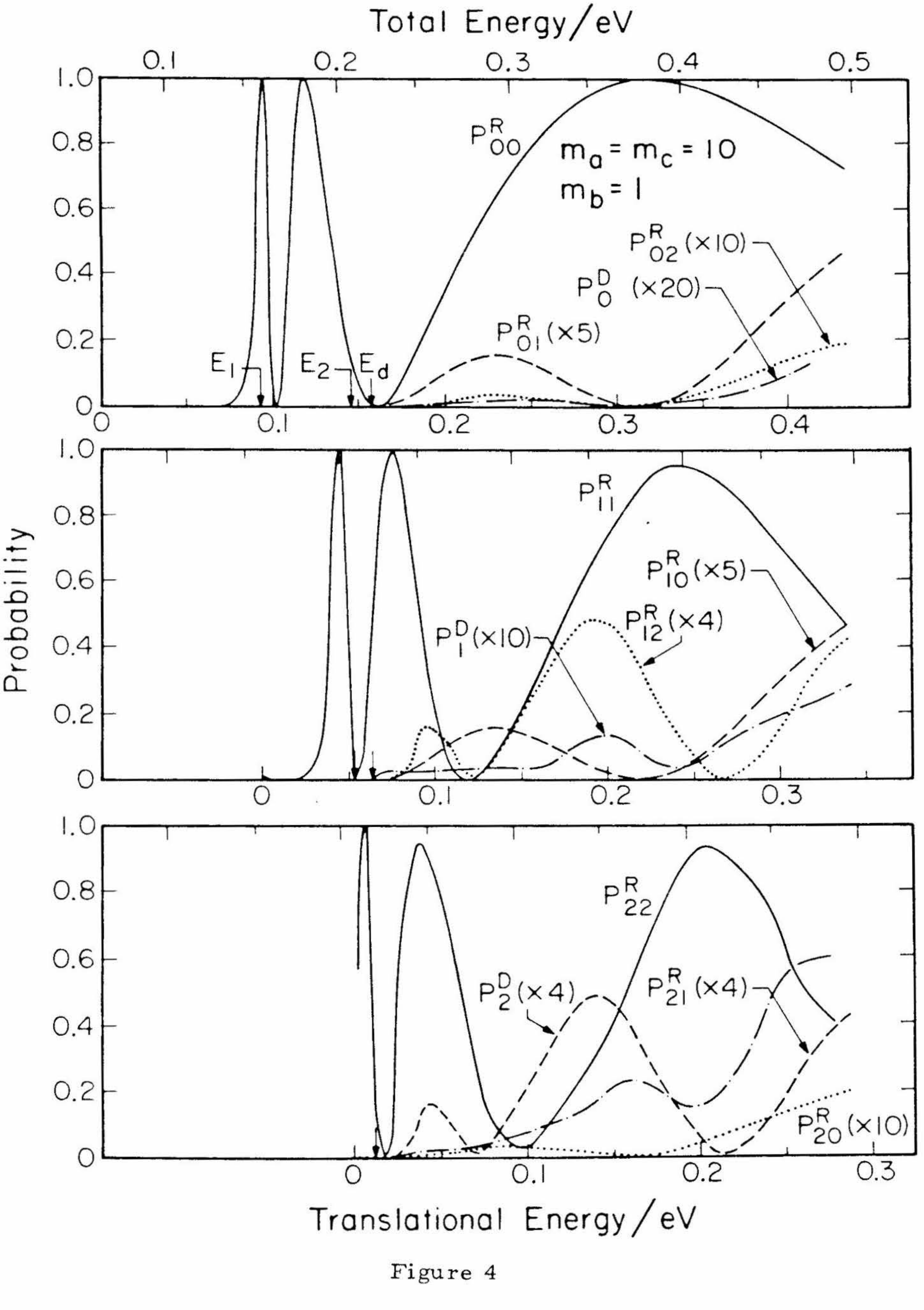
Total Energy/eV
0.1
0.2
0.3
0.4
0.5
1.0
0.8
0.6
0.4
0.2
0
P^R_{00}
$m_a = m_c = 10$
$m_b = 1$
P^R_{02} (×10)
P^D_0 (×20)
P^R_{01} (×5)
E_1
E_2
E_d
0
0.1
0.2
0.3
0.4
Probability
P^R_{11}
P^R_{10} (×5)
P^R_{12} (×4)
P^D_1 (×10)
0
0.1
0.2
0.3
P^R_{22}
P^D_2 (×4)
P^R_{21} (×4)
P^R_{20} (×10)
0
0.1
0.2
0.3
Translational Energy/eV

Figure 4

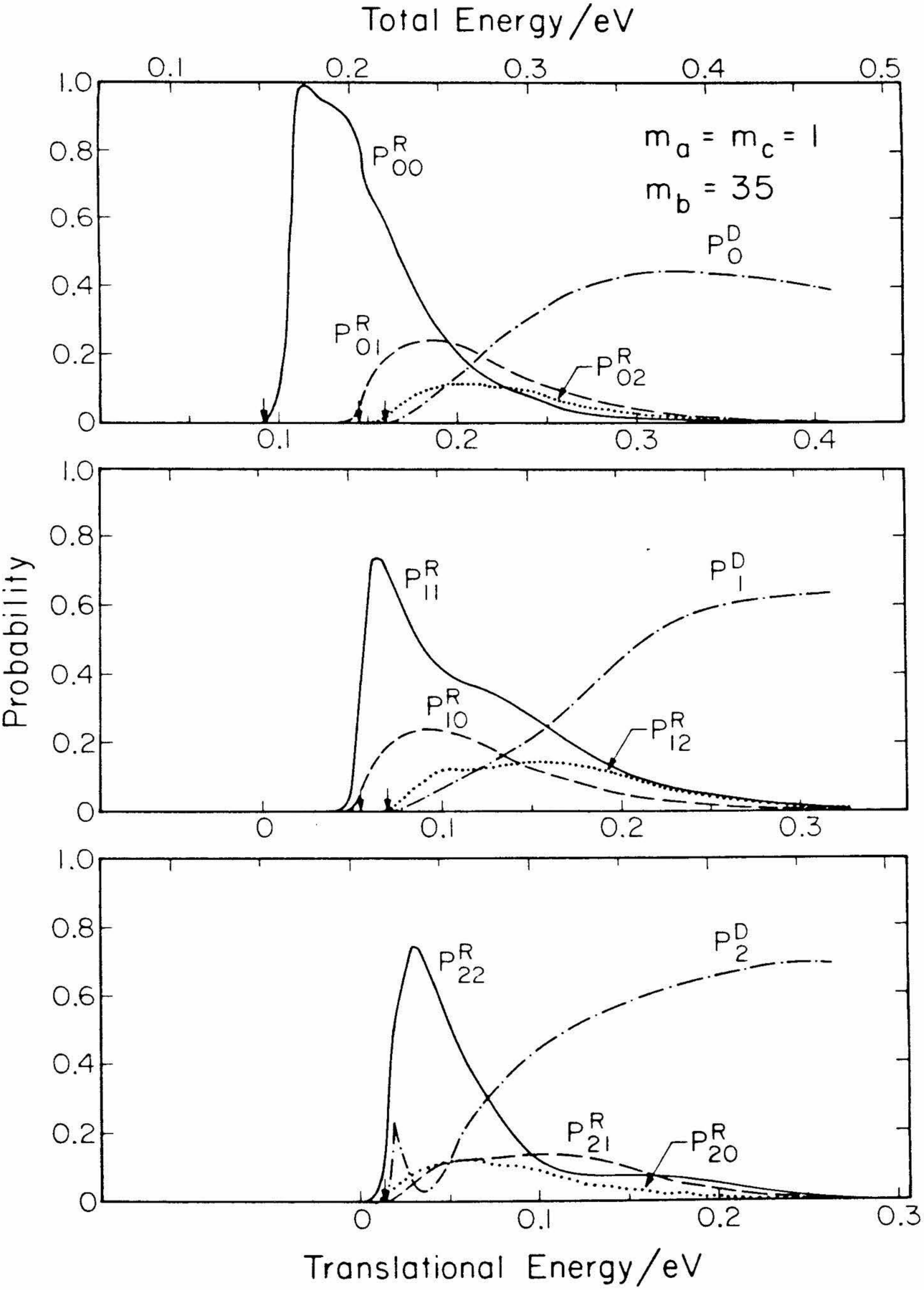
Total Energy/eV
0.1
0.2
0.3
0.4
0.5
1.0
0.8
0.6
0.4
0.2
0
$m_a = m_c = 1$
$m_b = 35$
P^R_{00}
P^D_0
P^R_{01}
P^R_{02}
0.1
0.2
0.3
0.4
Probability
P^R_{11}
P^D_1
P^R_{10}
P^R_{12}
0
0.1
0.2
0.3
P^R_{22}
P^D_2
P^R_{21}
P^R_{20}
0
0.1
0.2
0.3
Translational Energy/eV

Figure 5

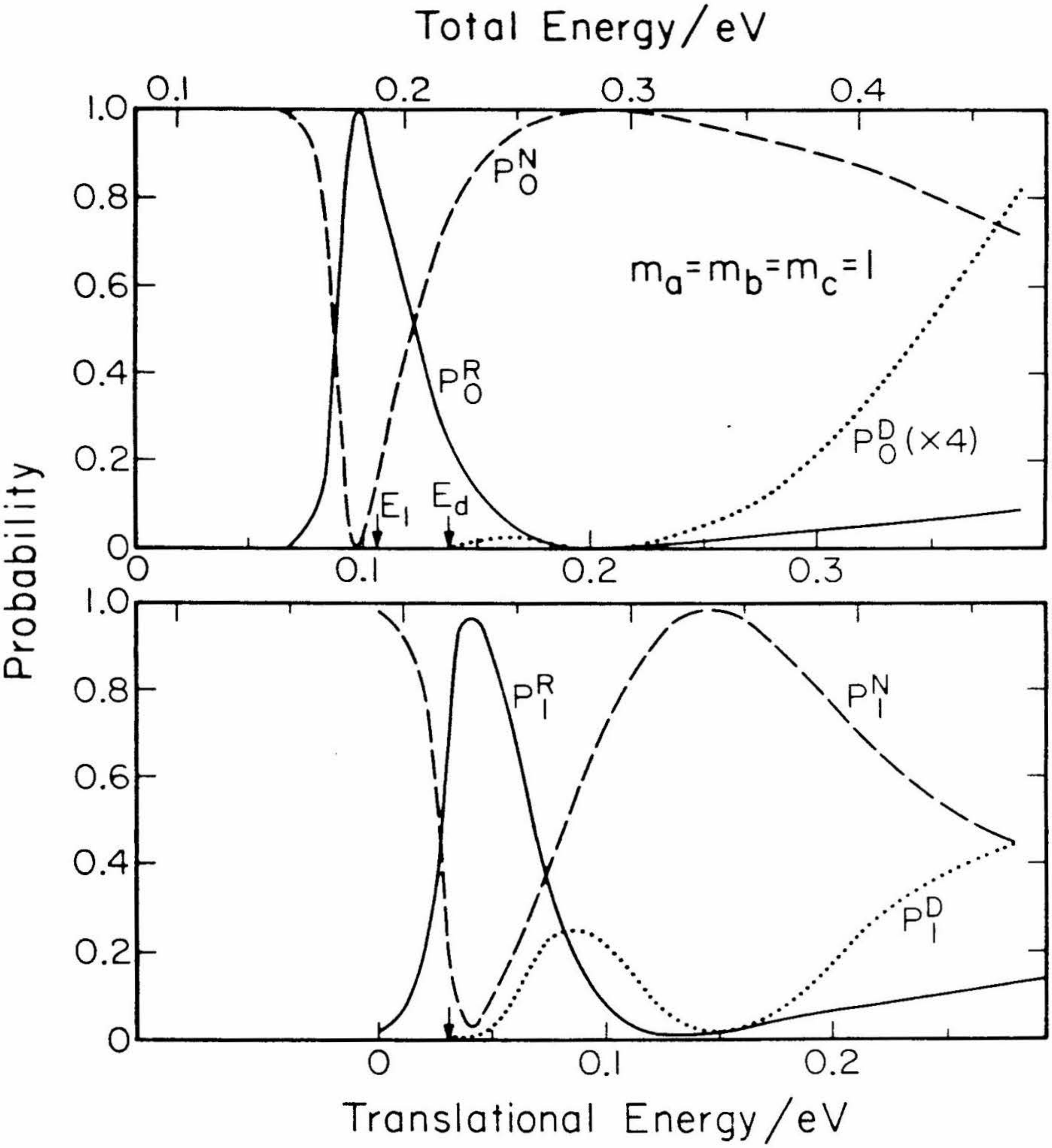
Total Energy/eV
0.1
0.2
0.3
0.4
1.0
0.8
0.6
0.4
0.2
0
P_0^N
$m_a = m_b = m_c = 1$
P_0^R
$P_0^D (\times 4)$
E_1
E_d
0
0.1
0.2
0.3
Probability
1.0
0.8
0.6
0.4
0.2
0
P_1^R
P_1^N
P_1^D
0
0.1
0.2
Translational Energy/eV

Figure 6

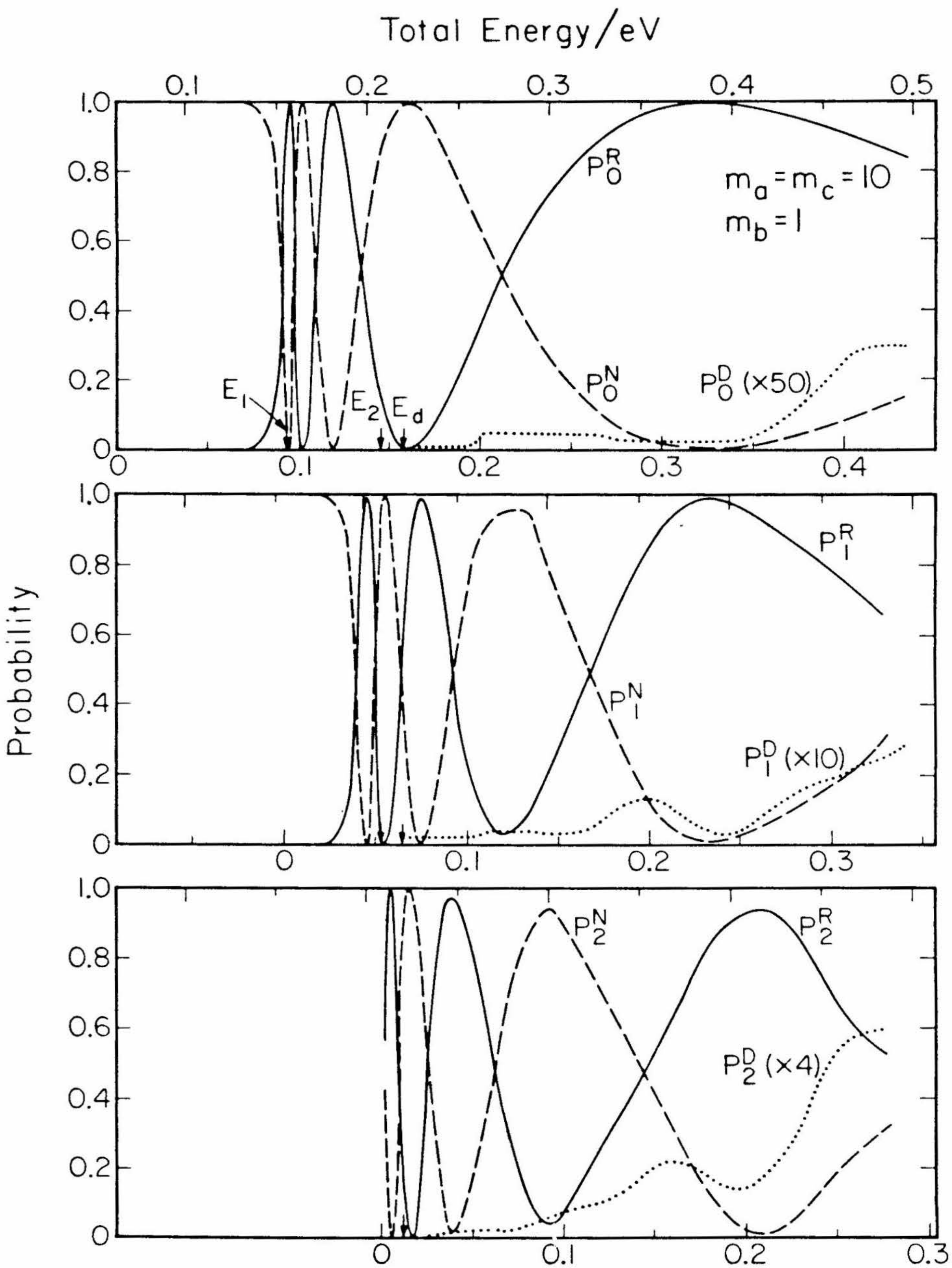
Total Energy/eV
0.1
0.2
0.3
0.4
0.5
1.0
0.8
0.6
0.4
0.2
0
P_0^R
$m_a = m_c = 10$
$m_b = 1$
P_0^N
P_0^D (×50)
E_1
E_2
E_d
0
0.1
0.2
0.3
0.4
P_1^R
P_1^N
P_1^D (×10)
0
0.1
0.2
0.3
P_2^N
P_2^R
P_2^D (×4)
0
0.1
0.2
0.3
Probability
Translational Energy/eV

Figure 7

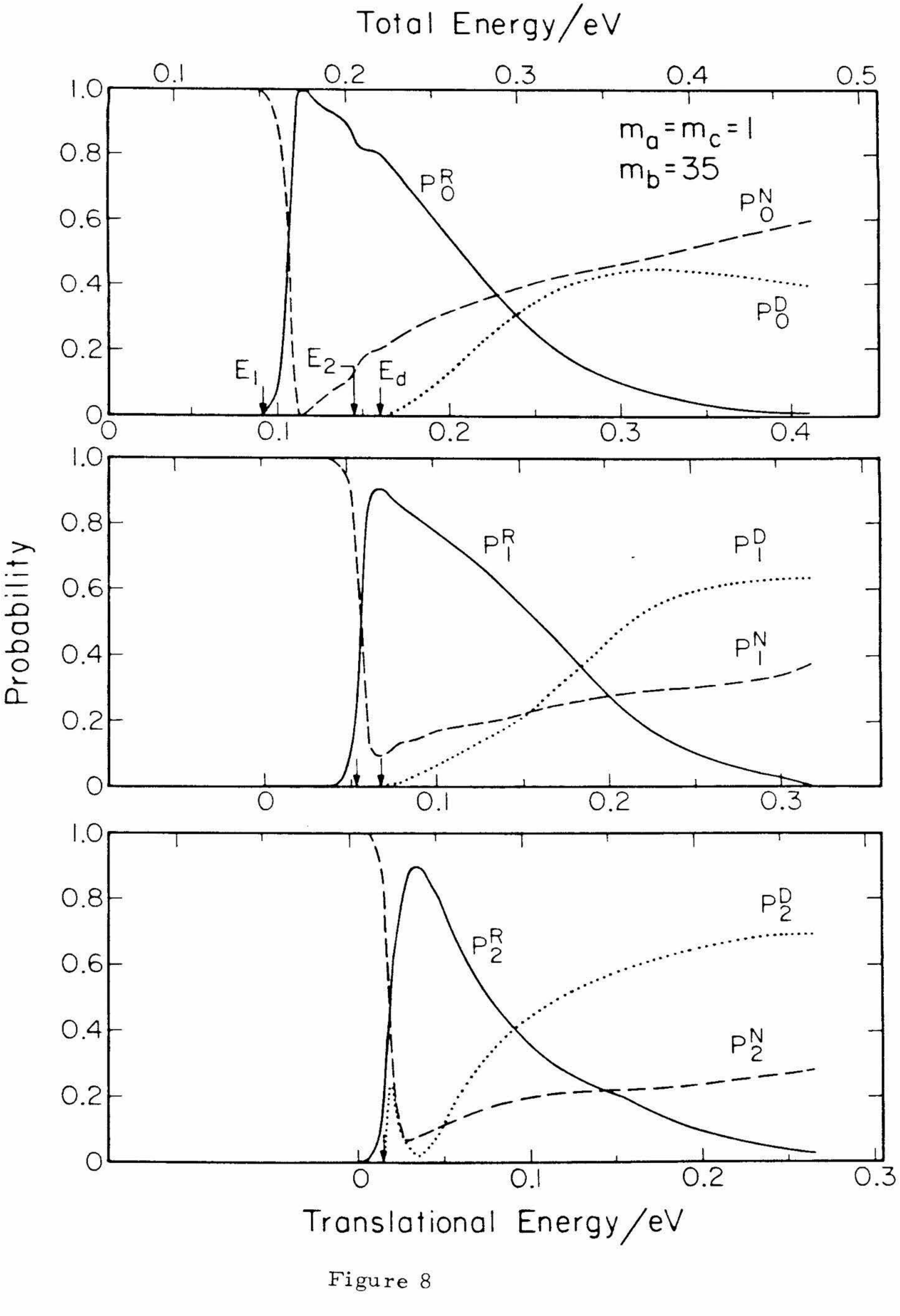
Total Energy/eV
0.1
0.2
0.3
0.4
0.5
1.0
0.8
0.6
0.4
0.2
0
$m_a = m_c = 1$
$m_b = 35$
P_0^R
P_0^N
P_0^D
E_1
E_2
E_d
0
0.1
0.2
0.3
0.4
Probability
P_1^R
P_1^D
P_1^N
0
0.1
0.2
0.3
P_2^R
P_2^D
P_2^N
0
0.1
0.2
0.3
Translational Energy/eV

Figure 8

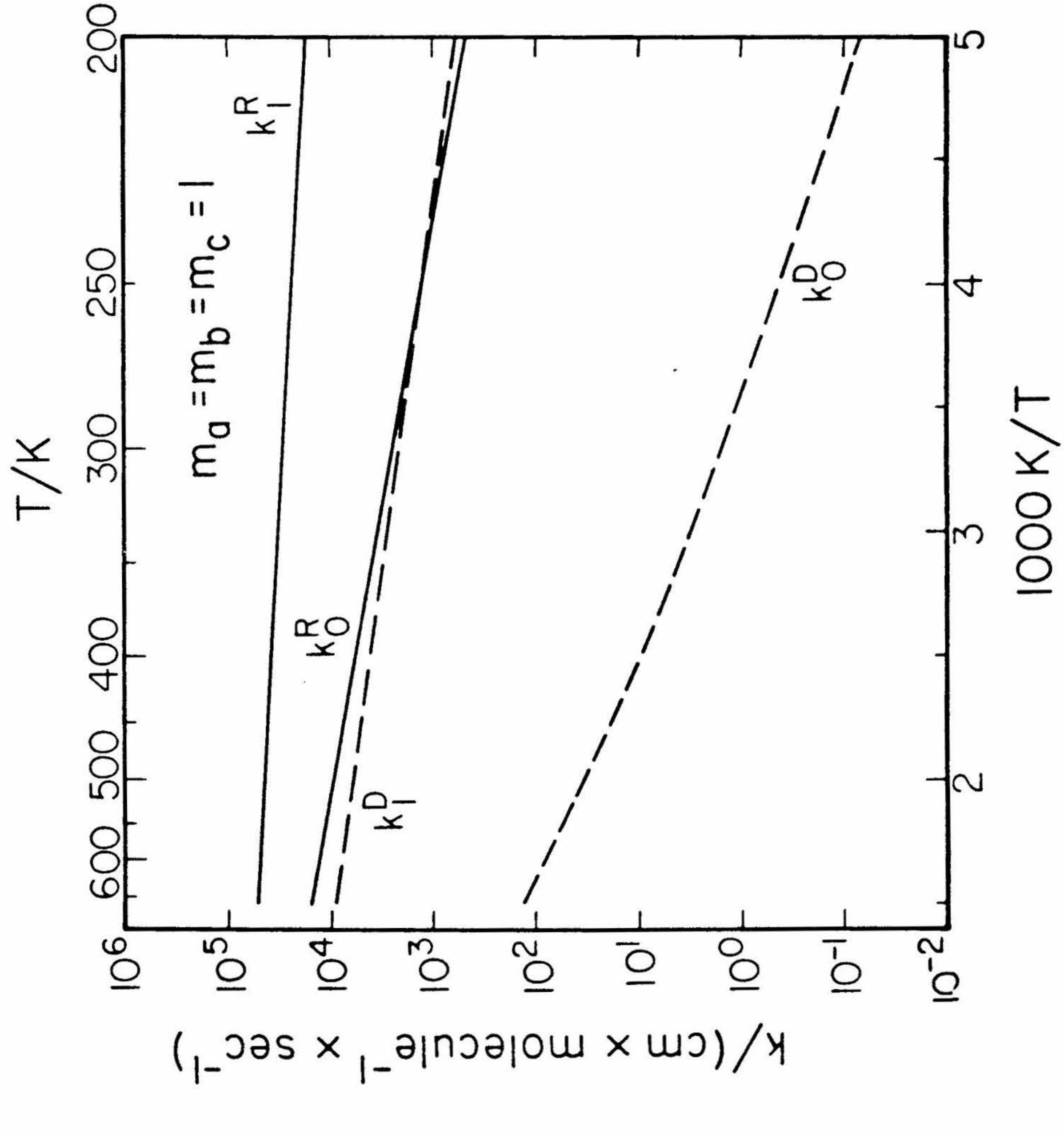
T/K
200
250
300
400
500
600
$m_a = m_b = m_c = 1$
k_1^R
k_0^R
k_1^D
k_0^D
10^6
10^5
10^4
10^3
10^2
10^1
10^0
10^{-1}
10^{-2}
k/(cm x molecule^{-1} x sec^{-1})
2
3
4
5
1000 K/T

Figure 9

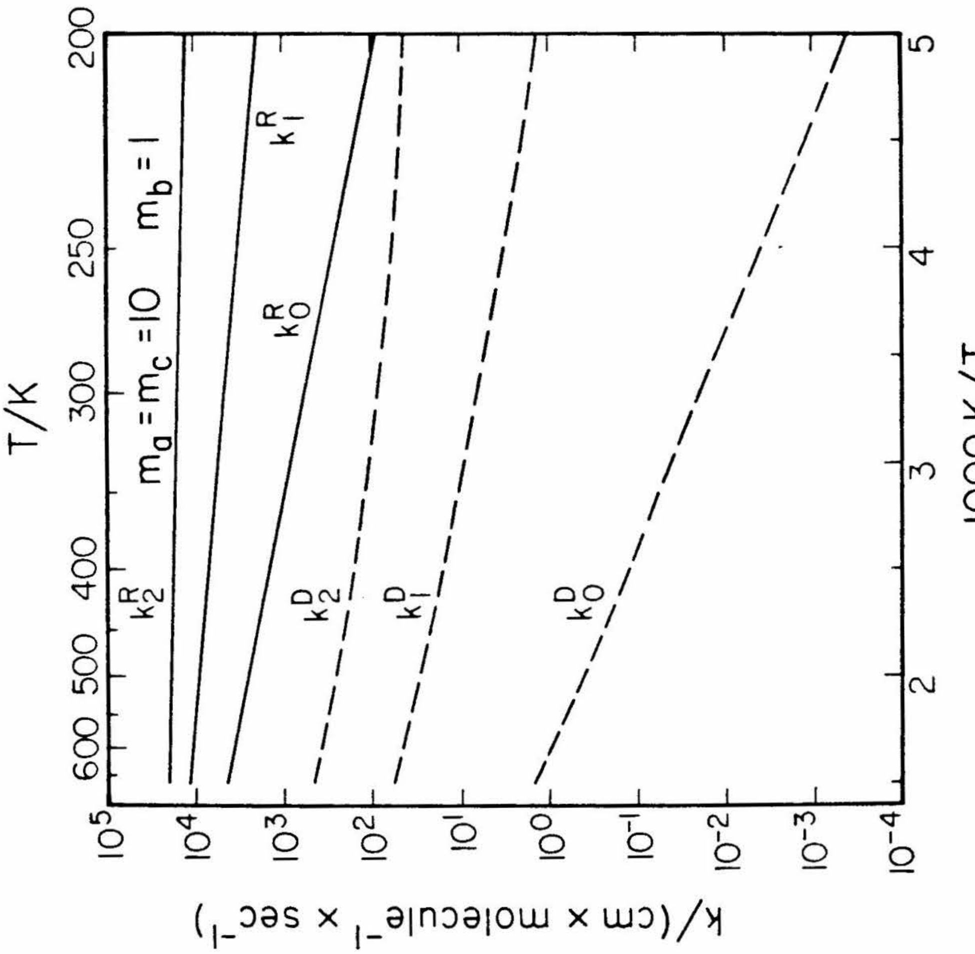
T/K
200
250
300
400
500
600
$m_a = m_c = 10 \quad m_b = 1$
k_2^R
k_1^R
k_0^R
k_2^D
k_1^D
k_0^D
10^5
10^4
10^3
10^2
10^1
10^0
10^{-1}
10^{-2}
10^{-3}
10^{-4}
$k/(\mathrm{cm} \times \mathrm{molecule}^{-1} \times \mathrm{sec}^{-1})$
1000 K/T
2
3
4
5

Figure 10

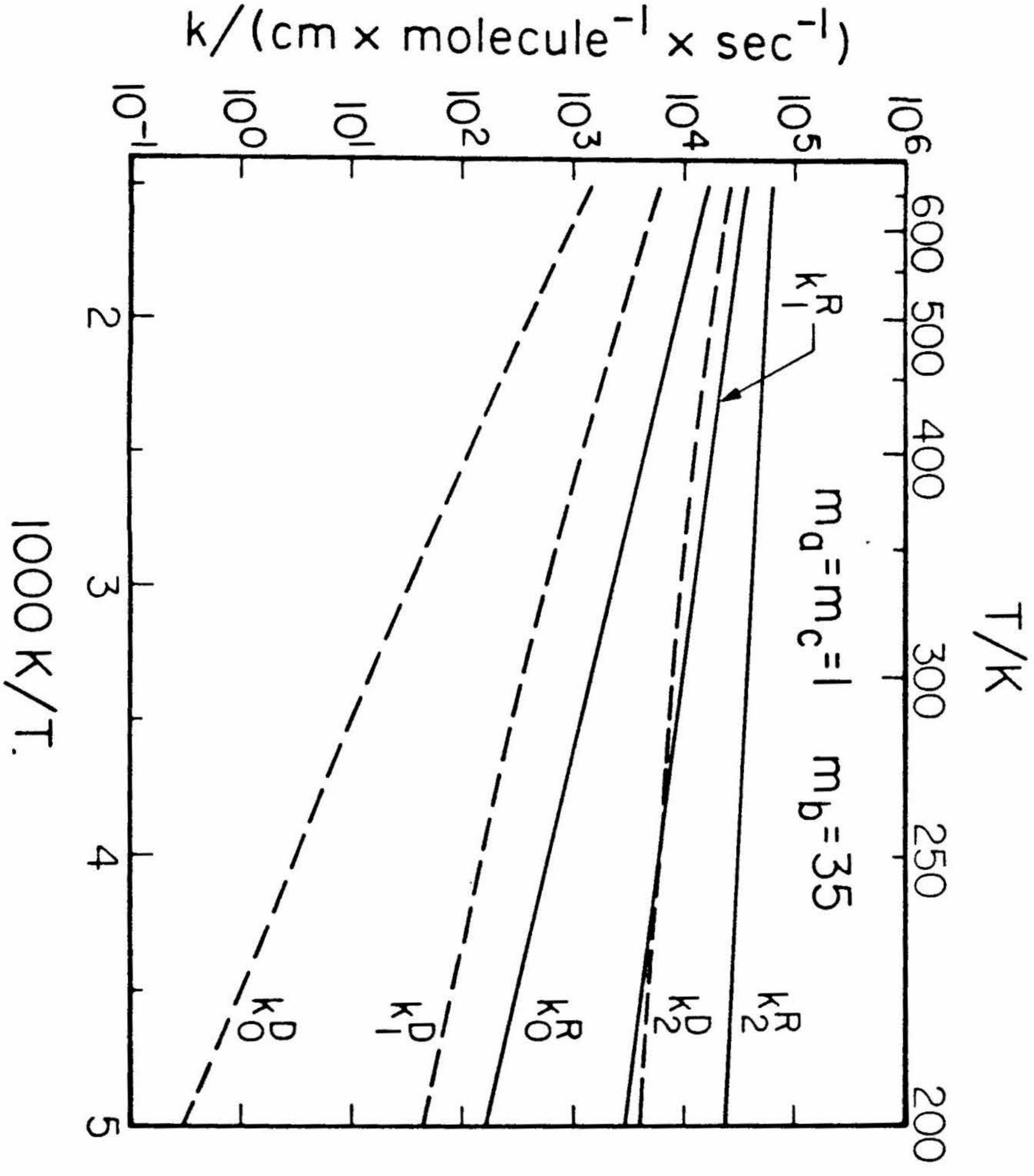
k/(cm × molecule^{-1} × sec^{-1})
10^6
10^5
10^4
10^3
10^2
10^1
10^0
10^{-1}
T/K
600
500
400
300
250
200
1000 K/T.
2
3
4
5
$m_a = m_c = 1$ $m_b = 35$
k_1^R
k_2^R
k_2^D
k_0^R
k_{-1}^D
k_0^D

Figure 11

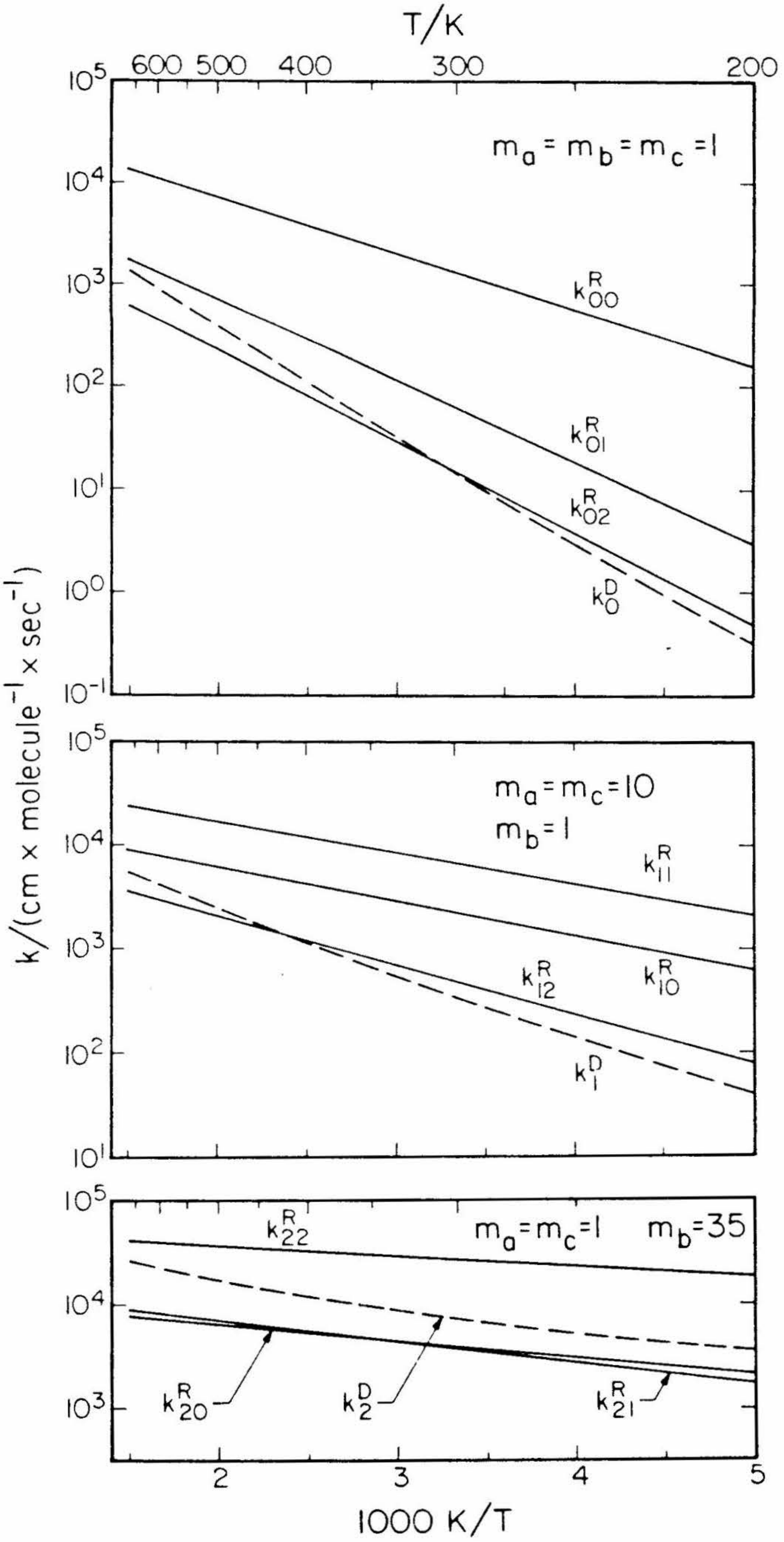
T/K
600
500
400
300
200
10^5
10^4
10^3
10^2
10^1
10^0
10^{-1}
$m_a = m_b = m_c = 1$
k^R_{00}
k^R_{01}
k^R_{02}
k^D_0
10^5
10^4
10^3
10^2
10^1
$m_a = m_c = 10$
$m_b = 1$
k^R_{11}
k^R_{12}
k^R_{10}
k^D_1
10^5
10^4
10^3
k^R_{22}
$m_a = m_c = 1$ $m_b = 35$
k^R_{20}
k^D_2
k^R_{21}
$k/(\mathrm{cm} \times \mathrm{molecule}^{-1} \times \mathrm{sec}^{-1})$
2
3
4
5
1000 K/T

Figure 12

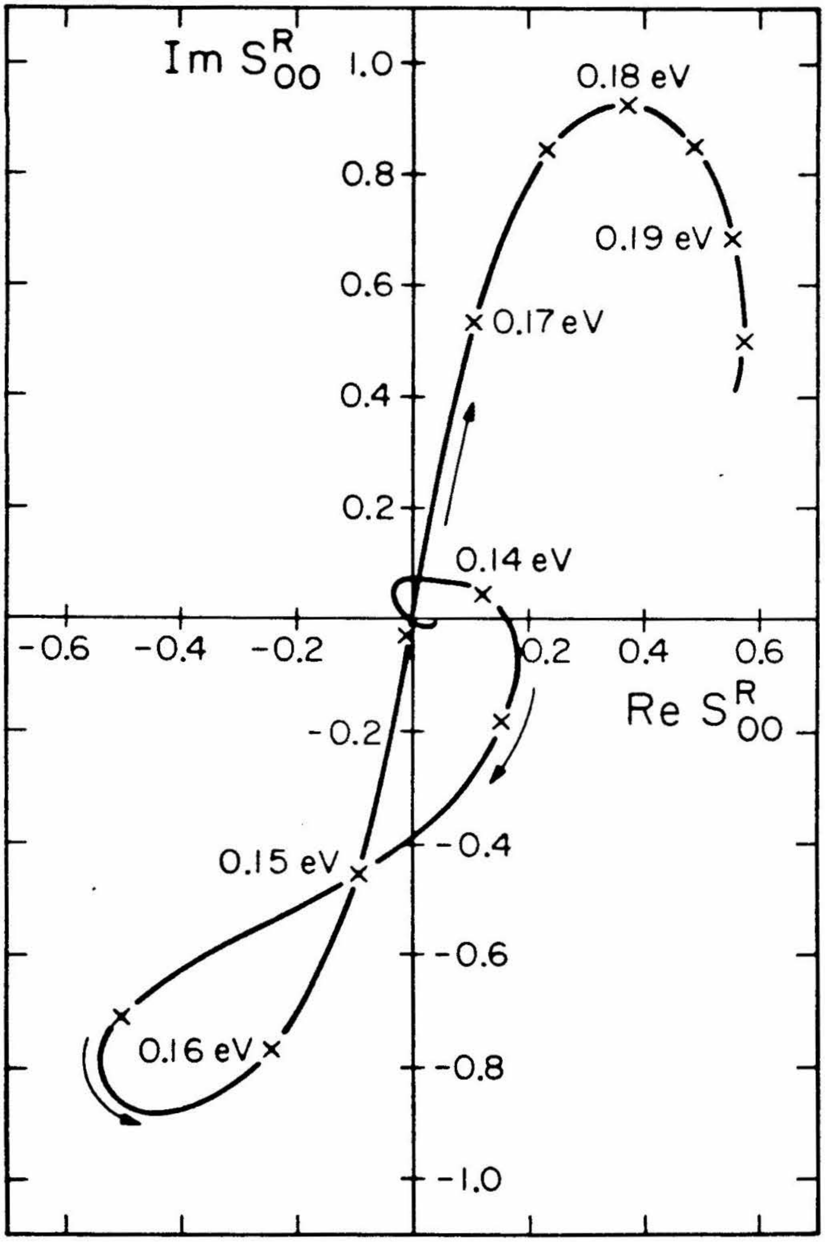
$\mathrm{Im}\ S^R_{00}$
1.0
0.8
0.6
0.4
0.2
-0.2
-0.4
-0.6
-0.8
-1.0
-0.6
-0.4
-0.2
0.2
0.4
0.6
$\mathrm{Re}\ S^R_{00}$
0.18 eV
0.19 eV
0.17 eV
0.14 eV
0.15 eV
0.16 eV

Figure 13

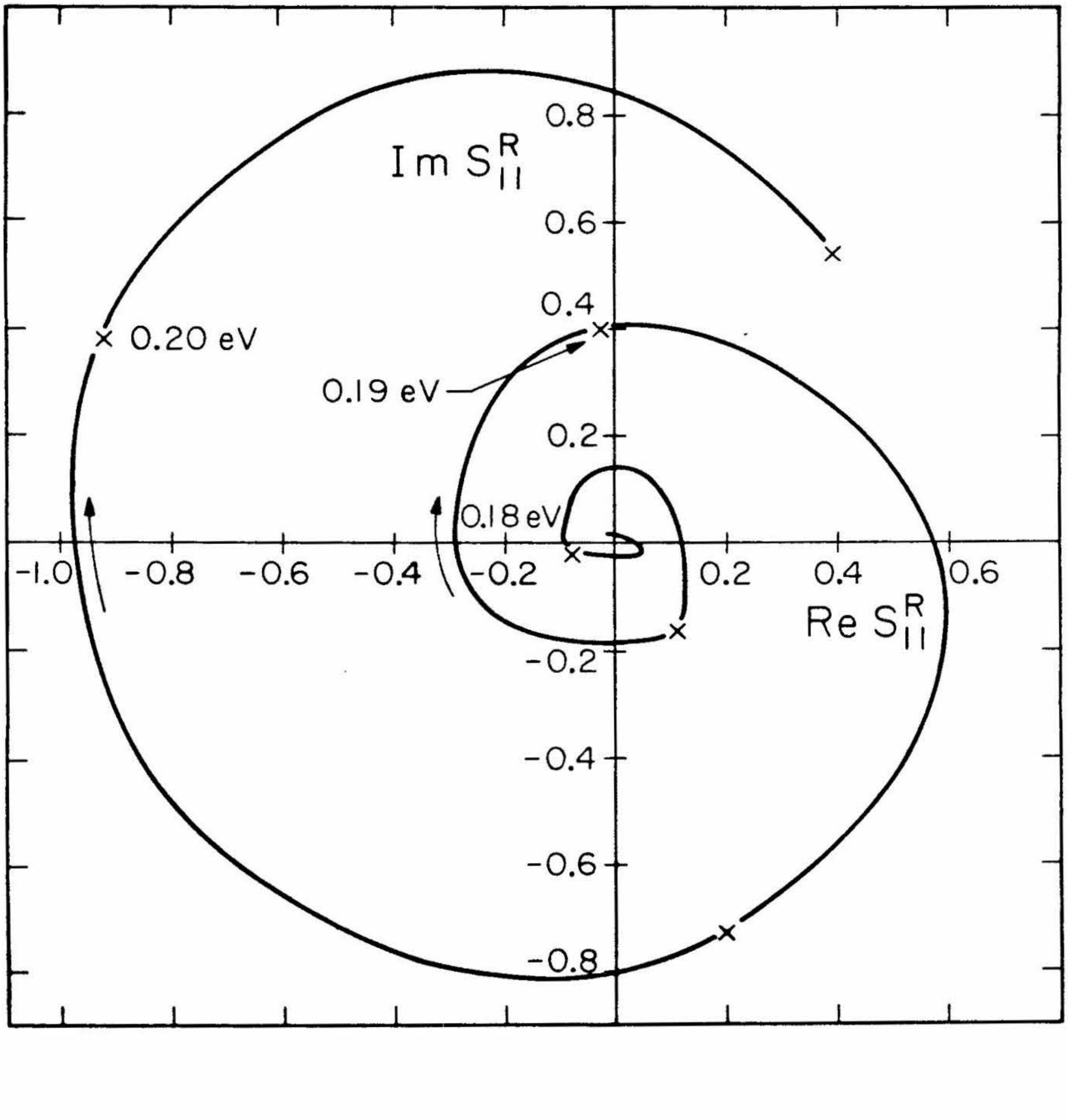
Im S_{11}^R
Re S_{11}^R
0.20 eV
0.19 eV
0.18 eV
0.8
0.6
0.4
0.2
-0.2
-0.4
-0.6
-0.8
-1.0
-0.8
-0.6
-0.4
-0.2
0.2
0.4
0.6

Figure 14

III. 5 COLLINEAR QUASI-CLASSICAL TRAJECTORY STUDY OF COLLISION-INDUCED DISSOCIATION ON A MODEL POTENTIAL ENERGY SURFACE

Collinear Quasi-Classical Trajectory Study of Collision-Induced Dissociation on a Model Potential Energy Surface.[a]

Jack A. Kaye[b] and Aron Kuppermann
Arthur Amos Noyes Laboratory of Chemical Physics,[c]
California Institute of Technology, Pasadena, California 91125

(Received)

Quasi-classical trajectory calculations have been carried out at energies above the threshhold for collision-induced dissociation for a model collinear atom-diatomic molecule system. Exact quantum mechanical calculations have shown that quasi-classical trajectories give a qualitatively correct picture of the dynamics in this system. Trajectories leading to dissociation are found to lie almost entirely in well defined reactivity bands, with the exception of a few occurring in a small chattering region in which the outcome of the trajectory is extremely sensitive to its initial conditions. The probability of dissociation leading to all possible distributions of the kinetic energy of the resulting atoms is obtained and is shown to vary substantially with initial conditions (reagent vibrational and translational energy). The form of these probability distributions is, to a major extent, determined by the position and width of the reactivity bands. The different dissociation reactivity bands are shown to be composed of different types of trajectories. Part of the vibrational enhancement of dissociation arises from the fact that the simplest possible trajectory leading to dissociation (one which crosses the symmetric stretch line once prior to the onset of dissociation) is not obtained with ground state reagents.

---

[a] This work was supported in part by a contract (No. F49620-79-C-0187) from the Air Force Office of Scientific Research.

[b] Work performed in partial fulfillment of the requirements for the Ph. D. degree in Chemistry at the California Institute of Technology.

[c] Contribution No.

I. INTRODUCTION

The collision-induced dissociation (CID) of diatomic molecules

$$A + BC \longrightarrow A + B + C \tag{1}$$

is a process of great fundamental interest in chemistry, particularly in the high temperature chemistry associated with shock waves, both in the laboratory (1) and in interstellar space (2). The ab initio calculation of CID rates has proven to be extremely difficult, as one must have accurate methods for calculating the potential energy surface for the collision, solving for the dynamics, and then integrating the coupled rate equations to obtain expressions for the rate of disappearance of the diatomic molecule.

The development of accurate methods for solving for the dynamics has been especially difficult. Kinematic and quasi-classical trajectory (QCT) calculations have been extensively used to study CID (3). The number of studies incorporating quantum mechanical effects, either by a semi-classical or a purely quantum mechanical approach, is much smaller (4). Most of these studies have been restricted to collinear collisions in which reactive collisions of the type

$$A + BC \longrightarrow AB + C \tag{2}$$

are not permitted. Non-collinear collisions in non-reactive systems have been studied by the semi-classical method by Rusinek (5). Exceptions to this are three purely quantum methods in which reaction and dissociation may compete (these are all restricted to collinear collisions at this time): the wave packet approach of Kulander (6), the hyperspherical coordinate coupled-channel method developed independently by Kaye and Kuppermann (7) and by Manz and Römelt (8), and the multiple collision approach of Beard and Micha (9) (which has been applied only to a non-reactive system).

The availability of accurate quantum mechanical (QM) results for CID has increased interest in QCT studies. In particular, Kaye and Kuppermann (7) have shown that for the model system they studied, the QCT results were qualitatively similar to the QM ones. Since the model system involves light masses (three hydrogen atoms) and weakly bound (0.22 eV) molecules, quantum effects might be expected to be important. This suggests that QCT calculations might be useful predictors of the gross features of CID in reactive systems. One must approach this with some caution, however, as in a non-reactive system, Gray, et al. (10) have obtained major differences in the dissociation probability between their QCT results and the QM results of Knapp and Diestler (11).

In order to help gain a better understanding of the dynamics of this model system, we have carried out a reactivity band analysis of the QCT results for this system. Such analyses have been extensively applied to reactive systems below dissociation (12, 13) and have also been applied to a non-reactive system above dissociation (10a). We examine bandedness in the plots of trajectory outcome (reaction, non-reaction, dissociation) as a function of initial vibrational phase of the diatomic molecule and the relative kinetic energy. We also consider the variation of the vibrational action of the diatomic product of non-reactive and reactive collisions with initial vibrational phase. In dissociative collisions we examine how the partitioning of the energy among the three product atoms varies with initial vibrational phase and reagent translational energy. We also examine individual trajectories in order to understand the nature of the trajectories comprising each of the reactivity bands.

II. METHOD OF CALCULATION

The QCT calculations have been performed using standard methods (14). The model potential enrgy surface used has been described previously (7); we repeat here its basic features. It is of the rotating Morse-cubic spline type (15), and has asymptotic Morse oscillator parameters (16) of $D_e = 0.22$ eV, $R_{eq} = 1.40083$ bohr, and $\beta = 1.6$ bohr^{-1}. There is a barrier to exchange of 0.14 eV. The surface is plotted in figure one of reference seven, and is replotted later in figures 23-31, in which we show selected trajectories . The trajectories are integrated with a time step of 5.41×10^{-17} sec. Energy is conserved to four digits in these calculations. Integration of trajectories began with the distance from the incident atom to the center of mass of the diatomic molecule at 12 bohr.

To determine dissociation probabilities and rough boundaries for reactivity bands, we have calculated 100 trajectories per energy at regularly spaced ($\pi/50$ radians) values of the initial vibrational phase. At selected energies, we have narrowed the phase grid substantially near the boundaries of the reactivity bands. Below dissociation we have calculated 50 trajectories per energy at regularly spaced ($\pi/25$ radians) values of the initial vibrational phase and successively narrowed the grid near the band boundaries.

We have also determined the partitioning of kinetic energy among the atoms after the collision. The quantity of greatest interest is the fraction f_X^D (X = A, B, C) of the available kinetic energy E' (the difference between the total energy E of the collision and the dissociation energy D_e of the diatomic molecule) in dissociative collisions in each of the atoms at the end of the collision. In dissociative collisions, the collision was defined to be over when both internuclear distances R_{AB} and R_{BC} were greater than 6.0 bohr and were increasing with time. The sum of the kinetic and potential energies of the AB and BC pairs was each required to be greater than D_e. We have extended this calculation to include this ratio for atom A in non-reactive collisions (f_A^N) and atom C in reactive collisions (f_C^R). Plots of these quantities vs. initial vibrational phase will connect smoothly to the f_A^D and f_C^D curves across the boundary of the reactivity bands . From the fractional energy vs. initial vibrational phase data, one may calculate the probability ${}^c\sigma_v^d$ of the kinetic energy of atom A after dissociation E_A being between E_A and $E_A + dE_A$ for a collision in which the diatomic molecule is in state v. This may be done by recognizing that this is related to the width of the region of phase d in which E_A will lie between E_A and $E_A + dE_A$

$$ {}^c\sigma_v^d(E_A) = (1/2\pi)\ |d\phi/dE_A| \tag{3} $$

The superscript c emphasizes the classical nature of this quantity. The $(1/2\pi)$ factor is included so that ${}^c\sigma_v^d(E_A)$ will be appropriately normalized:

$$ \int_{E_A^{\min}}^{E_A^{\max}} {}^c\sigma_v^d(E_A)dE_A = 1 \tag{4} $$

The limits of integration in eq. 4, $E_A^{\min}$ and $E_A^{\max}$, have been shown previously (17) to be $E'/6$ and $2E'/3$, respectively, when the masses of all atoms are equal. To simplify comparison of these partitioning probabilities from one energy to the next, we will plot the dimensionless partitioning probabilities $E' \cdot {}^c\sigma_v^d(E_A)$, which will be indicated by a bar over the quantity, vs. f_A for all values of the energy E', in which case the abscissa will always run from 1/6 to 2/3.

The evaluation of the derivative in eq. 3 is complicated by the possibility of minima or maxima in the E_A vs. curves; hence $\phi(E_A)$ may be a multiply valued function of ϕ . We separate those regions in which $d\phi/dE_A$ is positive and negative and then separately obtain the derivatives by a three-point finite difference procedure. The resulting derivatives are then used as an input for a cubic spline procedure wh which allows us to obtain approximate expressions for the derivatives as a function of E_A. We next sum the absolute values of the derivatives over all separated parts of each dissociative reactivity band and over all such dissociative reactivity bands, and divide by 2π for normalization. The resulting curve (called a partitioning probability curve) may contain some numerical noise associated with the numerical differentiation procedures; we have visually smoothed out the spline-induced oscillations.

III. RESULTS

Reaction and dissociation both occur in the energy range studied here (up to 0.25 eV above the dissociation energy of the diatomic molecule). Plots of the reaction and dissociation probability obtained from the trajectory calculations are shown for reagent states v = 0 and v = 1 (the only ones possible) in figures 1 and 2, respectively. For both reagent states, the reaction probability is zero below a threshhold energy, increases rapidly with energy to a large value (0.86 for v = 0, 0.96 for v = 1) and then decreases to zero (for v = 0) or a value just above zero (for v = 1). It then increases monotonically with energy. The dissociation probabilities for the v = 0 and v = 1 reagents behave quite differently from each other, however. In the v = 0 case, no dissociation is observed until one is substantially (0.08 eV) above its energetic threshhold; as the energy increases beyond that, the probability increases slowly, reaching a value of 0.27 eV at the highest energy studied. For the v = 1 case, dissociation sets in at 0.02 eV a above its energetic threshhold, increases rapidly with energy to a maximum of 0.33 and then decreases rapidly to 0.02 before again increasing with energy up to a value of 0.39 at the highest energy studied. It should be emphasized that all of these results are qualitatively similar to the exact quantum mechanical results for this system presented in reference 7.

We next examined bandedness in plots of trajectory outcome vs. initial vibrational phase and relative translational energy. Plots of the reactivity bands for this system are shown in figures 3 and 4 for reagent states v = 0 and 1, respectively, for energies above the threshhold for CID. Unlike reactivity band plots normally used in studies of reactive atom-diatomic molecule collisions at energies below dissociation, in which there are only two possible outcomes of a trajectory (reaction or non-reaction), there are three possible outcomes here: reaction (R), indicated by the shaded regions of the figures; dissociation (D), indicated by the speckled regions, and non-reaction (N), indicated by the clear regions. The dissociative band centered near 2.0 radians and 0.17 eV translational energy in figure 4 is enlarged in figure 5.

Fairly well defined bands are seen to exist above dissociation. When one narrows down the phase grid substantially (to on the order of 0.002 radians), one may find blurring of the boundaries and formation of a "chattering" region (18), in which the outcome of the trajectory varies strongly with small changes in the initial phase . This is most severe below 0.10 eV translational energy in the v = 1 case, where the high energy reaction and dissociation bands come to a "point" (see figure 4). For example, at 0.085 eV reagent translational energy, between 2.50 and 2.70 radians initial phase, there are four separate dissociation zones, two reaction zones, and one non-reaction zone obtained when the grid spacing of 0.002 radians is used. The total width of all the dissociative zones in this region is 0.52 radians. The dissociation probability produced by this region is only 0.8%, which is far smaller than the contribution at this energy from the large band centered at 5.5 radians. Chattering is also seen near the boundary between reactive and non-reactive bands at energies below dissociation.

We next consider the variation of the vibrational energy of the diatomic molecule resulting from reactive or non-reactive collisions. Normally, to examine this quantity one prepares plots of the action of the diatomic moledule at the end of the trajectory as a function of initial phase at a sequence of energies (10a, 12, 19, 20). At energies above dissociation, one cannot calculate the action in the usual way, and one is left with gaps in the action vs. phase plots. Examples of these plots are shown in figures 6 and 7 for the highest energies studied (reagent translational energies of 0.388 eV for v = 0 and 0.2815 eV for v = 1). Solid lines are used to indicate non-reactive zones and dashed lines are used to indicate reactive zones. The shaded regions mark those regions of initial phase in which the trajectories are dissociative and hence no action can be defined. In both of these figures, the dissociation is seen to occur in between regions of high final action in reactive and non-reactive collisions (the maximum allowable final action in this system is 1.981). This is quite reasonable behavior, as for dissociation to occur, there must be more than the dissociation energy present in each diatomic molecule, hence, the boundary between reactive or non-reactive regions is expected to occur where the final action of the diatomic molecule equals it maximum value.

A different sort of diagram is shown in figure 8, in which we plot the final action vs. initial phase in a collision with v = 1 reagent and a reagent translational energy of 0.1615 eV. Here there are three dissociative regions. Two are sandwiched between the reactive and non-reactive regions, and one is in the middle of the large non-reactive region. This dissociative region is part of the small dissociative band located near 2 radians initial phase between 0.15 and 0.20 eV reagent translational energy in figure 4 (and enlarged in figure 5). As the initial phase is varied so it closely approached that in the dissociative region, the final action increases, suggesting that the consideration of dissociation as a limiting case of vibrational excitation is an appropriate concept.

There is a substantial difference between the product state distribution in collisions with v = 1 reagent at relative energies of 0.2815 eV (figure 7) and at 0.1615 eV (figure 8). At the higher energy, the likelihood of vibrational deexcitation, as measured by the large region of initial phase over which the final action is substantially smaller than one, is much greater than at the lower energy. At the lower energy, from -0.5 radians to the second dissociative band (at 4.15 radians), the final action never becomes smaller than 0.8. Thus, increasing translational energy seems to lead to increasing vibrational non-adiabaticity in non-reactive collisions. The small likelihood of reaction in these energy regions makes it difficult to draw any conclusions concerning that process. A similar trend has been observed in the exact quantum mechanical calculations on this system (21).

Further evidence of the tendency towards vibrational adiabaticity at low energies can be seen by considering a collision with $v = 0$ molecules at an energy (0.178 eV relative translational energy) at which only non-reactive collisions occur - no dissociation or reaction was found. A plot of the final action as a function of initial phase for this collision is given in figure 9. The near adiabaticity may be seen by noting that the total range of final actions in the figure is from -0.12 to 0.19, corresponding to vibrational energies of 0.0639 eV and 0.1079 eV, respectively (the zero point energy is 0.0818 eV). Hence, at most 15% of the initial translational energy was converted to vibrational energy in the collision. Another interesting feature of this figure is the relatively complicated structure. In spite of the fact that all collisions are non-reactive and nearly adiabatic, there is still some systematic variation in the dependence of the final action on the initial phase.

To give some feeling for what happens when the boundary regions between the reactivity bands become blurred, we present in figure 10 a plot of final action vs. initial phase for the collision with $v = 1$ molecule at a relative translational energy of 0.085 eV for initial phases from 2.40 to 3.10 radians. In this region one sees five separate dissociative regions, four of which are found between 2.50 and 2.70 radians. These may be thought of as being distinct from the larger dissociative band between 2.90 and 3.10 radians. The latter band is part of the large dissociative band seen in the lower right hand portion of figure 4. The action vs. phase curves are fairly smooth in between the dissociative regions. Away from the lower tip of the large dissociation and reaction band in figure 4, the boundaries are smoother. This figure seems to represent, then, an upper limit to the complication of such a diagram.

We next consider the partitioning of kinetic energy among the three atoms in dissociative collisions and also the amount of kinetic energy of motion of the free atom in reactive and non-reactive collisions. The calculation of these quantities has been described earlier. Plots of these quantities as a function of the initial phase are shown for initial phases in or near which dissociation occurs for a variety of initial conditions in figures 11 - 16. A few important features are observed in these figures, and we review these here.

First, the curves are quite smooth in the dissociation region. At the border between reactive and dissociative collisions, f_C smoothly matches onto the f_C^R curve, and at the border between non-reactive and dissociative collisions, f_A smoothly matches onto the f_A^N curve. In all cases, the matching occurs at a value of the energy fraction of 2/3; this has been shown to be the maximum value f_A or f_C can take in the dissociative region for a system of three equal masses. The small values of f_B are also a requirement of the mass combination (for the case of three equal masses, f_B is required to be smaller than 1/6).

Second, two types of partitioning curves are seen. For those dissociative bands sandwiched between one reactive and one non-reactive band, f_A and f_C must both have regions where they are large (~2/3) and small (~1/6). For those bands sandwiched between two non-reactive bands, the f_A vs. phase curve must have a minimum. The presence of such a minimum will have a major effect on the partitioning probabilities to be presented below. In theory, one might obtain dissociative bands sandwiched between two reactive ones, but such bands have not been observed .

Finally, we present results for the partitioning probability $\overset{c}{\overline{\sigma_v}}{}^{d}$ defined earlier. These are shown in figures 17 - 22 for the six sets of initial conditions for which energy fractions were shown as a function of initial phase. They all appear quite different from each other, and we can rationalize much of their form simply from the reaction and dissociation probabilities, the kinematics of the system, and the existence of well defined dissociation bands in the reactivity band plots (figures 3-5). We will extensively examine this issue in the discussion section.

There are a few features of figures 17 - 22 which will prove to be of most interest. First is the tendency of the partitioning probabilities to have their maxima near the maximum allowable fraction of 2/3, although this is not uniformly true (see particularly figure 21, in which the partitioning probability diverges at a fraction of 0.25). Second, in four out of the six cases studied, the partitioning probability has divergences (figures 18 and 21) or sharp peaks (figures 19 and 20). Third, curves of the partitioning probability need not be smooth. If there is more than one dissociation band at a given energy, each of which has a very different slope or range of slopes in its corresponding fractional energy vs. phase curve, by summing the contributions from each band one may be adding one curve which is non-zero in the range $f_1 < f < f_2$ and another which is non-zero in the range $f_1' < f < f_2'$. Such a condition would result in a partitioning probability curve which is discontinuous at f_1' and f_2'. Normally, this will not be seen, as $f_1 = f_1' = 1/6$ and $f_2 = f_2' = 2/3$. If this is not true for a given band, discontinuities will be observed. This may be seen in figure 21, in which the hump in the region $0.42 < f < 0.49$ is due to the existence of a narrow dissociative band between 1.9930 and 2.0055 radians (not shown) in which the fractional energy varies from 0.497 to 0.415. Two additional narrow dissociative bands located from 1.8710 to

1.8758 radians and 1.9232 to 1.92825 radians make essentially no contribution to the partitioning probability because their narrowness means that the magnitude of the derivative $|d\phi/dE_A|$ will be small (unless, of course, E_A is essentially constant over the band, as is true in the additional band mentioned earlier).

IV. DISCUSSION

In this section we will consider first the implication of the bandedness of dissociative trajectories as seen in the reactivity band plots. In particular, we will focus on how this bandedness, when coupled with the calculated reaction probabilities and the pure kinematics of the collision, can be seen to lead to the general structure of the partitioning probability curves, such as those shown in figures 16 - 21. We will then consider the origins of the bandedness of the dissociative trajectories, and show that a strong relationship can be established between the separate bands and different types of trajectories leading to dissociation.

A. IMPLICATIONS OF THE DISSOCIATIVE REACTIVITY BANDS

Trajectories which lead to dissociation have been found to occur, as a general rule, in well defined bands in the reactivity band plots (figures 3 - 5). Exceptions to this trend are found for collisions of a $v = 1$ molecule in which the reagent translational energy is in the range from 0.07 to 0.10 eV. In this region, the trajectory outcome may vary substantially with small changes in the initial phase of the diatomic molecule. This is somewhat reminiscent of the observation of chattering regions in the final action vs. initial phase plots seen in reactive atom-diatomic collisions (at energies well below dissociation), particularly the $F + H_2$ (18, 20) and $Cl + HCl$(22) reactions. Unlike in those cases, where the outcome of the trajectory appears to be random, by the use of a sufficiently small grid spacing (0.002 radians), seemingly smooth (but quite short) curves of final action vs. initial phase can be obtained. We have found that only a few discrete regions of initial phase lead to dissociative trajectories. In all cases, the dissociation probability associated with these regions is quite small (no more than 1 % of all collisions) and can thus be neglected to that accuracy in the calculations of dissociation probabilities.

In most cases, dissociative trajectories can be thought of as limiting cases of reactive or non-reactive collisions giving rise to vibrational excitation of products. This is seen in two interrelated ways. For values of the initial phase only slightly different from those of the trajectories which lead to dissociation, the diatomic molecules remaining at the end of the collision will be highly vibrationally excited. If one considers the fractional energy, such as that plotted in figures 10-15, one sees that the curve for atom A smoothly matches onto that for atom A in non-reactive collisions and that for atom C smoothly matches onto that for atom C in reactive collisions. This is not necessarily true for dissociative collisions in the chattering region; as mentioned earlier, such regions may give rise to discontinuities in the partitioning probability curves.

The nature of the dissociative band (defined by the type of bands between which it is sandwiched at a given energy) will play a major role in determining the appearance of the partitioning probability curves. If the band is sandwiched between one reactive and one non-reactive band, the partitioning probability curve should cover essentially all the accessible region of energy fractions (1/6 to 2/3 in this case). If, on the other hand, the band is sandwiched between two non-reactive bands, the partitioning probability curves will cover only a subset of the allowable energy fractions and must have at least one place where they diverge. There will be no possibility of obtaining energy fractions lower than that at the lowest divergence. Thus, in such cases the partitioning probability curves for that dissociation band have the unusual property that they are zero below the diverging value, at which they jump discontinuously to infinity. At higher energy fractions, the curve is continuous. Such curves are observed in figures 18 and 21. These figures demonstrate that the value of the energy fraction at which the partitioning probability diverges can be quite close to its maximum or minimum permitted value. Precisely at what values of the energy fraction the partitioning probability diverges will depend on the shape of the dissociation and reaction reactivity bands at the energy being considered. If, for instance, one is at an energy fairly near the opening of the reaction band, the minimum in the energy fraction vs. phase plot will occur at a value of the energy fraction close to 1/6. This is the case in figure 21 (the important reaction and dissociation reactivity bands may be seen in figure 4). If the energy is such that one is not close to the opening of the reaction band, the minimum will occur at values of the energy fraction close to 2/3.

Certain types of curves of energy fraction vs. phase in dissociative collisions which might occur have not been obtained. For instance, in no cases were curves with more than one minimum or maximum observed. Hence, the partitioning probability diverges at one and only one point if it diverges at all. As mentioned earlier, no dissociative bands sandwiched between two reactive bands were observed. Such bands would lead to partitioning probability plots opposite to those in figures 18 and 21 - there would be no possibility of energy fractions above that at which the partitioning probability diverges of being populated. There seems to be no reason why such bands should not exist, so we assume that their absence is a function of the particular potential and mass combination studied.

The fact that reactive processes are less probable than non-reactive ones at the energies studied suggests that in dissociative collisions one may be more likely to find kinetic energy distributions in which atom A has the greatest portion of the available energy. This would give rise to the partitioning probability being dominated by high energy fractions. The range of energy fractions allowable is determined simply by the masses of the colliding particles, which explains why only certain numerical regions of the energy fraction are allowed (17). Changing the masses would, therefore, change the partitioning probabilities for two reasons. First, the dynamics of the system would change, and second, the ways in which kinetic energy could be distributed in dissociative collisions would be altered.

The structure of the reactivity band plots differs very strongly for v = 0 and v = 1 molecule collisions, and this fact, coupled with the definite manner in which the position and width of the reactivity bands have been shown to determine the partitioning probabilities, suggests that one might obtain substantially different kinetic energy distributions from dissociation from the two reagent states at the same total energy. The same statement applies to translational energy. The simplest way of obtaining such a case would be to locate an energy at which the dissociation from v = 0 occurs totally from a band which is sandwiched between two non-reactive bands, while that from v = 1 occurs from one or more bands sandwiched between one reactive and one non-reactive band. Thus, not only may the outcome of the collision (reaction, non-reaction, or dissociation) depend on the initial state, but the intimate details of dissociation may also be a function of the initial state.

B. ORIGIN OF THE DISSOCIATIVE REACTIVITY BANDS

Formation of reactivity bands in atom-diatomic molecule collisions has been observed in a variety of systems at energies below dissociation (12, 13); banding has also been observed in a non-reactive system studied at energies above dissociation (10a). The present study marks, to our knowledge, the first reactivity band study of dissociation in a reactive system. In studying the origin of reactivity bands, we are interested in getting a good physical picture as to what sort of trajectories comprise each band. In particular, we focus on two questions. First, we want to know whether each separate band corresponds to different types of trajectories. Second, we want to know what happens near the boundaries between bands, especially in the chattering regions, such as that shown in figure 10, in which the outcome of the trajectory is extremely sensitive to the initial conditions of the trajectory.

Wright and Tan (12c) have shown in their study of the collinear T + HT system on the SSMK surface (23) that the two lowest energy reaction reactivity bands are comprised of different types of trajectories. In the lower energy band, reactive trajectories cross the symmetric stretch line only once, while in the higher energy band, they cross the symmetric stretch line three times. Representative trajectories are shown in figure 8 of reference 12c. A similar correspondence can be drawn between the two reaction reactivity bands in figure 4 for collisions of v = 1 molecule. For collisions of v = 0 molecule in figure 3 we show only the high energy reaction reactivity band; there is another band at lower energies responsible for the large values of P_0^R at low energy seen in figure 1. Trajectories comprising the lower reaction reactivity band in the v = 1 case cross the symmetric stretch line once (figure 23) while those in the higher band cross the symmetric stretch line three times (figure 24). Reactive trajectories must cross the symmetric stretch line an odd number of times; thus, these are the simplest sort of reactive trajectories possible. The importance of reactive trajectories which cross the symmetric stretch line more than once indicate that a purely classical transition state theory would seriously overestimate the rate constant for reaction at high temperatures when these high energy trajectories become important (24). The same behavior is seen in collisions of ground state molecules; we do not show them here.

We next consider the nature of trajectories leading to dissociation. We will focus our attention first on the single dissociation band for collisions of ground state molecule and the two large bands for collisions of v = 1 molecules. We will consider the small band for v = 1 isolated in the large non-reactive band and the overall chattering region later. Typical dissociative trajectories are shown in figures 25 - 27 for the large band in v =0 collisions, the first band in v = 1 collision, and the second band in v = 1 collisions, respectively. In figures 25 and 27, the trajectory crosses the symmetric stretch line three times; in figure 26 the symmetric stretch lines is crossed only once. This suggests that the separate dissociation bands are each comprised of trajectories crossing the symmetric stretch line a different number of times, just as was seen for reactive transitions. Things are not quite so simple in the dissociation case, however, as the trajectory need not cross the symmetric stretch line an odd number of times. In fact, trajectories which cross it twice have been observed in both v = 1 reactivity bands. The last crossing of the symmetric stretch line may occur (as does that in the trajectory shown in figure 26) at large values of the internuclear coordinates. Whether or not such a crossing takes place will depend on the partitioning of energy in the three atoms. The final crossing, then, may be thought to occur while the atoms are in the process of dissociating, even if the crossing occurs at fairly small values of the internuclear coordinates. Thus, the first dissociation reactivity band in the reactivity band plot (in figure 4) may be thought of as being comprised of trajectories which cross the symmetric stretch line once prior to the process of actually dissociating (during which they may again cross that line). In the second dissociation band for v = 1 and the only such band for v = 0, two crossings take place prior to the onset of dissociation, after which a third crossing may occur.

These observations allow one to make a simply physical picture to account for the observed vibrational enhancement of CID in this system: The simplest trajectory which may lead to dissociation does not occur when the molecule is in its ground state. It occurs only when the molecule is in its excited state. Since more complicated trajectories appear to contribute only at higher energies, low energy dissociation is prevented in the ground state case. The qualitative agreement between the quasi-classical trajectory calculations and the exact quantum ones reported previously (7) indicates that this simple classical picture may be a reasonable one to use in attempting to understand the calculated vibrational enhancement of CID in this system.

We next wish to consider the small dissociation band seen in figure 4 (and enlarged in figure 5) near 2 radians and 0.18 eV reagent translational energy. A typical trajectory in this band is shown in figure 28. This trajectory is quite different from the dissociative ones seen in figures 25 and 27. This should not be surprising, however, as this small dissociation band is imbedded in a large non-reactive band and the other dissociation bands tend to be sandwiched between reactive and non-reactive bands. Examination of non-reactive trajectories near the boundaries between the non-reaction and dissociation reactivity bands indicates that differences between the trajectories within them are quite small and become important only at large values of the internuclear coordinates. This is a case, then, in which the final outcome of the trajectory is not determined until well after the collision might be thought to be finished (R_{AB} large and increasing, R_{BC} fairly small).

We finally consider the chattering region indicated in figure 9. In the region of initial phase from 2.5 to 2.7 radians, the outcome of the trajectory varies greatly with small changes in the initial phase. Such regions have been observed in studies of reactions below dissociation, particularly the $H + H_2$ (13) and $F + H_2$ (18, 20) reactions. In these regions, the trajectories become very complicated, frequently bouncing back and forth many times in the strong interaction region of the potential energy surface. Atom B is said to "chatter" between atoms A and C, hence the name chattering region.

In this case, the trajectories in the chattering region are not overly complicated. Three such trajectories are shown in figures 29 - 31 corresponding to initial conditions shown in figure 9. The initial phase differs by 0.01 radians (0.57°) between each trajectory. The dominant feature of the trajectories is clear : trajectories in this region involve motion more or less along the symmetric stretch line. The extreme sensitivity of the trajectory outcome to the initial phase can, therefore, be easily understood. Since, in moving along the symmetric stretch line, the trajectory has, to a first approximation, forgotten from where it was begun, it is reasonable that a small perturbation to the trajectory could seriously alter its course.

At energies below dissociation motion exactly along the symmetric stretch line would constitute that of a trapped trajectory - one which could oscillate back and forth forever, never leaving the interaction region of the potential energy surface (25). In the language of Pollak and Pechukas, such motion constitutes a trapped trajectory of the first kind (26). These trajectories are frequently found at the boundary between reactive and non-reactive bands in atom-diatomic molecule systems at energies below dissociation (12, 13, 20, 22). At energies above dissociation, trapped trajectories of the first kind (in which the trajectory oscillates back and forth forever between two different contours at the total energy) do not exist. A trajectory can change its character continuously from reactive to non-reactive or vice versa by going through an intermediate stage of dissociative trajectories. Thus, the requirement shown by Pechukas and Pollak that trapped trajectories must occur at the boundary between reactive and non-reactive bands at energies below dissociation seems not to apply at energies above dissociation (25). Nothing in these statements here, however, precludes the possibility of formation of trapped trajectories of the second or third kinds (26). No such trapped trajectories (or nearly trapped ones) were observed, although we have not carried out a systematic search for them.

V. CONCLUSIONS

We have performed a reactivity band analysis of CID in a model collinear reactive atom-diatomic molecule system. Quasi-classical trajectories are believed to provide a reasonable view of the dynamics in this system because of the qualitative similarity in the reaction and dissociation probabilities calculated by trajectories and by exact quantum mechanical calculations (7).

CID is shown to occur almost entirely in well defined bands, the exception being a small contribution from dissociative trajectories in a chattering region in which the outcome of the trajectory is extremely sensitive to the initial phase of the reagent molecule. Dissociation may be thought of as a limiting case of vibrational excitation, as non-dissociative (reactive or non-reactive) trajectories with initial conditions only slightly different from those leading to dissociation lead to a diatomic molecule product which is highly vibrationally excited. In most cases, dissociation reactivity bands are found sandwiched between one reactive and one non-reactive band; in the rest, they may be sandwiched between two non-reactive bands. In no instances were dissociative bands sandwiched between two reactive bands.

We have calculated the partitioning of kinetic energy among the three atomic products of dissociative collisions and showed that these quantities vary smoothly throughout the dissociation band. Kinematic considerations require that most of the available kinetic energy go into the end atoms (A or C). The fraction of the available kinetic energy in the end atoms, as a general rulse, matches smoothly onto that of the free atom in non-dissociative collisions (atom A in non-reactive collisions, atom C in reactive ones).

From the curves of energy fraction vs. initial phase we have been able to determine the partitioning probability, that is, the likelihood of the dissociation process to distribute the available energy in a given way. We have presented plots of the partitioning probabilities for six different sets of initial conditions (reagent vibrational state and translational energy), and found a wide range of appearance of the probability vs. energy fraction curves. We have shown that the general from of the partitioning probability curves can be inferred solely by examination of the reactivity band plots.

The different dissociation reactivity bands found for the reaction of vibrationally excited ($v = 1$) molecules have been shown to be comprised of different sorts of trajectories. The band which dominates at low energies (and shuts off at reagent translational energies above 0.12 eV) is seen to arise from trajectories which cross the symmetric stretch line only once prior to the onset of actual dissociation, while the higher energy band arises from trajectories which cross the symmetric stretch line twice prior to dissociation. During dissociation, the trajectories may or may not recross the symmetric stretch line an additional time. The single dissociation band observed in collisions of ground state molecules is seen to be made up of trajectories which cross the symmetric stretch line twice prior to dissociation. Hence, the vibrational enhancement of CID can be thought of as being due to the inability of ground state molecules to dissociate by the simplest possible trajectory; in that case dissociation is only possible by a more complex procedure, which only becomes important at higher energies.

The chattering region is seen to arise from trajectories which at some point follow the symmetric stretch line very closely. Since the available energy is greater than the dissociation energy, motion along the symmetric stretch line does not constitute a trapped trajectory. The existence of a dissociation channel allows for a smooth transition from reactive to non-reactive trajectories via an intermediate region of dissociative trajectories.

Our analysis here has been restricted to a single model potential energy surface for a collinear collision. In reactive systems, changes in the masses of the atoms have been shown to produce major changes in the structure of the reactivity bands (12b). Exact quantum mechanical calculations on "isotopically' substituted versions of the model system studied here (mass combinations 10-1-10 and 1-35-1) indicate that the effect of mass on dissociation is strong (22). Large changes in the reactivity band structure can be expected. Thus, one must use caution is attempting to generalize on the basis of the reactivity bands for one system.

Removal of the restriction to collinearity might be expected to lead to substantial changes in the reactivity bands (the model potential used here is defined solely for collinear configurations; we are addressing the general role of non-collinear collisions). In studies of the two and three dimensional T + HT reaction, Wright (12e) has shown a disappearance of the bandedness observed in the collinear reaction, which is due to the diminished importance of multiple collisions (which involve multiple crossing of the symmetric stretch line) in non-collinear collisions. Thus, in a more realistic (three-dimensional) system, the rich banded structure obtained here might be expected to be substantially blurred.

ACKNOWLEDGMENTS

The calculations reported here were performed on the Dreyfus-NSF Theoretical Chemistry Computer which was funded through grants from the Camille and Henry Dreyfus Foundation, the National Science Foundation (Grant No. CHE78-20235) and the Sloan Fund of the California Institute of Technology.

REFERENCES

1. R. L. Belford and R. A. Strehlow, Ann. Rev. Phys. Chem. 20, 247 (1969).

2. A. Dalgarno and W.G. Roberge, Astrophys J. 233, L25 (1979); D. Hollenbach and C. F. McKee, Astrophys J. Supp. Ser. 41, 555 (1979).

3. P. J. Kuntz, in: Atom-Molecule Collision Theory, ed. R. B. Bernstein (Plenum Press, New York, 1979), pp. 669-692 and references therein.

4. D. J. Diestler, in: Atom-Molecule Collision Theory, ed. R. B. Bernstein (Plenum Press, New York, 1979), pp. 655-667 and references therein.

5. I. Rusinek, J. Chem. Phys. 72, 4518 (1980).

6. K. C. Kulander, J. Chem. Phys. 69, 5064 (1978); Nucl. Phys. A353, 341c (1981).

7. J. A. Kaye and A. Kuppermann, Chem. Phys. Lett. 78, 466 (1981).

8. J. Manz and J. Römelt, Chem. Phys. Lett. 77, 172 (1980).

9. L. H. Beard and D. A. Micha, J. Chem. Phys. 73, 1193 (1980).

10. (a) J. C. Gray, G. A. Fraser, and D. G. Truhlar, Chem. Phys. Lett. 68, 359 (1979); (b) J. C. Gray, G. A. Fraser, D. G. Truhlar, and K. C. Kulander, J. Chem. Phys. 73, 5726 (1980).

11. E.-W. Knapp and D. J. Diestler, J. Chem. Phys. 67, 4969 (1977).

12. (a) J. S. Wright, G. Tan, K. J. Laidler, and J. E. Hulse, Chem. Phys. Lett. 30, 200 (1975); (b) J. S. Wright, K. G. Tan, and K. J. Laidler, J. Chem. Phys. 64, 970 (1976); (c) J. S. Wright and K. G. Tan, J. Chem. Phys. 66, 104 (1977); (d) K. G. Tan, K. J. Laidler, and J. S. Wright, J. Chem. Phys. 67, 5883 (1977); (e) J. S. Wright, J. Chem. Phys. 69, 720 (1978); (f) K. J. Laidler, K. G. Tan, and J. S. Wright, Chem. Phys. Lett. 46, 56 (1977).

13. R. E. Howard, A. C. Yates, and W.A. Lester, Jr., J. Chem. Phys. 66, 1960 (1977).

14. R. N. Porter and L. M. Raff, in: Dynamics of Molecular Collisions, Part B, ed. W. H. Miller (Plenum Press, New York, 1976), pp. 1-52; D. G. Truhlar and J. T. Muckerman, in: Atom-Molecule Collision Theory, ed. R. B. Bernstein (Plenum Press, New York, 1979), pp. 505-565.

15. J. M. Bowman and A. Kuppermann, Chem. Phys. Lett. 34, 523 (1975).

16. H. Eyring, J. Walter, and G. Kimball, Quantum Chemistry (Wiley, New York, 1944), pp. 272-273.

17. J. P. Dwyer, Ph. D. Thesis, California Institute of Technology, 1977, p. 126.

18. J. S. Hutchinson and R. E. Wyatt, J. Chem. Phys. 70, 3509 (1979).

19. J. W. Duff and D. G. Truhlar, Chem. Phys. Lett. 4, 1 (1974); J. R. Stine and R. A. Marcus, Chem. Phys. Lett. 29, 575 (1974); N. Sathyamurthy, Chem. Phys. Lett. 59, 95 (1978); M. S. Child and K. B. Whaley, Faraday Disc. Chem. Soc. Lond. 67, 57 (1979).

20. F. Schnabel and S. Chapman, Chem. Phys. Lett. 57, 189 (1978).

21. J. A. Kaye and A. Kuppermann, unpublished results.

22. J. A. Kaye and A. Kuppermann, manuscript in preparation.

23. I. Shavitt, R. M. Stevens, F. L. Minn, and M. Karplus, J. Chem. Phys. 48, 2700 (1968).

24. D. G. Truhlar and B. C. Garrett, Acc. Chem. Res. 13, 440 (1980).

25. P. Pechukas and E. Pollak, J. Chem. Phys. 67, 5976 (1977).

26. E. Pollak and P. Pechukas, J. Chem. Phys. 69, 1218 (1978).

FIGURE CAPTIONS

Figure 1. Probabilities for reaction P_0^R (solid line) and dissociation P_0^D (dashed line) in collisions of ground vibrational state molecules as determined by quasi-classical trajectory calculations as a function of the collision energy. The reagent translational energy E_0 is indicated on the lower abscissa; the total energy E (sum of vibrational and translational energy) is indicated on the upper abscissa. The arrow points to the energy at which the molecule dissociates.

Figure 2. Probabilities for reaction P_1^R (solid line) and dissociation P_1^D (dashed line) in collisions of vibrationally excited molecules as a function of the collision energy. The axes and markings are otherwise as in figure 1.

Figure 3. Reactivity band plot for reaction and dissociation in collisions of ground state molecule. Reactive (R) bands are indicated by shading; dissociative (D) bands are indicated by speckling. The solid white region is non-reactive (N). Both the translational energy E_0 (left ordinate) and the total energy E (right ordinate) are indicated.

Figure 4. Reactivity band plot for reaction and dissociation in collisions of vibrationally excited molecule. Band type is indicated as in figure 3. Axis labeling is also as in figure 3. No effort is made to accurately portray the band structure in the "chattering" region.

Figure 5. Enlarged view of the small dissociative band (from figure 4) in collisions of vibrationally excited molecule. All markings and axes are as in figure 3.

Figure 6. Final action v_f as a function of the initial phase ϕ_0 for a collision involving a ground state diatomic molecule at a reagent translational energy E_0 of 0.388 eV. A solid line is used to connect results of non-reactive trajectories; a dashed line is used to connect results of reactive

trajectories. The shaded areas indicate those regions of the initial phase giving rise to dissociative trajectories, in which the action cannot be defined in the usual way. N, D, and R indicate non-reactive, dissociative, and reactive regions, respectively. The trajectory was begun with the distance from atom A to the center of mass of BC being 12 bohr.

Figure 7. Final action v_f as a function of initial phase ϕ_o for a collision involving vibrationally excited molecules at a reagent translational energy E_1 of 0.2815 eV. All markings are as in figure 6.

Figure 8. Final action v_f as a function of initial phase ϕ_o for a collision involving vibrationally excited molecules at a reagent translational energy E_1 of 0.1615 eV. All markings are as in figure 6.

Figure 9. Final action v_f as a function of initial phase ϕ_o for a collision involving ground state molecules at a reagent translational energy E_o of 0.178 eV. All markings are as in figure 6. Note the expanded scale of the ordinate.

Figure 10. Final action v_f as a function of the initial phase ϕ_o for a collision involving vibrationally excited molecules at a reagent translational energy E_1 of 0.085 eV. The initial phases are limited to the chattering region described in the text and the regions to slightly lower and higher initial phase. All markings are as in figure 6.

Figure 11. Energy fractions f_X(X = A, B, C) (defined in section II) as a function of the initial phase ϕ_0 for the dissociative bands seen in collisions of ground state molecules at a reagent translational energy E_o of 0.388 eV. A solid line is used for atom A, a dashed line for atom B, and a dotted line for atom C. A dashed-dotted line marks the approximate boundary between bands. The curve for atom A is continued into the non-reactive region and the curve for atom C is continued into the reactive region by

a procedure described in the text. (a) the small band from 0.90 to 1.03 radians initial phase; (b) the large band from 5.10 - 6.60 radians.

Figure 12. Energy fractions f_X as a function of initial phase ϕ_o for dissociative bands in collisions of ground state molecules at a reagent translational energy E_0 of 0.233 eV. All markings are as in figure 11.

Figure 13. Energy fractions f_X as a function of initial phase ϕ_o for dissociative bands in collisions of vibrationally excited molecules at a reagent translational energy E_1 of 0.2815 eV. (a) the small band from 0.25 to 0.31 radians; (b) the large band from 3.20 to 5.50 radians. All markings are as in figure 11.

Figure 14. Energy fractions f_X as a function of initial phase ϕ_o for dissociative bands in collisions of vibrationally excited molecules at a reagent translational energy E_1 of 0.1815 eV. (a) band from 2.04 to 2.12 radians; (b) band from 4.25 to 4.80 radians; (c) band from 5.32 to 5.36 radians. All markings are as in figure 11.

Figure 15. Energy fractions f_X as a function of initial phase ϕ_o for dissociative bands in collisions of vibrationally excited moelcules at a reagent translational energy E_1 of 0.1015 eV.

Figure 16. Energy fractions f_X as a function of initial phase ϕ_o for dissociative bands in collisions of vibrationally excited molecules at a reagent translational energy E_1 of 0.0715 eV. All markings are as in figure 11.

Figure 17. Partitioning probability ${}^{c}\overline{\sigma}_{0}^{d}$ described in section II of the text for atom A for dissociation in collisions of ground state molecules at a reagent translational energy E_0 of 0.388 eV.

Figure 18. Partitioning probability ${}^{c}\overline{\sigma}_{0}^{d}$ for atom A for dissociation in collisions of ground state molecules at a reagent translational energy E_0 of 0.233 eV. The probability is zero for values of the energy fraction

f_A below that at which it diverges (~0.58).

Figure 19. Partitioning probability ${}^{c}\bar{\sigma}_{1}^{d}$ for atom A for dissociation in collisions of vibrationally excited molecules at a reagent translational energy E_1 of 0.2815 eV.

Figure 20. Partitioning probability ${}^{c}\bar{\sigma}_{1}^{d}$ for atom A for dissociation in collisions of vibrationally excited molecules at a reagent translational energy E_1 of 0.1815 eV.

Figure 21. Partitioning probability ${}^{c}\bar{\sigma}_{1}^{d}$ for atom A for dissociation in collisions of vibrationally excited molecules at a reagent translational energy of 0.1015 eV. The probability is zero for values of the energy fraction f_A below that at which it diverges (~0.25).

Figure 22. Partitioning probability ${}^{c}\bar{\sigma}_{1}^{d}$ for atom A for dissociation in collisions of vibrationally excited molecules at a reagent translational energy of 0.0715 eV.

Figure 23. Plot of a typical reactive trajectory in the low energy reaction reactivity band for collisions of vibrationally excited molecule. Trajectory is for initial conditions of E_1 = 0.0715 eV and initial vibrational phase of 3.4558 radians. The integration of the trajectory was begun with R = 12.8952 bohr. The trajectory is superimposed on a plot of the potential energy surface for the system in Delves mass-scaled coordinate system. Contours are drawn every 0.06 eV starting from 0.02 eV up to 0.50 eV with respect to a zero of energy at the bottom of the well of the isolatediatomic molecule. The X marks the saddle point for the reaction. Note that there is only one crossing of the symmetric stretch line.

Figure 24. Plot of a typical reactive trajectory in the high energy reaction reactivity band for collisions of vibrationally excited molecule. Trajectory is for initial condition of E_1 =0.2815 eV and initial vibrational

phase of 6.5649 radians. All markings are as in figure 23.

Figure 25. Plot of a typical dissociative trajectory in collisions of ground state molecules. Trajectory is for initial conditions of $E_0 = 0.388$ eV and initial phase of 0.3142 radians. All markings are as in figure 23.

Figure 26. Plot of a typical dissociative trajectory in the low energy dissociation reactivity band for collisions of vibrationally excited molecules. Trajectory is for initial conditions of $E_1 = 0.0715$ eV and initial phase of 5.3407 radians. All markings are as in figure 23.

Figure 27. Plot of a typical dissociative trajectory in the large, high energy dissociation reactivity band for collisions of vibrationally excited molecules. Trajectory is for initial conditions of $E_1 = 0.2815$ eV and initial phase of 5.3407 radians. All markings are as in figure 23.

Figure 28. Plot of a typical dissociative trajectory in the small dissociation reactivity band imbedded in the large non-reaction band for collisions of vibrationally excited molecules. Trajectory is for initial conditions of $E_1 = 0.1815$ eV and initial phase of 2.12 radians. All markings are as in figure 23.

Figure 29. Plot of a non-reactive trajectory in the chattering region shown in figure 10. Trajectory is for initial conditions of a vibrationally excited molecule, $E_1 = 0.085$ eV, and an initial phase of 2.65 radians. All markings are as in figure 23.

Figure 30. Plot of a dissociative trajectory in the chattering region shown in figure 10. Initial conditions are the same as for the trajectory in figure 29, except that the initial phase is 2.66 radians. All markings are as in figure 23.

Figure 31. Plot of a reactive trajectory in the chattering region shown in figure 10. Initial conditions are the same as for the trajectory

in figure 29, except that the initial phase is 2.67 radians. All markings are as in figure 23.

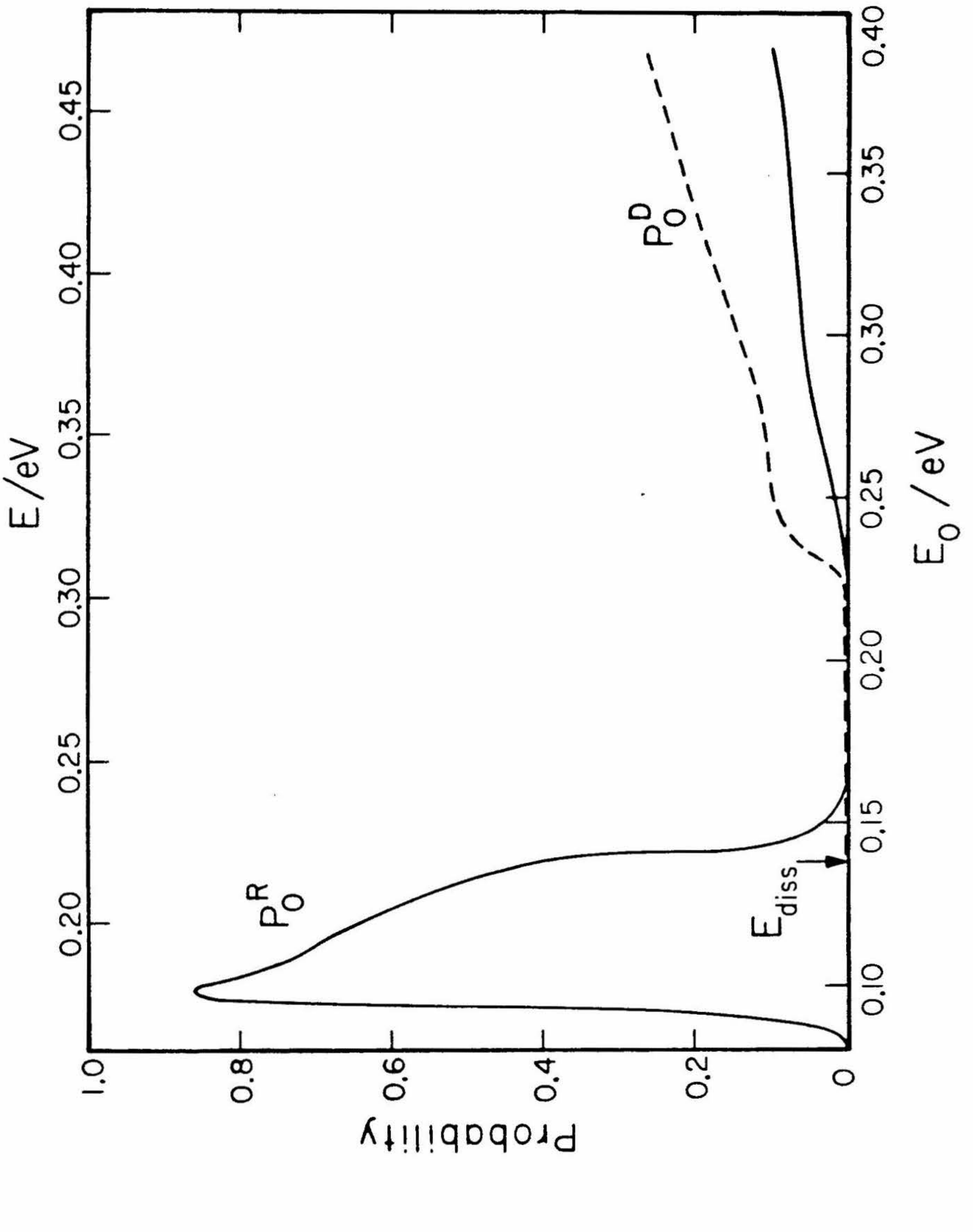
E /eV
0.20
0.25
0.30
0.35
0.40
0.45
Probability
1.0
0.8
0.6
0.4
0.2
0
E_0 /eV
0.10
0.15
0.20
0.25
0.30
0.35
0.40
P_0^R
P_0^D
E_{diss}

Figure 1

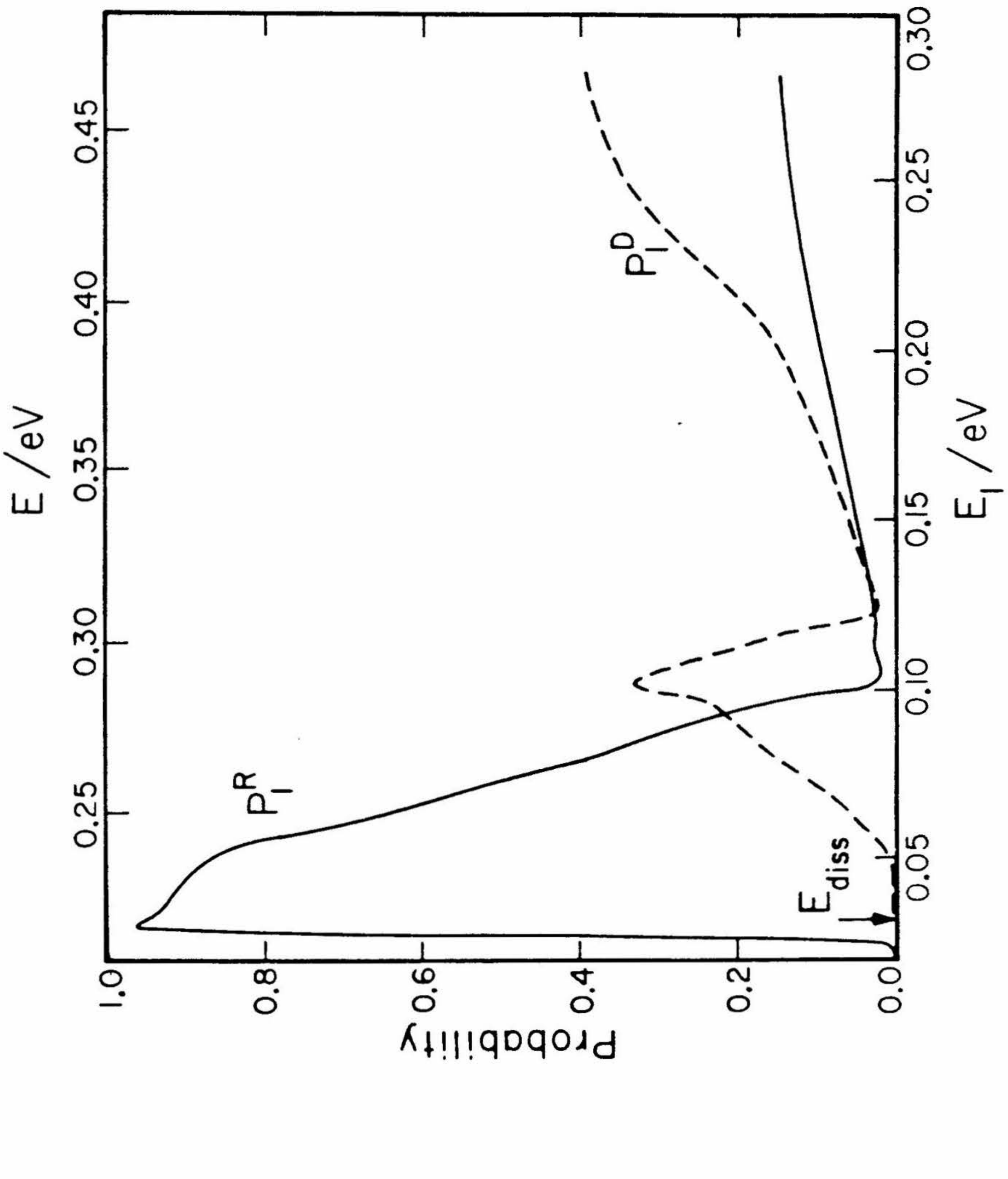
E /eV
0.25
0.30
0.35
0.40
0.45
Probability
1.0
0.8
0.6
0.4
0.2
0.0
E_I /eV
0.05
0.10
0.15
0.20
0.25
0.30
P_I^R
P_I^D
E_diss

Figure 2

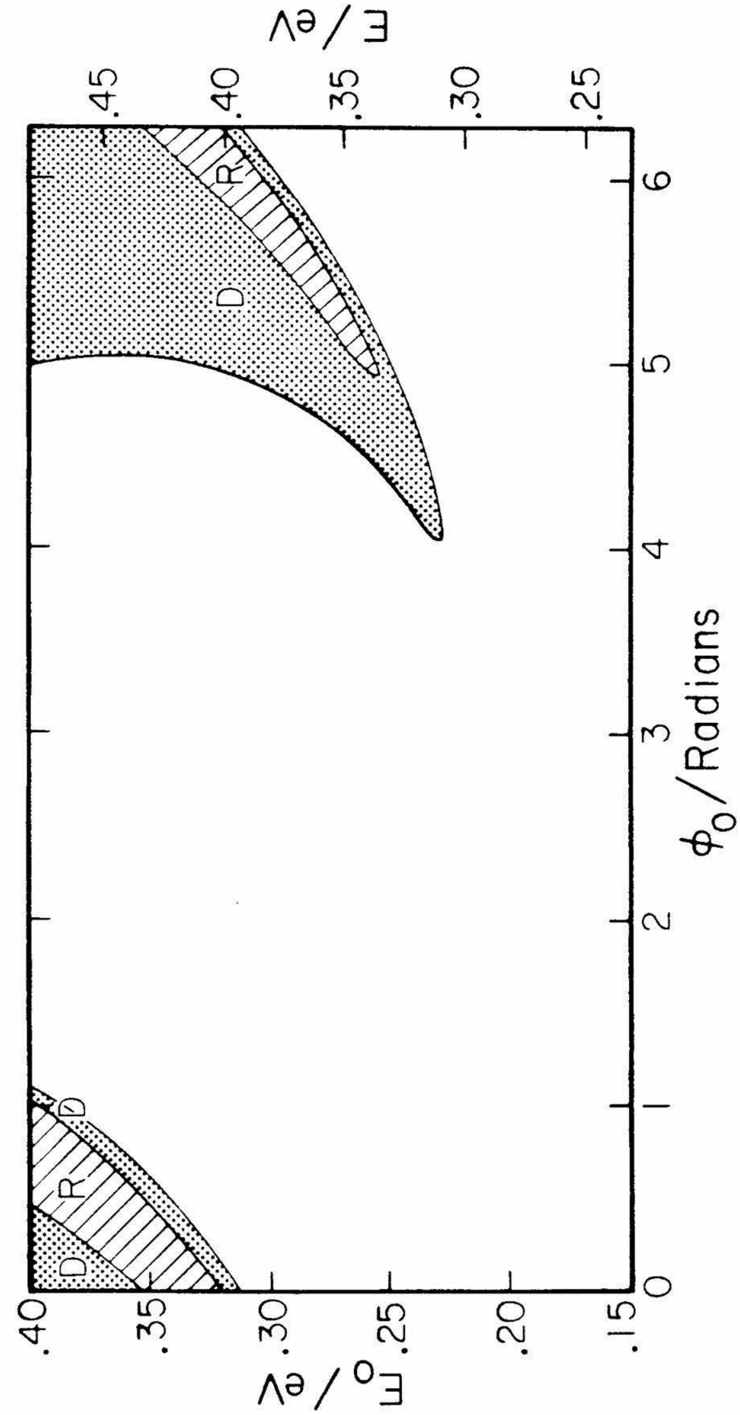
E / eV
.45
.40
.35
.30
.25
D
R
D
R
D
0
1
2
3
4
5
6
ϕ_0/Radians
.40
.35
.30
.25
.20
.15
E_0 / eV

Figure 3

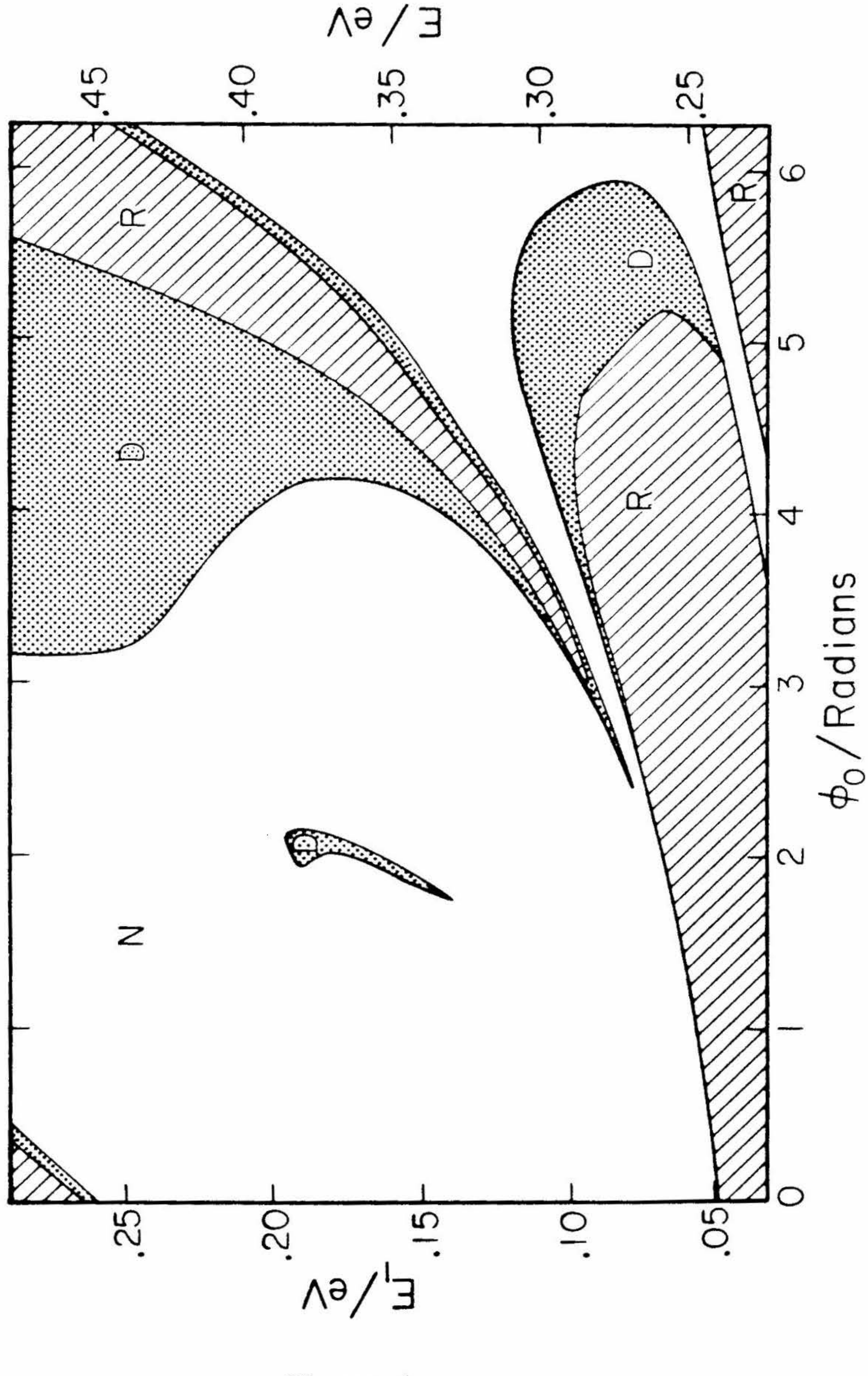
E / eV
.45
.40
.35
.30
.25
R
D
R
D
R
R
N
D
D
0
1
2
3
4
5
6
ϕ_0/Radians
.25
.20
.15
.10
.05
E_1/eV

Figure 4

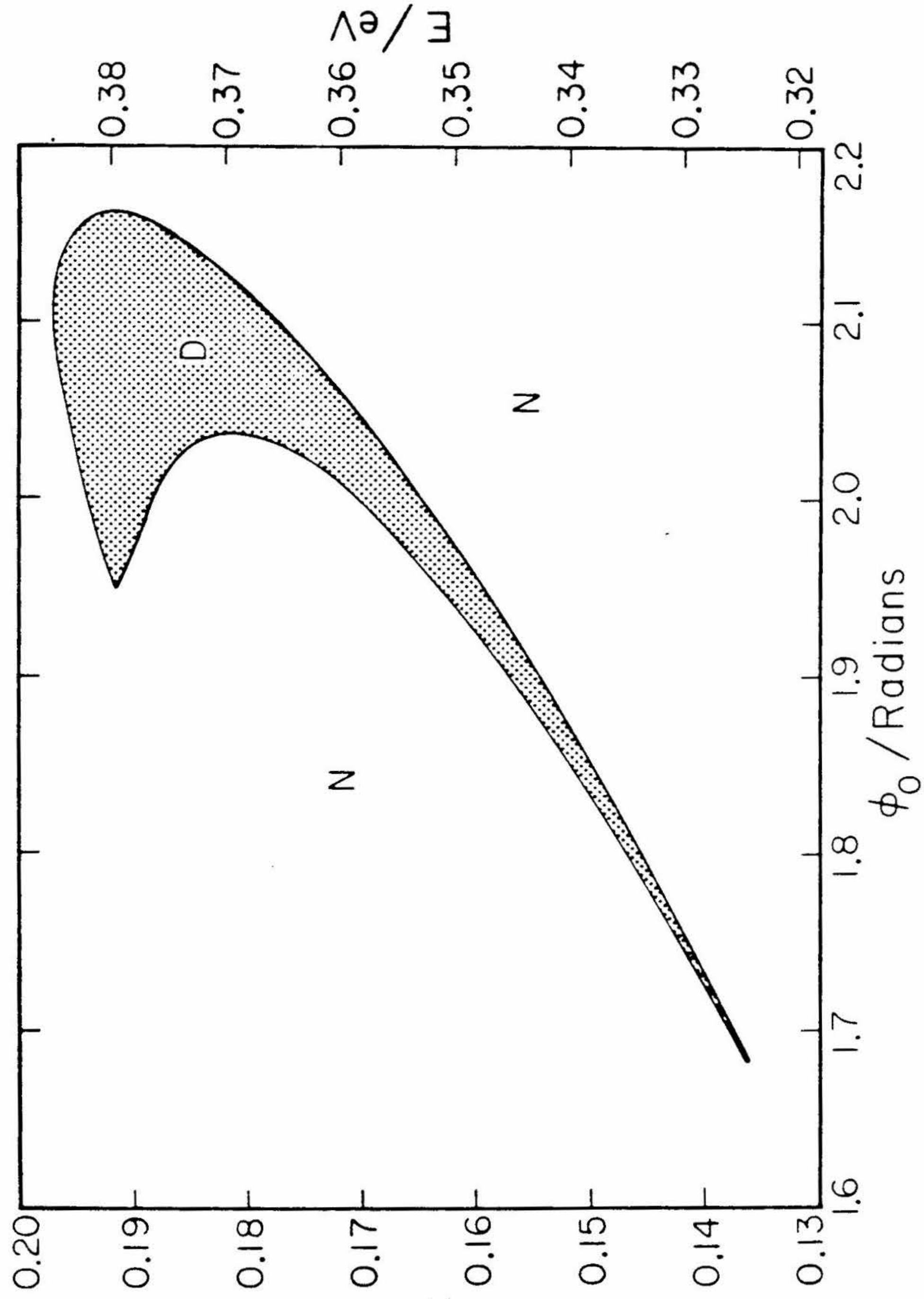
E / eV
0.38
0.37
0.36
0.35
0.34
0.33
0.32
E_1 / eV
0.20
0.19
0.18
0.17
0.16
0.15
0.14
0.13
ϕ_0 /Radians
1.6
1.7
1.8
1.9
2.0
2.1
2.2
D
N
N

Figure 5

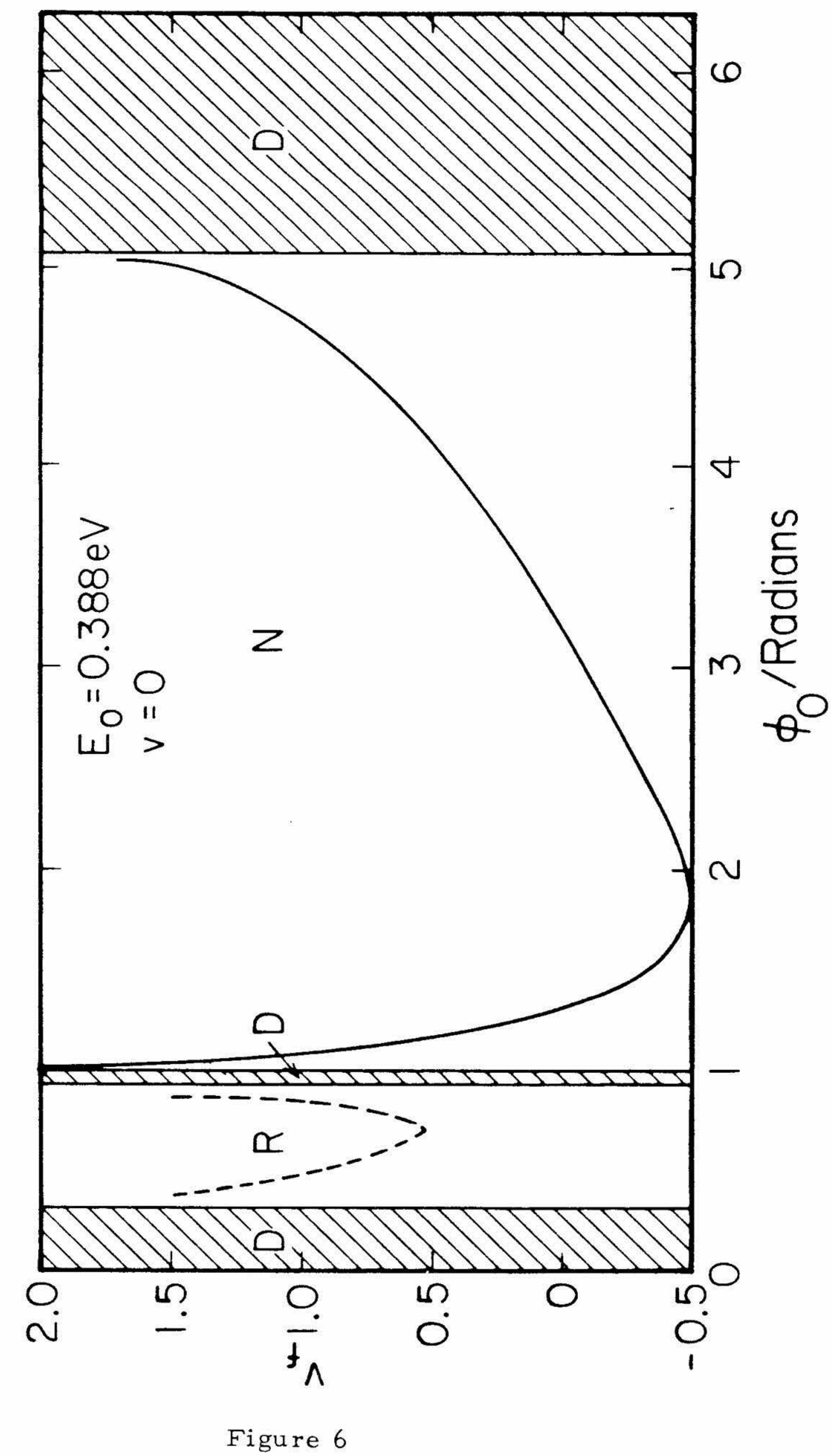

Figure 6

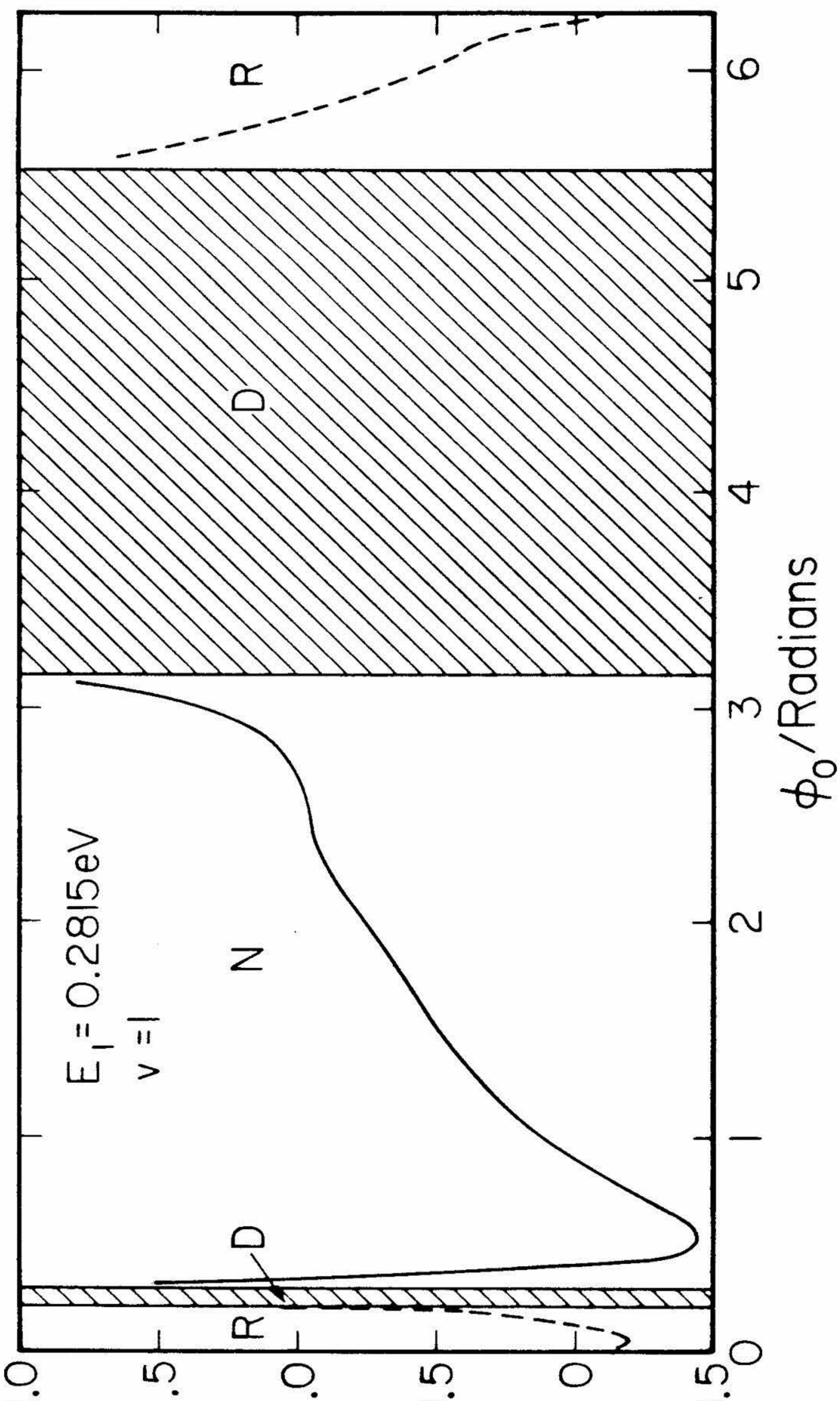

Figure 7

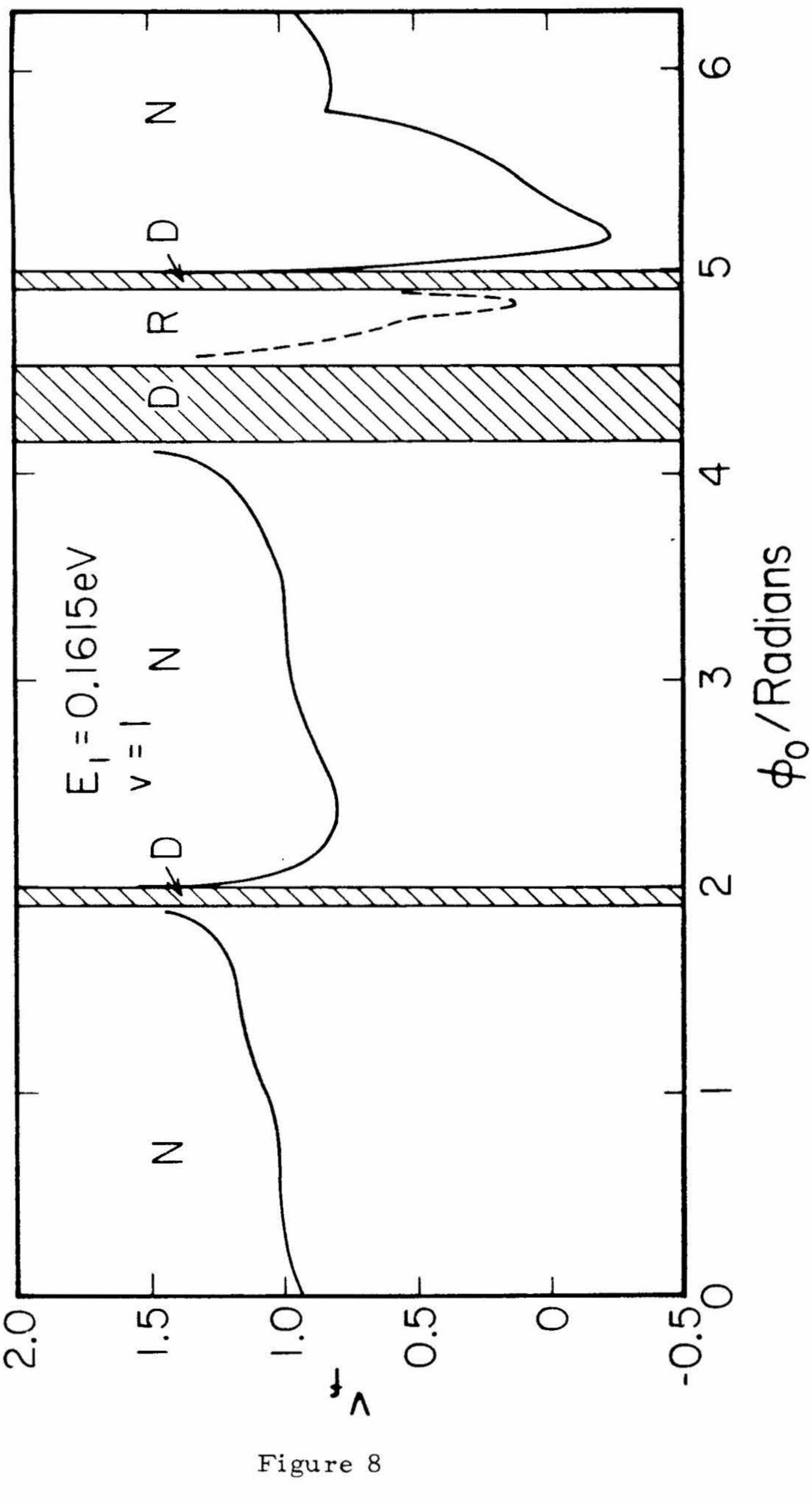
$E_1 = 0.1615\text{eV}$
$v = 1$
N
D
N
D
R
D
N
v_f
2.0
1.5
1.0
0.5
0
-0.5
0
1
2
3
4
5
6
ϕ_0/Radians

Figure 8

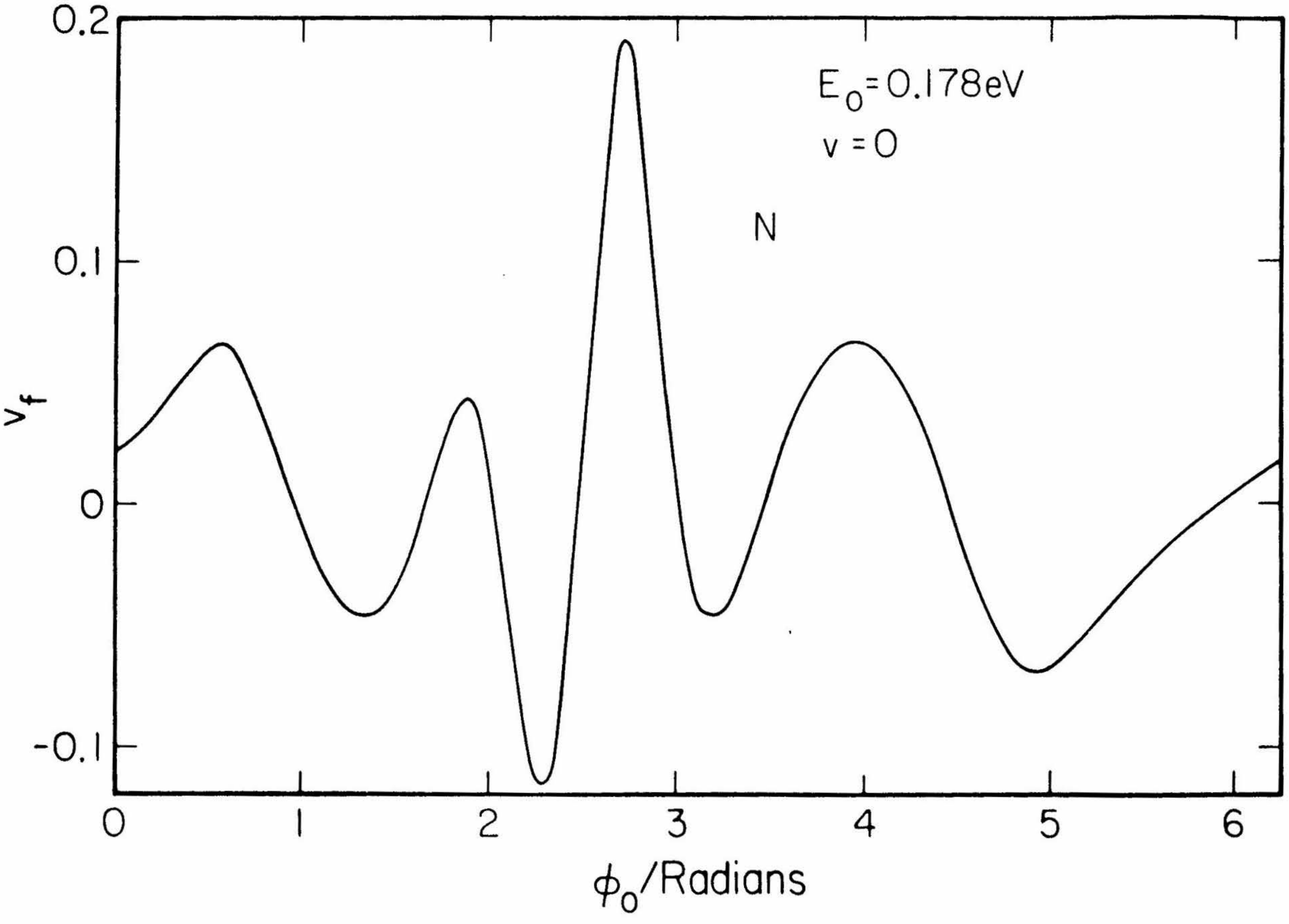

Figure 9

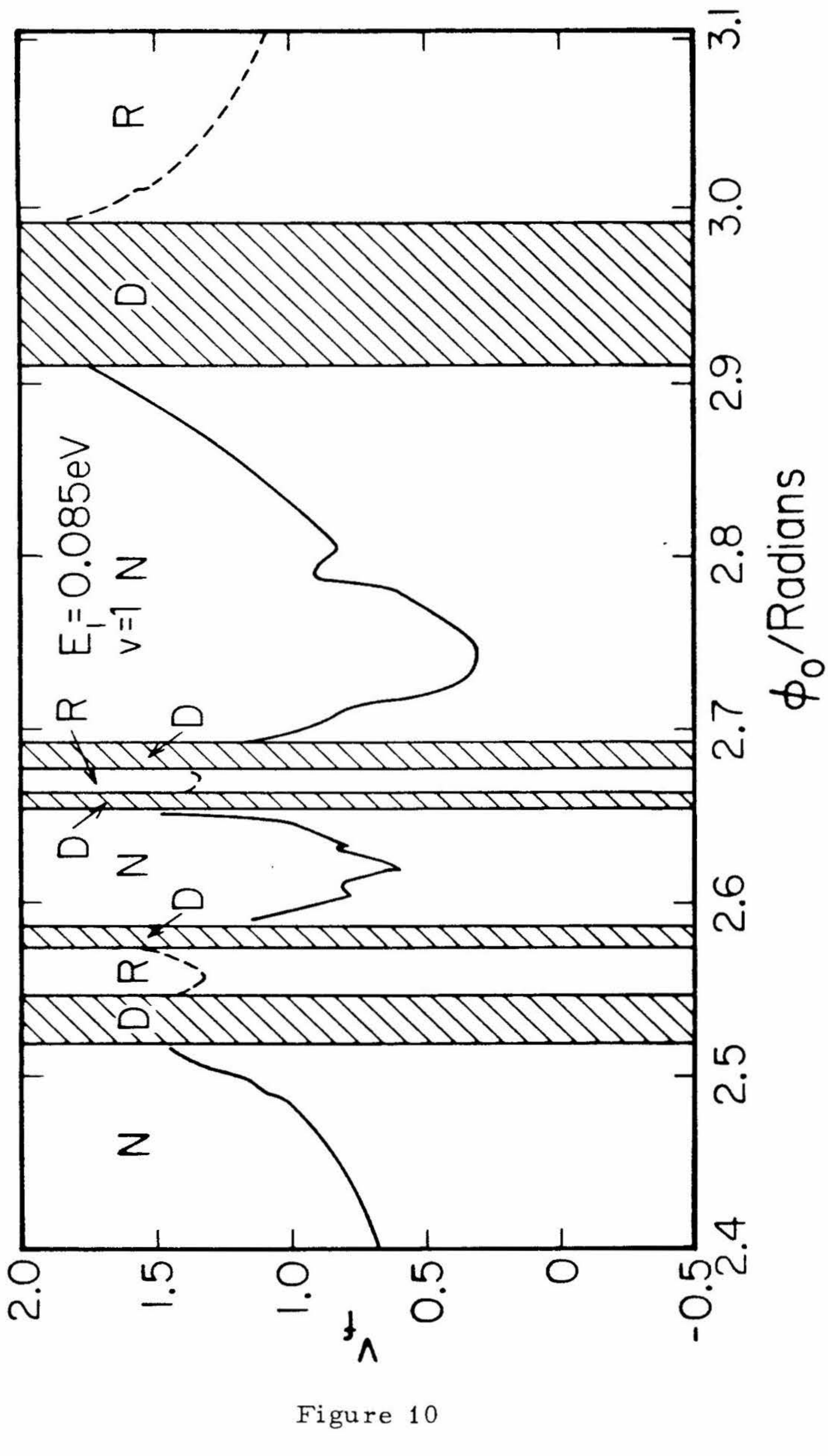
$E_I = 0.085$eV
$v=1$ N
N
D
R
D
N
D
R
D
D
R
V_f
2.0
1.5
1.0
0.5
0
-0.5
2.4
2.5
2.6
2.7
2.8
2.9
3.0
3.1
ϕ_o/Radians

Figure 10

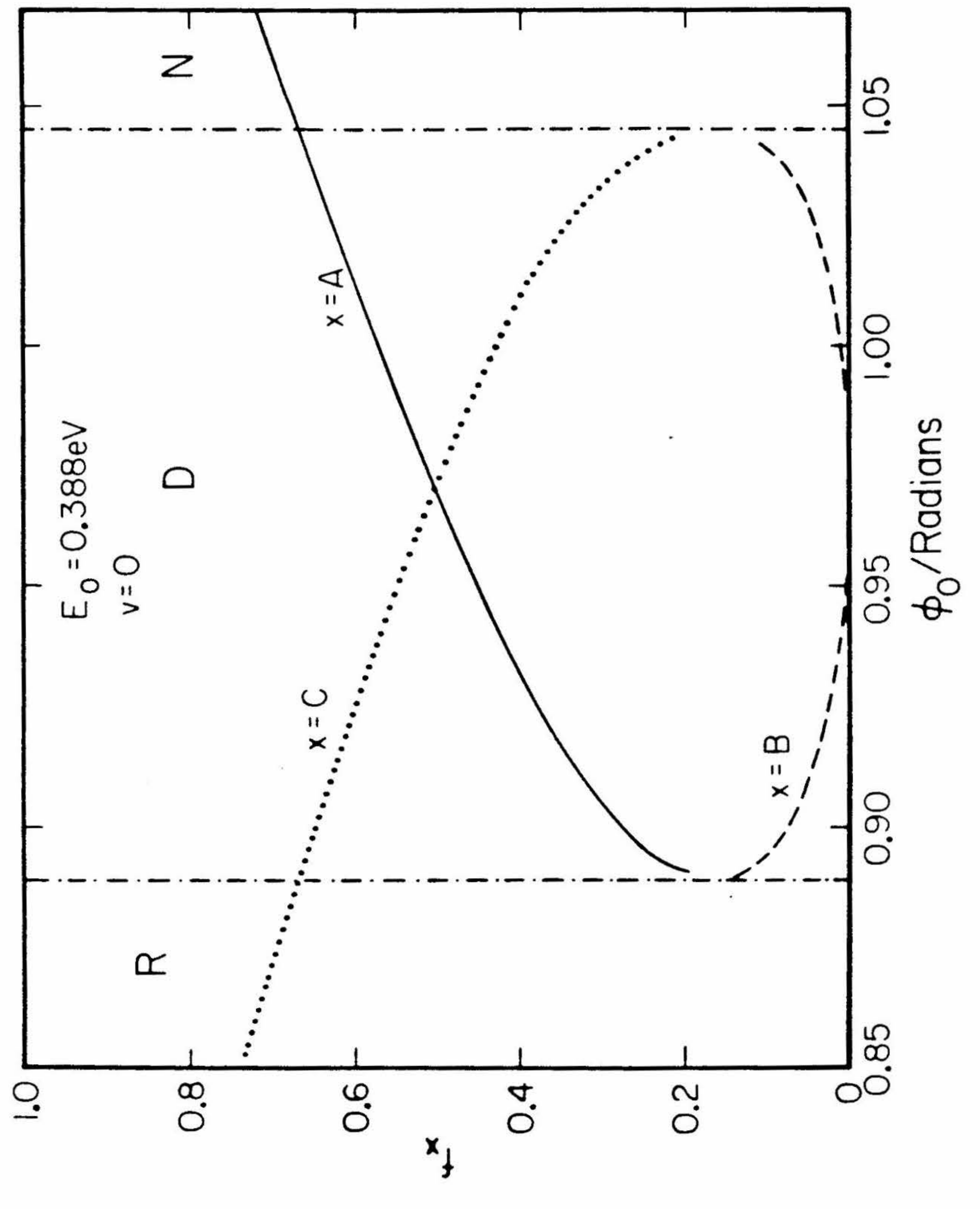
$E_0 = 0.388$eV
$v = 0$
R
D
N
x = A
x = B
x = C
x_f
1.0
0.8
0.6
0.4
0.2
0
0.85
0.90
0.95
1.00
1.05
ϕ_0/Radians

Figure 11a

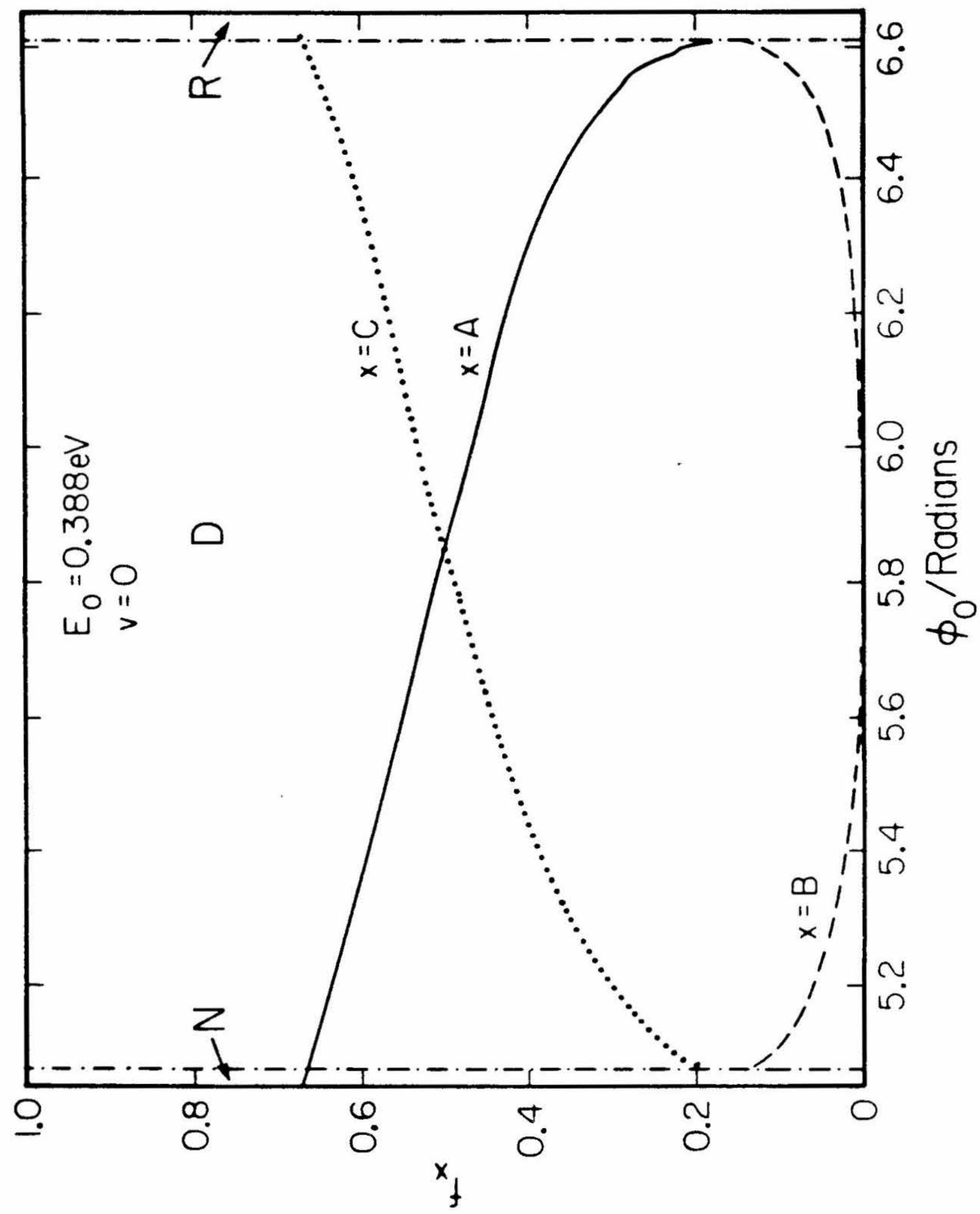
$E_0 = 0.388$eV
$v = 0$
D
N
R
x = C
x = A
x = B
1.0
0.8
0.6
0.4
0.2
0
f_x
5.2
5.4
5.6
5.8
6.0
6.2
6.4
6.6
ϕ_0/Radians

Figure 11b

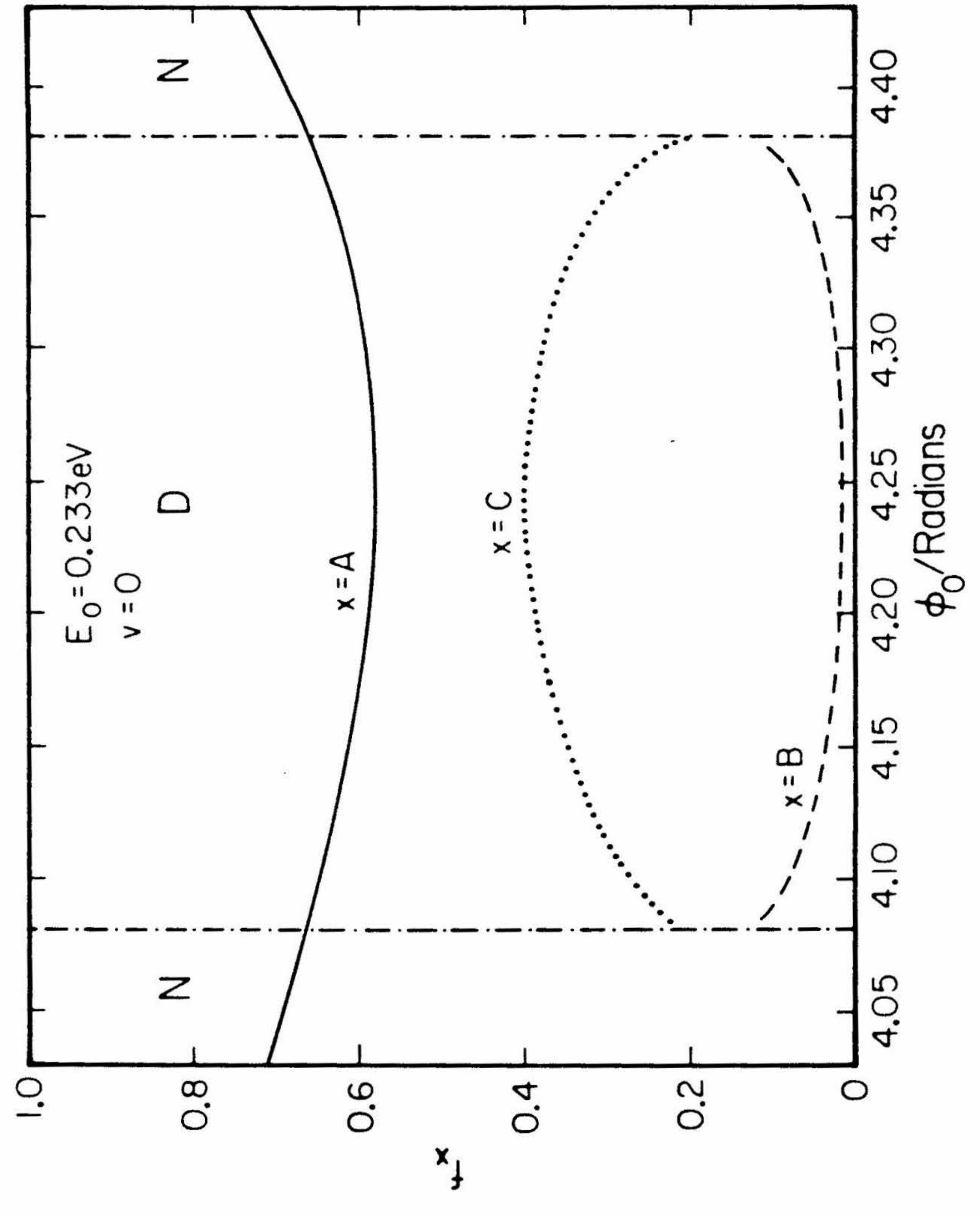
$E_0=0.233$eV
$v=0$
D
N
N
x = A
x = C
x = B
f_x
1.0
0.8
0.6
0.4
0.2
0
4.05
4.10
4.15
4.20
4.25
4.30
4.35
4.40
ϕ_0/Radians

Figure 12

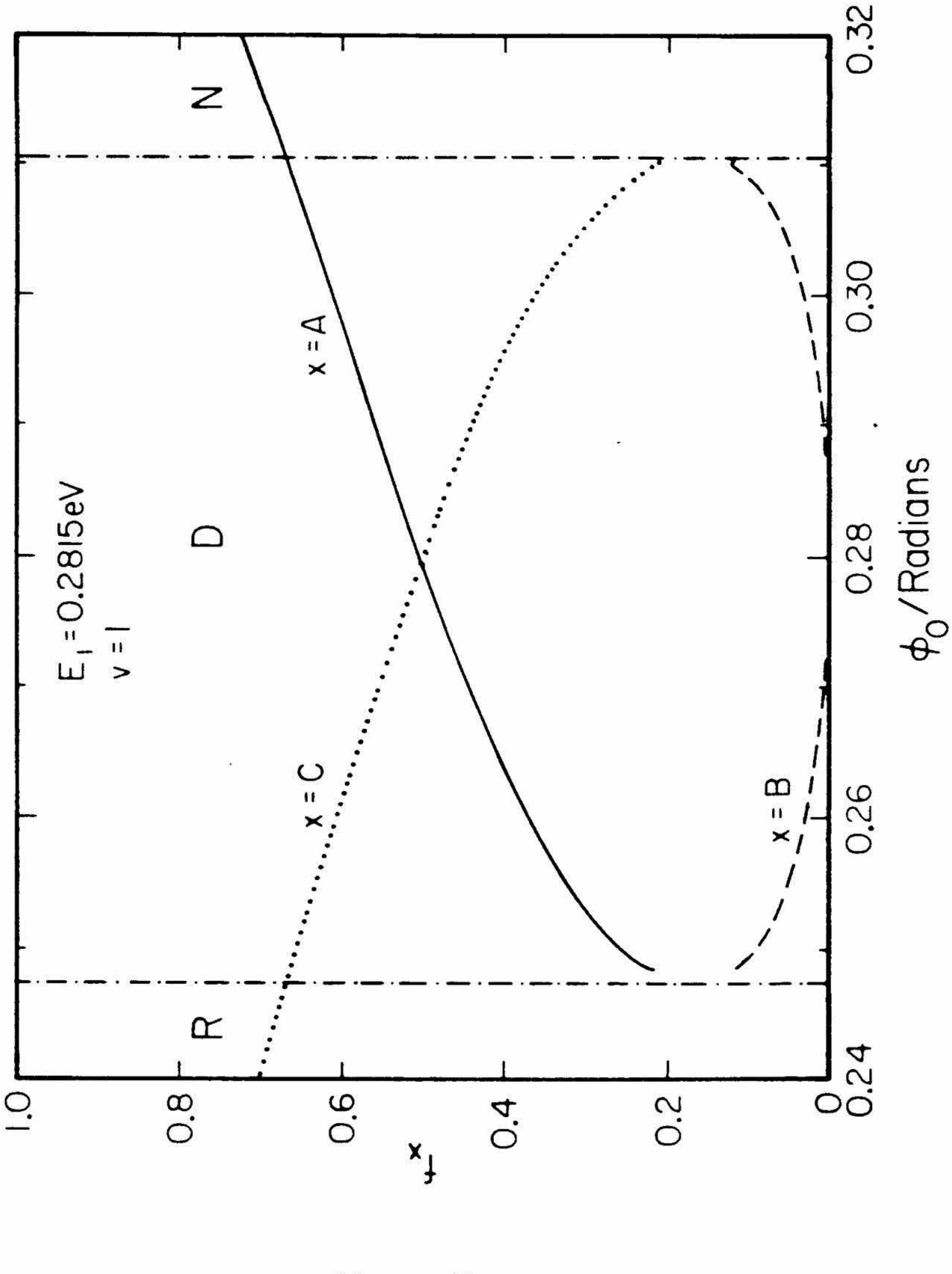
$E_1 = 0.2815$eV
$v = 1$
R
D
N
x = A
x = B
x = C
f_x
1.0
0.8
0.6
0.4
0.2
0
0.24
0.26
0.28
0.30
0.32
ϕ_0/Radians

Figure 13a

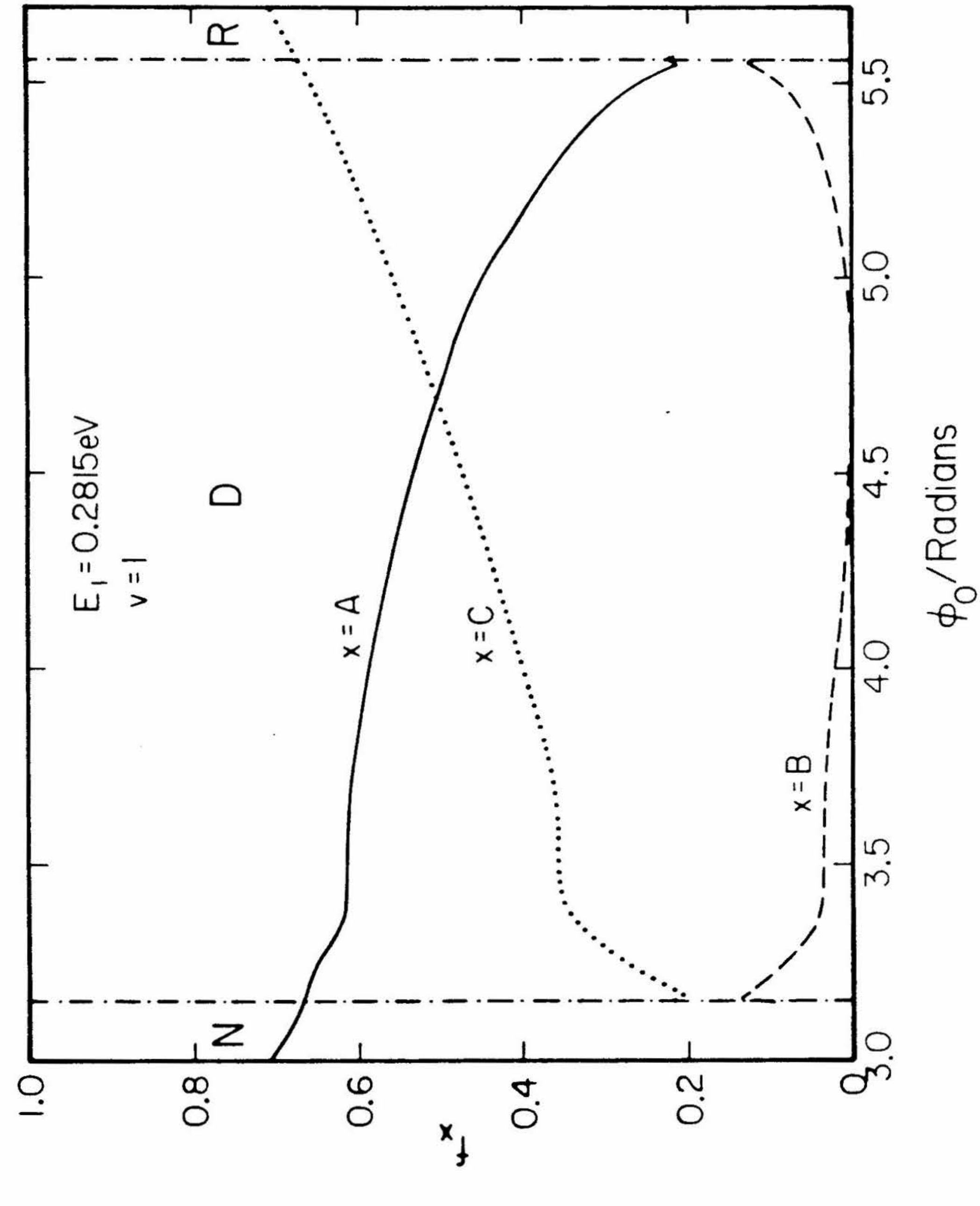
E_1=0.2815eV
v=1
N
D
R
x=A
x=C
x=B
f_x
φ_0/Radians
1.0
0.8
0.6
0.4
0.2
0
3.0
3.5
4.0
4.5
5.0
5.5

Figure 13b

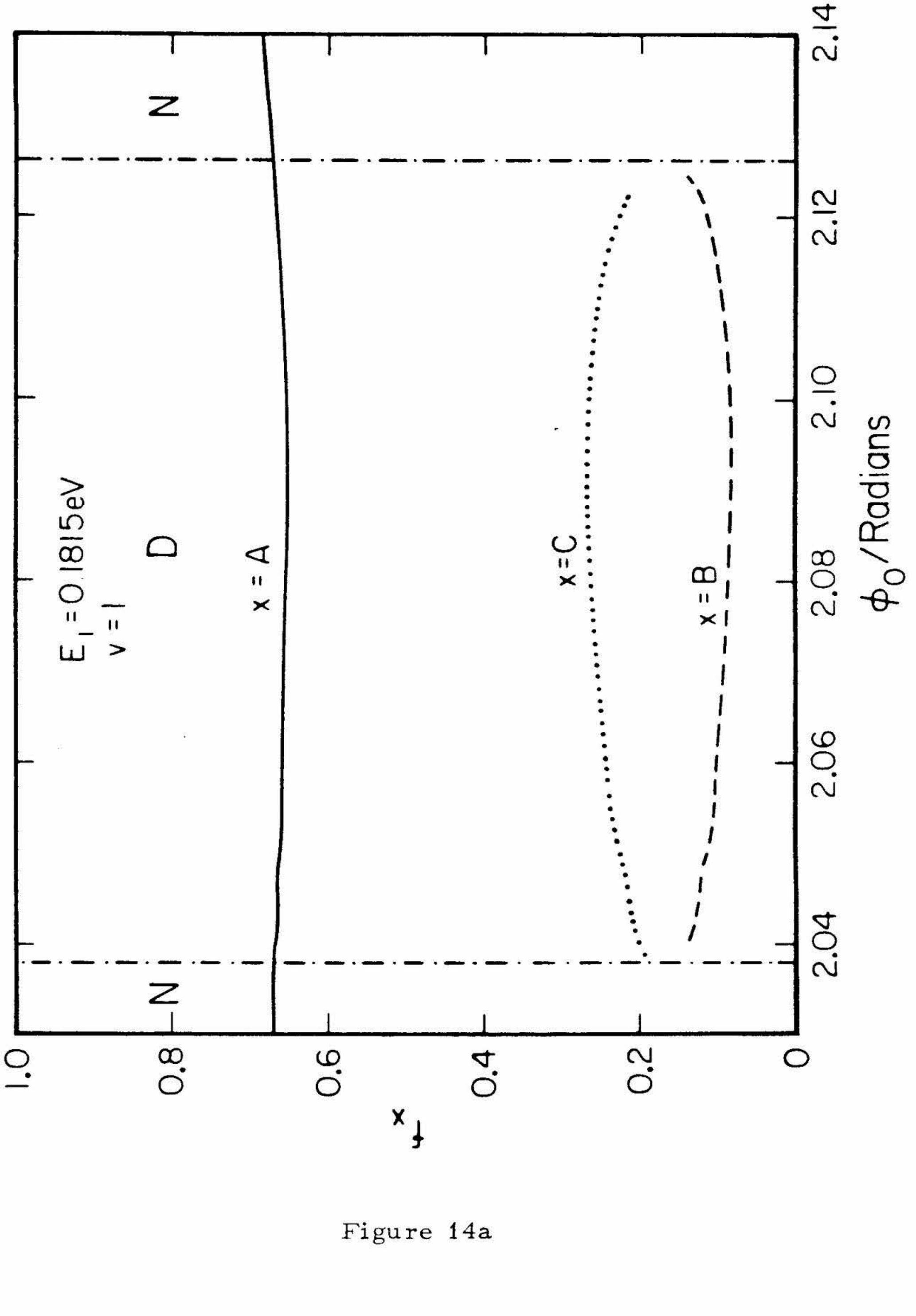
$E_1 = 0.1815$eV
$v = 1$
D
N
N
$x = A$
$x = C$
$x = B$
1.0
0.8
0.6
0.4
0.2
0
f_x
2.04
2.06
2.08
2.10
2.12
2.14
ϕ_0/Radians

Figure 14a

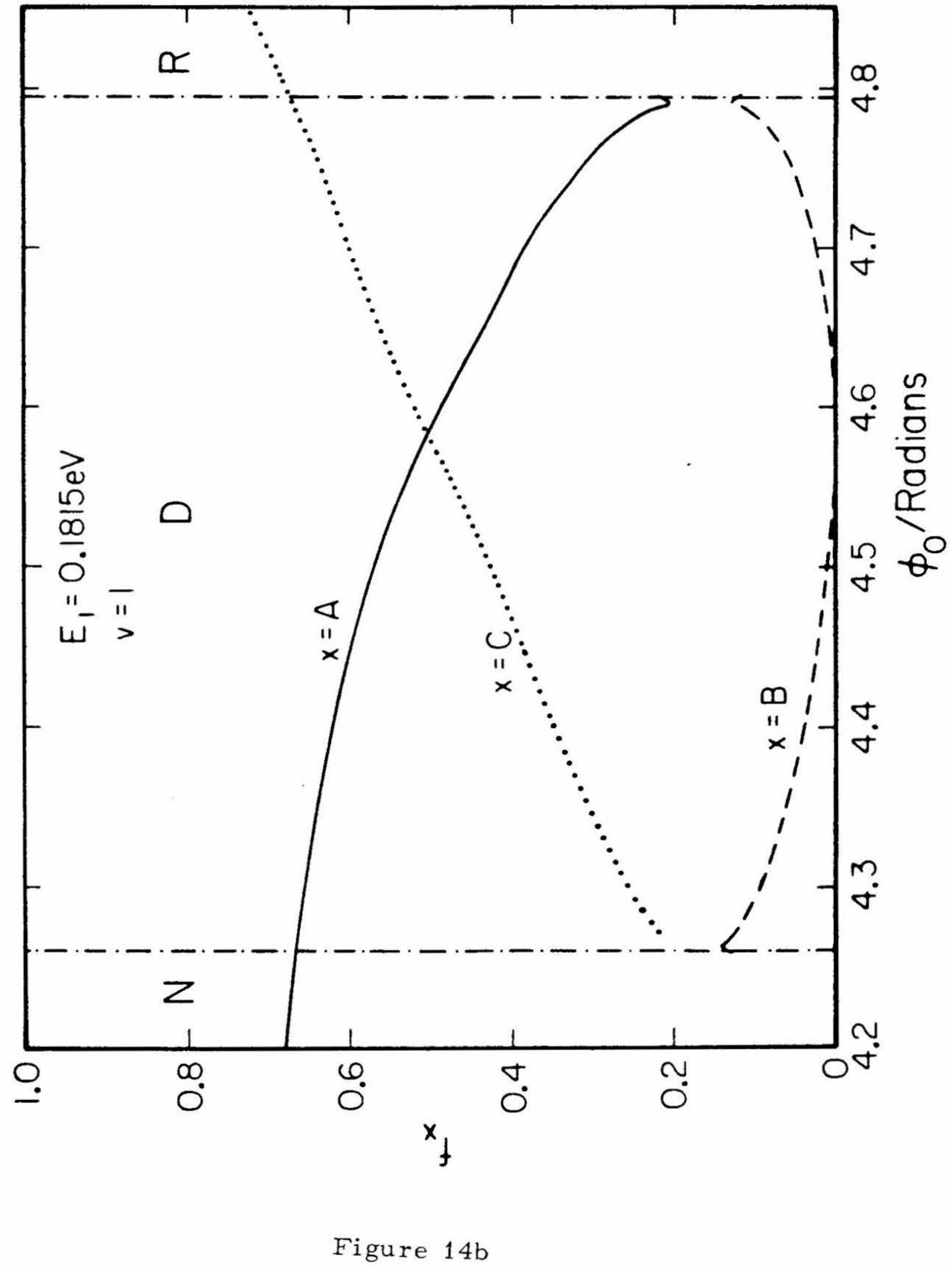
$E_1 = 0.1815$eV
v = 1
D
N
R
x = A
x = C
x = B
f_x
1.0
0.8
0.6
0.4
0.2
0
4.2
4.3
4.4
4.5
4.6
4.7
4.8
ϕ_0/Radians

Figure 14b

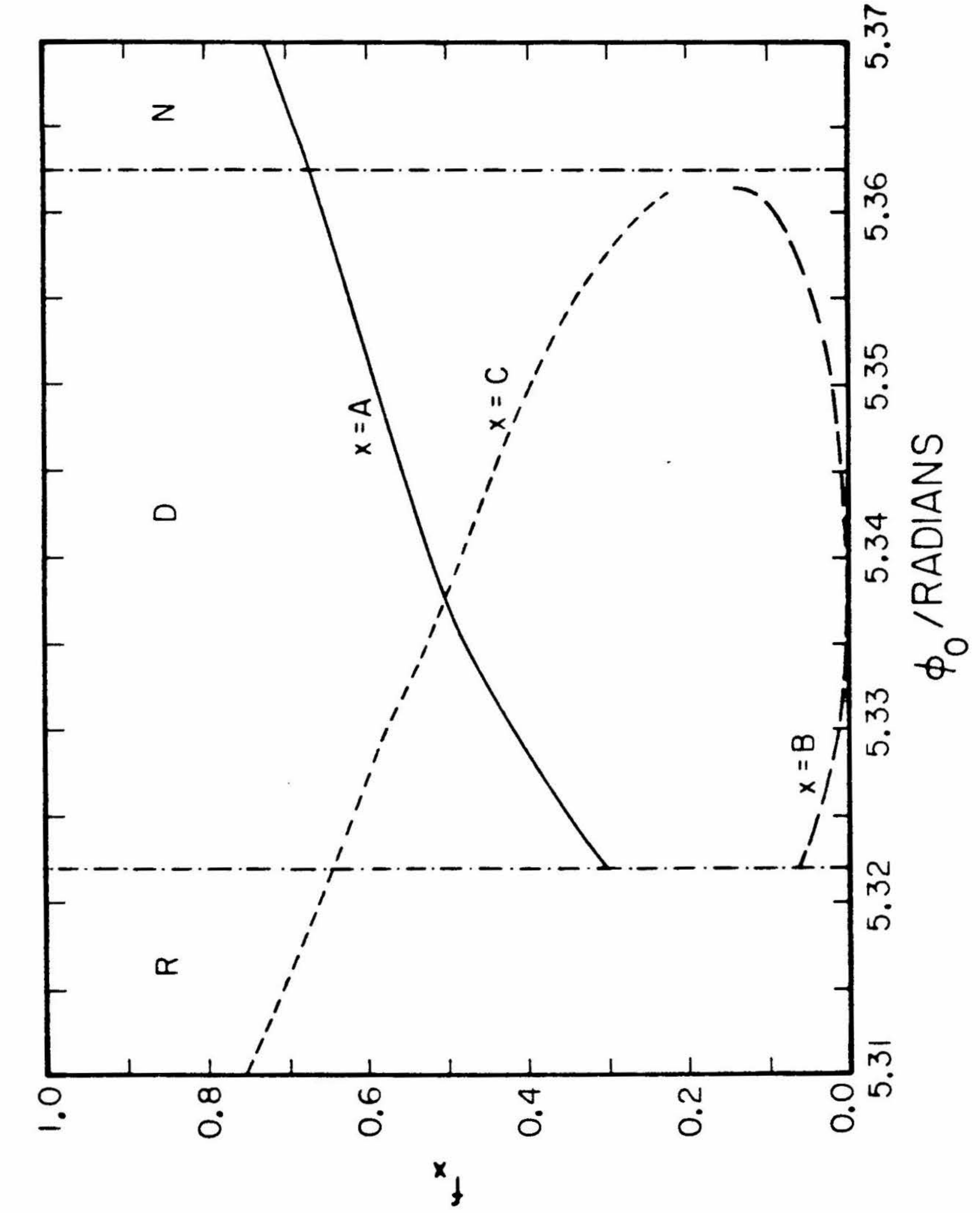
1.0
0.8
0.6
0.4
0.2
0.0
f_x
5.31
5.32
5.33
5.34
5.35
5.36
5.37
ϕ_0/RADIANS
R
D
N
x = A
x = C
x = B

Figure 14c

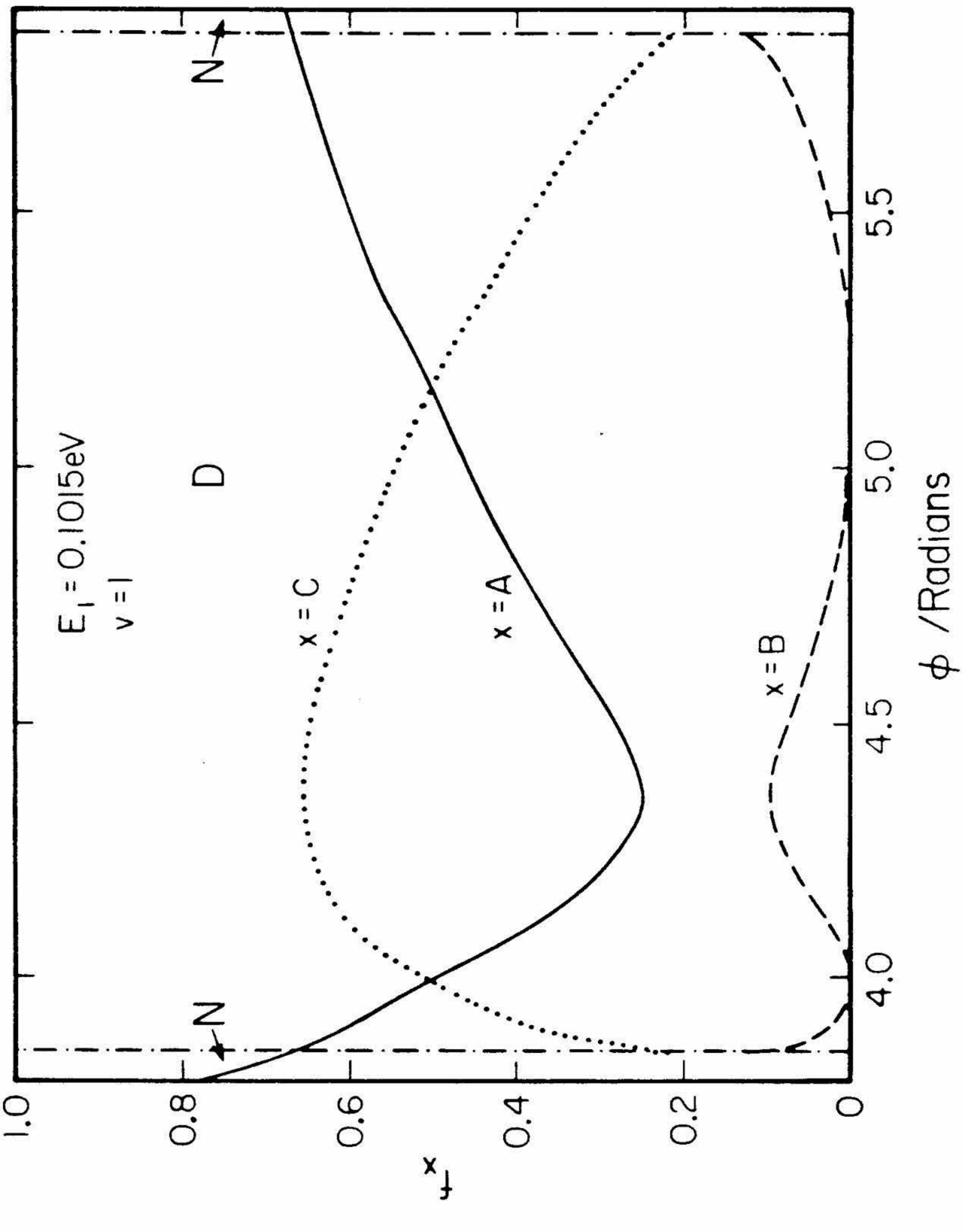
$E_1 = 0.1015$eV
v = 1
D
x = C
x = A
x = B
N
N
1.0
0.8
0.6
0.4
0.2
0
4.0
4.5
5.0
5.5
ϕ /Radians
f_x

Figure 15

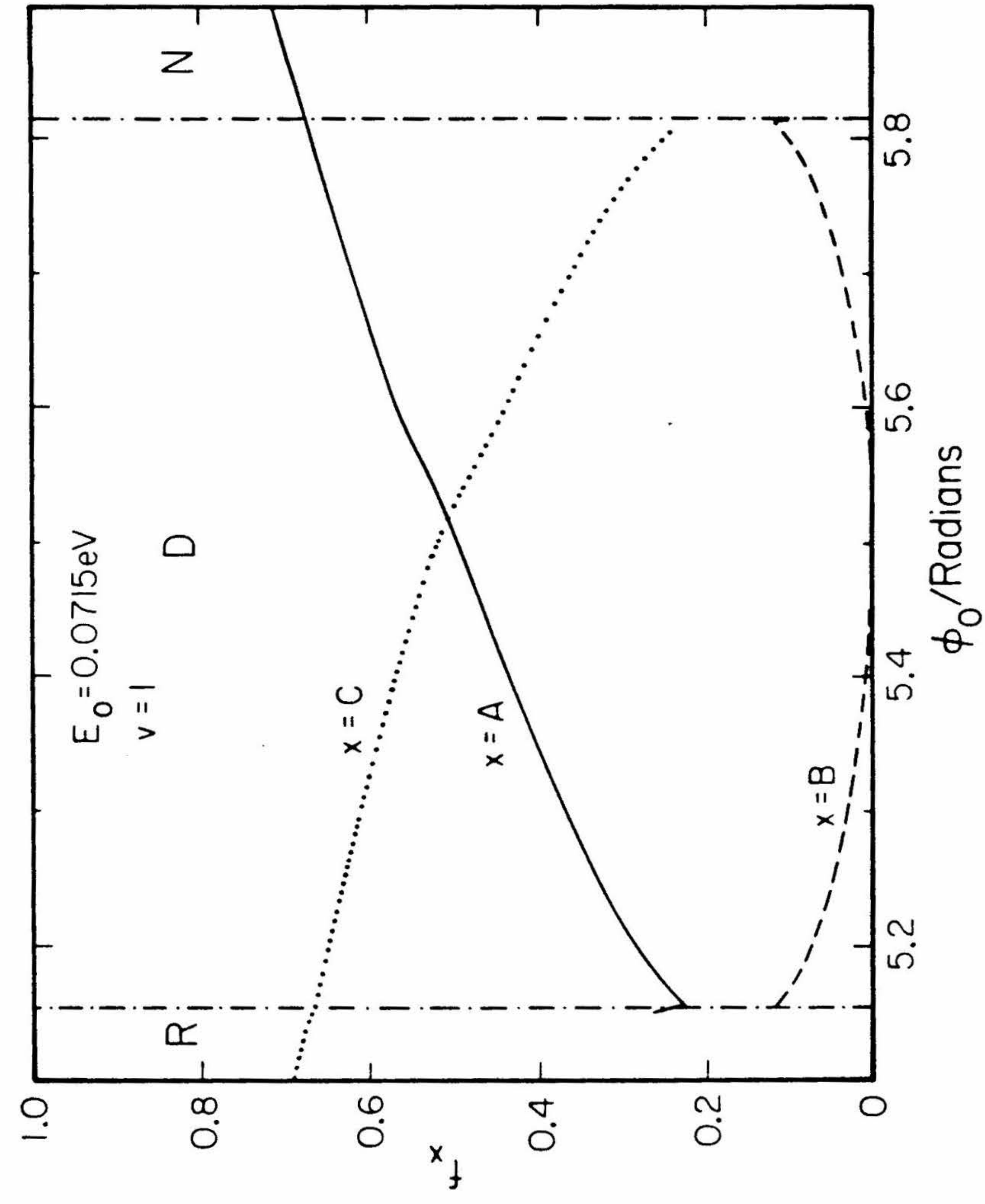
$E_o = 0.0715$eV
v = 1
R
D
N
x = C
x = A
x = B
f_x
0
0.2
0.4
0.6
0.8
1.0
5.2
5.4
5.6
5.8
ϕ_o/Radians

Figure 16

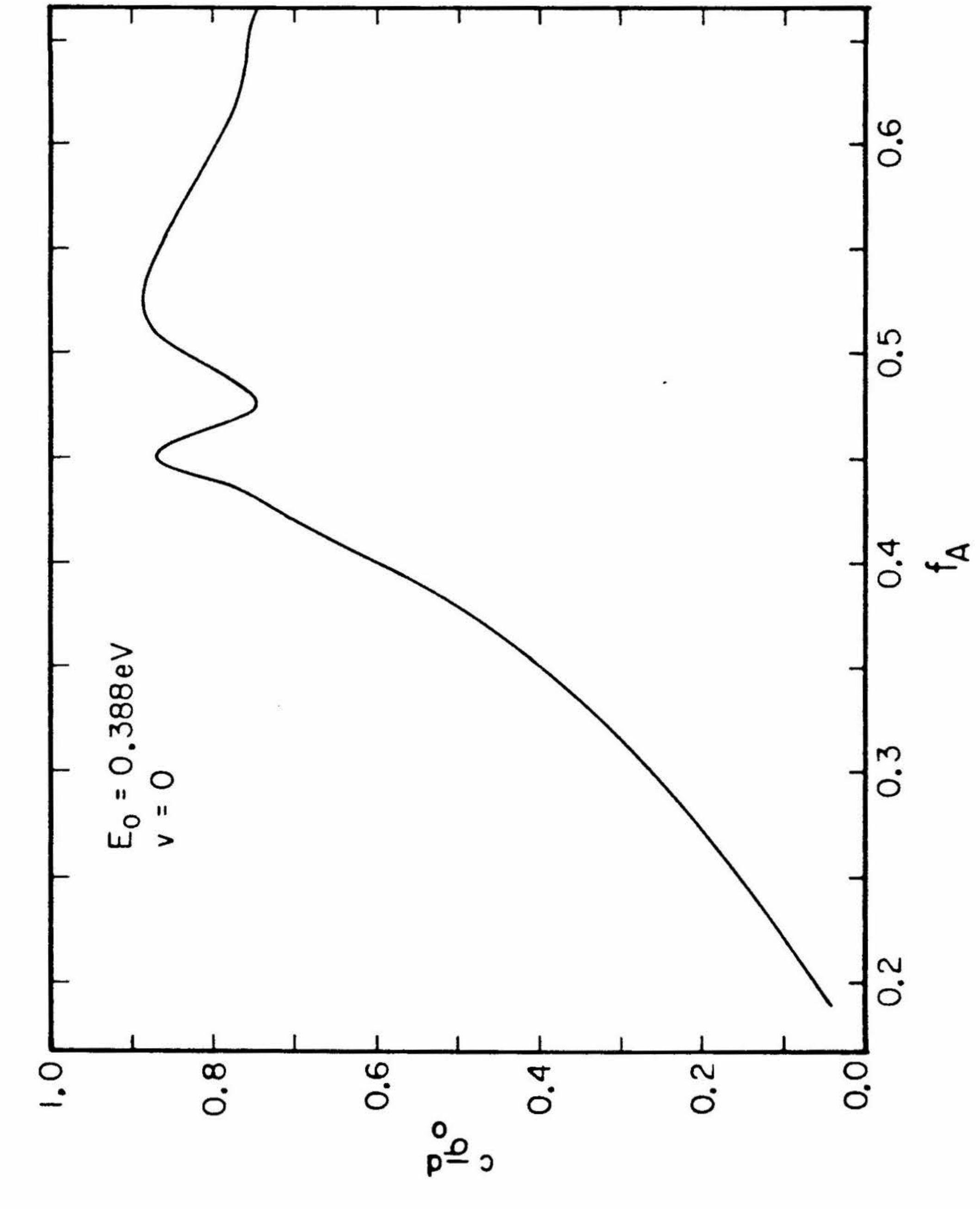

Figure 17

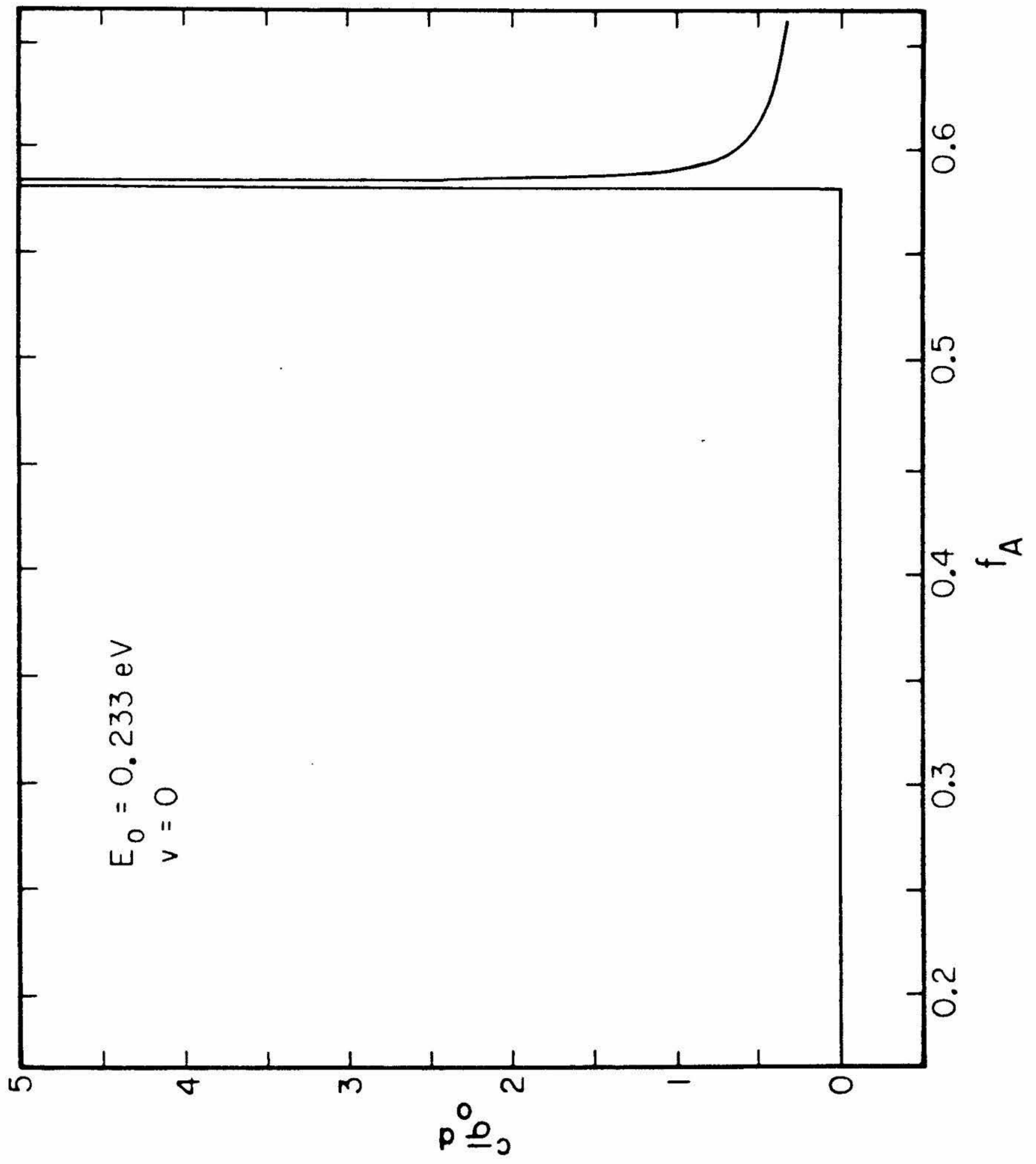

Figure 18

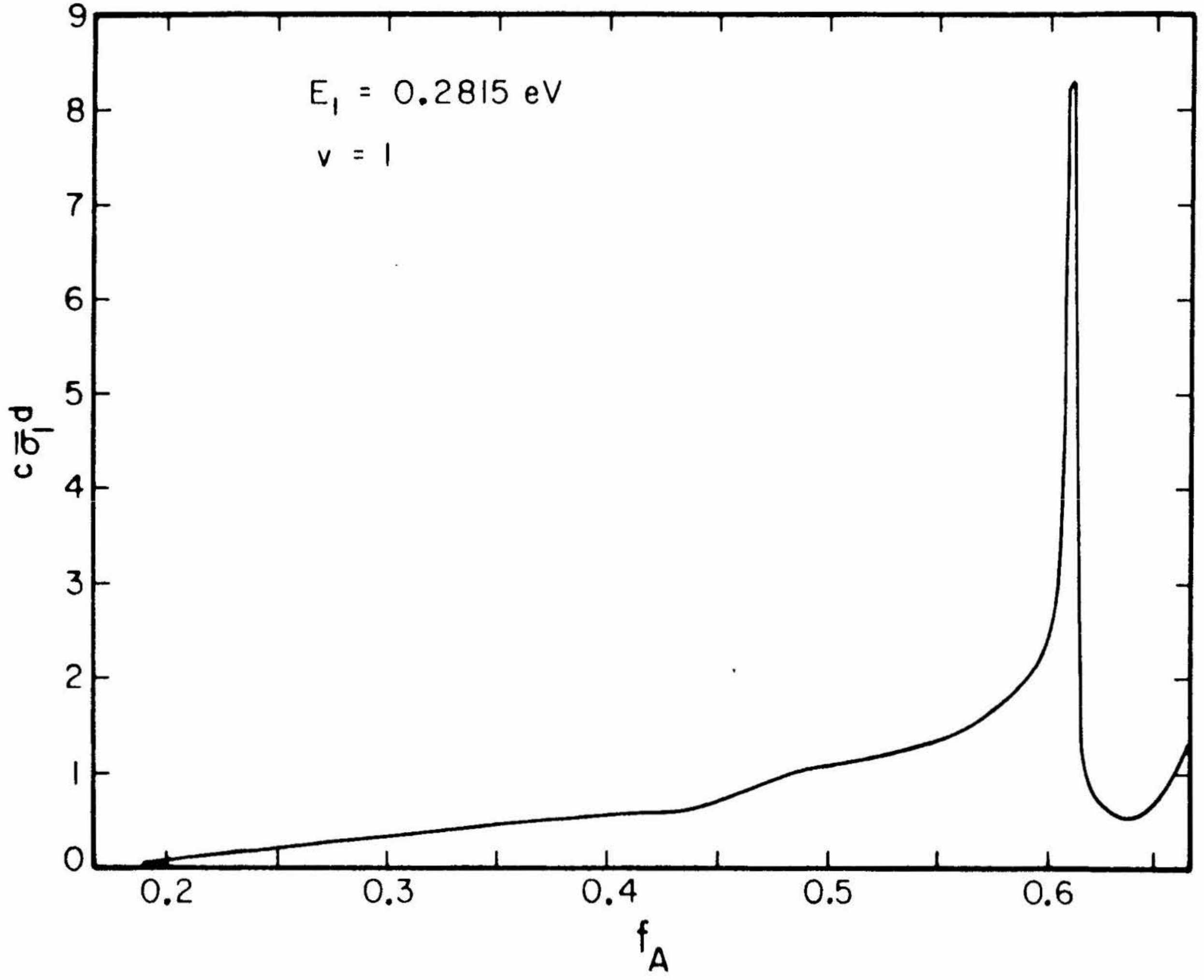

Figure 19

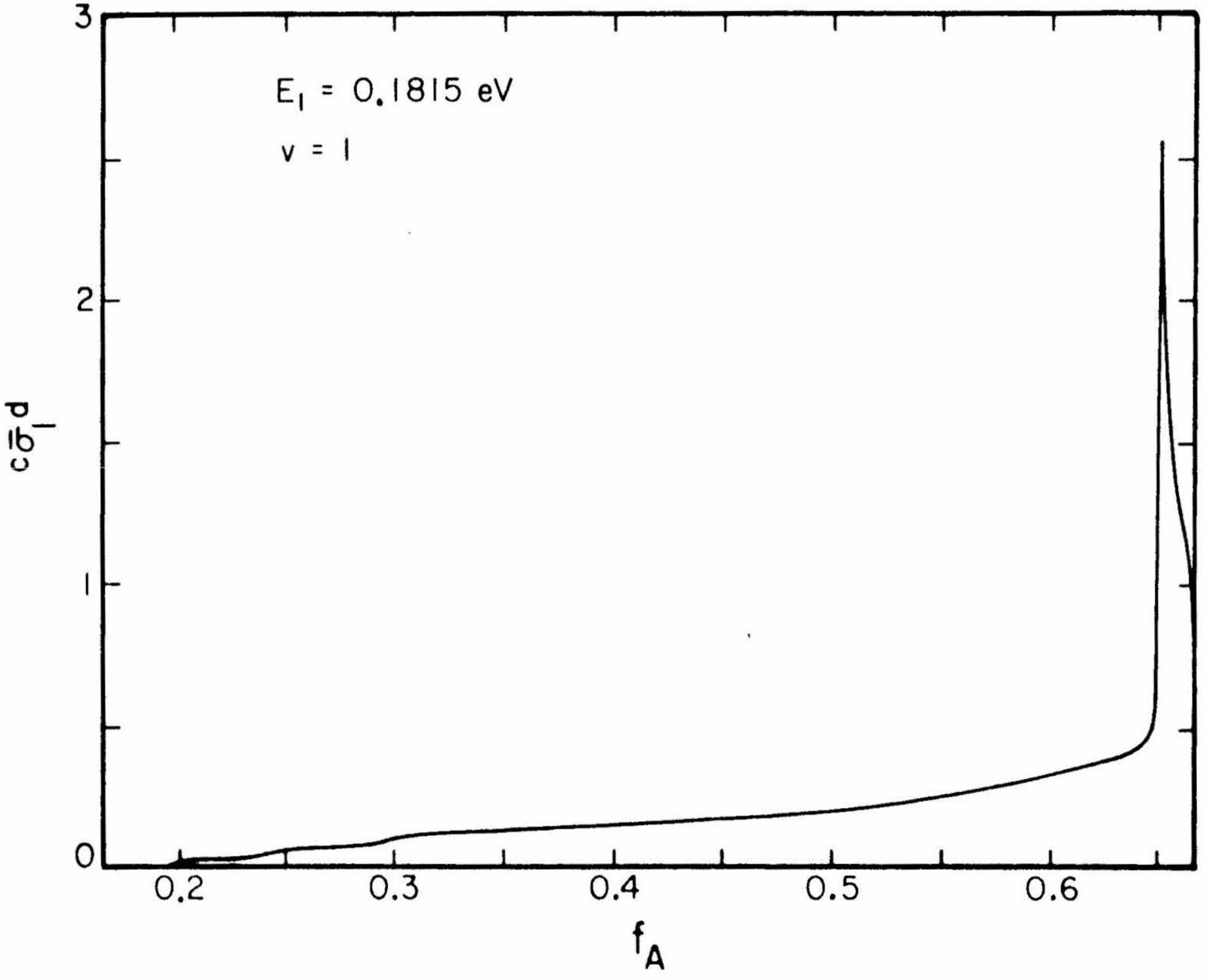

Figure 20

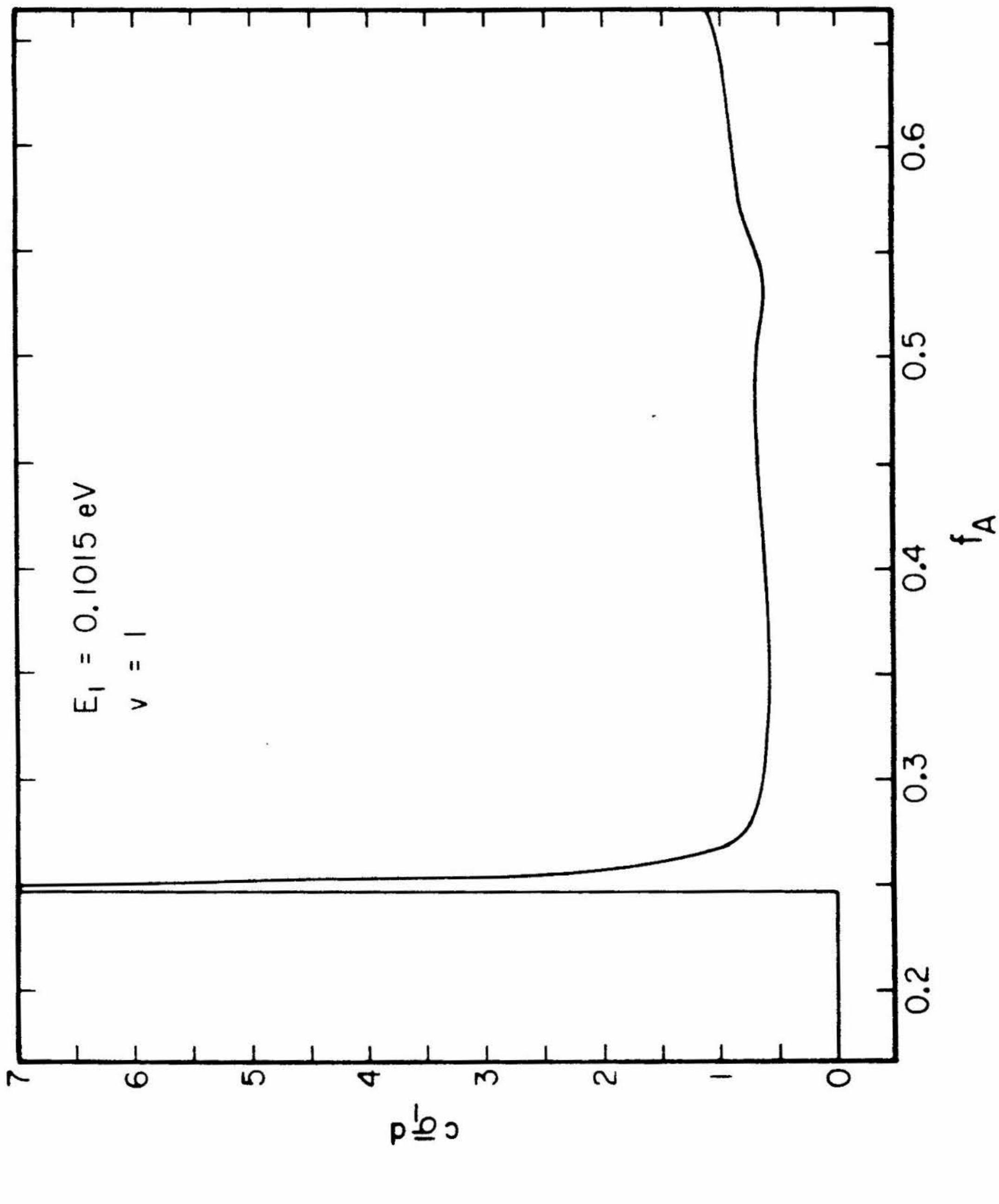

Figure 21

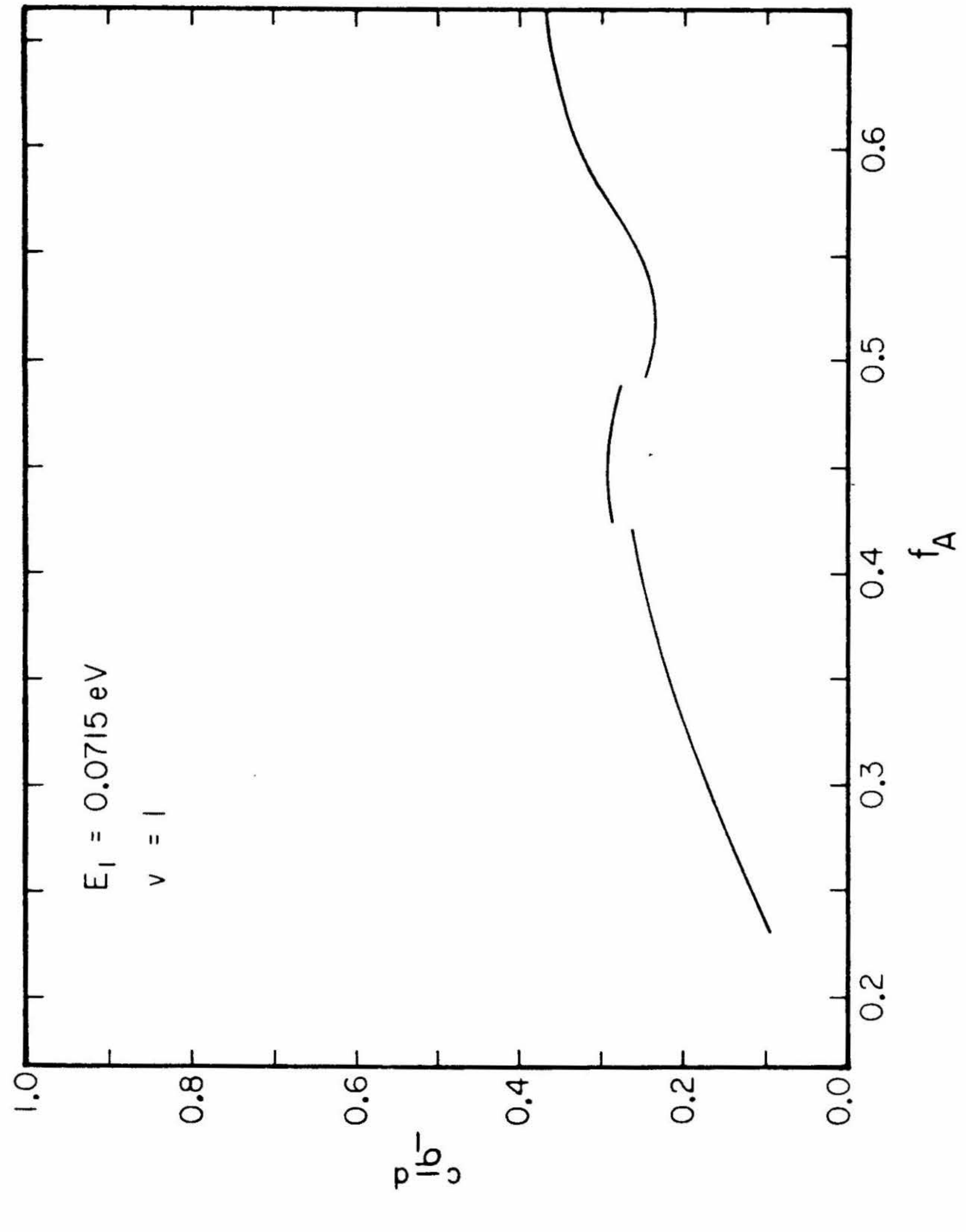

Figure 22

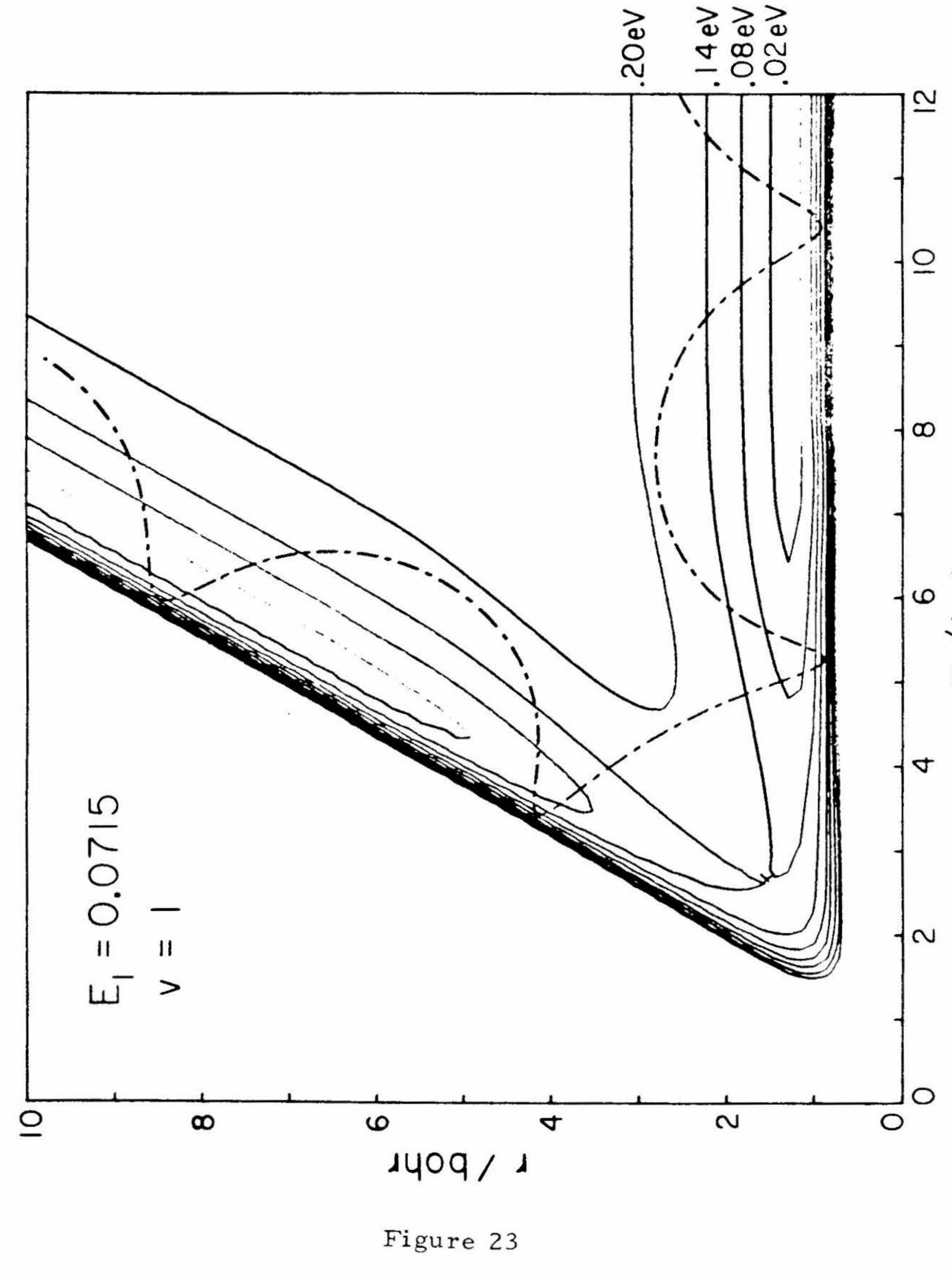

Figure 23

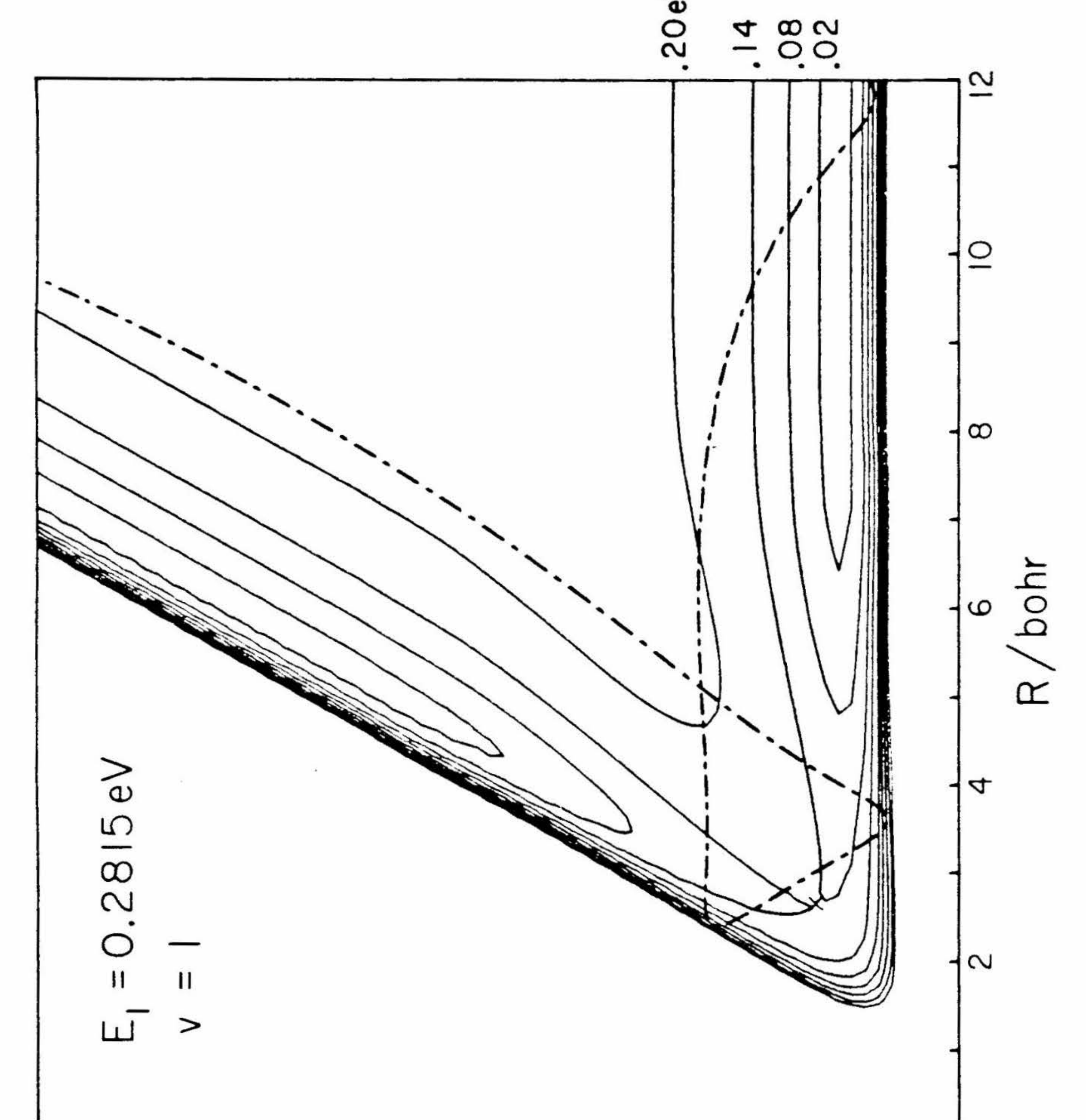
$E_I = 0.2815\,\mathrm{eV}$
$v = 1$
.20eV
.14
.08
.02
0
2
4
6
8
10
12
R/bohr
0
2
4
6
8
10
r / bohr

Figure 24

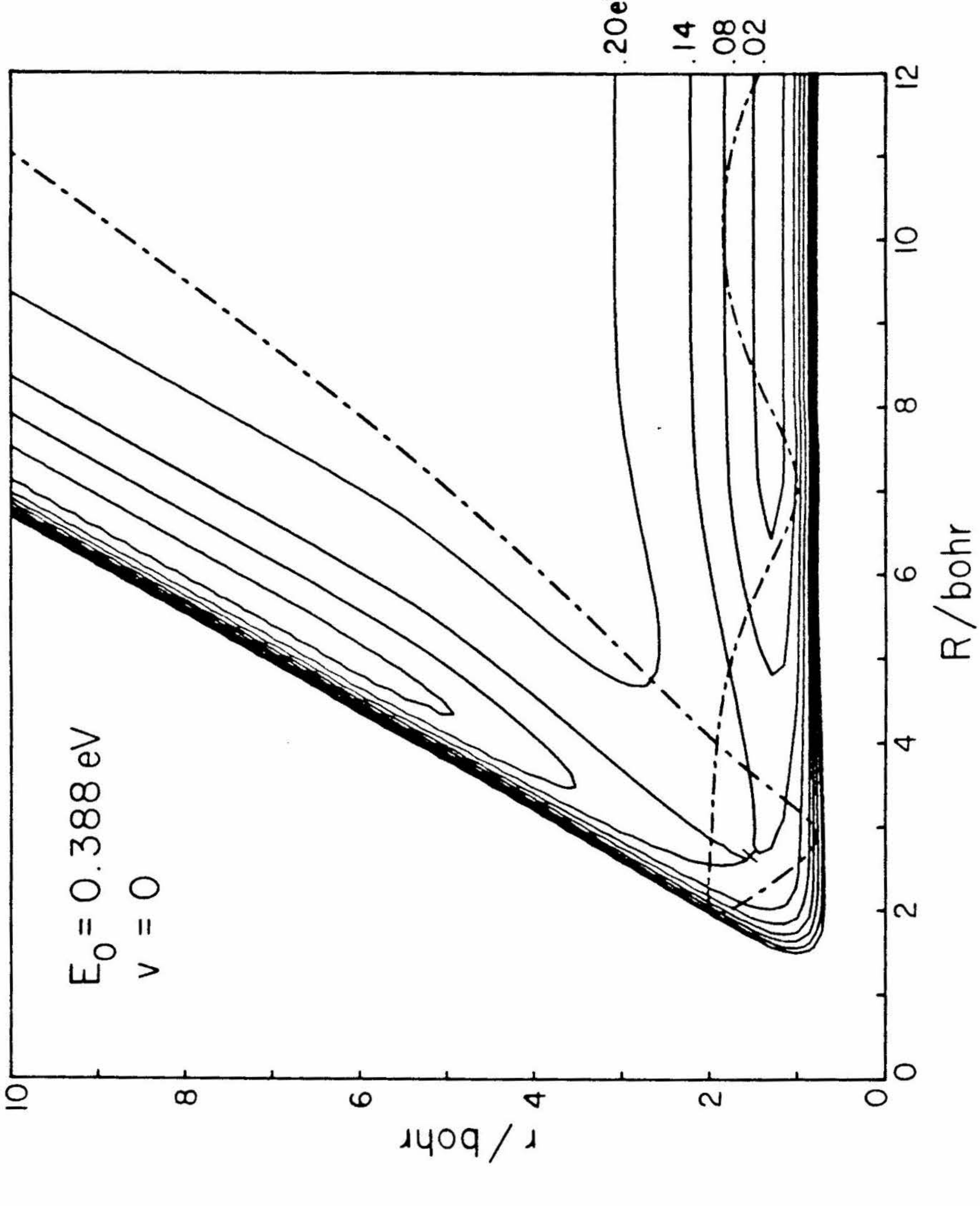

Figure 25

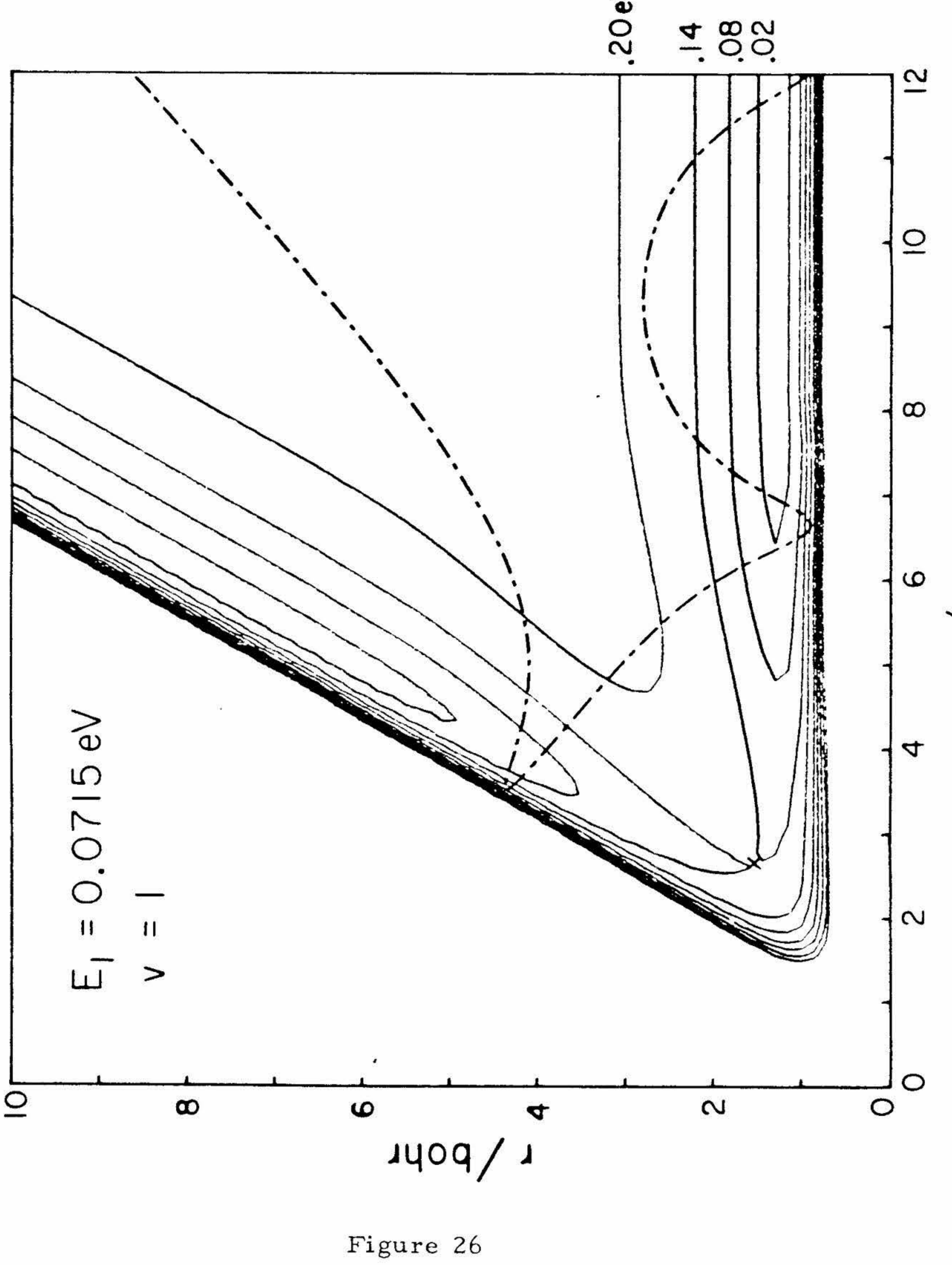

Figure 26

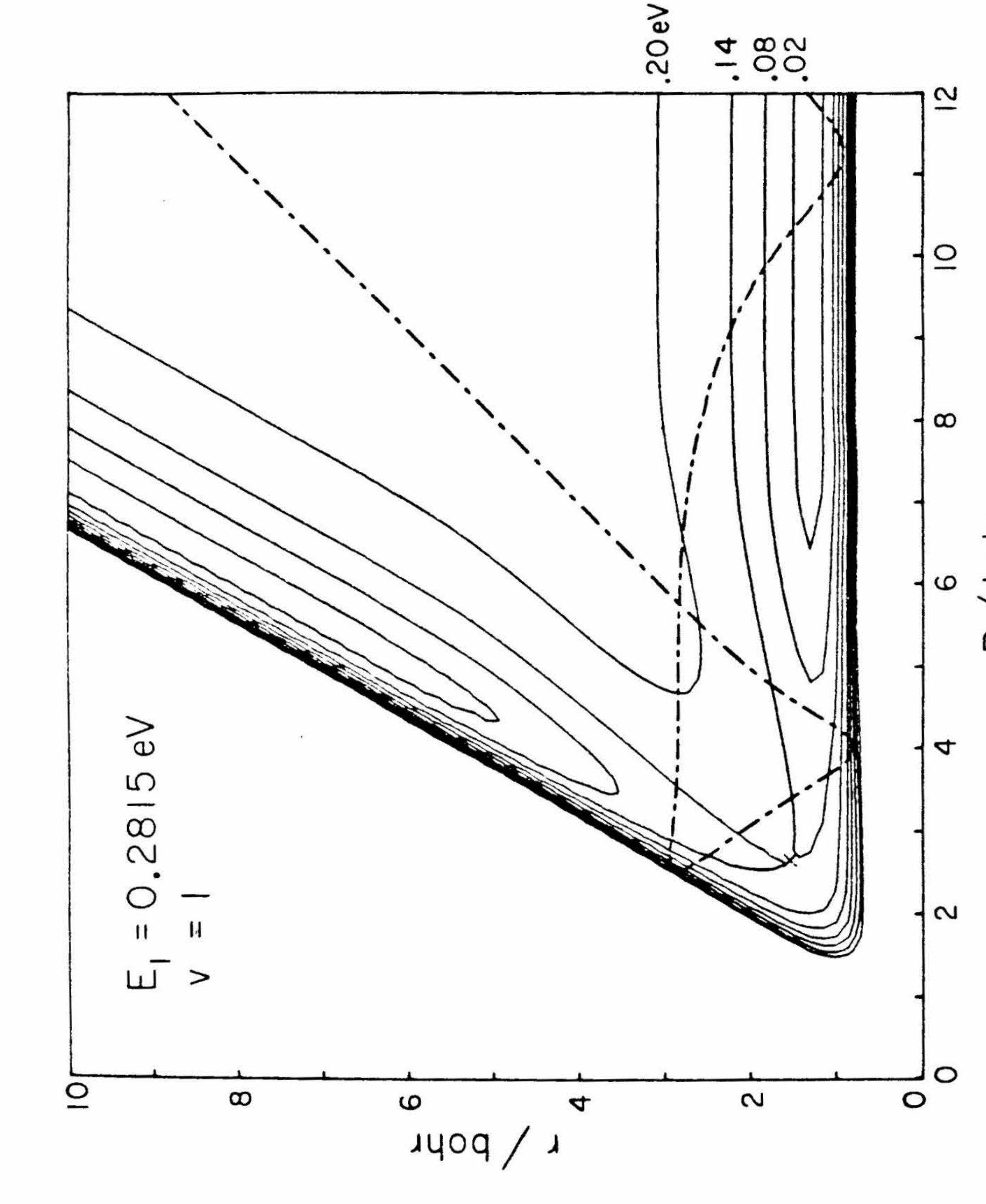

Figure 27

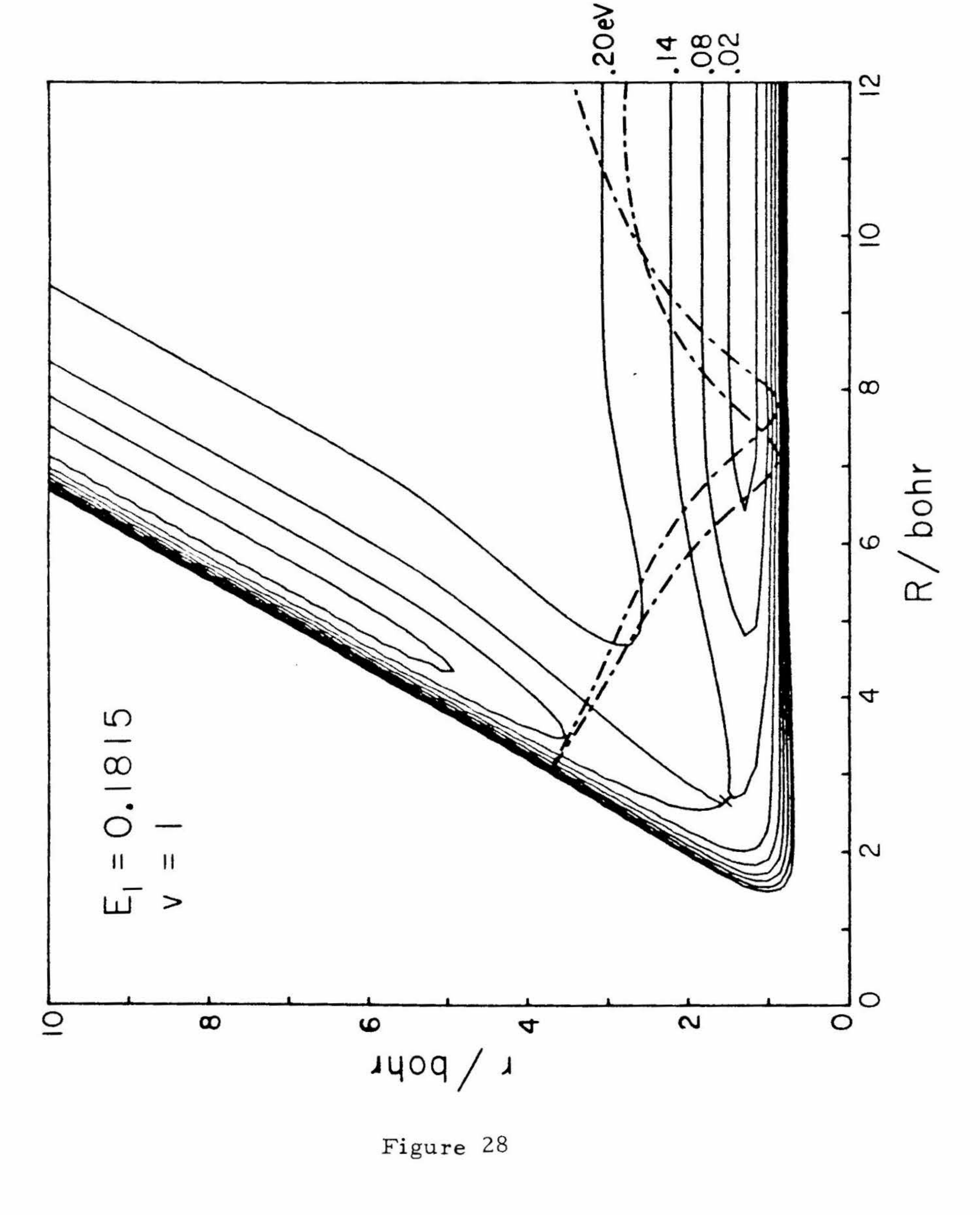

Figure 28

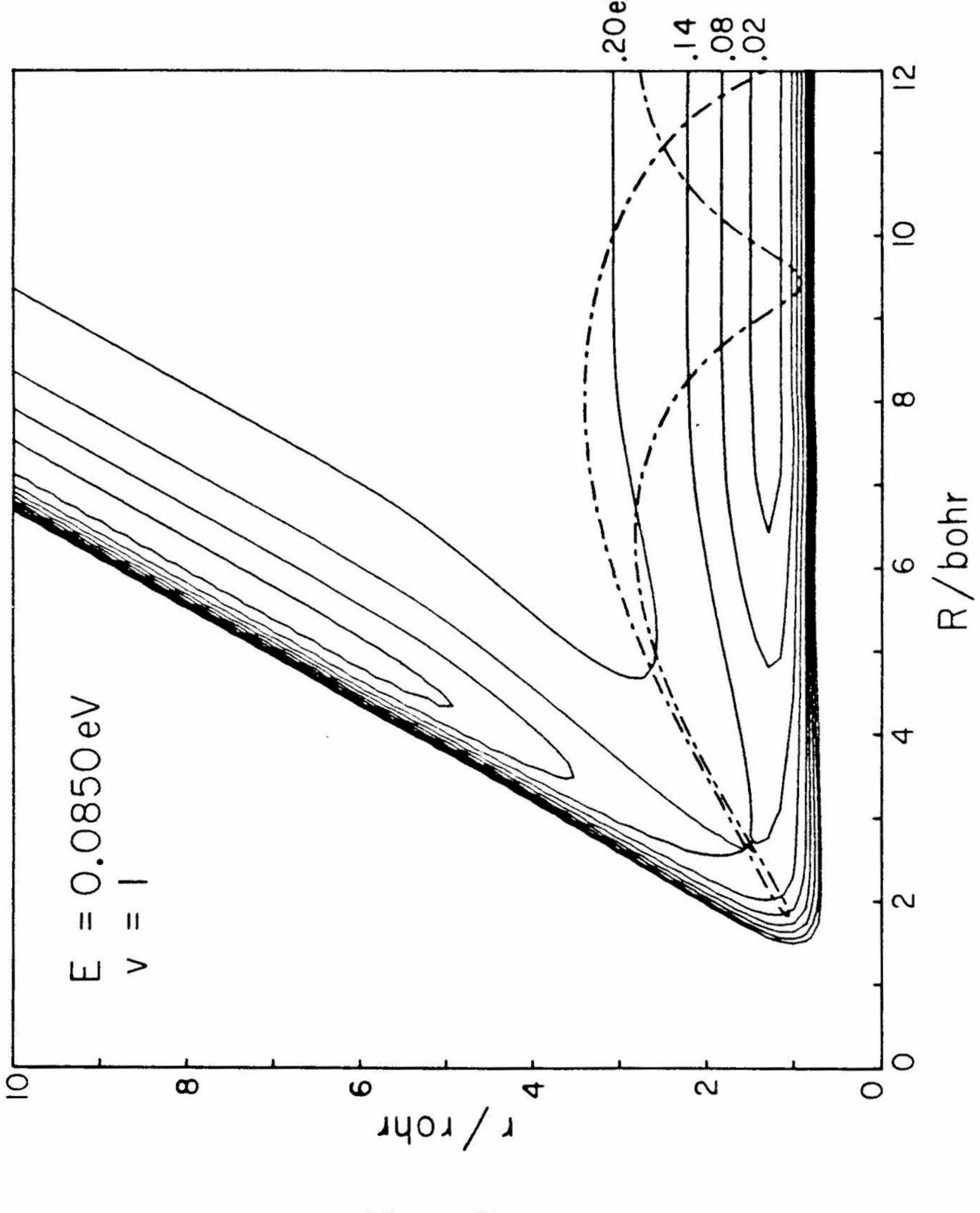

Figure 29

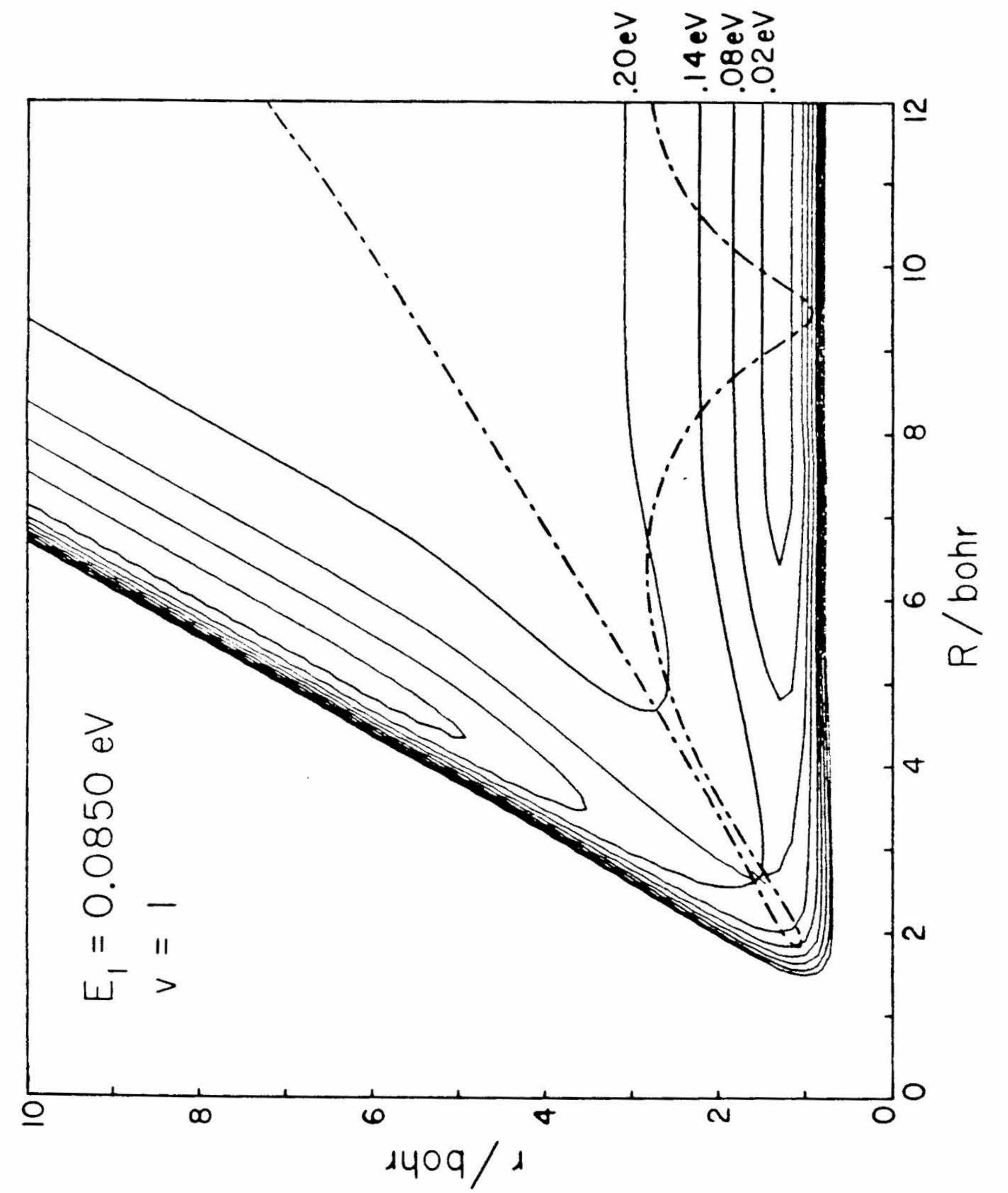

Figure 30

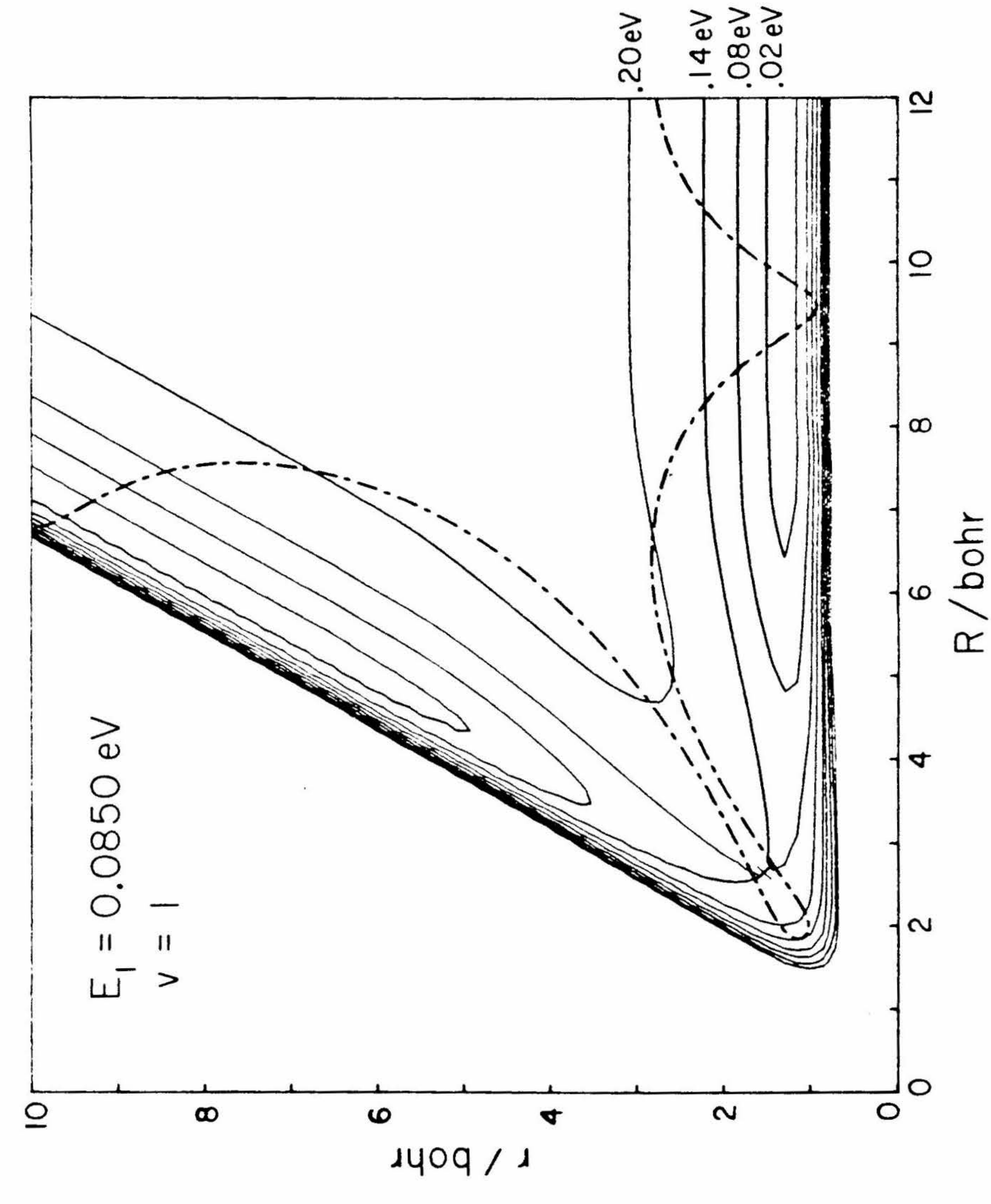

Figure 31

III.6 PARTITIONING OF KINETIC ENERGY AMONG REACTION PRODUCTS IN COLLISION-INDUCED DISSOCIATION IN COLLINEAR ATOM-DIATOMIC MOLECULE COLLISIONS FROM QUANTUM MECHANICAL AND CLASSICAL MECHANICAL CALCULATIONS

PARTITIONING OF KINETIC ENERGY AMONG REACTION PRODUCTS IN COLLISION INDUCED DISSOCIATION IN COLLINEAR ATOM-DIATOMIC MOLECULE COLLISIONS FROM QUANTUM AND CLASSICAL MECHANICAL CALCULATIONS*

Jack A. KAYE** and Aron KUPPERMANN
Arthur Amos Noyes Laboratory of Chemical Physics,†
California Institute of Technology,
Pasadena, California 91125, USA

(Received)

Results for the kinetic energy distributions of atomic products of the collision-induced dissociation

$$A + BC \rightarrow A + B + C$$

on a model reactive collinear system have been obtained by both quantum mechanical coupled channel and quasi-classical trajectory calculations. The results from the two methods are compared and discussed.

---

*This work was supported in part by a contract (No. F49620-79-C-0187) from the Air Force Office of Scientific Research.

**Work performed in partial fulfillment of the requirements for the Ph.D. degree in Chemistry at the California Institute of Technology.

†Contribution No.

1. Introduction

The distribution of energy among the various possible degrees of freedom (electronic, vibrational, rotational, and translational) in collisions of atoms or molecules with other molecules has been a subject of intense research, both experimental[1] and theoretical,[2] over the past 15 years. Most of this work has been concerned with the determination of the relative populations of the possible states of the molecular product; additional work has focussed on the relative rates of formation of different electronic states of atomic products.

In atom-diatomic molecule collisions at energies above the threshold for dissociation, collision-induced dissociation (CID)

$$A + BC \rightarrow A + B + C \tag{1}$$

may occur. In CID there are no molecular products; in electronically adiabatic collisions the only degrees of freedom in the product are translational. Far less is known about the dynamics of atom-diatomic molecule collisions at energies above dissociation than at those below;[3] in particular, little attention has been paid to the partitioning of the available energy among the three atoms in dissociative collisions.

This information can in principle be obtained from accurate calculations on the collision process. Their determination from classical trajectory calculations of the CID process is straightforward. One just calculates the kinetic energies of the three atoms when the collision is over for each trajectory resulting in dissociation, and then appropriately averages over all trajectories leading to dissociation. Their determination from quantum mechanical calculations is more complicated; they may be obtained from scattering calculations performed by the hyperspherical coordinates method.[4,5]

In this work we present results for the partitioning probabilities, that is, the probabilities of partitioning of the available energy among the three atoms in dissociative collisions by both quantum mechanical (QM) and quasi-classical trajectory (QCT) methods in a model collinear atom-diatomic molecule collision. We first review the methods by which these quantities are obtained. We will then compare the QM and QCT results and will discuss the origins of the difference between the results from the two methods.

2. Theory and Numerical Methods

A. Quantum Mechanical Method

The calculation of bound-continuum (dissociation) probabilities by the hyperspherical coordinate method has been outlined by us[4c] and by Manz and Römelt[5] previously. The basic formalism for the calculations of the partitioning probabilities has also been outlined previously.[4c,b] We present it here in more detail, emphasizing details appropriate to its numerical implementation.

First we recognize that in dissociative collisions, there is only one degree of freedom in the partitioning of the available energy among the three atoms.[8] This is best expressed as the angle α, which is one of the two variables in the hyperspherical coordinate treatment of collinear atom-diatomic molecule collisions.[4a] The kinetic energies of the three atoms are related by the expressions

$$\frac{E_A}{E'} = \frac{m_b + m_c}{M} \cos^2\alpha \tag{2a}$$

$$\frac{E_B}{E'} = \frac{m_b}{m_b + m_c} \left[\left(\frac{m_a}{M}\right)^{\frac{1}{2}} \cos\alpha - \left(\frac{m_c}{m_b}\right)^{\frac{1}{2}} \sin\alpha\right] \tag{2b}$$

$$\frac{E_c}{E'} = \frac{m_c}{m_b + m_c} \left[\left(\frac{m_a}{M}\right)^{\frac{1}{2}} \cos\alpha + \left(\frac{m_c}{m_b}\right)^{\frac{1}{2}} \sin\alpha\right] . \tag{2c}$$

where E′ is the energy of the collision measured with respect to that of three infinitely separated atoms and M is the sum of the atomic masses.

The probability $\sigma_d^{\lambda n_\lambda}(\alpha)$ of dissociating from a bound state λn_λ, where λ represents the reagent diatomic molecule (AB or BC) and n_λ is its vibrational quantum number to an angle α is given by the ratio of the total radial flux between α and $\alpha + d\alpha$ at some large value of ρ to the total incident flux $\hbar k_{\lambda n_\lambda}/\mu$, where $k_{\lambda n_\lambda}$ is the wavenumber appropriate to the incident state, and μ is the Delves[7] mass $(m_A m_B m_C/M)^{\frac{1}{2}}$

$$\sigma_d^{\lambda n_\lambda}(\alpha, \rho) = \mathrm{Im}\left[\psi^*\left(\frac{\partial\psi}{\partial\rho}\right)\right] \rho\, d\alpha , \tag{3}$$

where the dissociative part $\psi_d^{\lambda n_\lambda}$ (the only one of interest here) of the total wavefunction $\psi^{\lambda n_\lambda}$ (see eq. (3) of ref. 2) may be written (at large ρ) as

$$\psi_d^{\lambda n_\lambda} = \rho^{-\frac{1}{2}} \sum_{n=1} \exp(ik_n\rho)(k_{\lambda n_\lambda}/k_n) \quad S_n^{\lambda n_\lambda}\, \phi_n(\alpha;\rho) . \tag{4}$$

If numerical integration of the coupled channel equations were carried out to $\rho = \infty$, the eigenvalues of all continuum states would be identical (and zero) and all their wavenumbers k_n would be equal, and all terms in eq. (4) having a subscript n could be pulled outside the summation. In principle, the sum in eq. (4) is infinite; in practice it is truncated at some value N_d sufficiently large that the sum in eq. (4) has essentially converged to its true value. The dependence of $\sigma_d^{\lambda n_\lambda}$ on ρ should be quite small; if integration were carried out to infinity $\sigma_d^{\lambda n_\lambda}$ would be independent of ρ.

Combining eqs. (3) and (4) and performing the necessary algebra, we obtain the expression, assuming that the only ρ dependence in (4) is from the $\rho^{-\frac{1}{2}}$ and $\exp(ik_n\rho)$ terms,

$$\sigma_d^{\lambda n_\lambda}(\alpha,\rho) = \sum_{n,n'=1}^{N_d} \phi_n(\alpha;\rho)\,\phi_{n'}(\alpha;\rho)\,\frac{k^{\lambda n_\lambda}}{(k_n k_{n'})^{\frac{1}{2}}}\{A_{nn'}(\rho)[\mathrm{Re}S_{n'}^{\lambda n_\lambda}\,\mathrm{Re}S_n^{\lambda n_\lambda} + \mathrm{Im}S_{n'}^{\lambda n_\lambda}\,\mathrm{Im}S_n^{\lambda n_\lambda}] + B_{nn'}(\rho)[\mathrm{Re}S_{n'}^{\lambda n_\lambda}\,\mathrm{Im}S_n^{\lambda n_\lambda} - \mathrm{Re}S_\lambda^{\lambda n_\lambda}\,\mathrm{Im}S_{n'}^{\lambda n_\lambda}]\}\,d\alpha \tag{5}$$

where

$$A_{nn'}(\rho) = -\frac{1}{2\rho}\sin[(k_n - k_{n'})\rho] + k_n\cos[(k_n - k_{n'})\rho] \tag{6a}$$

$$B_{nn'}(\rho) = -\frac{1}{2\rho}\cos[(k_n - k_{n'})\rho] + k_n\sin[(k_n - k_{n'})\rho]\,. \tag{6b}$$

As mentioned earlier, as $\rho \to \infty$, $k_{n'} \to k_n$ for all n, n', so in the limit of infinite ρ we have

$$A_{nn'}(\rho \to \infty) \sim k_n \tag{7a}$$

$$B_{nn'}(\rho \to \infty) \sim 0\,. \tag{7b}$$

In that case, eq. (5) reduces to the form given previously.[4a, 6] In all numerical calculations we will use eq. (5) and not its limit as $\rho \to \infty$.

Rather than dealing with $\sigma_d^{\lambda n_\lambda}(\alpha,\rho)$, in which one calculates the probability of forming products corresponding to a given α, we prefer to consider the probability $\sigma_d^{\lambda n_\lambda}(E_A,\rho)$ of dissociation in which atom A has a center of mass energy E_A

$$\sigma_d^{\lambda n_\lambda}(E_A,\rho) = \left|\frac{d\alpha}{dE_A}\right| \sigma_d^{\lambda n_\lambda}(\alpha,\rho) . \tag{8}$$

These partitioning probabilities, when integrated over all possible values* of E_A give the total dissociation probability

$$P_d^{\lambda n_\lambda}(\rho) = \int_{E_A^{min}}^{E_A^{max}} \sigma_d^{\lambda n_\lambda}(E_A,\rho)dE_A \tag{9}$$

E_A^{min} and E_A^{max} are determined by eq. (2a) $\alpha = \alpha_{max} = \tan^{-1}(m_b M/m_a m_c)^{\frac{1}{2}}$ and $\alpha = 0$, respectively. For convenience's sake we will normally consider $\sigma_d^{\lambda n_\lambda}(E_A,\rho)$ as a function of the dimensionless quantity $f_A = E_A/E'$; to make $\sigma_d^{\lambda n_\lambda}(E_A,\rho)$ dimensionless we multiply it by E' to make a quantity $\bar{\sigma}_d^{\lambda n_\lambda}(E_A,\rho)$

$$\bar{\sigma}_d^{\lambda n_\lambda}(E_A,\rho) = E' \bar{\sigma}_d^{\lambda n_\lambda}(E_A,\rho) \tag{10}$$

Using these dimensionless quantities, the integral in eq. (9) becomes

---

*In eq. (8), ref. 4c, we mistakenly gave a value of 0 for the lower limit of integration. This is true only in the limit $\alpha_{max} \to \pi/2$; otherwise E_A^{min} is a finite non-zero quantity.

$$P_d^{\lambda n_\lambda}(\rho) = \int_{f_A^{min}}^{f_a^{max}} \bar{\sigma}_d^{\lambda n_\lambda}(E_{A,\rho})\, df_A \ . \tag{11}$$

B. Quasi-Classical Method

The details of the calculation of $\bar{\sigma}_d^{\lambda n_\lambda}(E_A)$ by the QCT method have been described elsewhere; we briefly outline them here.[8] The equation for ${}^{c-}\sigma^{\lambda n_\lambda}(E_A)$, where the superscript c indicates classical mechanics, is

$${}^{c-}\sigma_d^{\lambda n_\lambda}(E_A) = \frac{1}{2\pi} \sum_n \frac{1}{|df_A/d\phi_0|} \tag{12}$$

where ϕ_0 is the initial phase of the vibration of the diatomic molecule (in radians) and the summation is over all of the separate regions of the initial phase which lead to dissociation (in which E_A varies smoothly with ϕ_0). The coefficient $(1/2\pi)$ provides for correct normalization of ${}^{c-}\sigma_d^{\lambda n_\lambda}(E_A)$.

C. Potential Energy Surface

The potential energy surface used is of the rotating-Morse-cubic spline type,[9] and has been briefly described previously.[4c] For the mass combination studied ($m_A = m_B = m_C = 1$ in H-atom mass units), asymptotically there are two bound states, with energies of 0.0815 and 0.1885 eV with respect to the bottom of the diatomic molecue well (which is 0.22 eV deep). The Morse parameters[10] of the reagent molecule are $D_e = 0.22$ eV, $\beta = 1.6$ bohr^{-1}, $R_{eq} = 1.40083$ bohr.

D. Numerical Methods

In the hyperspherical coordinate calculations, six even and six odd basis functions were used. This is smaller than the basis set of 10 even and 10 odd functions used previously,[4c] and gave results that are qualitatively correct. Unitarity of the $\underset{=}{S}$ matrix was obtained approximately, with the deviation from unitarity increasing as the dissociation probability increases. Integration was carried out to $\rho = 190$ bohr; asymptotic analyses were carried out at 110, 130, 150, 170, and 190 bohr. As discussed above, at finite ρ, the dissociation probabilities $P_d^{\lambda n_\lambda}$ and the partitioning probabilities $\sigma_d^{\lambda n_\lambda}$ will vary weakly with ρ. The results we present are means of the values at the five different projection distances. We also indicate standard deviations of some of these quantities to provide a feeling as to the magnitude of their ρ dependence.

The quasiclassical trajectory calculations were carried out using standard methods.[11] The integration time step was 5.41×10^{-17} sec. Energy is conserved to four digits in these calculations. Integration of trajectories was begun with the distance $R_{A,BC}$ from the incident atom to the center of mass of the diatomic molecule of 12.0 bohr. Initially 100 trajectories were calculated per energy (and initial state), corresponding to a grid of initial phase of $\pi/50$ radians. Near the boundary between dissociative and either non-reactive or reactive regions of trajectory output the grid was cut down to 0.01 radians. The derivative in eq. (12) was evaluated by fitting a parabola to every group of three points and differentiating analytically; we then interpolated these derivatives by fitting to a cubic spline.

3. Results

We have calculated dissociation probabilities P^D as a function of energy at a number of energies up to 0.25 eV above dissociation when the reagent molecule is in vibrational state V. Values of dissociation probabilities, both quantum and quasi-classical, are given for four energies in Table 1. For the quantum results, we also present the worst unitarities WU (the largest sum of the squares of the elements in a given row or column of the $\underline{\underline{S}}$ matrix). Quantum mechanical results are all the means (indicated by angular brackets) of the five asymptotic analyses described above; standard deviations are given for all quantities (indicated by the letter s). We will focus our attention on the lowest and highest of the energies in Table 1: 0.04 and 0.25 eV, respectively.

Detailed data on the structure of the banding of QCT calculations are given in Table 2, in which we examine the number, width, and properties of the separate regions of the initial phase giving rise to dissociative trajectories. From Table 2 it is clear that there may be more than one region of initial phase leading to dissociation, and that these regions may have minima in their plots of f_A vs. initial phase. As has been shown earlier (and maybe seen from eq. (12)), minima in these plots give rise to divergences in $\sigma_d^{c-\lambda n_\lambda}$.

In considering the quantum results it is useful to have a feel for how the individual terms of the sum in eq. (5) will vary with the indices n and n′. To help establish a feeling for this, we present in Fig. 1 a plot showing the transition probability P^d_{vn} for going from the bound state v of the reagent diatomic molecule to the nth continuum state.

In this calculation $n, n' \leq 8$. These probabilities are obtained from the corresponding $\underset{=}{S}$ matrix elements by the expression

$$P^d_{vn} = |S^d_{vn}|^2 . \tag{13}$$

Hence a larger P^d_{vn} indicates a larger magnitude of S^d_{vn} and thus most likely a larger contribution to the summation in 5. From Fig. 1 we see that P^d_{vn} decreases appreciably (by more than two orders of magnitude) as n increases from 1 to 8, indicating that to first order, the truncation of the sum in eq. 5 should provide reasonable results. Note that in two of the three cases shown, there seems to be a strong preference for dissociation to symmetric continuum states (n = odd).

We next present plots of the quantum mechanical partitioning probabilities $\bar{\sigma}^v_d$ as a function of f_A for $E' = 0.04$ eV and 0.25 eV in Figs. 2 and 3. Because of the simplicity of this symmetric collinear atom-diatomic molecule system, we may replace the superscript λn_λ used previously by v, as that is the only initial quantity which may be varied. Error bars are used to indicate the standard deviations of the calculated partitioning probabilities from their mean. We deleted the portion of the curve nearest to $f_A = \frac{2}{3}$ as here the calculations are unreliable. This is due to the form of the $d\alpha/dE_A$ term in eq. (8):

$$\frac{d\alpha}{dE_A} = -\tfrac{1}{2}\left[E_A(E_A^{\max} - E_A)\right]^{-\frac{1}{2}} \tag{14}$$

When $E_A = E_A^{\max}$ (for this mass combination, when $f_A = \frac{2}{3}$), this factor diverges and the resulting $\bar{\sigma}^v_d$ may be large, as may their deviations.

In Figs. 4-6 we present plots of the classical partitioning probability ${}^{c\text{-}v}\sigma_d$ for three sets of initial conditions: $E' = 0.04$ eV and $v = 0$ and $E' = 0.25$ eV and $v = 0$ and $v = 1$, respectively. Note that the vertical scales are different in all the figures (except Figs. 4 and 5 do have the same vertical scale). In the ensuing discussion section we will discuss the differences in the forms of these curves as well as their differences from the quantum mechanical ones.

4. Discussion and Conclusions

The plots of the quantum mechanical partitioning probabilities $\bar{\sigma}_v^d$ in Figs. 2 and 3 all show the same basic structure. $\bar{\sigma}_v^d$ increases fairly smoothly as f'_A increases from its minimum to its maximum value. There does appear to be some structure in these curves as seen by the existence of shoulders and small maxima. The appearance of the error bars suggests that these wiggles might be real; from the data obtained one would certainly not remove the maximum in the $\bar{\sigma}_1^d$ curve near $f_A = 0.55$ in Fig. 3. It is premature to assign too much significance to these wiggles for two reasons. First, it has been seen in earlier calculations that termination of integration at a small value of ρ leads to spurious oscillations in the $\bar{\sigma}_v^d$ curves, which decrease in magnitude as ρ is increased. Second, the small basis set used in the calculations may lead to errors in the calculated values of $\bar{\sigma}_v^d$. Since the higher basis functions have more oscillations than do the lower ones, their contribution to the summation in eq. (3) may be such that, while its overall magnitude is small, it could affect the fine structure of the curves. We note that in general, the $\bar{\sigma}_0^d$ and $\bar{\sigma}_1^d$ curves have the same overall behavior.

The plots of ${}^{c}\bar{\sigma}_{v}^{d}$ (Figs. 4-6) have a richer structure in that the various curves are all fairly different. In Fig. 4 we see that ${}^{c}\bar{\sigma}_{1}^{d}$ increases fairly smoothly with f_A with the exception of a small dip near 0.52. In Fig. 5 we see that ${}^{c}\bar{\sigma}_{0}^{d}$ increases rapidly with f_A, reaches a maximum, exercises one fairly rapid oscillation and then decreases slowly with f_A. From Table 2 we see that there are two separate regions of initial phase contributing to dissociation; analysis of the contribution from each shows that only a small fraction ($\sim$ 10%) of the area under the curve in Fig. 4 comes from the first (narrow) dissociative region, and its contribution is nearly independent of f_A.

The curve for ${}^{c}\bar{\sigma}_{1}^{d}$ in Fig. 6 at the same total energy differs appreciably from that for ${}^{c}\bar{\sigma}_{0}^{d}$ in Fig. 5. The large spike in Fig. 6 arises because the plot of f_A vs. initial phase has a broad inflection region in which $dE_A/d\phi \sim 0$. Thus, by eq. 12, ${}^{c}\bar{\sigma}_{1}^{d}$ must become large. This is a somewhat unusual occurrence; more normally one finds minima in the plot of E_A vs. ϕ, giving rise to discontinuous jumps in the plot of ${}^{c}\bar{\sigma}_{v}^{d}$. These spikes or discontinuities in ${}^{c}\bar{\sigma}_{v}^{d}$ are purely a consequence of the way in which the classical trajectories behave, in particular the origin of well defined reactivity bands. How the reactivity band structure influences the form of the partitioning probability curves is discussed in detail elsewhere.[8]

Because there is not necessarily any close relationship between the reactivity band structure for collisions involving different reactant vibrational states,[8] the classical partitioning probabilities for different reactant states at the same total energies can have substantially different forms (i.e., have spikes or discontinuities). The quantum mechanical partitioning probabilities appear to be fairly similar for the different reactant states, however. Thus, it may be that classical mechanics, while giving a reasonable feel for the likelihood of dissociation, gives an incorrect feel for the details for the dissociation process. It is quite likely that in higher dimensionality, in which reactivity band structure blurs or disappears altogether,[12] more reasonable behavior might be obtained for classical partitioning probabilities.

In summary then, we feel we have obtained reasonably accurate (although probably not fully converged) probabilities for the partitioning of kinetic energy in collinear atom-diatomic molecule collisions by a quantum mechanical method on a model system. We have compared these results to those obtained by classical mechanics, and shown that while the classical ones may have the same overall behavior as the quantum ones they may have regions in which they behave quite differently.

Acknowledgments

The calculations reported here were performed on the Dreyfus-NSF Theoretical Chemistry Computer which was funded through grants from the Camille and Henry Dreyfus Foundation, the National Science Foundation (Grant No. CHE78-20235) and the Sloan Fund of the California Institute of Technology.

References

1. M. R. Levy, Prog. Reaction Kinetics 10 (1979) 1.
2. J. N. L. Connor, Computer Phys. Commun. 17 (1979) 117; R. B. Walker and J. C. Light, Ann. Rev. Phys. Chem. 31 (1980) 401.
3. D. J. Diestler, in Atom-Molecule Collision Theory, ed. R. B. Bernstein (Plenum Press, New York, 1979) pp. 655-657; P. J. Kuntz, in Atom-Molecule Collision Theory, ed. R. B. Bernstein (Plenum Press, New York, 1979) pp. 669-693.
4. (a) A. Kuppermann, J. A. Kaye, and J. P. Dwyer, Chem. Phys. Lett. 74 (1980) 257; (b) J. A. Kaye and A. Kuppermann, Chem. Phys. Lett. 77 (1981) 573; (c) J. A. Kaye and A. Kuppermann, Chem. Phys. Lett. 78 (1981) 546.
5. G. Hauke, J. Manz, and R. Römelt, J. Chem. Phys. 73 (1980) 5040; J. Römelt, Chem. Phys. Lett. 74 (1980) 263; J. Manz and J. Römelt, Chem. Phys. Lett. 76 (1980) 337; 77 (1981) 172; 81 (1981) 179.
6. J. P. Dwyer, Quantum Mechanical Studies of Molecular Scattering, Ph.D. Thesis, California Institute of Technology (1977).
7. L. M. Delves, Nucl. Phys. 9 (1959) 391; 20 (1960) 275.
8. J. A. Kaye and A. Kuppermann, manuscript in preparation.
9. J. M. Bowman and A. Kuppermann, Chem. Phys. Lett. 34 (1975) 523.
10. H. Eyring, J. Walter, and G. Kimball, Quantum Chemistry (Wiley, New York, 1964), pp. 272,273.

References (continued)

11. R. N. Porter and L. M. Raff, in: Dynamics of Molecular Collisions, Part B, ed. W. H. Miller (Plenum Press, New York, 1976), pp. 1-52; D. G. Truhlar and J. T. Muckerman, in Atom-Molecule Collision Theory, ed. R. B. Bernstein (Plenum Press, New York, 1979), pp. 505-565.

12. K. G. Tan, K. G. Laidler, and J. C. Wright, J. Chem. Phys. 67 (1977) 5883; J. S. Wright, J. Chem. Phys. 69 (1978) 720.

Table 1. Probabilities for Dissociation and Related Quantities

ϵ'/eV	$\langle WU \rangle$	$s(WU)$	$\langle P_0^\Gamma \rangle_{QM}$	$s(\langle P_0^\Gamma \rangle_{QM})$	$\langle P_1^\Gamma \rangle_{QM}$	$s(\langle P_1^\Gamma \rangle_{QM})$	$P_0^\Gamma QCT$	$P_1^\Gamma QCT$
0.04	1.0387	0.0020	0.0088	0.0007	0.1998	0.0016	0	0.107
0.08	1.0251	0.0023	0.0024	0.0004	0.1416	0.0007	0	0.215
0.16	1.0257	0.0012	0.0501	0.0022	0.1261	0.0036	0.137	0.150
0.25	1.0719	0.0029	0.2155	0.0017	0.4284	0.0033	0.268	0.390

Table 2. Detailed Structure of Dissociative Quasi-Classical Trajectory Bands

ϵ'/eV	$P_{0\,QCT}^{D}$	n_0^{D} (a)	$\Delta\phi_{0j}$ (b)	n_{0j}^{min} (c)	$P_{1\,QCT}^{D}$	n_1 (a)	$\Delta\phi_{1j}$ (b)	n_{1j}^{min} (c)
0.04	0.0	-	-	-	0.107	1	0.67	0
0.08	0.0	-	-	-	0.215	2	0.09	0
							1.26	1
0.16	0.137	2	0.77	0	0.150	3	0.20	1
			0.09	0			0.70	0
							0.04	0
0.25	0.277	2	0.15	0	0.39	2	0.05	0
			1.53	0			2.40	

(a) n_v^D is the number of separate regions of initial phase giving rise to dissociative trajectories in collisions of A + BC(v).

(b) $\Delta\phi_{vj}$ is the approximate width in radians of the jth separate region of initial phase giving rise to dissociative trajectories in collisions of A + BC(v) [$\Delta\phi_{vj} = \phi_{vj}^{max} - \phi_{vj}^{min}$, where ϕ_{vj}^{max} and ϕ_{vj}^{min} are the phases at the high and low phase ends of the jth dissociative region].

(c) n_{vj}^{min} is the number of minima in the plot of E_A vs. ϕ in the jth dissociation region for collisions of A + BC(v).

Figure Captions

FIG. 1. Plot of individual bound-continuum transition probabilities P^d_{vn} vs. the index n of the continuum state for three sets of initial collisions. $E' = 0.04$ eV, $v = 1$ (circles, solid line), $E' = 0.25$ eV, $v = 1$ (squares, dashed line); $E' = 0.25$ eV, $v = 0$ (triangles, dotted line). Values plotted are the means of the values obtained from five asymptotic anlyses. Error bars indicate one standard deviation about the mean. Where no error bars are shown, they are sufficiently small that they would be within the plotted symbol (circle, square, or triangle).

FIG. 2. Plot of the dimensionless quantum mechanical partitioning probabilities $\bar{\sigma}^d_v$ as a function of the fraction f_A of the available kinetic energy going to atom A at an energy $E' = 0.04$ eV with respect to three infinitely separated atoms. Curves are shown for both the $v = 1$ (solid line) and $v = 0$ (dashed line) initial states. The values of $\bar{\sigma}^0_d$ have been multiplied by ten before plotting. All values plotted are the means of the values obtained from the five asymptotic analyses; the error bars indicate one standard deviation about the mean. The plot has been cut off just above $f_A = 0.65$ for reasons described in the text.

FIG. 3. Plot of the dimensionless quantum mechanical partitioning probabilities $\bar{\sigma}^d_v$ as a function f_A of the available kinetic energy going to atom A at an energy $E' = 0.25$ eV with respect to three infinitely separated atoms. All markings are as in Fig. 2.

FIG. 4. Plot of the dimensionless classical mechanical partitioning probability σ^{c-d}_v as a function f_A of the available kinetic energy

Figure Captions (continued)

going to atom A at an energy $\mathbf{E}' = 0.04$ eV with respect to three infinitely separated atoms.

FIG. 5. Plot of the dimensionless classical mechanical partitioning probability ${}^{c-d}\sigma_0$ as a function f_A of the available kinetic energy going to atom A at an energy $\mathbf{E}' = 0.25$ eV with respect to three infinitely separated atoms.

FIG. 6. Plot of the dimensionless classical mechanical partitioning probability ${}^{c-d}\sigma_1$ as a function f_A of the available kinetic energy going to atom A at an energy $\mathbf{E}' = 0.25$ eV with respect to three infinitely separated atoms.

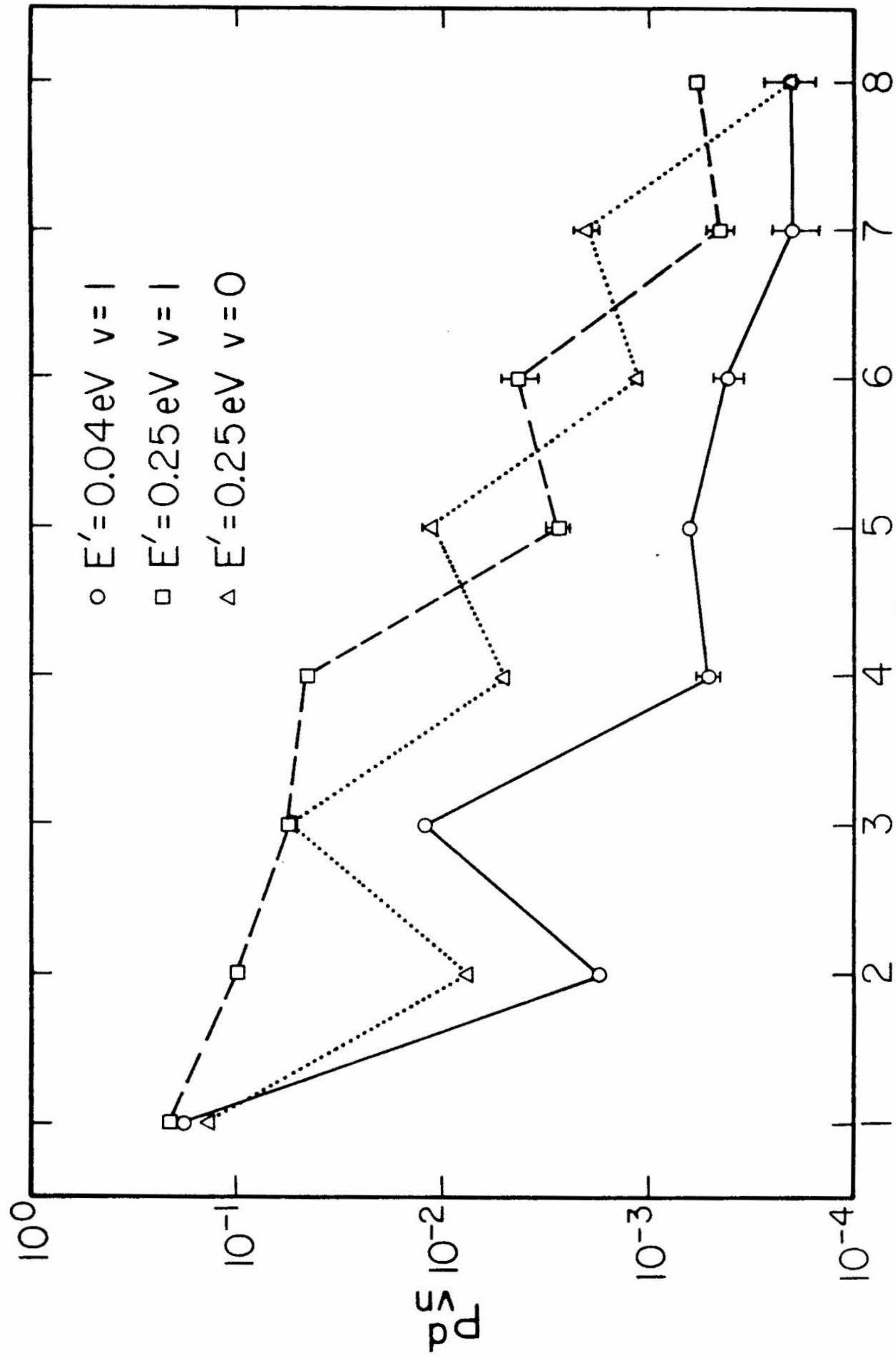
○ E′=0.04eV v=1
□ E′=0.25eV v=1
△ E′=0.25eV v=0
10^{0}
10^{-1}
10^{-2}
10^{-3}
10^{-4}
P^{d}_{vn}
1
2
3
4
5
6
7
8
n

Figure 1

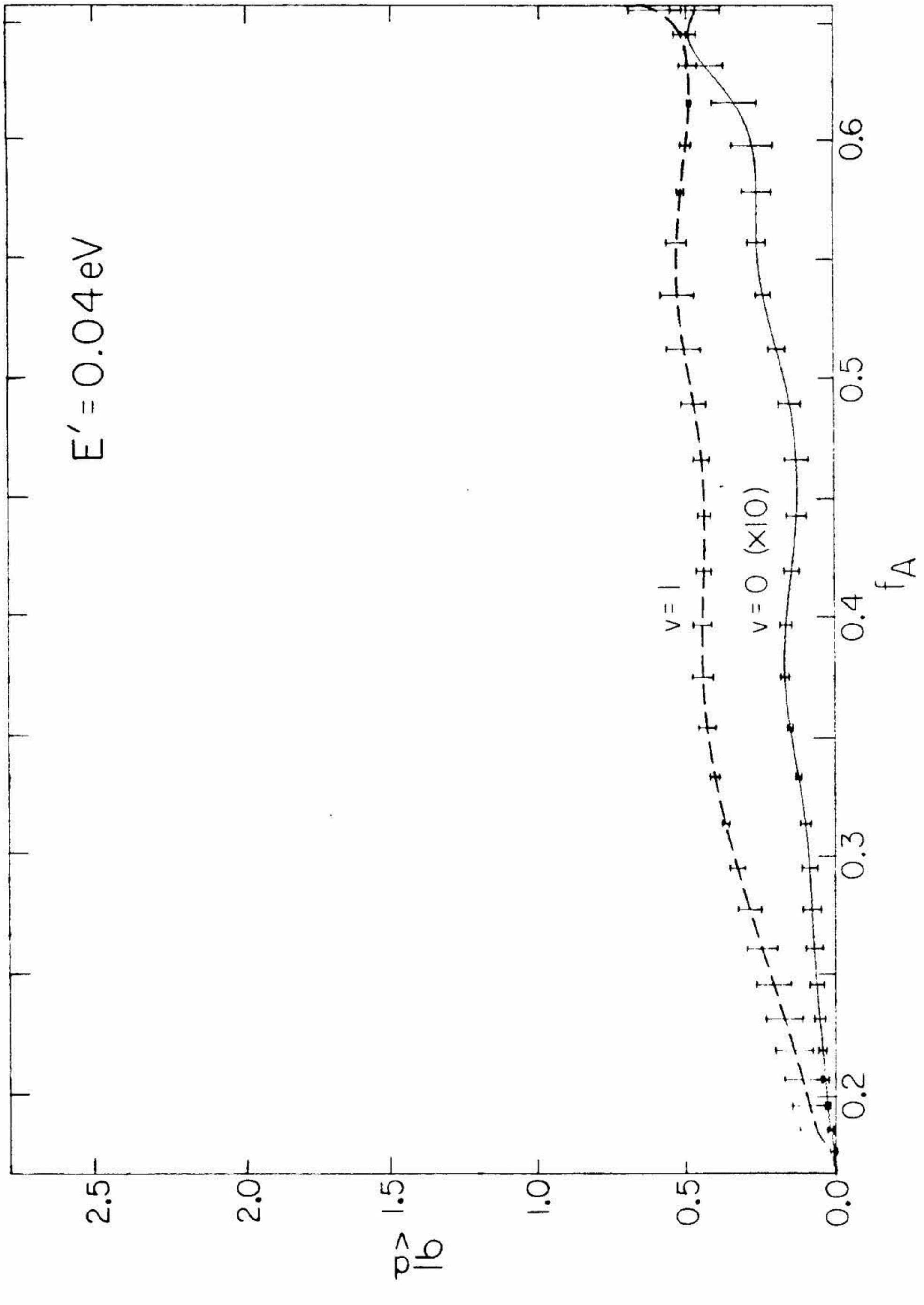

Figure 2

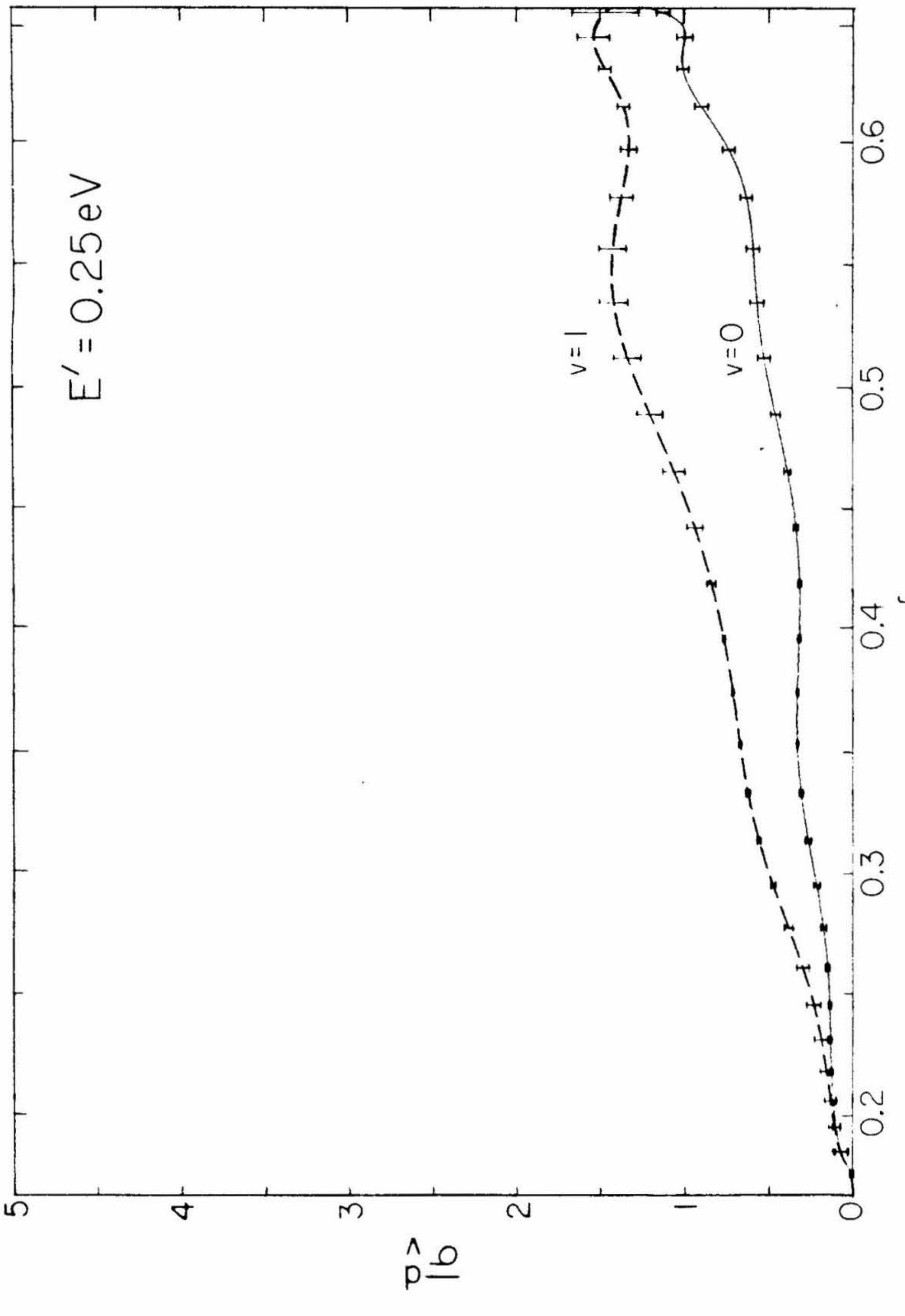

Figure 3

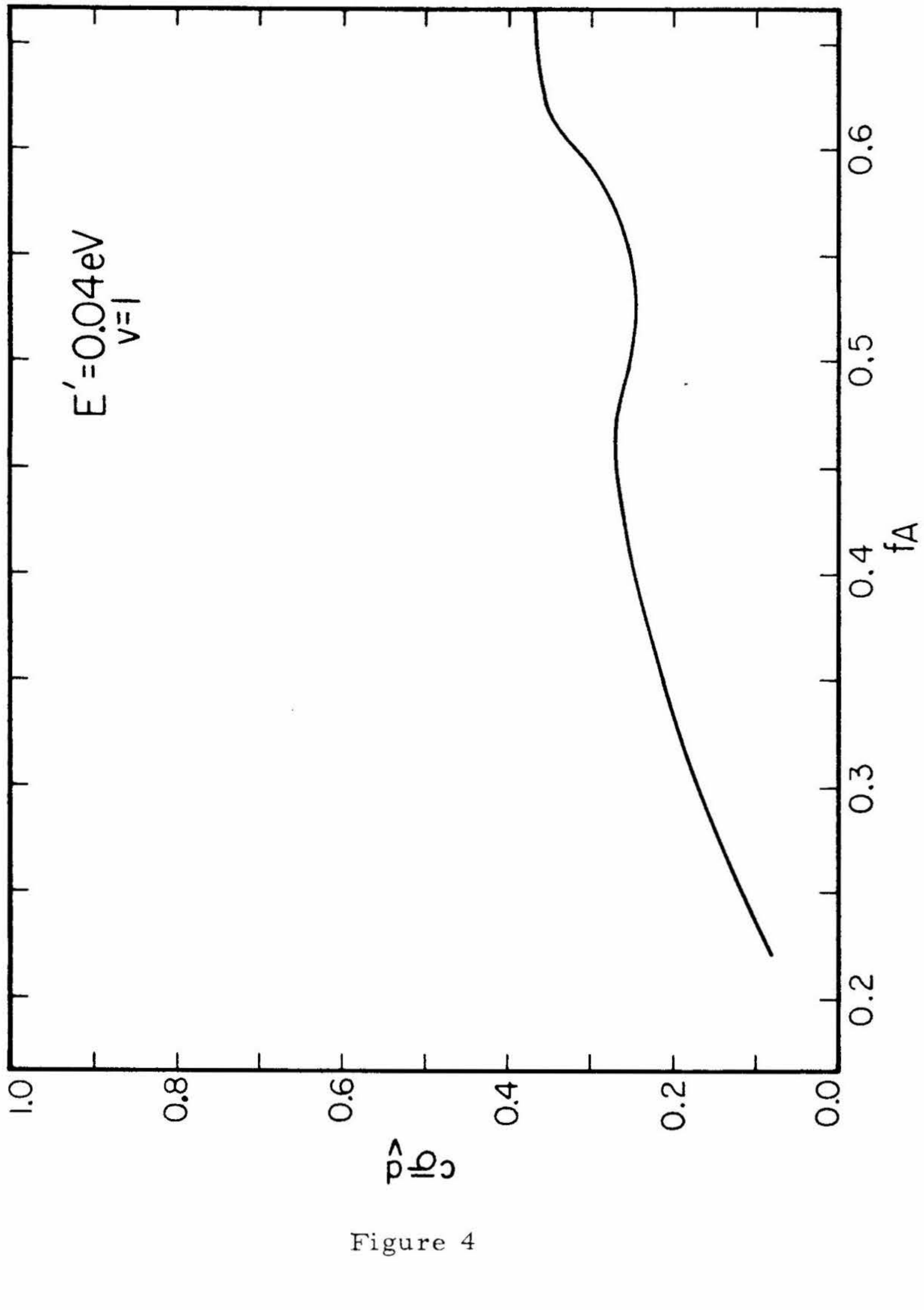
$E' = 0.04\text{eV}$
$v = 1$
f_A
0.2
0.3
0.4
0.5
0.6
$\frac{c\sigma}{\hat{p}}$
0.0
0.2
0.4
0.6
0.8
1.0

Figure 4

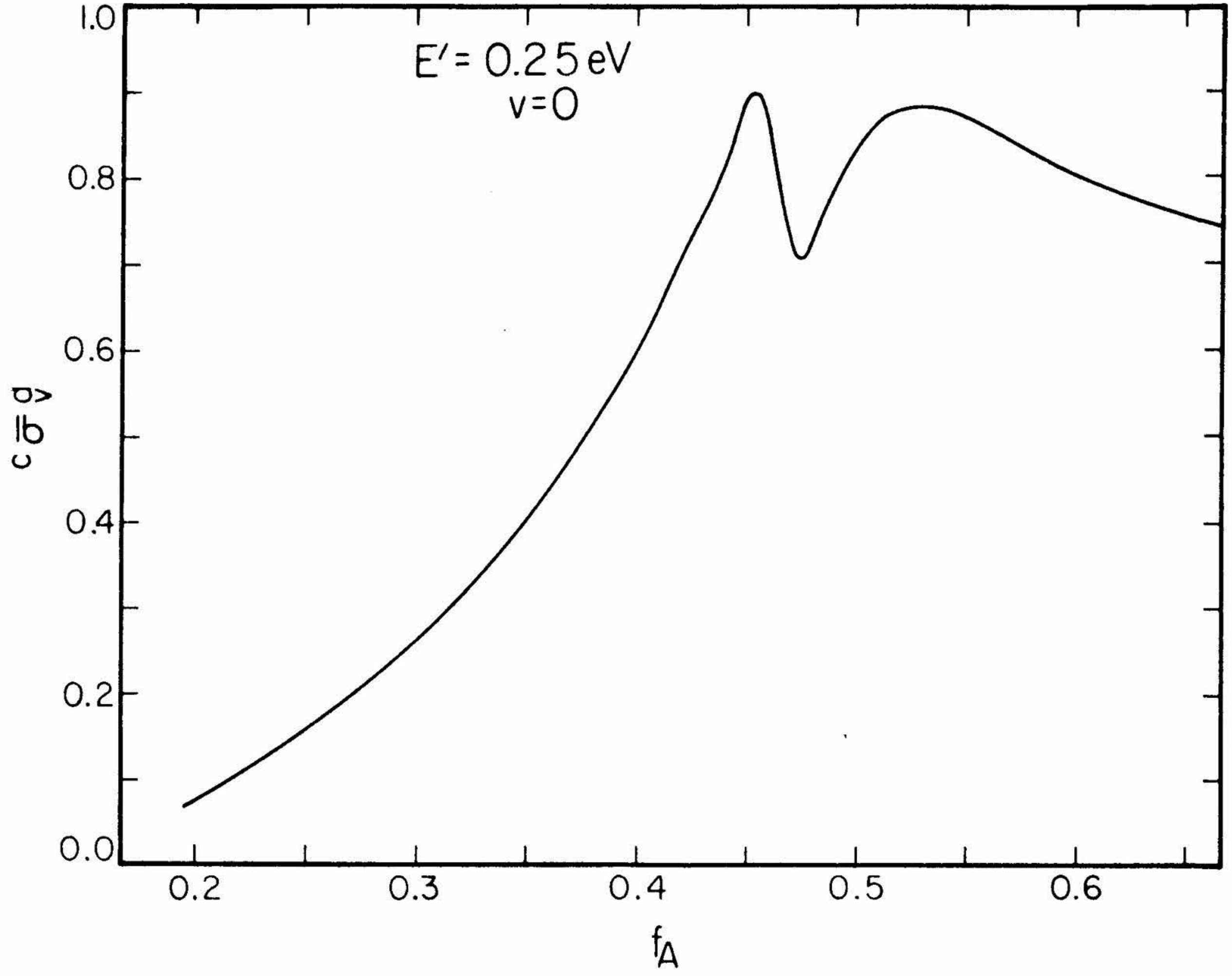

Figure 5

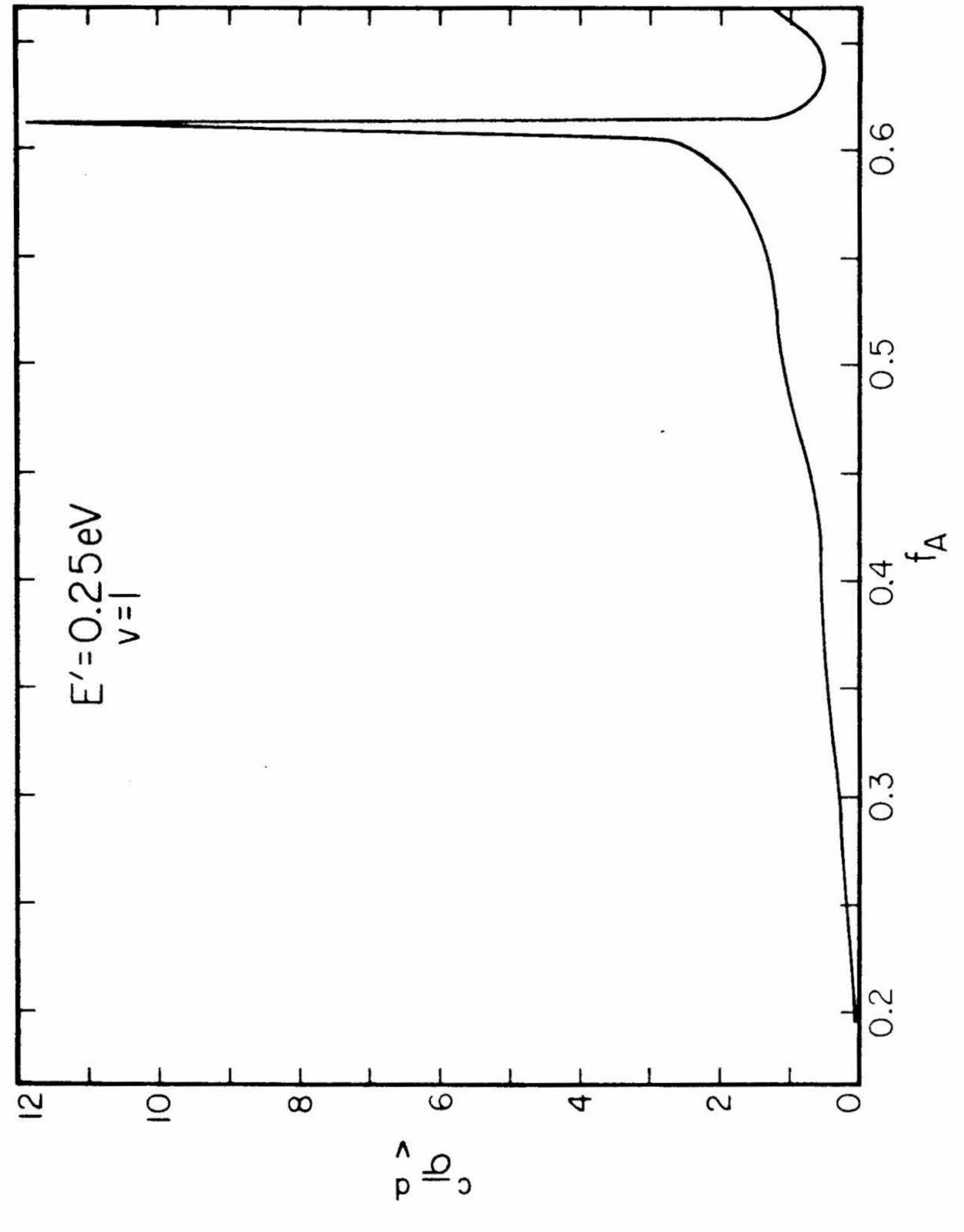

Figure 6

III.7 QUASI-CLASSICAL TRAJECTORY ANALYSIS OF THE EQUIVALENCE OF REACTIVE AND NON-REACTIVE DEACTIVATION IN THE COLLINEAR Cl' + HCl REACTION

QUASI-CLASSICAL TRAJECTORY ANALYSIS OF THE EQUIVALENCE OF REACTIVE AND NONREACTIVE DEACTIVATION IN THE COLLINEAR Cl′+ HCl SYSTEM*

Jack A. KAYE** and Aron KUPPERMANN

Arthur Amos Noyes Laboratory of Chemical Physics,[‡]
California Institute of Technology, Pasadena, California 91125, USA

Received

Near total equivalence of the reactive and nonreactive processes in vibrationally adiabatic collisions $Cl' + HCl(v) \rightarrow Cl' + HCl\ (v' < v)$, $Cl'H\ (v'' < v)$ has been observed in collinear quantum mechanical scattering calculations. Analysis of reactivity bands and individual trajectories in collinear quasi-classical trajectory calculations allows one to simply understand why this should be so.

---

* Research supported in part by the U. S. Air Force Office of Scientific Research (Contract No. F49620-79-C-0187).

** Work performed in partial fulfillment of the requirements for the Ph. D. in Chemistry at the California Institute of Technology.

[‡] Contribution No.

1. Introduction

Quasi-classical trajectory calculations have served an important role in the last 20 years in helping one gain insight into the dynamics of chemical reactions [1]. Information concerning the effect of reagent vibrational, rotational and translational excitation, and the product vibrational and rotational distributions has been obtained. In addition, by looking at trajectories, one is able to get a good physical picture of the collision process itself.

Such trajectory calculations have been particularly useful in the development of simple qualitative models for chemical reactions that allow one to understand how a change in a potential energy surface, isotopic substitution, or reagent excitation will affect the collision process [2]. These simple models and pictures are particularly useful in interpreting the results of quantum mechanical calculations [3], which, by themselves, give good values for reaction probabilities, but do not provide any insight as to how chemical reactions occur [4].

In this paper, we briefly report the results of quantum mechanical calculations on the collinear system

$$\mathrm{Cl'} + \mathrm{HCl}\ (v) \rightarrow \mathrm{Cl'} + \mathrm{HCl}\ (v' < v) \qquad (1a)$$

$$\rightarrow \mathrm{Cl'H}\ (v'' < v) + \mathrm{Cl} \qquad (1b)$$

on two potential energy surfaces. We focus in particular on one seemingly surprising aspect of the dynamics: in vibrationally nonadiabatic collisions, the probabilities, and thus the rates, of the nonreactive (1a) and reactive (1b) processes are almost equal, although this is not true for vibrationally adiabatic collisions. We show that this result is obtained approximately in collinear quasi-classical trajectory calculations, and that by analysis of reactivity bands and individual trajectories we can understand why this should be so.

In Section 2 we briefly describe the method of calculation and the potential energy surfaces used. In Section 3 we present the results of the quantum mechanical and quasi-classical trajectory calculations. In Section 4 we discuss and interpret the results obtained.

2. Computational Methods and Potential Energy Surfaces

The quantum mechanical calculations on reactions (1) were performed using the method of hyperspherical coordinates [5, 6]. This method allows one to treat heavy-light-heavy mass combinations without difficulty, in spite of the small skew angle (13.59°) between the two arrangement channels in Delves mass-weighted coordinate system [7]. This technique has previously been used by two different groups to study the reaction [5b, 6e]

$$I' + HI \rightarrow I'H + I \tag{2}$$

and similar results have been obtained, giving one substantial faith in its applicability to these mass combinations.

In the calculations reported here, eight even and eight odd basis functions were used at lower energies and 12 even and 12 odd at higher energies. Convergence of the transition probabilities (estimated by varying the basis set and integration stopping point) to ± 0.001 and flux to ± 0.0002 was obtained at nearly all energies. The highest energy for which calculations were performed was 1.24 eV above that of HCl ($v = 0$). Standard methods were used for the collinear quasi-classical trajectory calculations [1]. Trajectories were started with the distance from the Cl′ atom to the HCl center of mass, $R_{Cl', HCl}$ at 12 bohr, and were terminated when either distance, $R_{Cl', HCl}$ or $R_{Cl, HCl'}$, was more than 12 bohr.

Two different LEPS [8] surfaces were used. The molecular parameters for HCl and Cl_2 were those of Connor *et al.* [9]. Two values of the Sato parameter were chosen (0.138 for surface A; 0.185 for surface B). These correspond to surfaces (i) and (ii) of Smith [10], and have barrier heights of 6.21 and 1.89 kcal/mole, respectively. Parameters and properties of the potential energy surfaces are shown in table 1. The higher barrier height corresponds roughly to the experimental activation energy [11] and also to the upper limit to the barrier as predicted in ab initio calculations [12]; the lower barrier height is close to the predicted lower limit [12], and was found by Smith to lead to better agreement between quasi-classical trajectory calculations [10] and experiment [13] for the deactivation process

$$\mathrm{Cl} + \mathrm{H(D)Cl}\ (v = 1) \rightarrow \mathrm{Cl} + \mathrm{H(D)Cl}\ (v = 0). \qquad (3)$$

It is expected, then, that the actual barrier height is somewhere within these two limits. The potential surface is plotted in Delves [7] mass-weighted coordinates in figs. 4 and 5, where selected trajectories are plotted.

3. Results

In fig. 1, we present a plot of the probability versus energy curves for vibrationally nonadiabatic, nonreactive processes, defined as process (1a), with $v = 2$ and $v' = 0$ and 1 (P^V_{20} and P^V_{21}, respectively), and the corresponding reactive processes P^R_{20} and P^R_{21} for calculations on surface B. State-to-state rate constants are calculated from the reaction probability versus energy curves, and these are plotted in the form of Arrhenius plots for the four transitions in fig. 2. While the shape of the probability versus energy curves and rate constant curves are different on surface A, two of the most striking features are seen there also: the near equality of the corresponding reactive and nonreactive probabilities and rates, and also the dominance of single-quantum deactivating transitions. Hence, since the features of the dynamics of interest here are common to both surfaces, we will restrict further study to surface B.

The results of the quasi-classical trajectory calculations are presented in fig. 3 for a series of translational energies (energy above the $v = 2$ level). In the figure the final action of the diatomic product (HCl or HCl′) is plotted versus the initial vibrational phase of the HCl reagent. The reactive or nonreactive nature of the collision is also indicated. In addition, the duration of the trajectory is plotted.

One can clearly see that the trajectories giving rise to vibrationally nonadiabatic trajectories are localized in the two regions at the boundary between the reactive and nonreactive bands. As the energy decreases, the boundary region between the bands becomes diffuse, much more so for the activating transitions than the deactivating ones.

At the lowest energies, where quantum mechanically nc vibrational excitation is possible, the actions versus phase curve appears to be a collection of random points. The near symmetry of the reactive and nonreactive bands about a vertical line drawn through the center of the gap between the bands shows that one could expect nearly equal amounts of reactive and nonreactive products for vibrational deactivation, in agreement with the quantum mechanical results.

The funnel-shaped nature of the action versus phase curves near the boundary between the bands demonstrates the classical nature of the preference for single-quantum deactivations. Multiple quantum deactivations can only occur for a very small range of phases about the center of the gap. One can also see that the time for completion of the trajectory has a minimum at the deactivation gap (due no doubt to the fast nature of the exit process when all energy has been converted to translational energy) and a maximum at the activation gap. The fact that the trajectory time increases much more rapidly for activating collisions than it decreases for deactivating ones, especially at lower energies, suggests that for classically activating collisions the slowness is not a purely kinetic energy effect; the trajectories giving rise to vibrational excitation must be significantly more complex than those leading to relaxation.

4. Discussion and Conclusions

The increase in trajectory time and in the vibrational action of the diatomic product across a gap in the reactivity bands has been observed before by various workers in collisions of ground vibrational state molecules [14, 15]. Attention has seldom been directed to these phenomena in collisions of vibrationally excited molecules, however [16]. Nevertheless, the theory and intuition developed for the ground state case appears to carry over with some modification to the vibrationally excited state case considered here [14].

Pechukas and Pollak [17] have shown that the sharp increase of the final action and trajectory time versus phase plots across the band gaps is due to the existence of "trapped trajectories" that occur when the initial phase is quite close to that of the center of the gap. They have identified three different kinds of trapped trajectories [17], most importantly the first kind, in which the mass point vibrates forever between the two contours whose energy is that of the total energy present, and the second kind, in which the mass point vibrates in a way such that it touches only one of the energetically limiting trajectories. It is clear that motion along the symmetric stretch line would constitute a trapped trajectory of the first kind.

Our goal, then, is to determine what kind of trajectory, which must not be terribly different from a trapped trajectory, gives rise to vibrational deactivation. This trajectory must have the property that it causes the mass particle to "forget" from which arrangement channel it entered if there are to be equal reactive and nonreactive probabilities.

Since the trajectory time associated with vibrational deactivation is short, this trajectory cannot have that of an especially long-lived complex (one spending a far greater time in the saddle point region of the potential energy surface than a nearby less nonadiabatic trajectory). Examination of a number of trajectories shows that the limiting trapped trajectory for vibrational deexcitation is motion along the symmetric stretch line. In vibrationally deactivating collisions at some time the mass particle, the motion of which in Delves coordinates is equivalent to that of the actual system [the single particle of mass $m_{Cl}m_H^{\frac{1}{2}} \cdot (2m_{Cl} + m_H)^{-\frac{1}{2}}$], lies along the symmetric stretch line beyond the saddle point, and has its velocity directed along the line towards the saddle point, $(R_{Cl'-H} = R_{H+Cl} = R^{\ddagger})$. At that time, the trajectory obeys the equations

$$R_{Cl'-H} \approx R_{H-Cl} > R^{\ddagger} \tag{4a}$$

$$\frac{dR_{Cl'-H}}{dt} \approx \frac{dR_{H-Cl}}{dt} < 0 \, . \tag{4b}$$

A fairly typical trajectory resulting in substantial vibrational deactivation is shown in fig. 4a. Since this trajectory involves motion essentially along the symmetric stretch line, it means that to a good approximation, the mass particle has forgotten its channel of origin. That this type of trajectory leads to conversion of vibrational energy to translational energy has been observed by Wright et al. [15] in their study of the H + H_2 reaction. This effect is not observed in adiabatic reactions. A typical vibrationally adiabatic trajectory is shown in fig. 4b.

Examination of trajectories shows that trajectories leading to vibrational activation are in some ways the reverse of those leading to vibrational deactivation. Early on the trajectory first undergoes near-periodic motion near the saddle point (similar to a trapped trajectory of the second kind). At some time later the mass particle climbs the symmetric stretch line beyond the saddle point with its velocity directed towards dissociation. At lower energies, especially below the quantum mechanical energetic threshold for activation, the trajectory may then become highly complicated, undergoing near-periodic motion characteristic of motions of trapped trajectories of the first kind. For these trajectories roughly equal amounts of reactive and nonreactive products should be obtained. A typical trajectory resulting in vibrational excitation at high energy is shown in fig. 4c.

Three-dimensional trajectories have been calculated for the Cl + HCl system by a number of workers [10, 19]. The calculations show competitive rates for reactive and nonreactive deactivations. The uncertainty associated with the assignment of final quantum numbers in quasi-classical trajectory calculations makes a detailed comparison of the state-to-state deactivation rates difficult. The trajectory calculations all indicate that in three dimensions, the dominant pathway for vibrational relaxation is V → R energy transfer [10, 19], rather than V → T, as is necessarily the case in collinear collisions.

The fact that the same equality of reactive and nonreactive deactivation rates was obtained on the two potential energy surfaces suggests that this effect is not immensely dependent on the surface used (for a sufficiently high barrier, of course, the reactive probabilities will go to zero at low energies). As this near-equality is not obtained for the $H + H_2$ reaction (although as the reagent vibrational state increases, the reactive and nonreactive deactivation rates do approach one another [20]), it seems reasonable that this equality is a mass effect, arising from the small skew angle. We hope to document this in the future.

In a future publication, we will fully discuss the results of classical and quantum calculations on these systems [21].

Acknowledgements

The calculations reported here were performed on the Dreyfus-NSF Theoretical Chemistry Computer (VAX 11/780) which was funded through grants from the Camille and Henry Dreyfus Foundation, the National Science Foundation (Grant No. CHE78-20235), and the Sloan Fund of the California Institute of Technology, and on the IBM 370/158 computer of Ambassador College, Pasadena, California, for which we express our appreciation.

References

[1] R. N. Porter and L. M. Raff, in: Dynamics of Molecular Collisions, Part B, ed. W. H. Miller (Plenum Press, New York, 1976) pp. 1-52; D. G. Truhlar and J. T. Muckerman, in: Atom-Molecule Collision Theory, ed. R. B. Bernstein (Plenum Press, New York, 1979) pp. 505-565.

[2] J. C. Polanyi and J. L. Schreiber, in: Physical Chemistry, An Advanced Treatise, Vol. VIA, ed. W. Jost (Academic Press, New York, 1974), Chap. 6; P. J. Kuntz, in: Dynamics of Molecular Collisions, Part B, ed. W. H. Miller (Plenum Press, New York, 1976) pp. 53-120.

[3] A. Kuppermann, in: Theoretical Chemistry: Advances and Perspectives, Vol. 6A, ed. D. Henderson (Academic Press, New York, 1981) pp. 79-164.

[4] Some information concerning how the reaction takes place may be obtained by looking at probability densities and streamlines of probability current density that can be calculated from the wavefunctions in quantum mechanical scattering calculations. See, for example, E. A. McCullough, Jr., and R. E. Wyatt, J. Chem. Phys. 54 (1971) 3578; A. Kuppermann, J. T. Adams, and D. G. Truhlar, in: Electronic and Atomic Collisions, Abstracts of Papers of the 8th International Conference on the Physics of Electronic and Atomic Collisions, Belgrade, Yugoslavia, eds. B. C. Cǒbić and M. V. Kurepa (Institute of Physics, Belgrade, 1973) p. 229; S. L. Latham, J. F. McNutt, R. E. Wyatt, and M. J. Redmon, J. Chem. Phys. 69 (1978) 3740; J. F. McNutt

and R. E. Wyatt, in: Potential Energy Surfaces and Dynamics Calculations, ed. D. G. Truhlar (Plenum Press, New York, 1981) pp. 495-517.

[5] (a) A. Kuppermann, J. A. Kaye, and J. P. Dwyer, Chem. Phys. Letters 75 (1980) 257;

(b) J. A. Kaye and A. Kuppermann, ibid. 77 (1981) 573.

(c) J. A. Kaye and A. Kuppermann, ibid. 78 (1981) 546.

[6] (a) G. Hauke, J. Manz, and J. Römelt, J. Chem. Phys. 73 (1980) 5040.

(b) J. Römelt, Chem. Phys. Letters 74 (1980) 263.

(c) J. Manz and J. Römelt, ibid. 76 (1980) 333.

(d) J. Manz and J. Römelt, ibid. 77 (1981) 172.

(e) J. Manz and J. Römelt, ibid. 81 (1981) 179.

[7] L. M. Delves, Nucl. Phys. 9 (1959) 391; 20 (1960) 275.

[8] S. Sato, J. Chem. Phys. 23 (1955) 592, 2465.

[9] J. N. L. Connor, W. Jakubetz, J. Manz, and J. C. Whitehead, J. Chem. Phys. 72 (1980) 6209.

[10] I. W. M. Smith, J. Chem. Soc. Faraday Trans. II 71 (1975) 1970.

[11] F. S. Klein, A. Persky, and R. E. Weston, J. Chem. Phys. 41 (1964) 1799; F. S. Klein and A. Persky, ibid. 59 (1973) 2775.

[12] P. Botschwina and W. Meyer, Chem. Phys. Letters 44 (1976) 449.

[13] R. D. H. Brown, G. P. Glass, and I. W. M. Smith, J. Chem. Soc. Faraday Trans II 71 (1975) 1963. See also M. Kneba and J. Wolfram, J. Phys. Chem. 83 (1979) 69 and R. G. MacDonald

and C. B. Moore, J. Chem. Phys. 73 (1980) 1681, and references therein.

[14] F. T. Wall, L. A. Hiller, Jr., and J. Mazur, J. Chem. Phys. 29 (1958) 255; J. W. Duff and D. G. Truhlar, Chem. Phys. 4 (1974) 1; Chem. Phys. Letters 40 (1976) 251; J. R. Stine and R. A. Marcus, ibid. 29 (1974) 575; R. E. Howard, A. C. Yates, and W. A. Lester, Jr., J. Chem. Phys. 66 (1977) 1960; J. S. Hutchinson and R. E. Wyatt, ibid. 70 (1979) 3509.

[15] (a) J. S. Wright, G. Tan, K. J. Laidler, and J. E. Hulse, Chem. Phys. Letters 30 (1975) 200.

(b) J. S. Wright, K. G. Tan, and K. J. Laidler, J. Chem. Phys. 64 (1976) 970.

(c) J. S. Wright and K. G. Tan, ibid. 66 (1977) 104.

(d) K. G. Tan, K. J. Laidler, and J. S. Wright, ibid. 67 (1977) 5883.

[16] N. Sathyamurthy, Chem. Phys. Letters 59 (1978) 95; M. S. Child and K. B. Whaley, Disc. Faraday Soc. 67 (1979) 57; J. C. Gray, G. A. Fraser, and D. G. Truhlar, Chem. Phys. Letters 68 (1979) 359.

[17] P. Pechukas and E. Pollak, J. Chem. Phys. 67 (1977) 5976.

[18] E. Pollak and P. Pechukas, J. Chem. Phys. 69 (1978) 1218.

[19] D. L. Thompson, J. Chem. Phys. 56 (1972) 3570; R. L. Wilkins, ibid. 63 (1975) 534.

[20] J. A. Kaye and A. Kuppermann, unpublished results.

[21] J. A. Kaye and A. Kuppermann, manuscript in preparation.

Table 1

Parameters and properties of LEPS potential energy surfaces A and B. [a)]

		HCl	Cl_2
β/bohr^{-1}		0.9892	1.0626
R_e/bohr		2.4060	3.7791
D_e/eV		4.6258	2.5169
Δ	A	0.138	
	B	0.185	
saddle point location/bohr			
A		(1.459, 1.459)	
B		(1.443, 1.443)	
barrier height/(kcal/mole)			
A		6.21	
B		1.89	
HCl zero point energy/eV			
A		0.1838	
B		0.1836	

---

a) Masses used: $m_{Cl} = 34.6974\ m_H$.

Figure Captions

Figure 1. Cubic spline fit to quantum mechanical probabilities of state-to-state transitions versus reagent translational energy for vibrational deactivation in collinear collisions of Cl + HCl (v = 2): P_{20}^{V} (solid line), P_{21}^{V} (dashed line), P_{20}^{R} (dotted line), and P_{21}^{R} (dashed-dotted line). Note expanded vertical scale (full scale corresponds to probability of 0.04).

Figure 2. Arrhenius plots of state-to-state rate constants for vibrational activation in collinear collisions of Cl + HCl (v = 2). The rate constants were calculated from the quantum mechanical transition probabilities. The lines represent the same transitions as in fig. 1; markers represent the points calculated. k_{20}^{V} (○), k_{21}^{V} (Δ), h_{20}^{R} (+), k_{21}^{R} (x).

Figure 3. Plots of final vibrational action (left ordinate) versus initial phase of reagent HCl (v = 2) in collinear collisions of Cl + HCl (v = 2). In the region in which the curves are smooth, a solid line represents reactive collisions and a dashed line represents nonreactive collisions. In the non-smooth regions, open circles are used to indicate reactive collisions and open squares to indicate nonreactive collisions. The time of the trajectory (the time scale is on the right ordinate) is shown by a dotted line in its smooth region and by closed circles elsewhere. Curves are for translational energies of 0.5 eV (top), 0.3 eV (middle), and 0.1 eV (bottom).

Figure 4. Plots of typical trajectories (dashed-dotted line) superimposed on a contour plot of the potential energy surface (surface B) in Delves mass-weighted coordinate system. Contours are drawn every 0.4 eV from 0.2 to 3.0 eV, measured with respect to the bottom of the

HCl well. An x is drawn at the saddle point. The trajectories were started at R = 24.75 bohr in the entrance channel (at the lower right) and terminated in the exit channel (upper right), well past the limits of the plot. Trajectories shown are for a translational energy of 0.3 eV. (a) Vibrationally adiabatic trajectory-initial phase = 0.50 radians, final action = 1.981; (b) vibrational deactivating trajectory-initial phase = 2.9293 radians, final action = -0.115; (c) vibrationally activating trajectory-initial phase = 4.09 radians, final action = 2.821.

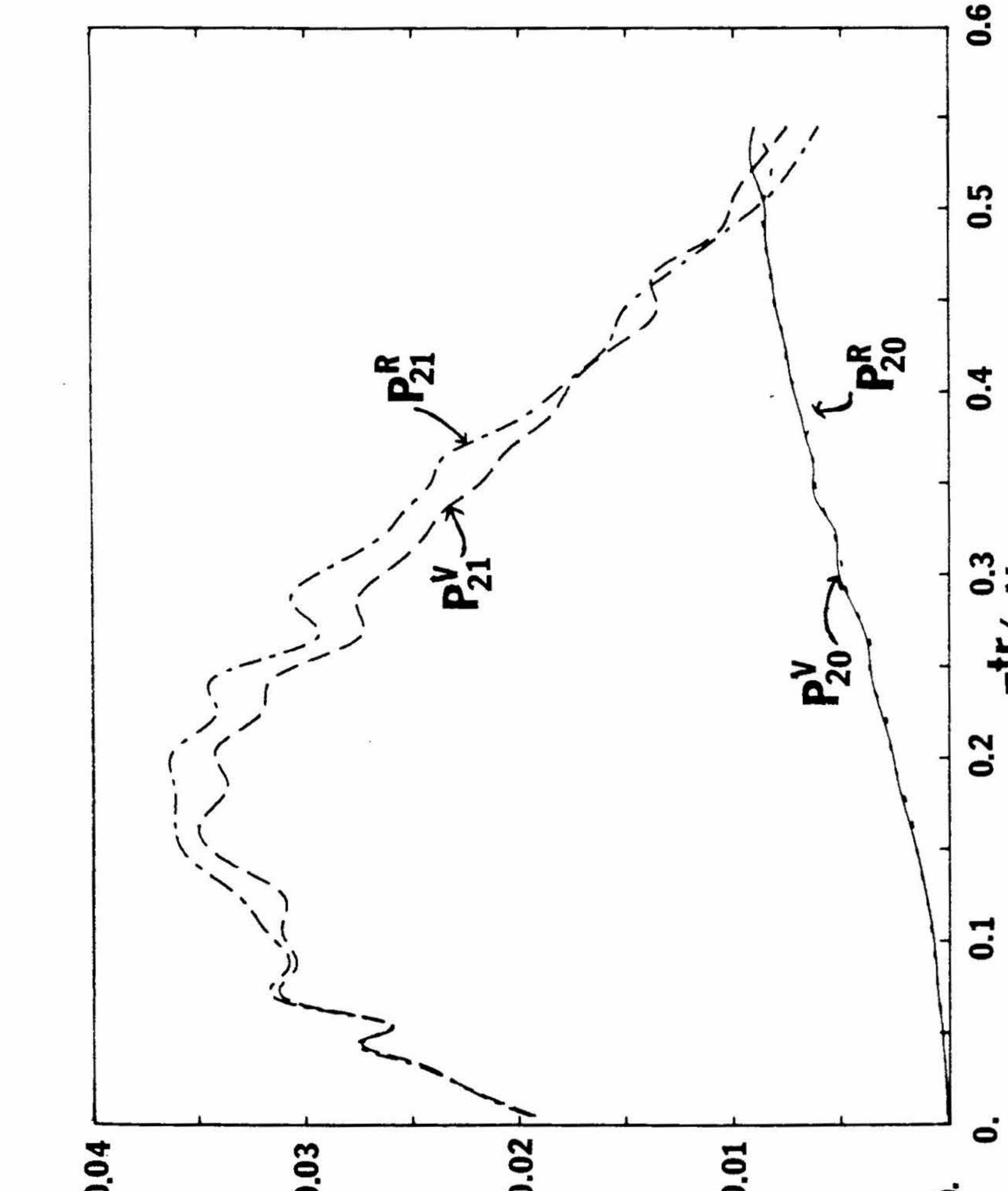
Probability
0.04
0.03
0.02
0.01
0.
0.
0.1
0.2
0.3
0.4
0.5
0.6
E^{tr}/eV
P^R_{21}
P^V_{21}
P^V_{20}
P^R_{20}

Figure 1

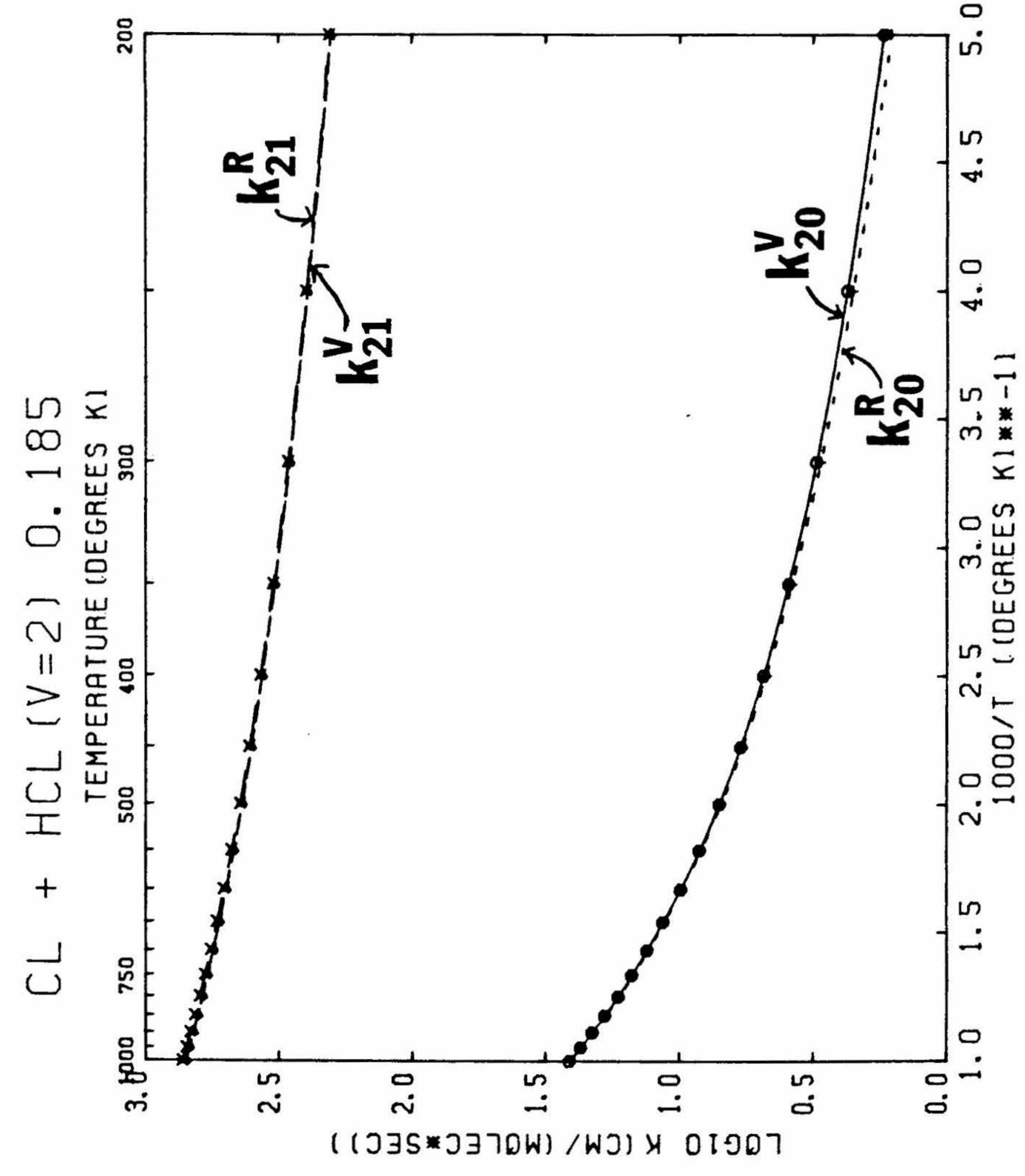
CL + HCL (V=2) 0.185
TEMPERATURE (DEGREES K)
1000
750
500
400
300
200
LOG10 K (CM/(MOLEC*SEC))
3.0
2.5
2.0
1.5
1.0
0.5
0.0
1000/T ((DEGREES K)**-1)
1.0
1.5
2.0
2.5
3.0
3.5
4.0
4.5
5.0
k^R_{21}
k^V_{21}
k^V_{20}
k^R_{20}

Figure 2

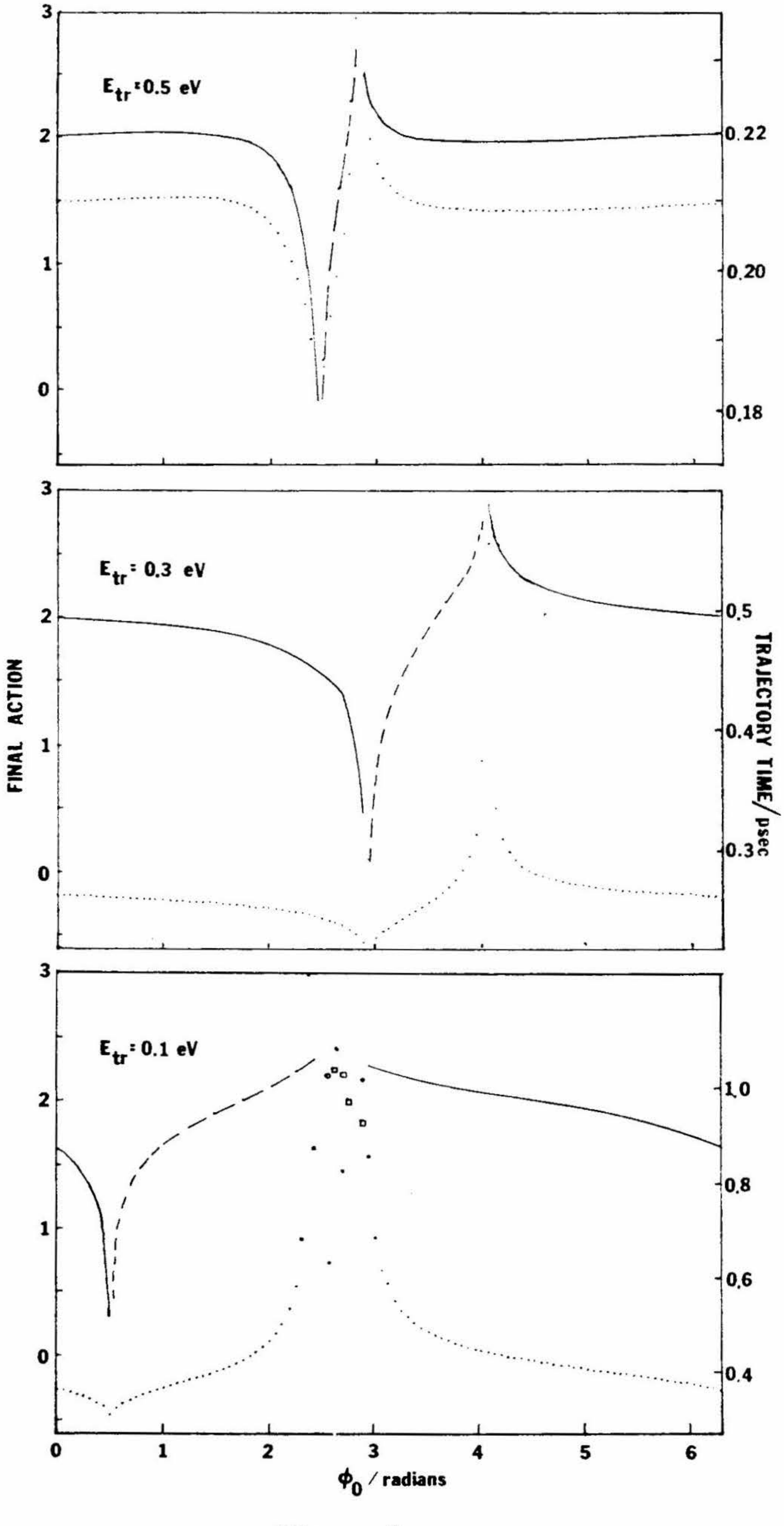
Etr = 0.5 eV
Etr = 0.3 eV
Etr = 0.1 eV
FINAL ACTION
TRAJECTORY TIME/psec
φ0 / radians
3
2
1
0
0.22
0.20
0.18
0.5
0.4
0.3
1.0
0.8
0.6
0.4
0
1
2
3
4
5
6

Figure 3

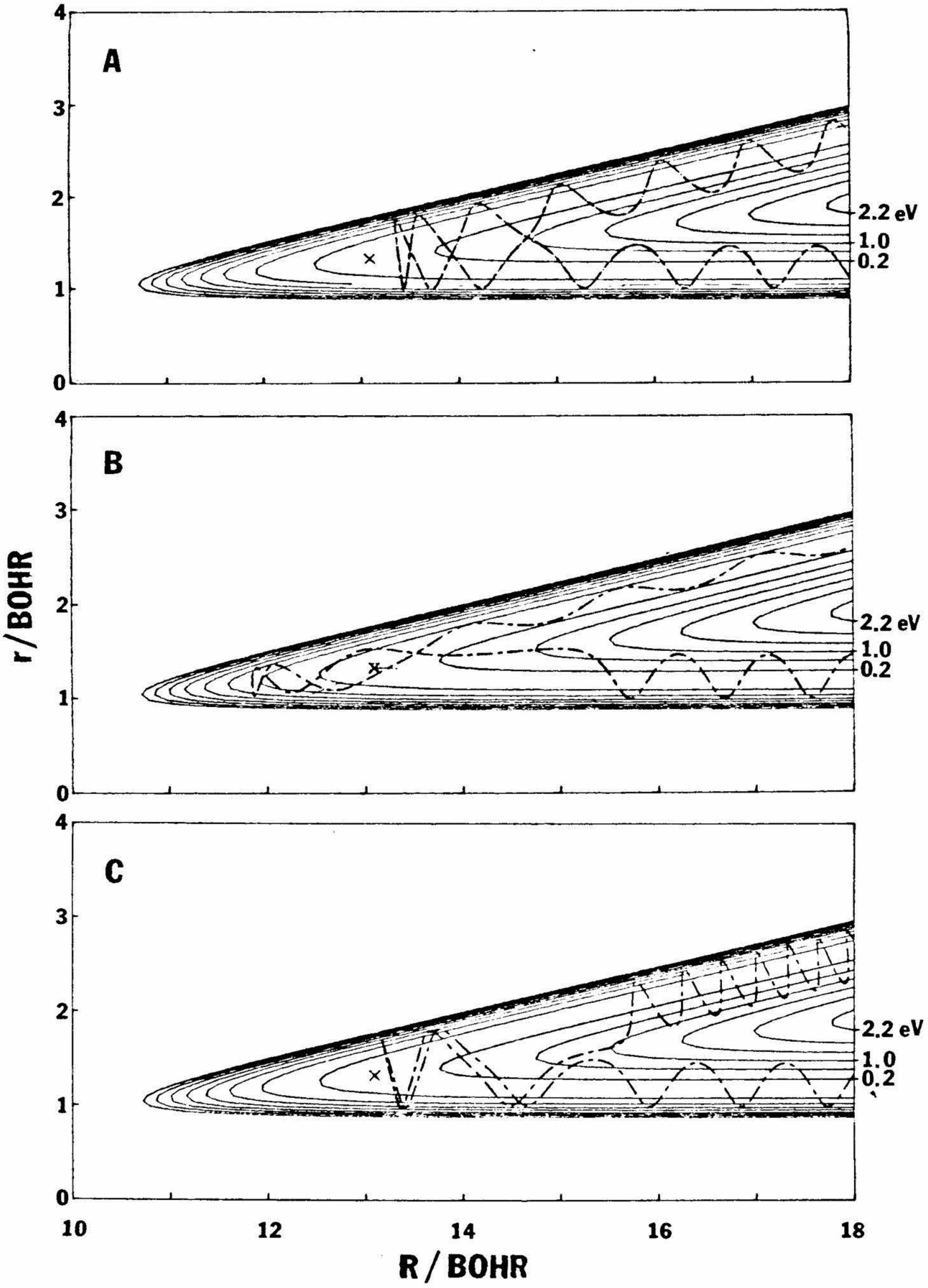

Figure 4

III.8 COLLINEAR QUANTUM MECHANICAL PROBABILITIES AND RATE CONSTANTS FOR THE Br + HCl(v=2, 3, 4) REACTION USING HYPERSPHERICAL COORDINATES

COLLINEAR QUANTUM MECHANICAL PROBABILITIES AND RATE CONSTANTS FOR THE Br + HCl(v=2, 3, 4) REACTION USING HYPERSPHERICAL COORDINATES[*]

Jack A. KAYE[**] and Aron KUPPERMANN
Arthur Amos Noyes Laboratory of Chemical Physics[‡]
California Institute of Technology
Pasadena, California 91125 USA

Received (   )

Calculations of quantum mechanical probabilities and rate constants for the collinear reaction Br + HCl(v=2, 3, 4) $\rightarrow$ BrH + Cl, Br + HCl($v' < v$) were performed using hyperspherical coordinates. Removal of vibrationally excited HCl proceeds mainly by reaction to a nearly degenerate HBr state. Collisions displaying a large change in the internal energy of the reactant occur with low probabilities.

---

[*] Research supported in part by the US Air Force Office of Scientific Research (Contract No. F49620-79-C-0187)

[**] Work performed in partial fultilment of the requirements for the Ph.D. in Chemistry at the California Institute of Technology

[‡] Contribution No.

I. INTRODUCTION

Reactions of halogen atoms (X) with hydrogen halides (HY) of the type

$$X + HY \longrightarrow XH + Y \tag{1}$$

have been the subject of a great deal of experimental and theoretical work (1). Exothermic reactions of this type produce inverted population distributions of vibrational levels (2) and can thus be used as the pumping step in chemical lasers (3). The fairly small energy difference between the ground ($^2P_{3/2}$) and first excited ($^2P_{1/2}$) state of the halogen atom allows one to look at the possibility of electronically non-adiabatic processes (4). Endoergic reactions of this type are known to be greatly accelerated by vibrational excitation of the hydrogen halide reagent (5).

Theoretical treatments of these reactions are more difficult, however. Not only must one have an accurate potential energy surface in order to perform reliable scattering calculations, but one must also consider the possibility of multiple-surface collisions. Single-surface quasi-classical trajectory calculations on these systems have usually been able to match experimental product state distributions, but have not had much success in duplicating other experimental results (isotope effects, temperature dependence, rate constants) (6).

Quantum mechanical treatments of these reactions have been limited, because the traditional methods of attacking collinear atom-diatomic molecule collisions (7, 8) are not well suited to collisions in which a light atom is transferred between two heavy ones. This difficulty has recently been overcome by the development of the collinear hyperspherical coordinates technique (9, 10), which allows one to perform reactive scattering calculations efficiently for heavy-light-heavy (H-L-H) systems. Studies of systems of this type using this method have previously been limited to exchange reactions of identical atoms (symmetric systems), such as (9b, 10e)

$$I' + HI \longrightarrow I'H + I \quad (2)$$

In this work we report the results of calculations on the asymmetric system Br + HCl for the processes

$$Br + HCl(v=2,3,4) \longrightarrow BrH(v') + Cl \quad (3a)$$

$$\longrightarrow Br + HCl(v' < v) \quad (3b)$$

These processes (5, 11) and the reverse reaction (12)

$$Cl + HBr \longrightarrow ClH + Br \quad (4)$$

have been studied experimentally and in three dimensional quasi-classical trajectory calculations (5, 13). A preliminary account of a collinear quantum mechanical calculation on reaction 4 has been reported previously (14).

In section 2 we briefly discuss the application of the hyperspherical coordinate method to asymmetric systems and the surface used. In section 3 we present and discuss the results, and in section 4 we summarize the results and conclusions.

II. COMPUTATIONAL METHOD AND POTENTIAL ENERGY SURFACE

We have discussed our hyperspherical coordinate method for symmetric systems previously (9), and the modification of the method for asymmetric systems is straightforward. The basic idea of the method is to express the problem in the polar coordinates ρ, α, and expand the wave function in a set of eigenfunctions of the hamiltonian at constant ρ. Two simple changes are involved in going from symmetric to asymmetric systems.

a) Whereas in symmetric systems the integration of the coupled channel equations could be done for the symmetric and antisymmetric solutions separately, such a decoupling is no longer possible

b) At large values of ρ, it previously sufficed to project the wave function onto a basis set of the eigenfunctions of one diatomic molecule only; two such projections, for HX and HY, are now required.

We have verified the accuracy of our asymmetric hyperspherical coordinates program by performing scattering calculations on the $F + H_2$ system on the $F + H_2$ system on the Muckerman V surface (15), and achieved agreement with previous results (16) to within 3% or better at energies near the resonance. A plot showing probabilities for the reaction $F + H_2(v=0) \longrightarrow FH(v=2) + H$ obtained by the hyperspherical coordinate method and previous method is shown in figure 1. The rapid convergence of this technique with respect to the number of basis functions seen for the $H + H_2$ system (9a) is also seen for the $F + H_2$ system; with sufficiently frequent changes of basis functions, results converged to approximately ±0.02 in the low energy region (up to 0.10 eV translational energy) can be obtained with 7 basis functions (5 open, 2 closed, correlating asymptotically to one closed state of each of the H_2 and HF molecules).

12-14 basis functions were used in all the calculations reported here. This is far more than needed in the lowest energy region (equivalent results were obtained with only 8 channels in this energy region). Transition probabilities should be good to ±0.002 for nearly all transitions and energies; in many cases they are probably good to better than ±0.001. Small transition probabilities (i.e. those significantly smaller than 0.001) probably have fairly large relative errors (~10%) as seen by oscillations in the probability vs. energy curves to be shown below. Flux was normally conserved to better than ±0.001. Deviation of the scattering matrix from unitarity increased gradually with energy until at the highest energies studied (1.15 eV above the HBr ground state) flux was converged to ±0.008.

The potential energy surface used is essentially that of Baer (14). It is an LEPS (17) surface, with all Sato parameters set to 0.154. The Morse oscillator parameters are those of Douglas, et al (5). The surface has a barrier to exhange of 1 kcal/mole. This surface is not designed to accurately mimic the real one; inadequacies are suggested by the difference between the observed (12) and calculated (14) vibrational product state distribution for reaction 4. A plot of the surface in the Delves coordinate system (7c, 9a) is shown in figure 2.

III. RESULTS AND DISCUSSION

A plot of the energies of the basis functions as a function of the propagation coordinate ρ is shown in figure 3. Transition probabilities for reactions 3a and 3b are presented as a function of reagent translational energy in figure 4 for $v = 2$ (figure 4a), $v = 3$ (4b), and $v = 4$ (4c for reaction 3a and 4d for 3b). Corresponding Arrhenius plots of the thermal rate constants for these transitions are presented in figure 5.

There are three major features of the dynamics, as may be readily seen by examination of figures 4 and 5:

a) The only transition probability which can achieve a substantial value (greater than 0.1) is that for reaction to the energetically nearest HBr state. Thus, Br + HCl (v=2, 3, 4) reacts predominantly to form HBr(v=0, 1, 2), respectively. The near-degeneracy of HCl(v) and HBr(v-2) may be seen in figure 3.

b) Transitions involving a large change in vibrational quantum number are far less likely than those involving a smaller change. This may be seen especially clearly by considering the state-to-state rate constants in figure 5, where the large separation between the curves is indicative of the large difference in rate constants and thus reaction probabilities.

c) Probabilities and rates of transitions to near-degenerate product states are nearly equal: this may be seen for three pairs of reactions:

$$\mathrm{Br} + \mathrm{HCl}(v{=}3) \longrightarrow \mathrm{BrH}(v{=}0) + \mathrm{Cl}\,, \quad \mathrm{Br} + \mathrm{HCl}(v{=}2)$$
$$\mathrm{Br} + \mathrm{HCl}(v{=}4) \longrightarrow \mathrm{BrH}(v{=}1) + \mathrm{Cl}\,, \quad \mathrm{Br} + \mathrm{HCl}(v{=}3)$$
$$\longrightarrow \mathrm{BrH}(v{=}0) + \mathrm{Cl}\,, \quad \mathrm{Er} + \mathrm{HCl}(v{=}2)$$

The calculation of the transition probability to the energetically nearest HBr state as the only one reaching an appreciable value is in agreement with the results of experimental studies (5) of the removal of HCl(v=2, 3, 4) by Br atoms; in particular, the observation that the greater rapidity of removal of these levels of HCl than of the v=1 level must be due to chemical reaction (process 3a) and not inelastic non-reactive collisions (process 3b). While we have not extended our calculations below the HBr(v=0) level, as is necessary to calculate rates for the deactivation rate from HCl(v=1), it seems quite reasonable to expect that that rate would be significantly slower than those shown here. The relative rates of removal of HCl(v) obtained here do not agree with those determined experimentally, however. We calculate HCl(v=3) to be removed more rapidly than either HCl(v=2) or HCl(v=4); experiments show the rate to increase as v is increased from 1 to 4 (5).

This disagreement is not surprising, however, as it has been seen in symmetric collisions that the probability vs. energy curves (rate constants) for the vibrationally adiabatic exchange reaction X' + HX(v) ⟶ X'H(v) + X for X = Cl (18) and X = I (10e, 18) vary substantially and irregularly with reagent excitation. In contrast, for the H + H_2 reaction, the differences between successive probability vs. energy curves for vibrationally adiabatic reaction are much more regular (9a). The irregularity observed is most likely due to a combination of the H-L-H mass combination and the restriction to collinearity. Three-dimensional quasi-classical trajectory calculations performed on a similar but not identical surface (13b) show no such irregular behavior, while one-dimensional quasi-classical trajectory calculations performed on this surface show irregularity roughly similar to that of the quantum results reported here (19).

A substantial difference between collinear (theoretical) and experimental results for this system is quite reasonable in the light of experimental results on various exoergic X + HY reactions, which suggest that, at least at low energies, the reaction proceeds by attack of the X atom on the Y end of the HY molecule, with subsequent H atom migration and HX bond formation as the HY bond breaks (12, 20).

The low probabilities of multi-quantum transitions in non-reactive collisions and of reactive transitions to all but the near-degenerate level can be understood classically, as can the near equality of the probabilities of reactive and non-reactive transitions to near degenerate states. This has been demonstrated in studies of the Cl + HCl reaction (21). Transitions involving a large change in vibrational action (analogous to vibrational quantum number) occur at the boundary between reactivity bands (22) in plots of the final action versus initial vibrational phase. Near the boundary, the final action varies rapidly with initial vibrational phase, forming a cusp about some central boundary phase (21). Transitions involving a large change in quantum number can only occur for collisions in a very limited range of initial phase and are thus unlikely. In symmetric systems such as Cl + HCl, these transitions involved motion essentially along the symmetric stretch line. To a first approximation, then, the system has "forgotten" in which channel it began its motion, giving rise to the near equivalence of reactive and non-reactive transitions to degenerate energy levels.

One must take great care in relating the results obtained here to experimental ones. The collinearity restriction is undoubtedly a severe one and can be expected to lead to qualitatively incorrect results. The surface used was chosen mainly for its simplicity and although it displays the correct energetics of the system it need not otherwise bear a close similarity to the correct one. Indeed, Smith (13b) performed three dimensional quasi-classical trajectory calculations on a related potential energy surface (LEPS with Sato parameters of 0.17) and could not get good agreement with experimental results. Finally, one must consider the possibility of collisions involving more than one electronic potential energy surface. Their possible importance has been considered previously, but the results are inconclusive.

IV. CONCLUSIONS

We have shown that the hyperspherical coordinate method is well-suited to the study of reactions (1) and have applied it to the Br + HCl(v=2, 3, 4) system. The major features of the dynamics include the dominance of the removal of vibrationally excited HCl by reaction to the near-degenerate HBr level, the small probability of collisions involving a large change in internal energy, and the near-equivalence of reactive and non-reactive processes to near-degenerate HCl and HBr levels. Because of the restriction to collinear motion, uncertainty in the potential energy surface, and the possible role of collisions involving more than one electronic potential energy surface, these calculations do not have predictive quantitative value, and comparison with experiment should be done very cautiously.

V. ACKNOWLEDGMENTS

The calculations reported were performed on the Dreyfus-NSF Theoretical Chemistry Computer which was funded through grants from the Camille and Henry Dreyfus Foundation, the National Science Foundation (Grant No. CHE78-20235), and the Sloan Fund of the California Institute of Technology, and on the IBM 370/158 computer of Ambassador College, for which we express our appreciation.

REFERENCES

1. M. R. Levy, Prog. Reac. Kin. 10 (1979) 1.
2. See, for example, K. Tamagake, D. W. Setser, and J. P. Sung, J. Chem. Phys. 73 (1980) 2203; N. B. H. Jonathan, P. V. Sellers, and A. J. Stace, Mol. Phys. 43 (1981) 215.
3. J. R. Airey, J. Chem. Phys. 52 (1970) 156.
4. J. W. Hepburn, K. Liu, R. G. Macdonald, F. J. Northrup, and J. C. Polanyi, J. Chem. Phys. 75 (1981) 3353.
5. D. J. Douglas, J. C. Polanyi, and J. J. Sloan, J. Chem. Phys. 59 (1973) 6679; Chem. Phys. 13 (1976) 15.
6. C. A. Parr, J. C. Polanyi, and W. H. Wong, J. Chem. Phys. 58 (1973) 5.
7. a) A. Kuppermann, in: Proceedings of the Conference on Potential Energy Surfaces in Chemistry, ed. W. A. Lester, (U. Calif., Santa Cruz, 1970), pp. 121-124; b) in: Proceedings of the 7th International Conference on the Physics of Electronic and Atomic Collisions (North-Holland, Amsterdam, 1971), pp. 3-5; c) in: Theoretical Chemistry, Advances and Perspectives, Vol. 6a, ed. D. Henderson (Academic Press, New York, 1981), pp. 79-162.
8. C. C. Rankin and J. C. Light, J. Chem. Phys. 51 (1969) 1701; G. Miller and J. C. Light, J. Chem. Phys. 54 (1971) 1635, 1643.
9. a) A. Kuppermann, J. A. Kaye, and J. P. Dwyer, Chem. Phys. Lett. 74 (1980) 257; b) J. A. Kaye and A. Kuppermann, Chem. Phys. Lett. 77 (1981) 573; c) J. A. Kaye and A. Kuppermann, Chem. Phys. Lett. 78 (1981) 546.
10. a) G. Hauke, J. Manz, and J. Römelt, J. Chem. Phys. 73 (1980) 5040; b) J. Römelt, Chem. Phys. Lett. 74 (1980) 263; c) J. Manz and J. Römelt, Chem. Phys. Lett. 76 (1980) 337; d) J. Manz and J. Römelt, Chem. Phys. Lett. 77 (1981) 172;

e) J. Manz and J. Römelt, Chem. Phys. Lett. 81 (1981) 179.

11. D. Arnoldi, K. Kaufmann, and J. Wolfrum, Phys. Rev. Lett. 34 (1975) 1597; D. Arnoldi and J. Wolfrum, Ber. Bunsenges. Phys. Chem. 80 (1976) 892; R. G. Macdonald and C. B. Moore, J. Chem. Phys. 73 (1980) 1681.

12. D. H. Maylotte, J. C. Polanyi, and K. B. Woodall, J. Chem. Phys. 57 (1972) 1547; F. J. Wodarczyk and C. B. Moore, Chem. Phys. Lett. 26 (1974) 484; C.-C. Mei and C. B. Moore, J. Chem. Phys. 67 (1977) 3936.

13. a) J. C. Brown, H. E. Bass, and D. L. Thompson, J. Phys. Chem. 81 (1977) 479; b) I. W. M. Smith, Chem. Phys. 20 (1977) 437.

14. M. Baer, J. Chem. Phys. 62 (1975) 305.

15. J. T. Muckerman, in: Theoretical Chemistry: Advances and Perspectives, Vol. 6a, ed. D. Henderson (Academic Press, New York, 1981), pp. 1-77.

16. G. C. Schatz, J. M. Bowman, and A. Kuppermann, J. Chem. Phys. 63 (1975) 674.

17. S. Sato, J. Chem. Phys. 23 (1955) 592, 2465.

18. J. A. Kaye and A. Kuppermann, unpublished results.

19. We have performed collinear quasi-classical trajectory calculations for the forward and reverse reaction and will present these results later.

20. C.-C. Mei and C. B. Moore, J. Chem. Phys. 70 (1979) 1759; E. Wurzberg and P. L. Houston, J. Chem. Phys. 72 (1980) 5915.

21. J. A. Kaye and A. Kuppermann, manuscript in preparation.

22. J. S. Wright, G. Tan, K. J. Laidler, and J. E. Hulse, Chem. Phys. Lett. 30 (1975) 200; J. S. Wright, K. G. Tan, and K. J. Laidler, J. Chem. Phys. 64 (1976) 970; J. S. Wright and K. G.

Tan, J. Chem. Phys. 66 (1977) 104; K. G. Tan, K. J. Laidler, and J. S. Wright, J. Chem. Phys. 67 (1977) 5883.

FIGURE CAPTIONS

Figure 1. Probability of the reaction $F + H_2(v=0) \longrightarrow FH(v=2) + H$ on the Muckerman V surface as a function of reagent energy. The solid line connects results obtained previously; the points represent results obtained with the method of hyperspherical coordinates using up to 8 basis functions.

Figure 2. Equipotential contour plot for the Br + HCl system. The solid curves are the contours and are equally spaced in increments of 0.4 eV from 0.2 to 3.8 eV. The zero of energy is the bottom of the HCl well. The surface is plotted in the Delves coordinate system.

Figure 3. Hyperspherical coordinate eigenvalues $E_n(\rho)$ as a function of the propagation coordinate ρ. Values of n for the curves are shown at the top of the figure. The asymptotic states to which each of the curves correlates is indicated at the right of the figure.

Figure 4. Transition probabilities $P_{vv'}^R$ and $P_{vv'}^V$ for the processes $Br + HCl(v=2, 3, 4) \longrightarrow HBr(v') + Cl$, $Br + HCl(v' < v)$ as a function of initial relative translational energy. The lines are cubic spline fits to the points shown. Line types and symbol meanings are indicated in the figures. a) v = 2; b) v = 3; c) v = 4 - reactive only; d) v = 4 - non-reactive only.

Figure 5. Arrhenius plots of state-to-state rate constants $k_{vv'}^R$, $k_{vv'}^V$ for the processes $Br + HCl(v) \longrightarrow HBr(v') + Cl$, $Br + HCl(v' < v)$. The four plots are similar to the corresponding four plots in figure 4 with respect to line and symbol usage.

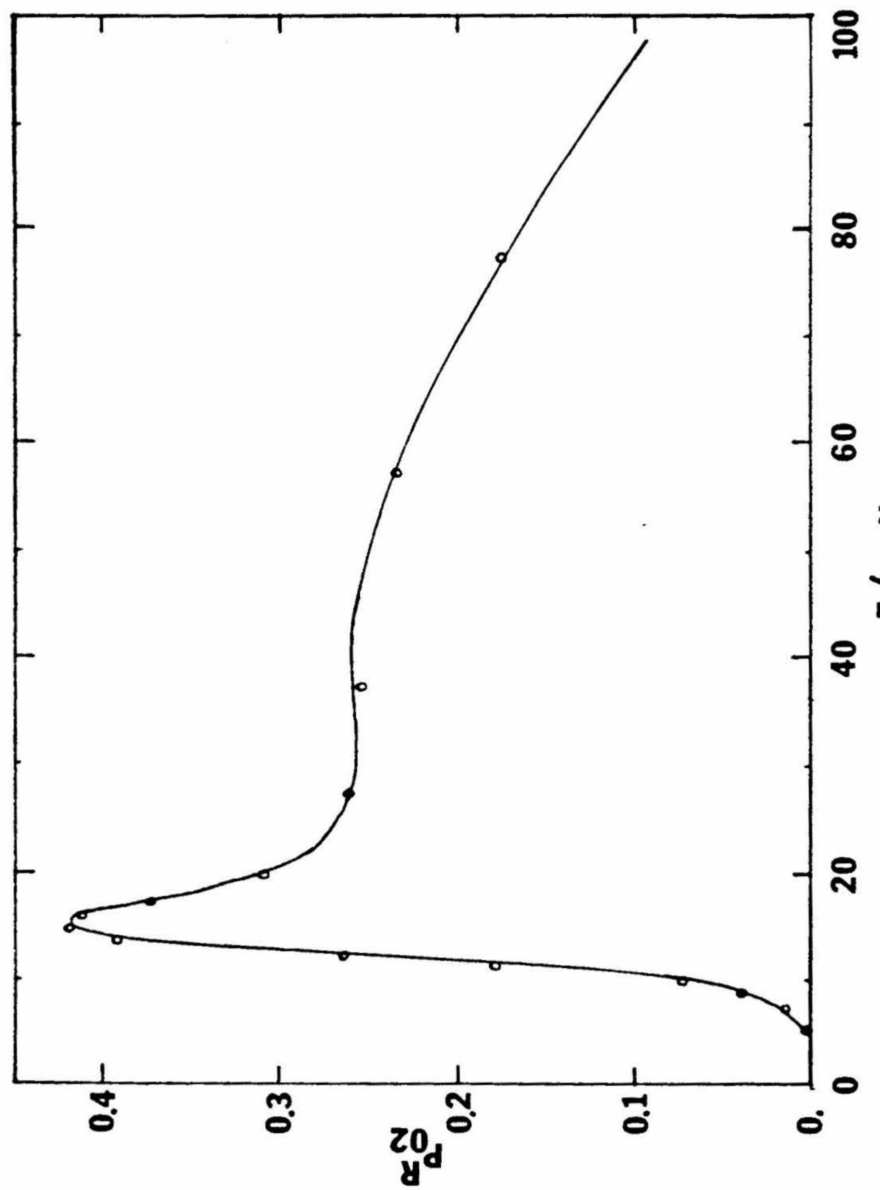

Figure 1

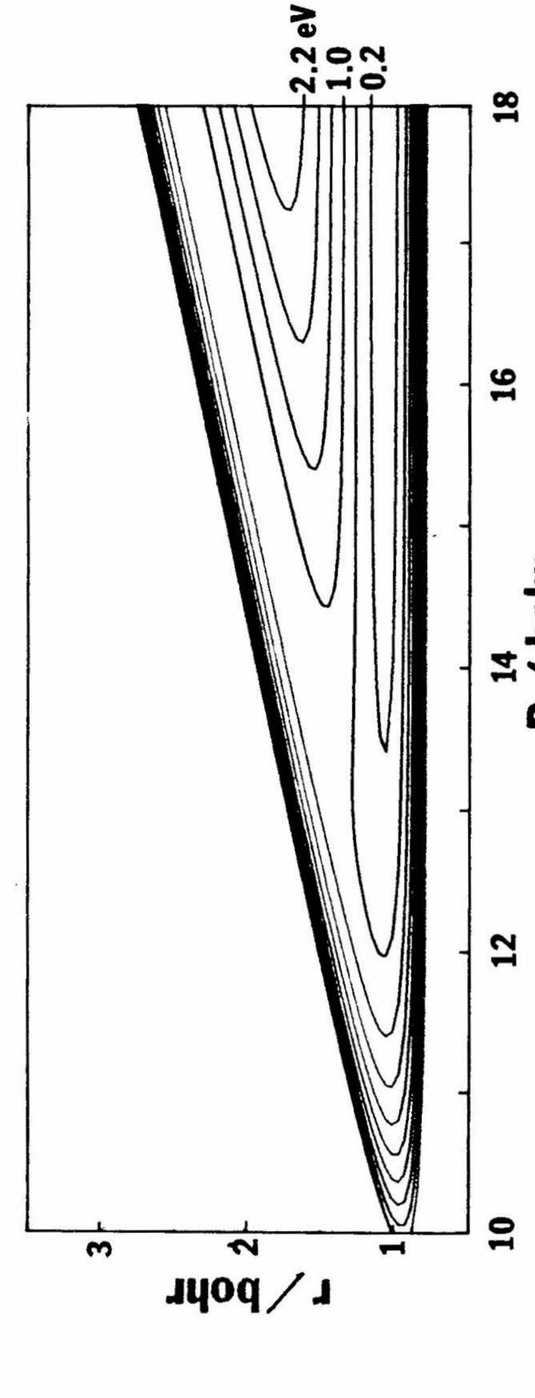

Figure 2

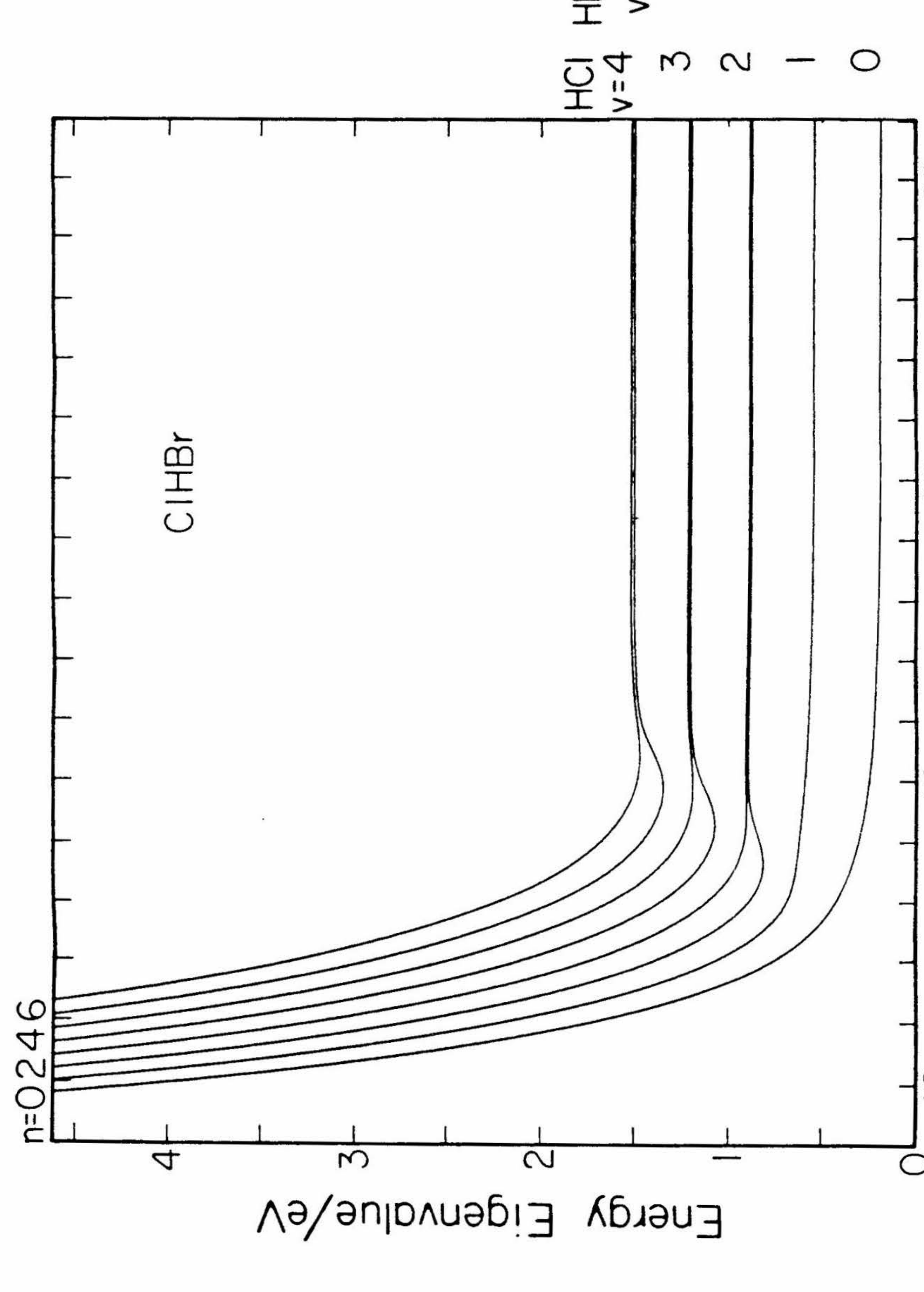
ClHBr
HCl
v=4
3
2
1
0
HBr
v=2
1
0
n=0246
10
15
20
25
ρ/bohr
0
1
2
3
4
Energy Eigenvalue/eV

Figure 3

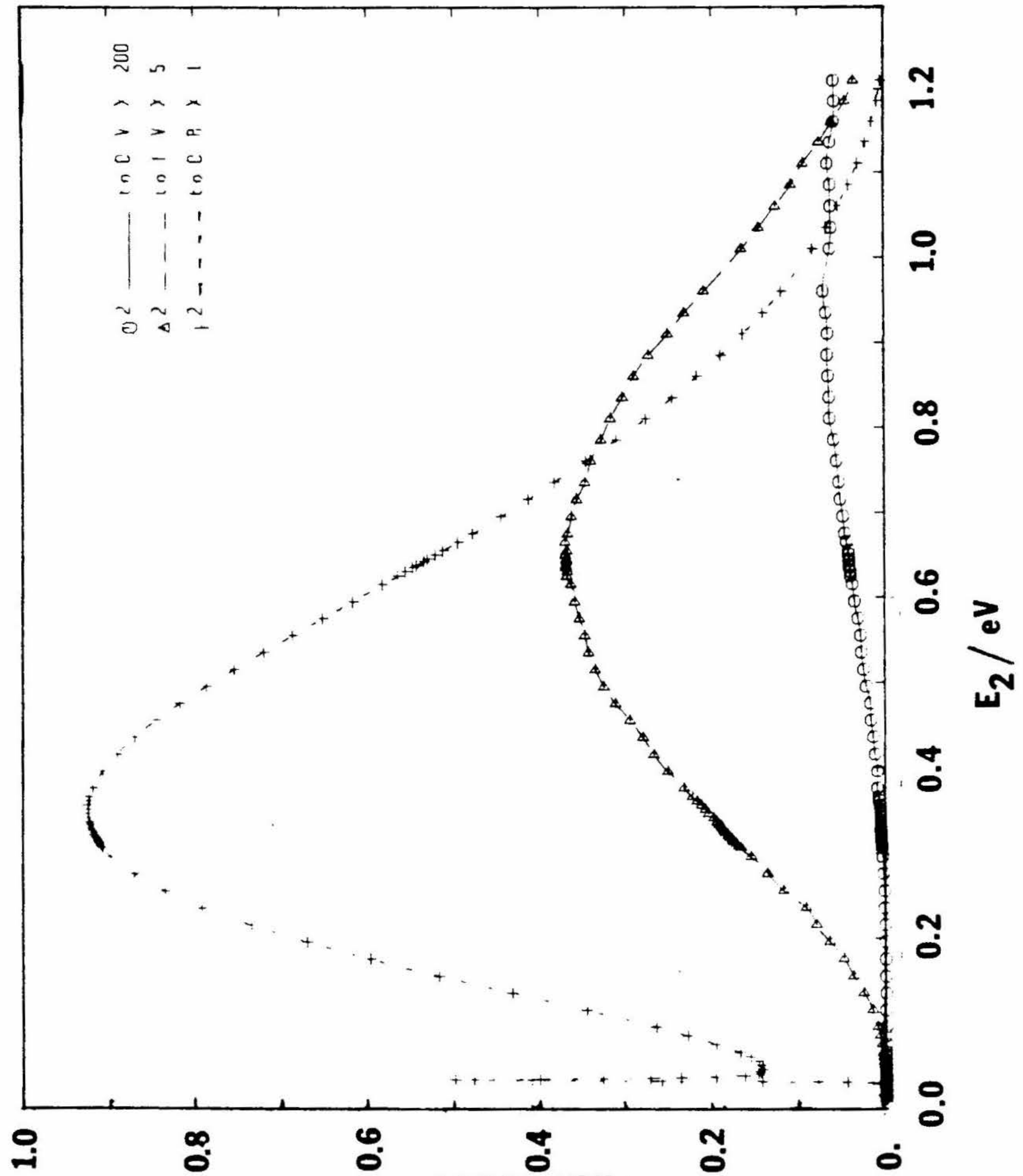
PROBABILITY
1.0
0.8
0.6
0.4
0.2
0.
E$_2$/eV
0.0
0.2
0.4
0.6
0.8
1.0
1.2
⊖ 2 ——— to C V > x 200
△ 2 — — — to 1 V > x 5
+ 2 — + — to C R > x 1

Figure 4a

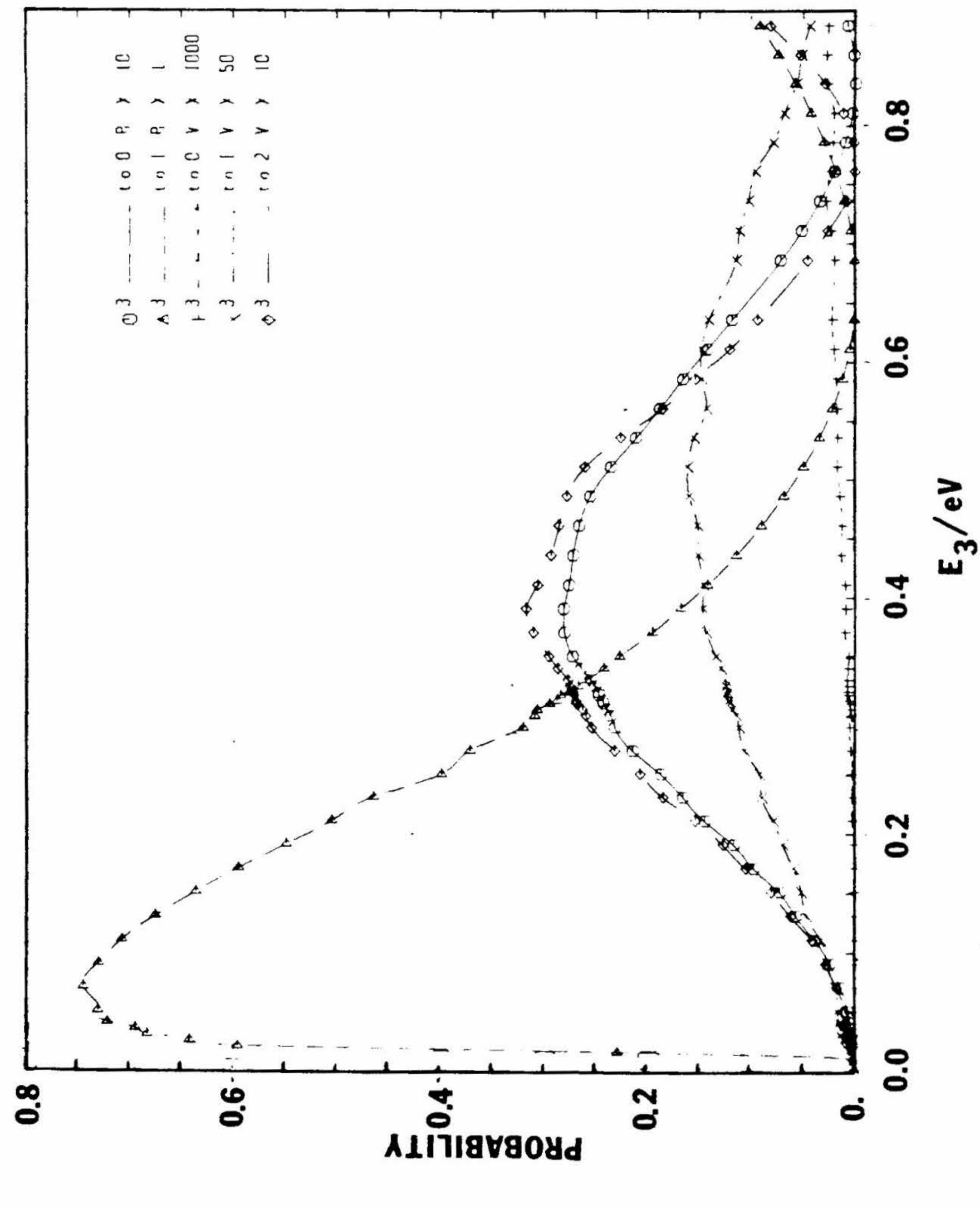
3 to 0 R x 10
3 to 1 R x 1
3 to 0 V x 1000
3 to 1 V x 50
3 to 2 V x 10
PROBABILITY
0.
0.2
0.4
0.6
0.8
E$_3$/eV
0.0
0.2
0.4
0.6
0.8

Figure 4b

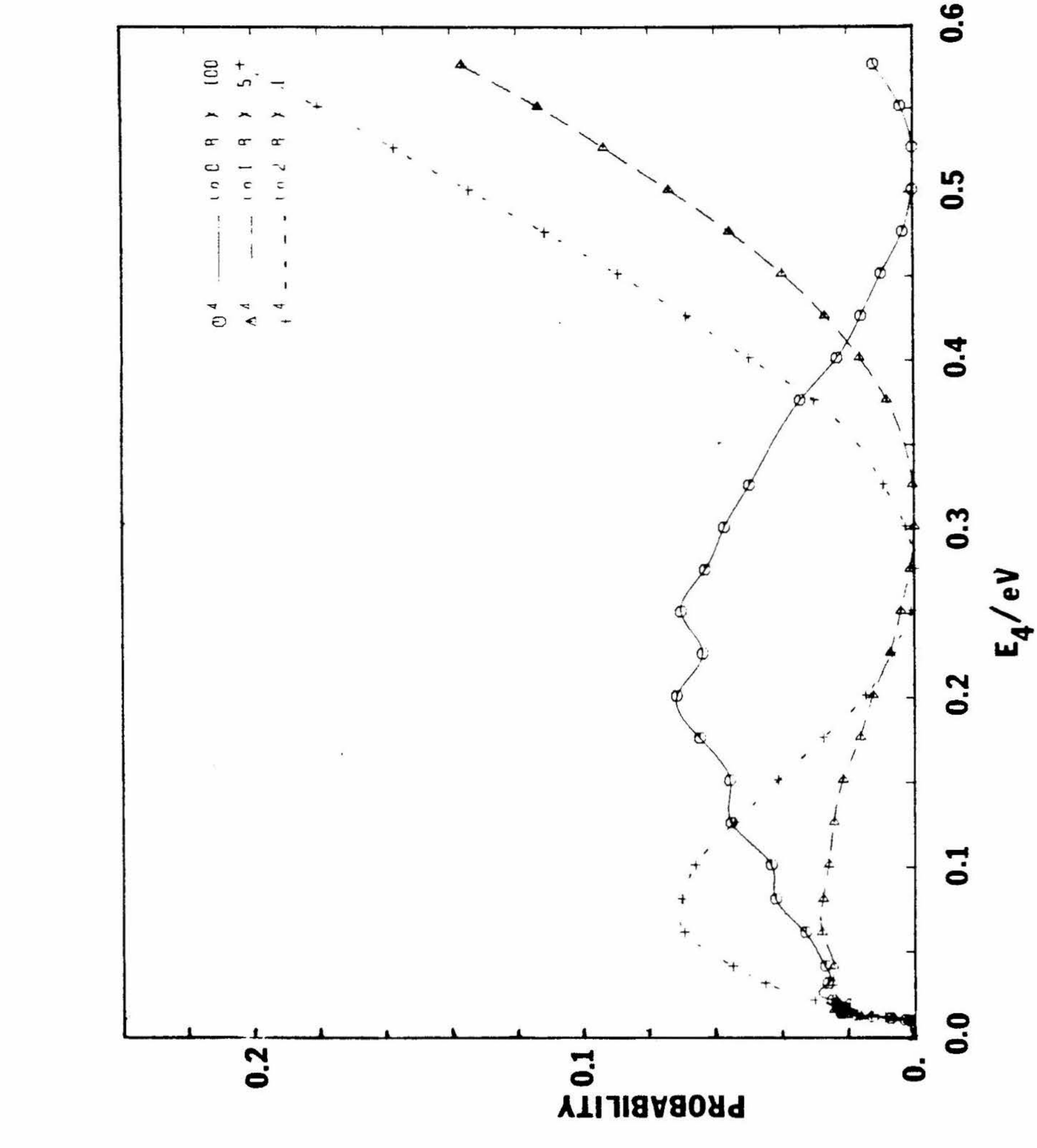
4 (n 0 R) x 100
4 (n 1 R) x 5
4 (n 2 R) x 1
PROBABILITY
0.
0.1
0.2
E$_4$/eV
0.0
0.1
0.2
0.3
0.4
0.5
0.6

Figu re 4c

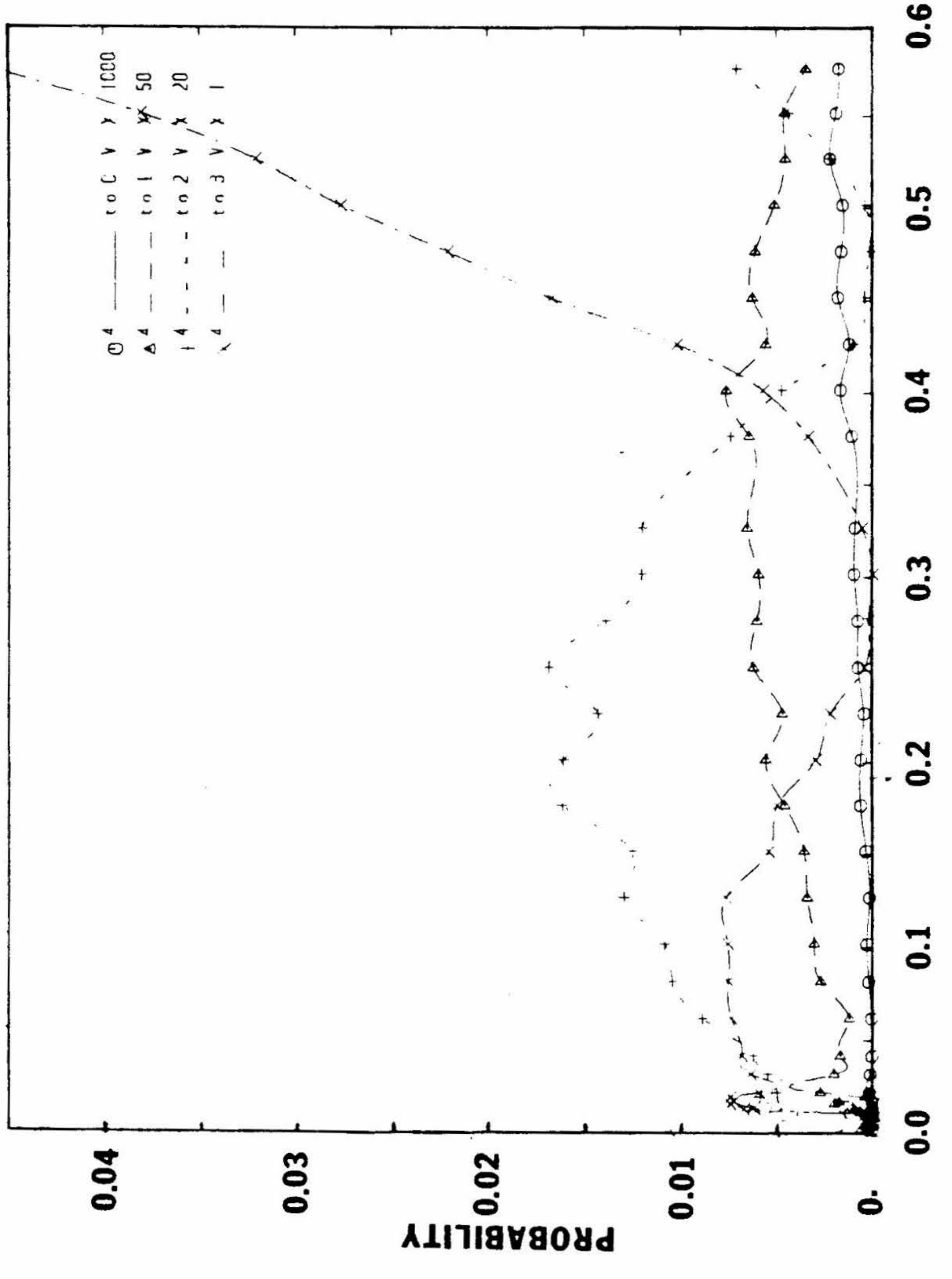
4 to 0 v x /1000
4 to 1 v x 50
4 to 2 v x 20
4 to 3 v x 1
PROBABILITY
0.
0.01
0.02
0.03
0.04
E_4/eV
0.0
0.1
0.2
0.3
0.4
0.5
0.6

Figure 4d

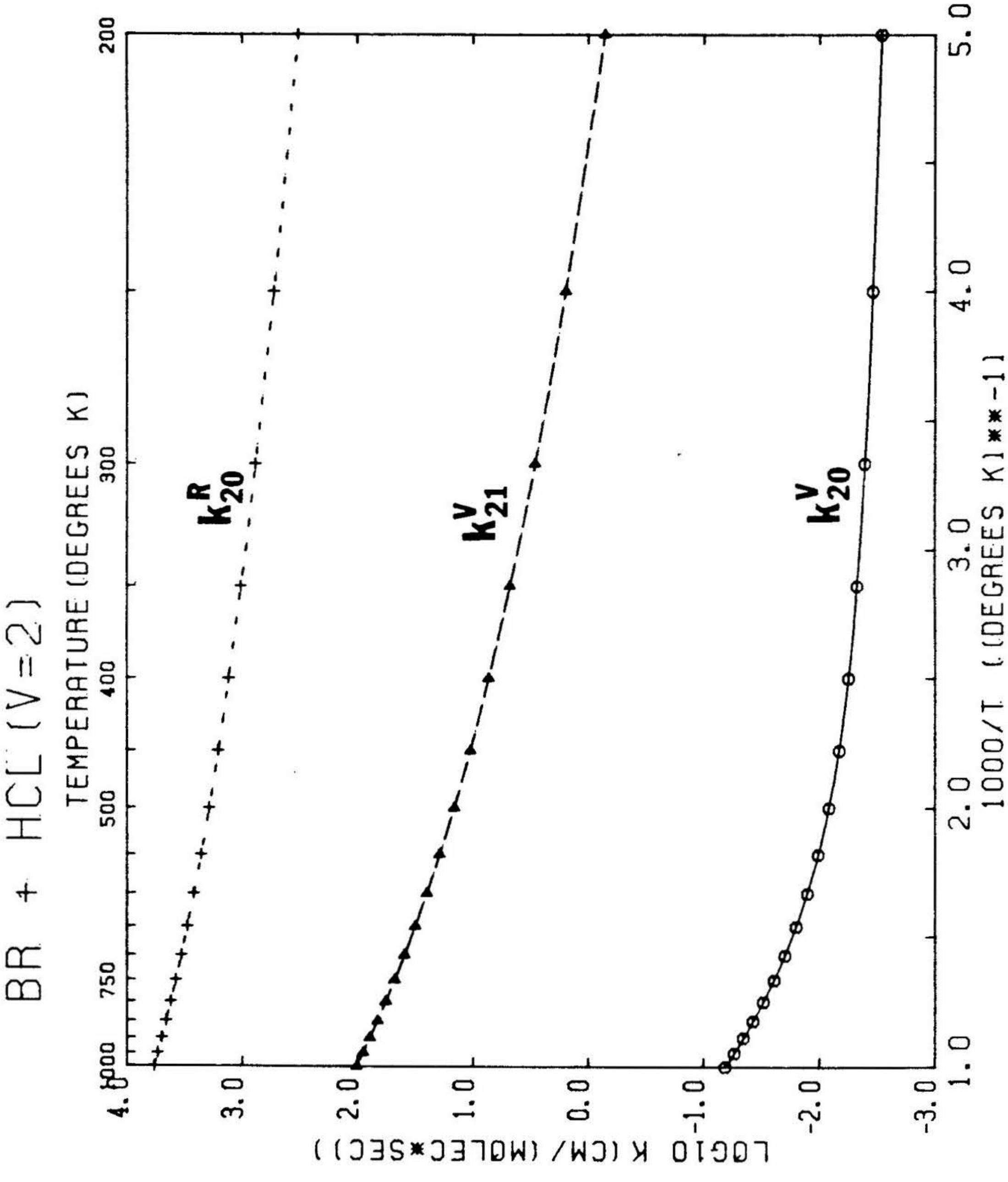
BR + HCL (V=2)
TEMPERATURE (DEGREES K)
1000
750
500
400
300
200
LOG10 K (CM/(MOLEC*SEC))
4.0
3.0
2.0
1.0
0.0
-1.0
-2.0
-3.0
1000/T ((DEGREES K)**-1)
1.0
2.0
3.0
4.0
5.0
k^R_{20}
k^V_{21}
k^V_{20}

Figure 5a

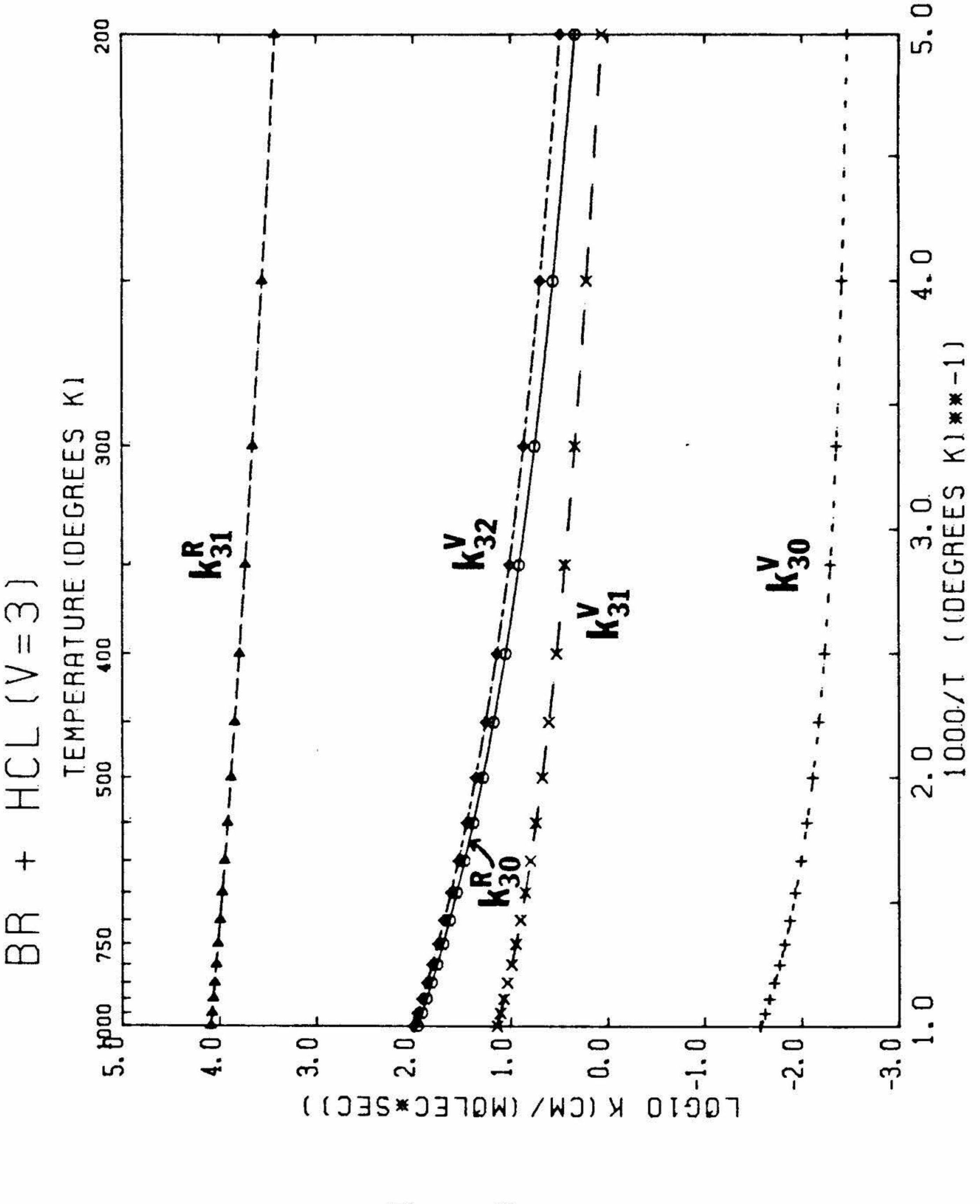
BR + HCL (V=3)
TEMPERATURE (DEGREES K)
1000
750
500
400
300
200
LOG10 K (CM/(MOLEC*SEC))
5.0
4.0
3.0
2.0
1.0
0.0
-1.0
-2.0
-3.0
1000/T ((DEGREES K)**-1)
1.0
2.0
3.0
4.0
5.0
k^R_{31}
k^V_{32}
k^V_{31}
k^V_{30}
k^R_{30}

Figure 5b

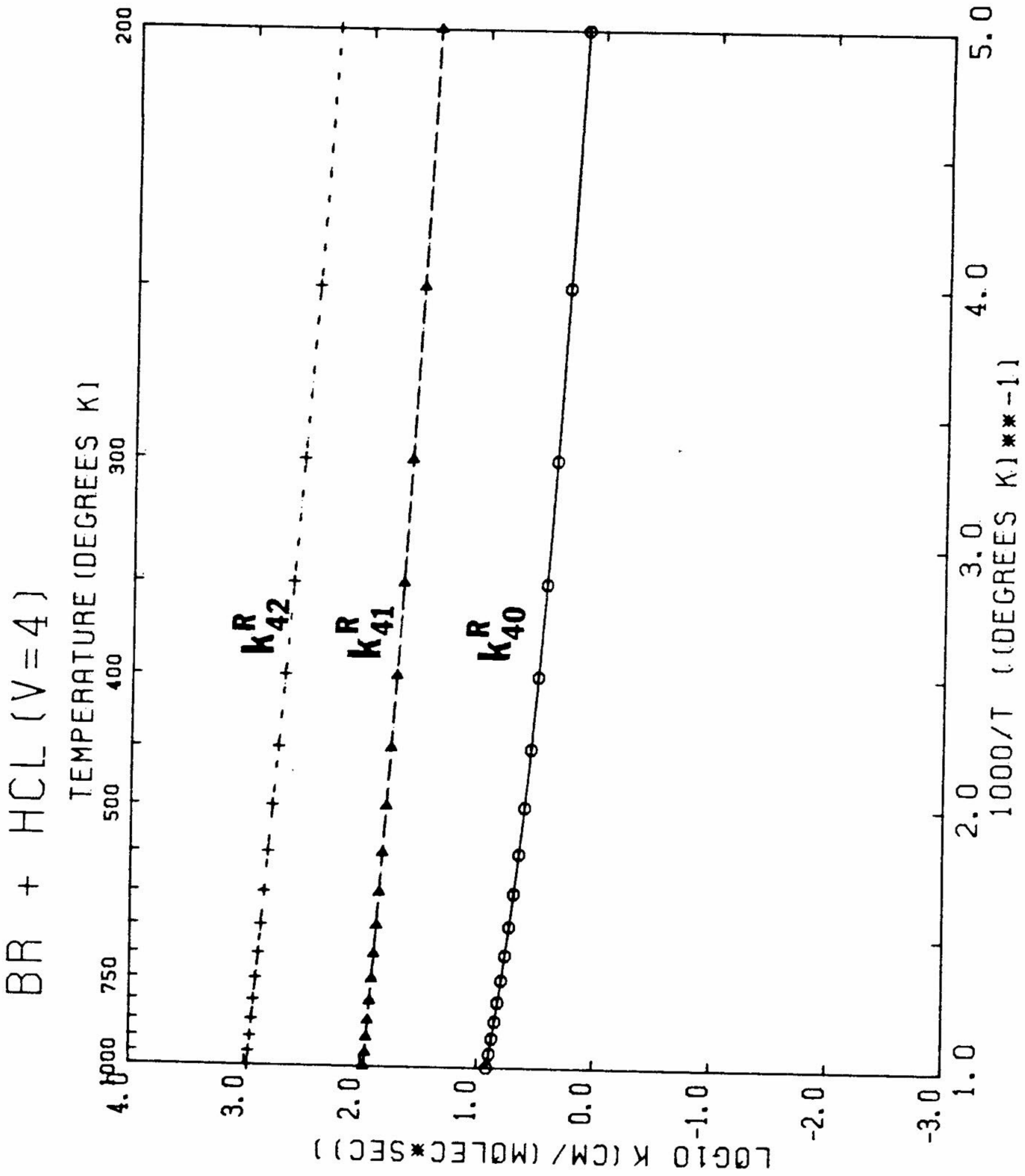
BR + HCL (V=4)
TEMPERATURE (DEGREES K)
1000
750
500
400
300
200
k^R_{42}
k^R_{41}
k^R_{40}
LOG10 K (CM/(MOLEC*SEC))
4.0
3.0
2.0
1.0
0.0
-1.0
-2.0
-3.0
1.0
2.0
3.0
4.0
5.0
1000/T ((DEGREES K)**-1)

Figure 5c

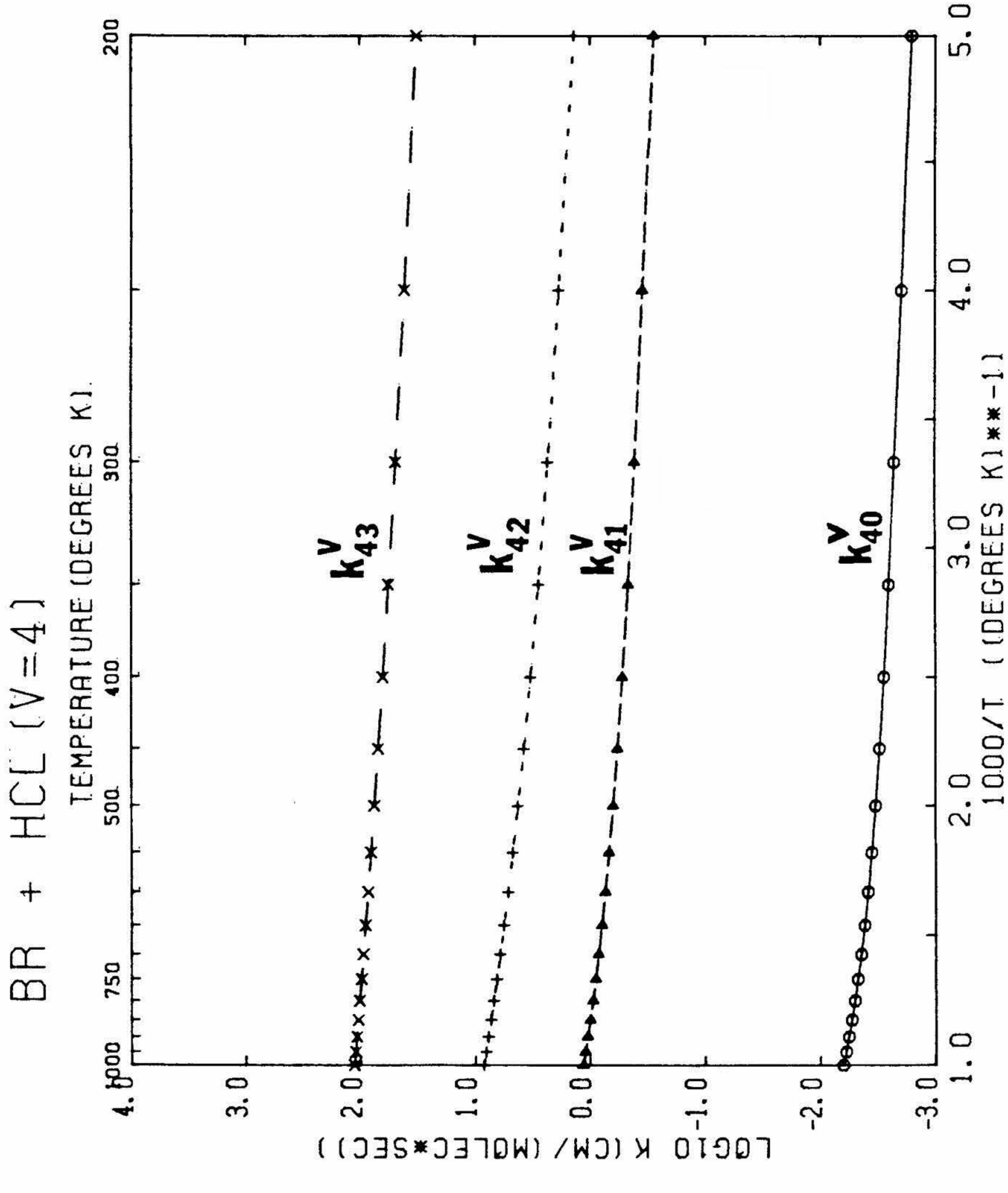
BR + HCL (V=4)
TEMPERATURE (DEGREES K)
1000
750
500
400
300
200
k^v_{43}
k^v_{42}
k^v_{41}
k^v_{40}
4.0
3.0
2.0
1.0
0.0
-1.0
-2.0
-3.0
LOG10 K (CM/(MOLEC*SEC))
1.0
2.0
3.0
4.0
5.0
1000/T ((DEGREES K)**-1)

Figure 5d

III.9 ASYMPTOTIC PROPERTIES OF HYPERSPHERICAL COORDINATE BASIS FUNCTIONS AND THEIR MATRIX ELEMENTS IN THE ADIABATIC REPRESENTATION

ASYMPTOTIC PROPERTIES OF HYPERSPHERICAL COORDINATE BASIS FUNCTIONS AND THEIR MATRIX ELEMENTS IN THE ADIABATIC REPRESENTATION[†]

Jack A. KAYE[‡] and Aron KUPPERMANN

Arthur Amos Noyes Laboratory of Chemical Physics,
California Institute of Technology
Pasadena, California 91125, USA

Asymptotic properties of two different sets of basis functions for a hyperspherical coordinate treatment of the reactive collinear atom-diatomic molecule collision have been determined by numerical calculation. One of the basis sets is the one used in previous hyperspherical coordinate calculations on H + H_2, I + HI, and a model problem allowing for collision-induced dissociation; the other involves a cut through the potential energy surface consisting of two straight lines connected by an arc. Eigenvalues of the basis functions and elements of the matrices which couple the equations when the problem is formulated in the adiabatic representation have been obtained on two potential energy surfaces. Analysis of the properties of these matrices yields predictions of properties of the matrices which are verified in the numerical calculations. Asymptotic behavior of the eigenvalues and matrix elements of the eigenfunctions and the potential has been studied, as

---

[†] This work was supported in part by a Contract (No. F49620-79-C0187) from the US Air Force Office of Scientific Research.

[‡] Work performed in partial fulfillment of the requirements for the Ph.D degree in Chemistry at the California Institute of Technology.

have the differences between the matrix elements with the two basis functions. The implications of the large ρ behavior observed on the asymptotic properties of the radial Schrödinger equation will be discussed. Preliminary results of numerical integration of the adiabatic equations are presented and interpreted in terms of a simple 2×2 model.

I. Introduction

The method of hyperspherical coordinates has been demonstrated to be a simple and effective one for the quantum mechanical study of the collinear reactive collision of an atom with a diatomic molecule.[1-8] Using this technique, transition probabilities have been determined for the $H + H_2$[1] and $I + HI$[2,8] systems, as well as for a model system above the threshold for collision-induced dissociation (CID).[2,6]

One major consideration in using the hyperspherical coordinates in quantum mechanical studies of reactive scattering is the value of the radius ρ to which one must integrate in order for transition probabilities to converge. If this value is too large, then the calculation becomes impactical. So far, essentially converged transition probabilities, both above and below dissociation, have been obtained without the need for integrating so far out that the value of ρ becomes inconveniently large.

In considering the CID problem, however, one is interested not only in transition probabilities, but in partitioning probabilities, that is, the probability for producing dissociated products for which the center-of-mass energy of the product is distributed in a given way. At a large value of ρ (76 bohr in the mode, CID case) where CID probabilities essentially converged (the calculated probabilities are probably good to ± 0.01), these partitioning probabilities have not converged with respect to the stopping point of the numerical integration. If integration is continued further (to 110 bohr) they do begin to show signs of convergence. The partitioning probabilities are discussed elsewhere.[9] The interaction between the particles has died off at a much smaller value of ρ, however, hence, the variation in the differential probabilities must be due to coupling introduced into the equations by the coordinate system (inaccuracies in the projection of the bound states onto Cartesian coordinate basis functions could also be partly responsible).

At large values of ρ, then, the problem to be considered is essentially that of a particle moving in a potential which varies in a known way with ρ. Since this variation with ρ is fairly simple, one hopes that either an analytic approach or a numerical one based on properties of the basis functions used (and their matrix elements) could allow one to introduce the correct asymptotic behavior without integration to large values of ρ.

In this paper we consider two different aspects of basis functions for a hyperspherical coordinate treatment at the reactive collinear atom-diatom molecule collision. We calculate these basis functions at large values of ρ ($\rho \leq 5000$ bohr) and obtain the matrices responsible for coupling equations when written in the adiabatic representation. Particular interest is paid to the ρ dependence of these quantities, especially when there exist relationships of the form

$$Q_{\lambda k} \propto \rho^{-\nu}$$

where $Q_{\lambda k}$ is some quantity (eigenvalue, matrix element) and ν is a limiting exponent of some sort. Finally, of the two different sets of basis functions studied, we consider whether one is superior in terms of its asymptotic properties.

The outline of the paper is as follows. In section II we review the hyperspherical coordinate picture and the equations which the two different basis sets satisfy. We then formulate the coupled channel problem in the adiabatic representation (an earlier description of the method[1] used the diabatic representation) and deduce some properties of the coupling matrices and some matrices generated in the course of integrating the coupled equations in the adiabatic representation. In section III we review the numerical techniques used in all the calculations reported here, and results of the calculations are given in section IV. In section V the results are discussed, and section VI consists of a summary of conclusions.

II. Theory

A. The Hyperspherical Coordinate Picture

The details of the hyperspherical coordinate system have been given in reference 1 so we will only review those portions of it relevant to the calculation of basis functions. Recall that each solution ψ_j of the Schrödinger equation is expanded in terms of an infinite and discrete set of orthonormal basis functions $\phi_i(\alpha;\bar{\rho})$ which are calculated at only certain values of $\rho = \bar{\rho}$:

$$\psi_j = \rho^{-\frac{1}{2}} \sum_i{}' \phi_i(\alpha;\bar{\rho}) g_{ij}(\rho;\bar{\rho}) \tag{2}$$

Each basis function ϕ_i satisfied the equation

$$-\frac{\hbar^2}{2\mu\rho^2}\frac{\partial^2}{\partial\alpha^2}\phi_i(\alpha;\bar{\rho}) + V(\alpha;\bar{\rho})\phi_i(\alpha;\bar{\rho}) = E_i(\rho)\phi_i(\alpha;\bar{\rho}) \tag{3}$$

subject to the boundary conditions

$$\phi_i(\alpha = 0;\bar{\rho}) = \phi(\alpha = \alpha_{max};\bar{\rho}) = 0 \tag{4}$$

where the value of α_{max} is determined by the masses of a, b, and c. We will be interested in the appearance of the basis functions $\phi_i(\alpha;\bar{\rho})$ in the limit of large ρ. As mentioned earlier at very large ρ there is essentially no interaction between at least two of the particles.

In the diabatic picture, the coupled channel equations which must be integrated are coupled by the potential term - i.e., terms of the form

$$V_{ij}(\rho;\bar{\rho}) = \int_0^{\alpha_{max}} \phi_i(\alpha;\bar{\rho})\, V(\rho,\alpha)\, \phi_j(\alpha;\bar{\rho})\, d\alpha \tag{5a}$$

and

$$V_{ij}(\bar{\rho}) = \int_0^{\alpha_{max}} \phi_i(\alpha;\bar{\rho})\, V(\bar{\rho};\alpha)\, \phi_j(\alpha;\bar{\rho})\, d\alpha\ . \tag{5b}$$

One would expect the $V_{ij}(\rho;\bar{\rho})$ term to vary discontinuously with distance because the basis functions change for every new $\bar{\rho}$. This complicates analysis of the large ρ (and $\bar{\rho}$) properties of these matrix elements.

To avoid this complication, one may work instead in the adiabatic representation, in which basis functions are calculated at all values of ρ. These basis functions will solve a form of eq. (3) in which $\bar{\rho}$ is everywhere replaced by ρ. Since the basis functions are now explicit functions of ρ, one must differentiate them with respect to ρ in substituting an expansion similar to that of eq. (2) into the Schrödinger equation for the problem (eq. (4) in ref. 1).

After some algebra one may show that the radial wavefunction elements $g_{kj}(\rho)$ satisfy the following equation:

$$\frac{d^2 g_{kj}}{d\rho^2}(\rho) + 2\sum_i{}' \overset{(1)}{T}_{ki}(\rho)\,\frac{dg_{ij}}{d\rho}(\rho) + \sum_i{}' \overset{(2)}{T}_{ki}(\rho)\,g_{ij}(\rho)$$

$$= -\frac{2\mu}{\hbar^2}\left\{E - E_k(\rho) + \frac{\hbar^2}{8\mu\rho^2}\right\} g_{kj}(\rho)\,, \tag{6}$$

where the matrix elements $\overset{(1)}{T}_{kj}(\rho)$ and $\overset{(2)}{T}_{kj}(\rho)$ are defined as follows:

$$\overset{(1)}{T}_{kj}(\rho) = \int_0^{\alpha_{\max}} \phi_k(\rho)\,\frac{\partial\phi_j}{\partial\alpha}(\rho)\,d\alpha \tag{7a}$$

$$\overset{(2)}{T}_{kj}(\rho) = \int_0^{\alpha_{\max}} \phi_k(\rho)\,\frac{\partial^2\phi_j}{\partial\alpha^2}(\rho)\,d\alpha\,, \tag{7b}$$

and $E_k(\rho)$ is the eigenvalue associated with a given $\phi_k(\rho)$. In matrix form equation (6) may be written as

$$\underline{\underline{g}}'' + 2\,\underline{\underline{T}}^{(1)}\,\underline{\underline{g}}' + \underline{\underline{T}}^{(2)}\,\underline{\underline{g}} = \underline{\underline{\epsilon}}\,\underline{\underline{g}} \tag{8}$$

where the matrix $\hat{\underline{\underline{\epsilon}}}(\rho)$ is a diagonal matrix whose elements are given by the relationships

$$\hat{\epsilon}_{ij}(\rho) = \begin{cases} -\dfrac{2\mu}{\hbar^2}\left\{E - E_i(\rho) + \dfrac{\hbar^2}{8\mu\rho^2}\right\} & i = j \\ 0 & i \neq j \end{cases} \tag{9}$$

Hence, the equations to be integrated are coupled by matrix elements of the basis functions and their ρ-derivatives. Since in the adiabatic representation the basis functions vary smoothly with ρ, the matrices $\underline{\underline{T}}^{(1)}$, $\underline{\underline{T}}^{(2)}$, and $\underline{\underline{\epsilon}}$ should vary smoothly with ρ, simplifying analysis of their large ρ behavior.

B. An Alternative Basis Set

The basis functions ϕ, used in section A (and in reference 1), are calculated along an arc cut through the potential surface at a constant value of ρ = constant. It is known that for bound states, at small values of ρ, these do not provide a good description of the bound states of the molecule, which are instead best described by basis functions calculated along cuts of r_λ = constant [recall $\rho = (R_\lambda^2 + r_\lambda^2)^{\frac{1}{2}}$]. By projecting the wavefunction onto a set of Cartesian coordinate basis functions, at a moderate value of ρ ($\sim$ 7 bohr) Kuppermann et al.[1] were able to converge their $H + H_2$ transition probabilities far sooner than Römelt whose probabilities continued to oscillate at larger values of ρ. This suggests that a better basis set than the purely polar ones defined in eq. (3) might be developed by using, rather than an arc at constant ρ, a cut which is at constant R_λ and R_k in the $\lambda + \nu\kappa$ and $\lambda\nu + \kappa$ arrangement channels, respectively, and an arc at some constant ρ' (operationally defined in Fig. 1) in the intermediate region, corresponding to the dissociative plateau. This coordinate system is pictured in Fig. 1 (for comparison purposes, an arc at constant ρ is drawn in also). The point at which one switches over from a straight line to an arc is arbitrary; ideally it should be sufficiently close to the dissociation limit that its energy is above that of all the bound states of the isolated molecules.

These basis functions, which will be called $\chi_n(R, S)$ to distinguish them from the purely polar $\phi_n(\rho, \alpha)$ used above, satisfy the following equations

$$\left.\begin{aligned} &[-\frac{\hbar^2}{2\mu}\frac{\partial^2}{\partial r_\lambda^2} + V(R_\lambda, r_\lambda)]\chi_n^{(1)}(R,S) = E_n(R)\,\chi_n^{(1)}(R,S) \\ &-\frac{\hbar^2}{2\mu\rho^2}\frac{\partial^2}{\partial\alpha^2} + V(\rho', \alpha')]\,\chi_n^{(2)}(R,S) = E_n(R)\,\chi_n^{(2)}(R,S) \\ &-\frac{\hbar^2}{2\mu}\frac{\partial^2}{\partial r_\kappa{}^2} + V(R_\kappa, r_\kappa)]\,\chi_n^{(3)}(R,S) = E_n(R)\,\chi_n^{(3)}(R,S) \end{aligned}\right\} \qquad (10)$$

where the superscripts (1), (2), and (3) represent the regions at the potential surface marked in Fig. 1, R is as defined as in Fig. 1, and S is a transverse variable which is a distance in region 1 and 3 and an angle (α') in region 2.

Across the boundaries the following continuity equations hold:

$$\begin{aligned} &\chi_n^{(1)}(R_\lambda, r_\lambda = r_0) = \chi_n^{(2)}(\bar{\rho} = R - R_0,\ \alpha' = 0) \\ &\left(\frac{\partial\chi_n^{(1)}}{\partial r}\right)_{\substack{r=r_0\\ R=\text{const}}} = \frac{1}{R-R_0}\left(\frac{\partial\chi_n^{(2)}}{\partial\alpha'}\right)_{\substack{\alpha'=0\\ \rho'=R-r_0}} \qquad (11) \\ &\chi_n^{(2)}(\rho' = R-R_0,\ \alpha' = \alpha'_{max}) = \chi_n^{(3)}(R',\ r_{\kappa'} = r'_{\kappa_0}) \\ &\left(\frac{\alpha\chi_n^{(3)}}{\partial r_k}\right)_{\substack{r_\kappa=r_0\\ R'}} = -\frac{1}{R-r_0}\left(\frac{\partial\chi_n^{(2)}}{\partial\alpha'}\right)_{\substack{\alpha'=\alpha'_{max}\\ \rho'=R-R_0=R'-R'_0}} \end{aligned}$$

The boundary conditions are simply

$$\chi_n^{(1)}(R, r_\lambda = 0) = \chi_n^{(3)}(R', r_\kappa = 0) = 0 . \tag{12}$$

Alternatively, one may cast the eqs. (10) in terms of a variable s which is a smoothly varying distance coordinate which is a distance in regions (1) and (3), and an arc length $= (\rho' \cdot \alpha')$ in region (2).

$$s = r_\lambda \qquad \text{for } 0 < r_\lambda < r_{\lambda_0} \quad \text{(region (1))}$$

$$s = r_{\lambda_0} + \rho' \alpha' \qquad \text{for } r_\lambda > r_{\lambda_0},\ r_\kappa > r_{\kappa_0} \quad \text{(reg. (2))}$$

$$s = r_{\lambda_0} + \rho' \alpha'_{\max} + (r_{\kappa_0} - r_\kappa) \quad \text{for } 0 < r_\kappa < r_{\kappa_0} \quad \text{(region (3))}$$

Since s smoothly varies (and is always a distance) there is no need to impose continuity equations of the form of eqs. (1).

The χ_n are normalized as follows:

$$\int_0^{r_{\lambda_0}} \chi_n^{(1)} \chi_{n'}^{(1)} \, dr_\lambda + \int_0^{\alpha'_{\max}} \chi_n^{(2)} \chi_{n'}^{(2)} \rho' \, d\alpha' + \int_{r_{\kappa_0}}^{0} \chi_n^{(3)} \chi_{n'}^{(3)} \, dr_\kappa = \delta_{nn'}$$

(14

The ρ' term in the region (2) portion of the normalization integral becomes important in the calculation of the adiabatic matrix elements $T^{(1)}$ and $T^{(2)}$ and causes them to have different properties when calculated using the "hybrid" basis functions $\chi_n(R, S)$ than when calculated using the "purely polar" basis functions $\phi_n(\alpha; \bar{\rho})$. These differences will be outlined below.

C. Integrating the Coupled Equations in the Adiabatic Representation

When integrating the coupled second-order differential equations developed in a coupled-channel calculation, it is frequently convenient to have no first derivative term. For example, the Gordon integrator[10] in which the term multiplying the $\underline{\underline{g}}$ term in an equation of the form

$$\underline{\underline{g}}'' + \underline{\underline{f}}(x)\underline{\underline{g}} = \underline{\underline{0}} \tag{15}$$

is assumed to be linear in x, allows no first derivative term. When developed in the adiabatic representation, the coupled channel eqs. 8 do contain a first derivative term, which must be removed if one is to use an integrator such as Gordon's. The use of such an integrator, in which one follows the coefficients of the terms in the differential equation rather than following the wavefunction directly (i.e., by a brute force numerical integration of the differential equation) is particularly important in the CID problem at large ρ, when all channels are energetically accessible and thus highly oscillatory at sufficiently high energy.

To remove the first derivative term, one may define a modified radial wavefunction $\underline{\underline{y}}$ by the transformation

$$\underline{\underline{g}} = \underline{\underline{M}}\,\underline{\underline{y}}\ , \tag{16}$$

where $\underline{\underline{M}}$ is to be determined from the requirement that there be no first derivative term in the differential equation for $\underline{\underline{y}}$. Substitution of eq. (16) into eq. (8) and the imposition of this requirement for $\underline{\underline{M}}$ give the following two equations

$$\underline{\underline{M}}' + \underline{\underline{T}}^{(1)}\underline{\underline{M}} = \underline{\underline{0}} \tag{17a}$$

$$\underline{\underline{y}}'' + \underline{\underline{M}}^{-1}\{-(\underline{\underline{T}}^{(1)})^2 - (\underline{\underline{T}}^{(1)})' + \underline{\underline{T}}^{(2)}\}\,\underline{\underline{M}}\,\underline{\underline{y}} = \underline{\underline{M}}^{-1}\underline{\underline{\epsilon}}\,\underline{\underline{M}}\,\underline{\underline{y}}\,. \tag{17b}$$

All of these matrices depend on ρ; we suppress this dependence for convenience. For simplicity, we define the matrix $\underline{\underline{P}}$ (not to be confused with the matrix of reaction probabilities) to be the bracketed term in eq. (17b)

$$\underline{\underline{P}} = -(\underline{\underline{T}}^{(1)})^2 - (\underline{\underline{T}}^{(1)})' + \underline{\underline{T}}^{(2)} \tag{17c}$$

hence, eq. (17b) may be rewritten as

$$\underline{\underline{y}}'' + \underline{\underline{M}}^{-1}\,\underline{\underline{P}}\,\underline{\underline{M}}\,\underline{\underline{y}} = \underline{\underline{M}}^{-1}\underline{\underline{\epsilon}}\,\underline{\underline{M}}\,\underline{\underline{y}}\,. \tag{17d}$$

Thus, in the limit of large ρ, we are interested in the behavior of the matrices $\underline{\underline{M}}^{-1}\underline{\underline{P}}\,\underline{\underline{M}}$ and $\underline{\underline{M}}^{-1}\underline{\underline{\epsilon}}\,\underline{\underline{M}}$. The matrix $\underline{\underline{M}}$ may be obtained by solution of eq. (17a), which is a first-order matrix differential equation. Since at sufficiently large ρ, $\underline{\underline{T}}^{(1)}$ is expected to become small (numerical studies of $\underline{\underline{T}}^{(1)}$, $\underline{\underline{T}}^{(2)}$, and P will be presented below), $\underline{\underline{M}}$ might then be expected to become essentially independent of ρ. Further, $\underline{\underline{M}}$ and $\underline{\underline{P}}$ are independent of energy, hence calculation of $\underline{\underline{P}}$ and integration of eq. (17a) to obtain $\underline{\underline{M}}$ need only be done once to get a good understanding of the asymptotic properties of eq. (17d) (we also need to know the ρ dependence of ϵ, but this may be determined simply from consideration of the eigenvalues associated with the basis functions ϕ_n or χ_n.

D. Properties of the Adiabatic Coupling Matrix Elements

Before we attempt to calculate the adiabatic coupling matrix elements $\underline{\underline{T}}^{(1)}$, $\underline{\underline{T}}^{(2)}$, and $\underline{\underline{P}}$, it is useful to consider properties imposed on them by their definition. In particular, we are interested in fundamental differences between the matrices calculated for the purely polar basis functions ϕ_n and the hybrid basis functions χ_n.

1. Purely Polar Basis Functions

The $T^{(1)}$ matrix can be shown to be skew-symmetric, that is, to have the property

$$T^{(1)}_{ij} = -T^{(1)}_{ji} \tag{18a}$$

as a simple consequence of the normalization property of the ϕ_n. We suppress the ρ dependence of these quantities. The ϕ_n are real and orthonormal: hence

$$\int_0^{\alpha_{\max}} \phi_n \phi_{n'}\, d\alpha = \delta_{nn'} \tag{19a}$$

so $$\frac{\partial}{\partial\rho}\left[\int_0^{\alpha_{\max}} \phi_n \phi_{n'}\, d\alpha\right] = \int_0^{\alpha_{\max}} \frac{\partial\phi_n}{\partial\rho}\phi_{n'}\, d\alpha + \int_0^{\alpha_{\max}} \phi_n \frac{\partial\phi_n}{\partial\rho}\, d\alpha = 0 \tag{19b}$$

$$= T^{(1)}_{n'n} + T^{(1)}_{nn'} = 0$$

hence

$$T^{(1)}_{nn'} = -T^{(1)}_{n'n} \quad .$$

No similar symmetry condition exists for the $T^{(2)}$ matrix, however. This may be shown by differentiating eq. (19b) with respect to ρ:

$$\int_0^{\alpha_{\max}} \frac{\partial^2\phi_n}{\partial\rho^2}\,\phi_{n'}\,d\alpha + 2\int_0^{\alpha_{\max}} \frac{\partial\phi_n}{\partial\rho}\,\frac{\partial\phi_{n'}}{\partial\rho}\,d\alpha + \int_0^{\alpha_{\max}} \phi_n\,\frac{\partial^2\phi_{n'}}{\partial\rho}\,d\alpha = 0 \tag{20a}$$

so $$\underline{\underline{T}}^{(2)}_{n'n} + \underline{\underline{T}}^{(2)}_{nn'} = -2\langle\frac{\partial\phi_n}{\partial\rho}\,|\,\frac{\partial\phi_{n'}}{\partial\rho}\rangle\ . \tag{20b}$$

For the diagonal matrix elements $\underline{\underline{T}}^{(2)}_{nn'}$, then, one sees that

$$T^{(2)}_{nn} = -\langle\frac{\partial\phi_n}{\partial\rho}\,|\,\frac{\partial\phi_n}{\partial\rho}\rangle \tag{20c}$$

where brackets represent integrals over α. Since the integrand on the right-hand side of eq. (20c) is everywhere positive, the diagonal elements of $T^{(2)}$ must be negative.

We may also differentiate the equation for $\underline{\underline{T}}^{(1)}$ to obtain an expression for $(\underline{\underline{T}}^{(1)})'$, which is one of the components of $\underline{\underline{P}}$.

$$\underline{\underline{T}}^{(1)}_{nn'} = \langle\,\phi_n\,|\,\frac{\partial\phi_n}{\partial\rho}\,\rangle$$

$$(\underline{\underline{T}}^{(1)}_{nn'})' = \frac{\partial}{\partial\rho}\,\langle\,\phi_n\,|\,\frac{\partial\phi_{n'}}{\partial\rho}\,\rangle = \langle\frac{\partial\phi_n}{\partial\rho}\,|\,\frac{\partial\phi_{n'}}{\partial\rho}\rangle + \langle\,\phi_n\,|\,\frac{\partial^2\phi_{n'}}{\partial\rho}\,\rangle$$

so $$(\underline{\underline{T}}^{(1)}_{nn'})' = \langle\frac{\partial\phi_n}{\partial\rho}\,|\,\frac{\partial\phi_{n'}}{\partial\rho}\rangle + \underline{\underline{T}}^{(2)}_{nn'}\ . \tag{21}$$

Substitution of eq. (21c) into eq. (17) allows us to write $\underline{\underline{P}}$ by the following expression

$$\underline{\underline{P}}_{nn'} = -(\underline{\underline{T}}^{(1)})^2_{nn'} - \langle\frac{\partial\phi_n}{\partial\rho}\,|\,\frac{\partial\phi_{n'}}{\partial\rho}\rangle\ . \tag{22}$$

It is obvious that the second matrix on the right-hand side of eq. (22) is symmetric, and $(\underline{\underline{T}}^{(1)})^2$ can be shown to be symmetric as a consequence of the skew-symmetry of $\underline{\underline{T}}^{(1)}$:

$$(\underline{\underline{T}}^{(1)})^2_{ij} = \sum_k T^{(1)}_{ik}\, T^{(1)}_{kj} = \sum_k (-1)\, T^{(1)}_{ki}\, T^{(1)}_{kj} = \sum_k (-1)^2 T^{(1)}_{ki}\, T^{(1)}_{jk} = \sum_k T^{(1)}_{jk} T^{(1)}_{ki}$$

$$(\underline{\underline{T}}^{(1)})^2_{ij} = (\underline{\underline{T}}^{(1)})^2_{ji} \tag{23}$$

Hence, since both terms on the right-hand side of eq. (23) are symmetric, $\underline{\underline{P}}$ is symmetric.

Some properties of the matrix $\underline{\underline{M}}$ defined by eq. (16) may be ascertained by considering the effect of the skew-symmetry of $\underline{\underline{T}}^{(1)}$ in this coordinate system. This is best seen in the two-state case, in which an analytic treatment of the differential equation (17a) becomes possible. In this case, there is only one independent non-zero $T^{(1)}$ matrix element, which can be represented by the expression $f(\rho)$. We will later examine the case where $f(\rho)$ behaves asymptotically like $\rho^{-\nu}$ where ν less than or equal to one, as we are especially interested in the asymptotic behavior of $\underline{\underline{M}}$. Writing

$$T^{(1)} = \begin{pmatrix} 0 & f(\rho) \\ -f(\rho) & 0 \end{pmatrix}. \tag{24}$$

We recognize that $T^{(1)}$ may be diagonalized by the transformation

$$\underline{\underline{\lambda}} = \underline{\underline{\Lambda}}^{-1}\, \underline{\underline{T}}^{(1)}\, \underline{\underline{\Lambda}} \ , \tag{25}$$

where the eigenvalues $\lambda_\pm$ aregiven by the expression

$$\lambda_{\pm} = \pm\, i f(\rho) \tag{26}$$

and the matrix $\underline{\underline{\Lambda}}$ has the form

$$\underline{\underline{\Lambda}} = \begin{pmatrix} 1/\sqrt{2} & 1/\sqrt{2} \\ i/\sqrt{2} & -i/\sqrt{2} \end{pmatrix} \tag{27}$$

If we define a new matrix $\underline{\underline{N}}$ by the expression

$$\underline{\underline{M}} = \underline{\underline{\Lambda}}\, \underline{\underline{N}}\,, \tag{28}$$

one can show, given the ρ independence of $\underline{\underline{\Lambda}}$, that the differential equation becomes

$$\underline{\underline{N}}' = -\underline{\underline{\lambda}}\, \underline{\underline{N}}. \tag{29}$$

Since λ is diagonal, one had four uncoupled differential equations for the elements N_{ij} of $\underline{\underline{N}}$. If we start integrating eq. (29) at some value of $\rho = \rho_0$ where $N_{ij}(\rho_0) = N^{o}_{ij}$, then the solutions of eq. (29) are given by the equations

$$N_{1j}(\rho) = N^{o}_{1j}\, e^{-i\int f(\rho)d\rho} = N^{o}_{ij}\, F_{-}(\rho) \tag{30a}$$

$$N_{2j}(\rho) = N^{o}_{ij}\, e^{i\int f(\rho)d\rho} = N^{o}_{ij}\, F_{+}(\rho) \tag{30b}$$

where $j = 1, 2$.

Without loss of generality, let us take $\underline{\underline{M}}(\rho_0) = \underline{\underline{I}}$. Then

$$\underline{\underline{N}}(\rho_0) = \underline{\underline{\Lambda}}^{-1} = \begin{pmatrix} 1/\sqrt{2} & -i/\sqrt{2} \\ 1/\sqrt{2} & i/\sqrt{2} \end{pmatrix} \tag{31}$$

and one can show that

$$M = \begin{pmatrix} C(\rho) & -D(\rho) \\ D(\rho) & C(\rho) \end{pmatrix} \quad (32)$$

where

$$C(\rho) = F_+(\rho) + F_-(\rho) = \cos \int f(\rho)\, d\rho \quad (33a)$$

$$D(\rho) = -i[F_+(\rho) - F_-(\rho)] = \sin \int f(\rho)\, d\rho \quad (33b)$$

An important point is to be learned from eqs. (32) and (33): These elements of $\underline{\underline{M}}$ will oscillate with ρ at a frequency which will vary with ρ depending on the way in which the off-diagonal element of $T^{(1)}$ varies with ρ.

In the case that $f(\rho)$ has the form given by eq. (1)

$$f(\rho) = a\rho^{-\nu} \quad (34)$$

we may easily evaluate the integral in eqs. (33) a d obtain explicit expressions for $C(\rho)$ and $D(\rho)$. If ν is a positive number greater than one, we may write

$$C(\rho) = \cos \bar{f}(\rho) \quad (35a)$$

$$D(\rho) = \sin \bar{f}(\rho) \quad (35b)$$

where $$\bar{f}(\rho) = \frac{a}{1-\nu}\rho^{1-\nu} \quad (36a)$$

Thus, as ρ increases, $\rho^{1-\nu}$ decreases and the frequency of oscillations of $C(\rho)$ and $D(\rho)$ will decrease with increasing ρ. If ν equals one, eqs. (35) will hold with $\bar{f}(\rho)$ defined by

$$\bar{f}(\rho) = a \ln(\rho) \quad . \tag{36b}$$

Thus, a plot of the elements of $\underline{\underline{M}}$ would be expected to oscillate with ρ at a frequency which is independent of $a \ln(\rho)$. We will present numerical results for a more realistic system later.

Let us now briefly consider the behavior of the other matrices in eqs. (17), in particular $\underline{\underline{\epsilon}}$, $\underline{\underline{P}}$, and the form in which they appear in eqs. 17d

$$\underline{\underline{R}} = \underline{\underline{M}}^{-1}\, \underline{\underline{\epsilon}}\, \underline{\underline{M}} \tag{37a}$$

$$\underline{\underline{Q}} = \underline{\underline{M}}^{-1}\, \underline{\underline{P}}\, \underline{\underline{M}} \quad . \tag{37b}$$

Note that this $\underline{\underline{R}}$ should not be confused with the reactance matrix. From its definition in eq. (9) we recall that $\underline{\underline{\epsilon}}$ is diagonal. At the large values of ρ at which we are mainly interested, the $\hbar^2/2\mu\rho^2$ may be safely neglected. Hence we may write

$$\epsilon_{ij} \approx [- \frac{2\mu}{\hbar^2}\, (E - E_i(\rho))]\, \delta_{ij} \quad . \tag{38}$$

This matrix may be broken up into two parts: one bound ($\underline{\underline{\epsilon}}^b$) and one continuum ($\underline{\underline{\epsilon}}^c$):

$$\underline{\underline{\epsilon}}_{ij} = \begin{pmatrix} \underline{\underline{\epsilon}}^b & \underline{\underline{0}} \\ \underline{\underline{0}} & \underline{\underline{\epsilon}}^c \end{pmatrix} \tag{39}$$

$\underline{\underline{\epsilon}}^b$ and $\underline{\underline{\epsilon}}^c$ are square matrices of dimensions $N_b \times N_b$ and $N_d \times N_d$, respectively, where N_b is the number of bound states and N_d is the number of dissociative states being integrated. We assume that at the large values of ρ being considered here, the eigenvalues $E_i(\rho)$ above dissociation will be sufficiently small that they are much less than the energy **E** (this assumption will obviously not be correct at energies very close to the threshold for dissociation). Thus the matrix $\underline{\underline{\epsilon}}^c$ is a constant matrix of a scalar whose elements are given by

$$\epsilon_i^c \approx -\frac{2\mu E}{\hbar^2} \tag{40}$$

(the notation reminds us that $\underline{\underline{\epsilon}}^d$ is diagonal). For the bound states we expect that the eigenvalues $E_i(\rho)$ become independent of ρ at large ρ and thus the matrix $\underline{\underline{\epsilon}}^b$ will become independent of ρ. Unlike $\underline{\underline{\epsilon}}^c$, however, $\underline{\underline{\epsilon}}^b$ is not a matrix of a scalar; its elements are given by eq. (38). Since $\underline{\underline{\epsilon}}^b$ is diagonal, we will use only a single subscript as we did with $\underline{\underline{\epsilon}}^d$.

For the simple 2 × 2 case considered here, we may evaluate $\underline{\underline{R}}$ in terms of the elements of $\underline{\underline{M}}$ and $\underline{\underline{\epsilon}}^b$ (we assume in the 2 × 2 case we are integrating two bound states). If we define $C = c(\rho)$ and $D = D(\rho)$, we may write

$$\underline{\underline{R}} = \underline{\underline{M}}^{-1}\underline{\underline{\epsilon}}\,\underline{\underline{M}} = \begin{pmatrix} C & D \\ -D & C \end{pmatrix}\begin{pmatrix} \epsilon_0^b & 0 \\ 0 & \epsilon_1^b \end{pmatrix}\begin{pmatrix} C & -D \\ D & C \end{pmatrix} = \begin{pmatrix} \epsilon_0^b C^2 + \epsilon_1^b D^2 & (\epsilon_1^b - \epsilon_0^b)CD \\ (\epsilon_1^b - \epsilon_0^b)CD & \epsilon_0^b D^2 + \epsilon_1^b C^2 \end{pmatrix} \tag{41}$$

We emphasize that ϵ_0^b and ϵ_1^b are essentially independent of ρ, so that the ρ dependence in $\underline{\underline{R}}$ will come entirely from that of $\underline{\underline{M}}$.

We now consider the behavior of $\underline{\underline{Q}}$ in the 2 × 2 case. Recalling that $\underline{\underline{P}}$ is symmetric, we write

$$\underline{\underline{P}} = \begin{pmatrix} t & u \\ u & v \end{pmatrix} \tag{42}$$

and can show that

$$\underline{\underline{Q}} = \begin{pmatrix} t\,C^2 + v\,S^2 + 2u\,CS & (v-t)\,CS + u\,C_2 \\ (v-t)\,CS + u\,C_2 & t\,S^2 + v\,C^2 - 2u\,CS \end{pmatrix} \tag{43}$$

where $$C_2 = \cos 2\bar{f}(\rho) \tag{44}$$

Assuming that t, u, and v defined in eq. (42) will all decay fairly rapidly with ρ, we expect that the matrix element of $\underline{\underline{Q}}$ will also decrease fairly rapidly. Superimposed on this decay, however, will be oscillations produced by the C^2, S^2, and CS terms. While this form for $\underline{\underline{Q}}$ is quite complicated, we note that as $\underline{\underline{Q}}$ decreases with increasing ρ, $\underline{\underline{R}}$ will oscillate with a rate determined by the oscillations in C and D, and the differential eq. (17d) becomes, at large ρ

$$\underline{\underline{y}}'' = \underline{\underline{R}}\,\underline{\underline{y}} \ . \tag{45}$$

This equation will not yield to simple analytic solution in spite of its being only a 2 × 2 matrix equation, because of the ρ dependence of $\underline{\underline{R}}$. Since $\underline{\underline{R}}$ derived in eq. (41) is symmetric, it can be diagonalized with real eigenvalues and eigenvectors which will vary with ρ. It is this ρ variation which makes a simple analytic integration of eq. (45) impossible, and we would be forced, even in the 2 × 2 case, to evaluate y'' numerically. Because of the absence of the first derivative term, standard integrators, such as Gordon's method (10) should be able to be used with little or no difficulty.

As a result of the simple form of eq. (45) and the relationship of $\underline{\underline{R}}$ to $\underline{\underline{\epsilon}}$, we expect that for closed channels $\underline{\underline{y}}$ will experience exponential growth, while for open channels $\underline{\underline{y}}$ will undergo oscillations. Thus, at energies above dissociation, $\underline{\underline{y}}$ should grow exponentially when ρ is small because the eigenvalues $E_i(\rho)$ may be greater than the energy, but at large ρ, when all channels are open, $\underline{\underline{y}}$ should stop growing and should instead oscillate at some variable frequency.

2. Hybrid Basis Functions

Matrix elements of the hybrid basis functions χ_n must be broken up into three portions, corresponding to regions (1), (2), and (3) in Fig. 1 and discussed above. We will use angular brackets to denote the sum of the three separate integrals. In this notation, the normalization condition in eq. (14a) may be written simply as

$$\langle \chi_n | \chi_{n'} \rangle = \delta_{nn'} \ . \tag{46}$$

When working with the hybrid basis functions, the equations for the radial wavefunction matrix are the same as in the purely polar case (eq. 8) except that all derivatives are with respect to R rather than ρ. Since R, the propagation variable most appropriate in region 1, is simply related to the more appropriate propagation variables ρ' in region 2 and R′ in region 3, the derivative with respect to R in region 1 can be equated to one with respect to ρ' in region 2 and R′ in region 3.

The major differences between the properties of the adiabatic coupling matrix elements in the purely polar and hybrid basis functions can be shown to result from the presence of the ρ' term in the region 2 portion of the normalization integral in eq. (46). For example, $\underline{\underline{T}}^{(1)}$ may be studied by differentiating the normalization eq. (46) as follows:

$$\frac{\partial}{\partial R}\langle \chi_n | \chi_{n'} \rangle = \frac{\partial}{\partial R}\left\{ \int_0^{r_{\lambda_0}} \chi_n^{(1)} \chi_{n'}^{(1)}\, dr_\lambda + \int_0^{\alpha'_{\max}} \chi_n^{(2)} \chi_{n'}^{(2)} \rho'\, d\alpha \right.$$

$$\left. + \int_{\kappa_0}^{0} \chi_n^{(3)} \chi_{n'}^{(3)}\, dr_\kappa \right\} = 0. \qquad (47)$$

The $\underline{\underline{T}}^{(1)}$ matrix may be written in the following way:

$$\underline{\underline{T}}^{(1)}_{nn'} = \langle \chi_n | \frac{\partial \chi_{n'}}{\partial R} \rangle = \int_0^{r_{\lambda_0}} \chi_n^{(1)} \frac{\partial \chi_{n'}^{(1)}}{\partial R}\, dr_\lambda + \int_0^{\alpha'_{\max}} \chi_n^{(2)} \left(\frac{\partial \chi_{n'}^{(2)}}{\partial \rho'}\right) \rho'\, d\alpha$$

$$+ \int_{r_{\kappa_0}}^{0} \chi_n^{(3)} \frac{\partial \chi_{n'}^{(3)}}{\partial R'}\, dr_\kappa \,, \qquad (48)$$

hence,

$$\underline{\underline{T}}^{(1)}_{nn'} + \underline{\underline{T}}^{(1)}_{n'n} = -\int_0^{\alpha'_{\max}} \chi_n^{(2)} \chi_{n'}^{(2)}\, d\alpha. \qquad (49)$$

The integral on the right-hand side of eq. (49) is equal to $1/\rho'$ times the portion of the normalization integral coming from region 2. For diagonal terms corresponding to dissociative χ_n, essentially all of the contribution to the normalization eq. should come from region 2, and hence the right-hand side of eq. (26) may be replaced by $-\frac{1}{\rho'}$ for dissociative states. Hence, for diagonal dissociative terms

$$T^{(1)}_{nn} \approx -\frac{1}{2\rho'} \qquad n > n_{\text{diss}} \quad . \qquad (50)$$

For diagonal bound terms the right-hand side of eq. (26) should be close to zero, as the bound χ_n should be vanishingly small in the region 2. Therefore the bound diagonal terms $T^{(1)}_{nn}$, $n < n_{diss}$ should be zero, and their magnitude should decrease as n decreases.

By differentiation of eq. (24), one may obtain the following expression for the $T^{(2)}$ matrix:

$$T^{(2)}_{nn'} + T^{(2)}_{n'n} + 2\langle \frac{\partial \chi_n}{\partial R} \,|\, \frac{\partial \chi_{n'}}{\partial R} \rangle + 2 \int_0^{\alpha'_{max}} \chi^{(2)}_{n'} \frac{\partial \chi_n}{\partial \rho'} \, d\alpha' + 2 \int_0^{\alpha'_{max}} \chi^{(2)}_{n} \frac{\partial \chi_{n'}}{\partial \rho'} \, d\alpha' = 0. \tag{51}$$

For diagonal elements, then

$$T^{(2)}_{nn} = -\langle \frac{\partial \chi_n}{\partial R} \,|\, \frac{\partial \chi_n}{\partial R} \rangle - 2 \int_0^{\alpha'_{max}} \chi^{(2)}_{n} \frac{\partial \chi^{(2)}_n}{\partial \rho'} \, d\alpha'. \tag{52}$$

By an argument analogous to that used in obtaining eq. (50), we may assume for dissociative states that the second integral on the right-hand side of eq. (52) is given by $\frac{1}{\rho'} \underline{\underline{T}}^{(1)}_{nn}$. Using eq. (41), which gives a formula for the dissociative diagonal elements of $\underline{\underline{T}}^{(1)}$, we may write

$$T^{(2)}_{nn} \approx -\langle \frac{\partial \chi_n}{\partial R} \,|\, \frac{\partial \chi_n}{\partial R} \rangle + \frac{1}{\rho'^2} \ . \tag{53}$$

Similarly to $T^{(1)}_{nn}$, the bound diagonal elements of $\underline{\underline{T}}^{(2)}$ may be expected to be dominated by the first term on the right-hand side of eq. (53), as the bound χ_n are essentially zero in region 2.

Just as an expression relating $(\underline{\underline{T}}^{(1)})'$ to $\underline{\underline{T}}^{(2)}$ was obtained in the purely polar case (eq. (21)), an analogous expression may be obtained for this hybrid case

$$(T^{(1)}_{nn'})' = \langle \frac{\partial \chi_n}{\partial R} \Big| \frac{\partial \chi_{n'}}{\partial R} \rangle + \underline{\underline{T}}^{(2)}_{nn'} + \int_0^{\alpha'_{max}} \chi_n^{(2)} \frac{\partial \chi_{n'}^{(2)}}{\partial \rho'} \, d\alpha'. \tag{54}$$

Hence, one may rewrite the $\underline{\underline{P}}$ matrix in the hybrid case by the following expression:

$$\underline{\underline{P}}_{nn'} = -(\underline{\underline{T}}^{(1)})^2_{nn'} - \langle \frac{\partial \chi_n}{\partial R} \Big| \frac{\partial \chi_{n'}}{\partial R} \rangle - \int_0^{\alpha'_{max}} \chi_n^{(2)} \frac{\partial \chi_{n'}^{(2)}}{\partial \rho'} \, d\alpha'. \tag{55}$$

Since the $\underline{\underline{T}}^{(1)}$ matrix in the hybrid case is not skew-symmetric, the $(\underline{\underline{T}}^{(1)})^2$ matrix is not necessarily symmetric; obviously the third term on the right-hand side of eq. (50) need not give rise to a symmetric matrix. Hence, the $\underline{\underline{P}}$ matrix in the hybrid case need not be symmetric.

The presence of additional terms in the expressions for the $\underline{\underline{T}}^{(1)}$, $\underline{\underline{T}}^{(2)}$, and $\underline{\underline{P}}$ matrices in the hybrid coordinate system implies that the $\underline{\underline{P}}$ matrix in this system (and also the $\underline{\underline{M}}$ matrix) may have a very different behavior than in the purely polar system. Which one will prove superior (earlier onset of simple analytic behavior and/or more rapid decay of the appropriate matrix elements) will be considered in the subsequent discussion. Because in this hybrid coordinate system $\underline{\underline{T}}^{(1)}$ is not skew-symmetric, the simple analysis employed at the end of the previous section of the ρ dependence of $\underline{\underline{M}}$ does not apply. Since we will only present numerical results for $\underline{\underline{M}}$ and the matrices obtained from it for the purely polar basis functions, we will not attempt to perform such an analysis here.

E. Flat Channel Case in the Purely Polar System

To help provide some guidance for the analysis of the data for the continuum states obtained, we consider, in the purely polar coordinate system, the properties of the eigenfunctions $\phi_n(\rho, \alpha)$ and their associated eigenvalues $E_n(\rho)$ at large values of ρ for a particle moving in the one-dimensional potential

$$\left.\begin{aligned} V(S=0) &= V(S = \rho\alpha_{\max}) = \infty . \\ V(0 < S < \rho\alpha_{\max}) &= 0. \end{aligned}\right\} \tag{5}$$

This is just the one-dimensional particle-in-a-box problem, except that the box becomes longer as ρ increases (in fact, the box length is directly proportional to ρ). This model is not as irrelevant to the problem under consideration here as might first appear. At sufficiently large ρ, the wells in the actual potential $V(\rho, \alpha)$ are extremely narrow, and might be expected to have only a minor influence on the dissociative basis functions $\phi_n(\rho, \alpha)$. Since the true potential $V(\rho, \alpha)$ does go to zero at $\alpha = 0$ and $\alpha = \alpha_{\max}$ and is essentially zero for $\delta\alpha < \alpha < \alpha_{\max} - \delta\alpha$ where $\delta\alpha$ is a small quantity (which decreases as ρ increases), the flat channel case is a reasonable model for the continuum states.

We now consider the implications of the flat channel model for the asymptotic behavior of the eigenvalues $E_n(\rho)$. Since the length of the box, ℓ, in this model is given by

$$\ell = \rho \cdot \alpha_{\max} , \tag{57}$$

The well known equation for energy levels of a particle-in-a-box becomes

$$E_n(\rho) = \frac{h^2 n^2}{8m\alpha_{\max}^2 \rho^2} . \tag{58}$$

The eigenfunctions ϕ_n^{model} are, however, independent of ρ. Hence all matrices of the type $\underline{\underline{T}}^{(1)}$, $\underline{\underline{T}}^{(2)}$, and $\underline{\underline{P}}$ will be zero in this model. The reasonableness of this model will be shown by examining some of the basis functions $\phi_n(\rho, \alpha)$ at moderately large (for this paper) values of ρ, as well as by examining the behavior of the eigenvalues $E_n(\rho)$ at large ρ.

III. Numerical Techniques and Potential Energy Surface Used

A. Numerical Techniques

The second-order differential equations for the basis functions (i.e., eq. (3) for the purely polar and eqs. (10) for the hybrid) are solved by a finite difference procedure.[11] The tridiagonal matrix obtained by substituting in the second difference for the second derivative is then treated by a Givens-Householder technique[12] in order to obtain the appropriate set of eigenvalues and eigenvectors. This treatment is particularly simple when a constant grid size is used in the discretization of the potential and the basis functions, that is, when the basis functions are to be determined at a set of values x_n, where $x_{n-1} - x_n = h$, a constant, for all n. When this is the case, the second-order difference used is just

$$\left(\frac{d^2y}{dx^2}\right)_{x=x_n} = \frac{y_{n+1} - 2y_n + y_{n-1}}{2h} , \tag{59}$$

where $y_n = y(x_n)$, etc., and the tridiagonal matrix obtained is symmetric.

At the large values of ρ considered in this study, however, a constant grid size is not an efficient one, as there will be large numbers of oscillations of the basis functions in the well region with smaller numbers, if any, in the plateau region. The larger ρ gets, the narrower the wells become (viewed as a function of α) and the greater the difference between the grid size needed in the well and the plateau regions. This may be seen by examination of Fig. 3 of Ref. 1, which shows cuts of the potential at constant $\bar{\rho}$. At 20 bohr, the largest value of $\bar{\rho}$ for which the potential is pictured, the wells occupy roughly 33% of the range of α, the potential is zero over roughly 50% of the range of α. The smallness of the width of the well at large ρ suggests that at large ρ a multi-tiered grid is needed. In the well region, then, a constant stepsize of h_1 might be needed, whereas in the plateau region, a larger step size of h_2 might be used. The relative ratio of h_2 to h_1 can be expected to increase as ρ increases. It turns out that numerical instability appears to result whenever the ratio of step sizes h_2/h_1 gets too large. To eliminate this problem, we found it necessary to introduce a third, very narrow region of α space between the well and the plateau regions in which the step size is the geometric mean of that in in the two regions. This division of the arc into three regions is pictured schematically in Fig. 2. A similar division of the discretization was performed in calculations of the hybrid basis functions, these various relationships between the step sizes were tried, with the general feature that at large R, $h_{\text{plateau}} \gg h_{\text{int}} \gg h_{\text{well}}$, where each h is measured in terms of distance [r_λ in region (1), $\rho'\alpha'$ in region 2, r_κ in region 3].

Once a non-uniform grid has been introduced into the calculation, two complications occur. First, a new more general finite difference expression for the second derivative must be used, as eq. (59) only applies to a regularly spaced grid of points. We choose to approximate the basis function by a quadratic in each three-point interval. In the case of equally space points, the finite difference expression reduces to eq. (59); when points are not equally spaced, which occurs at the boundary between the areas of different step size, the following difference procedure is used:

$$\left(\frac{d^2y}{dx^2}\right)_{x=x_n} = \frac{2\left[y_{n+1}(x_n - x_{n-1}) - y_n(x_{n-1} - x_{n-1}) + y_{n-1}(x_{n-1} - x_n)\right]}{(x_{n+1} - x_n)(x_{n+1} - x_{n-1})(x_n - x_{n-1})} . \tag{60}$$

Second, the tridiagonal matrix obtained is no longer symmetric, which means that one must symmetrize it before using the Givens-Householder method to obtain the eigenvalues. This symmetrization may be performed providing corresponding sub- and super-diagonal elements are both zero, both positive, or both negative.[13] Since in this problem, they are both positive (except in certain cases when the potential is symmetric and the calculation runs over the entire range of α; then both are zero), so the symmetrization can always be performed. The transformations necessary are described in reference 13, and computer programs employing them were obtained from an EISPACK guide.[14]

In all calculations reported here, little, if any, attempt was made to converge all the numbers (eigenvalues, eigenfunctions, adiabatic coupling matrix elements) to absolutely correct values. Since we are mainly concerned with rough power-law type behavior, such as that indicated in eq. (1), we simply chose what seemed to be reasonable parameters (number of points, relative step sizes, boundary between step sizes) and performed an entire set of calculations with these parameters. It is assumed the the general features of the dependence of the quantities of interest are independent of the exact parameters used. Where information as to sensitivity has been obtained, it will be commented on.

Adiabatic coupling matrices were obtained by calculating the eigenfunctions ϕ_n or χ_n at three closely spaced values of ρ or R, respectively. A finite difference form of the derivative with respect to ρ was then used to calculate the derivatives of the basis functions with respect to the propagation variable (ρ or R).

$$\left(\frac{\partial\phi}{\partial\rho}(\rho,\alpha)\right)_{\rho=\rho_0} = \frac{1}{2(\delta\rho)}\left(\phi(\rho_0+\delta\rho,\alpha) - \phi(\rho_0-\delta\rho,\alpha)\right) \tag{61a}$$

$$\left(\frac{\partial^2\phi}{\partial\rho^2}(\rho,\alpha)\right)_{\rho=\rho_0} = \frac{1}{(\delta\rho)^2}\left(\phi(\rho_0+\delta\rho,\alpha) - 2\phi(\rho_0,\alpha) + \phi(\rho_0-\delta\rho,\alpha)\right) \tag{61b}$$

Similar expressions were obtained for $\partial\chi/\partial R$ and $\partial^2\chi/\partial R^2$. In all cases, the values of the $\underline{\underline{T}}^{(1)}$ and $\underline{\underline{T}}^{(2)}$ matrices were found to vary very weakly with δ_ρ. Normally δ_ρ was no more than 0.0025ρ and was frequently much smaller. Integrals were evaluated via trapezoidal rule approximation. Some tests of the accuracy of the numerical calculations employed were provided by the properties of the adiabatic coupling matrices outlined in section 2, such is the skew-symmetry of $\underline{\underline{T}}^{(1)}$ and the symmetry of $\underline{\underline{P}}$ for the purely polar basis set. We will comment on the ability of the calculation to obtain these properties later.

B. Potential Energy Surfaces

Calculations were performed on two different potential energy surfaces. The first (and the one to which most attention will be paid) is the Porter-Karplus surface for $H + H_2$.[15] This is the surface used in the calculations discussed in refs. 1 and 4 and is typical of realistic potential surfaces for reactive scattering. The second ("the dissociative" surface) is the same used in the model study of CID in reference 3. This surface is of the rotating Morse-cubic spline type,[16] and for the hydrogen atom masses used here and in ref. 3, supports only two bound states in each arrangement channel. A major reason for looking at the second surface is that we have substantial information on the rate of convergence of bound-continuum transition probabilities with the stopping point of the integration, and we hope to be able to relate that to the relative magnitude of the adiabatic coupling matrix elements. We also want to learn how, if at all, the limiting exponents of the type in eq. (1)

depend on the exact surface used. We will use this dissociative surface in our numerical integration of eqs. (17).

IV. Results

In this section we will present some of the results of the calculations performed on the two potential energy surfaces using both the purely polar and the hybrid basis functions. We will emphasize our work on the ρ dependence of the adiabatic coupling matrix elements on the PK H_3 surface, and will briefly present some of the results obtained on the dissociative surface. First we will consider the purely polar basis functions, then we will consider the hybrid ones. In the ensuing discussion we will compare some of the properties of the quantities of interest. For both basis sets, we will consider the eigenvalues as a function of the propagation variable, and will then consider the adiabatic coupling matrix elements. We will also show some plots of the purely polar basis functions, which should help in understanding some of the results obtained for that set of basis functions. We will close by presenting results of numerical integration of the adiabatic equations on this surface.

A. Purely Polar Coordinate Basis Functions

1. Appearance of the basis functions at large ρ

Intuition tells us that at large ρ, the bound basis functions should be localized into the well region of the potential, while the dissociative basis functions should be spread out over the entire range of α. One question of particular interest is the relative fraction of the dissociative basis functions located in the well region. If it turns out that the dissociative basis functions are small in the well region, then the particle-in-a-box model for dissociative states outlined above should be valid.

Plots of the 17th, 19th, and 21st even eigenfunctions for the PK H_3 surface at 50 and 100 bohr are presented in Figs. 3 and 4, respectively. The 17th even eigenfunction is the highest even bound eigenfunction. Only the $0 < \alpha < \alpha_{max}|2$ range is plotted due to the symmetry of the eigenfunction. It is clear for the figures that at large ρ the dissociative basis functions are essentially confined to the plateau region; their amplitude in the well region is quite small compared to that in the plateau region. The small α part of these basis functions is blown up and presented in Figs. 5 and 6 for 50 and 100 bohr, respectively. One can see that the location at the maxima and minima in the dissociative basis functions shown are independent of quantum number and that as ρ increases, their oscillatory part is compressed into an ever decreasing range of α. Finally, in Figs. 7 and 8, we plot the basis functions vs. $\rho \cdot \sin\alpha$ at 50 and 100 bohr, respectively. It is clear that the positions of the minima and maxima at both distances occur at the same values of $\rho \cdot \sin\alpha$ (note that $\rho \cdot \sin\alpha$ is just the distance r_λ).

2. Eigenvalues at large ρ

We will be concerned mainly with the eigenvalues $E_{n_d}(\rho)$ of the dissociative states n_d, but will comment on those of the bound states also. In Fig. 9, the eigenvalues of the eight lowest even dissociative states are plotted vs. ρ in a log-log plot. It is seen that for a given quantum number, there is a linear relationship between the logarithm of the eigenvalue and that of ρ. Slopes are in the range from -2.06 to -2.11. Recall for a particle in a box, these would be related by a line with slope -2. Another test of the validity of the particle-in-a-box model can be made by examining the relationship between the eigenvalues of the dissociative states and their derivatives with respect to ρ. In the particle-in-a-box model, the energy levels are given by eq. (58). Differentiation of that expression gives expressions for $dE_{n_d}(\rho)/d\rho$ and $d^2E_{n_d}(\rho)/d\rho^2$

$$\frac{dE_{n_d}(\rho)}{d\rho} = -\frac{2h^2 n_d^2}{8m\alpha_{max}^2 \rho^3} = -\frac{2}{\rho}\left[E_{n_d}(\rho)\right] \qquad (62a)$$

$$\frac{d^2E_{n_d}(\rho)}{d\rho^2} = \frac{6h^2 n_d^2}{8m\alpha_{max}^2 \rho^4} = \frac{6}{\rho^2}\left[E_{n_d}(\rho)\right] = -\frac{3}{\rho}\,\frac{dE_{n_d}(\rho)}{d\rho} \qquad (62b)$$

Values of these derivatives and some of the ratios to each other and to the eigenvalues are given in Table 1. It may be seen that at large ρ ($\geq$ 500 bohr) eq. (62a) is fairly well obeyed (to 5%); eq. (62b) is less well obeyed, and the quality of obeying deteriorates once ρ gets beyond 500 bohr. Some of this deterioration may be due to numerical instabilities, it is clear, however, that eq. (62b) is substantially less well approximated by the data. In testing the validity of the particle-in-a-box model, it is also worth checking whether $E_{n_d}(\rho) \propto n_d^2$ for a given ρ. The logarithm of $E_{n_d}(\rho)$ plotted vs. log n_d is displayed in Fig. 10, and the resulting curves for a given ρ are linear with slopes very close to 2.

We have also looked at the eigenvalues of the seven highest even bound states. Plots of the log of the difference between the eigenvalue for three of these vs. log of ρ are presented in Fig. 11. There is no well defined behavior in these curves, although the similarity between r = 10 and n = 13 curves is obvious. It will be seen shortly that the eigenvalues of the bound states are far more constant in the hybrid basis set.

3. Adiabatic coupling matrix elements

We next consider the elements of $\underline{\underline{T}}^{(1)}$, $\underline{\underline{T}}^{(2)}$, and P as a function of ρ. Several $T_{ij}^{(1)}$ are plotted vs. ρ (in a log-log plot) in Fig. 12. The bound-bound (b-b) $T^{(1)}$ matrix elements form a linear plot for ρ above 50 bohr with slope close to -1; the bound-continuum (b-c) ones are linear over a fairly broad range of ρ, although curvature sets in near $\rho \approx 1000$ bohr. The linear ranges of these plots have slopes in the range -2.3 to -2.5. The continuum-continuum (c-c) ones are linear over a shorter range, and have slopes of roughly -1.9. These data are summarized in Table 2.

In all cases, the diagonal elements of $\underline{\underline{T}}^{(1)}$ are many orders of magnitude smaller than nearby off-diagonal ones. For example, at 15 bohr, $T_{18,18}^{(1)} = 1.4 \times 10^{-5}$, while $T_{20,18}^{(1)} = 0.34$; at 2500 bohr the numbers are 9.6×10^{-11} and 2.1×10^{-5}, respectively. Thus, to a very good degree of approximation, the diagonal elements of $\underline{\underline{T}}^{(1)}$ are zero, which is a necessary consequence of the predicted skew-symmetry of $\underline{\underline{T}}^{(1)}$. The skew-symmetry may be checked explicitly by comparing appropriate matrix elements. For all elements studied at all distances, approximate skew-symmetry was observed. In some cases, skew-symmetry to four figures was obtained; in others it was only 10%. On the whole, the approximate skew-symmetry obtained provides a good check in the numerical methods used in the calculation of $\underline{\underline{T}}^{(1)}$.

Plots of some b-b and b-c off-diagonal elements of $\underline{\underline{T}}^{(2)}$ are given in Fig. 13. For b-b and b-c elements, the plots are linear over a fairly broad range of ρ, although the deviation from linearity becomes substantial at large ρ ($\gtrsim$ 1000 bohr). The off-diagonal c-c curves have no real region of linearity and are not shown. As in the $T^{(1)}$ case, the slopes differ depending on the matrix element. The b-b matrix elements give rise to a line with slope close to -2; the b-d ones lead to a slope in the range -3.1 to -3.3. The diagonal $T^{(2)}$ matrix elements (not shown) show similar behavior. The b-b diagonal matrix elements give rise to plots with slopes very close to -2; their value varies only slightly from element to element. The c-c diagonal matrix elements behave quite differently. The slopes on the corresponding plots vary widely (from -3.85 for $n = 22$ to -5.5 for $n = 17$), and as a result, at moderate ρ, the magnitudes of the matrix elements vary substantially from element to element. At large ρ (the exact value of which increases as n increases), deviation from linearity occurs.

The elements of $\underline{\underline{P}}$ behave similarly to those of $\underline{\underline{T}}^{(2)}$. Their values and ρ-dependence are determined largely by the type of matrix element (b-b, b-c, c-c). This segregation can be seen quite clearly in Fig. 14. Slopes of the b-b, b-c, and c-c plots are in the range of -1.9, -3.2, and -4.0 to 4.5, respectively. All of the slope data are summarized in Table 2.

B. The Hybrid Basis Functions

Although the propagation variable in the hybrid coordinates is R, we will plot eigenvalues and matrix elements of the hybrid basis functions as a function of ρ'. This should be a more appropriate variable for the continuum states, which are the ones in which we are most interested. Recall that in deriving approximate expressions for the diagonal dissociative terms of $T^{(1)}$ and $T^{(2)}$, ρ' came into the final answer in a simple way.

1. Eigenvalues at large ρ'

The eigenvalues of the hybrid basis functions are calculated to vary as ρ'^{-2} (slopes of the appropriate log-log plot ranged from 1.98 to 2.00). This behavior is very similar to that of the eigenvalues of the purely polar basis functions. Also as in the purely polar case, the eigenvalues obey a relationship of the type $E_n(\rho') \propto n^2$, where n is the effective quantum number of the dissociative state (n = 1 for the first even dissociative state, 2 for the first odd dissociative state, etc.) This is approximately true for all R > 50 bohr; at smaller R, the log E vs. log n has pronounced curvature at low n. The eigenvalues of the bound states calculated in the hybrid basis set are far more stable with respect to a change in the propagation variable than those calculated with the purely polar basis set. This may be seen in Fig. 15, in which the log of the energy difference between the eigenvalue at a given ρ' and the corresponding one at $\rho' = 4989$ bohr is plotted vs. the log of ρ'. For all but the highest bound state, these curves are essentially flat over the whole range of ρ' considered. The change in eigenvalues at the largest values of ρ' is probably due to numerical instability resulting from the large disparity between the step sizes in the three regions along the cut through the potential (see Fig. 2).

2. Adiabatic coupling matrix elements

The adiabatic coupling matrix elements are plotted vs. ρ' as log-log plots in Figs. 16 through 18. In Fig. 16 various $T^{(1)}$ matrix elements are considered and in Fig. 17 the $T^{(2)}$ ones are examined. In both, three main features are apparent. First, at large values of ρ', the diagonal matrix elements are the largest. Second, there are only two different classes of lines, as determined by their slopes. The b-b matrix elements have slopes close to -1 for $T^{(1)}$ and -2 for $T^{(2)}$; the b-d and c-c ones have slopes close to -2.5 for $T^{(1)}$ and -3.5 for $T^{(2)}$. (Some matrix elements, especially for $T^{(1)}$ changed sign once or twice over the ρ' range examined and were not plotted on these plots.) Third, the b-b matrix elements involving more deeply bound states are orders of magnitude smaller than those of higher states. For example, $T^{(2)}_{14,16}(\rho' = 1000) \approx 1000\, T^{(2)}_{12,16}$ ($\rho' = 1000$ bohr). The diagonal b-b $T^{(1)}_{nn}$ and $T^{(2)}_{nn}$ matrix elements have also been examined, and we have found that in both cases, linear log-log plots are obtained with slopes close to -1 for $T^{(1)}_{nn}$ and -2 for $T^{(2)}_{nn}$. The decreases in the matrix elements as n decreases are substantial, as was predicted in section II-D. This is in contrast to the c-c diagonal elements, which for large ρ are nearly independent of n. We present the logarithm of the absolute value of some diagonal elements of $\underline{\underline{T}}^{(1)}$ and $\underline{\underline{T}}^{(2)}$ in Table 3. Selected elements of $\underline{\underline{P}}$ are displayed in Fig. 18. Again, two clusters of slopes were obtained, -2 for the b-b and c-c, and -3.5 for the b-c. The curves are linear or nearly linear over the entire range of ρ' examined. For the b-b and b-c elements examined, the same behavior observed for the $T^{(1)}$ and $T^{(2)}$ was obtained, namely that those matrix elements involving more deeply bound states are substantially smaller than those involving lesser bound ones. Also, the magnitude of the c-c matrix elements decreases as one moves away from the diagonal.

C. Eigenvalues and Matrix Elements on the Dissociative Surface

We have calculated some of the $T^{(1)}$ and $T^{(2)}$ matrix elements for both the purely polar and hybrid basis functions on the dissociative surface. Our interest in performing these calculations is twofold. First, we wish to determine whether the general behavior of the adiabatic coupling matrix elements is independent of the surface being used. Second, we wish to use them so that we may integrate eq. 17 (for the purely polar basis set) to calculate $\underline{\underline{M}}$, $\underline{\underline{Q}}$, $\underline{\underline{R}}$, and $\underline{\underline{Y}}$ as defined earlier. We find that the ρ dependences of $\underline{\underline{T}}^{(1)}$ and $\underline{\underline{T}}^{(2)}$ are quite similar for this surface for the purely polar basis set as may be seen in Figs. 19 and 20, respectively. The only non-zero b-b matrix element, $T^{(1)}_{01}$, yields a linear plot with a slope of -0.99, and all the b-c $\underline{\underline{T}}^{(1)}$ elements examined lead to plots with slopes in the vicinity of -2.5. Again, at large ρ, the b-b matrix element is much larger than any of the b-c ones examined. No $T^{(1)}$ c-c matrix elements are plotted, as they did not lie along straight lines in a log $|T^{(1)}_{ij}|$ vs. log ρ plot (some changed sign once of twice in the region of ρ considered). A similar behavior was obtained for $\underline{\underline{T}}^{(2)}$ (see Fig. 20). Two b-b elements have slopes near -2; four b-c ones have slopes near -3.5.

It is seen that linearity for the b-c matrix elements does not set in until fairly large values of ρ, the exact value increasing with the quantum number of the dissociative state.

Analogous calculations have been performed using the hybrid basis functions, and elements of $\underline{\underline{T}}^{(1)}$ and $\underline{\underline{T}}^{(2)}$ are plotted in Figs. 21 and 22, respectively. The b-b $T^{(1)}$ matrix elements lead to linear plots with slopes of nearly -1 (see Fig. 30), while the b-c ones give two different slopes. Those involving the ground state gave slopes near -1.6, those involving the first (and only excited) state gave slopes near -2. The one c-c element shown gave a slope of -2; a number of off-diagonal c-c elements calculated for higher n ($10 \leq n \leq 23$) gave similar slopes. The diagonal element $T^{(1)}_{10,10}$ gave a slope of -1. Log-log plots of $\underline{\underline{T}}^{(2)}$ only became linear at very large values of ρ' (see Fig. 22). The b-b matrix elements gave a slope of roughly -2; the b-c elements involving the $n = 0$ state gave slopes of -2.6, while those involving the $n = 1$ state gave slopes closer to -3. In both the $T^{(1)}$ and $T^{(2)}$ cases, b-c matrix elements involving $n = 0$ are much smaller than those involving $n = 1$. The one c-c element shown gave a slope of -3, other higher c-c off-diagonal elements give slopes near -2.8, the diagonal $T^{(2)}_{10,10}$ element gave a slope of -1.92.

In general, the behavior observed on this surface is similar to that observed on the PK surface. The c-c matrix elements on this surface are less well behaved (i.e., give rise less readily to linear plots) than on the PK surface. On both surfaces the matrix elements segregate the same way, i.e., with the purely polar basis functions the b-b matrix elements become much larger than the b-c ones at large ρ, and with the hybrid basis functions matrix elements involving lower energy bound states are smaller than those involving higher energy ones.

D. Integration of the Adiabatic Equations on the Dissociative Surface

We have performed some preliminary calculations in which we numerically integrated the Eqs. (17) on the dissociative surface using the purely polar coordinate basis functions. We will briefly review this integration here and present the results which were obtained.

The problem which we studied was that of the four lowest energy even eigenfunctions only, hence the matrices generated were 4 × 4 and there were 16 coupled differential equations to be solved. Integration was begun at $\rho = 1$ bohr and carried out to $\rho = 5000$ bohr. The integrator used was an Adams-Moulton integrator with a Runge-Katta-Gill initiation procedure.^{17} A cubic spline procedure was used to interpolate the various matrices needed for the integration; note in this interpolation the independent variable was the logarithm of ρ rather than ρ itself.

We examine selected elements of the $\underline{\underline{M}}$, $\underline{\underline{Q}}$, $\underline{\underline{R}}$, and $\underline{\underline{y}}$ matrices defined earlier. As in our treatment of the simple 2 × 2 case, our initial condition in the integration of eq. (17a) is that $\underline{\underline{M}}(\rho_0 = 1) = \underline{\underline{I}}$. We then plot the elements of M obtained in a semi-log plot of M_{ij} vs. $\log_{10}(\rho)$. Plots of seven such matrix elements are shown in Figs. 23 and 24. There are two striking features of these graphs. First, the curves vary substantially from matrix element to matrix element, and with distance, although their values are always between minus one and plus one. Second, one sees at small values of ρ, the variation of the elements with distance is highly irregular, while at larger values of ρ (~ 300 bohr) two types of variation set in--either ρ independence, found for all elements shown except M_{14} and M_{24}, or oscillations which occur with a magnitude and frequency which is independent of $\log \rho$. The elements M_{11}, M_{12}, and M_{13}, not shown, also oscillate at large ρ in a similar manner. These results suggest that oscillatory behavior should be the rule in rows corresponding to bound states (n this four-channel case, rows 1 and 2), while those in rows corresponding to continuum states will become independent of ρ. We recall that oscillatory behavior of the type observed (frequency independent of $\log \rho$) was predicted to occur in the 2×2 case, in which open states only were included. Thus, the usefulness of the 2×2 model is verified.

We next consider some elements of $\underline{\underline{R}}$. $\underline{\underline{R}}$ is, of course, dependent on the energy, but for simplicity we will show only a few elements of $\underline{\underline{R}}$ at the energy $E = 0.10$ eV (measured with respect to a zero of energy of three infinitely separated atoms). Selected diagonal and off-diagonal elements of $\underline{\underline{R}}$ are shown in Figs. 25 and 26, respectively. There are three major features of Figs. 25 and 26. First, at small values of ρ (< 30 bohr), the diagonal elements of $\underline{\underline{R}}$ decrease substantially with increasing ρ, while its off-diagonal elements vary in a much less regular way. Second, at moderate values of ρ (> 30 bohr), all elements of $\underline{\underline{R}}$ have seemed to settle down to some sort of asymptotic values, about which they may or may not oscillate, and if so, the oscillation may be smooth as for the diagonal elements R or may have cusps, as is seen for its off-diagonal elements. Third, at large ρ, the off-diagonal elements are substantially smaller than the diagonal elements.

A number of these observations can be simply explained. For example, the large decrease in the diagonal elements R_i with increasing ρ at small ρ is due mainly to the fact that the eigenvalues $E_i(\rho)$ are very large at small ρ and decrease substantially with increasing ρ. The difference between the small ρ dependence of the diagonal and off-diagonal elements of $\underline{\underline{R}}$ is partially due to the initial choice of $\underline{\underline{M}}$ $(\rho = 1)$ as the unit matrix. Thus, the off-diagonal elements can only grow, at least initially, as $\underline{\underline{R}}$ $(\rho = 1) = \underline{\underline{\epsilon}}$ $(\rho = 1)$, and $\underline{\underline{\epsilon}}$ is diagonal.

The reason for the existence of smooth oscillations in the plots of the diagonal elements of $\underline{\underline{R}}$ and cusps in those of the off-diagonal ones can be understood by consideration of the 2×2 model. From Eq. (41) we see that the diagonal terms involve only squares of sine and cosine terms, while the off-diagonal ones involve products of sine and cosine terms. Since at energies above dissociation ϵ_0^b and ϵ_1^b will have the same sign, the diagonal elements of $\underline{\underline{R}}$ will always have the same sign, while the off-diagonal elements of $\underline{\underline{R}}$ may change sign. The cusps in Fig. 26 come from taking the absolute value of a number whose sign is changing. We note that the cusps observed in Fig. 26 at large ρ occur at regular values of log ρ; this is consistent with the result in Eq. (4).

We next consider the ρ dependence of the elements of $\underline{\underline{Q}}$. Selected diagonal and off-diagonal elements of $\underline{\underline{Q}}$ are shown in Figs. 27 and 28, respectively. There are major features in these graphs. First, all matrix elements decrease rapidly with increasing ρ, by a relationship in the neighborhood of ρ^{-2}. Second, all the matrix elements change sign periodically as ρ increases and the frequency of these sign changes is fairly insensitive to log (ρ). This behavior is very different from that of $\underline{\underline{R}}$, whose diagonal elements became essentially independent of ρ at large ρ (except for the small oscillations, without cusps, seen in Fig. 25.

Again, the behavior of the elements of $\underline{\underline{Q}}$ may be easily understood. The rapid decrease in the magnitude of the elements of $\underline{\underline{Q}}$ will come from the rapid decrease in those of $\underline{\underline{P}}$. In Table 2 we saw that the b-b elements of $\underline{\underline{P}}$ (on the $H + H_2$ surface, but the results presented earlier indicate that the ρ dependence of all matrix elements should be independent of the surface) decrease as ρ^{-2}. Since the elements of $\underline{\underline{M}}$ are everywhere of order unity, the elements of $\underline{\underline{Q}}$ should decay as the slowest decaying ones of $\underline{\underline{P}}$, and this is what is observed. The reason for the existence of sign changes in the diagonal elements of $\underline{\underline{Q}}$ (unlike in $\underline{\underline{R}}$) may be seen by consideration of the 2×2 case. In Eq. (43) we showed that the diagonal elements of $\underline{\underline{Q}}$ are composed of two kinds of terms--those that involve the square of a sine or a cosine term, and those involving the product. The product term will change sign with ρ, so the entire diagonal element may also (depending on the relative values of t, u, and v). Because the elements of $\underline{\underline{Q}}$ decrease so much more rapidly than those of $\underline{\underline{R}}$, we see that to a good degree of approximation, eq. (45) is satisfied at large ρ. Examination of Figs. 25 and 26 indicates that at large ρ, at the energy shown, the diagonal elements of $\underline{\underline{Q}}$ are roughly one order of magnitude greater than the off-diagonal ones, and eqs. (45) would approximately decouple. Thus, in principle the analysis of $\underline{y}$ might involve only the solution of uncoupled differential equations. We will not pursue this line of reasoning, showing instead the results of a numerical solution of Eq. 17d.

We present plots of the diagonal elements of $\underline{\underline{y}}$ in Figs. 29 and 30 for energies above and below dissociation, respectively. The initial conditions for the integration were the usual for the integration of a radial Schrödinger equation

$$\underline{\underline{y}}(\rho_0) = \underline{\underline{0}} \qquad (63a)$$

$$\underline{\underline{y}}'(\rho_0) = \underline{\underline{I}} \qquad (63b)$$

From the figures we can see that the expectations of section II-D-1 are correct: at the energy above dissociation (Fig. 29), $\underline{\underline{y}}$ grows rapidly at small ρ, begins to change sign at moderate ρ, and settles into some highly oscillatory but otherwise ρ independent state at large ρ. At the energy below dissociation (Fig. 30), $\underline{\underline{y}}$ grows rapidly at all ρ (disregarding small local effects of sign changes) finally running off the scale of the figure $\rho = 1000$ bohr.

V. Discussion and Conclusions

Substantial information concerning the ρ-dependence of the eigenvalues and adiabatic coupling matrix elements has been obtained in these calculations. In particular we have found the existence of fairly well-defined asymptotic behavior for these quantities, the exponents associated with which vary depending on the nature of the quantity. We have found some major differences between the matrix elements coming from the purely polar and hybrid basis functions. In this section, we will review some of the major features of the quantities studied.

For both basis functions, at moderate and large ρ, the eigenvalues of the dissociative states are approximately related to ρ (for simplicity we will say ρ, although for the hybrid basis functions the appropriate quantity is ρ') by the expression

$$E_{n_d}(\rho) \sim n_d^2/\rho^2 \tag{64}$$

where n_d is the effective quantum number of the dissociative state as defined earlier. This expression is exactly what would be expected from a model of a particle in a one-dimensional box. The reason for the applicability of the model is clear from the appearance of the purely polar eigenfunctions at large ρ --they are small in the well region, and can thus be thought to reside only in the plateau region. Some deviation of the eigenvalues from the particle-in-a-box model is seen. Their ρ derivatives obey the particle-in-a-box relationships less well than do the eigenvalues themselves. The bound eigenvalues change far less with ρ for the hybrid basis functions than they do for the purely polar ones.

The adiabatic coupling matrices $T^{(1)}$ and $T^{(2)}$ both have the basic structure required by their definitions--ex. a skew-symmetric $T^{(1)}$ for the purely polar basis functions. The asymptotic relationships of the individual matrix elements are determined largely by the nature of the matrix element--bound-to-bound, bound-to-continuum, or continuum-to-continuum. In most cases log-log plots of the matrix element vs. ρ give rise to straight lines, although sometimes linearity does not set in immediately, and is frequently less well obtained for continuum-to-continuum matrix elements. Deviation from linearity at very large values of ρ ($>$1000 bohr) is probably due to numerical error. Similar behavior for the matrix elements is obtained on both potential energy surfaces studied.

Major differences were obtained between matrix elements for the purely polar and hybrid basis functions, however. Most of these, i.e., the lack of skew-symmetry, the $1/\rho'$ dependence of the diagonal $T^{(1)}$ and the observed $1/(\rho')^2$ dependence of the diagonal $T^{(2)}$ matrix elements, were predicted from a fairly straightforward analysis of the implications of its definition. Also, the $T^{(1)}$ and $T^{(2)}$ matrix elements for the hybrid basis functions do not segregate themselves into clusters (on basis of magnitude) depending on their b-b, b-d, or c-c nature. Instead, they segregate on the basis of their lowest component quantum number--the lower that becomes, the smaller the matrix element will be.

The $\underline{\underline{P}}$ matrix calculated from the $\underline{\underline{T}}^{(1)}$, $\underline{\underline{T}}^{(2)}$, and $\underline{\underline{T}}^{(1)\prime}$ matrices for the two basis functions differ from each other in the same way as the $\underline{\underline{T}}^{(2)}$ matrices do. This is reasonable enough, as both have the same units (distance^{-2}). The $\underline{\underline{P}}$ matrix, or more precisely the matrix product $\underline{\underline{Q}} = \underline{\underline{M}}^{-1}\,\underline{\underline{P}}\,\underline{\underline{M}}$, will be the crucial factor in determining the asymptotic properties of the differential equation for the radial wavefunction. Comparing the $\underline{\underline{P}}$ matrices, one sees that the one calculated with the hybrid basis functions appears to be more linear than that calculated with the purely polar ones. This suggests that the hybrid basis functions might be superior to the purely polar ones for the purposes of formulating the asymptotic analysis of the radial wavefunction Schrödinger equation. This superiority may be cancelled out by the slower die-off with distance of the c-c $\underline{\underline{P}}$ matrix elements for the hybrid basis functions. Also, the different clustering properties of the elements of $\underline{\underline{P}}$ (and also those of $\underline{\underline{T}}^{(1)}$, which determine those of $\underline{\underline{M}}$) make the comparison between the basis sets less clear. The lack of simple analytic properties of the coupling matrices (i.e., skew-symmetry of $\underline{\underline{T}}^{(1)}$, symmetry of $\underline{\underline{P}}$) in the hybrid case might make the understanding of the adiabatic equations more difficult with the hybrid basis than with the purely polar ones.

We have integrated the adiabatic equations in a preliminary way on the dissociative surface for the purely polar basis set. We have obtained values for the elements of $\underline{\underline{M}}$, $\underline{\underline{R}}$, $\underline{\underline{Q}}$, and $\underline{\underline{y}}$ out to very large ρ. The bulk of the results obtained are predicted by the analytic 2×2 model considered in detail. A result of major importance is that some elements of $\underline{\underline{M}}$ can oscillate between -1 and 1 even at very large ρ; these oscillations are found to occur with a frequency that is independent of $\log(\rho)$. This introduces oscillations into the elements of $\underline{\underline{R}}$, $\underline{\underline{Q}}$, and $\underline{\underline{y}}$. We emphasize that all of these oscillations are implied in the 2×2 case. The existence of thes oscillations presents a problem in that it prevents us from being able to simply describe the large ρ properties of $\underline{\underline{y}}$. The results of the numerical integration do suggest that whatever this asymptotic behavior is, it sets in in the neighborhood of $\rho = 100$-300 bohr. This may be an indication that converged partitioning probabilities for dissociation (defined earlier) can only be obtained by integrating to a value of ρ of that magnitude. Preliminary results do indicate that integration past $\rho = 110$ bohr (in the diabatic representation) leads to reasonably well converged partitioning probabilities. These will be presented elsewhere.

VI. Acknowledgments

The calculations reported here were performed on the Dreyfus-NSF Theoretical Chemistry Computer which was funded through grants from the Camille and Henry Dreyfus Foundation, the National Science Foundation (Grant No. CHE78-20235), and the Sloan Fund of the California Institute of Technology.

References

1. A. Kuppermann, J. A. Kaye, and J. P. Dwyer, Chem. Phys. Lett. 74 (1980) 257.
2. J. A. Kaye and A. Kuppermann, Chem. Phys. Lett. 77 (1981) 573.
3. J. A. Kaye and A. Kuppermann, Chem. Phys. Lett. 78 (1981) 550.
4. J. Römelt, Chem. Phys. Lett. 74 (1980) 263.
5. G. Hauke, J. Manz, and J. Römelt, J. Chem. Phys. 73 (1980) 5040.
6. J. Manz and J. Römelt, Chem. Phys. Lett. 76 (1980) 337.
7. J. Manz and J. Römelt, Chem. Phys. Lett. 77 (1980) 172.
8. J. Manz and J. Römelt, Chem. Phys. Lett. 81 (1981) 179.
9. J. A. Kaye and A. Kuppermann, unpublished results.
10. R. G. Gordon, J. Chem. Phys. 51 (1969) 14.
11. D. G. Truhlar, J. Comp. Phys. 10 (1972) 123.
12. J. Ortega, in Mathematical Methods for Digital Computers, Vol. 2, ed. A. Ralston and H. S. Wilf (Wiley, N.Y., 1967) p. 94.
13. J. H. Wilkinson, The Algebraic Eigenvalue Problem (Clarendon Press, Oxford, 1965) pp. 335-337.
14. B. T. Smith, J. M. Boyle, J. J. Dongarra, B. S. Farbow, Y. Ikebe, V. C. Klema, C. B., Moler, in Matrix Routines - EISPACK Gude, Lecture Notes in Computer Science", G. Goos and J. Hartmanis, eds., Springer-Verlag, Berlin, 1976.
15. R. N. Porter and M. Karplus, J. Chem. Phys. 40 (1964) 1105.

References (continued)

16. J. M. Bowman and A. Kuppermann, Chem. Phys. Lett. 34 (1975) 523.

17. S. P. Conte and C. deBoor, Elementary Numerical Analysis; An Algorithmic Approach, 2nd ed. (McGraw-Hill, New York, 1972) pp. 336-356.

Table 1. Calculated Eigenvalues and Their Derivatives for Seven Lowest Symmetric Continuum States (PK Surface, purely polar basis functions)

	n_d	E_j/eV^*	$\frac{dE_j}{d\rho}(\mathrm{eV\cdot bohr^{-1}})$	$\frac{d^2E_j}{d\rho^2}(\mathrm{eV\cdot bohr^{-2}})$	$\frac{dE_j/d\rho}{E_j}(\mathrm{bohr^{-1}})$	$\frac{d^2E_j/d\rho^2}{dE_j/d\rho}(\mathrm{bohr^{-1}})$
$\rho = 100$ bohr	1	1.4361(-5)	-3.377(-7)	1.236(-8)	-2.353(-2)	-3.660(-2)
	3	1.2972(-4)	-3.055(-6)	1.118(-7)	-2.355(-2)	-3.660(-2)
	5	3.6253(-4)	-8.551(-6)	3.121(-7)	-2.359(-2)	-3.650(-2)
	7	7.1536(-4)	-1.688(-5)	6.134(-7)	-2.360(-2)	-3.634(-2)
	9	1.1899(-3)	-2.805(-5)	1.013(-6)	-2.357(-2)	-3.611(-2)
	11	1.7865(-3)	-4.203(-5)	1.507(-6)	-2.353(-2)	-3.586(-2)
	13	2.5046(-3)	-5.873(-5)	2.092(-6)	-2.345(-2)	-3.562(-2)
	predicted by eq. 62				-2.000(-2)	-3.000(-2)
	deviation from eq. 62				17%	19%
$\rho = 200$ bohr	1	3.2123(-6)	-3.502(-8)	6.128(-10)	-1.090(-2)	-1.750(-2)
	3	2.8921(-5)	-3.152(-7)	5.511(-9)	-1.090(-2)	-1.750(-2)
	5	8.0392(-5)	-8.763(-7)	1.529(-8)	-1.090(-2)	-1.745(-2)
	7	1.5772(-4)	-1.719(-6)	2.991(-8)	-1.090(-2)	-1.740(-2)
	9	2.6101(-4)	-2.844(-6)	4.932(-8)	-1.090(-2)	-1.734(-2)
	11	3.9038(-4)	-4.253(-6)	7.347(-7)	-1.089(-2)	-1.727(-2)
	13	5.4591(-4)	-5.945(-6)	1.023(-7)	-1.089(-2)	-1.721(-2)
	predicted by eq. 62				-1.000(-2)	-1.500(-2)
	deviation from eq. 62				8.9%	15%
$\rho = 500$ bohr	1	4.8116(-7)	-2.002(-9)	1.364(-11)	-4.161(-3)	-6.813(-3)
	3	4.3304(-6)	-1.801(-8)	1.227(-10)	-4.159(-3)	-6.813(-3)
	5	1.2029(-5)	-5.004(-8)	3.407(-10)	-4.160(-3)	-6.809(-3)
	7	2.3576(-5)	-9.807(-8)	6.674(-10)	-4.160(-3)	-6.805(-3)
	9	3.8973(-5)	-1.621(-7)	1.102(-9)	-4.159(-3)	-6.798(-3)
	11	5.8218(-5)	-2.421(-7)	1.644(-9)	-4.158(-3)	-6.791(-3)
	13	8.1312(-5)	-3.381(-7)	2.293(-9)	-4.158(-3)	-6.782(-3)
	predicted by eq. 62				-4.000(-3)	-6.000(-3)
	deviation from eq. 62				4.0%	13%
$\rho = 1000$ bohr	1	1.1771(-7)	-2.414(-10)	8.287(-13)	-2.051(-3)	-3.433(-3)
	3	1.0594(-6)	-2.172(-9)	7.457(-12)	-2.050(-3)	-3.433(-3)
	5	2.9425(-6)	-6.034(-9)	2.071(-11)	-2.051(-3)	-3.432(-3)
	7	5.7670(-6)	-1.183(-8)	4.058(-11)	-2.051(-3)	-3.430(-3)
	9	9.5324(-6)	-1.955(-8)	6.705(-11)	-2.051(-3)	-3.430(-3)
	11	1.4238(-5)	-2.919(-8)	1.001(-10)	-2.050(-3)	-3.429(-3)
	13	1.9884(-5)	-4.077(-8)	1.397(-10)	-2.050(-3)	-3.427(-3)
	predicted by eq. 62				-2.000(-3)	-3.000(-3)
	deviation eq. 62				2.5%	14%
$\rho = 1500$ bohr	1	5.1935(-8)	-7.073(-11)	1.653(-13)	-1.362(-3)	-2.337(-3)
	3	4.6741(-7)	-6.366(-10)	1.488(-12)	-1.362(-3)	-2.337(-3)
	5	1.2983(-6)	-1.768(-9)	4.131(-12)	-1.362(-3)	-2.337(-3)
	7	2.5445(-6)	-3.465(-9)	8.095(-12)	-1.362(-3)	-2.336(-3)
	9	4.2057(-6)	-5.728(-9)	1.338(-11)	-1.362(-3)	-2.336(-3)
	11	6.2819(-6)	-8.555(-9)	1.998(-11)	-1.362(-3)	-2.335(-3)
	13	8.7726(-6)	-1.195(-8)	2.789(-11)	-1.362(-3)	-2.334(-3)
	predicted by eq. 62				-1.333(-3)	-2.000(-2)
	deviation from eq. 62				2.2%	17%
$\rho = 2500$ bohr	1	1.8584(-8)	-1.518(-11)	2.284(-14)	-8.169(-4)	-1.506(-3)
	3	1.6725(-7)	-1.366(-10)	2.055(-13)	-8.168(-4)	-1.504(-3)
	5	4.6455(-7)	-3.794(-10)	5.708(-13)	-8.167(-4)	-1.504(-3)
	7	9.1046(-7)	-7.436(-10)	1.119(-12)	-8.167(-4)	-1.506(-3)
	9	1.5049(-6)	-1.229(-9)	1.848(-12)	-8.167(-4)	-1.504(-3)
	11	2.2478(-6)	-1.836(-9)	2.760(-12)	-8.168(-4)	-1.503(-3)
	13	3.1390(-6)	-2.564(-9)	3.854(-12)	-8.168(-4)	-1.503(-3)
	predicted by eq. 62				-8.000(-4)	-1.200(-3)
	deviation eq. 62.				2.1%	25%

*Numbers in parentheses are powers of ten by which other number should be multiplied.

Table 2. Limiting Exponents (ν) for Adiabatic Coupling Matrix Elements $F_{nn'}$, $F = T^{(1)}, T^{(2)}, P$. (PK Surface, Symmetric Eigenfunctions Only)

		Purely Polar		Hybrid	
		(n, n')	ν	(n, n')	ν
$\mathbf{T}^{(1)}$	b-b	(12,16)	0.97	(14,14)	1.06
		(14,16)	0.93	(16,16)	0.98
				(12,14)	1.03
				(12,16)	1.09
				(14,16)	1.16
	b-c	(14,20)	2.38	(14,22)	2.83
		(14,18)	2.44	(20,16)	2.43
		(18,16)	2.47	(18,16)	2.43
		(20,16)	2.33		
	c-c	(20,22)	1.88	(18,22)	2.52
		(18,22)	1.88	(20,18)	2.08
		(20,18)	1.89	(18,18)	1.02
$\mathbf{T}^{(2)}$	b-b	(16,16)	1.97	(14,14)	2.10
		(14,16)	1.95	(16,16)	2.01
		(12,16)	1.98	(12,14)	1.98
		(10,10)	2.00	(12,16)	1.98
				(14,16)	1.95
	b-c	(14,20)	3.18	(20,16)	3.47
		(14,18)	3.33	(18,16)	3.47
		(18,16)	3.33		
		(20,16)	3.12		
	c-c	(18,18)	4.68	(18,22)	3.30
		(20,20)	4.15	(20,18)	3.40
		(23,23)	3.85	(18,18)	2.01
$\mathbf{P}$	b-b	(16,16)	1.91	(16,16)	1.98
		(14,16)	1.92	(14,16)	2.09
				(12,16)	2.08
				(12,14)	2.13
	b-c	(20,16)	3.16	(20,16)	3.51
		(18,16)	3.29	(18,16)	3.55
				(14,22)	3.60
				(14,18)	3.64
				(12,18)	3.83
				(10,20)	~4.24
	c-c	(20,20)	4.08	(18,18)	2.03
		(18,22)	4.24	(20,18)	2.02
		(20,18)	4.40	(20,22)	2.09
				(18,22)	2.14

Table 3. Common Logarithm of $|T_{nn}^{(1)}|$ and $|T_{nn}^{(2)}|$ for Hybrid Basis Functions on PK surface at $\rho' = 2316$ bohr ($\log \rho' = 2.5$). (Note n = 17 is first symmetric continuum state.)

n	$\log_{10}\|T_{nn}^{(1)}\|$	$\log_{10}\|T_{nn}^{(2)}\|$
17	-2.77	-5.10
16	-2.91	-5.75
15	-3.68	-6.8
14	-5.40	-7.85
13	-7.71	-10.19
12	-10.61	-13.10
11	-13.22	<-14

Figure Captions

FIG. 1. Schematic picture of the breakup of the potential energy surface into subregions for the construction of the hybrid basis set. Region 1 is the A + BC region in which the hybrid basis functions are calculated along a line at constant R_λ; Region 2 is the dissociative plateau in which they are calculated along an arc at constant ρ', region 3 is the AB + C region in which they are calculated at a line at constant R_κ. For comparison, an arc at constant ρ, along which the purely polar basis functions are calculated is pictured also. The definition of the (ρ, α) and (ρ', α') coordinate systems is shown. Note that the angles α and α' are equal only for the case of $\alpha = \alpha' = \alpha_{\max}|2$; however $\alpha_{\max} = \alpha'_{\max}$.

FIG. 2. Schematic representation of the breakup of the grid for the calculation of the basis functions at large ρ when a three-tiered grid must be used. Note that the point density is highest nearest the ends and lowest in the middle; in the transition regions, the grid spacing h_2 is the geometric mean of that in the end and center regions.

FIG. 3. Plot of the symmetric purely polar basis functions $\phi_N^{(s)}$ (ρ = 50 bohr) for H_3 on the Porter-Karplus surface for N = 16, 18 and 20 (N = 16 is the highest symmetric bound basis function) as a function of the angle α in the range $0 \leq \alpha \leq \pi/6$ radians. The $\phi_N^{(s)}$ are normalized over the entire range of α.

FIG. 4. Plot of $\phi_N^{(s)}$ (ρ = 100 bohr) for N = 16, 18, and 20 vs. α as in Fig. 3.

Figure Captions (continued)

FIG. 5. Plot of $\phi_N^{(s)}$ (ρ = 50 bohr) for N = 16, 18, and 20 vs. α in the range $0 \leq \alpha \leq 6$ degrees. Otherwise, plot is as in Fig. 3. Normalization of $\phi_N^{(s)}$ is over all α.

FIG. 6. Plot of $\phi_N^{(s)}$ (ρ = 100 bohr) for N = 16, 18, and 20 vs. α as in Fig. 5.

FIG. 7. Plot of $\phi_N^{(s)}$ (ρ = 50 bohr) for N = 16, 18, and 20 vs. $\rho \cdot \sin\alpha$ in the range $0 < \rho \sin\alpha < 12$ bohr. Otherwise, plot is as in Fig. 3. Normalization of $\phi_N^{(s)}$ is over all α.

FIG. 8. Plot of $\phi_N^{(s)}$ (ρ = 100 bohr) for N = 16, 18, and 20 vs. $\rho \sin\alpha$ as in Fig. 7.

FIG. 9. Log-log plot of eigenvalues $E_{n_d}(\rho)$ of dissociative purely polar basis functions on the PK surface as a function of ρ. Only eigenvalues of symmetric states are shown; hence the restriction to odd values of n_d.

FIG. 10. Log-log plot of eigenvalues $E_{n_d}(\rho)$ of dissociative purely polar basis functions on the PK surface as a function of the index n, at seven different values of ρ (labeled in bohr).

FIG. 11. Log-log plot of the absolute value of the deviation of the eigenvalue $E_n(\rho)$ of the nth symmetric bound state of the purely polar basis functions on the PK surface from its value at ρ = 3000 bohr as a function of ρ for n = 10 (dashed line), n = 13 (dotted line), and n = 15 (solid line).

FIG. 12. Log-log plot of the absolute value of selected elements of the Matrix $\underline{\underline{T}}^{(1)}$ calculated for symmetric purely polar basis functions on the PK surface vs. ρ. Bound-to-bound (b-b)

Figure Captions (continued)

matrix elements are indicated by solid lines; bound-to-continuum (b-c) by dotted lines, and continuum-to-continuum by dashed lines. Each T_{ij} is represented by a letter code: $A = T^{(1)}_{14,16}$; $B = T^{(1)}_{12,16}$, $C = T^{(1)}_{14,20}$, $D = T^{(1)}_{14,18}$, $E = T^{(1)}_{20,22}$, $F = T^{(1)}_{20,22}$. Curvature at $\rho > 1000$ bohr is probably due to numerical inaccuracies.

FIG. 13. Log-log plot of the absolute value of selected elements of the matrix $\underline{\underline{T}}^{(2)}$ calculated for symmetric purely polar basis functions on the PK surface <u>vs</u>. ρ. Symbols and lines are as used in Fig. 12. Curvature at $\rho > 1000$ bohr is probably due to numerical inaccuracies.

FIG. 14. Log-log plot of the absolute value of selected elements of the matrix $\underline{\underline{P}}$, calculated for symmetric purely polar basis functions on the PK surface <u>vs</u>. ρ. Line types represent different types of matrix elements as used in Fig. 12, the letter code for each P_{ij} is as follows: $A = P_{14,16}$, $B = P_{12,16}$, $C = B_{20,16}$, $D = P_{18,16}$, $E = P_{20,20}$, $F = P_{18,22}$, $G = P_{20,18}$.

FIG. 15. Log-log plot of the absolute value of the deviation of the eigenvalue $E_n(\rho')$ of the nth symmetric bound state of the hybrid basis functions on the PK surface from its value at $\rho' = 4989$ bohr as a function of ρ' for $n = 13$ (dashed-dotted line), $n = 14$ (dotted line), $n = 15$ (dashed line), and $n = 16$ (solid line).

FIG. 16. Log-log plot of the absolute value of selected elements of the matrix $\underline{\underline{T}}^{(1)}$ calculated for symmetric hybrid basis functions

Figure Captions (continued)

on the PK surface vs. ρ'. Line types represent different types of matrix elements as used in Fig. 12. Where lines are not extended to the smallest or largest ρ, deviation from linearity of the plots was severe. The letter code for each $T^{(1)}_{ij}$ is as follows: A = $T^{(1)}_{16,16}$, B = $T^{(1)}_{14,14}$, C = $T^{(1)}_{12,16}$, D = $T^{(1)}_{12,14}$, E = $T^{(1)}_{20,16}$, F = $T^{(1)}_{20,18}$, G = $T^{(1)}_{18,18}$, H = $T^{(1)}_{18,22}$.

FIG. 17. Log-log plot of the absolute v lue of selected elements of the matrix $\underline{\underline{T}}^{(2)}$ calculated for symmetric hybrid basis functions on the PK surface vs. ρ'. Line types represent different types of matrix elements as used in Fig. 12; letter codes are identical to those used in Fig. 16.

FIG. 18. Log-log plot of the absolute value of selected elements of the matrix $\underline{\underline{P}}$ calculated for symmetric hybrid basis functions on the PK surface vs. ρ'. Line types represent different types of matrix elements as used in Fig. 12; the letter codes are as follows: A = $P_{16,16}$, B = $P_{14,16}$, C = $P_{12,16}$, D = $P_{12,14}$, E = $P_{20,16}$, F = $P_{20,18}$, G = $P_{12,18}$, H = $P_{10,20}$, I = $P_{18,18}$, J = $P_{18,22}$.

FIG. 19. Log-log plot of the absolute value of selected elements of the matrix $\underline{\underline{T}}^{(1)}$ calculated for symmetric purely polar basis functions on the dissociative surface vs, ρ. Line types represent different types of matrix elements as used in Fig. 12, the letter codes are as follows: A: $T^{(1)}_{0,1}$, B: $T^{(1)}_{1,6}$, C: $T^{(1)}_{0,9}$, D: $T^{(1)}_{0,3}$, E: $T^{(1)}_{0,2}$.

Figure Captions (continued)

FIG. 20. Log-log plot of the absolute value of selected elements of the matrix $\underline{\underline{T}}^{(2)}$ calculated for symmetric purely polar basis functions on the dissociative surface vs. ρ. Line types represent different types of matrix elements as used in Fig. 12; the letter codes are as follows: A: $T^{(2)}_{0,0}$, B: $T^{(2)}_{0,1}$, C: $T^{(2)}_{0,9}$, D: $T^{(2)}_{0,3}$, E: $T^{(2)}_{0,2}$.

FIG. 21. Log-log plot of the absolute value of selected elements of the matrix $\underline{\underline{T}}^{(1)}$ calculated for symmetric hybrid basis functions on the dissociative surface vs. ρ. Line types represent different types of matrix elements as used in Fig. 12; the letter codes are as follows: A: $T^{(1)}_{1,1}$, B: $T^{(1)}_{0,1}$, C: $T^{(1)}_{0,0}$, D: $T^{(1)}_{1,5}$, E: $T^{(1)}_{1,2}$, F: $T^{(1)}_{0,3}$, G: $T^{(1)}_{5,9}$.

FIG. 22. Log-log plot of the absolute value of selected elements of the matrix $\underline{\underline{T}}^{(2)}$ calculated for symmetric hybrid basis functions on the dissociative surface vs. ρ'. Line types represent different types of matrix elements as used in Fig. 12; the letter codes are as follows: A: $T^{(2)}_{1,1}$, B: $T^{(2)}_{1,5}$, C: $T^{(2)}_{1,2}$ D: $T^{(2)}_{0,3}$, E: $T^{(2)}_{5,9}$. The small number of curves at all but the largest values of ρ' reflects irregular variation in the $T^{(2)}_{ij}$ which would make the plots highly non-linear.

FIG. 23. Selected values of elements of the matrix $\underline{M}$ (defined in eq. (17a)) as a function of the logarithm of ρ for the first four symmetric purely polar eigenfunctions on the dissociative surface. The initial values of N_{ij} (ρ = 1 bohr) = δ_{ij} were used. A different line type is used for each element shown.

Figure Captions (continued)

FIG. 24. Additional elements of $\underline{\underline{M}}$ as a function of the logarithm of ρ for the case treated in Fig. 23.

FIG. 25. Absolute values of the diagonal elements of the matrix $\underline{\underline{R}}$ (defined in eq. (37a)) vs. the logarithm of ρ for the case treated in Fig. 23 for an energy of E = 0.10 eV (measured with respect to three infinitely separated atoms).

FIG. 26. Absolute values of selected elements of the matrix $\underline{\underline{R}}$ vs. the logarithm of ρ for the case treated in Fig. 23 at an energy E = 0.10 eV.

FIG. 27. Absolute values of the diagonal elements of the matrix $\underline{\underline{Q}}$ (defined in eq. (37b)) vs. the logarithm of ρ for the case treated in Fig. 23.

FIG. 28. Absolute values of selected elements of the matrix $\underline{\underline{Q}}$ vs. the logarithm of ρ for the case treated in Fig. 23.

FIG. 29. Absolute values of diagonal elements of the matrix $\underline{\underline{y}}$ (defined in eq. (17d)) vs. the logarithm of ρ for the case treated in Fig. 23 for an energy of E = 0.10 eV (measured with respect to three infinitely separated atoms). Initial conditions for the integration of eq. (17d)) were $y_{ij}(\rho = 1 \text{ bohr}) = 0$; $y'_{ij}(\rho = 1 \text{ bohr}) = \delta_{ij}$.

FIG. 30. Absolute values of diagonal elements of the matrix $\underline{\underline{y}}$ vs. the logarithm of ρ for the case treated in Fig. 23 for an energy of E = -0.02 eV. Initial conditions and energy origin are the same as those used in Fig. 29.

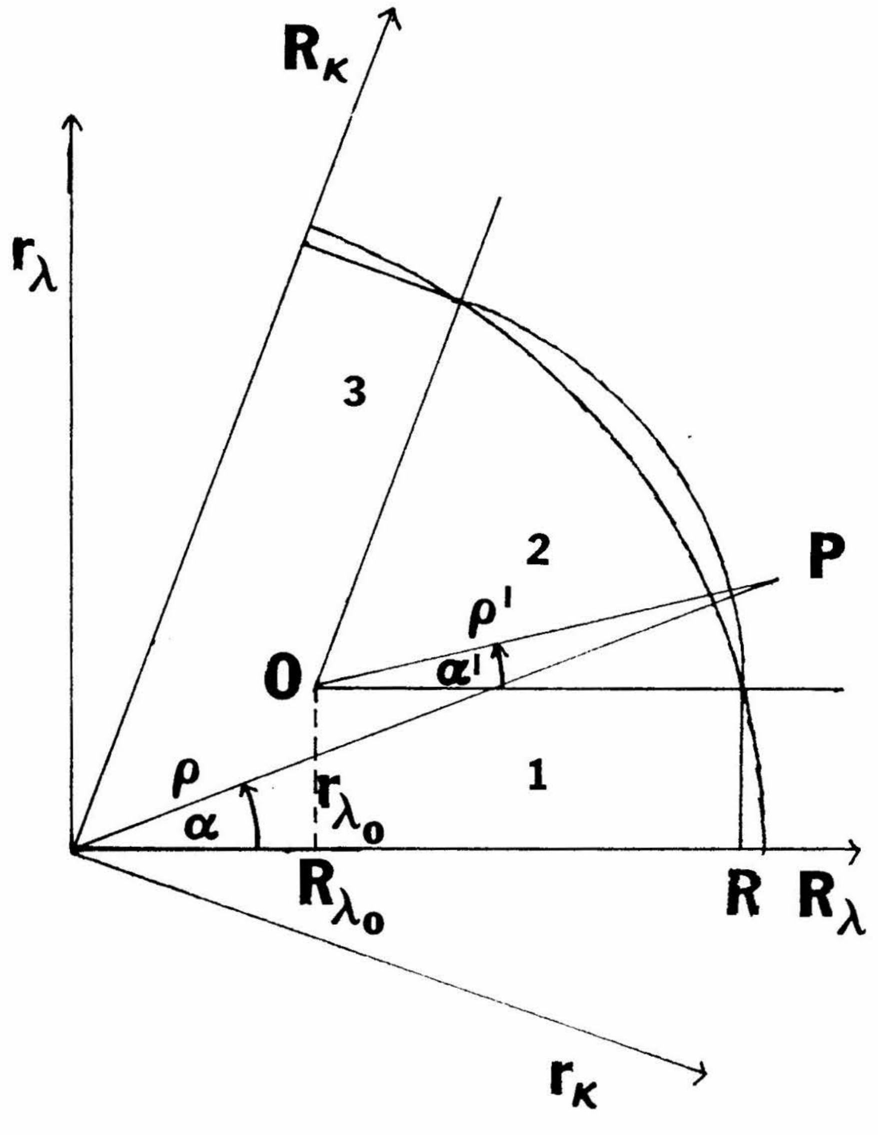
R_κ
r_λ
3
2
P
ρ'
O
α'
ρ
r_{λ_0}
1
α
R_{λ_0}
R
R_λ
r_κ

Figure 1

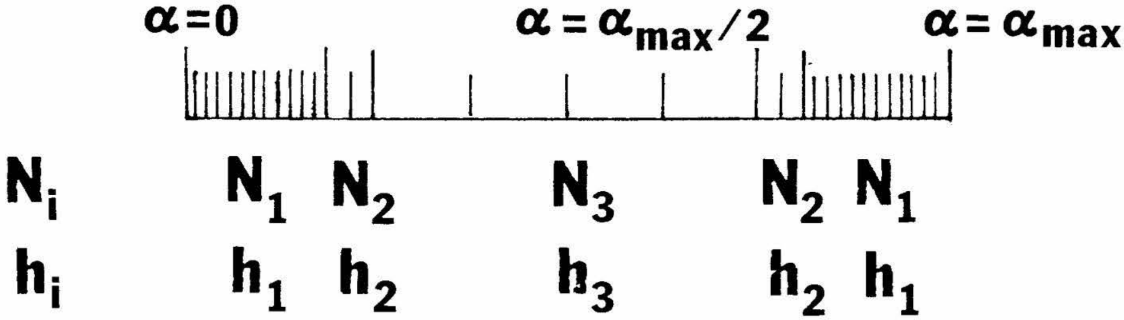

Figure 2

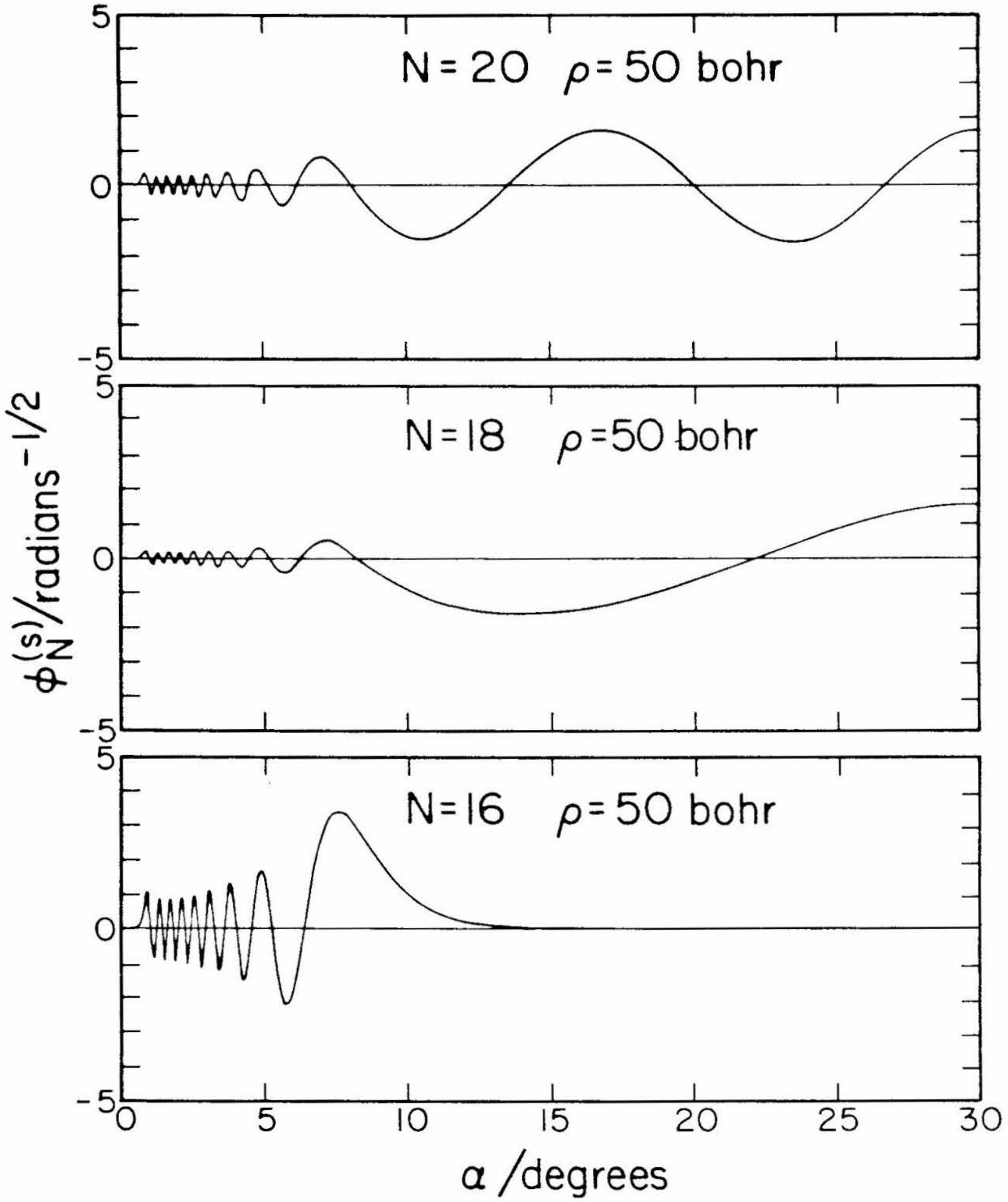
N = 20 ρ = 50 bohr
N = 18 ρ = 50 bohr
N = 16 ρ = 50 bohr
$\phi_N^{(s)}$/radians$^{-1/2}$
α /degrees
5
0
-5
0
5
10
15
20
25
30

Figure 3

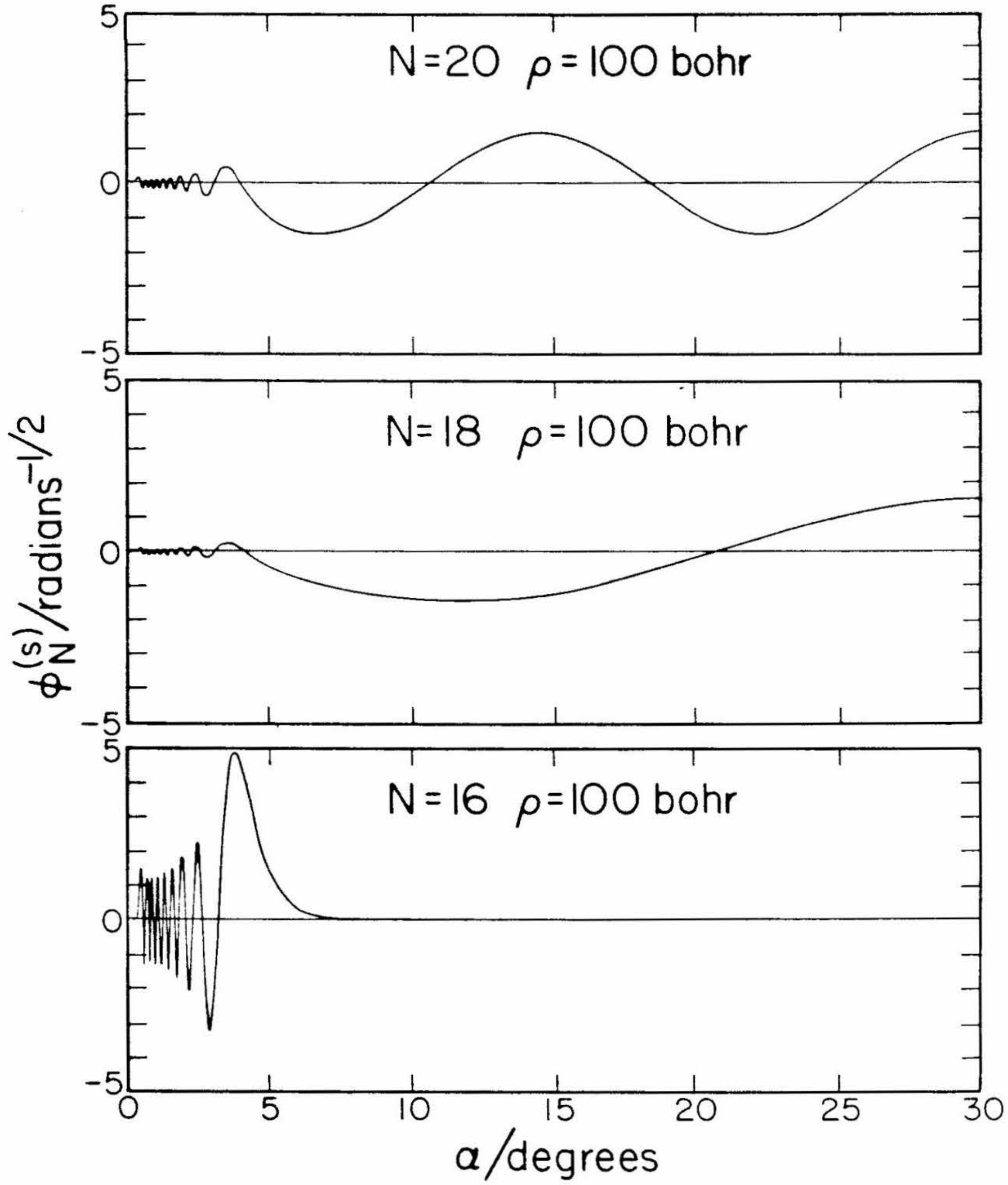
N=20 ρ=100 bohr
N=18 ρ=100 bohr
N=16 ρ=100 bohr
$\phi_N^{(s)}$/radians$^{-1/2}$
α/degrees
5
0
-5
0
5
10
15
20
25
30

Figure 4

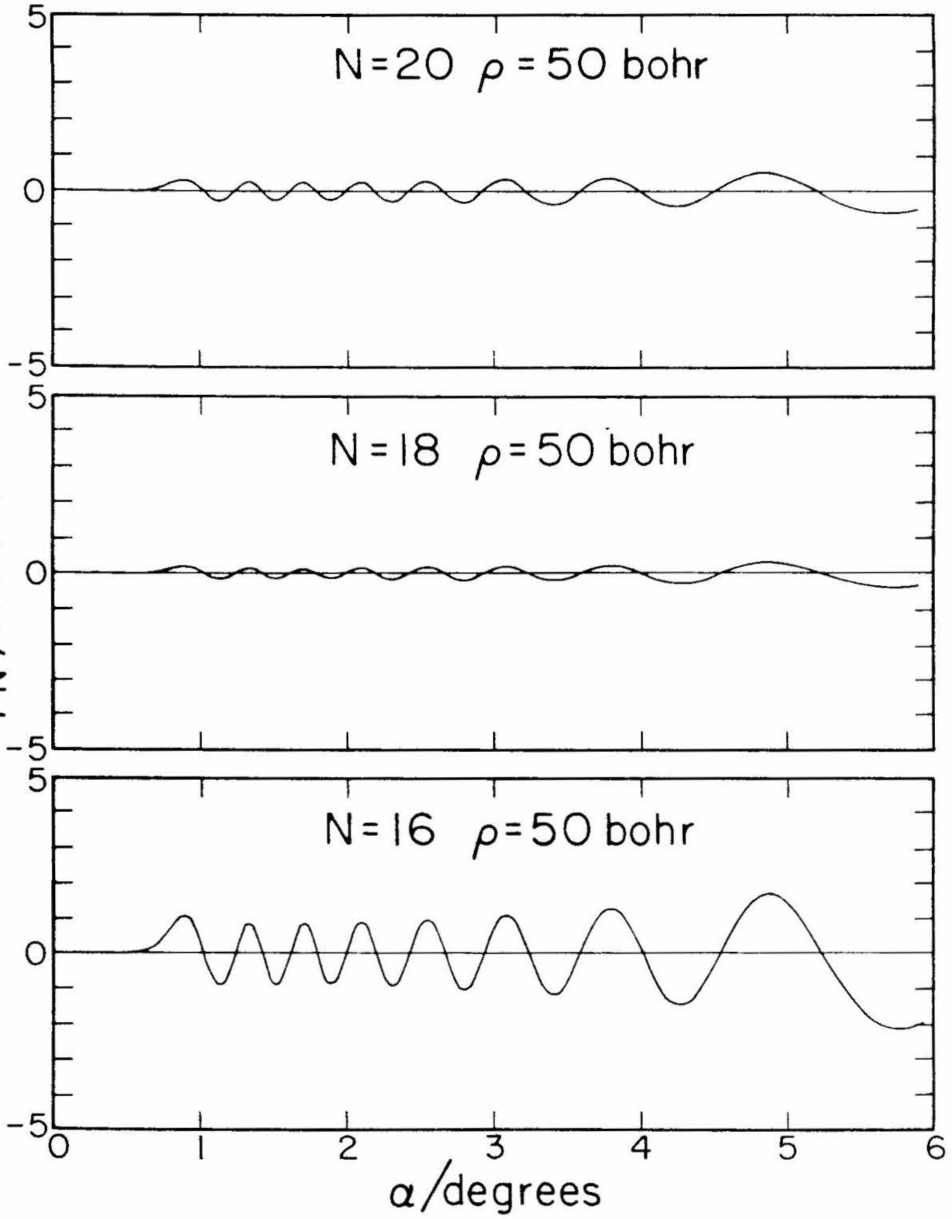

N=20 ρ=50 bohr
N=18 ρ=50 bohr
N=16 ρ=50 bohr
5
0
-5
$\phi_N^{(s)}$/radians$^{-1/2}$
0
1
2
3
4
5
6
α/degrees

Figure 5

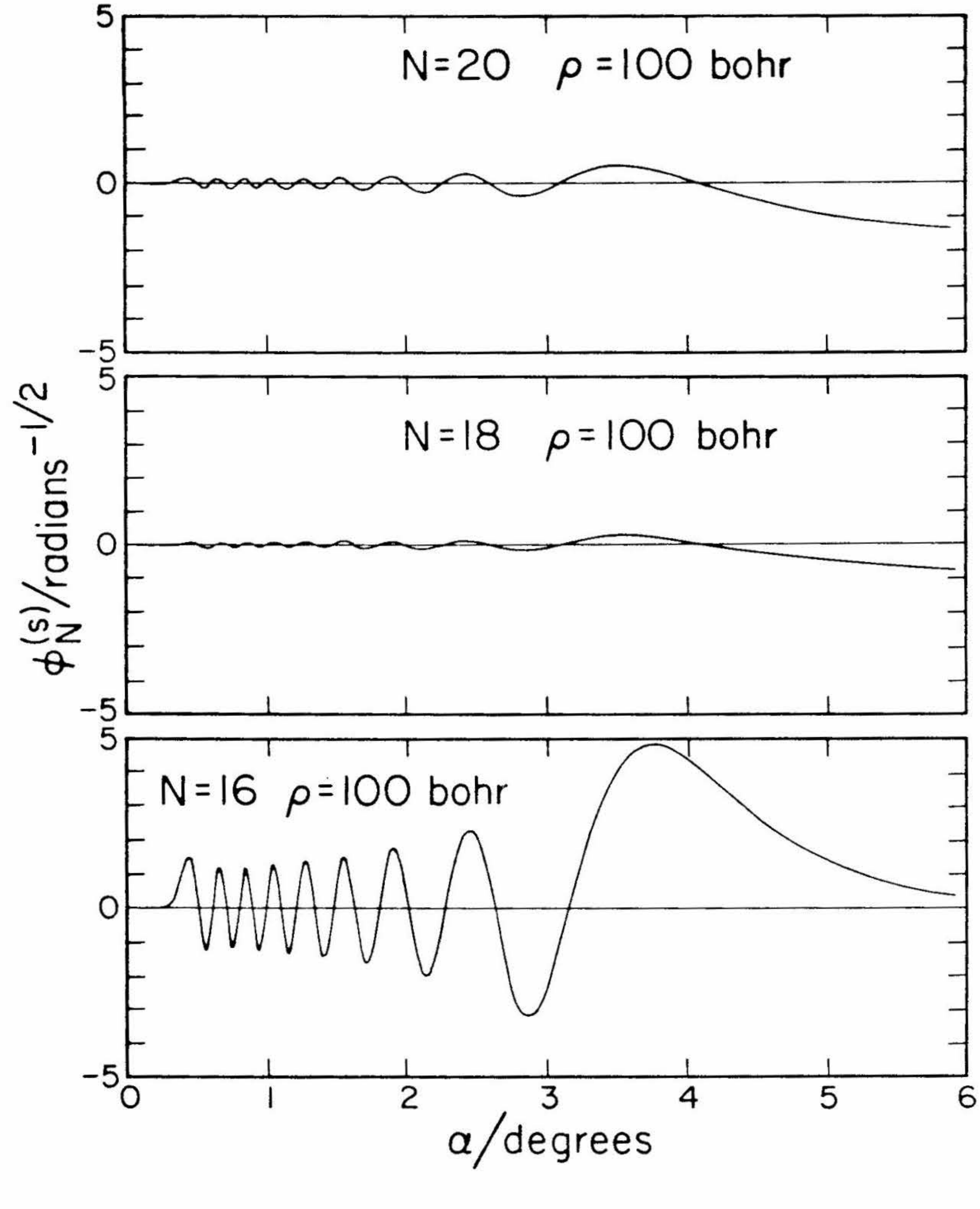
N=20 ρ=100 bohr
N=18 ρ=100 bohr
N=16 ρ=100 bohr
$\phi_N^{(s)}$/radians$^{-1/2}$
5
0
-5
5
0
-5
5
0
-5
0
1
2
3
4
5
6
α/degrees

Figure 6

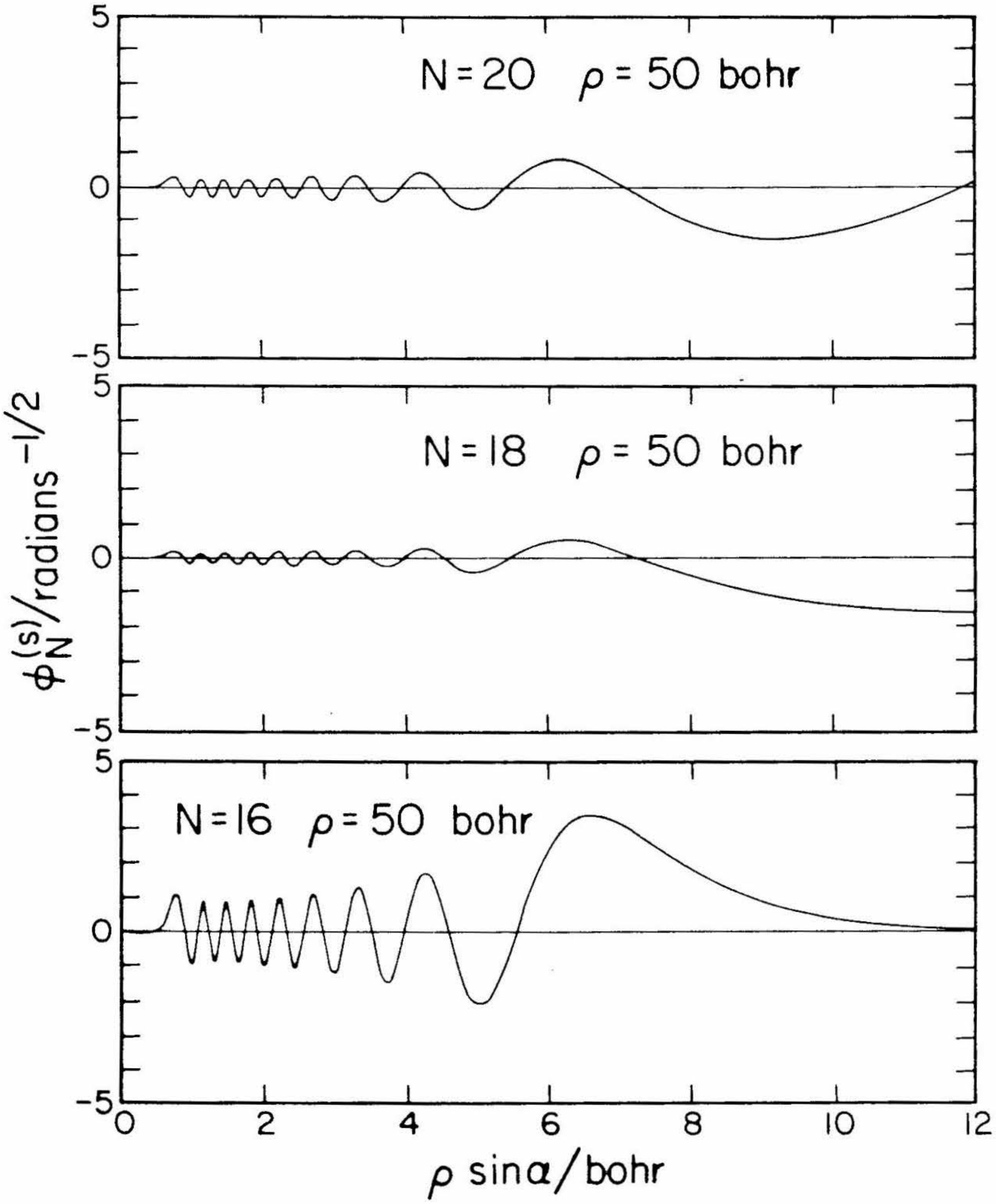
N = 20 ρ = 50 bohr
N = 18 ρ = 50 bohr
N = 16 ρ = 50 bohr
5
0
-5
0
2
4
6
8
10
12
$\phi_N^{(s)}$/radians$^{-1/2}$
ρ sinα/bohr

Figure 7

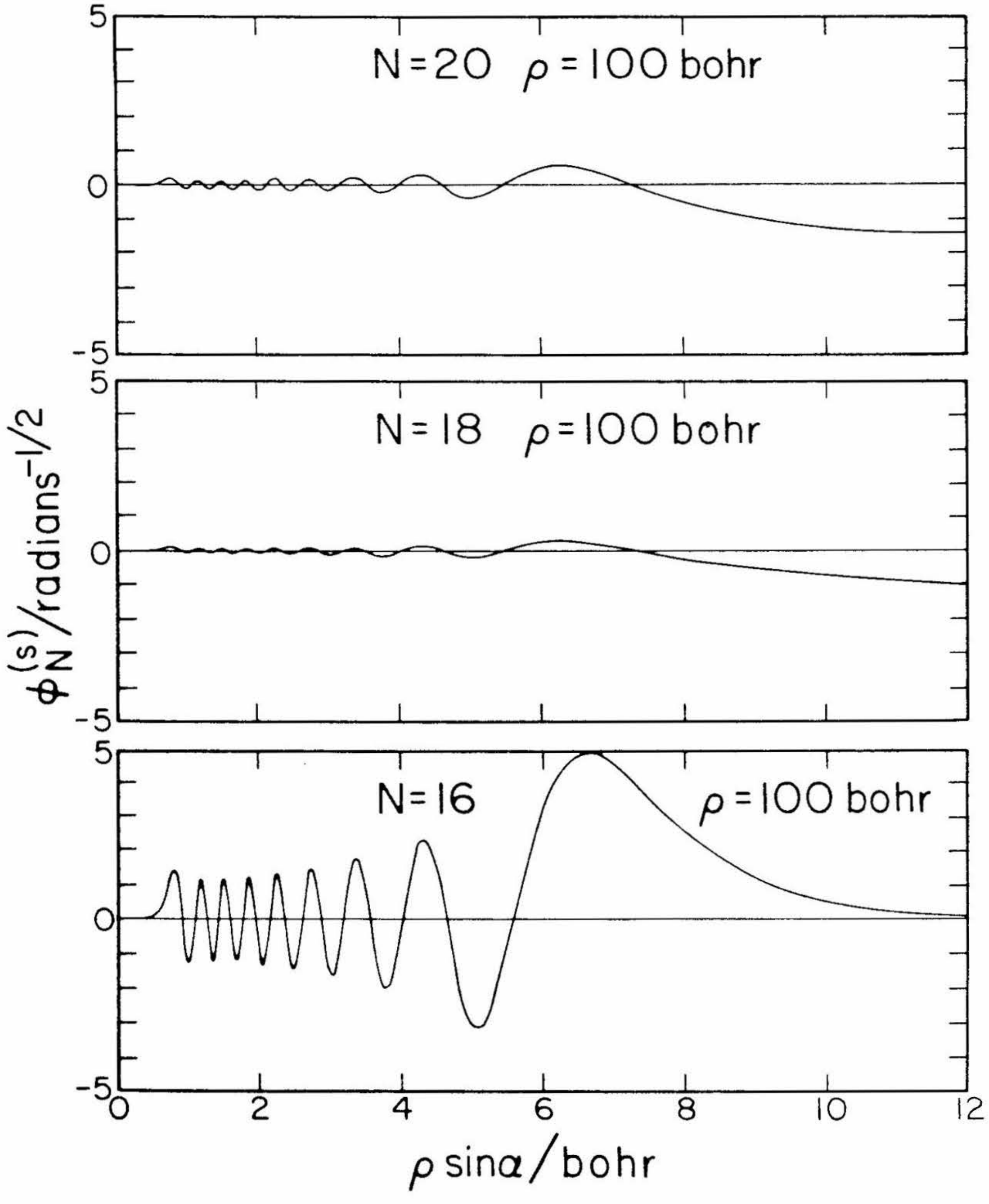
N=20 ρ=100 bohr
N=18 ρ=100 bohr
N=16 ρ=100 bohr
$\phi_N^{(s)}$/radians$^{-1/2}$
5
0
-5
0
2
4
6
8
10
12
ρ sinα/bohr

Figure 8

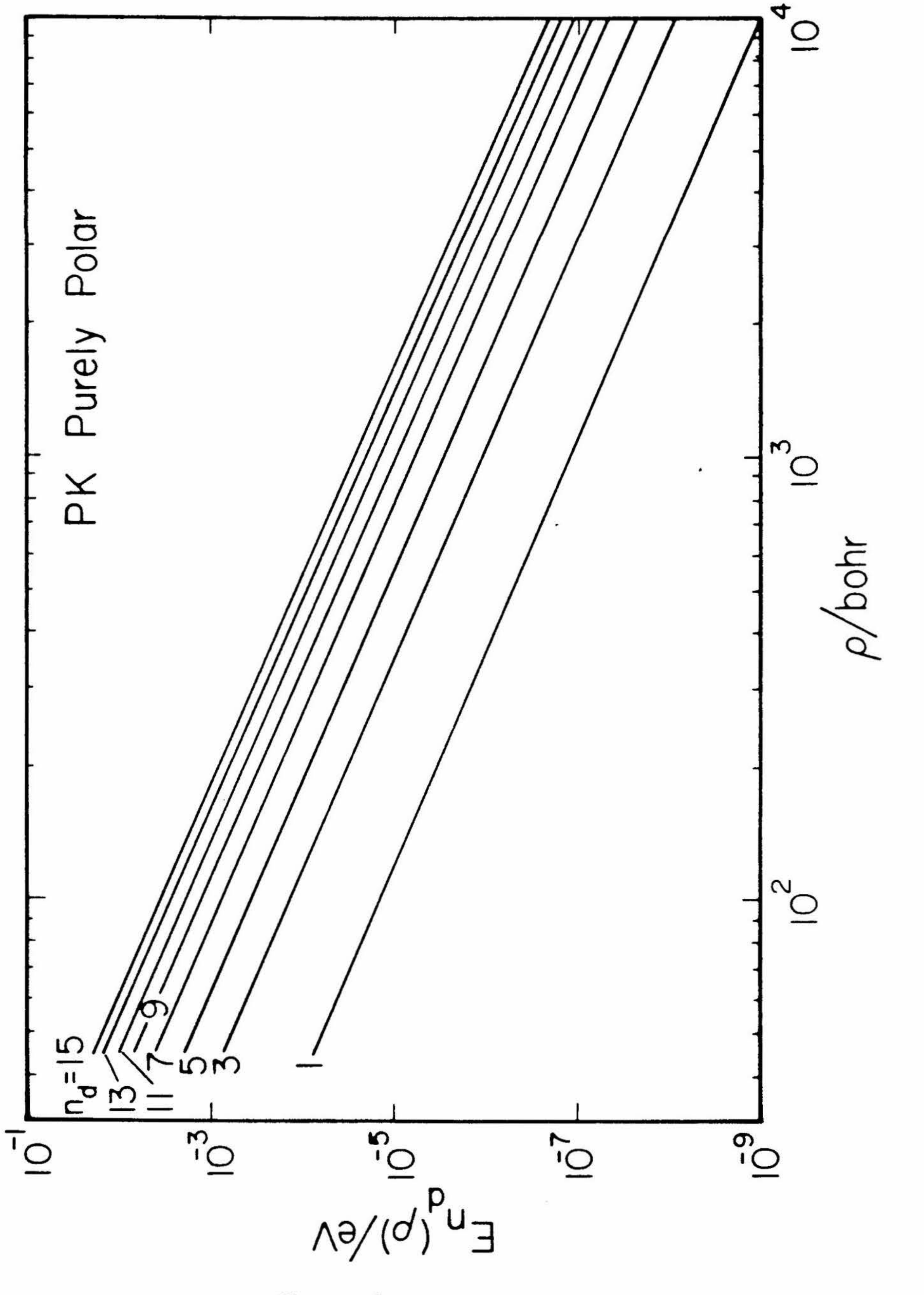
PK Purely Polar
n_d=15
13
11
9
7
5
3
1
10^-1
10^-3
10^-5
10^-7
10^-9
10^2
10^3
10^4
ρ/bohr
E_{n_d}(ρ)/eV

Figure 9

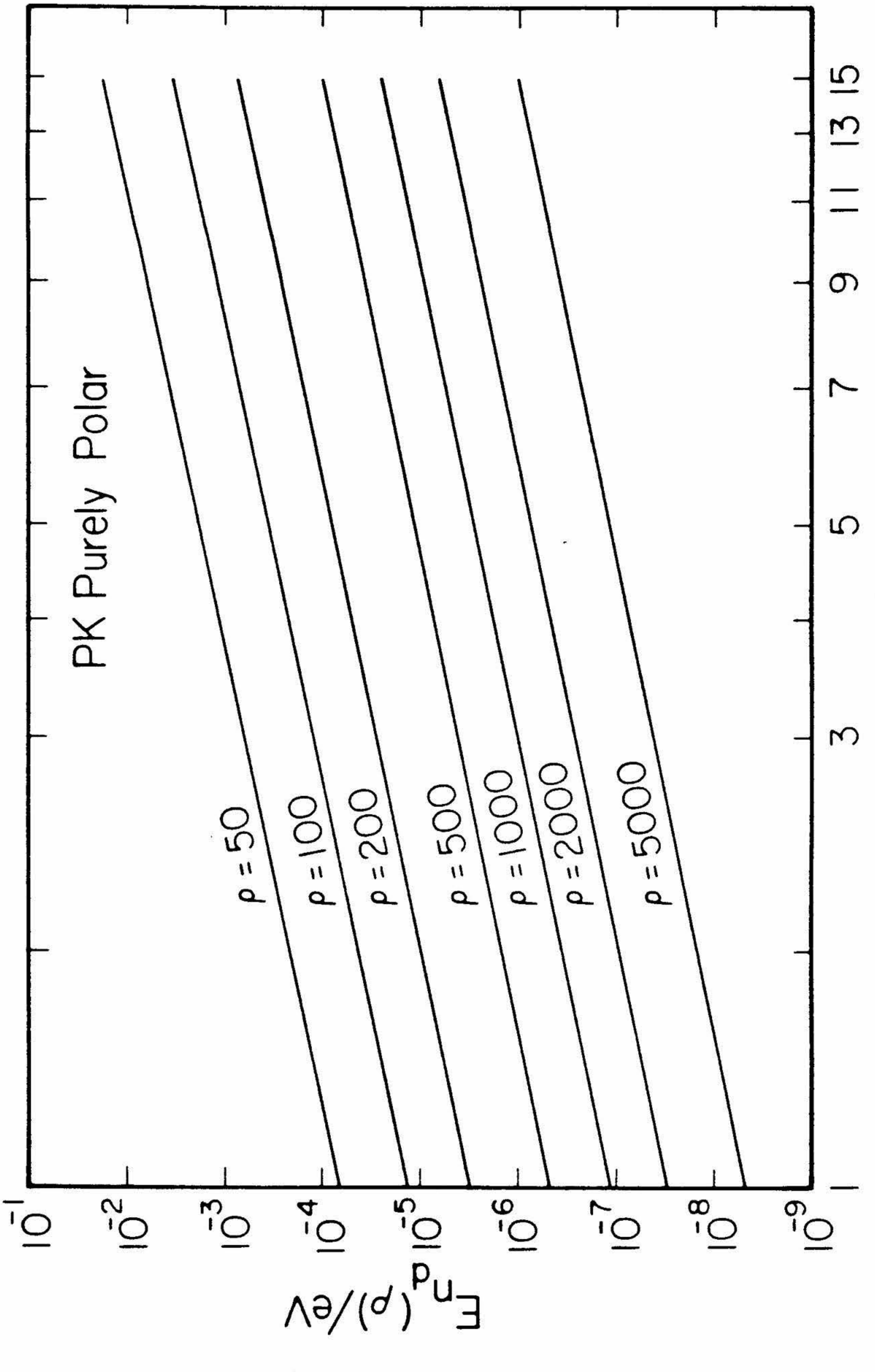
PK Purely Polar
ρ = 50
ρ = 100
ρ = 200
ρ = 500
ρ = 1000
ρ = 2000
ρ = 5000
3
5
7
9
11
13
15
n_d
10^{-1}
10^{-2}
10^{-3}
10^{-4}
10^{-5}
10^{-6}
10^{-7}
10^{-8}
10^{-9}
$E_{n_d}(\rho)/eV$

Figure 10

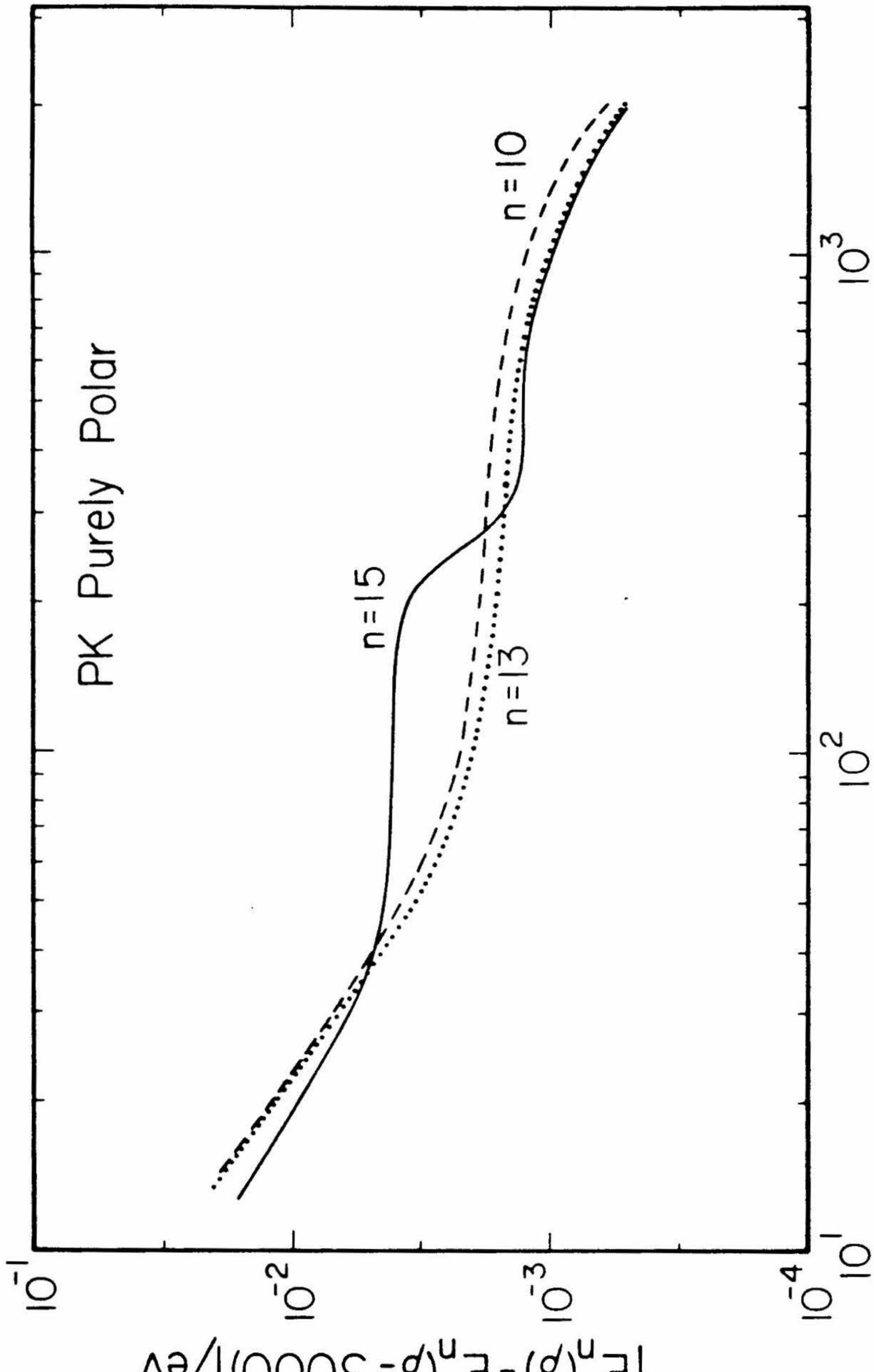
PK Purely Polar
n=15
n=13
n=10
10^{-1}
10^{-2}
10^{-3}
10^{-4}
10^{1}
10^{2}
10^{3}
ρ/bohr
$|E_n(\rho) - E'_n(\rho = 3000)|$/eV

Figure 11

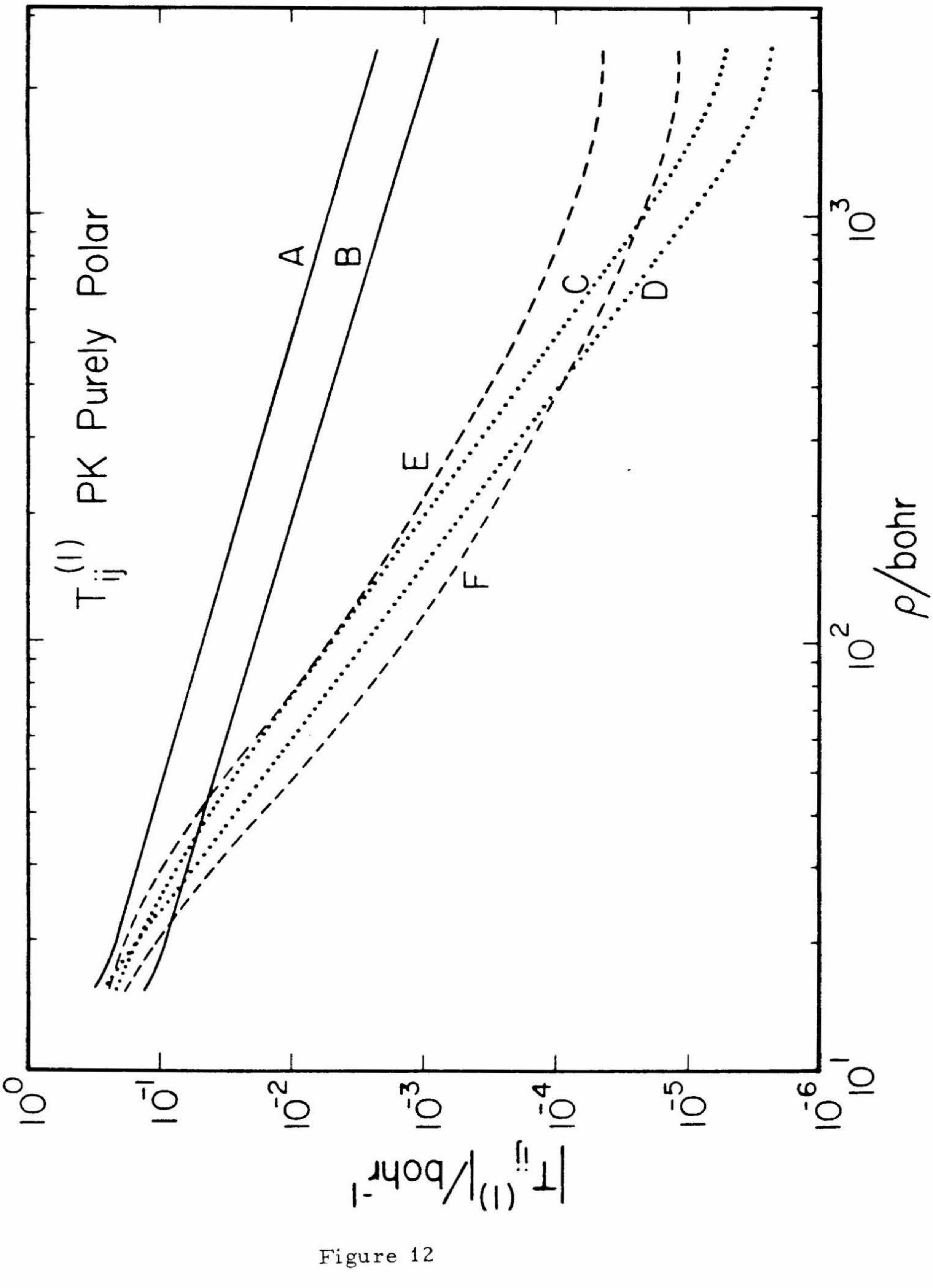
$T_{ij}^{(1)}$ PK Purely Polar
A
B
C
D
E
F
10^0
10^{-1}
10^{-2}
10^{-3}
10^{-4}
10^{-5}
10^{-6}
10^1
10^2
10^3
ρ/bohr
$|T_{ij}^{(1)}|$/bohr^{-1}

Figure 12

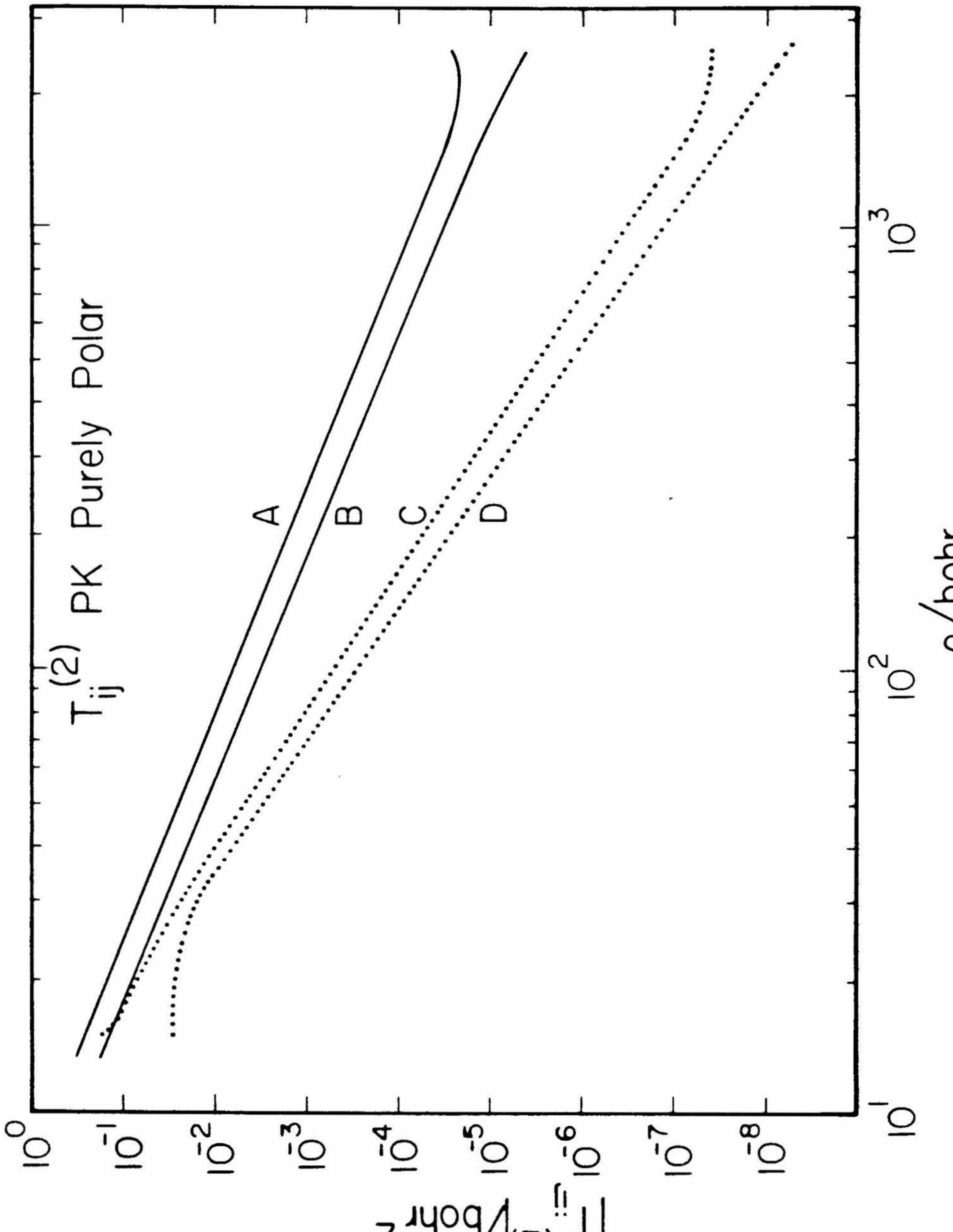
$T_{ij}^{(2)}$ PK Purely Polar
A
B
C
D
10^0
10^{-1}
10^{-2}
10^{-3}
10^{-4}
10^{-5}
10^{-6}
10^{-7}
10^{-8}
$|T_{ij}^{(2)}|$/bohr^{-2}
10^1
10^2
10^3
ρ/bohr

Figure 13

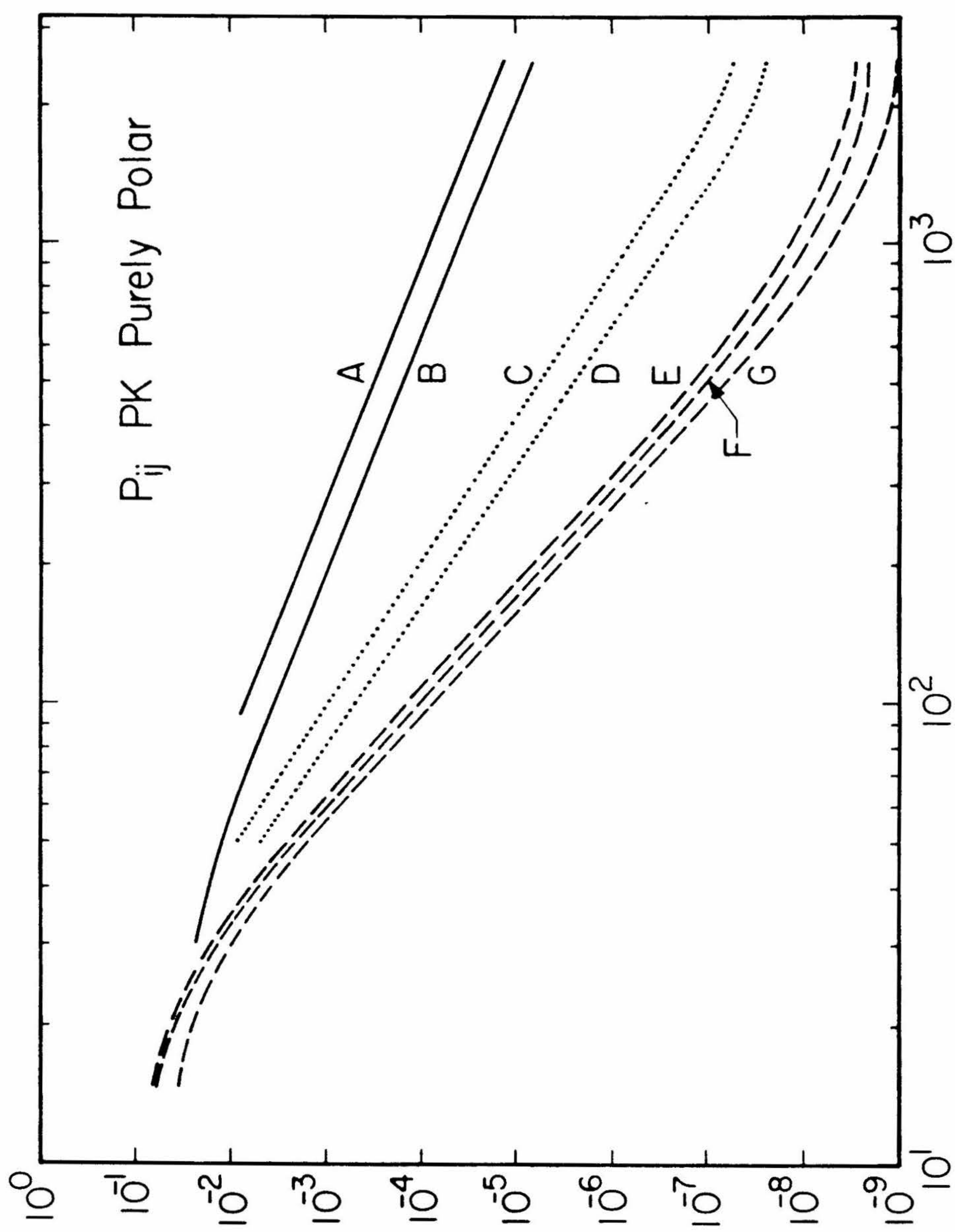
P_{ij} PK Purely Polar
A
B
C
D
E
F
G
10^{0}
10^{-1}
10^{-2}
10^{-3}
10^{-4}
10^{-5}
10^{-6}
10^{-7}
10^{-8}
10^{-9}
$|P_{ij}|$/bohr^{-2}
10^{1}
10^{2}
10^{3}
ρ/bohr

Figure 14

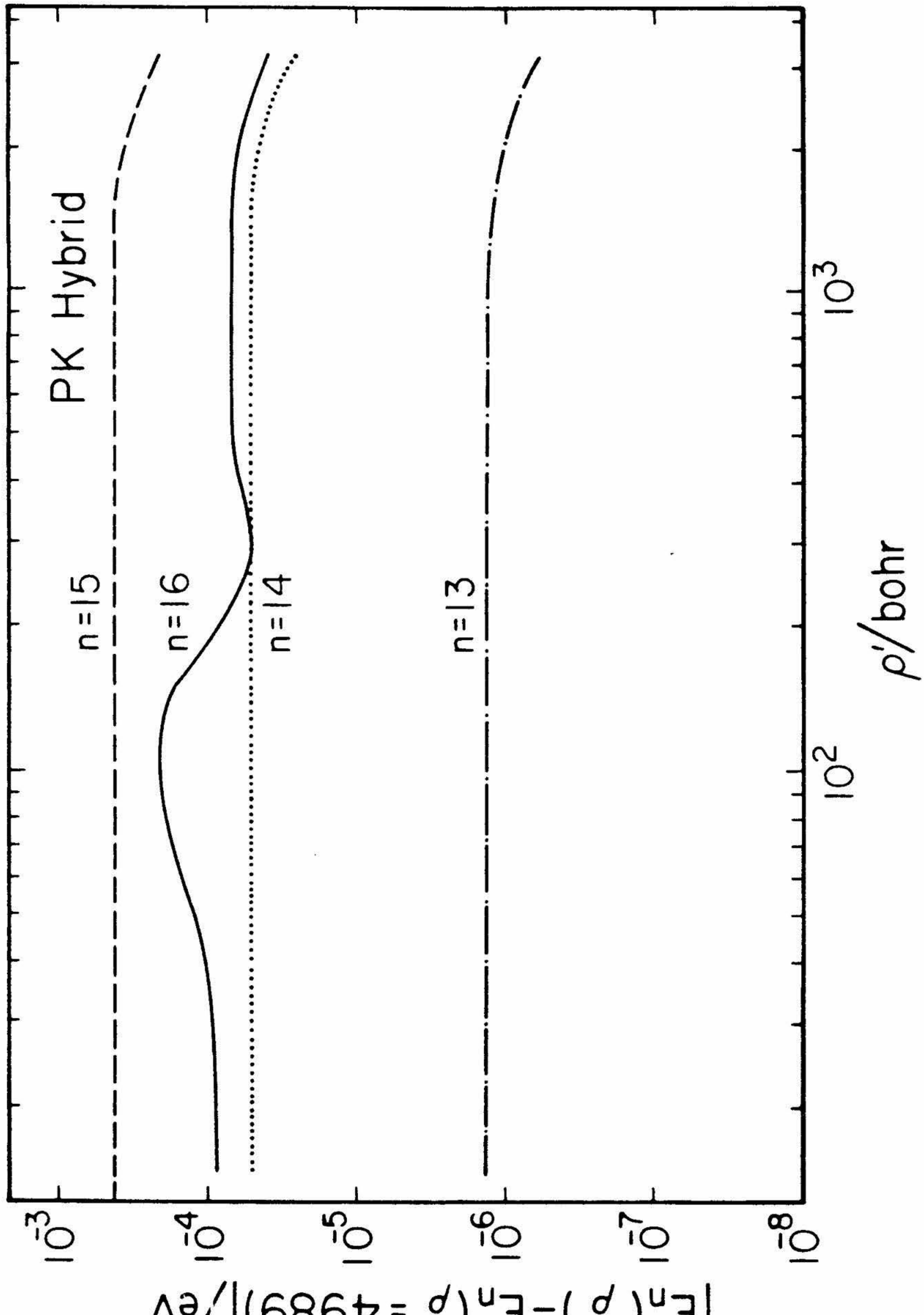
PK Hybrid
n=15
n=16
n=14
n=13
10^{-3}
10^{-4}
10^{-5}
10^{-6}
10^{-7}
10^{-8}
10^{2}
10^{3}
ρ'/bohr
$|E_n(\rho')-E_n(\rho'=4989)|$/eV

Figure 15

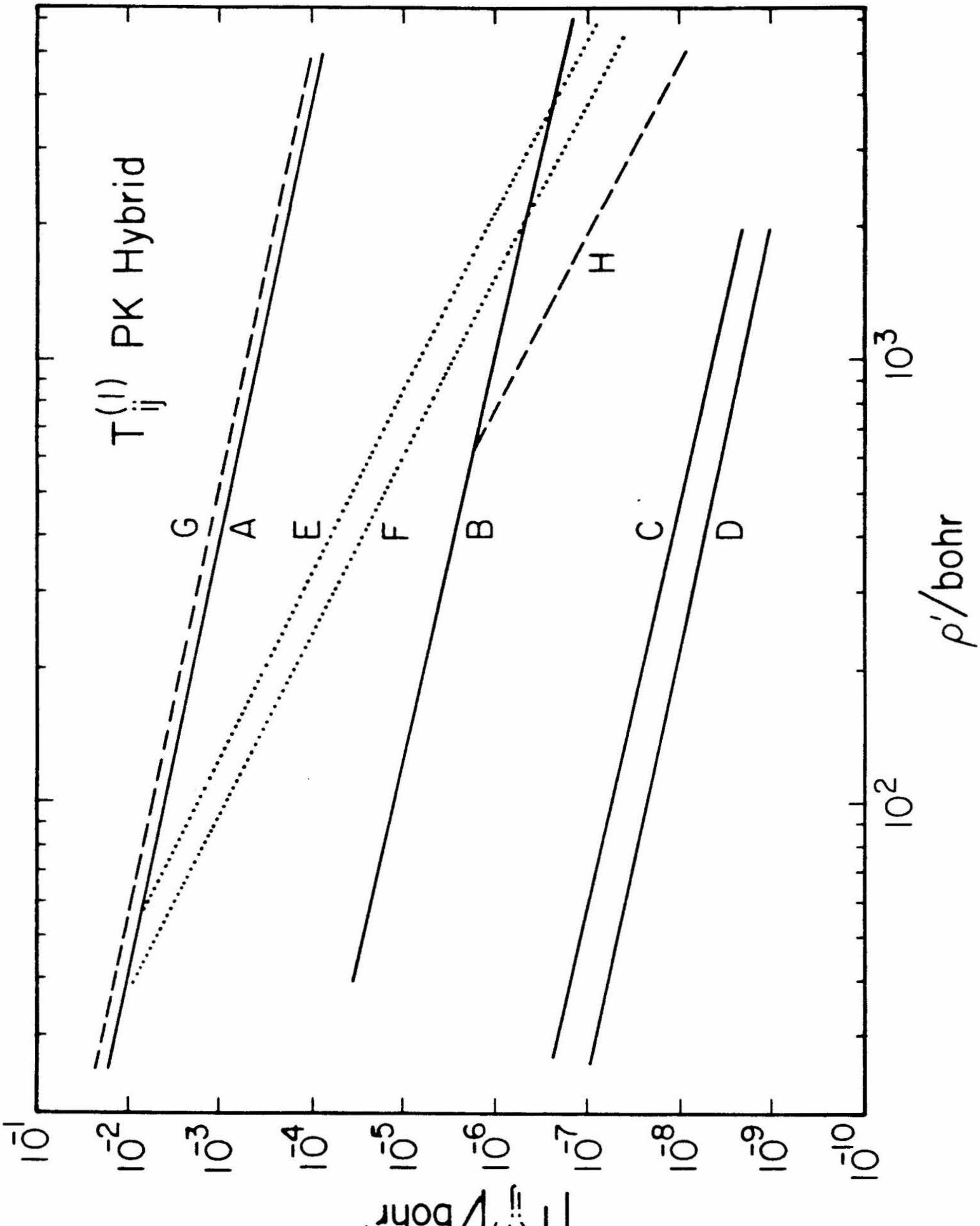
$T_{ij}^{(I)}$ PK Hybrid
G
A
E
F
B
C
D
H
10^{-1}
10^{-2}
10^{-3}
10^{-4}
10^{-5}
10^{-6}
10^{-7}
10^{-8}
10^{-9}
10^{-10}
$|T_{ij}^{(I)}|$/bohr^{-1}
10^{2}
10^{3}
ρ'/bohr

Figure 16

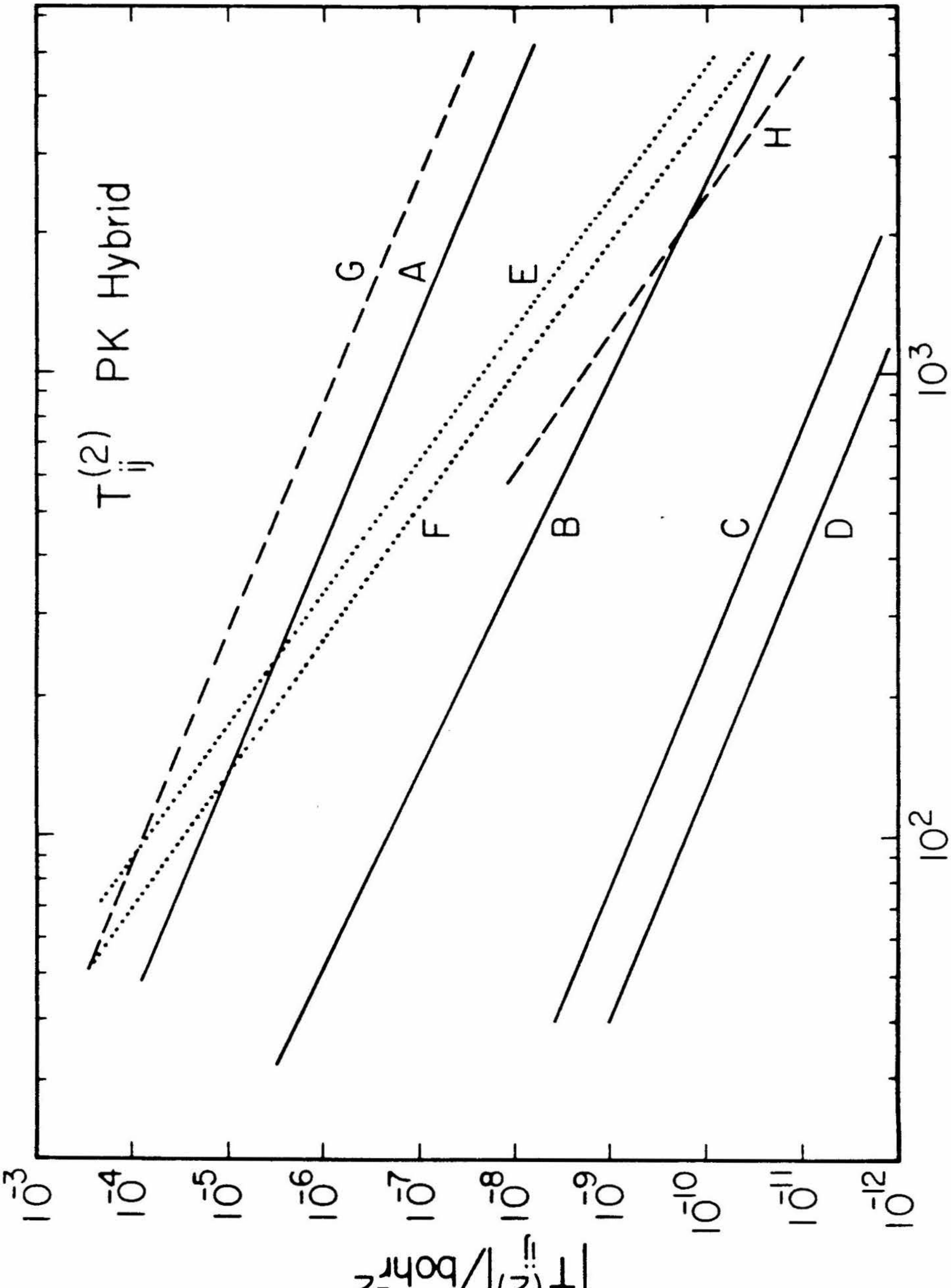
$T_{ij}^{(2)}$ PK Hybrid
$|T_{ij}^{(2)}|$/bohr^{-2}
ρ'/bohr
10^{-3}
10^{-4}
10^{-5}
10^{-6}
10^{-7}
10^{-8}
10^{-9}
10^{-10}
10^{-11}
10^{-12}
10^{-13}
10^{2}
10^{3}
G
A
E
F
B
H
C
D

Figure 17

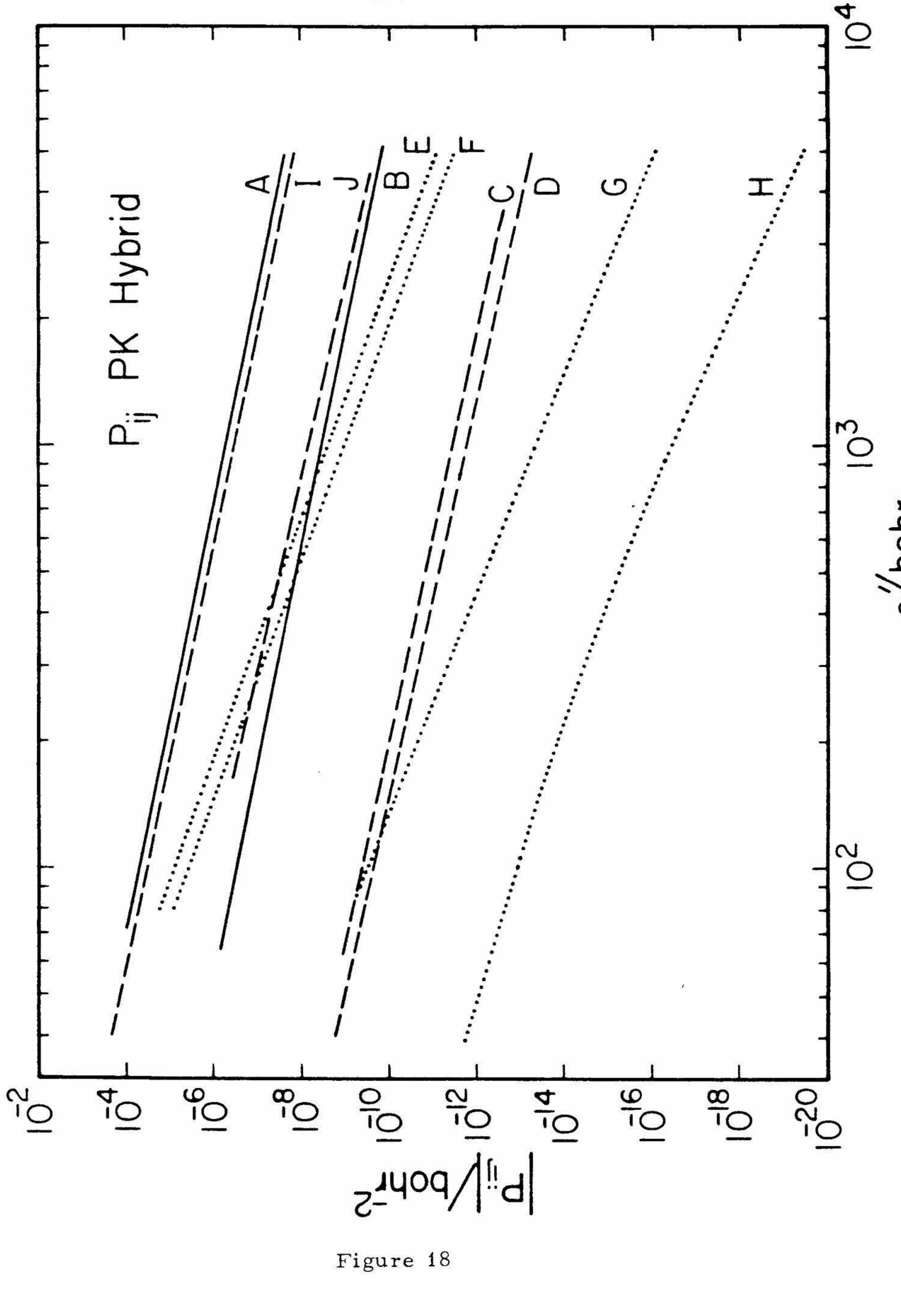
P_{ij} PK Hybrid
A
I
J
B
E
F
C
D
G
H
10^2
10^3
10^4
ρ/bohr
10^{-2}
10^{-4}
10^{-6}
10^{-8}
10^{-10}
10^{-12}
10^{-14}
10^{-16}
10^{-18}
10^{-20}
$|P_{ij}|$/bohr^{-2}

Figure 18

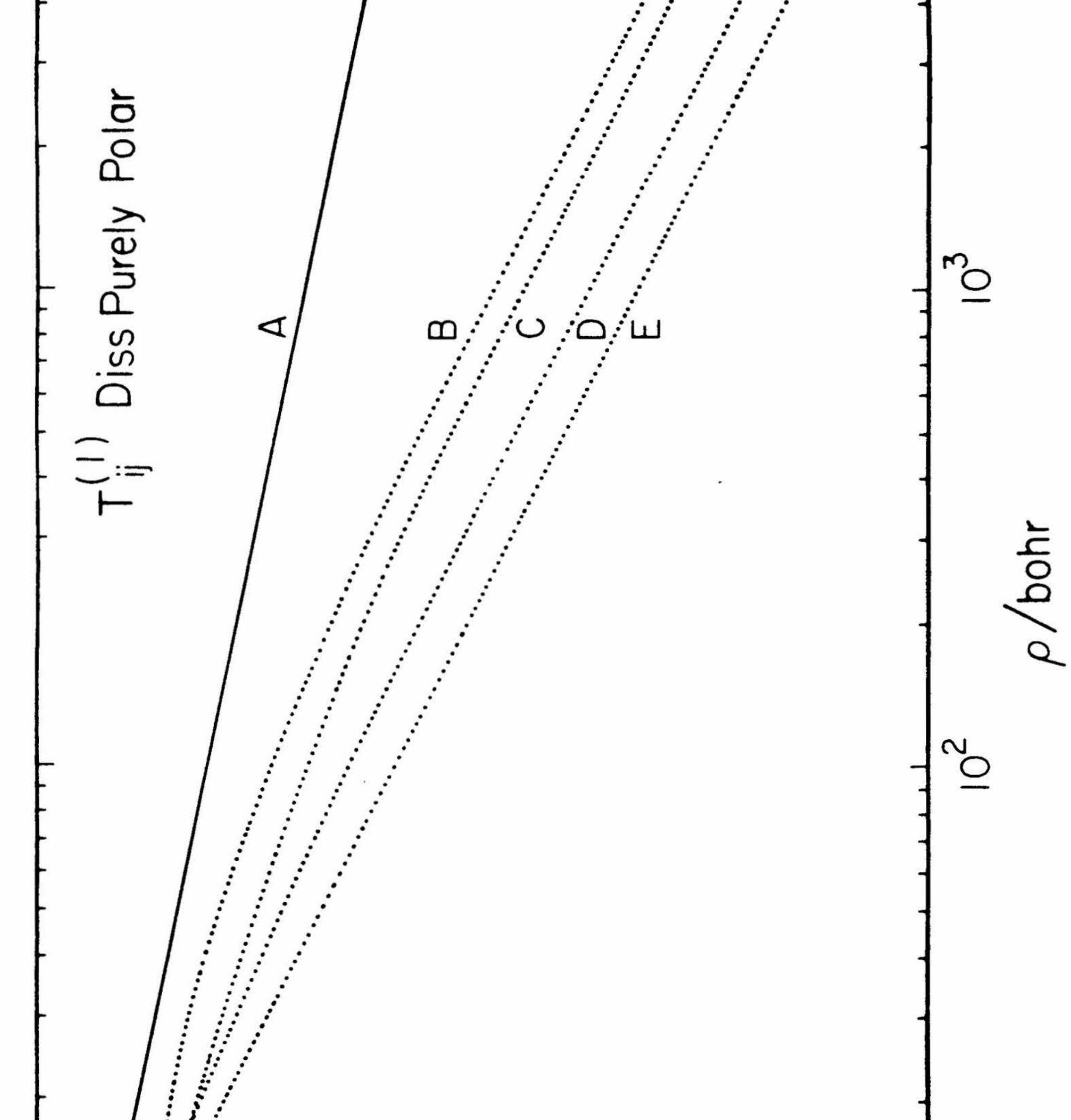
$T_{ij}^{(1)}$ Diss Purely Polar
A
B
C
D
E
10^{0}
10^{-1}
10^{-2}
10^{-3}
10^{-4}
10^{-5}
10^{-6}
10^{-7}
10^{-8}
10^{-9}
10^{1}
10^{2}
10^{3}
ρ /bohr
$|T_{ij}^{(1)}|$ / bohr^{-1}

Figure 19

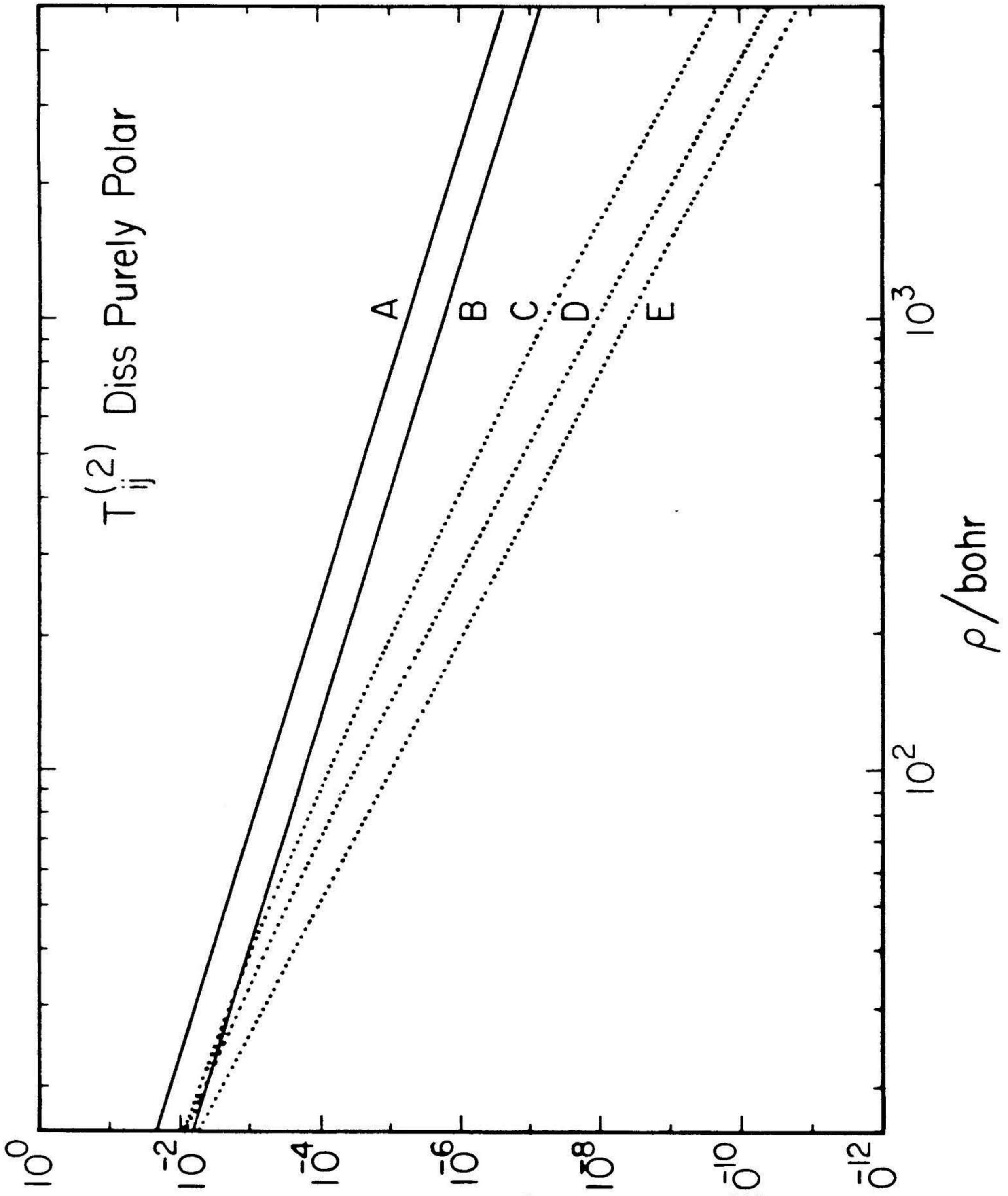
$T_{ij}^{(2)}$ Diss Purely Polar
A
B
C
D
E
10^0
10^{-2}
10^{-4}
10^{-6}
10^{-8}
10^{-10}
10^{-12}
$|T_{ij}^{(2)}|/\mathrm{bohr}^{-2}$
10^2
10^3
ρ/bohr

Figure 20

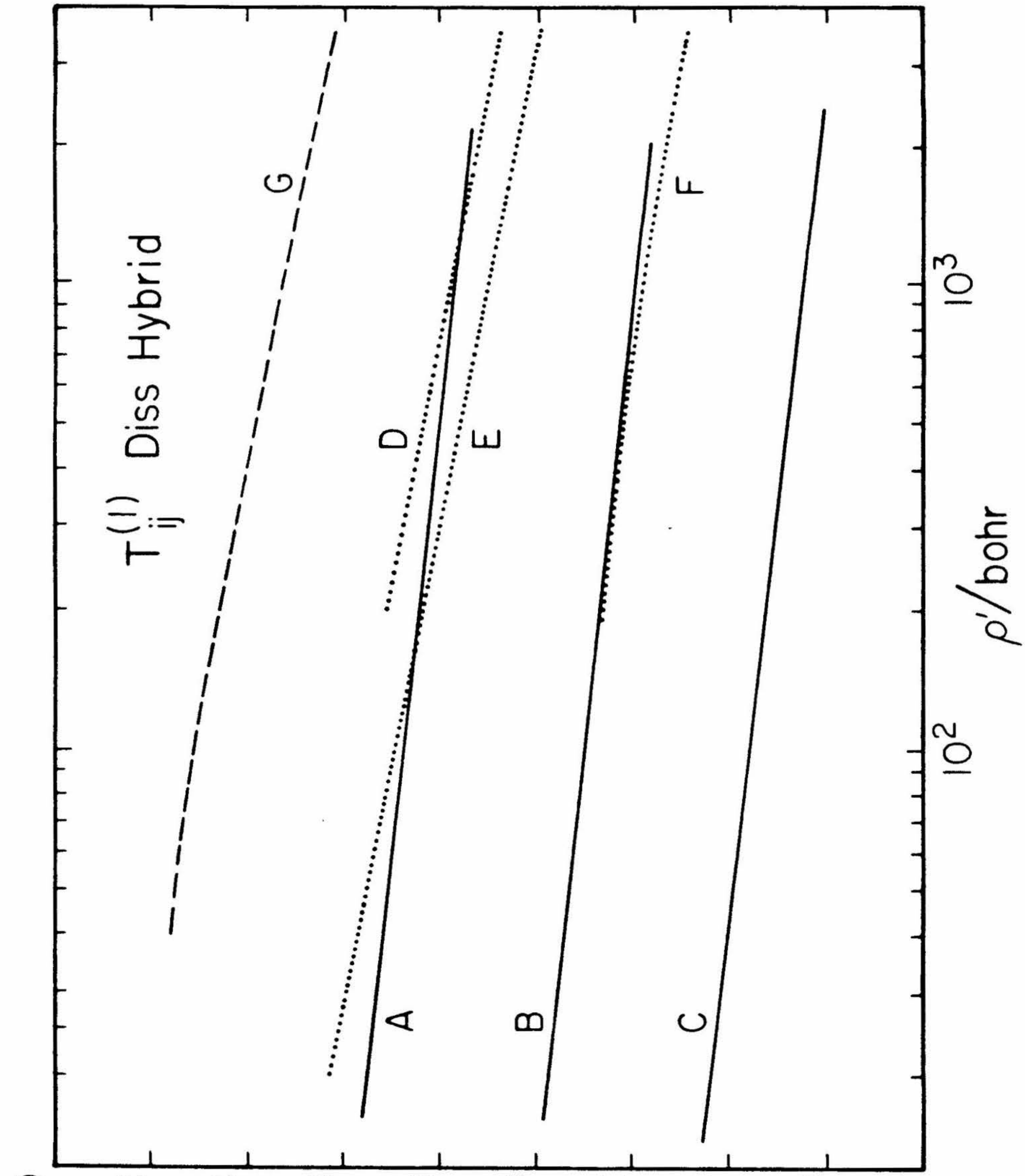
$T_{ij}^{(1)}$ Diss Hybrid
A
B
C
D
E
F
G
10^{0}
10^{-2}
10^{-4}
10^{-6}
10^{-8}
10^{-10}
10^{-12}
10^{-14}
10^{-16}
10^{-18}
10^{2}
10^{3}
ρ'/bohr
$|T_{ij}^{(1)}|$/bohr^{-1}

Figure 21

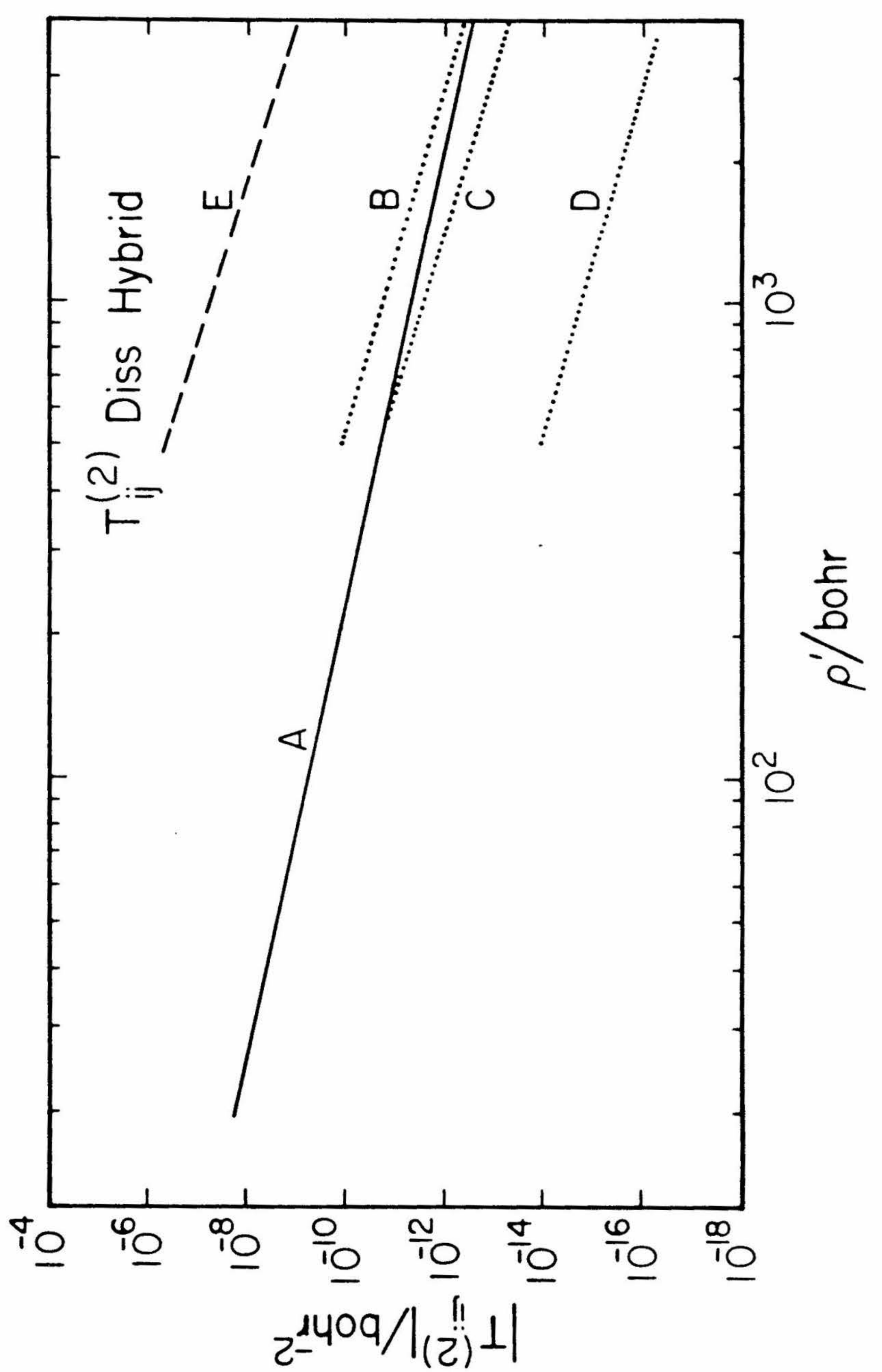
$T_{ij}^{(2)}$ Diss Hybrid
A
B
C
D
E
10^{-4}
10^{-6}
10^{-8}
10^{-10}
10^{-12}
10^{-14}
10^{-16}
10^{-18}
$|T_{ij}^{(2)}|$/bohr^{-2}
10^2
10^3
ρ'/bohr

Figure 22

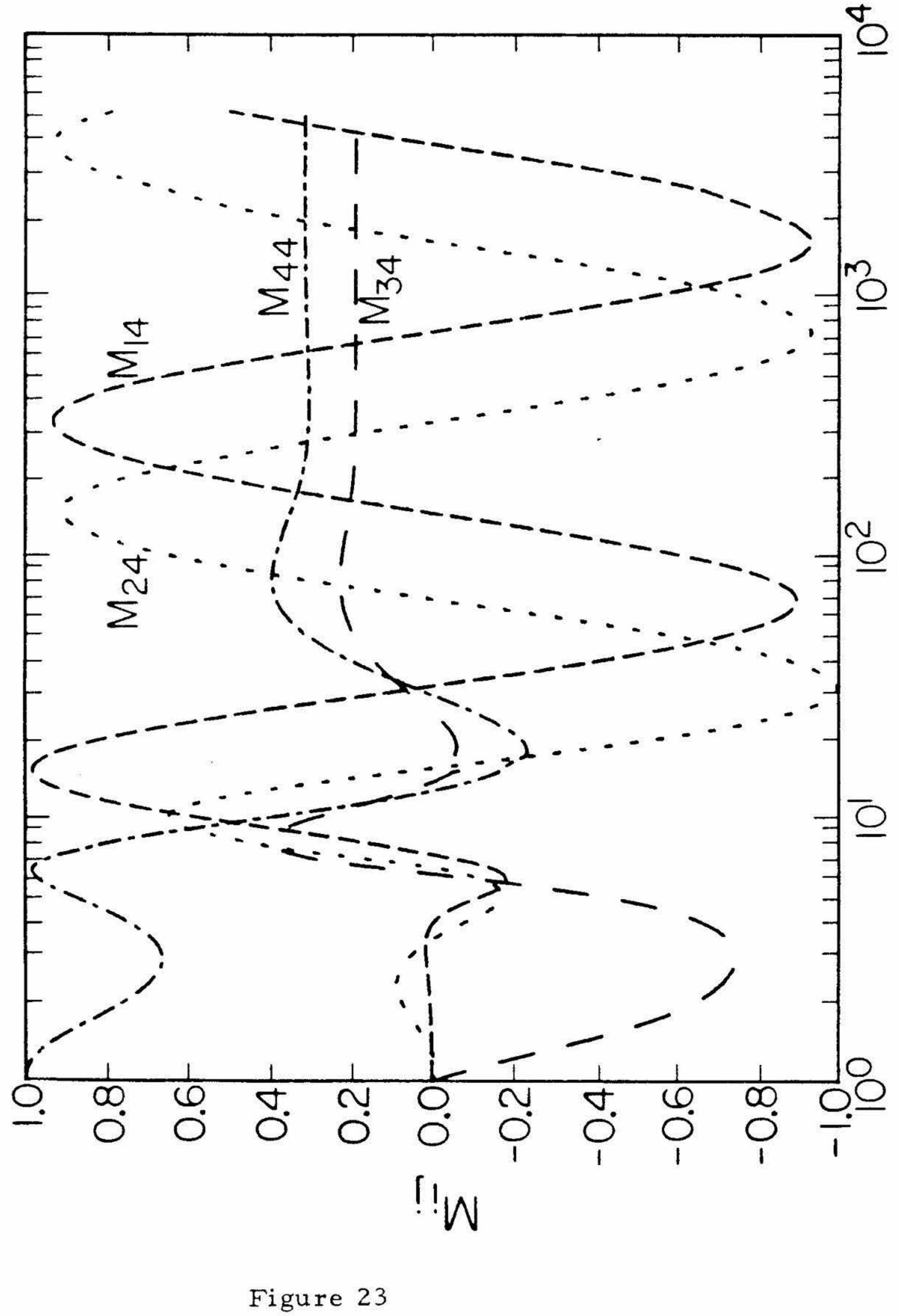
M_{ij}
1.0
0.8
0.6
0.4
0.2
0.0
-0.2
-0.4
-0.6
-0.8
-1.0
10^0
10^1
10^2
10^3
10^4
ρ/bohr
M_{14}
M_{24}
M_{44}
M_{34}

Figure 23

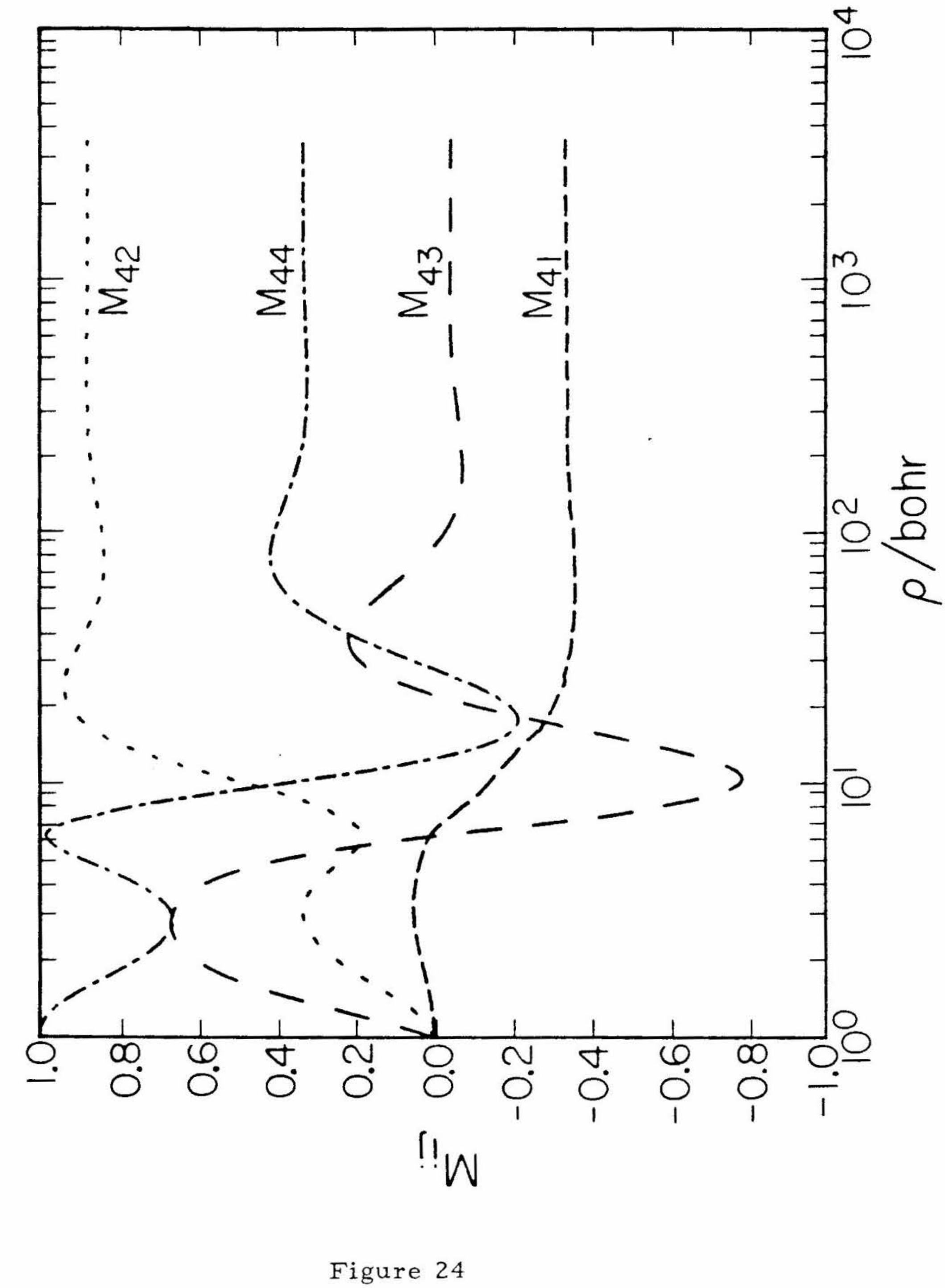
M$_{42}$
M$_{44}$
M$_{43}$
M$_{41}$
1.0
0.8
0.6
0.4
0.2
0.0
-0.2
-0.4
-0.6
-0.8
-1.0
10^0
10^1
10^2
10^3
10^4
ρ/bohr
M$_{ij}$

Figure 24

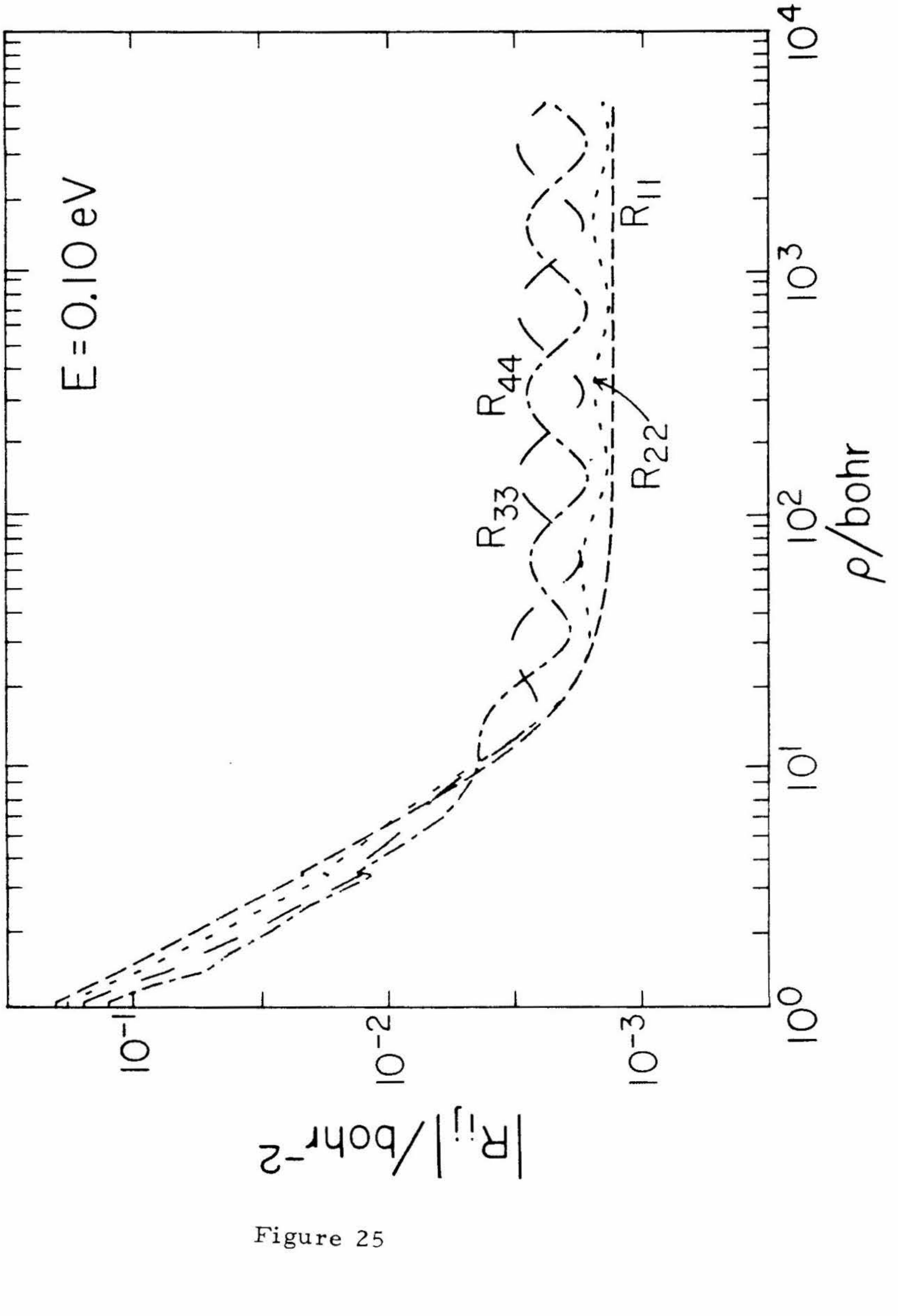
E=0.10eV
R_33
R_44
R_22
R_11
10^0
10^1
10^2
10^3
10^4
ρ/bohr
10^-1
10^-2
10^-3
|R_ij|/bohr^-2

Figure 25

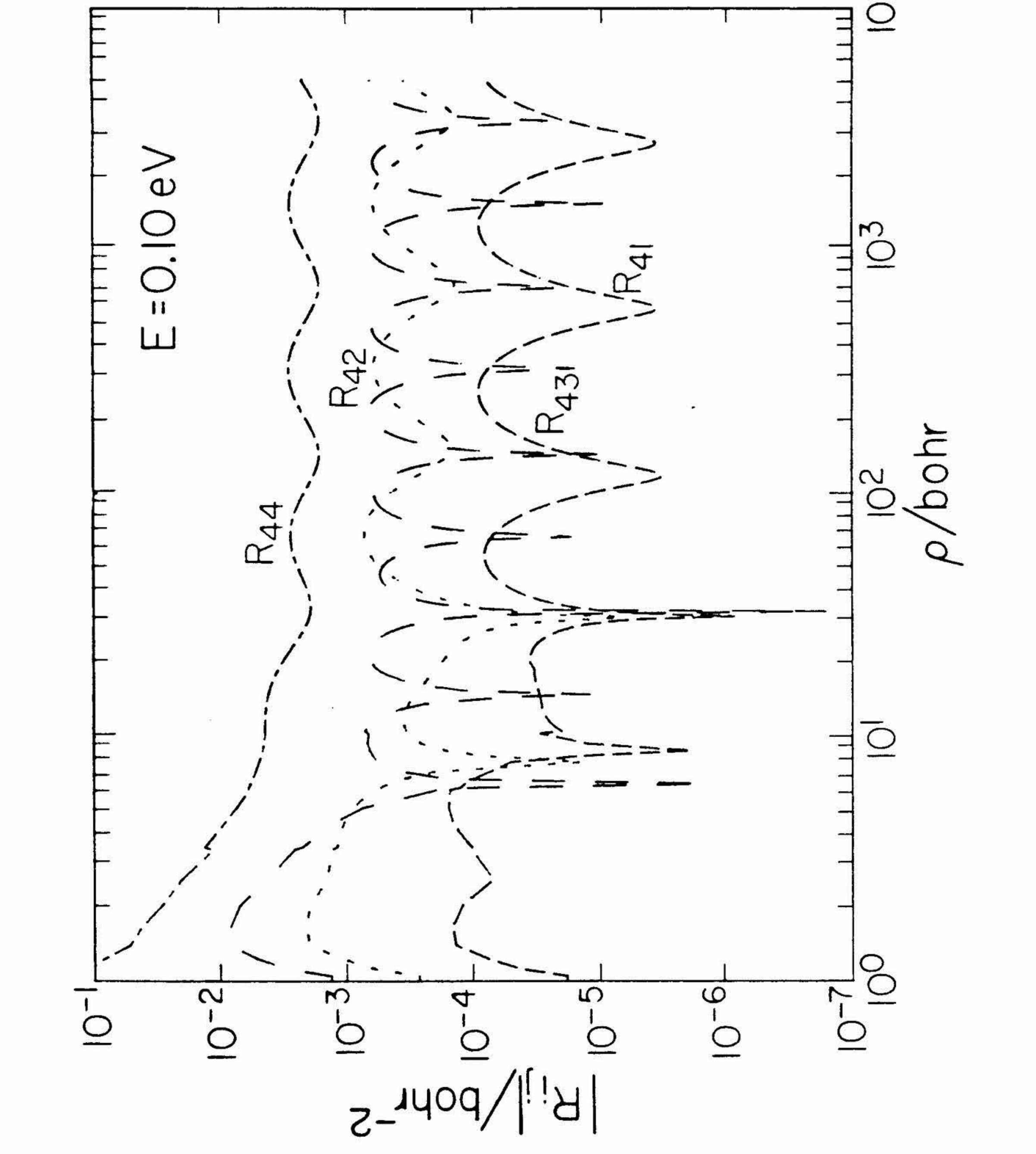
E=0.10eV
R44
R42
R431
R41
10^0
10^1
10^2
10^3
10^4
ρ/bohr
10^-1
10^-2
10^-3
10^-4
10^-5
10^-6
10^-7
|Rij|/bohr^-2

Figure 26

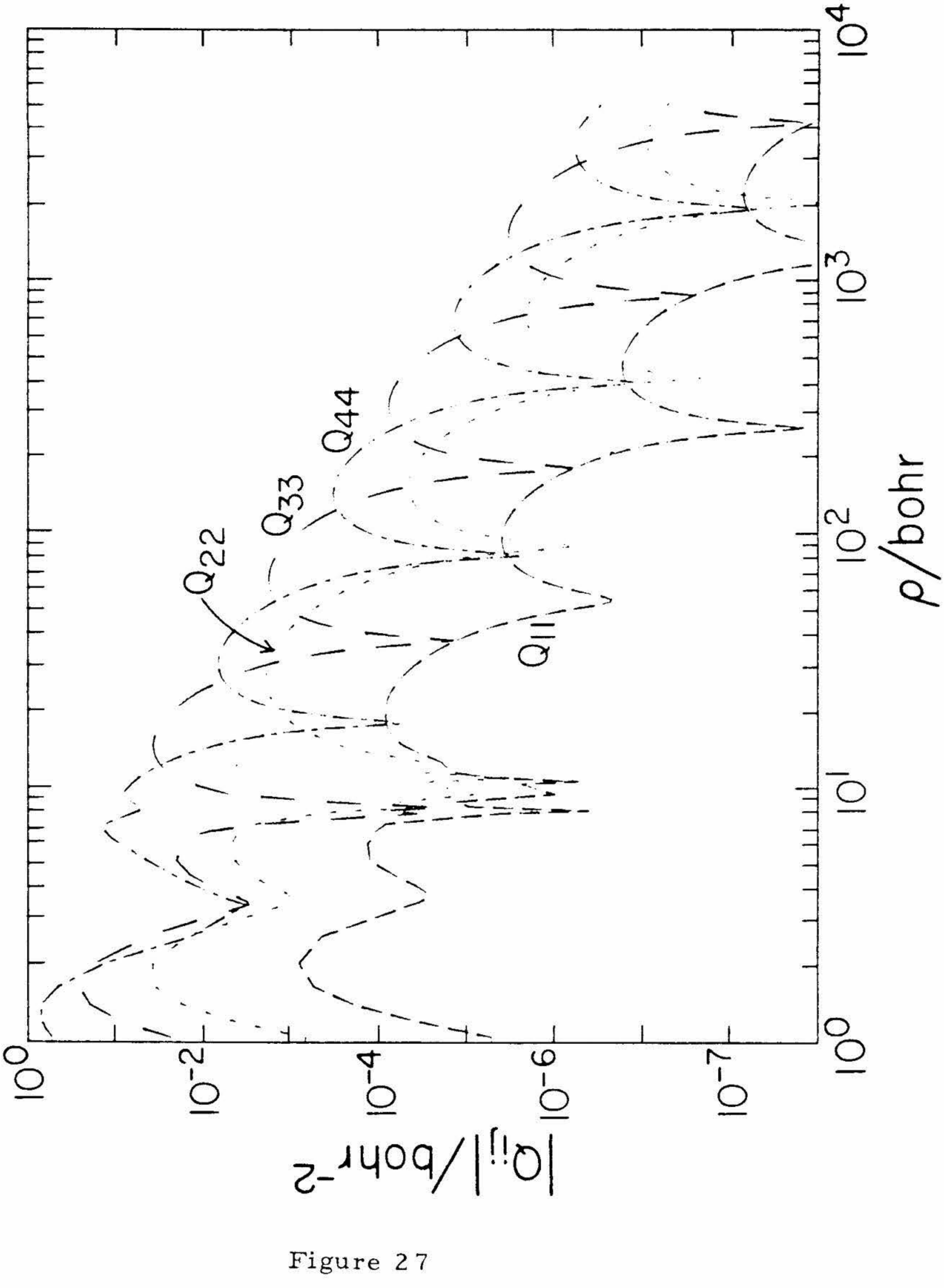
$|Q_{ij}|$/bohr^{-2}
10^0
10^{-2}
10^{-4}
10^{-6}
10^{-7}
ρ/bohr
10^0
10^1
10^2
10^3
10^4
Q_{11}
Q_{22}
Q_{33}
Q_{44}

Figure 27

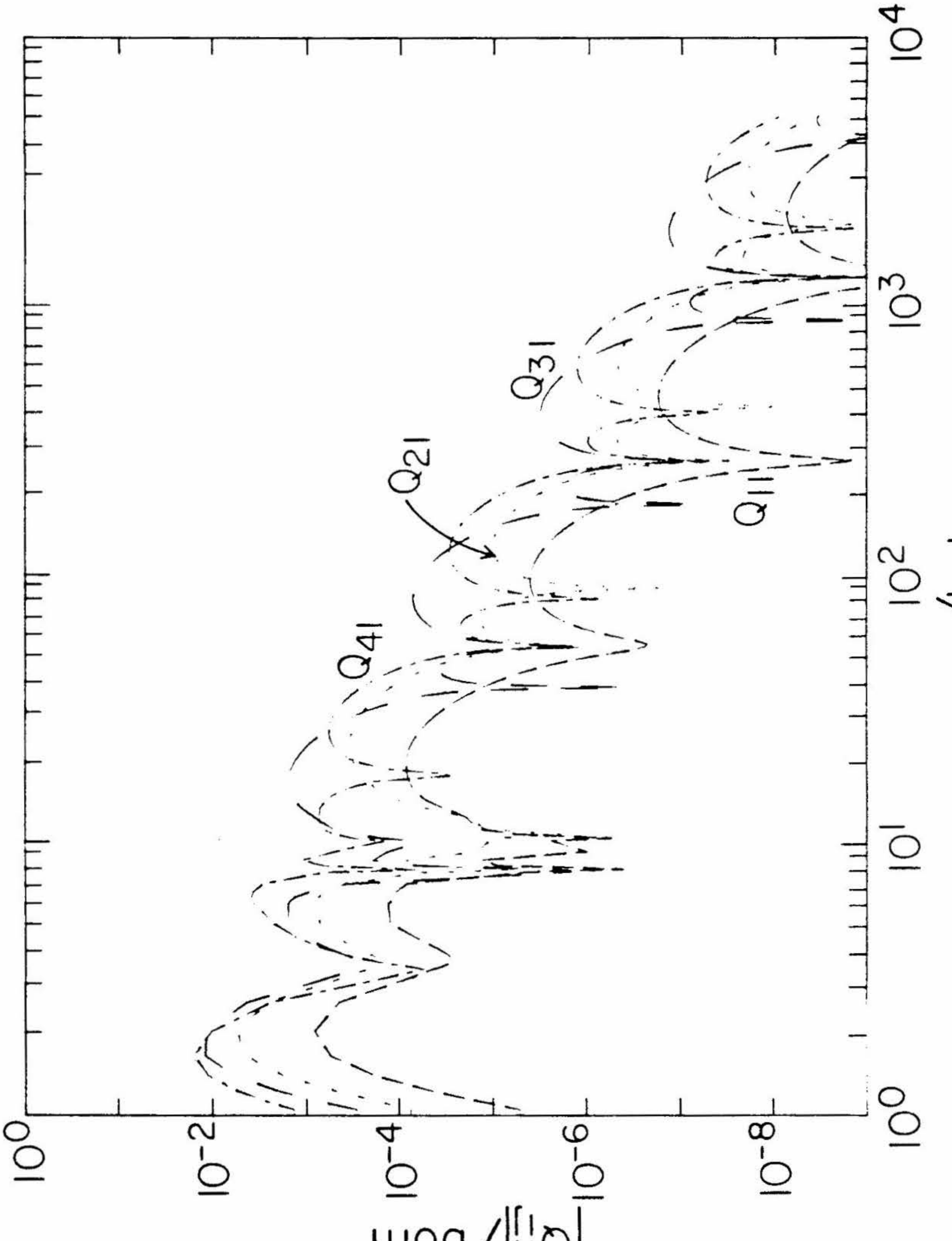
10^0
10^-2
10^-4
10^-6
10^-8
|Q_ij|/bohr^-2
10^0
10^1
10^2
10^3
10^4
ρ/bohr
Q41
Q21
Q31
Q11

Figure 28

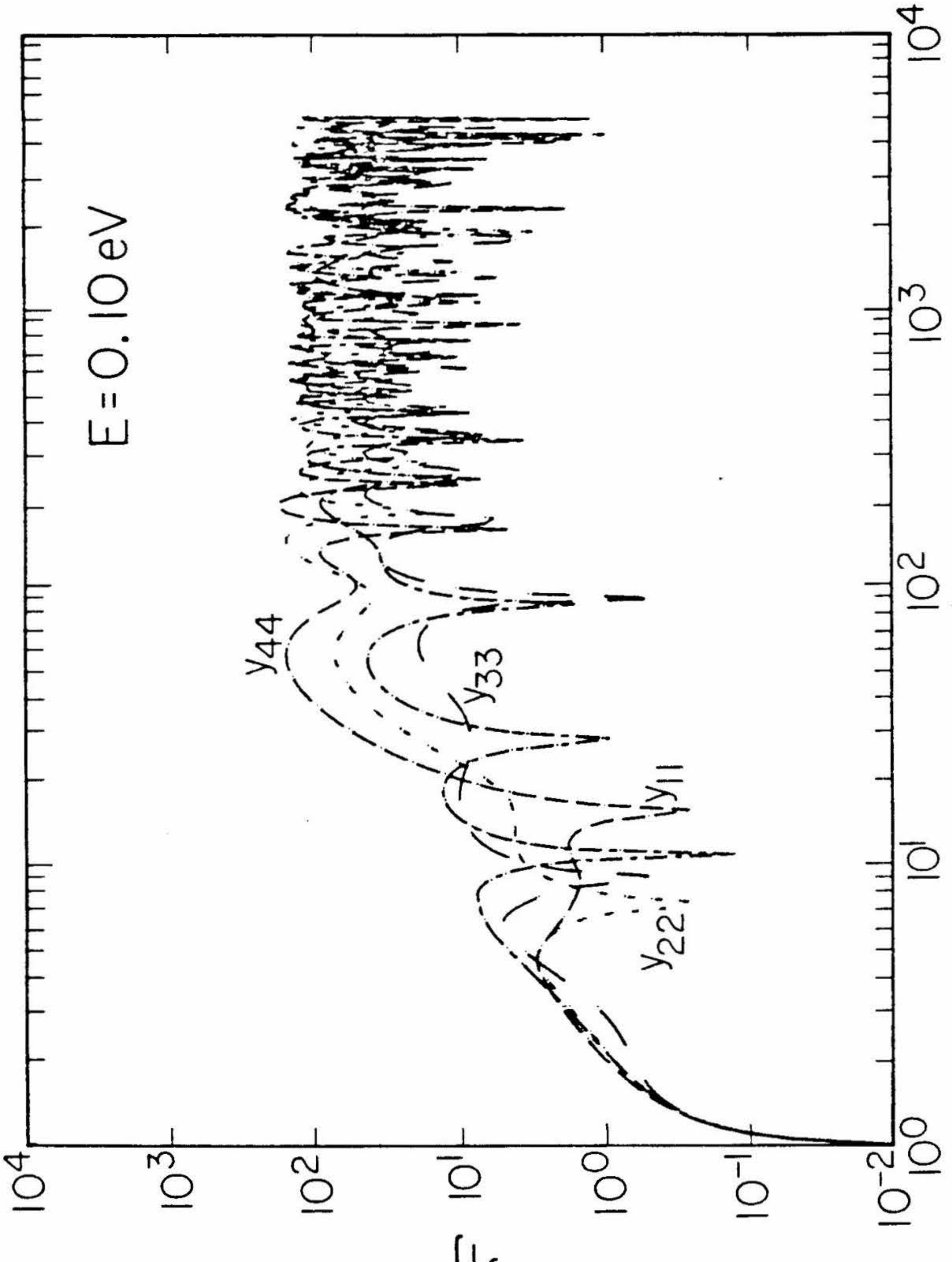
E = 0.10 eV
y44
y33
y11
y22
y_ij
10^4
10^3
10^2
10^1
10^0
10^-1
10^-2
10^0
10^1
10^2
10^3
10^4
ρ/bohr

Figure 29

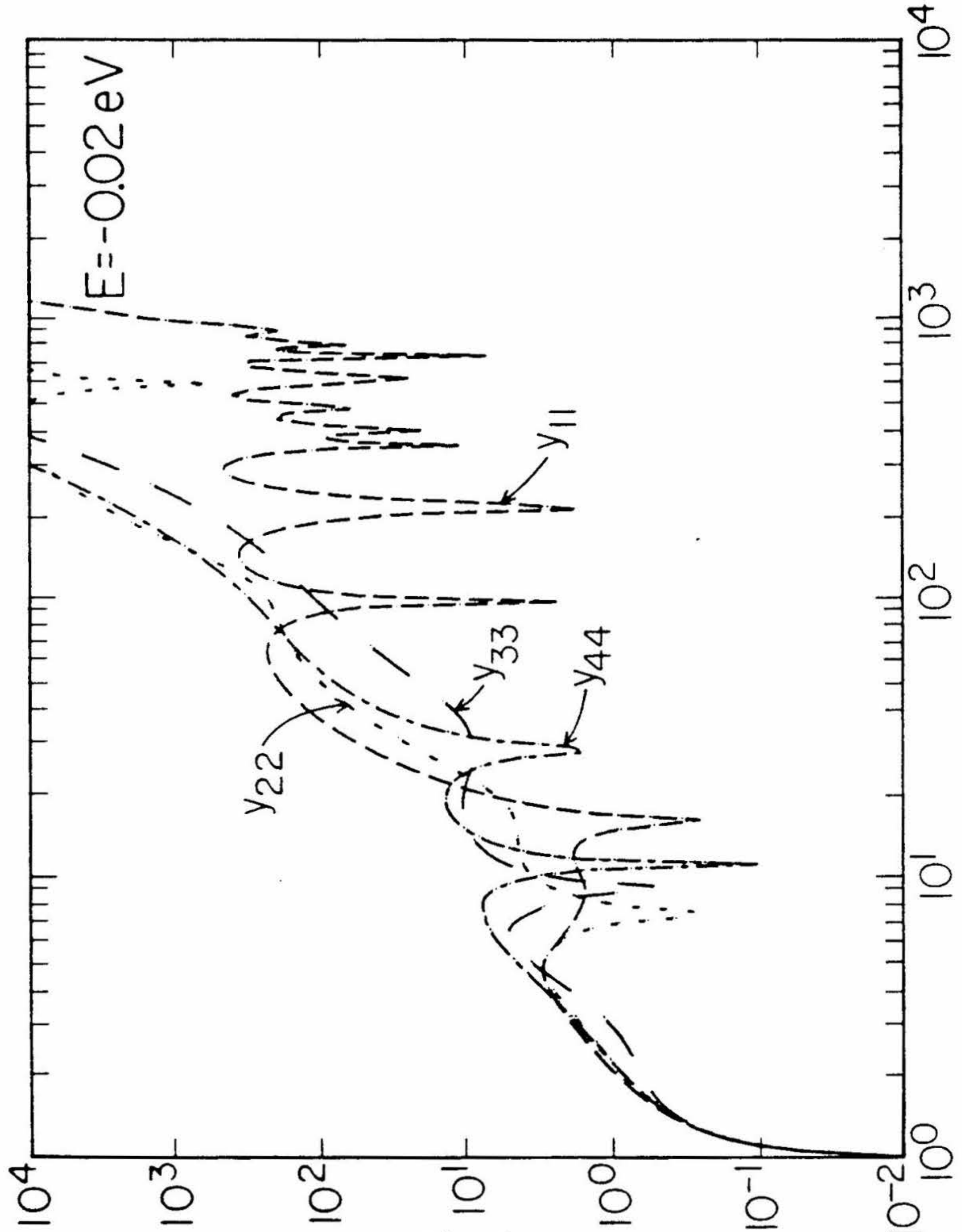
E=-0.02eV
y_{11}
y_{22}
y_{33}
y_{44}
$|y_{ii}|$
ρ/bohr
10^{0}
10^{1}
10^{2}
10^{3}
10^{4}
10^{-2}
10^{-1}
10^{0}
10^{1}
10^{2}
10^{3}
10^{4}

Figure 30

III.10 CALCULATION OF PROBABILITY DENSITY, PROBABILITY CURRENT DENSITY, AND TUNNELING FRACTIONS USING HYPERSPHERICAL COORDINATES AND APPLICATION TO THE COLLINEAR H + H_2 SYSTEM

CALCULATION OF PROBABILITY DENSITY, PROBABILITY CURRENT DENSITY, AND TUNNELING FRACTIONS USING HYPERSPHERICAL COORDINATES AND APPLICATION TO THE COLLINEAR H + H_2 SYSTEM*

Jack A. KAYE** and Aron KUPPERMANN

Arthur Amos Noyes Laboratory of Chemical Physics,
California Institute of Technology
Pasadena, California 91125, USA

We have developed a procedure for generating consistent physical wavefunctions from hyperspherical coordinate coupled channel calculations of collinear atom-diatom molecule collisions. Both the formal and numerical aspects of this procedure are developed in detail. The procedure is applied to the collinear $H + H_2$ reaction on the Porter-Karplus surface over the energy range in which the probability of the reaction $H + H_2 (v = 0) \rightarrow H_2 (v = 0) + H$ increases rapidly with increasing energy. Using the wavefunctions generated, we calculate preliminary results of probability densities, probability current densities, and tunneling fractions. These results, although not converged, do show qualitatively correct behavior, including delocalization of probability density with increasing energy, decreased importance of tunneling at high energies, and the formation of a vortex in the field of streamlines of probability current density high energies. Possible methods for improvement in these results are discussed.

---

*Research supported in part by the US Air Force Office of Scientific Research (Contract No. F49620-79-C-0187).

**Work performed in partial fulfilment of the requirements for the Ph.D. in Chemistry at the California Institute of Technology.

1. Introduction

Quantum mechanical scattering calculations and quasi-classical trajectory calculations of chemical reactions have provided a great deal of information about the dynamics of chemical reactions.[1] In addition to allowing one to calculate reaction probabilities as a function of energy, and thus rate constants as a function of temperature, these calculations have proven useful by helping to provide answers to some fundamental questions in chemical dynamics. These questions include such problems as the effect of small changes in the potential energy surface on the dynamics, the importance of quantum mechanical effects, in particular dynamical resonances, and the relative effectiveness of different kinds of internal energy in promoting reaction.

Reaction probabilities as a function of energy are not all that one wishes to know about chemical reactions, however. One would like to be able to answer the question "How does a chemical reaction occur?" Classical trajectories[2] have proven to be very helpful in this regard, as they allow one to see physically what sort of relative motion leads to chemical reaction and the importance of multiple crossings of a barrier to reaction, which has important implications for the application of classical transition state theory.[3] Purely classical trajectories cannot help one to understand quantum mechanical effects, such as tunneling and dynamical resonances, however.

The additional information desired can be obtained by examination of the wavefunctions, ψ_j, generated (in principle if not explicitly) in the course of quantum mechanical scattering calculations. In particular, one wishes to examine the probability density[4]

$$\rho_j(\underset{\sim}{R}) = \psi_j^*(\underset{\sim}{R})\,\psi_j(\underset{\sim}{R}) \qquad (1)$$

everywhere on the potential energy surface (j represents the quantum states of the colliding partners and $\underset{\sim}{R}$ is a vector including all possible coordinates) and the probability current density[4]

$$\underset{\sim}{J}_j(\underset{\sim}{r}) = \frac{i\hbar}{2m}\,[\psi_j \underset{\sim}{\nabla}\,\psi_j^* - \psi_j^* \underset{\sim}{\nabla}\,\psi_j] \qquad (2)$$

(and the streamlines). By consideration of the former quantity, we can examine the variation of the probability density with energy through a resonance. Large changes in it should be seen at some position on the potential energy surface, and these given the "location" of the resonance on the surface. From the latter, by analogy with hydrodynamic streamlines,[5] one can see what portions of the potential energy surface are most sampled in the reaction. One can also get from it a quantitative measure of the extent of tunneling.

Such calculations have been performed by a number of workers. Wyatt and coworkers have examined these quantities for the collinear $H + H_2$[6] and $F + H_2$[7] reactions and the three-dimensional ($J = 0$) $F + H_2$ reaction[8] and found a number of interesting effects; similar observations were made by Kuppermann et al.[9] in their study of the collinear $H + H_2$ reaction. The most interesting observation was that of vortex formation. These vortices have been maned "quantum whirlpools." In a series of papers, Hirschfelder[10] and coworkers have examined streamlines to the probability current density for various simple systems.

The methods used in the calculation of the scattering wavefunctions have had serious limitations. Wyatt and coworkers[6-8] obtained their wavefunctions from coupled channel calculations based on natural collision coordinates, which do not efficiently permit one to study systems of the type

$$H + LH \rightarrow HL + H \tag{3}$$

where H and L represent heavy and light atoms, respectively. In the earliest work, McCullough and Wyatt[6] obtained their wavefunctions by solving the time-dependent Schrödinger equation. Kuppermann et al.[9] obtained their wavefunctions from a modified version[11] of the finite difference boundary value method of Diestler and McKoy.[12]

The H-L-H case is one of the most interesting ones for the application of wavefunction and probability current density analysis as the nature of the mass combination leads to a large skewing of the axes when viewed in an appropriate mass-weighted coordinate system.[13] A result of this skewing demonstrated in Fig. 1 or ref. 14 by the potential energy surface for the reaction

$$I' + HI \rightarrow I'H + I \tag{4}$$

is that the reaction probably does not follow the minimum energy path; instead it involves crossing from one well to another at substantially greater distances. This type of motion is permissible at all energies, as the zero-point energy of HI is far greater than the barrier height. Another factor adding to the interest in these systems is the existence of very sharp resonances, which are extremely sensitive to the exact details of the potential energy surface.[14,15] Such reactions can now be easily studied (collinearly) by the hyperspherical coordinates method.[16,17]

In this paper we further develop the hyperspherical coordinates method[16,17] to extract the scattering wavefunction so that probability densities and probability current densities can be calculated (the latter obtained using a previously developed computer program[18] for generating them from wavefunctions in collinear atom-diatom molecule collisions). We outline the theory necessary for this advance and discuss both the theoretical and numerical aspects of its implementation. We show preliminary results for these quantities as calculated for the collinear $H + H_2$ reaction on the Porter-Karplus[19] surface. Numerical difficulties have made further progress difficult; we discuss possible methods to get around them. Finally, we discuss some improvements that may be made in the calculation of the probability current density from the wavefunction specifically when the wavefunction is generated by a coupled channel technique (rather than by a finite difference technique as used previously).

2. Theory

The theoretical questions to be dealt with may be broken down into a set of interrelated ones. First, one must consider how the wavefunction is represented in the hyperspherical coordinate approach[16] to reactive scattering. One must then consider how the physical wavefunction, corresponding to the collision of the diatomic molecule in a specific vibrational state with the incident atom, may be constructed from the wavefunctions generated in the course of the solution of the scattering equations and the final $\underline{\underline{S}}$ matrix. We need to examine both the formal and numerical spects of this step. Finally, we must take these physical wavefunctions and from them obtain the probability density and probability current densities.

Since the first[16] and third[18] of these have been dealt with elsewhere, we will focus our attention on the second. Nevertheless, we will briefly review the first and third questions for the sake of completeness.

A. The hyperspherical coordinates wavefunction

The fundamental idea of the hyperspherical coordinates approach to the collinear reactive atom-diatomic molecule scattering problems is simple. As the two coordinates necessary to describe the system, one uses one distance, ρ, and one angle, α, (this technique is described more fully in ref. 16, where ρ and α are defined. The wavefunction is expanded in terms of a basic set of eigenfunctions $\phi_i(\alpha,\bar{\rho})$ of a cut through the potential at a constant value of $\rho = \bar{\rho}$.

$$\psi_j(\rho,\alpha) = \rho^{-\frac{1}{2}} \sum_{i=0}^{N} g_{ij}(\rho;\bar{\rho})\,\phi_i(\alpha;\bar{\rho}) \qquad (5)$$

where the $g_{ij}(\rho,\bar{\rho})$, the so-called radial wave functions, are solutions of the differential equation (expressed in matrix form)

$$-\frac{\hbar^2}{2\mu}\,\frac{d^2\underline{\underline{g}}(\rho,\bar{\rho})}{d\rho^2} + \underline{\underline{W}}(\rho,\bar{\rho})\,\underline{\underline{g}}(\rho,\bar{\rho}) = \underline{\underline{E}}(\rho,\bar{\rho})\,\underline{\underline{g}}(\rho,\bar{\rho}) \qquad (6)$$

where the matrix elements W_{ij} and E_{ij} are given by the expression

$$W_{ij}(\rho,\bar{\rho}) = \langle J|V(\alpha,\rho) - \left(\frac{\bar{\rho}}{\rho}\right)^2 V(\alpha,\bar{\rho})|i\rangle \tag{7}$$

$$E_{ij}(\rho,\bar{\rho}) = [E + \hbar^2/8\,\mu\rho^2 - E_i(\bar{\rho})]\,\delta_{ij} \tag{8}$$

where $|j\rangle = \phi_j(\alpha,\bar{\rho})$, $E_i(\bar{\rho})$ is the eigenvalue of $\phi_i(\alpha;\bar{\rho})$, E is the total energy of the system measured with respect to the bottom of the isolated reagent molecular well, and the integration in eq. (7) is over the angle α.

In solving the differential equation, one starts at a value of ρ sufficiently small that all eigenvalues E_i are much greater than the energy E. In that case, the wavefunction will be sufficiently small that, to a very good approximation, it will be zero, and we may take as our initial conditions

$$\underline{\underline{g}}(0,\bar{\rho}) = \underline{\underline{O}} \tag{9a}$$

$$\underline{\underline{g}}'(0,\bar{\rho}) = \underline{\underline{I}}\ . \tag{9b}$$

The matrix differential equation (6) is then integrated numerically to a value of ρ sufficiently large that the interaction between the particles is such that the diatomic molecules only barely feel the influence of the remaining atom. At that point the ψ_j are then numerically projected onto the bound state eigenfunctions of the BC and AB diatomic molecules; we then obtain the reaction ($\underline{\underline{R}}$), scattering ($\underline{\underline{S}}$), and probability ($\underline{\underline{P}}$) matrices from these wavefunctions.

A crucial point to be made is that the wavefunctions ψ_j generated in the course of integrating eq. (6) do not correspond to the physical wavefunctions desired. The boundary conditions which insure that one is solving the proper problem are only imposed after eq. 6 has been integrated. Thus, in order to obtain a physical wavefunction, we need to use both the wavefunctions generated in the course of the integration and the $\underline{\underline{S}}$ matrix determined in the asymptotic analysis.

B. Calculating the Physical Wavefunction— Formal Aspects

The problem of obtaining the physical wavefunction ψ_j^{phys} from the ψ_j available from the $g_{ij}(\rho,\bar{\rho})$ determined in the integration of eq. 6 reduces to that of finding the correct linear combination of the ψ_j We will call the ψ_j the primitive wavefunctions, because they are what is generated in the program. Mathematically, we want to determine the coefficient matrix $\underline{\underline{W}}$, where

$$\psi_j^{\text{phys}} = \sum_{i=1}^{N} \psi_i^{\rho r} W_{ij}\ , \qquad 1 \le j \le N_{op} \le N \tag{10}$$

where N, the total number of primitive wavefunctions determined, is greater than the number N_{op} of asymptotically open vibrational states ($j = 1$ would correspond to only one state open in either the reagent or product channel, but not both, with no possibility for other than elastic scattering).

The quantity of greatest interest in the analysis that follows is the radial wavefunction matrix $\underline{\underline{h}}$ determined in the projection of the wavefunction onto eigenfunctions χ_i of the AB and BC diatomic potentials:

$$\psi_j^{\rho r} = \rho^{-\frac{1}{2}} \sum_{i=1}^{N} g_{ij}\, \phi_i = \sum_{i=1}^{N} h_{ij}\, \chi_i \tag{11}$$

where we have suppressed the coordinate dependencies of the various wavefunctions. In the ensuing discussion, we will restrict consideration to $\underline{\underline{h}}$. Once we have the matrix $\underline{\underline{W}}$, we will then return to considering the full wavefunction ψ. The asymptotic analysis, which is discussed in detail elsewhere,[20] says that at large values of the distances R_λ, R_γ (defined in ref. 20) we may write $\underline{\underline{h}}$ in one of the two asymptotic forms

$$\underline{\underline{h}}_R = \underline{\underline{v}}^{-\frac{1}{2}} (\underline{\underline{\mathcal{S}}}\,\underline{\underline{C}} + \underline{\underline{\mathcal{C}}}\,\underline{\underline{D}}) \tag{12a}$$

$$\underline{\underline{h}}_S = \underline{\underline{v}}^{-\frac{1}{2}} (\underline{\underline{\mathcal{I}}}\,\underline{\underline{A}} + \underline{\underline{\mathcal{O}}}\,\underline{\underline{B}}) \tag{12b}$$

(where $\underline{\underline{h}}_R = \underline{\underline{h}}_S = \underline{\underline{h}}$)

where $\underline{\underline{v}}$ is a diagonal matrix given by

$$V_{\lambda n_\lambda} = \delta_{nn'} \hbar |k_{\lambda n_\lambda}| / \mu \tag{13}$$

where the wavenumber $k_{\lambda n_\lambda}$ is given by the expression

$$k_{\lambda n_\lambda} = \frac{1}{\hbar} [2\mu (E - E_{\lambda n_\lambda})]^{\frac{1}{2}} \tag{14}$$

where λ denotes the arrangement channel ($\lambda = A + BC$, $\kappa = AB + C$) and the $E_{\lambda n_\lambda}$ are the vibrational energies of the diatomic molecule in channel λ and

$$\underline{\underline{\mathcal{I}}}_{\lambda n_\lambda}(R_\lambda) = \begin{cases} \exp(-ik_{\lambda n_\lambda} R_\lambda) & \text{for open channels} \\ \exp(|k_{\lambda n_\lambda}| R_\lambda) & \text{for closed channels} \end{cases} \tag{15}$$

$$\underline{\underline{\mathcal{O}}}_{\lambda n_\lambda}(R_\lambda) = \begin{cases} \exp(ik_{\lambda n_\lambda} R_\lambda) & \text{for open channels} \\ \exp(-|k_{\lambda n_\lambda}| R_\lambda) & \text{for closed channels} \end{cases} \tag{16}$$

$$\underline{\underline{\mathcal{S}}}_{\lambda n_\lambda}(R_\lambda) = \begin{cases} \sin(k_{\lambda n_\lambda} R_\lambda) & \text{for open channels} \\ \exp(|k_{\lambda n_\lambda}| R_\lambda) & \text{for closed channels} \end{cases} \tag{17}$$

$$\underline{\underline{\mathcal{C}}}_{\lambda n_\lambda}(R_\lambda) = \begin{cases} \cos(k_{\lambda n_\lambda} R_\lambda) & \text{for open channels} \\ \exp(-|k_{\lambda n_\lambda}| R_\lambda) & \text{for closed channels} \end{cases} \tag{18}$$

Similar expressions may be derived for the derivatives $\underline{\underline{h}}'_R$ and $\underline{\underline{h}}'_S$, where $\underline{\underline{\mathcal{S}}}$, $\underline{\underline{\mathcal{C}}}$, $\underline{\underline{\mathcal{I}}}$, and $\underline{\underline{\mathcal{O}}}$ are replaced by their R_λ derivatives $\underline{\underline{\mathcal{S}}}'$, $\underline{\underline{\mathcal{C}}}'$, $\underline{\underline{\mathcal{I}}}'$, and $\underline{\underline{\mathcal{O}}}'$, respectively.

The $\underline{\underline{h}}_R$ form is more convenient from a computational point of view, as then only real quantities are involved. The matrices $\underline{\underline{C}}$ and $\underline{\underline{D}}$ may be obtained from $\underline{\underline{h}}_R$, $\underline{\underline{h}}'_R$, $\underline{\underline{\mathcal{S}}}$, $\underline{\underline{\mathcal{C}}}$, $\underline{\underline{\mathcal{S}}}'$, and $\underline{\underline{\mathcal{C}}}'$. The reactance matrix $\underline{\underline{R}}$ is obtained by the expression

$$\underline{\underline{R}} = \underline{\underline{D}}\,\underline{\underline{C}}^{-1}. \tag{19}$$

When only reaction probabilities are desired, one may consider only the "open" part of the $\underline{\underline{R}}$ matrix ($N_{op} \times N_{op}$ instead of $N \times N$) and calculate the open part of the $\underline{\underline{S}}$ matrix and from that the probabilities in the usual way.

The $\underline{\underline{h}}_S$ form is closer to the physical wavefunction however, as it involves incoming and outgoing waves in all states and in all channels. What we seek is the wavefunction in which there is an incoming wave in only one state in one channel (but all possible outgoing states in both channels are allowed). The $\underline{\underline{S}}$ matrix may be obtained analogously to the manner in which $\underline{\underline{R}}$ was obtained. The matrices $\underline{\underline{A}}$ and $\underline{\underline{B}}$ may be obtained from $\underline{\underline{h}}_S$, $\underline{\underline{h}}'$, $\underline{\underline{\mathcal{I}}}$, $\underline{\underline{\mathcal{I}}}'$, $\underline{\underline{\mathcal{O}}}$, and $\underline{\underline{\mathcal{O}}}'$, and then by the expression

$$\underline{\underline{S}} = \underline{\underline{B}}\,\underline{\underline{A}}^{-1} . \tag{20}$$

Substituting eq. (19) into eq. (12a) and eq. (20) into eq. (12b), we get

$$\underline{\underline{h}}_R = v^{-\frac{1}{2}}(\underline{\underline{\mathcal{S}}} + \underline{\underline{\mathcal{C}}}\,\underline{\underline{R}})\,\underline{\underline{C}} \tag{21a}$$

$$\underline{\underline{h}}_S = v^{-\frac{1}{2}}(\underline{\underline{\mathcal{D}}} - \underline{\underline{\mathcal{O}}}\,\underline{\underline{S}})\,\underline{\underline{A}} . \tag{21b}$$

We may construct a "physical matrix" solution from the primitive solution by right multiplying by $\underline{\underline{C}}^{-1}$ so

$$\underline{\underline{h}}_R^{\text{phys}} = \underline{\underline{h}}_R\,\underline{\underline{C}}^{-1} = \underline{\underline{v}}^{-\frac{1}{2}}(\underline{\underline{\mathcal{S}}} + \underline{\underline{\mathcal{C}}}\,\underline{\underline{R}}) . \tag{22}$$

We similarly define the "physical S matrix" solution

$$\underline{\underline{h}}_S^{\text{phys}} = \underline{\underline{h}}_S\,\underline{\underline{A}}^{-1} = \underline{\underline{v}}^{-\frac{1}{2}}(\underline{\underline{\mathcal{D}}} - \underline{\underline{\mathcal{O}}}\,\underline{\underline{S}}) . \tag{23}$$

We need then relate $\underline{\underline{h}}_R^{\text{phys}}$ and $\underline{\underline{h}}_S^{\text{phys}}$, we may do this by the matrix equation

$$\underline{\underline{h}}_S^{\text{phys}} = \underline{\underline{h}}_R^{\text{phys}}\,\underline{\underline{V}} . \tag{24}$$

Substitution of eqs. (22) and (23) into eq. (24) gives us, formally at least, $\underline{\underline{V}}$ and $\underline{\underline{S}}$:

$$(\underline{\underline{\mathcal{D}}} - \underline{\underline{\mathcal{O}}}\,\underline{\underline{S}}) = (\underline{\underline{\mathcal{S}}} + \underline{\underline{\mathcal{C}}}\,\underline{\underline{R}})\,\underline{\underline{V}} . \tag{25}$$

We may get both $\underline{\underline{S}}$ and $\underline{\underline{V}}$ because each submatrix (the open and closed parts) contains two different types of terms: sines and cosines in the open parts and $\exp(|\kappa|R)$ and $\exp(-|\kappa|R)$ in the closed parts. We will return to this later.

The last step involves conversion of the "physical S matrix" solution to the actual physical solution. The solution we have now is very close to the desired asymptotic form

$$\psi^{\text{phys}}_{\lambda' n'_{\lambda'}} \sim \sum_{\lambda n_\lambda} [\delta^{\lambda' n'_{\lambda'}}_{\lambda n_\lambda} \exp(-i\kappa'_{\lambda n_\lambda} R_\lambda) + f^{\lambda' n'_{\lambda'}}_{\lambda n_\lambda} \exp(i k_{\lambda n_\lambda} R_\lambda)]\, \chi_{\lambda n_\lambda}(r_\lambda) \tag{26}$$

where r_λ is the internal coordinate of the diatomic molecule in the λ channel. The $\underline{\underline{f}}$ and $\underline{\underline{S}}$ matrix elements are related in the following way:

$$f^{\lambda' n'_{\lambda'}}_{\lambda n_\lambda} = \left(\frac{v_{\lambda' n'_{\lambda'}}}{v_{\lambda n_\lambda}} \right)^{\frac{1}{2}} S^{\lambda' n'_{\lambda'}}_{\lambda n_\lambda} \; . \tag{27}$$

Hence, the desired physical wavefunction $\underline{\underline{h}}^{\text{phys}}$, is related to $\underline{\underline{h}}^{\text{phys}}_S$ by the expression

$$\underline{\underline{h}}^{\text{phys}} = \underline{\underline{h}}^{\text{phys}}_S \, \underline{\underline{v}}^{\frac{1}{2}} \; . \tag{28}$$

Rewriting things in terms of the actual wavefunction

$$\psi^{\text{phys}}_j = \psi^{\text{phys}}_{sj} \, v_j^{\frac{1}{2}} \tag{29}$$

which, combined with eq. (24), (20), and (10) lets us write

$$\underline{\underline{W}} = \underline{\underline{C}}^{-1} \underline{\underline{V}}\, \underline{\underline{v}}^{\frac{1}{2}} \tag{30}$$

so

$$\psi^{\text{phys}}_j = \sum_{\kappa \ell} \psi^{\text{pr}}_\ell (C^{-1})_{\ell \kappa} V_{\kappa j} v_j^{\frac{1}{2}} \; . \tag{31}$$

Now we need only evaluate $\underline{\underline{V}}$. To do this, we break eq. (25) up into a set of four equations

$$\left[\begin{pmatrix} \underline{\underline{\mathcal{S}}}_o & 0 \\ 0 & \underline{\underline{\mathcal{S}}}_c \end{pmatrix} + \begin{pmatrix} \underline{\underline{\mathcal{C}}}_o & 0 \\ 0 & \underline{\underline{\mathcal{C}}}_c \end{pmatrix} \begin{pmatrix} \underline{\underline{R}}_{oo} & \underline{\underline{R}}_{oc} \\ \underline{\underline{R}}_{co} & \underline{\underline{R}}_{cc} \end{pmatrix}\right] \begin{pmatrix} \underline{\underline{V}}_{oo} & \underline{\underline{V}}_{oc} \\ \underline{\underline{V}}_{co} & \underline{\underline{V}}_{cc} \end{pmatrix} = \begin{pmatrix} \underline{\underline{\mathcal{J}}}_o & 0 \\ 0 & \underline{\underline{\mathcal{J}}}_c \end{pmatrix} - \begin{pmatrix} \underline{\underline{\mathcal{O}}}_o & 0 \\ 0 & \underline{\underline{\mathcal{O}}}_c \end{pmatrix} \begin{pmatrix} \underline{\underline{S}}_{oo} & \underline{\underline{S}}_{oc} \\ \underline{\underline{S}}_{co} & \underline{\underline{S}}_{cc} \end{pmatrix} \tag{32}$$

From eqs. (15)-(18),

$$\underline{\underline{\mathcal{S}}}_c = \underline{\underline{\mathcal{J}}}_c \tag{33a}$$

$$\underline{\underline{\mathcal{C}}}_c = \underline{\underline{\mathcal{O}}}_c \tag{33b}$$

$$\underline{\underline{\mathcal{J}}}_o = \underline{\underline{\mathcal{C}}}_o - i\,\underline{\underline{\mathcal{S}}}_o \tag{33c}$$

$$\underline{\underline{\mathcal{O}}}_o = \underline{\underline{\mathcal{C}}}_o + i\,\underline{\underline{\mathcal{S}}}_o \quad . \tag{33d}$$

By substituting eqs. (33) into eq. (32) and equating the coefficients of $\underline{\underline{\mathcal{S}}}_o$ and $\underline{\underline{\mathcal{C}}}_o$, we get eight equations (we will suppress the fact that all these quantities, except i, are matrices)

$$V_{oo} = -i\,(I + S_{oo}) \tag{34a}$$

$$R_{oo}V_{oo} + R_{oc}V_{co} = I - S_{oo} \tag{34b}$$

$$V_{oc} = -i\,S_{oc} \tag{34c}$$

$$R_{oo}V_{oc} + R_{oc}V_{cc} = -S_{oc} \tag{34d}$$

$$V_{co} = 0 \tag{34e}$$

$$R_{co}V_{oc} + R_{cc}V_{co} = -S_{co} \tag{34f}$$

$$V_{cc} = I \tag{34g}$$

$$R_{co}V_{oc} + R_{cc}V_{cc} = -S_{co} \quad . \tag{34h}$$

Combining eq. (34a, b, e) we can show

$$S_{oo} = (I - iR_{oo})^{-1}(I + iR_{oo}) \tag{35a}$$

$$V_{oo} = -2i(I - iR_{oo})^{-1}. \tag{35b}$$

It may be shown (Appendix A) that eq. (35a) is equivalent to the usual form[20]

$$S_{oo} = (I + iR_{oo})(I - iR_{oo})^{-1} . \tag{35c}$$

Combining eq. (34c, d, g) we can show

$$S_{oc} = -(I - iR_{oo})^{-1} R_{oc} \tag{36a}$$

$$V_{oc} = i(I - iR_{oo})^{-1} R_{oc} . \tag{36b}$$

We may then write expressions for S_{co} and S_{cc}:

$$S_{co} = 2iR_{co}(I - iR_{oo})^{-1} \tag{37a}$$

$$S_{cc} = -R_{cc} - R_{co}\, i(I - R_{oo})^{-1} R_{oc} . \tag{37b}$$

Equations (36a and 37) are presented for the sake of completeness; they will not be needed in what follows. The only part of $\underline{\underline{S}}$ actually used is S_{oo}, from which reaction probabilities are calculated. We need only the open columns of $\underline{\underline{V}}$. We will construct the entire $\underline{\underline{V}}$ matrix, however. From eqs. (34e), (34g), (35b) and (36b) we see that it may be written as

$$\underline{\underline{V}} = \begin{pmatrix} -2i(I - iR_{oo})^{-1} & i(I - iR_{oo})^{-1} R_{oc} \\ 0 & I \end{pmatrix} . \tag{38}$$

It is noted that $\underline{\underline{R}}_{oc}$ will be needed in the calculation of the closed columns of $\underline{\underline{V}}$. Evaluation is straightforward in that one must use both the open and closed columns of $\underline{\underline{h}}$, $\underline{\underline{h}}'$, $\underline{\underline{\mathcal{S}}}$, $\underline{\underline{\mathcal{C}}}$, $\underline{\underline{\mathcal{S}}}'$, and $\underline{\underline{\mathcal{C}}}'$.

At this point, we have expressions for the three matrices $\underline{\underline{v}}^{\frac{1}{2}}$, $\underline{\underline{V}}$, and $\underline{\underline{C}}^{-1}$, from which $\underline{\underline{W}}$ may be obtained and thus the physical wavefunction may be obtained from the primitive wavefunction.

C. Calculating the Primitive Wavefunctions

The primitive wavefunction ψ_j^{pr} needed for the construction of the physical wavefunctions by eq. (10) are in principle available from the radial wavefunction obtained in the integration of eq. (6), the basis functions $\phi_n(\alpha, \bar{\rho})$ and the value of the propagation coordinate ρ by eq. (5). The successful application of eq. (5) requires that the product

$$\rho^{\frac{1}{2}} \psi_j^{pr} = \sum_{i=1}^{N} \phi_i g_{ij} \tag{39}$$

be continuous. This is not normally the case during the integration of eq. (6) for two reasons.

First, to maintain the linear independence of the N columns of the radial wavefunction being integrated, it is necessary to perform some sort of stabilizing transformation that inhibits the exponential growth associated with the closed channels. This requirement is really numerical in origin. Given a computer with infinite precision, no such transformation would be necessary. The stabilizing transformation used with the hyperspherical coordinates technique is the reorthogonalization procedure of Riley and Kuppermann.[21] In this procedure, the radial wavefunction matrix and its derivative are periodically right-multiplied by the inverse of the current radial wavefunction matrix to give modified matrices as follows:

$$\underline{\underline{g}}_{\mathrm{new}} = \underline{\underline{g}}_{\mathrm{old}}\, \underline{\underline{g}}^{-1}_{\mathrm{old}} = \underline{\underline{I}} \tag{40a}$$

$$\underline{\underline{g}}'_{\mathrm{new}} = \underline{\underline{g}}'_{\mathrm{old}}\, \underline{\underline{g}}^{-1}_{\mathrm{old}} \; . \tag{40b}$$

In this transformation, the logarithmic derivative $\underline{\underline{\ell}}$, given by

$$\underline{\underline{\ell}} = \underline{\underline{g}}'\,\underline{\underline{g}}^{-1} \; , \tag{41}$$

is unchanged. This transformation, which will not affect the reaction probabilities, corresponds to a change of the initial conditions for the integration of eq. (6). Clearly, it does lead to discontinuities in $\underline{\underline{g}}$ which must be corrected for prior to the insertion of $\underline{\underline{g}}$ into eq. (5).

Second, to maintain the magnitude of the radial wavefunction matrix elements, the numerical integrator used[22] "renormalizes" the wavefunction and its derivative after each integration step by right multiplication by a diagonal matrix:

$$\underline{\underline{g}}_{\mathrm{new}} = \underline{\underline{g}}_{\mathrm{old}} \cdot \underline{\underline{c}} \tag{42a}$$

$$\underline{\underline{g}}_{\mathrm{new}} = \underline{\underline{g}}_{\mathrm{old}} \cdot \underline{\underline{c}} \tag{42b}$$

where $\underline{\underline{c}}$ has been defined elsewhere.[22] Substitution of eqs. (42) into eq. (41) shows that the logarithmic derivative $\underline{\underline{\ell}}$ is unchanged by this transformation. Corrections for this renormalization must be made prior to the application of eq. (5).

The problem of construction of a "consistent" $\underline{\underline{g}}$ (that which leads to a continuous ψ_j^{pr}) is in principle exactly the same as that faced in the numerical projection of the wavefunction onto a basis set of BC and AB diatomic molecule eigenfunctions. In that case, the projection procedure requires the radial wavefunction over a range of ρ, which necessitates the propagation of a consistent wavefunction. Because in the case of the projection, a consistent wavefunction is needed over only a small range of ρ (usually ≤ 1 bohr) where the eigenvalues $E_n(\bar{\rho})$ have essentially settled down to their asymptotic values, numerical difficulties are few. In the construction of the consistent $\underline{\underline{g}}$ necessary for the probability density and probability current density calculation, numerical difficulties are quite severe, and we discuss these later.

As presently formulated, the program by which we calculate probability current density from the physical wavefunction ψ_j^{phys} requires them at a regular grid of points (in internuclear coordinates).[18] In the course of the hyperspherical coordinate program, one does not obtain the wavefunction on any regular grid, however. The numerical integrator chooses its own step size in order to meet certain restrictions on the error in each step, meaning that before the calculation is performed, one does not even know at what point the wavefunction will be available. Another difficulty is that the number of grid points desired, usually in the range of 1000-5000 (the grid size normally ranges from 30×30 to 70×70), is sufficiently large that we cannot force the numerical integrator to explicitly integrate from each grid point to the next. Rather, it is desired to permit the integrator to proceed as it would and to obtain the wavefunction at the grid points by an accurate numerical interpolation scheme.

This may be demonstrated by the following example. A typical step size for the integrator in the collinear H + H_2 reaction is 0.03 bohr; a typical range of ρ is from 1 to 10 bohr. Hence, a total of 300 steps for each of the symmetric and antisymmetric solutions will be needed. A typical grid size for a probability density and probability current density study of this reaction might require 1600 points. Thus, if one were to integrate from one grid point to the next, 5 times as many integration steps would be needed. This requirement would impose an unsatisfactory computational burden and is, therefore, unacceptable. The importance of an accurate and efficient numerical interpolation scheme is clearly seen.

Fortunately, the numerical integrator used[22] provides for an efficient means of performing such an interpolation. Again, a similar problem has been faced in the projection of the wavefunction onto the BC and AB diatomic basis sets, where the wavefunction is needed at a large number (100-200) of points over a small ($\lesssim$ 1 bohr) range of ρ. The interpolation method used is the same in both cases. Since the wavefunction is the product of two parts, one angular (given by the basis set), and one radial, we must perform two interpolations to evaluate the wavefunction at an arbitrary grid point.

The angular part of the interpolation is simple. The basis functions are represented numerically as vectors, each element of which corresponds to a value of the angular coordinate α. To obtain the angular part of the wavefunction at some intermediate value of α, one may interpolate by some simple approximation scheme, such as assuming that the

ϕ_n are piecewise linear (as is done for the grid points), or by approximating the entire ϕ_n by a cubic spline and then evaluating the derivative from the spline coefficients at the desired value of α (as is done in the projection region).

For the radial part of the wavefunction, we take advantage of the particular nature of the Gordon integrator.[22] In this integrator, the potential is approximated by a series of linear portions. The resulting differential equations are analytically solvable in terms of the Airy functions Ai and Bi. Within each integration step, the radial wavefunction matrices may be expressed as linear combinations of Ai and Bi functions of the appropriate arguments (see ref. 22, for a full description of the method).

$$\underline{\underline{g}}(\rho) = \underline{\underline{A}}(\rho)\,\underline{\underline{a}}(\rho) + \underline{\underline{B}}(\rho)\,\underline{\underline{b}}(\rho) \tag{43a}$$

$$\underline{\underline{g}}'(\rho) = \underline{\underline{A}}'(\rho)\,\underline{\underline{a}}(\rho) + \underline{\underline{B}}'(\rho)\,\underline{\underline{b}}'(\rho)\,, \tag{43b}$$

where $\underline{\underline{A}}$ and $\underline{\underline{B}}$ are the matrices of Ai and Bi, respectively, and $\underline{\underline{a}}$ and $\underline{\underline{b}}$ are coefficient matrices. It is assumed that the dependence of $\underline{\underline{a}}$ and $\underline{\underline{b}}$ on ρ is sufficiently small such that their deviation from a constant matrix can be determined by perturbation theory. We then make the additional assumption that the perturbation corrections $\underline{\underline{P}}$ and $\underline{\underline{P}}'$ to $\underline{\underline{g}}$ and $\underline{\underline{g}}'$ are linear over the step. We then write

$$\underline{\underline{g}}(\rho) = A(\rho)\,a(\rho_0) + B(\rho)\,b(\rho_0) + \underline{\underline{P}}(\rho) \tag{44a}$$

$$\underline{\underline{g}}'(\rho) = A(\rho)\,a'(\rho_0) + B(\rho)\,b'(\rho_0) + \underline{\underline{P}}'(\rho) \tag{44b}$$

where ρ_0 is the value of ρ at the beginning of the integration step.

The evaluation of $\underline{\underline{a}}$, $\underline{\underline{b}}$, $\underline{\underline{P}}$, and $\underline{\underline{P}}'$ is fully described in ref. 22.

Equations (44) provide a relatively simple and efficient means of interpolating the radial part of the wavefunction. All that is required for the evaluation of $\underline{\underline{g}}(\rho)$ at a grid point is the evaluation of the matrices $\underline{\underline{A}}$ and $\underline{\underline{B}}$ at the value of ρ appropriate to it and the multiplication of the perturbation corrections by the ratio of the quantity $\rho-\rho_0$ to the full stepsize.

With these methods for the interpolation of the angular and radial parts of the wavefunction, we have all the necessary data for the construction of an accurate ψ_j^{pr} at any grid point.

To actually generate consistent primitive wavefunctions, we need, therefore, to undo the stabilizing and normalizing transformations performed on the radial wavefunction. There is a certain amount of freedom associated with this consistency establishment: one can force the wavefunction to be consistent with respect to any given point on the surface (providing one uses a wavefunction consistent with respect to the same point in doing the asymptotic analysis described earlier). The simplest choices are to make it consistent with respect to the beginning of the integration of eq. (6) (eqs. (9)), or to make it consistent with respect to the end of the integration of eq. (6). The former method (forward consistency) is conceptually simpler and requires less computational effort, but has some numerical difficulties associated with the consistency generation. The latter method (backward consistency) is perhaps more elegant, but requires substantially greater computational effort and may have numerical difficulties of its own. We now describe both these methods.

To generate a forward consistent wavefunction one must calculate, every time a reorthogonalization or renormalization is performed, a "transformed unit matrix" by the expressions

$$\underline{\underline{U}}_{\text{new}} = \underline{\underline{U}}_{\text{old}}\, \underline{\underline{g}}_{\text{old}}^{-1} \tag{45a}$$

at reorthogonalizations and

$$\underline{\underline{U}}_{\text{new}} = \underline{\underline{U}}_{\text{old}}\, \underline{\underline{b}} \tag{45b}$$

at renormalizations. At the start of integration, $\underline{\underline{U}} = \underline{\underline{I}}$ (hence the name transformed unit matrix). To generate a consistent radial wavefunction from the inconsistent one propagated in the hyperspherical coordinates program, one need only perform the operation

$$\underline{\underline{g}}^{\text{cons}} = \underline{\underline{g}}^{\text{incons}}\, \underline{\underline{U}}^{-1} \,. \tag{46}$$

This clearly has the effect of undoing all the transformations associated with reorthogonalizations and renormalizations.

Numerical difficulties arise mainly from the reorthogonalization transformations in the following way. Since closed channels lead to exponential growth in the wavefunction, reorthogonalizations involve multiplication of the wavefunction by a matrix, the magnitude of whose elements are less than one. The more closed the channels, the smaller the elements of the matrix will be. After a number of such transformations, the matrix will have elements whose magnitudes are much less than one, and the inversion procedure may prove difficult. Linear dependence may creep into the transformed matrix $\underline{\underline{U}}$, making inversion impossible. In some ways, hyperspherical coordinates are the worst coordinate system in which to generate a forward consistent wavefunction, as at the smallest values of ρ, all channels are closed by many eV. The exponential growth in the wavefunction will, therefore, be quite rapid, and one will encounter numerical difficulties fairly early in the integration, even where the wavefunction is small.

A backward consistent wavefunction may also be obtained. To do this, one must multiply the inconsistent primitive wavefunction by the product of all reorthogonalization and renormalization transformation matrices that are used during subsequent integration. If we write the radial wavefunction $\underline{\underline{g}}$ at some value of $\rho = \rho_n$ as $\underline{\underline{g}}_n$ and transformation matrices at each $\rho_{n'}$ as $\underline{\underline{T}}_{n'}$, then the backward consistent wavefunction at $\rho = \rho_n$ may be written as

$$\underline{\underline{g}}_n^{\text{cons}} = \underline{\underline{g}}_n^{\text{incons}} \prod_{i=1}^{k_n} \underline{\underline{T}}_{n+i} \tag{47}$$

where k_n is the number of transformations (renormalizations and reorthogonalizations) remaining. The numerical advantages of this method are that no inversions are necessary and that the matrices being multiplied will be small (its elements have magnitude less than one). As n decreases ($n = 0$ at the start of integration) the matrices T_n will get smaller, and the worst numerical problem that should develop is underflows in their product. That may not be a major limitation, however, as it may be satisfactory in that case to let $\underline{\underline{g}}_n^{\text{cons}} = \underline{\underline{0}}$.

The computational simplicity associated with the forward consistent wavefunction derives from the fact that it can be constructed from previous transformations during the integration procedure. Thus, only N matrix elements must be stored (recall that at a grid point, each ψ_j^{pr} is given by a single real number) at each grid point. To calculate a backward consistent wavefunction, one must store not only N inconsistent matrix elements at each grid point, but also each transformation matrix $\underline{\underline{T}}_n$ over the entire range of the integration. Only then can one go about the calculation of the consistent wavefunction.

In the work to be described we have employed the forward consistent method and have had progress seriously impeded by numerical difficulties. It seems that the deciding factor in the choice of which type of consistency to use is the nature of the computer being used. If the computer represents floating point numbers in a way such that the maximum exponent available is small or does not carry enough digits to avoid linear dependence problems in the calculation and inversion of $\underline{\underline{U}}$, the forward consistent method will not work, and the backward consistent method should be used. If one has a computer with a wide dynamic range for floating point numbers and sufficient digits for accurate inversion of $\underline{\underline{U}}$, the forward method seems advisable because of its simplicity. As a result of our difficulties, we plan at some future time to allow for backwards consistency.

D. Calculation of Probability Density and Probability Current Density

The calculation of the probability density, ρ_j, from the physical wavefunction is straightforward. One simply substitutes the value of the physical wavefunction ψ_j^{phys} into eq. (1) to calculate ρ, and then displays the information in whatever way desired, normally a contour plot.

The probability current density calculation is a bit more complicated, and the method used in the calculation is described elsewhere.[18] We mention only a few of the most crucial elements of this calculation here. The objects which are normally plotted are not the current densities but their streamlines - curves which are everywhere tangent to the probability current density vectors. The streamlines are especially useful because of their similarity to streamlines of fluid flow and thus the clarity with which the hydrodynamical analogy to quantum mechanics may be made.

In order to calculate the probability current density $\underset{\wedge}{J}$ as defined in eq. (2), one needs to transform the coordinate system so that there is only one mass in the kinetic energy operator. There are several such choices for this coordinate system. The one used here is one in which the variables X_3 and X_2 are defined by the relationship:

$$X_3 = \left(\frac{\mu_{a,bc}}{\mu_{bc}}\right)^{\frac{1}{2}} \left(R_{AB} + \frac{\mu_{bc}}{n_b} R_{BC}\right) \tag{48a}$$

$$X_2 = R_{BC}, \tag{48b}$$

where R_{AB} and R_{BC} are the A-B and B-C internuclear distances and the μ are the reduced masses as defined in the usual way. Another choice for this system might be the usual Delves coordinates.[13]

$$R = \left(\frac{\mu_{a,bc}}{\mu_{bc}}\right)^{\frac{1}{4}} \left(R_{AB} + \frac{\mu_{bc}}{\mu_b} R_{BC}\right) = \left(\frac{\mu_{bc}}{\mu_{a,bc}}\right)^{\frac{1}{4}} X_3 \tag{49a}$$

$$r = \left(\frac{\mu_{bc}}{\mu_{a,bc}}\right)^{\frac{1}{4}} R_{BC} = \left(\frac{\mu_{bc}}{\mu_{a,bc}}\right)^{\frac{1}{4}} X_2 . \tag{49b}$$

The skew angle (the angle made in the new coordinate system between lines of R_{AB} = constant and R_{BC} = constant) in these two coordinate systems is the same. Plots of streamlines of probability current density and tunnelling fractions displayed in the results section will be in the X_3, X_2 coordinate system as defined in eqs. 48.

In addition to plotting the streamlines of probability current density, we can use the current densities to calculate "tunneling fractions" in the following way. Boundary streamlines may be calculated which are tangent to the contours whose energy is the same as the energy of the calculation. The region of the potential energy surface between the two boundary streamlines represents a "classical river", as a streamline that lies outside this river at any point on the potential energy surface must go through a classically forbidden region somewhere on the surface. From this definition, it is easy to establish the tunneling fractions on both the repulsive wall and dissociative plateau sides.

3. Numerical Results

We will present plots of probability densities and streamlines of probability current density, and results of calculations of tunneling fractions for the H + H_2 reaction or the Porter-Karplus surface[19] using a wavefunction obtained from the hyperspherical coordinates wavefunction. Because of our choice of a forward consistent wavefunction, numerical difficulties associated with closed channels were a severe problem, and we were limited to 2 channel (2 symmetric and 2 antisymmetric) calculations. Inclusion of an additional closed channel leads to fatal numerical errors. It has been shown[16] that a 2 channel calculation of this system gives good reaction probabilities in the low energy region; we have no information on the convergence of the wavefunction. Reaction probabilities for the energies considered here are given in Table 1 (these are the probabilities calculated in the 2 channel runs from which the physical wavefunctions were obtained).

The first step in the calculation of the physical wavefunction after the performance of the scattering calculation is the construction of the coefficient matrix $\underline{\underline{W}}$. We emphasize that we are only interested in the columns of $\underline{\underline{W}}$ corresponding to asymptotically open channels; there is nothing at all physical about the wavefunction associated with the collision in a channel in which there is insufficient energy for any collision to occur! Thus, we will consider a non-square $\underline{\underline{W}}$ of N rows and N_{op} columns. In the $H + H_2$ collision, the symmetry of the collision imposes a restriction on $\underline{\underline{W}}$:

$$W_{i,N_{op}+j} = (-1)^{i+1} W_{i,j} \tag{50}$$

A manifestation of this restriction will be seen in the probability density plots, where ψ_1^{phys} and ψ_2^{phys} (the only possible ones in the energy range considered) give probability density plots which are reflections of each other about the R_{AB}- R_{BC} symmetric stretch line.

Let us first consider the structure of the $\underline{\underline{W}}$ matrix for this system. The exact form of the matrix will depend on the details of the construction of the physical wavefunction, in particular the choice of forward or backward consistency. When a forward consistent wavefunction is used, it will be large at large ρ where integration is terminated. Since $\underline{\underline{W}}$ is related to the inverse of the final consistent radial wavefunction and derivative matrices via the matrix $\underline{\underline{C}}^{-1}$, $\underline{\underline{W}}$ will be small in the forward consistent case. Values of $\underline{\underline{W}}$ at a series of energies are displayed in Table 2. The calculation of $\underline{\underline{W}}$ is somewhat complicated because of the existence of a wide range of exponents associated with the $\exp(\pm|\kappa|R)$ terms in the evaluation of $\underline{\underline{R}}_{oo}$ and $\underline{\underline{R}}_{oc}$. These difficulties are exacerbated by the use of a forward consistent wavefunction. A scheme for avoiding potential pitfalls in the evaluation of $\underline{\underline{W}}$ is given in Appendix B.

A. Probability Densities

Contour plots of the probability density are shown for six different energies in Figs. 1-6 (total energies of 0.4466, 0.4866, 0.5266, 0.5666, 0.6066, and 0.6466 eV measured with respect to the bottom of the H_2 well). These plots are for the physical wavefunction corresponding to an A + BC collision; the collision process can be thought of as starting at the lower right hand corner of the plot. These plots have been made in internuclear coordinates; for interpretation a plot in Delves coordinates would be best. Contours are drawn at intervals of 0.25 of the common logarithm of ρ. (The wavefunction is normalized to unit incident flux.) Two features are immediately apparent. First, there are constrictions in the entrance channel which decrease in severity and move closer to the saddle point as the energy increases. Between these constrictions lie regions of increased probability density, which also wash out with increasing energy. Second, at low energy, there is little amplitude in the region of the potential energy surface corresponding to reaction products. As the energy increases, the probability distribution becomes almost symmetric about the symmetric stretch line. At these highest energies, the reaction probability is almost unity. The physical interpretation of these data, then, is that at high energies, where the exit channel of the surface is sampled, the probability density will be uniformly spread along the minimum energy path. At energies where the reaction probability has not yet become appreciable, the wavefunction is forced to be localized in the entrance channel, giving rise to the maxima at the three lowest energies shown. The origin of the constrictions is not clear from the plots.

The jagged nature of the contours of constant probability density in Figs. 1-6 is probably due to the large grid size used (0.1 bohr). With a smaller distance between grid points, it is expected that smoother curves would be generated. As the current work is only really at the preliminary level, we chose not to pursue this particular point. With this grid size and range used, there are 1024 grid points, which already requires a fairly substantial computational effort in terms of computer time and disk usage. With some relatively simple modifications, an L-shaped grid region rather than a square one as is presently used might be employed, which would allow for a higher density of points in the entrance and exit channels and in the saddle point region, and a lower density of points high upon the dissociative plateau. In the latter region, the physical wavefunction can clearly have no amplitude in the energy range considered, as it is classically forbidden (quantum mechanically one might say that the lowest energy eigenfunctions ϕ_i have zero amplitude in this region).

B. Probability Current Density

In Figs. 7-13 we present plots of the streamlines of probability current density. The streamlines are broken up into a series of curves, the head of each of which is marked by an arrow. The length of the arrow is proportional to the current density at its center. The streamline plots are superimposed on a contour diagram of the potential energy surface in order to display the relationship between the streamlines and the surface. These plots are in the (X_3, X_2) coordinate system defined in eqs. (48). The minimum energy path is marked by a dashed line, the saddle point is indicated by a cross. Contours are drawn every 0.2 eV from 0.2 eV to 1.6 eV, measured with respect to the bottom of the H_2 well. An additional contour is drawn at the energy of the calculation.

The plots for energies of 0.4866, 0.5266, 0.5666, 0.6066, 0.6466, 0.6966, and 0.7466 eV display a few key features. At the lowest energies, nearly all of the flux to reaction occurs at greater distances than those corresponding to the saddle point (Fig. 7, 8), while at the highest energies there is appreciable flux through and to the left of the saddle point. At the two highest energies, we can also see the development of a vortex in the streamline diagram just to the right of the saddle point region. It appears that at higher energies this vortex might close on itself, forming a quantum whirlpool. Such whirlpools have been previously seen for this system.[6]

It is clear from these figures that a fair amount of the reaction at low energies occurs via tunneling. We will try to quantify this in the next subsection. For example, at 0.5266 eV (Fig. 8), one can see three streamlines crossing the contour at that energy, transporting flux through the dissociative plateau in spite that region's classical inaccessibility. At the higher energies, it is similarly clear that very little flux is transported by tunneling. As a result of the vortex, flux is shifted into smaller values of X_3 and X_2.

There are some unsatisfactory features in these streamline plots which indicate lack of convergence, instabilities, or outright errors in the analysis (most likely in the manipulation of the hyperspherical coordinates wavefunction into a form suitable for the streamlines program). For example, in Fig. 7, the two streamlines shown starting at the smallest values of X_2 coalesce near $X_3 = 3.5$ bohr and remain essentially indistinguishable until about $X_2 = 2.40$ bohr, where they suddenly separate. Similarly, in Figs. 8-11, the streamline starting at the smallest value of X_2 makes a sharp turn to smaller values of X_2 before rounding the corner at unusually small values of X_3 and X_2.

It is quite possible that some of this unphysical behavior is a direct manifestation of the large grid spacing used (0.1 bohr) in these calculations, and redoing the calculations with a smaller spacing might alleviate this problem. Improvement might also be made by using a partially analytic expression for the derivative of the physical wavefunction based on the derivative of the radial wavefunction which is available from the scattering calculations. Such a procedure might provide a better estimate for the partial derivatives of the radial wavefunction than the numerical procedure currently used (it should certainly be more efficient). We will develop this further in the final section.

C. Tunneling Fractions

The calculation of the tunneling fraction has been outlined earlier. To obtain the tunneling fraction, we need to calculate the flux normal to a set of lines normal to the minimum energy path in the (X_3, X_2) coordinate system. The tunneling fraction is the fraction of this flux which lies outside the boundary streamlines defined earlier. We have calculated these tunneling fractions along six lines normal to the reaction path at the energies shown in Figs. 8-13. The values of the currents normal to each line and the fractions which can be classified as tunneling through the wall, classical, and tunneling through the plateau, are presented for each line at each energy in Table 2.

It has been shown[18] that when there is no dissociation, given that the lines extend sufficiently far into the wall and the plateau region, the current normal to each line should be the same for a given energy. This will not be true in practice because of errors in the physical wavefunction used and the approximations inherent in the numerical methods used in the calculation of the current density, most probably the numerical interpolation and differentiation of the wavefunction. A measure of how well this condition has been satisfied may be seen by comparing the various currents in Table 3. These data are summarized in Table 4, in which we list average currents, their average deviation, and the % deviation at the seven energies studied.

The current normal to each of the cuts is clearly not equal at a given energy, as may be seen for the large % deviations in Table 3. This measure of the relative error seems to be decreasing with energy at the lower energies dropping from 12.2% to 8.8%, although at the highest energies, it appears to have reached some sort of limiting value. This deviation is far worse than the normal deviation of $\leq 0.5\%$ obtained in the study of the $H + H_2$ reaction on the scaled SSMK surface performed previously.[18] The current work differs substantially from that study in the method of generation of the wavefunction (coupled channel hyperspherical coordinate method as opposed to finite difference method). In addition, a large grid spacing was used in these calculations (0.1 bohr); we have not yet examined how a reduction in this parameter will influence the results.

A pictorial representation of these tunneling fractions is given in Figs. 14-20 for the same energies in which the streamlines of probability current density were examined in Figs. 7-13, respectively. The lines normal to the minimum energy path are clear. They are numbered from one to six (see Table 3); 1 being at the lower right-hand portion of the figure, corresponding to A + BC, while 6 is in the upper center, corresponding to AB + C. The current normal to the lines is indicated by the heavy solid curve; the distance from the line along which the normal current is calculated to the curve is proportional to the magnitude of the current at each point along the line. The boundary streamlines are indicated by short dashed lines. As in Figs. 7-13, the plots are superimposed on a contour plot of the potential energy surface.

From Figs. 14-20, a few features are most visible. First, the classical river defined by the boundary streamlines is very narrow in the entrance and exit channels at low energies; it widens substantially as energy increases. At the highest energies (0.6966 and 0.7466 eV) one can see the distortion related to the vortex formation seen quite clearly in the streamlines in Figs. 12 and 13. In the entrance channel and the exit channel, the current normal to the lines is strongly peaked about the minimum energy path (centered slightly on the plateau side), whereas in the saddle point region, along the symmetric stretch line, the distribution is much broader.

The tunneling fractions for each line have been listed in Table 3. Two major results are evident. First, as the energy increases, the fraction of reaction occurring by tunneling decreases substantially. For example, along the symmetric sketch line, 63.6% of the current lies outside the classical river region defined by the two boundary streamlines at 0.4866 eV, while only 3.8% goes outside it at 0.7466 eV. This decrease in the importance of tunneling at high energies is to be expected; these calculations thus serve to verify our chemical intuition. Second, the fraction of the current lying outside the classical river region is usually smallest on the symmetric stretch line; it is always greatest at the lines farthest in the entrance and exit channel. This can be seen to arise for the narrowness of the classical river in the entrance and exit channels, which essentially forces current into the tunneling regions as the current profile does not change that much in these channels. Only near the saddle point does the current profile change substantially, and then the boundary streamlines separate to form a wider classical river, meaning that more of the current can be in this classical region. Since a small change in the boundary streamlines in the entrance and exit channels could produce a fairly large change in the tunnelling fractions, the absolute values of these numbers should not have too much significance attached to them. The trend of decreasing importance of tunneling with increasing energy should be valid, however.

4. Discussion and Conclusion

We have successfully calculated the physical wavefunctions from a coupled channel calculation for the H + H_2 reaction using the hyperspherical coordinates technique. Using these wavefunctions, we have obtained plots of probability density and of streamlines of probability current density, and have calculated tunneling fractions over the energy range from 0.4866 eV to 0.7466 eV. In this energy range the reaction probability rises essentially from zero to unity.

A number of results were obtained for this system. Plots of the probability density show that at low energy, the physical wavefunction is isolated in the entrance channel and has one or more regions of maximum amplitude separated by regions of constriction. As the energy is increased, both become less pronounced, until at the highest energies considered, they have disappeared and there is a maximum in the saddle point region. The streamlines of probability density show that at low energies a fair amount of the reaction flux will pass over the edge of the dissociation plateau rather than following the minimum energy path. As the energy increases, less of the flux goes over the plateau, and at the highest energies, flux is efficiently routed away from the plateau by the formation of a vortex in the streamline field. The formation of this vortex can also be seen in the probability density plots at these energies.

The tunneling fractions yield two major results. First, as the energy increases, the relative importance of tunneling decreases substantially. Second, the tunneling fraction is least at or near the symmetric stretch line and highest far out in the entrance and exit channel. The condition that the current normal to the lines normal to the minimum energy path is only approximately satisfied ($\sim 10\%$), with the error greatest ($\sim 12\%$) at the lowest energy and least ($\sim 9\%$) at the highest energies.

The calculations reported here are, at the very best, preliminary. We have not yet established convergence of any of the quantities reported with respect to either the number of channels in the hyperspherical coordinate calculation or the grid spacing in the probability density and probability current density calculation. Testing of the former can only be performed after the method of consistent primitive wavefunction calculation is changed from forward consistent to backward consistent. Testing the influence of the grid spacing can be easily accomplished, however. One must finally consider the accuracy of the numerical interpolation and differentiation procedures used in the probability current density calculation. These were found to be sufficiently accurate in previous calculations; the switch in method of wavefunction calculation (from finite difference to hyperspherical coordinate coupled channel) should not alter this conclusion.

One fairly simple improvement which might be made is the pseudo-analytic calculation of the derivatives necessary in the evaluation of the current density. Since in a previous application the wavefunction was generated by a finite difference method, the derivative had to be constructed by using a finite difference approximation to the derivative operator. In the hyperspherical coordinate coupled channel method used here for the generation of the wavefunctions, one has access not only to the wavefunction, but the ρ derivative of the radial wavefunction. If one approximates the α derivative of the basis function by a finite difference procedure, one can obtain an expression for the derivative of the primitive wavefunctions (and hence the physical ones) with respect to ρ and α. By appropriate transformation of variables, these derivatives can be evaluated in any desired coordinate system. This procedure is developed in detail in Appendix C.

The preliminary results of the work reported here suggest that after reprogramming to allow for a numerically less dfficult way of calculating a consistent wavefunction and after some numerical testing to establish a maximum grid spacing for convergence of current densities and tunneling fractions, we will have a general and efficient means of the calculation of probability densities, current densities, and tunneling fractions for collinear atom-diatomic molecule reactions. This method should be applicable to all such reactions, including heavy-light-heavy reactions. It should also allow the calculation of streamlines of probability current density in reactions involving collision-induced dissociation,[23,24] as these may also be studied by the hyperspherical coordinate method.

Appendix A. Demonstration of the Equivalence of Eqs. 35a and 35c.

(We suppress the fact that $\underline{\underline{R}}_{oo}$, $\underline{\underline{S}}_{oo}$, and $\underline{\underline{I}}$ are matrices.) We show here that the expression for S_{oo} obtained in eq. (35a) is equivalent to the usual definition of eq. (35c). This derivation relies solely on the facts that R_{oo} is real and symmetric and that the inverse of the transpose of a matrix is equal to the transpose of the inverse of a matrix.

$$R_{oo} = R_{oo}{}^{+} \tag{A-1}$$

$$(A^{+})^{-1} = (A^{-1})^{+} . \tag{A-2}$$

We start with eq. (35a)

$$S_{oo} = (I - iR_{oo})^{-1} (I + iR_{oo}) . \tag{A-3}$$

The hermitian adjoint of S_{oo} is given by

$$S_{oo}{}^{+} = (I + iR_{oo})^{+} [(I - iR_{oo})^{-1}]^{+},$$

which by eqs. (A-1) and (A-2) can be shown to be equivalent to

$$S_{oo}{}^{+} = (I - iR_{oo})(I + iR_{oo})^{-1}$$

$$S_{o}(S_{oo}{}^{+})^{-1} = (I + iR_{oo})(I - iR_{oo}),$$

which is the usual form of S_{oo} (eq. (35c)). Thus, if we can show that S_{oo} as written in eq. (A-3) is unitary, then we can show that the two forms of S_{oo} are equivalent.

We write
$$\begin{aligned}
S_{oo}{}^{+} S_{oo} &= (I - iR_{oo})(I + iR_{oo})^{-1}(I - iR_{oo})^{-1}(I + iR_{oo}) \\
&= (I - iR_{oo})\left[(I - iR_{oo})(I + iR_{oo})\right]^{-1}(I + iR_{oo}) \\
&= (I - iR_{oo})(I + R_{oo}{}^{2})^{-1}(I + iR_{oo}) \\
&= (I + R_{oo}{}^{2})^{-1} + R_{oo}(I + R_{oo}{}^{2})^{-1} R_{oo} + \\
&\qquad i[(I + R_{oo}{}^{2})^{-1} R_{oo} - R_{oo}(I + R_{oo}{}^{2})^{+}] . \qquad \text{(A-4)}
\end{aligned}$$

This equals the unit matrix I if we can show that

$$(I + R_{oo}{}^{2})^{-1} R_{oo} = R_{oo}\,(I + R_{oo}{}^{2})^{-1} . \qquad \text{(A-5)}$$

This can be shown quite easily (letting $x = R_{oo}$)

$$\begin{aligned}
(I + x^{2})^{-1} x &= (x x^{-1} + x^{2})^{-1} x = [x(x^{-1} + x)]^{-1} x = (x^{-1} + x)^{-1} x^{-1} x \\
&= (x^{-1} + x)^{-1},
\end{aligned}$$

and similarly,

$$\begin{aligned}
x(I + x^{2})^{-1} &= x(x^{-1} x + x^{2})^{-1} = x[(x^{-1} + x)x]^{-1} = x \cdot x^{-1}(x^{-1} + x)^{-1} \\
&= (x^{-1} + x)^{-1}.
\end{aligned}$$

Since (A-5) is true, the imaginary part of the right hand side of eq. (A-4) is zero, and the real part can be simply shown to reduce to the unit matrix:

$$\begin{aligned}
(I + R_{oo}{}^{2})^{-1} + R_{oo}(I + R_{oo}{}^{2})^{-1} R_{oo} &= (I + R_{oo}{}^{2})^{-1} + R_{oo}{}^{2}(I + R_{oo}{}^{2})^{-1} \\
&= (I + R_{oo}{}^{2})(I + R_{oo}{}^{2})^{-1} = I.
\end{aligned}$$

Thus S_{oo} is unitary and by definition

$$S_{oo}^{+} = S_{oo}^{-1}$$

so

$$(S_{oo}^{+})^{-1} = S_{oo} \, .$$

Hence eq. (35a) implies eq. (35c) (and vice versa).

Appendix B. Scheme for the Evaluation of $\underline{\underline{W}}$.

We wish to evaluate $\underline{\underline{W}}$ by the following expression (all quantities are matrices)

$$\underline{\underline{W}} = \underline{\underline{C}}^{-1}\,\underline{\underline{V}}\,\underline{\underline{v}}^{\frac{1}{2}}, \tag{B-1}$$

which on breaking up into its open and closed parts (we suppress the fact that the quantities considered are matrices)

$$\begin{pmatrix} W_{oo} & W_{oc} \\ W_{co} & W_{cc} \end{pmatrix} = \begin{pmatrix} (C^{-1})_{oo} & (C^{-1})_{oc} \\ (C^{-1})_{co} & (C^{-1})_{cc} \end{pmatrix} \begin{pmatrix} V_{oo} & V_{oc} \\ V_{co} & V_{cc} \end{pmatrix} \begin{pmatrix} v_o^{\frac{1}{2}} & O \\ O & v_c^{\frac{1}{2}} \end{pmatrix}, \tag{B-2}$$

where $\underline{\underline{V}}$ is given in eq. (38).

Using this formula for $\underline{\underline{V}}$, one may write the two blocks of $\underline{\underline{W}}$ desired ($\underline{\underline{W}}_{oo}$, $\underline{\underline{W}}_{oo}$) as

$$W_{oo} = (C^{-1})_{oc}\,V_{oo}\,v_o^{\frac{1}{2}} \tag{B-3a}$$

$$W_{co} = (C^{-1})_{co}\,V_{oo}\,v_o^{\frac{1}{2}} \tag{B-3b}$$

and using the equality

$$(I - iR_{oo})^{-1} = (I + iR_{oo})(I + R_{oo}{}^{2})^{-1}$$

one may write

$$W_{oo} = -2i\,(C^{-1})_{oo}(I + iR_{oo})(I + R_{oo}{}^{2})^{-1}\;v_o^{\frac{1}{2}} \tag{B-5a}$$

$$W_{co} = -2i\,(C^{-1})_{co}(I + iR_{oo})(I + R_{oo}{}^{2})^{-1}\;v_o^{\frac{1}{2}} \tag{B-5b}$$

so

$$\mathrm{Re}\,W_{oo} = 2(C^{-1})_{oo}\,R_{oo}\,(I + R_{oo}^{\;2})^{-1}\,v_o^{\frac{1}{2}}$$

$$\mathrm{Im}\,W_{oo} = -2(C^{-1})_{oo}\,(I + R_{oo}^{\;2})^{-1}\,v_o^{\frac{1}{2}}$$

$$\mathrm{Re}\,W_{co} = +2(C^{-1})_{co}\,R_{oo}(I + R_{oo}^{\;2})^{-1}\,v_o^{\frac{1}{2}}$$

$$\mathrm{Im}\,W_{co} = -2(C^{-1})_{co}\,(I + R_{oo}^{\;2})^{-1}\,v_o^{\frac{1}{2}} \quad .$$

The desired parts of the inverse of $\underline{\underline{C}}$ may be constructed from the blocks of $\underline{\underline{C}}$ and their inverses.

$$(C^{-1})_{oo} = [C_{oo} - C_{oc}\,(C_{cc})^{-1}\,C_{co}]^{-1} \tag{B-6a}$$

$$(C^{-1})_{co} = -(C_{cc})^{-1}\,C_{co}[C_{oo} - C_{oc}(C_{cc})^{-1}\,C_{co}]^{-1}$$

$$= -(C_{oc})^{-1}\,C_{co}(C^{-1})_{oo} . \tag{B-6b}$$

Difficulty enters in that $\underline{\underline{C}}$ has terms which decay exponentially and we wish to remove the decaying terms prior to inversion. This may be done in the following way:

$$\begin{pmatrix} C_{oo} & C_{oc} \\ C_{co} & C_{cc} \end{pmatrix} = \begin{pmatrix} I & O \\ O & \frac{1}{2}e^{-|k|R} \end{pmatrix} \begin{pmatrix} C_{oo} & C_{oc} \\ f_{co}^{(c)} & f_{cc}^{(c)} \end{pmatrix} \tag{B-7}$$

where $e^{-|\kappa|R}$ is a diagonal matrix whose elements are given by the expression

$$(e^{-|k|R})_{ij} = \delta_{ij}\,e^{-|k_j|R} \quad . \tag{B-8}$$

On substituting the expressions obtainable from (B-7) for C_{co} and C_{cc} in terms of $f_{co}^{(c)}$ and $f_{cc}^{(c)}$ and eqs. (B-6) into eqs. (B-5), one obtains the expressions

$$\mathrm{Re}\, W_{co} = -(f_{cc}^{(c)})^{-1} (f_{co}^{(c)})\, \mathrm{Re}\, W_{oo} \tag{B-9a}$$

$$I_m\, W_{co} = -(f_{cc}^{(c)})^{-1} (f_{co}^{(c)})\, \mathrm{Im}\, W_{oo}\, . \tag{B-9b}$$

A word should be said about the evaluation of R_{oo}. A formula for the entire matrix $\underline{\underline{R}}$ is given in eq. (19), and on breaking it up into its submatrices we can see easily that

$$R_{oo} = D_{oo}\,(C^{-1})_{oo} + D_{oc}\,(C^{-1})_{co}\, .$$

The matrix $\underline{\underline{D}}$ has terms which grow exponentially only in the rows of D corresponding to asymptotically closed channels (subblocks D_{co}, D_{cc}). Hence, it is not necessary to define a modified $\underline{\underline{D}}$ as was done for $\underline{\underline{C}}$ in eq. (B-7) and we can use eq. (B-6b) to write

$$R_{oo} = [D_{oo} - D_{oc}\,(f_{cc}^{(c)})^{-1}\, f_{co}^{(c)}\,](C^{-1})_{oo}\, , \tag{B-9}$$

which may be substituted in eqs. (B-5) and (B-9) to evaluate W_{oo} and W_{co}. The evaluation of R_{oo} then, should have no difficulties other than those produced by the presence of large values of the radial wave-functions going into the calculation of C_{oo}, C_{oc}, $f_{co}^{(c)}$, $f_{cc}^{(c)}$, D_{oo}, and D_{oc}, and these can be removed by making the substitution

$$\overline{D} = DN \tag{B-10a}$$

$$\overline{C} = CN, \tag{B-10b}$$

where the elements of $\underline{\underline{N}}$ are sufficiently small that the elements of $\underline{\underline{\overline{D}}}$ are close to unity. A convenient choice is to make N diagonal so that

$$\overline{R} = \overline{D}\,\overline{C}^{-1} = DN \circ N^{-1} C^{-1} = DC^{-1} = R \ .$$

If $\underline{\underline{N}}$ is diagonal, then we may write

$$\overline{C}_{oo} = C_{oo} N_o$$

$$\overline{C}_{oc} = C_{oc} N_c$$

$$\overline{f}^{(c)}_{co} = f_{co} N_o$$

$$\overline{f}^{(c)}_{cc} = f_{cc} N_c$$

so

$$\mathrm{Re}\, W_{oo} = 2N_o [\overline{C}_{oo} - \overline{C}_{oc} (\overline{f}^{(c)}_{cc})^{-1} \overline{f}^{(c)}_{co}]^{-1} R_{oo} (I + R_{oo}^2)^{-1} v_o^{\frac{1}{2}} \quad \text{(B-11a)}$$

$$\mathrm{Im}\, W_{oo} = -2N_o [\overline{C}_{oo} - \overline{C}_{oc}\ \overline{f}^{(c)}_{cc})^{-1} \overline{f}^{(c)}_{co}]^{-1} (I + R_{oo}^2)^{-1} v_o^{\frac{1}{2}} \quad \text{(B-11b)}$$

$$\mathrm{Re}\, W_{co} = -N_c^{-1} (\overline{f}^{(c)}_{cc})^{-1} \overline{f}^{(c)}_{co} N_o \mathrm{Re}\, W_{oo} \quad \text{(B-11c)}$$

$$\mathrm{Im}\, W_{co} = -N_c^{-1} (f^{(c)}_{cc})^{-1} \overline{f}^{(c)}_{co} N_o\, \mathrm{Im}\, W_{oo} \quad \text{(B-11d)}$$

Appendix C. Construction of Pseudo-Analytic Derivative of the Wavefunction.

In the evaluation of the derivatives of the physical wavefunction required by eq. (2) for the probability current density, we wish to use the fact that we are propagating not only the radial wavefunction $\underline{\underline{g}}$ but its derivative $\underline{\underline{g}}'$. Starting with eq. (5) for the primitive wavefunction:

$$\psi_j^{pr} = \rho^{-\frac{1}{2}} \sum_i \phi_i(\alpha;\bar{\rho})\, g_{ij}(\rho;\bar{\rho}) \tag{C-1}$$

and eqs. (49) relating the $(X_3\,X_2)$ coordinate system to the Delves coordinates (R, r) which are simply related to the hyperspherical coordinates

$$\rho = (R^2 + r^2)^{\frac{1}{2}} = a\,(X_3^2 + X_2^2)^{\frac{1}{2}} \tag{C-2a}$$

$$\alpha = \tan^{-1}(r/R) = \tan^{-1}(X_2/X_3) \tag{C-2b}$$

$$\text{where } a = \left(\frac{\mu_{bc}}{\mu_{a,bc}}\right)^{\frac{1}{4}}$$

we may write

$$\left(\frac{\partial \psi_j^{pr}}{\partial X_3}\right)_{X_2} = \sum_i \Bigg[-\tfrac{1}{2}\rho^{-\frac{3}{2}}\left(\frac{\partial\rho}{\partial X_3}\right)_{X_2} \phi_i g_{ij} + \rho^{-\frac{1}{2}}\left(\frac{\partial\phi_j}{\partial\alpha}\right)\left(\frac{\partial\alpha}{\partial X_3}\right)_{X_2} g_{ij}$$
$$+ \rho^{-\frac{1}{2}}\phi_i\left(\frac{\partial g_{ij}}{\partial\rho}\right)\left(\frac{\partial\rho}{\partial X_3}\right)_{X_2}\Bigg] \tag{C-3a}$$

$$\left(\frac{\partial\psi_j^{pr}}{\partial X_2}\right)_{X_2} = \sum_i \left[-\tfrac{1}{2}\,\rho^{-\frac{3}{2}}\left(\frac{\partial\rho}{\partial X_2}\right)_{X_3}\phi_i g_{ij} + \rho^{-\frac{1}{2}}\left(\frac{\partial\phi_j}{\partial\alpha}\right)\left(\frac{\partial\alpha}{\partial X_2}\right)_{X_3} g_{ij}\right.$$

$$\left. + \rho^{-\frac{1}{2}}\phi_i\left(\frac{\partial g_{ij}}{\partial\rho}\right)\left(\frac{\partial\rho}{\partial X_2}\right)_{X_3}\right] . \qquad \text{(C-3b)}$$

The α derivative of the basis functions $\phi_i(\alpha;\bar{\rho})$ may be approximated by any convenient technique. In that case, to evaluate eqs. (C-3), one needs only to determine expressions for the partial derivatives of ρ and α, which are given below:

$$\left(\frac{\partial\rho}{\partial X_3}\right)_{X_2} = a^2 X_3/\rho \qquad \text{(C-4a)}$$

$$\left(\frac{\partial\rho}{\partial X_2}\right)_{X_3} = a^2 X_2/\rho \qquad \text{(C-4b)}$$

$$\left(\frac{\partial\alpha}{\partial X_3}\right)_{X_2} = -a^2 X_2/\rho^2 \qquad \text{(C-4c)}$$

$$\left(\frac{\partial\alpha}{\partial X_2}\right)_{X_3} = a^2 X_3/\rho^2 \ . \qquad \text{(C-4d)}$$

Combining eqs. (C-3) and (C-4), we may obtain an expression for $(\partial\psi_j^{pr}/2X_3)_{X_2}$ and $(\partial\psi_j^{pr}/\partial X_2)_{X_3}$

$$\left(\frac{\partial\psi_j^{pr}}{\partial X_3}\right)_{X_2} = a\rho^{-\frac{3}{2}}\sum_i\left[-\frac{\cos\alpha}{2}\,\phi_i g_{ij} - \sin\alpha\left(\frac{\partial\phi_i}{\partial\alpha}\right)g_{ij} + \rho\cos\alpha\,\phi_i\left(\frac{\partial g_{ij}}{\partial\rho}\right)\right] \qquad \text{(C-5a)}$$

$$\left(\frac{\partial\psi_j^{pr}}{\partial X_3}\right)_{X_2} = a\rho^{-\frac{3}{2}}\sum_i\left[-\frac{\sin\alpha}{2}\,\phi_j g_{ij} + \cos\alpha\left(\frac{\partial\phi_i}{\partial\alpha}\right)g_{ij} + \rho\sin\alpha\,\phi_i\left(\frac{\partial g_{ij}}{\partial\rho}\right)\right] \qquad \text{(C-5b)}$$

If one wanted to obtain a higher order approximation to the primitive wavefunction ψ_j^{pr}, one could evaluate higher order derivatives using the second derivative of the radial wavefunction, which may be obtained from the radial wavefunction by substitution into the Schrödinger eq. which it satisfies (eq. (6)). An additional derivative of the basis functions ϕ_i could be obtained by another numerical approximation. One would then expand the wavefunction in a Taylor series about each grid point.

Numerical testing of these modifications to the differentiation and interpolation procedures used seems in order, although the success of previous calculations of the current density suggests that they should not be necessary. Nevertheless, they do seem more elegant, and the differentiation procedure should result in a time savings in these steps.

References

1. R. B. Bernstein, ed. Atom-Molecule Collision Theory (Plenum Press, New York, 1979).
2. R. E. Howard, A. C. Yates, and W. A. Lester, Jr., J. Chem. Phys. 66, 1960 (1977); F. Schnabel and S. Chapman, Chem. Phys. Lett. 57, 189 (1978); J. S. Hutchinson and R. E. Wyatt, J. Chem. Phys. 70, 3509 (1977).
3. D. G. Truhlar and B. C. Garrett, Acc. Chem. Res. 13, 440 (1980).
4. L. J. Schiff, Quantum Mechanics, 3rd Ed. (McGraw-Hill, New York, 1968), pp. 25-27.
5. R. B. Bird, W. E. Stewart, and E. W. Lightfoot, Transport Phenomena (John Wiley, New York, 1960), p. 135.
6. E. A. McCullough and R. W. Wyatt, J. Chem. Phys. 54, 3578 (1971).
7. S. L. Latham, J. F. McNutt, R. E. Wyatt, and M. J. Redmon, J. Chem. Phys. 69, 3746 (1978).
8. J. F. McNutt and R. E. Wyatt, in: Potential Energy Surfaces and Dynamics Calculations, ed. D. G. Truhlar (Plenum Press, New York, 1981), pp. 495-517.
9. A. Kuppermann, J. T. Adams, and D. G. Truhlar, 8th International Conference on the Physics of Electronic and Atomic Collisions, 1973, Belgrade, Yugoslavia, p. 149 of Abstracts.
10. J. O. Hirschfelder, A. C. Cristoph, and W. E. Palke, J. Chem. Phys. 61, 5435 (1974); J. O. Hirschfelder, C. J. Goebel, and L. W. Bruch, J. Chem. Phys. 61, 5456 (1974); J. O. Hirschfelder and K. T. Tang, J. Chem. Phys. 64, 760 (1976); 65, 470 (1976).

References (continued)

11. D. C. Truhlar and A. Kuppermann, J. Chem. Phys. 56, 2232 (1972).

12. D. J. Diestler and V. McKoy, J. Chem. Phys. 48, 2951 (1968).

13. L. M. Delves, Nucl. Phys. 9, 391 (1959); 20, 275 (1960).

14. J. A. Kaye and A. Kuppermann, Chem. Phys. Lett. 77, 573 (1981).

15. J. Manz and J. Römelt, Chem. Phys. Lett. 81, 179 (1981).

16. A. Kuppermann, J. A. Kaye, and J. P. Dwyer, Chem. Phys. Lett. 74, 257 (1980).

17. G. Hauke, J. Manz, and J. Römelt, J. Chem. Phys. 73, 5040 (1980); J. Römelt, Chem. Phys. Lett. 74, 263 (1980).

18. A. Kuppermann, J. T. Adams, and D. G. Truhlar, manuscript in preparation.

19. R. N. Porter and M. Karplus, J. Chem. Phys. 40, 1105 (1964).

20. A. Kuppermann, in Theoretical Chemistry: Advances and Perspectives, Vol. 6A, ed. D. Henderson (Academic Press, New York, 1981), pp. 79-164.

21. M. E. Riley and A. Kuppermann, Chem. Phys. Lett. 1, 537 (1968).

22. R. G. Gordon, J. Chem. Phys. 51, 14 (1969); the integrator used has been modified by A. Wagner and V. McKoy.

23. J. A. Kaye and A. Kuppermann, Chem. Phys. Lett. 78, 546 (1981).

24. J. Manz and J. Römelt, Chem. Phys. Lett. 77, 172 (1981).

Table 1. Reaction probabilities obtained in the scattering calculations (2 even and 2 odd channels) from which the wavefunctions were obtained. Energies are with respect to the bottom of the H_2 well.

E (eV)	P^R_{00}
0.4466	0.0360
0.4666	0.1588
0.4866	0.4004
0.5066	0.6923
0.5266	0.8527
0.5466	0.9445
0.5666	0.9828
0.6066	0.9994
0.6466	0.9998
0.6966	0.9947
0.7466	0.9851

Table 2: Values of the elements of the matrix $\underline{\underline{W}}^*$

E_{tot}/eV	$\underline{\underline{W}}$	
0.4766	-1.6734(-16)	-1.6734(-16)
	-6.3208(-19)	6.3208(-19)
	-1.5705(-17)	-1.5705(-17)
	-6.7711(-20)	6.7711(-20)
0.5266	-2.6546(-16)	-2.6546(-16)
	-3.4571(-19)	3.4571(-19)
	-2.4897(-17)	-2.4897(-17)
	-3.7002(-20)	3.7002(-20)
0.5666	-2.9972(-16)	-2.9972(-16)
	9.4603(-19)	-9.4603(-19)
	-2.8091(-17)	-2.8091(-17)
	1.0117(-19)	-1.0117(-19)
0.6066	-2.2044(-16)	-2.2044(-16)
	3.1179(-18)	-3.1179(-18)
	-2.0645(-17)	-2.0645(-17)
	3.3313(-19)	-3.3313(-19)
0.6466	2.9423(-17)	2.9423(-17)
	5.4057(-18)	-5.4057(-18)
	2.7537(-18)	2.7537(-18)
	5.7707(-19)	-5.7707(-19)
0.6966	5.8046(-16)	5.8046(-16)
	6.0622(-18)	-6.0622(-18)
	5.4278(-17)	5.4278(-17)
	6.4605(-19)	-6.4605(-19)
0.7466	1.2884(-15)	1.2884(-15)
	1.3619(-18)	-1.3619(-18)
	1.2037(-16)	1.2037(-16)
	1.4506(-19)	-1.4506(-19)

[*] Numbers in parentheses indicate the power of 10 by which the non-enclosed number should be multiplied.

Table 3. Data on Tunneling Fractions[*]

	line #[†]	current(au)	% wall	% classical	% plateau	% tunneling
E = 0.4866	1	1.549(-2)	16.06	19.61	64.34	80.39
	2	1.742(-2)	8.86	15.74	75.40	84.26
	3	1.563(-2)	3.73	33.00	63.28	67.00
	4	9.622(-3)	6.13	36.36	57.51	63.64
	5	1.637(-2)	8.35	19.61	72.04	80.39
	6	1.657(-2)	12.52	11.96	75.52	88.04
E = 0.5266	1	3.498(-2)	20.18	35.60	44.22	64.40
	2	3.939(-2)	14.07	43.68	42.26	56.32
	3	3.646(-2)	3.59	51.79	44.62	48.21
	4	2.417(-2)	5.33	50.04	44.63	49.96
	5	3.944(-2)	4.32	46.48	49.20	53.52
	6	3.729(-2)	16.82	40.63	42.55	59.37
E = 0.5666	1	4.296(-2)	25.71	39.98	34.31	60.02
	2	4.674(-2)	16.23	51.49	32.28	48.51
	3	4.540(-2)	3.11	69.43	27.46	30.57
	4	3.180(-2)	3.88	67.53	28.59	32.47
	5	5.040(-2)	4.43	65.50	30.07	34.50
	6	4.512(-2)	21.65	45.29	30.06	54.71
E = 0.6066	1	4.662(-2)	28.01	46.89	25.10	53.11
	2	5.000(-2)	16.29	59.20	24.51	40.80
	3	4.930(-2)	2.97	80.33	16.70	19.67
	4	3.594(-2)	2.76	81.83	15.41	18.17
	5	5.588(-2)	5.08	77.37	17.55	22.63
	6	4.918(-2)	23.88	52.51	23.61	47.49
E = 0.6466	1	4.942(-2)	25.38	57.74	16.88	42.26
	2	5.361(-2)	14.81	72.56	12.66	27.47
	3	5.176(-2)	3.41	89.35	7.24	10.65
	4	3.880(-2)	2.67	92.59	4.74	7.41
	5	5.988(-2)	5.89	85.31	8.80	14.69
	6	5.263(-2)	20.91	64.11	14.97	35.89
E = 0.6966	1	5.255(-2)	22.67	63.96	13.36	36.04
	2	5.835(-2)	14.00	77.36	8.64	22.64
	3	5.378(-2)	4.02	91.62	4.36	8.38
	4	4.122(-2)	2.83	94.16	3.01	5.84
	5	6.205(-2)	6.51	89.12	6.37	12.88
	6	5.570(-2)	18.67	69.86	11.47	30.14
E = 0.7466	1	5.534(-2)	23.94	66.02	10.04	33.98
	2	6.189(-2)	16.16	77.34	6.51	22.66
	3	5.543(-2)	4.85	91.27	3.88	8.73
	4	4.286(-2)	3.18	96.14	0.65	3.83
	5	6.365(-2)	6.64	86.77	6.59	13.23
	6	5.394(-2)	19.93	72.01	8.06	27.99

---

[*] Numbers in parentheses represent the powers of 10 by which the unenclosed number should be multiplied.

[†] Lines are numbered sequentially along the minimum energy path: 1 = A + BC; 6 = AB + C.

Table 4. Average Currents and Deviations

E/eV	Avg. Current	Avg. Dev. Curr.	% Dev.
0.4806	1.519(-2)	1.854(-3)	12.21
0.5266	3.529(-2)	3.808(-3)	10.79
0.5666	4.375(-2)	4.245(-3)	9.70
0.6066	4.782(-2)	4.362(-3)	9.12
0.6466	5.093(-2)	4.551(-3)	8.94
0.6966	5.394(-2)	4.760(-3)	8.82
0.7466	5.619(-2)	4.976(-3)	8.86

Figure Captions

FIG. 1. Plot of the probability density ($\psi^* \psi$) of the physical wavefunction corresponding to the collision H + H_2 (v = 0) at E = 0.4466 eV in internuclear (R_{AB}, R_{BC}) coordinates. Contours are plotted at equally spaced increments (0.25) of the common logarithm. The lowest contour is at 0.0; the highest is at 1.75. The wavefunction is normalized to unit incident flux. A 32 × 32 grid was used in the calculations generating the physical wavefunction whose amplitude is pictured here. Most of the irregular features of the graph should be due to the use of this large grid size, as well as the nature of the contour plotting routine used.

FIG. 2. Plot of probability density as in Fig. 1 for E = 0.4866 eV. The contours run from 0.00 to 2.0.

FIG. 3. Plot of probability density as in Fig. 1 for E = 0.5266 eV. The contours run from 0.0 to 1.75.

FIG. 4. Plot of probability density as in Fig. 1 for E = 0.5666 eV. The contours run from 0.0 to 1.50.

FIG. 5. Plot of probability density as in Fig. 1 for E = 0.6066 eV. The contours run from 0.0 to 1.50.

FIG. 6. Plots of probability density as in Fig. 1 for E = 0.6466 eV. The contours run from 0.0 to 1.50.

FIG. 7. Plot of streamlines of probability current density for the collision at H + H_2 (v = 0) at E = 0.4866 eV. The arrows point in the direction of the current density vector; the length of the arrows is proportional to the magnitude of the current density

Figure Captions (continued)

at its midpoint. The streamlines are superimposed on a contour plot of the potential energy surface; contours are drawn every 0.2 eV from 0.2 eV to 1.6 eV, measured with respect to the bottom of the H_2 well. Contours are also drawn at the energy **E** of the collision. The minimum energy path is indicated by a dashed line; the saddle point is marked by a cross. The coordinate system is the (X_3, X_2) system defined in eqs.(48).

FIG. 8. Plot of streamlines of probability current density as in Fig. 7 for **E** = 0.5266 eV.

FIG. 9. Plot of streamlines of proability current density as in Fig. 7 for **E** = 0.5666 eV.

FIG. 10. Plot of streamlines of probability current density as in Fig. 7 for **E** = 0.6066 eV.

FIG. 11. Plot of streamlines of probability current density as in Fig. 7 for **E** = 0.6466 eV.

FIG. 12. Plot of streamlines of probability current density as in Fig. 7 for **E** = 0.6966 eV.

FIG. 13. Plot of streamlines of probability current density as in Fig. 7 for **E** = 0.7466 eV.

FIG. 14. Plot showing the boundary streamlines defined in the text, six lines normal to the minimum energy path, and the magnitude of the current normal to these lines at **E** = 0.4866 eV. The boundary streamlines are shown by short dashes. The plot is superimposed on a contour plot of the potential energy surface

Figure Captions (continued)

as was used in Fig. 7. The magnitude of the currents is proportional to the distance from the line to the corresponding curve.

FIG. 15. Plot showing boundary streamlines and currents in direction of minimum energy path for $E = 0.5266$ eV.

FIG. 16. Plot showing boundary streamlines and currents in direction of minimum energy path for $E = 0.5666$ eV.

FIG. 17. Plot showing boundary streamlines and currents in direction of minimum energy path for $E = 0.6066$ eV.

FIG. 18. Plot showing boundary streamlines and currents in direction of minimum energy path for $E = 0.6466$ eV.

FIG. 19. Plot showing boundary streamlines and currents in direction of minimum energy path for $E = 0.6966$ eV.

FIG. 20. Plot showing boundary streamlines and currents in direction of minimum energy path for $E = 0.7466$ eV.

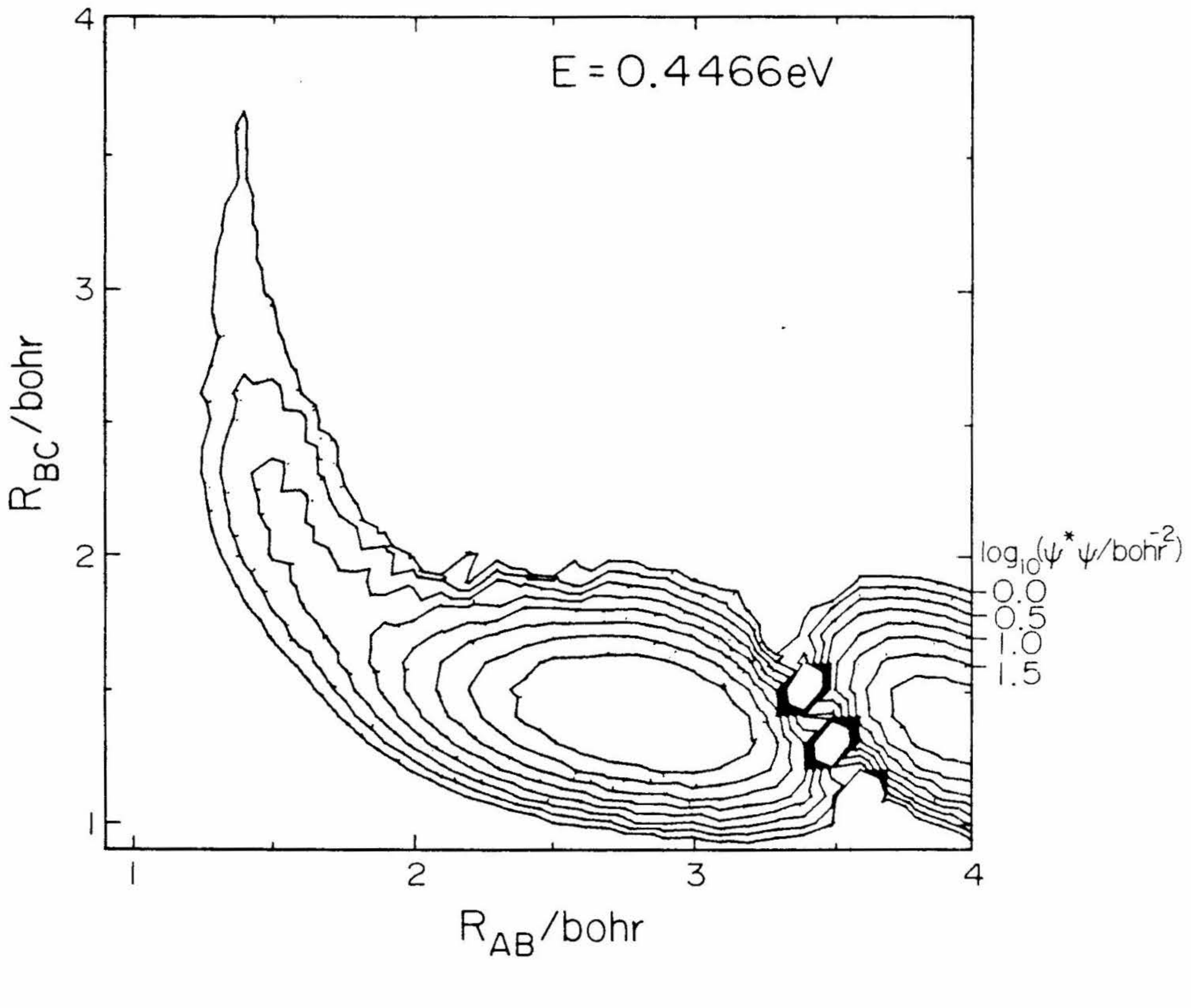
E = 0.4466eV
R_{BC}/bohr
R_{AB}/bohr
4
3
2
1
1
2
3
4
$\log_{10}(\psi^*\psi/\text{bohr}^{-2})$
0.0
0.5
1.0
1.5

Figure 1

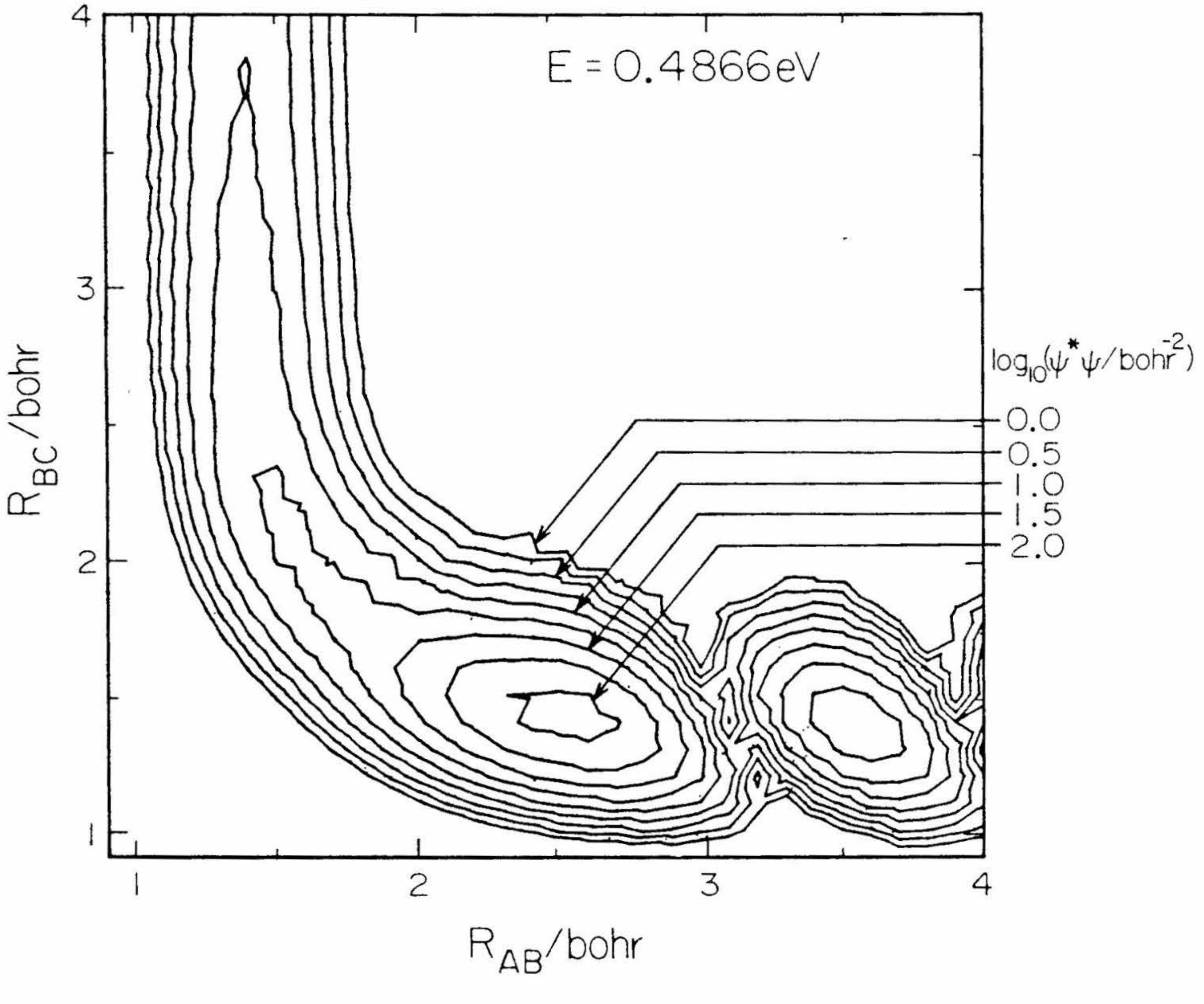
E = 0.4866eV
R_{BC}/bohr
R_{AB}/bohr
$\log_{10}(\psi^*\psi/\mathrm{bohr}^{-2})$
0.0
0.5
1.0
1.5
2.0
1
2
3
4
1
2
3
4

Figure 2

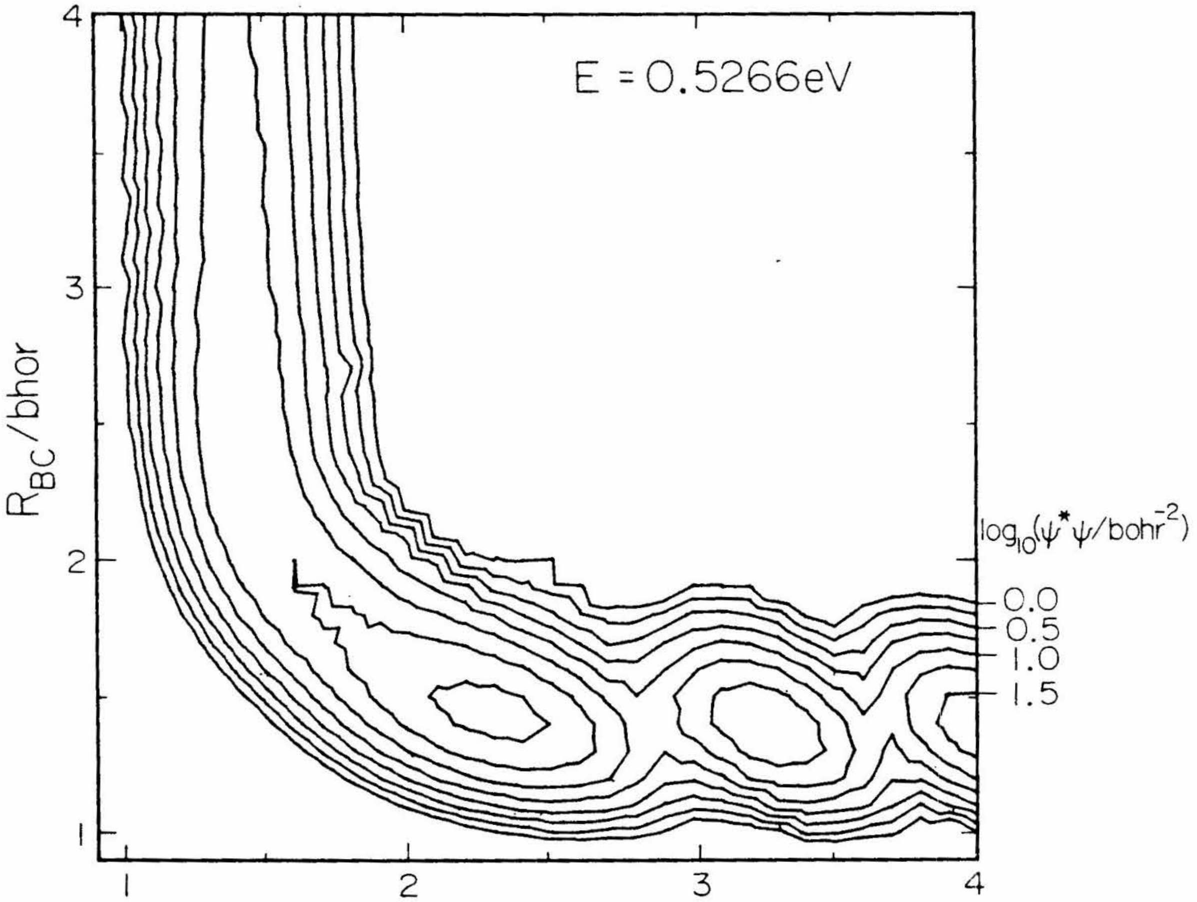
E = 0.5266eV
R_BC/bhor
R_AB/bohr
log10(ψ*ψ/bohr^-2)
0.0
0.5
1.0
1.5
1
2
3
4
1
2
3
4

Figure 3

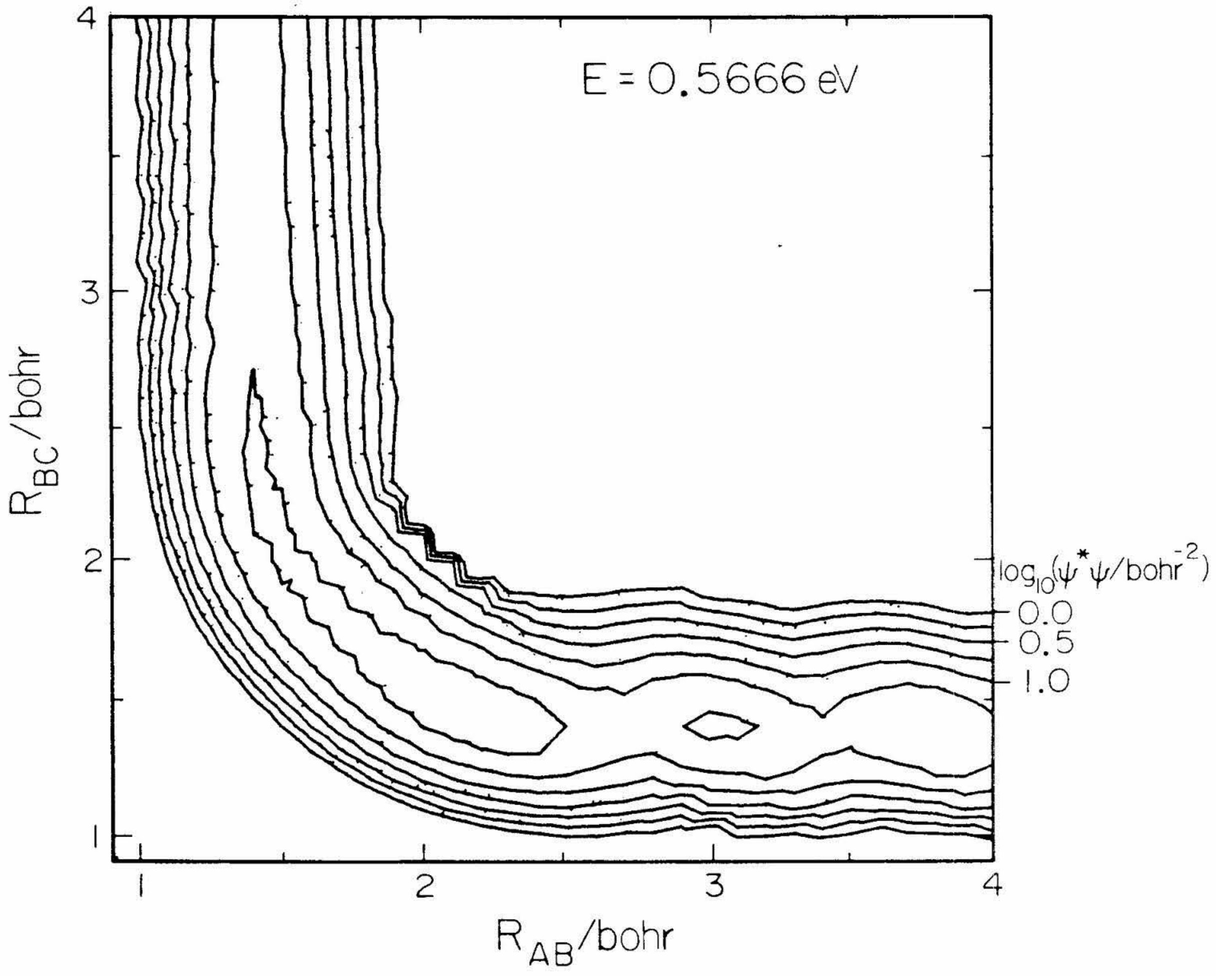
E = 0.5666 eV
R_{BC}/bohr
R_{AB}/bohr
1
2
3
4
1
2
3
4
$\log_{10}(\psi^* \psi/\text{bohr}^{-2})$
0.0
0.5
1.0

Figure 4

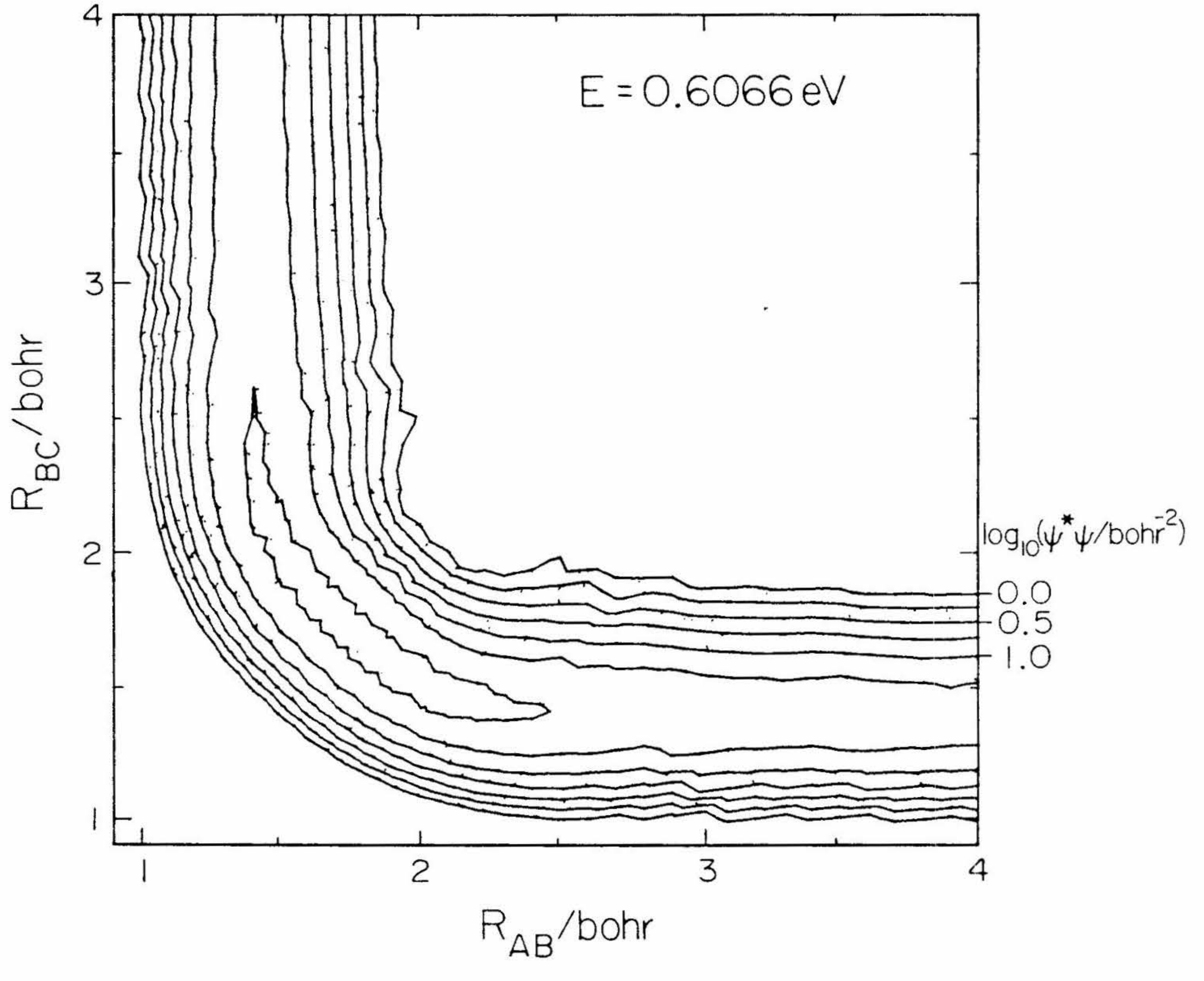
E = 0.6066 eV
R_{BC}/bohr
R_{AB}/bohr
$\log_{10}(\psi^*\psi/\text{bohr}^{-2})$
0.0
0.5
1.0
1
2
3
4
1
2
3
4

Figure 5

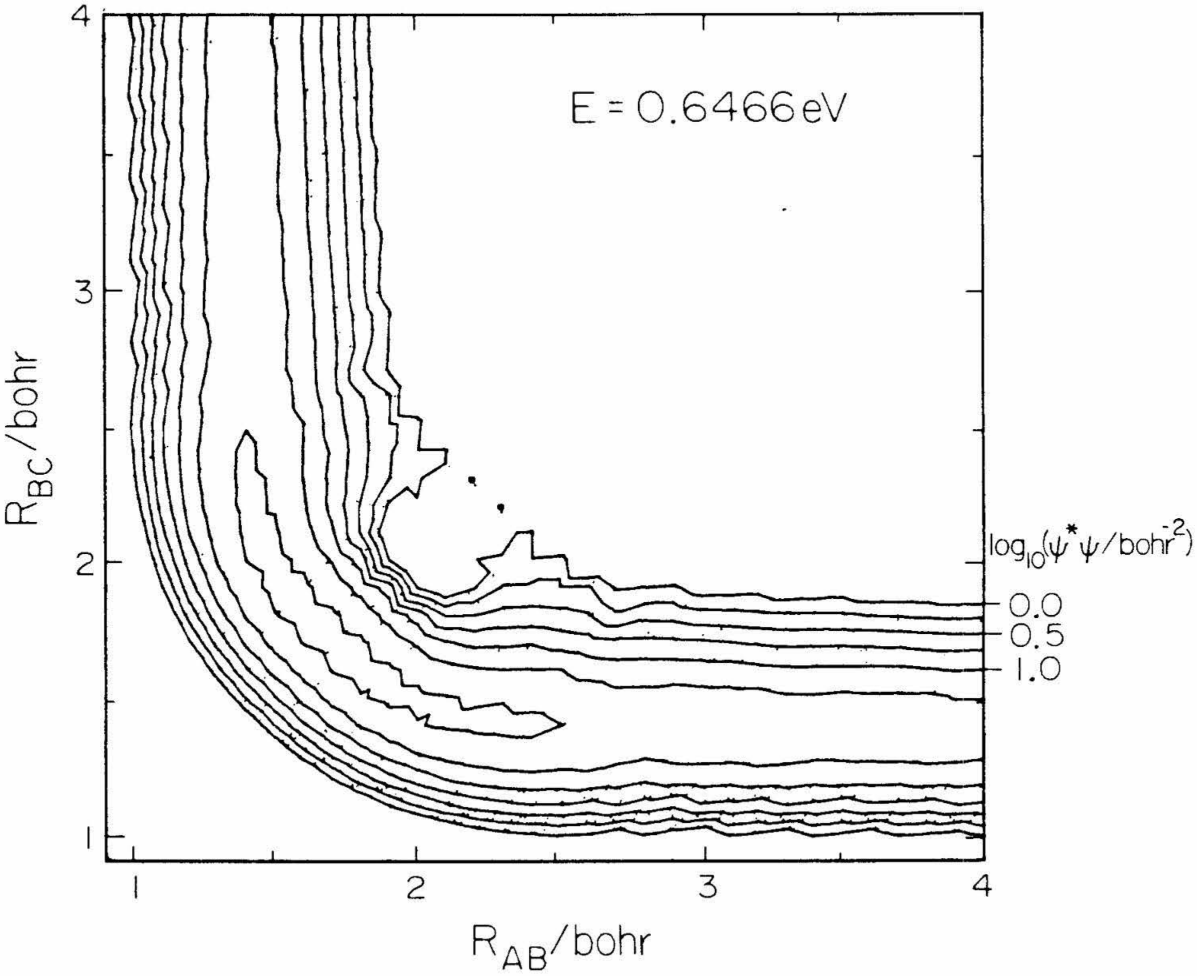
E = 0.6466 eV
R_{BC}/bohr
R_{AB}/bohr
$\log_{10}(\psi^*\psi/\text{bohr}^{-2})$
0.0
0.5
1.0
1
2
3
4
1
2
3
4

Figure 6

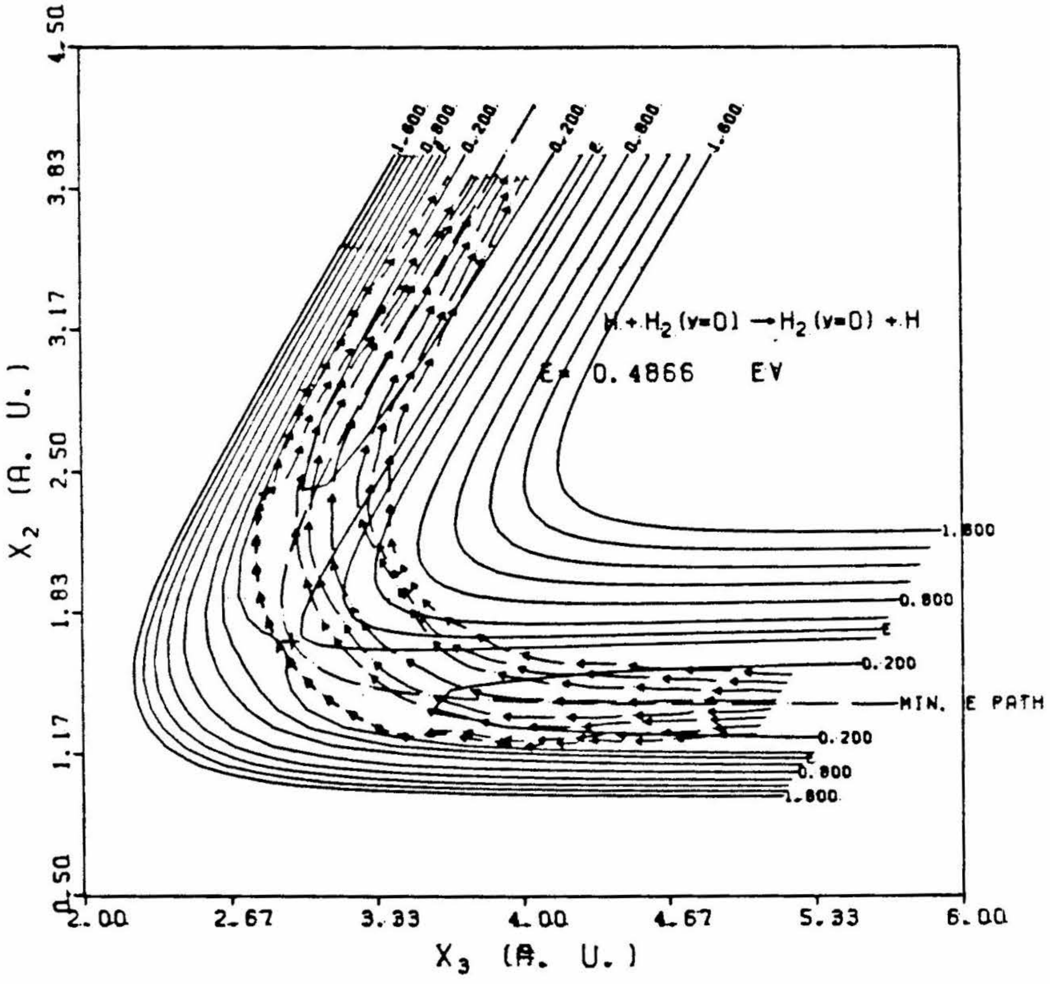
H + H_2 (v=0) → H_2 (v=0) + H
E= 0.4866 EV
1.800
0.800
0.200
E
MIN. E PATH
0.50
1.17
1.83
2.50
3.17
3.83
4.50
2.00
2.67
3.33
4.00
4.67
5.33
6.00
X_2 (A. U.)
X_3 (A. U.)

Figure 7

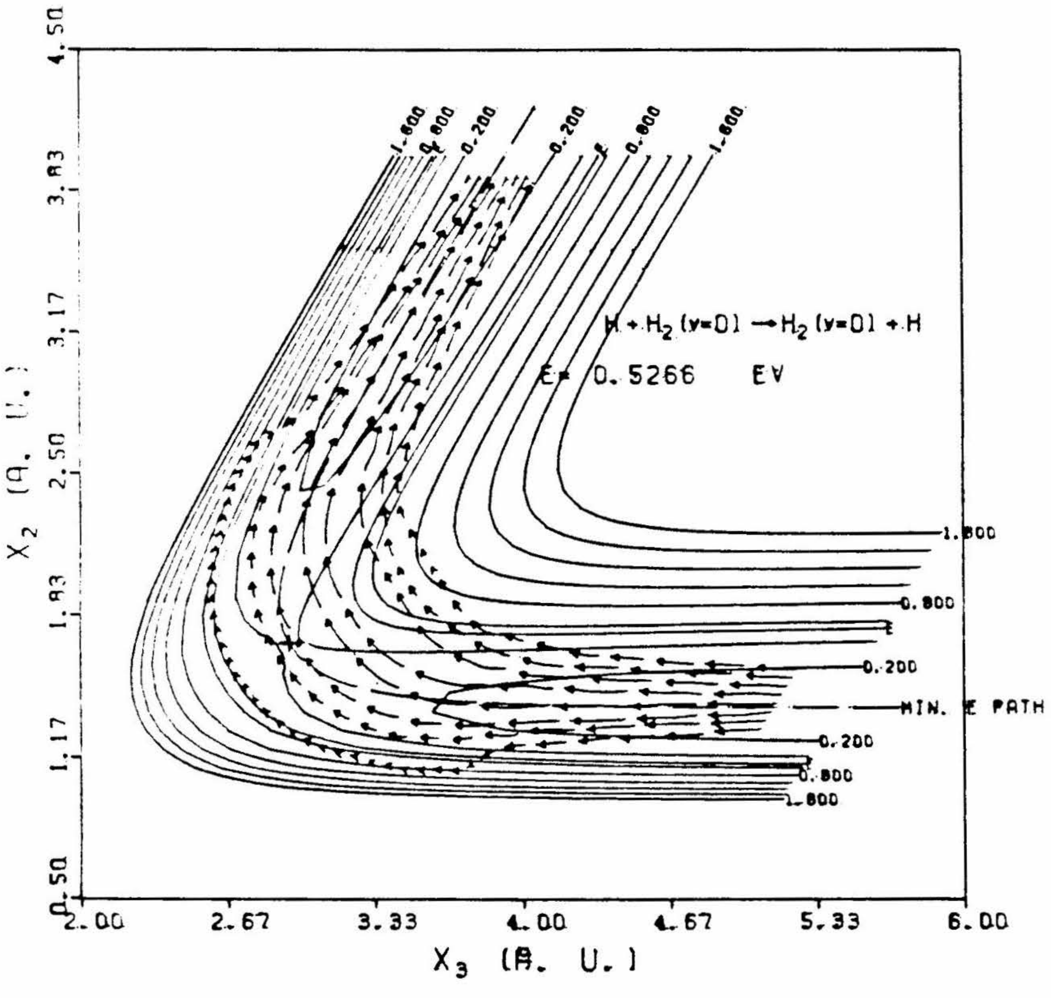
H + H₂ (v=0) → H₂ (v=0) + H
E= 0.5266 EV
1.800
0.800
0.200
0.200
E
0.800
1.800
1.800
0.800
E
0.200
MIN. E PATH
0.200
0.800
1.800
X₂ (A. U.)
4.50
3.83
3.17
2.50
1.83
1.17
0.50
2.00
2.67
3.33
4.00
4.67
5.33
6.00
X₃ (A. U.)

Figure 8

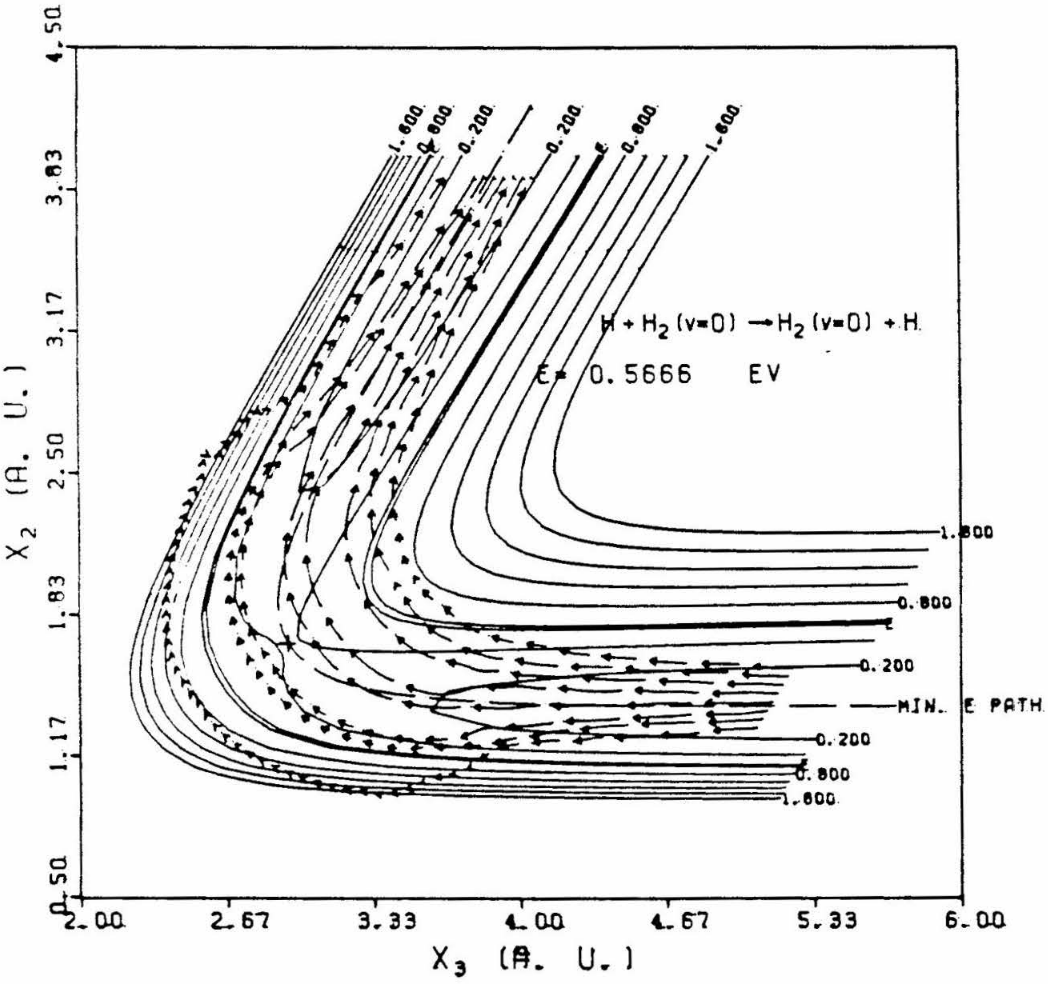
H + H2 (v=0) → H2 (v=0) + H
E= 0.5666 EV
1.800
0.800
0.200
0.200
0.800
1.800
1.800
0.800
0.200
MIN. E PATH
0.200
0.800
1.800
E
E
X2 (A. U.)
4.50
3.83
3.17
2.50
1.83
1.17
0.50
2.00
2.67
3.33
4.00
4.67
5.33
6.00
X3 (A. U.)

Figure 9

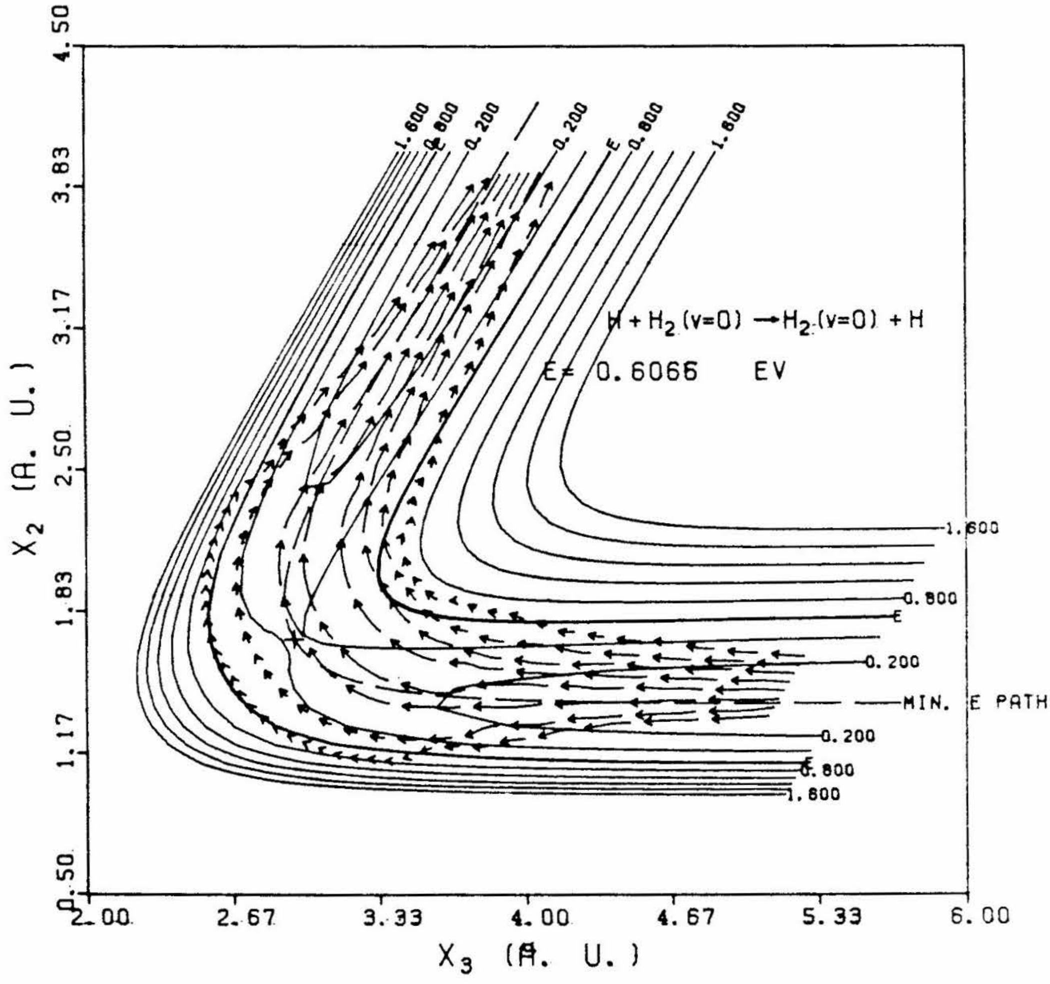
H + H_2 (v=0) → H_2 (v=0) + H
E= 0.6066 EV
1.600
0.800
E
0.200
0.200
E
0.800
1.600
1.600
0.800
E
0.200
MIN. E PATH
0.200
E
0.800
1.600
X_2 (A. U.)
4.50
3.83
3.17
2.50
1.83
1.17
0.50
2.00
2.67
3.33
4.00
4.67
5.33
6.00
X_3 (A. U.)

Figure 10

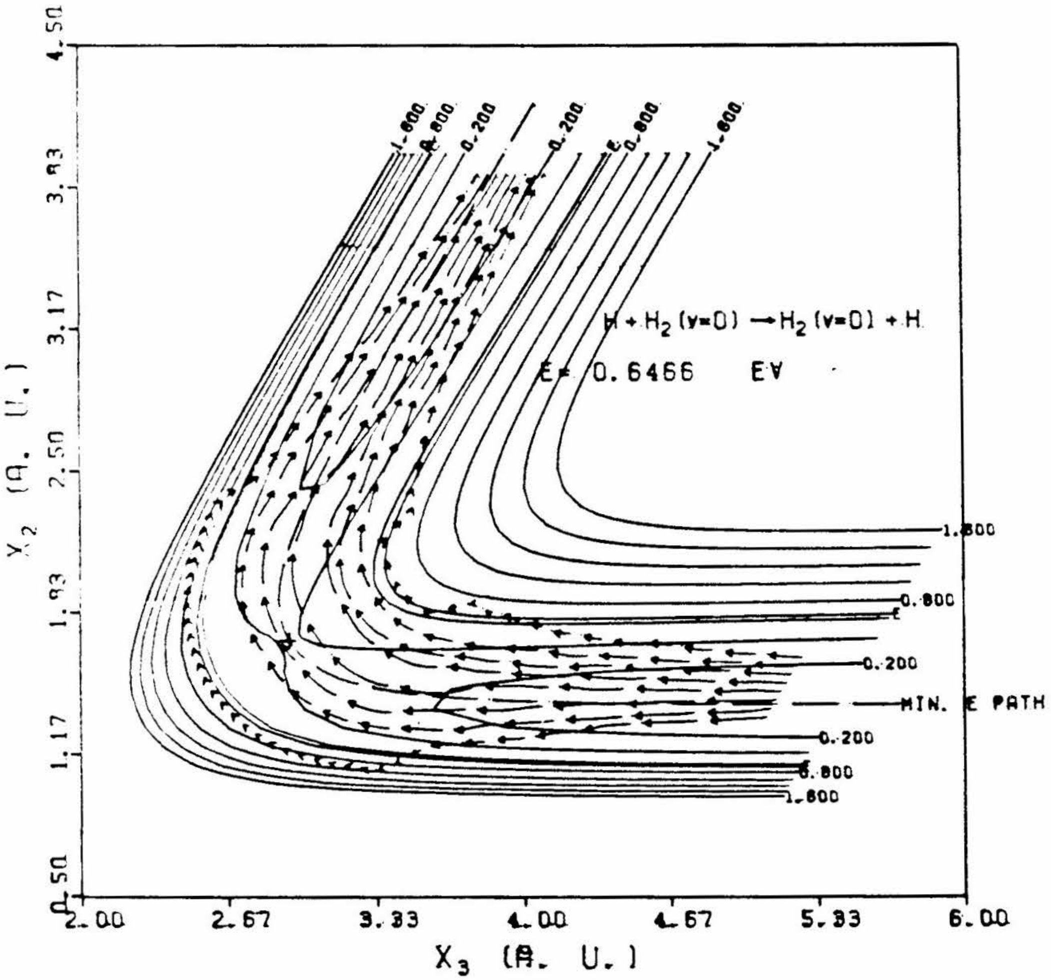
H + H_2 (v=0) → H_2 (v=0) + H
E= 0.6466 EV
1.800
0.800
0.200
0.200
0.800
1.800
1.800
0.800
0.200
MIN. E PATH
0.200
0.800
1.800
Y_2 (A. U.)
4.50
3.83
3.17
2.50
1.83
1.17
0.50
2.00
2.67
3.33
4.00
4.67
5.33
6.00
X_3 (A. U.)

Figure 11

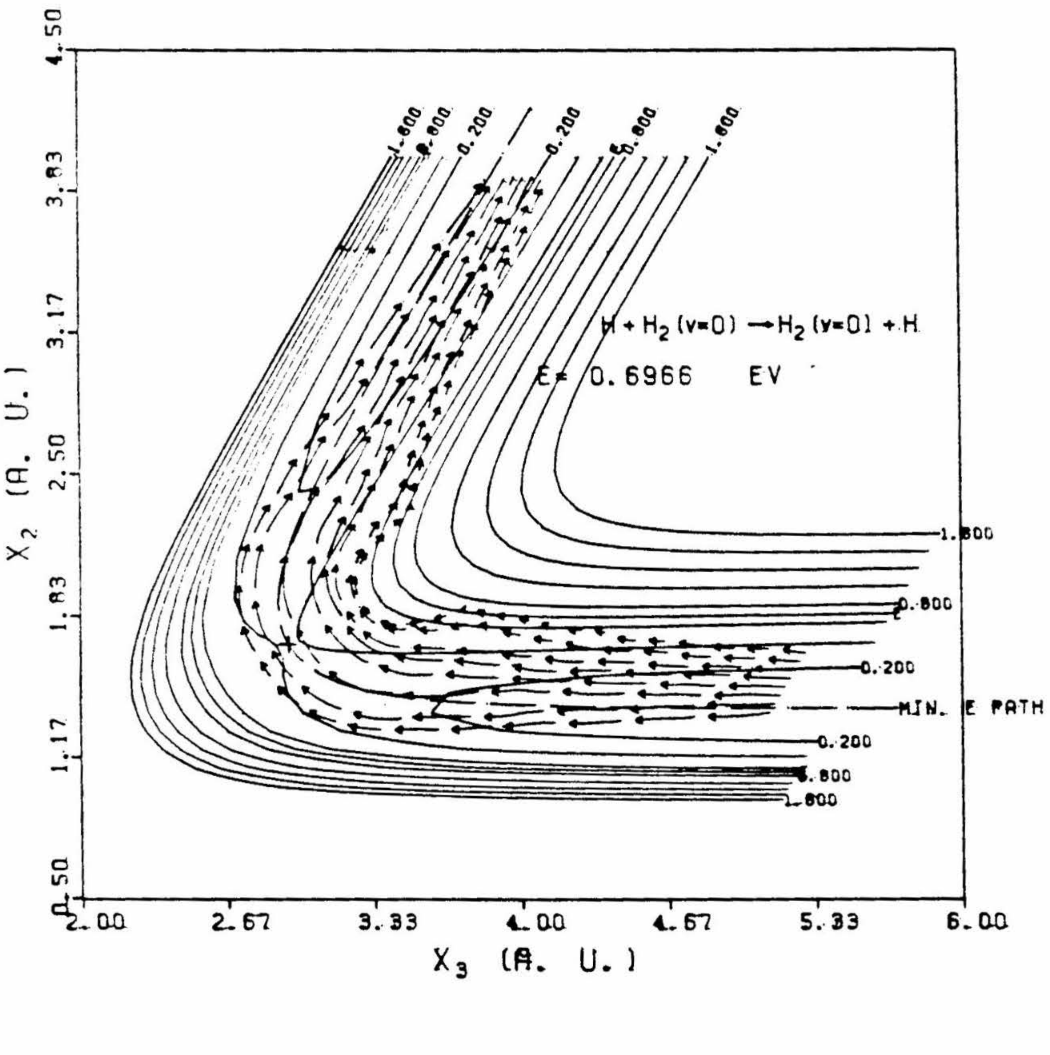
H + H$_2$ (v=0) → H$_2$ (v=0) + H
E= 0.6966 EV
MIN. E PATH
1.600
0.800
0.200
X$_2$ (A. U.)
X$_3$ (A. U.)
0.50
1.17
1.83
2.50
3.17
3.83
4.50
2.00
2.67
3.33
4.00
4.67
5.33
6.00

Figure 12

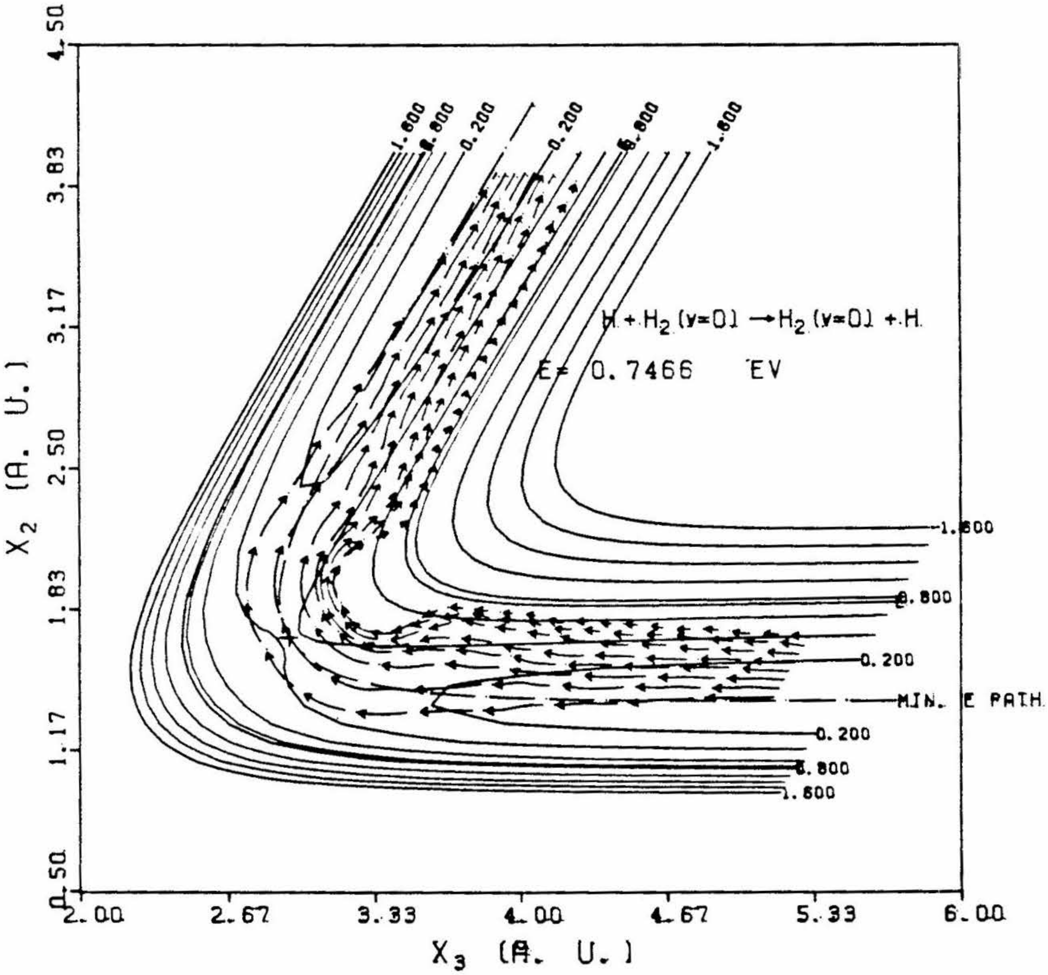
H + H_2 (v=0) → H_2 (v=0) + H
E= 0.7466 EV
1.600
0.800
0.200
MIN. E PATH
X_2 (A. U.)
X_3 (A. U.)
4.50
3.83
3.17
2.50
1.83
1.17
0.50
2.00
2.67
3.33
4.00
4.67
5.33
6.00

Figure 13

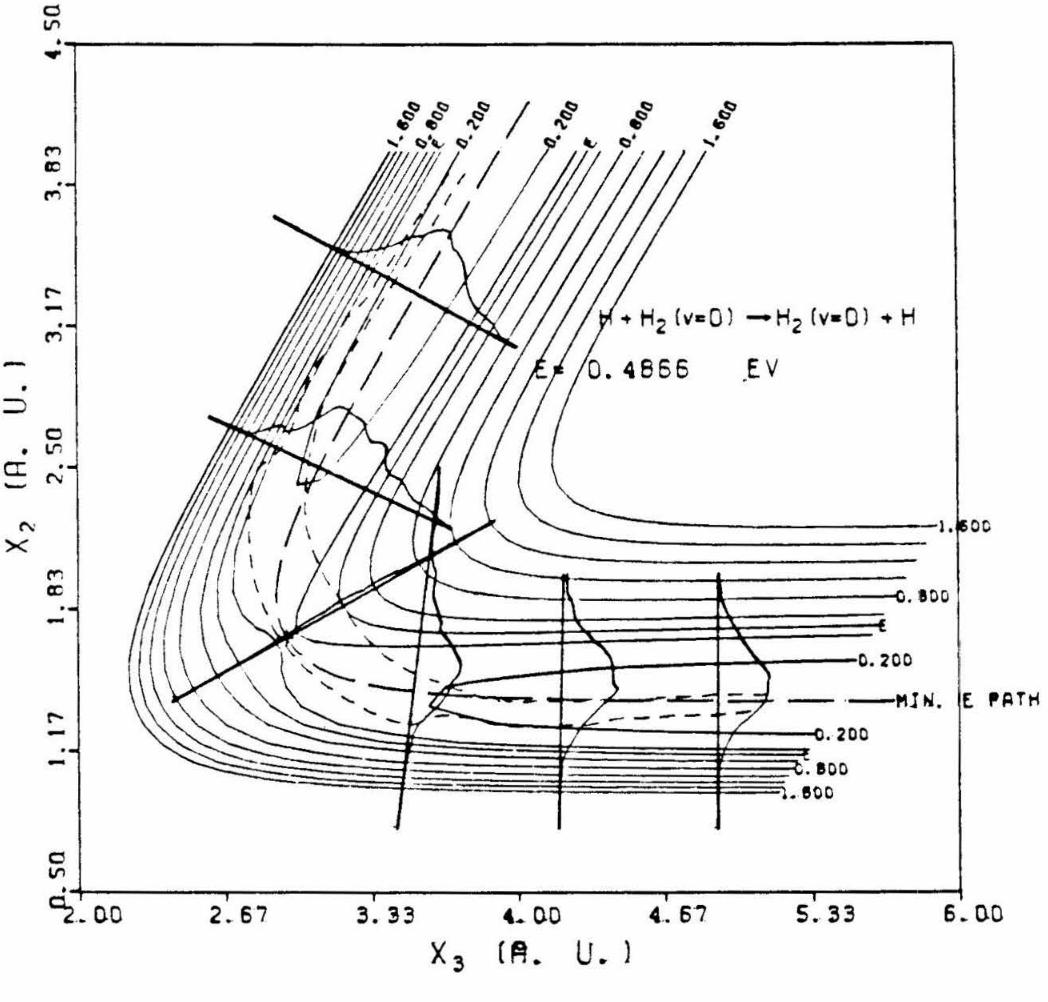
$H + H_2 (v=0) \rightarrow H_2 (v=0) + H$
E= 0.4866 EV
1.600
0.800
E
0.200
0.200
E
0.800
1.600
1.600
0.800
E
0.200
MIN. E PATH
0.200
E
0.800
1.600
X_2 (A. U.)
X_3 (A. U.)
0.50
1.17
1.83
2.50
3.17
3.83
4.50
2.00
2.67
3.33
4.00
4.67
5.33
6.00

Figure 14

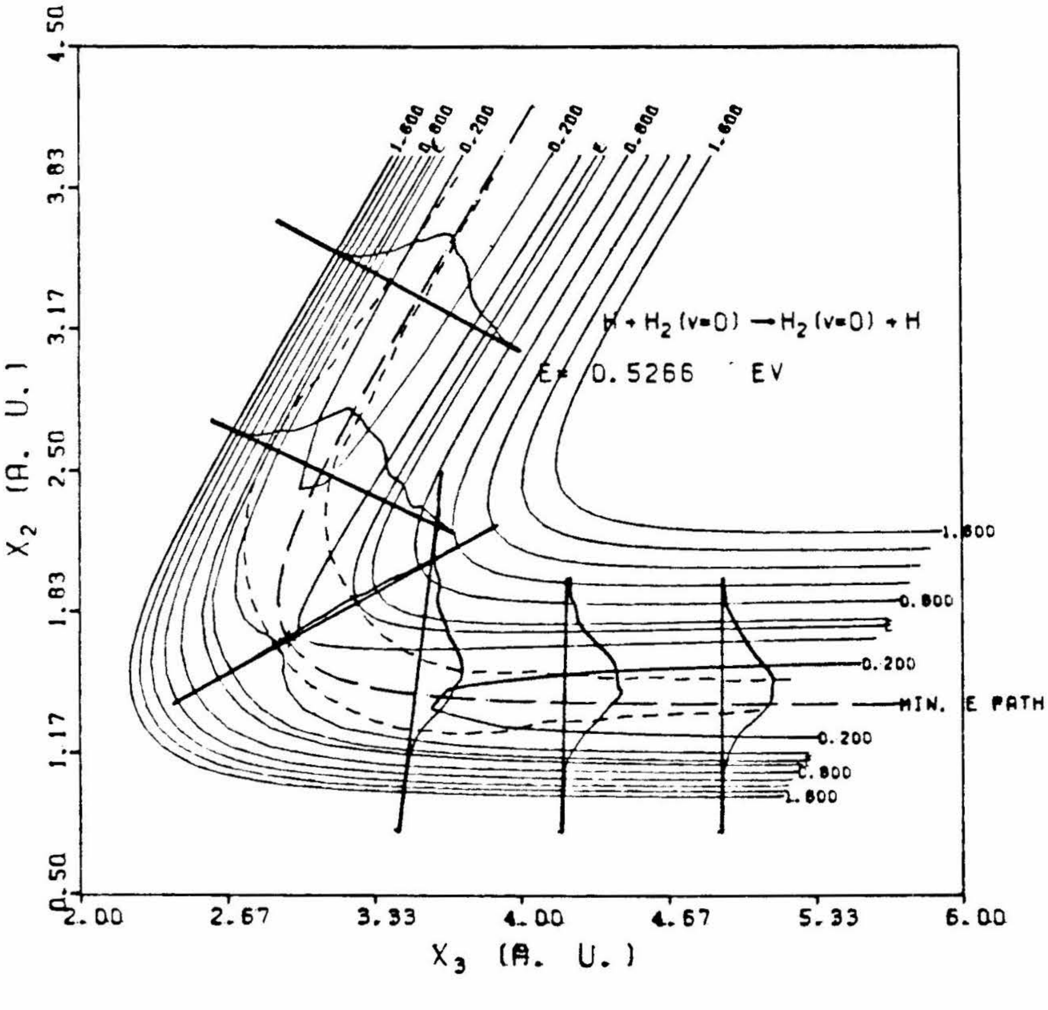
H + H$_2$(v=0) → H$_2$(v=0) + H
E= 0.5266 EV
X$_2$ (A. U.)
X$_3$ (A. U.)
4.50
3.83
3.17
2.50
1.83
1.17
0.50
2.00
2.67
3.33
4.00
4.67
5.33
6.00
1.600
0.800
E
0.200
MIN. E PATH

Figure 15

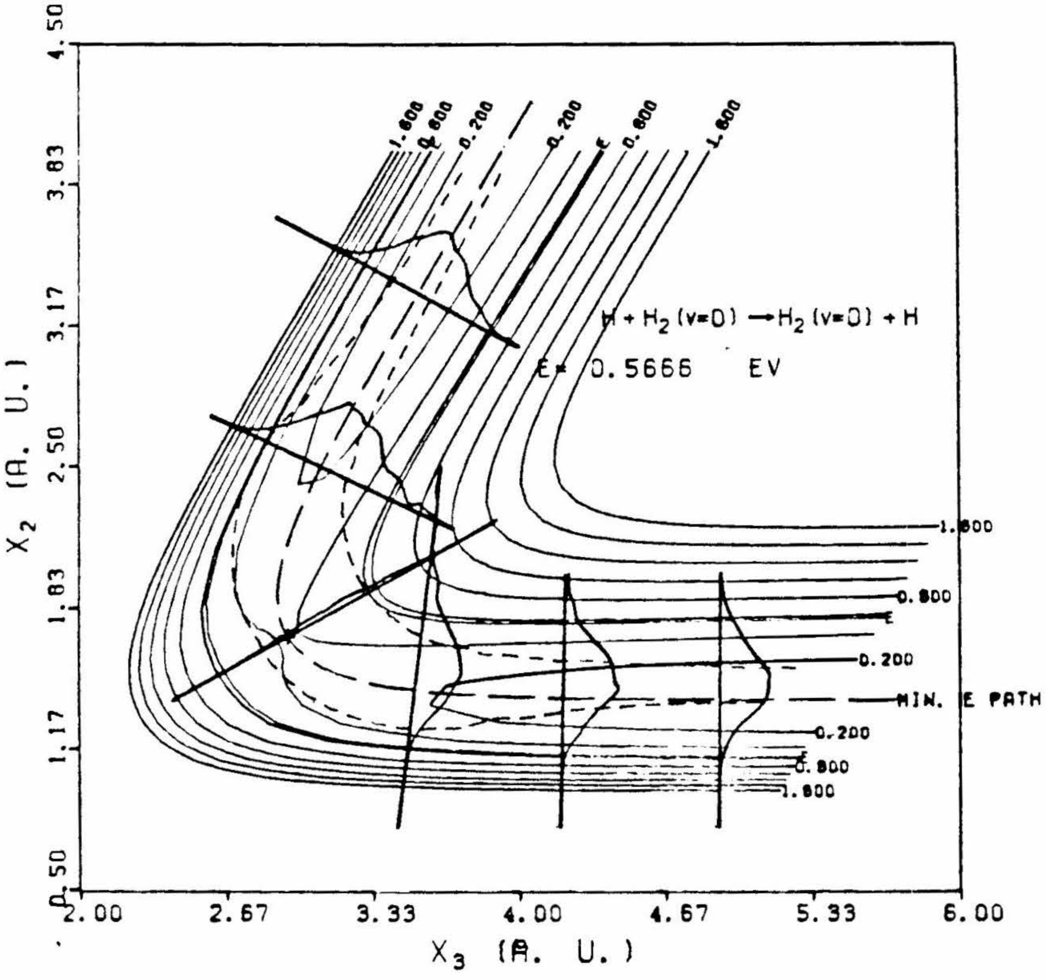
1.600
0.800
0.200
0.200
E
0.800
1.600
H + H2 (v=0) → H2 (v=0) + H
E= 0.5666 EV
1.600
0.800
E
0.200
MIN. E PATH
0.200
E
0.800
1.600
4.50
3.83
3.17
2.50
1.83
1.17
0.50
X2 (A. U.)
2.00
2.67
3.33
4.00
4.67
5.33
6.00
X3 (A. U.)

Figure 16

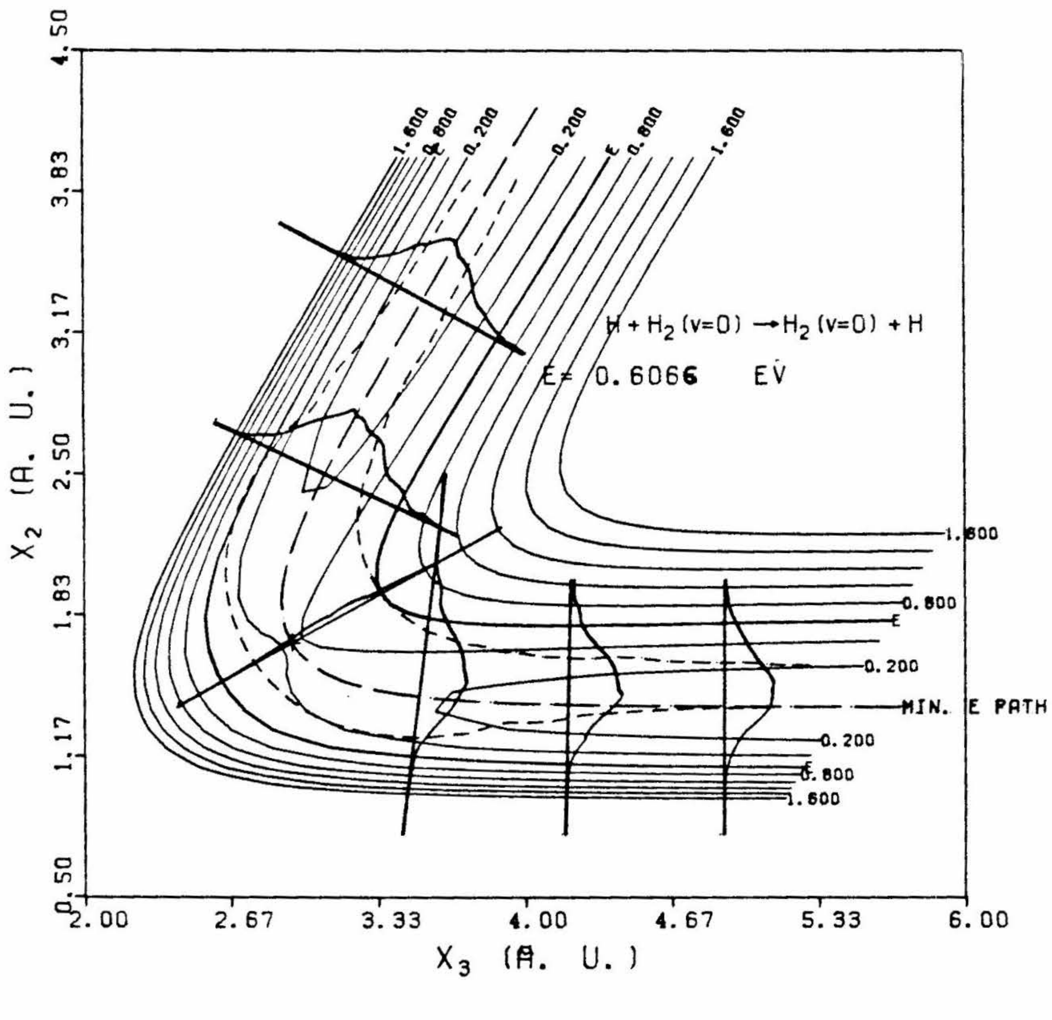
H + H_2 (v=0) → H_2 (v=0) + H
E= 0.6066 EV
1.600
0.800
E
0.200
MIN. E PATH
X_2 (A. U.)
X_3 (A. U.)
0.50
1.17
1.83
2.50
3.17
3.83
4.50
2.00
2.67
3.33
4.00
4.67
5.33
6.00

Figure 17

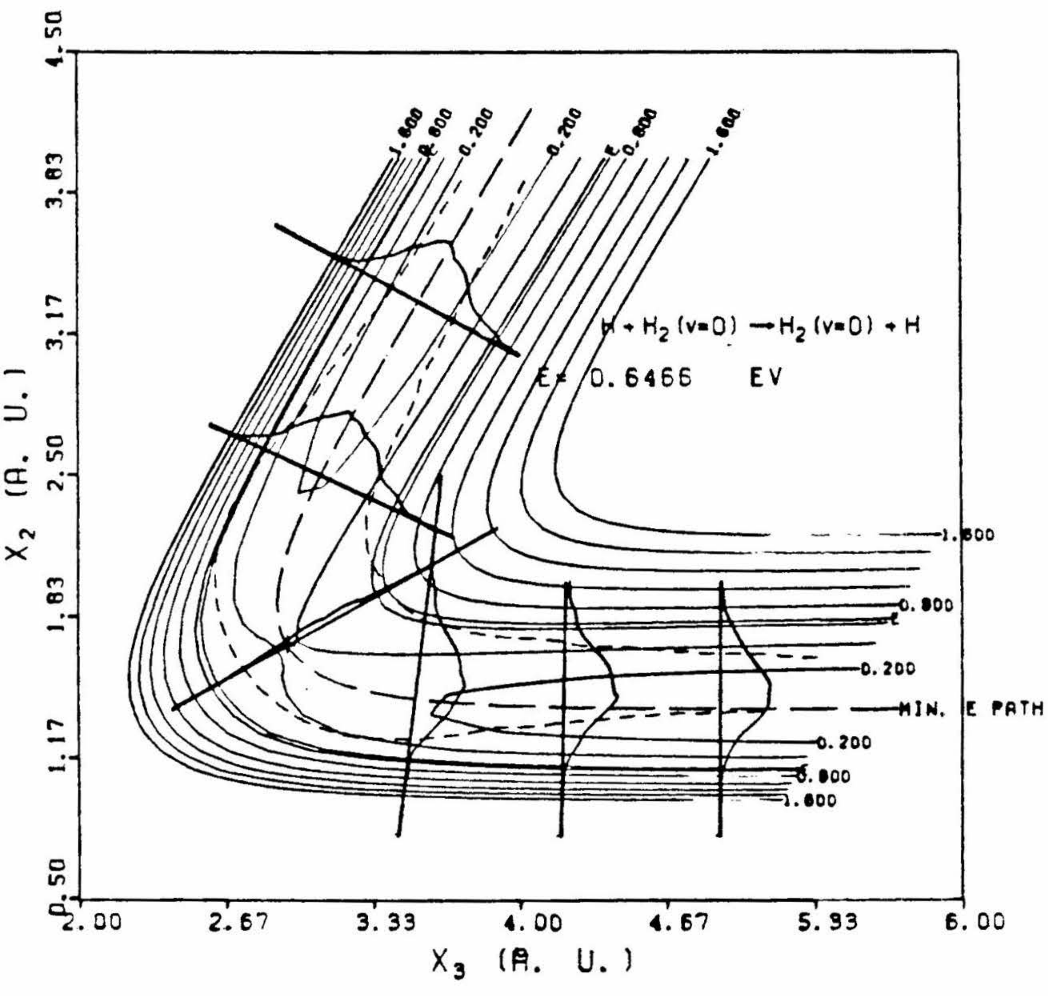
1.600
0.800
0.200
0.200
E
0.800
1.600
H + H2 (v=0) → H2 (v=0) + H
E= 0.6466 EV
1.600
0.800
E
0.200
MIN. E PATH
0.200
0.800
1.600
X2 (A. U.)
4.50
3.83
3.17
2.50
1.83
1.17
0.50
2.00
2.67
3.33
4.00
4.67
5.33
6.00
X3 (A. U.)

Figure 18

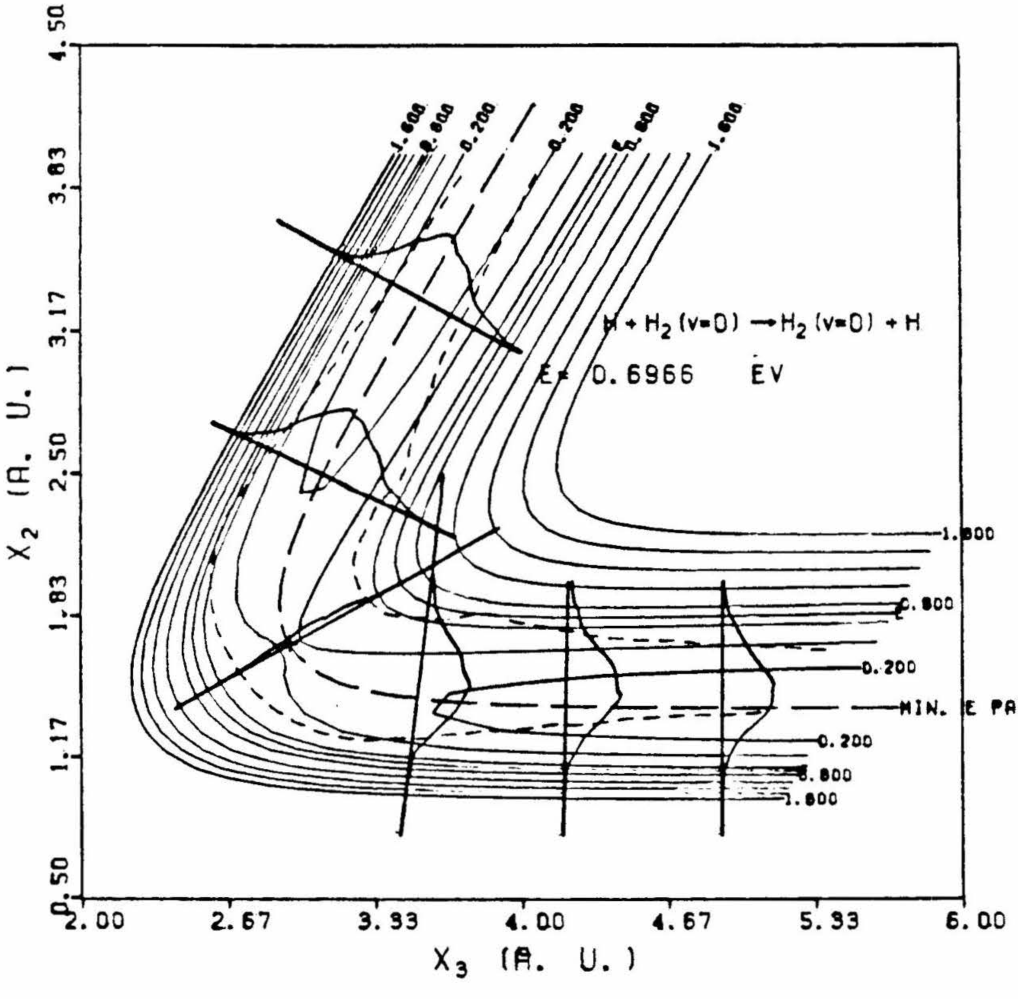
H + H2 (v=0) → H2 (v=0) + H
E= 0.6966 EV
1.600
0.800
0.200
0.200
0.800
1.600
1.600
0.800
0.200
MIN. E PATH
0.200
0.800
1.600
X2 (A. U.)
0.50
1.17
1.83
2.50
3.17
3.83
4.50
X3 (A. U.)
2.00
2.67
3.33
4.00
4.67
5.33
6.00

Figure 19

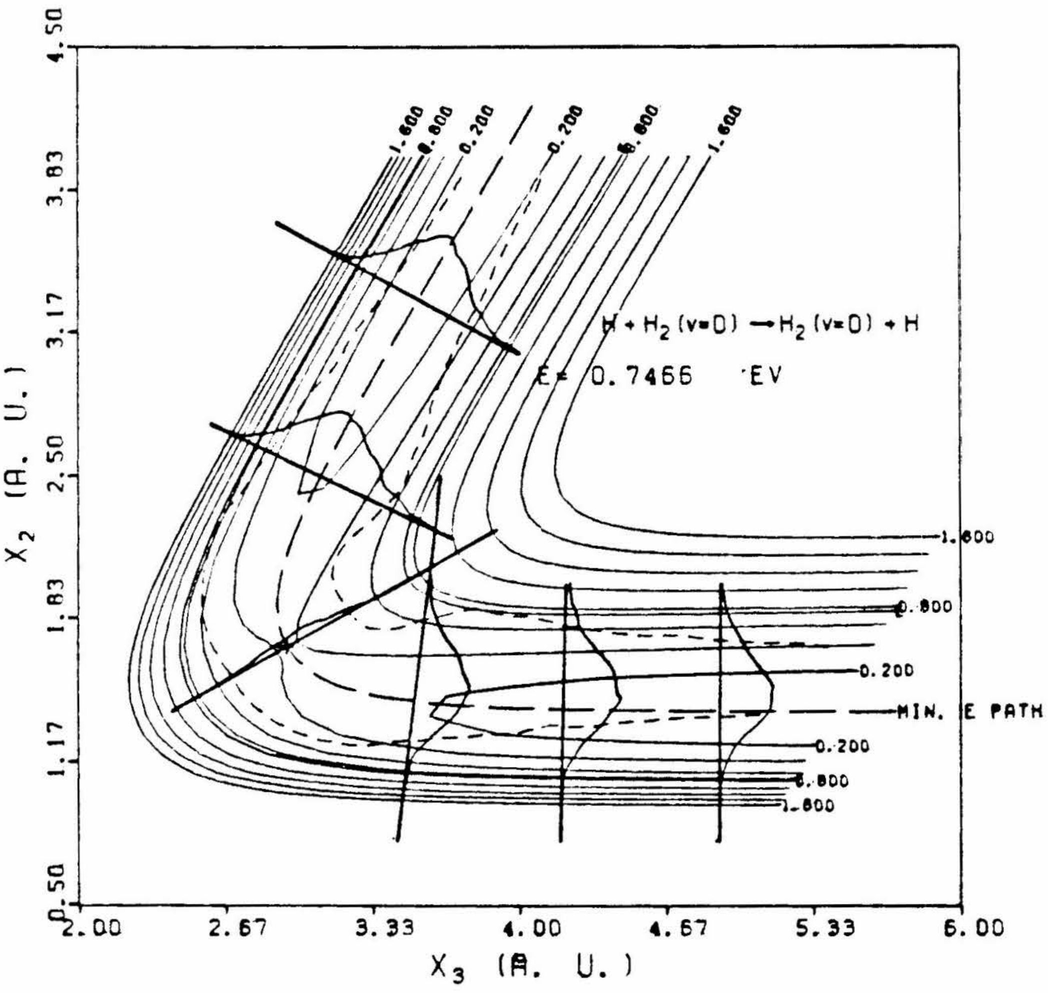
1.600
0.800
0.200
0.200
0.800
1.600
H + H₂ (v=0) → H₂ (v=0) + H
E= 0.7466 EV
1.600
0.800
0.200
MIN. E PATH
0.200
0.800
1.600
X₂ (A. U.)
4.50
3.83
3.17
2.50
1.83
1.17
0.50
2.00
2.67
3.33
4.00
4.67
5.33
6.00
X₃ (A. U.)

Figure 20

III. 11 HYPERSPHERICAL COORDINATES IN COLLINEAR ATOM-DIATOMIC MOLECULAR COLLISIONS: CONVERGENCE PROPERTIES

HYPERSPHERICAL COORDINATES IN COLLINEAR ATOM-DIATOMIC MOLECULE COLLISIONS: CONVERGENCE PROPERTIES[a)]

Jack A. KAYE[b)], Aron KUPPERMANN, and John P. DWYER[c)]

Arthur Amos Noyes Laboratory of Chemical Physics[d)]
California Institute of Technology, Pasadena, California 91125, USA

(Received)

The hyperspherical coordinates method for studying the collinear reactions of atoms and diatomic molecules is presented in some detail. We apply the method to the low energy $H + H_2$ and $F + H_2$ reactions, and focus on the behavior of the reaction probabilities and scattering matrix element phases with the number of basis functions and the projection distance (essentially termination point of integration). For $H + H_2$ probabilities and phases converge quite rapidly with the number of basis functions; the convergence of $F + H_2$ is less rapid. In $H + H_2$ one must integrate to $\gtrsim 10$ bohr to get nearly converged absolute phases which agree well with those obtained from another method; relative phases are obtained accurately at much smaller ρ. The phases for $F + H_2$ appear to be converging (slowly) with projection distance, but not to the values obtained from another method.

---

a) This work was supported in part by a contract (No. F49629-79-C-0187) from the Air Force Office of Scientific Research.

b) Work performed in partial fulfillment of the requirements for the Ph.D. degree in Chemistry at the California Institute of Technology.

c) Present address: Supreme Court of the United States, Washington, D.C. 20543.

d) Contribution No.

1. Introduction

Quantum mechanical studies of chemical reactions have provided substantial insight into the dynamics of chemical reactions, particularly reactions of systems containing hydrogen atoms, in which quantum mechanical effects are expected to play a major role.[1-3] Exact three-dimensional quantum mechanical calculations are quite difficult to perform, however, and have been limited to the reaction

$$H + H_2 \rightarrow H_2 + H \tag{1}$$

at low energy.[4-6] Approximate three-dimensional quantum mechanical calculations have been performed on both this system[7] and the reaction[8]

$$F + H_2 \rightarrow FH + H. \tag{2}$$

A far more tractable problem is that of a collinear collision of an atom and a diatomic molecule. In such a collision, the atoms are constrained to lie on a single straight line, which vastly simplifies the formalism and reduces the numerical effort in solving the appropriate Schrödinger equation compared to the three-dimensional case.[1-3] A number of methods have been developed to study collinear atom-diatomic molecule collisions within the framework of quantum mechanics, including coupled channel methods based on natural collision coordinates[9] and on the hybrid Cartesian coordinate/modified polar coordinate method of Kuppermann.[10] In addition, the two-dimensional partial differential equation has been solved directly by finite element methods (without expansion of the wavefunction in terms of some orthonormal basis set).[11]

While the coupled channel techniques have been used quite successfully for a number of chemical reactions, they cannot be used to study two interesting classes of reaction: Heavy-light-heavy (H-L-H) reactions in which a light atom is transferred between two heavy ones, and collision induced dissociation: (CID).

$$A + BC \rightarrow A + B + C \tag{3}$$

in which the reagent molecule is dissociated by the collision with the incident atom. H-L-H reactions are difficult to treat because the large amounts of skewing introduced into the potential energy surface by conversion to an appropriate set of mass-scaled coordinates causes an undesirably large number of basis functions to be needed. For example, Baer[12] reported needing 40 states in his calculations on the reaction

$$Cl + HBr \rightarrow ClH + Br. \tag{4}$$

CID has been difficult to treat because the previous coupled channel methods have expanded the wavefunction in terms of a basis set which is zero in the dissociative (A + B + C) region of the potential energy surface. Quantum mechanical studies of CID have been performed in non-reactive systems, in which chemical reaction of the type

$$A + BC \rightarrow AB + C \tag{5}$$

does not compete with CID[13] (process 3). The finite element method mentioned earlier has been applied to CID in non-reactive systems.[14] The first successful treatment of CID in reactive systems was the wave-packet approach of Kulander, who solved the time-dependent

Schrödinger equation for the collision.[15]

We have recently shown that collinear atom-diatomic molecule collisions can be studied easily and efficiently by the methods of hyperspherical coordinates,[16] and that this method can be applied without difficulty to both the H-L-H[17] and ClD[18] systems which have previously defied easy treatment. A similar approach has been developed by Manz et al.[19,20] and applied to the H-L-H[21,22] and ClD[23] problem. Our work[16-18] has shown that not only is the hyperspherical coordinates method desirable because of its ability to treat heretofore difficult problems, but that for certain problems which can be treated by the previous methods, fewer basis functions are needed when using hyperspherical coordinates.

In this paper we will review the formalism of the hyperspherical coordinates method, emphasizing those aspects of the method which differ from the treatment of Manz et al. We will then present results (reaction probabilities and scattering matrix element phases) for reactions 1 and 2 and, in particular, how these results depend on certain aspects of the numerical procedures. Finally, we will give an assessment of the method in light of the results obtained.

2. Theory

In the hyperspherical coordinates approach to collinear atom-diatomic molecule collisions, the two independent coordinates are the polar coordinates ρ, α, which are related to the usual Delves[24] coordinates R, r by the transformation

$$\rho^2 = (R_\alpha^2 + r_\alpha^2) = (R_\gamma^2 + r_\gamma^2) \tag{6a}$$

$$\alpha = \tan^{-1}(r_\alpha/R_\gamma), \tag{6b}$$

where the indices α and γ refer to the A + BC and AB + C arrangement channels, respectively. The Delves coordinates R_α, r_α are related to the r'_α, the distance between the two atoms in the bound molecular pair, and R'_α, the distance from the free atom to the center of mass of the diatomic molecule by the relationship

$$R_\alpha = aR'_\alpha \tag{7a}$$

$$r_\alpha = a^{-1} r'_\alpha \tag{7b}$$

where

$$a = \left(\frac{\mu_{\alpha,\beta\gamma}}{\mu_{\beta\gamma}}\right)^{\frac{1}{4}}, \tag{8}$$

where μ represents the reduced mass defined in the usual way. Similar expressions to (7) hold for R_γ and r_γ with the roles of α and γ in Eq. 8 reversed.

In Delves coordinates, the hamiltonian for nuclear motion is given by

$$H = -\frac{\hbar^2}{2\mu}\left[\frac{\partial^2}{\partial R_\lambda^2} + \frac{\partial^2}{\partial r_\lambda^2}\right] + V_\lambda(R_\lambda, r_\lambda); \qquad \lambda = \alpha, \gamma \tag{9}$$

where

$$\mu = [m_\alpha m_\beta m_\gamma/M]^{\frac{1}{2}} \tag{10a}$$

where

$$M = m_\alpha + m_\beta + m_\gamma$$

is a reduced mass and is independent of arrangement channel. $V_\lambda(R_\lambda, r_\lambda)$ is the electronically adiabatic potential energy surface for the triatomic system in λ coordinates.

In hyperspherical coordinates, the hamiltonian becomes

$$H(\rho,\alpha) = -\frac{\hbar^2}{2\mu}\left[\frac{\partial^2}{\partial\rho^2} + \frac{1}{\rho}\frac{\partial}{\partial\rho} + \frac{1}{\rho^2}\frac{\partial^2}{\partial\alpha^2}\right] + V(\alpha,\rho). \tag{11}$$

We desire a set of independent solutions $\{\psi^n(\rho,\alpha)\}$ to the Schrödinger equation

$$H(\rho,\alpha)\,\psi^n(\rho,\alpha) = E\,\psi^n(\rho,\alpha)\ . \tag{12}$$

To solve this equation we proceed to expand the wavefunction $\psi^n(\rho,\alpha)$ in terms of a set of orthonormal eigenfunctions $\{\phi_{n'}(\alpha;\bar{\rho})\}$ of the potential along the line $\rho = \bar{\rho}$

$$\psi^n(\rho,\alpha) = \rho^{-\frac{1}{2}} \sum_{n'=0}^{N} g^n_{n'}(\rho;\bar{\rho})\,\phi_{n'}(\alpha;\bar{\rho})\ , \tag{13}$$

where the $\rho^{-\frac{1}{2}}$ term is included to remove the first derivative term seen in eq. (11) from the hamiltonian, and N is the number of states included in the calculation. Because the potential $V(\rho,\alpha)$ becomes infinite at $\alpha = 0$ and $\alpha = \alpha_{max} = \tan^{-1}(m_\beta M/m_\alpha m_\gamma)^{\frac{1}{2}}$, (these correspond to the interatomic distances R_{BC} and R_{AB} being zero, respectively) the eigenfunctions $\phi_{n'}(\alpha;\bar{\rho})$ satisfy the boundary conditions

$$\phi_{n'}(0;\bar{\rho}) = \phi_{n'}(\alpha_{\max};\bar{\rho}) = 0 \tag{14}$$

and the differential equation

$$-\frac{\hbar^2}{2\mu\bar{\rho}^2}\frac{\partial^2\phi_{n'}}{\partial\alpha^2}(\alpha;\bar{\rho}) + V(\alpha,\bar{\rho})\,\phi_n(\alpha,\rho) = \mathbf{E}_n\,\phi_n(\alpha,\rho)\,. \tag{15}$$

As a result of these boundary conditions, this set of eigenfunctions is infinite and discrete. It is this property of the basis set that allows one to treat CID with no artificial "discretization of the continuum", as the basis set is already discrete, even at energies above dissociation. Of course, we use only a finite number (N) of these basis functions. These are calculated numerically by a finite difference procedure.[25]

The differential equation to be solved then is, in matrix form,

$$-\frac{\hbar^2}{2\mu}\frac{d^2\underline{\underline{g}}}{d\rho^2}(\rho;\bar{\rho}) + \underline{\underline{W}}(\rho;\bar{\rho})\,\underline{\underline{g}}(\rho;\bar{\rho}) = \underline{\underline{E}}(\rho;\bar{\rho})\,g(\rho;\bar{\rho}), \tag{16}$$

where

$$W^n_{n'}(\rho;\bar{\rho}) = \langle n|\,V(\alpha;\rho) - (\bar{\rho}^2/\rho^2)\,V(\alpha,\bar{\rho})\,|n'\rangle \tag{17a}$$

$$\mathbf{E}^n_{n'}(\rho;\bar{\rho}) = [\mathbf{E} + \hbar^2/8\,\mu\rho^2 - \mathbf{E}_n(\bar{\rho})]\,\delta^n_{n'} \tag{17b}$$

where $|n'\rangle = \phi_{n'}(\alpha;\bar{\rho})$ and the angular brackets represent integration over the angle α, and $\mathbf{E}_n(\bar{\rho})$ is the eigenvalue associated with the basis function $\phi_{n'}(\alpha;\bar{\rho})$.

Integration of the eq. (16) begins from some value of $\rho = \rho_0$ which is sufficiently small that all the eigenvalues of the eigenvectors $\phi_n(\alpha;\rho_0)$ are sufficiently greater than the total energy **E** of the collision. In this case we may assume the following initial conditions:

$$\underline{\underline{g}}(\rho_0;\rho_0) = \underline{\underline{0}} \tag{18a}$$

$$\underline{\underline{g}}(\rho_0;\rho_0) = \underline{\underline{I}}\ . \tag{18b}$$

Given these initial conditions, eq. (16) is numerically integrated by any convenient procedure (we have chosen to use the method of Gordon)[26]. Eq. (16) is formulated in the diabatic representation. One can formulate the problem in the adiabatic representation, in which the basis functions vary continuously with ρ; in that case an equation very different from (16) is developed; we have derived these equations in the adiabatic representation elsewhere.[27]

Two points concerning the numerical integration should be mentioned. First, since closed channels [states whose eigenvalue $E_n(\rho)$ is greater than the total collision energy E] are normally included in the calculation (except in calculations of CID at large ρ, when all states are open), one must prevent the exponential growth associated with the closed channels. This is particularly severe in the hyperspherical coordinates approach at small ρ, when all channels are closed. This growth is prevented by the reorthogonalization procedure of Riley and Kuppermann.[28] Second, since we are working in a diabatic representation, we must modify the radial wavefunction $\underline{\underline{g}}$ when changing basis functions in order to maintain continuity of $\psi^n(\rho;\alpha)$ and its derivative $\psi'^n(\rho,\alpha)$ across the boundary. This is accomplished by the transformation

$$\underline{\underline{g}}(\rho;\bar{\rho}_\kappa) = \underline{\underline{O}}\,\underline{\underline{g}}(\rho;\bar{\rho}_\kappa) \tag{19a}$$

$$g'(\rho';\bar{\rho}_\kappa) = O'g'(\rho;\bar{\rho}_\kappa) \tag{19b}$$

where the overlap matrix $\underline{\underline{O}}$ is defined by the expression

$$O^n_{n'} = \langle \phi_{n'}(\rho;\bar{\rho}_{\kappa+1}) | \phi_n(\rho;\bar{\rho}_\kappa)\rangle \ . \qquad (20)$$

Ideally $\underline{\underline{O}}$ should be an orthogonal matrix; deviations from orthogonality which will prodcue a loss of flux, are produced by use of a finite basis set.

At large values of ρ, at which the regions of the potential energy surface corresponding to bound AB and BC diatomic molecules are localized to small and large α, respectively, we may project the bound wave function $\psi^n(\rho,\alpha)$ onto basis functions appropriate to the diatomic molecules. These basis functions $\{\chi^n(r_\lambda;\bar{R}_\lambda)\}$ are solutions of the differential equation

$$-\frac{\hbar^2}{2\mu}\frac{d^2\chi^\lambda_n}{dr^2_\lambda}(r_\lambda;\bar{R}_\lambda) + V_\lambda(r_\lambda,\bar{R}_\lambda)\,\chi^\lambda_n(r_\lambda;\bar{R}_\lambda) = E_n(\bar{R}_\lambda)\,\chi^\lambda_n(r_\lambda;\bar{R}_\lambda). \qquad (21)$$

In terms of this basis set, the wavefunction ψ^n may be written

$$\psi^n = \rho^{-\frac{1}{2}} \sum_{n'} g^n_{n'}(\rho;\bar{\rho})\,\phi_{n'}(\alpha;\bar{\rho}) = \sum_{n''} h^n_{n''}(r_\lambda;\bar{R}_\lambda)\,\chi^\lambda_{n''}(r_\lambda;\bar{R}_\lambda) \qquad (22)$$

The matrix elements $h^n_{n''}$ are evaluated from eq. (22) by taking advantage of the orthogonality of the $\{\chi^\lambda_n(r_\lambda;\bar{R}_\lambda)\}$ and assuming that the basis sets $\{\phi\}$ and $\{\chi\}$ are orthogonal. This is a very good approximation when only bound states are considered; it is less good when considering continuum states. The $h^n_{n''}$ are obtained from the expression

$$h^n_{n''} = \int_{r^{\min}_\lambda}^{r^{\max}_\lambda} \chi^\lambda_{n''}(r_\lambda;\bar{R}_\lambda)\,e^{-\frac{1}{2}} \sum_{n'} g^n_{n'}(\rho;\bar{\rho})\,\phi_{n'}(\alpha;\bar{\rho})\,dr_\lambda \qquad (23)$$

where ρ, r_λ, and R_λ are related by eqs. 6.

We have discussed elsewhere[27] the methods by which a $\underline{\underline{g}}$ suitable for use in eq. (23) is generated (one must correct for reorthogonalizations and renormalizations by the Gordon integrator). In many cases the width of the channel $r_\lambda^{\min} < r_\lambda < r_\lambda^{\max}$ is sufficiently large that one needs to use more than one polar coordinate basis set $\phi_{n'}(\alpha;\bar{\rho}_\kappa)$ in order to accurately represent the wavefunction $\psi^n(\rho,\alpha)$. In that case, the integral in eq. (23) must be broken up into m parts, where m is the number of basis sets used in the integration from $\rho_{\min}$ to $\rho_{\max}$ in polar coordinates, where

$$\rho_{\min}^2 = \bar{R}_\lambda^2 + (r_\lambda^{\min})^2 \tag{24a}$$

$$\rho_{\max}^2 = \bar{R}_\lambda^2 + (r_\lambda^{\max})^2 . \tag{24b}$$

The new form of eq. (23) is

$$h_{n''}^{n}(R_\lambda;\bar{R}_\lambda) = \sum_\kappa \int_{(r_\lambda^{\min})_\kappa}^{(r_\lambda^{\max})_\kappa} \chi_{n''}^{\lambda}(r_\lambda;\bar{R}_\lambda)\,\rho^{-\frac{1}{2}} \sum_m g_{n'}^{n}(\rho;\bar{\rho}_\kappa)\,\phi_{n'}(\alpha;\bar{\rho}_\kappa)\,dr_\lambda \tag{25}$$

where $r_\lambda^{\min}$ and $r_\lambda^{\max}$ now depend on the index κ. Note that the overlap matrix defined in eqs. (19) and (20) above insures that the integrand in eq. (25) is continuous across the boundaries between basis sets.

An equation similar to (23) (or 25) is needed for the derivative $\underline{\underline{h}}'$ of the matrix $\underline{\underline{h}}$. This is obtained by differentiating eq. 23 with respect to R_λ; the result is

$$(h^{n}_{n''})'(R_\lambda;\bar{R}_\lambda) = \int_{r_\lambda^{\min}}^{r_\lambda^{\max}} \chi^{\lambda}_{n''}(r_\lambda;\bar{R}_\lambda)\Big\{-\tfrac{1}{2}\rho^{-\frac{3}{2}}\sum_{n'} g^{n}_{n'}(\rho;\bar{\rho})\,\phi_{n'}(\alpha;\bar{\rho})$$

$$+\sum_{n'}\rho^{-\frac{1}{2}}\,\frac{dg^{n}_{n'}}{d\rho}(\rho;\bar{\rho})\,\Big(\frac{\partial\rho}{\partial R_\lambda}\Big)\,\phi_{n'}(\alpha;\bar{\rho}) + \sum_{n'}\rho^{-\frac{1}{2}}\,g^{n}_{n'}(\rho;\bar{\rho})\,\frac{d\phi_{n'}(\alpha;\bar{\rho})}{d\alpha}\Big(\frac{\partial\alpha}{\partial R_\lambda}\Big)\Big\}\,dr_\lambda \tag{26}$$

When more than one basis set is used in the projection region, the integral in eq. (26) may be simply broken up into portions as in eq. (25). The matrices $\underline{\underline{h}}$ and $\underline{\underline{h}}'$ are used in the asymptotic analysis and calculation of the $\underline{\underline{R}}$, $\underline{\underline{S}}$, and $\underline{\underline{\rho}}$ matrices by the usual procedure.[3, 29]

When including "continuum" states, that is those whose asymptotic eigenvalues are greater than the dissociation energy of the diatomic molecules, the continuum states are treated differently from the bound states. This case is described in detail elsewhere.

In symmetric collisions (where atom C is identical to atom A), the potential energy function $V(\alpha,\rho)$ is symmetric about the line $\alpha = \alpha_{\max}/2$, and one can separately integrate symmetric and antisymmetric eigenfunctions, as there is no coupling between these two sets of eigenfunctions. One could then project onto symmetric and anti-symmetric linear combinations of the diatomic molecule basis functions $\chi^{\lambda}_{n}(r_\lambda;\bar{R}_\lambda)$ and evaluate symmetric and antisymmetric scattering matrices could be evaluated and then combined to get reactive and non-reactive ones. Instead, we have projected separately onto bound states in each channel and evaluated a scattering matrix only once. We note that Manz et al.[19-23] perform no such projection, using instead their polar coordinate radial wavefunctions (the equivalent of our $\underline{\underline{g}}$) directly in their asymptotic analysis.

3. Results

We have extensively tested the hyperspherical coordinate method on reactions 1 and 2 on the Porter-Karplus[30] and Muckerman V[31] surfaces respectively. Calculations on these systems have been performed previously in this laboratory[32, 33-36] and we compare our results with these previous results. A number of other workers have performed calculations on reactions 1 and 2 also (referred to in refs. 1 and 2). The quantities on which we will focus our attention are certain state-to-state reaction probabilities (P^R_{00} for the H + H_2 reaction; P^R_{02} (for the F + H_2 reaction) and scattering matrix element phases (ϕ^R_{00} for the H + H_2 reaction; ϕ^R_{02} for the F + H_2 reaction). We note that scattering matrix element phases are determined only modulo 2π, and we make no effort to assign absolute values to any of the phases. We will examine these reaction probabilities and scattering matrix element phases as a function of two parameters: the number of basis functions being included in the calculation and the stopping point of the integration (essentially the value of $\bar{R}_\lambda$ defined earlier).

A. The H + H_2 Reaction

In Table 1 we present results for the reaction probability P^R_{00} in the energy range from 0.25-1.75 eV with respect to the bottom of the H_2 well. We have results for $2 \leqslant N \leqslant 6$, where N is the number of symmetric (and of anti-symmetric) basis functions used in the calculation. Results from a previous calculation (10 basis functions) are also included. Numerical parameters used in the integration of eq. (16) are given in Table 2.

We have also obtained P^R_{00} as a function of the projection distance ρ_{pr}, which is related to the distance $\bar{R}_\lambda$ by the equation

$$\rho^2_{pr} = \bar{R}^2_\lambda + r^{eq^2}_\lambda \tag{27}$$

where

$$r^{eq}_\lambda = a^{-1}_\lambda r'^{eq}_\lambda . \tag{28}$$

These calculations were made with four even and four odd basis functions for $5 \leq \rho_{pr} \leq 12$ bohr. These probabilities are tabulated in Table 3, along with the previous results. Averages and standard deviations of the probabilities are given in Table 4. Both Tables 1 and 3 contain only a fraction of the energies at which we have calculated probabilities and phases. The dependence of the scattering matrix element phase ϕ^R_{00} on the number of basis functions is indicated by the data in Table 5, and on projection distance in Table 6. Additionally, we have plotted ϕ^R_{00} over a range of energies for the different projection distances in Fig. 1, and in Figs. 2 and 3 we compare the phases obtained here at energies near the first and second resonance with those from extensions of the previous calculations on this system.

B. The F + H_2 Reaction

In Table 7 we present results for the reaction probability P^R_{02} in the energy range from 0.0-0.5 eV with respect to the zero-point energy of HF, with points concentrated near the low energy resonance in this system. We have results for $7 \leq N \leq 9$, where N is now the total number of basis functions used in the calculations. Results from previous calculations on this system (13 basis functions) are also included. Numerical parameters used in the integration of eq. (16) are given in Table 2. In Table 8 we present results for P_{02}^{R} as a function of the projection distance ρ_{pr} for a calculation with nine basis functions. We have examined $\rho_{pr} = 10$, 12, and 14 bohr. Note in the asymmetric case $r_{\alpha}^{eq} \neq r_{\gamma}^{rq}$, for simplicity we require $r_{\gamma}^{eq} = r_{\alpha}^{eq}$ so $\bar{R}_{\alpha} = \bar{R}_{\gamma}$. Tables of the phase ϕ_{02}^{R} of the scattering matrix element S_{02}^{R} as a function of basis set and projection distance are given in Table 9 and Table 10, along with their values from calculations by the previous method.

4. Discussion and Conclusions

From the results in the tables and figures, it is clear that reaction probabilities and scattering matrix element phases converge quite rapidly with basis set for the $H + H_2$ reaction, while similar convergence has not yet set in for the $F + H_2$ system. Convergence in the former system is quite remarkable (and fast) at certain energies above the threshold region, the probabilities sometimes vary by less than ± 0.0001 on addition of basis functions. The general conclusions from Tables 1 and 5 is that in the $H + H_2$ system, with two closed channels of each symmetry type one should have an adequate basis set, given the frequency of basis set calculations (every 0.10 bohr) used.

Convergence of the reaction probabilities with projection distance is less rapid. The results scatter about an average value; the scatter is fairly narrow, as we see from Table 4 that the largest standard deviation of the P_{00}^{R} is 0.007 (and that occurs essentially in the center of the first resonance, where data scatter might be expected to be large). This convergence is impressive when compared to the results of Römelt[20] for this reaction on the Porter-Karplus surface. He obtained good reaction probabilities by interpolating between the limits of a highly oscillatory P_{00}^{R} vs. integration stopping point (he did no projection). For example, at an energy of 0.0404 au even at ρ = 14 bohr, P_{00}^{R} is oscillating with amplitudes of ± 0.075 about the correct probability. Since the major conceptual difference between his work and our work is our inclusion of a projection;[16, 19, 20] it appears that it must be the projection which causes our transition probabilities to reach their accurate values so rapidly.

While the reaction probabilities for $H + H_2$ become more or less independent of the projection distance at fairly small ρ, we see that the same is not true for the scattering matrix element phases. These approach a limiting value as the projection distance increases, and approach it uniformly from above (see Fig. 1). As with the probabilities, the phases compare quite well with those of the previous method (see Figs. 2 and 3). The probabilities for $F + H_2$ behave fairly well in terms of basis set and projection distance convergence (though not as well as those for $H + H_2$). The phases (Tables 9 and 10) also converge fairly well with respect to basis set, but do not appear to converge rapidly as the projection distance increases. Further, they do not appear to be approaching the correct phases (as determined in the previous calculations). In particular, the small region of increasing phase with energy seen by the previous method is not reflected when ρ_{pr} = 10-12 bohr, and is only minimally reflected when ρ_{pr} = 14 bohr.

We have no reason why the phases for FH_2 should not be converging to the seemingly correct answer.

The rapid convergence of the reaction probabilities and phases with basis set bodes well for future development of hyperspherical coordinate methods for three-dimensional reactive scattering,[37] as it is hoped that in that case a smaller number of basis functions might be needed to treat 3D H + H_2 than in the previous calculations.[5]

Acknowledgments

The calculations reported here were performed on the Dreyfus-NSF Theoretical Chemistry Computer which was funded through grants from the Camille and Henry Dreyfus Foundation, the National Science Foundation (Grant No. CH 978-20235), and the Sloan Fund of the California Institute of Technology, and or the IBM 370/158 Computer of Ambassador College, Pasadena, California, for which we express our appreciation.

References

1. J. N. L. Connor, Comp. Phys. Comm. **17**, 117 (1979).
2. R. B. Walker and J. C. Light, Ann. Rev. Phys. Chem. **31**, 401 (1980).
3. A. Kuppermann, in Theoretical Chemistry: Advantages and Perspectives, Vol. 6A, ed. D. Henderson (Academic Press, New York, 1981) pp. 79-164.
4. A. B. Elkowitz and R. E. Wyatt, J. Chem. Phys. **62**, 2504 (1975); **63**, 702 (1975).
5. A. Kuppermann and G. C. Schatz, J. Chem. Phys. **62**, 2502 (1975); G. C. Schatz and A. Kuppermann, J. Chem. Phys. **65**, 4642 (1976); **65**, 4668 (1976).
6. R. B. Walker, E. B. Stechel, and J. C. Light, J. Chem. Phys. **69**, 2922 (1978).
7. M. Baer, V. Khare, and D. J. Kouri, Chem. Phys. Lett. **68**, 378 (1979); D. J. Kouri, V. Khare, and N. Baer, J. Chem. Phys. **75**, 1179 (1981); J. M. Bowman and K. T. Lee, Chem. Phys. Lett. **64**, 291 (1979); J. Chem. Phys. **72**, 5071 (1980).
8. M. J. Redmon and R. E. Wyatt, Chem. Phys. Lett. **63**, 209 (1979); J. Jellinek, M. Baer, V. Khare, and D. J. Kouri, Chem. Phys. Lett. **75**, 460 (1980); V. Khare, D. J. Kouri, J. Jellinek, and M. Baer, in: Potential Energy Surfaces and Dynamics Calculations, ed. D. G. Truhlar (Plenum Press, New York, 1981) pp. 475-493.
9. C. C. Rankin and J. C. Light, J. Chem. Phys. **51**, 1701 (1969); G. Miller and J. C. Light, J. Chem. Phys. **54**, 1635, 1643 (1971).

References (continued)

10. A. Kuppermann, in: Proceedings of the Conference on Potential Energy Surfaces in Chemistry, ed. W. A. Lester (U. Calif., Santa Cruz, 1970) pp. 121-124; in: Proceedings of the 7th International Conference on the Physics of Electronic and Atomic Collisions (North-Holland, Amsterdam, 1971) pp. 3-5.

11. H. Rabitz, A. Askar, and A. S. Cakmak, Chem. Phys. 29, 61 (1978); A. Askar, A. S. Cakmak, and H. A. Rabitz, Chem. Phys. 33, 267 (1978).

12. M. Baer, J. Chem. Phys. 62, 305 (1975).

13. D. J. Diestler, in Atomic Molecule Collision Theory, ed. R. B. Bernstein (Plenum Press, New York, 1979) pp. 655-667 and references therein.

14. G.-D. Barg and A. Askar, Chem. Phys. Lett. 76, 609 (1980).

15. K. C. Kulander, J. Chem. Phys. 69, 5064 (1978); Nucl. Phys. A353, 34c (1981).

16. A. Kuppermann, J. A. Kaye, and J. P. Dwyer, Chem. Phys. Lett. 74, 257 (1980).

17. J. A. Kaye and A. Kuppermann, Chem. Phys. Lett. 77, 573 (1981).

18. J. A. Kaye and A. Kuppermann, Chem. Phys. Lett. 78, 546 (1981).

19. G. Hauke, J. Manz, and J. Römelt, J. Chem. Phys. 73, 5040 (1980).

20. J. Römelt, Chem. Phys. Lett. 74, 263 (1980).

21. J. Manz and J. Römelt, Chem. Phys. Lett. 76, 337 (1980).

References (continued)

22. J. Manz and J. Römelt, Chem. Phys. Lett. 81, 179 (1981).

23. J. Manz and J. Römelt, Chem. Phys. Lett. 77, 172 (1981).

24. L. M. Delves, Nucl. Phys. 9, 391 (1959); 20, 275 (1960).

25. D. G. Truhlar, J. Comput. Phys. 10, 123 (1972).

26. R. G. Gordon, J. Chem. Phys. 51, 14 (1969).

27. J. A. Kaye, Ph.D. Thesis, California Institute of Technology, 1982.

28. M. E. Riley and A. Kuppermann, Chem. Phys. Lett. 1, 537 (1968).

29. A. M. Lane and R. G. Thomas, Rev. Mod. Phys. 30, 257 (1958).

30. R. N. Porter and M. Karplus, J. Chem. Phys. 40, 1105 (1964).

31. J. T. Muckerman, in: Theoretical Chemistry: Advances and Perspectives, Vol. 6A, ed. D. Henderson (Academic Press, New York, 1981) pp. 1-77.

32. G. C. Schatz and A. Kuppermann, Phys. Rev. Lett. 35, 7266 (1975); unpublished results.

33. G. C. Schatz, J. M. Bowman, and A. Kuppermann, J. Chem. Phys. 58, 4023 (1973); 63, 674 (1975).

34. A. Kuppermann, in: Potential Energy Surfaces and Dynamics Calculations, ed. D. G. Truhlar (Plenum Press, New York, 1981) pp. 375-420.

35. A. Kuppermann and J. A. Kaye, J. Phys. Chem. 85, 1969 (1981).

36. J. A. Kaye and A. Kuppermann, manuscript in preparation.

37. R. T. Ling and A. Kuppermann, in: Electronic and Atomic Collisions, Abstracts of Papers of the 9th International Conference

References (continued)

on the Physics of Electronic and Atomic Collisions, ed. J. S. Risley and R. Geballe (U. Wash., Seattle, 1975) pp. 353-354; J. K. C. Wong and A. Kuppermann, in: Abstracts of Papers, Pacific Conference on Chemistry and Spectroscopy, Pasadena, California, 10-12 October 1979, p. 39.

Table 1. $H + H_2$ Reaction Probabilities as a Function of Basis Set.

			P_{00}^{R} a)			
N= ε/au.	2	3	4	5	6	prev. method
0.0120	0.1802(-6)	0.3468(-6)	0.2467(-6)	0.2620(-6)	0.1390(-6)	0.1985(-6)
0.0140	0.3526(-3)	0.3179(-3)	0.3183(-3)	0.3070(-3)	0.3142(-3)	0.3256(-3)
0.0160	0.3135(-1)	0.3103(-1)	0.3103(-1)	0.3101(-1)	0.3107(-1)	0.3052(-1)
0.0170	0.1589	0.1569	0.1569	0.1568	0.1569	0.1554
0.0180	0.4740	0.4596	0.4596	0.4596	0.4596	0.4597
0.0190	0.8059	0.7842	0.7843	0.7843	0.7843	0.7876
0.0210	0.9902	0.9838	0.9836	0.9836	0.9836	0.9860
0.0240	0.9959	0.9968	0.9969	0.9969	0.9970	0.9976
0.0300	0.9096	0.9289	0.9301	0.9302	0.9302	0.9306
0.0320	-- b)	0.1797	0.1768	0.1765	0.1770	0.1738
0.0340	--	0.7110	0.7121	0.7115	0.7115	0.7127
0.0380	--	0.5187	0.5219	0.5222	0.5218	0.5210
0.0420	--	0.2991	0.299	0.3010	0.3011	0.2998
0.0450	--	0.2496	0.2251	0.2254	0.2253	0.2208
0.0470	--	--	0.3516	0.3557	0.3558	0.3546
0.0480	--	--	0.7050	0.7120	0.7120	0.7037
0.0490	--	--	0.1329	0.1331	0.1328	0.1288
0.0500	--	--	0.1131	0.1153	0.1155	0.1158
0.0530	--	--	0.1339	0.1330	0.1329	0.1361
0.0570	--	--	0.1157	0.1161	0.1160	0.1217
0.0610	--	--	--	0.6369(-1)	0.6383(-1)	0.6452(-1)
0.0640	--	--	--	0.1193	0.1206	0.1161

a) The number enclosed in parentheses is the power of 10 by which the non-enclosed number should be multiplied.

b) Lack of unitarity of the scattering matrix indicated that this calculation was unreliable.

Table 2. Numerical Parameters for Integration of Eq. 16.

		$H + H_2$	$F + H_2$
ρ_{pr}	=	10 bohr	10 bohr
r_λ^{min}	=	0.25 bohr	0.3 bohr
r_λ^{max}	=	4.0 bohr	3.3 bohr
ρ_0	=	1.5 bohr	2.0 bohr
$\Delta\bar{\rho}$ b)	=	0.1 bohr	0.1 bohr
N c)		250	300-380
NBPT d)		150	150

a) $\rho_{pr}^2 = (\bar{R}_\lambda^2 + r_\lambda^{eq^2})$ where $r_\lambda^{eq} = a^{-1} r_\lambda^{\prime eq}$.

b) Distance between successive basis set calculations.

c) Minimum number of points in eigenfunctions $\phi_n(\alpha;\bar{\rho})$.

d) Number of points in eigenfunctions $\chi_n^\lambda(r_\lambda;\bar{R}_\lambda)$

Table 3. H + H_2 Reaction Probabilities as a Function of Projection Distances

ρ_{pr} = ϵ/au.	5	6	7	8	9	10	11	12	prev. method
0.0120	0.4367(-6)	0.1941(-6)	0.3558(-6)	0.2372(-6)	0.2063 -6)	0.2487(-6)	0.2830(-6)	0.2990(-6)	0.1985(-6)
0.0140	0.3146(-3)	0.3284(-3)	0.3260(-3)	0.3110(-3)	0.3164(-3)	0.3183(-3)	0.3239(-3)	0.3247(-3)	0.3256(-3)
0.0160	0.3047(-1)	0.2975(-1)	0.3005(-1)	0.3059(-1)	0.3113(-1)	0.3103(-1)	0.3048(-1)	0.2998(-1)	0.3052(-1)
0.0170	0.1564	0.1585	0.1570	0.1523	0.1524	0.1569	0.1577	0.1540	0.1554
0.0180	0.4684	0.4612	0.4604	0.4737	0.4653	0.4596	0.4714	0.4672	0.4597
0.0190	0.7808	0.7833	0.7929	0.7770	0.7909	0.7843	0.7822	0.7911	0.7876
0.0210	0.9872	0.9844	0.9876	0.9837	0.9880	0.9836	0.9877	0.9843	0.9860
0.0240	0.9984	0.9968	0.9970	0.9983	0.9981	0.9969	0.9972	0.9982	0.9976
0.0300	0.9347	0.9357	0.9354	0.9340	0.9320	0.8301	0.9289	0.9285	0.9306
0.0320	0.1958	0.1735	0.1793	0.1774	0.1749	0.1768	0.1785	0.1775	0.1738
0.0340	0.7140	0.7132	0.7115	0.7100	0.7102	0.7121	0.7118	0.7100	0.7127
0.0380	0.5256	0.5222	0.5299	0.5190	0.5296	0.5219	0.5254	0.5254	0.5210
0.0420	0.3007	0.3021	0.3010	0.3014	0.3036	0.2999	0.3014	0.3039	0.2998
0.0450	0.2231	0.2187	0.2173	0.2213	0.2228	0.2251	0.2212	0.2209	0.2208
0.0470	0.3518	0.3538	0.3532	0.3541	0.3512	0.3516	0.3513	0.3516	0.3546
0.0480	0.7114	0.7103	0.7071	0.7078	0.7051	0.7050	0.7047	0.7052	0.7037
0.490	0.1258	0.1318	0.1320	0.1340	0.1311	0.1329	0.1322	0.1319	0.1288
0.0500	0.1126	0.1113	0.1105	0.1129	0.1126	0.1131	0.1135	0.1129	0.1158
0.0530	0.1234	0.1267	0.1265	0.1269	0.1249	0.1236	0.1252	0.1257	0.1361

Table 4. Average and Standard Deviation of H + H_2 Reaction Probabilities. (From Table 3.)

ϵ/au.	$\langle P_{00}^R \rangle$	std. dev.	std. dev. $\langle P_{00} \rangle$
0.012	2.826(-7)	8.127(-8)	28.8%
0.014	3.204(-4)	6.193(-6)	1.93%
0.016	0.03044	0.00049	1.61%
0.017	0.1557	0.0024	1.55%
0.018	0.4659	0.0052	1.12%
0.019	0.7853	0.0057	0.72%
0.021	0.9858	0.0020	0.20%
0.024	0.9976	0.0007	0.07%
0.030	0.9324	0.0029	0.32%
0.032	0.1792	0.0070	3.89%
0.034	0.7116	0.0015	0.21%
0.038	0.5249	0.0038	0.72%
0.042	0.3018	0.0014	0.46%
0.045	0.2213	0.0025	1.12%
0.047	0.3523	0.0012	0.33%
0.048	0.7071	0.0026	0.37%
0.049	0.1315	0.0024	1.86%
0.050	0.1124	0.0010	0.90%
0.053	0.1254	0.0014	1.08%

Table 5. H + H_2 Phases as a Function of Basis Set

	ϕ_{00}^{R} /radians				
N =	2	3	4	5	6
ϵ/au.					
0.021	8.149	8.083	8.082	8.082	8.082
0.024	5.787	5.787	5.784	5.784	5.785
0.026	4.338	4.323	4.319	4.319	4.319
0.028	2.949	2.950	2.946	2.946	2.946
0.030	1.717	1.705	1.701	1.700	1.700
0.0305	1.506	1.427	1.423	1.422	1.423
0.031	1.197	1.183	1.180	1.180	1.180
0.0315	0.675	1.021	1.022	1.021	1.021
0.032	0.196	0.715	0.577	0.581	0.579
0.0325	-- a)	-0.291	-0.259	-0.260	-0.259
0.033	--	-0.454	-0.442	-0.443	-0.443
0.0335	--	-0.608	-0.664	-0.664	-0.664
0.034	--	-0.916	-0.913	-0.914	-0.914
0.035	--	-1.431	-1.431	-1.431	-1.431
0.036	--	-1.958	-1.960	-1.961	-1.961
0.038	--	-2.971	-2.977	-2.989	-2.989
0.040	--	-3.999	-3.998	-4.000	-4.000

a) Lack of unitarity of the scattering matrix indicated that this calculation was unreliable.

Table 6. H + H_2 Phases as a Function of Projection Distance.

	ϕ_{00}^{R}/radians							
ρ_{pr} ϵ/au.	5	6	7	8	9	10	11	12
0.021	12.713	10.364	9.196	8.576	8.247	8.082	8.003	7.966
0.024	9.853	7.797	6.771	6.222	5.931	5.785	5.715	5.683
0.026	8.110	6.199	5.240	4.726	4.456	4.319	4.254	4.225
0.028	6.507	4.714	3.813	3.330	3.075	2.946	2.884	2.856
0.030	5.068	3.374	2.522	2.065	1.823	1.701	1.641	1.614
0.031	4.473	2.821	1.988	1.539	1.301	1.180	1.124	1.337
0.032	3.779	2.161	1.342	0.902	0.684	0.577	0.514	0.474
0.033	2.688	1.120	0.326	-0.102	-0.328	-0.442	-0.496	-0.517
0.034	2.151	0.613	-0.161	-0.579	-0.802	-0.911	-0.965	-0.991
0.036	0.979	-0.489	-1.239	-1.641	-1.853	-1.961	-2.008	-2.034
0.038	-0.162	-1.584	-2.289	-2.684	-2.892	-2.990	-3.046	-3.002
0.040	-1.270	-2.636	-3.325	-3.701	-3.904	-4.000	-4.051	-4.069

Table 7. $F + H_2$ Reaction Probabilities as a Function of Basis Set

N = ϵ/au.	7	P^{R}_{02} a) 8	9	previous method
0.010	0.1290(-2)	0.1286(-2)	0.1357(-2)	0.1245(-2)
0.0102	0.4354(-1)	0.4363(-1)	0.4363(-1)	0.4457(-1)
0.0103	0.1834	0.1843	0.1962	0.2038
0.0104	0.3856	0.3882	0.402	0.4108
0.0105	0.3752	0.3765	0.3744	0.3550
0.0108	0.2611	0.2621	0.2666	0.2630
0.011	0.2537	0.2545	0.2602	0.2562
0.012	0.2438	0.2453	0.2404	0.2338
0.013	0.1497	0.1476	0.1456	NA c)
0.014	-- b)	0.7077(-1)	0.6927(-1)	NA
0.015	0.5563(-1)	0.6106(-1)	0.6029(-1)	0.5717(-1)
0.0175	--	0.5529(-1)	0.5738(-1)	0.5477(-1)
0.020	--	0.3539(-1)	0.3623(-1)	0.3493(-1)
0.025	--	0.1162(-2)	0.1154(-2)	0.1101(-2)

a) The number enclosed in parentheses is the power of 10 by which the non-enclosed number should be multiplied.

b) Lack of unitarity of the scattering matrix (> 10%) indicated that this calculation was unreliable.

c) Not available.

Table 8. F + H_2 Reaction Probabilities as a Function of Projection Distance

		P_{02}^{R} a)		
ρ_{pr} ϵ/au.	10	12	14	previous method
0.010	0.1357(-2)	0.1205(-2)	0.1151(-2)	0.1245(-2)
0.0101	0.8221(-2)	0.7622(-2)	0.7897(-2)	0.8036(-2)
0.0102	0.4363(-1)	0.4445(-1)	0.4128(-1)	0.4457(-1)
0.01025	0.9666(-1)	0.9895(-1)	0.9666(-1)	0.9690(-1)
0.0103	0.1962	0.1969	0.2010	0.2038
0.010335	0.2870	0.2842	0.2908	0.3044
0.010365	0.3560	0.3502	0.3560	0.3711
0.0104	0.4025	0.3941	0.3963	0.4108
0.0105	0.3744	0.3719	0.3701	0.3777
0.0106	0.3176	0.3199	0.3197	0.3081
0.017	0.2839	0.2825	0.2786	0.2709
0.0108	0.2666	0.2641	0.2659	0.2630
0.011	0.2602	0.2660	0.2621	0.2562
0.0114	0.2608	0.2623	0.2618	0.2597
0.0118	0.2517	0.2475	0.2528	0.2461
0.0122	0.2231	0.2264	0.2269	0.2183
0.0125	0.1978	0.1961	0.193	0.1933

Table 9. F + H_2 Phases as a Function of Basis Set.

	ϕ_{02}^{R}/radians			
ρ_{pr} ϵ/au.	7	8	9	previous method
0.010	7.664	7.645	7.754	5.748
0.0102	5.233	5.240	5.246	4.180
0.0103	4.764	4.746	4.769	4.003
0.0104	4.652	4.637	4.681	4.157
0.0105	4.448	4.432	4.477	4.157
0.0108	3.251	3.234	3.237	3.420
0.011	2.377	2.359	2.387	2.854
0.0115	0.550	0.529	0.533	NA[a)]
0.012	-1.063	-1.089	-1.086	0.400
0.0125	-2.544	-2.576	-2.553	-0.701
0.013	-3.875	-3.924	-3.928	-1.762

a) Not available.

Table 10. F + H_2 Phases as a Function of Projection Distance

	ϕ_{02}^{2} /radians			
ρ_{pr} ϵ/au.	10	12	14	previous results
0.010	7.754	7.246	6.692	5.748
0.0101	6.209	5.511	5.434	4.760
0.0102	5.246	4.765	4.558	4.180
0.01025	4.942	4.411	4.297	4.034
0.0103	4.769	4.276	4.179	4.003
0.010335	4.718	4.242	4.160	4.028
0.010365	4.701	4.235	4.161	4.090
0.01004	4.681	4.226	4.158	4.157
0.0105	4.477	4.048	3.983	4.157
0.0106	4.104	3.708	3.650	3.972
0.0107	3.676	3.367	3.248	3.649
0.0108	3.237	2.878	2.816	3.420
0.011	2.387	2.065	2.028	2.854
0.0114	0.885	0.590	0.563	1.826
0.0118	-0.460	-0.720	-0.748	0.859
0.0122	-1.456	-1.921	-1.953	-0.700(-1)
0.125	-2.558	-2.783	-2.811	-0.701

Figure Captions

FIG. 1. Phase ϕ_{00}^{R} of the scattering matrix element S_{00}^{R} for the $H + H_2$ reaction as a function of the total energy **E** for different values of the projection distance ρ_{pr}. Data for $\rho_{pr} = 11, 12$ bohr are not plotted because of their similarity to the 10 bohr results. Scattering calculations were performed with four even and four odd basis functions; other numerical parameters have their values in Table 2.

FIG. 2. Phase ϕ_{00}^{R} of the scattering matrix element S_{00}^{R}, for the $H + H_2$ reaction as a function of the total energy $\mathbf{E}_n$ near the first resonance by the previous method (line) and present method (circle). Scattering calculations used $\rho_{pr} = 10$ bohr; all other parameters are as in Fig. 1.

FIG. 3. Phase ϕ_{00}^{R} of the scattering matrix element S_{00}^{R} for the $H + H_2$ reaction as a function of the total energy **E** near the second resonance. Symbols are as in Fig. 2.

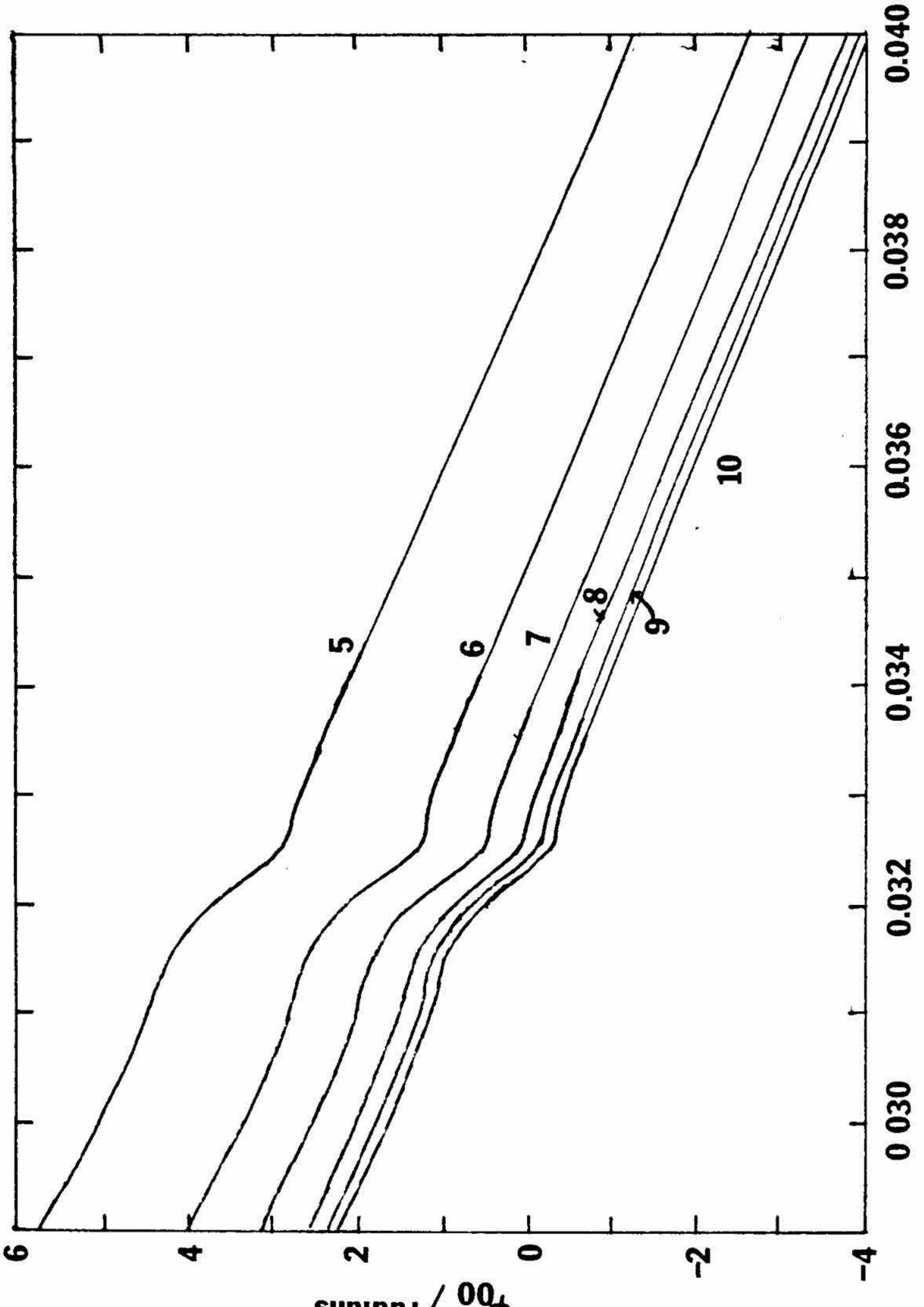
6
4
2
0
-2
-4
ϕ_R^{00} /radians
0 030
0.032
0.034
0.036
0.038
0.040
E/au
5
6
7
8
9
10

Figure 1

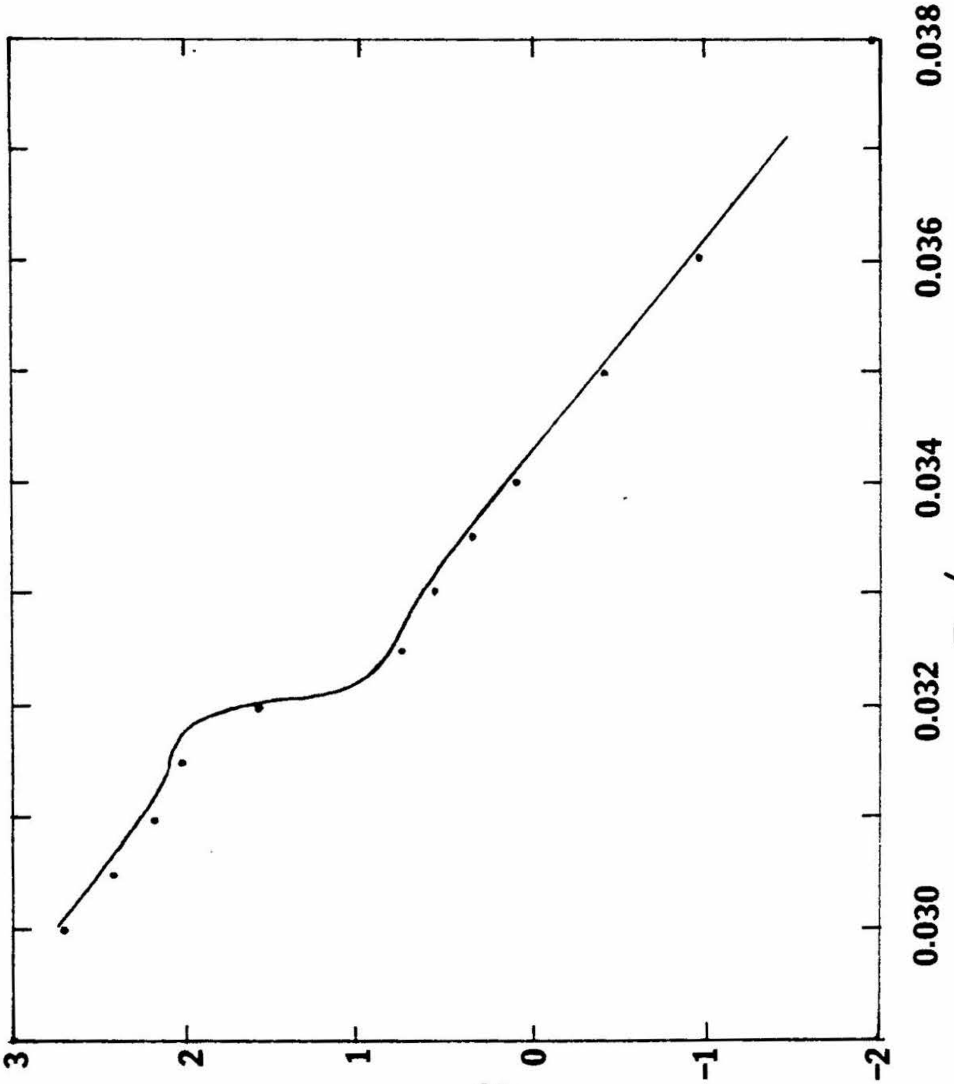

Figure 2

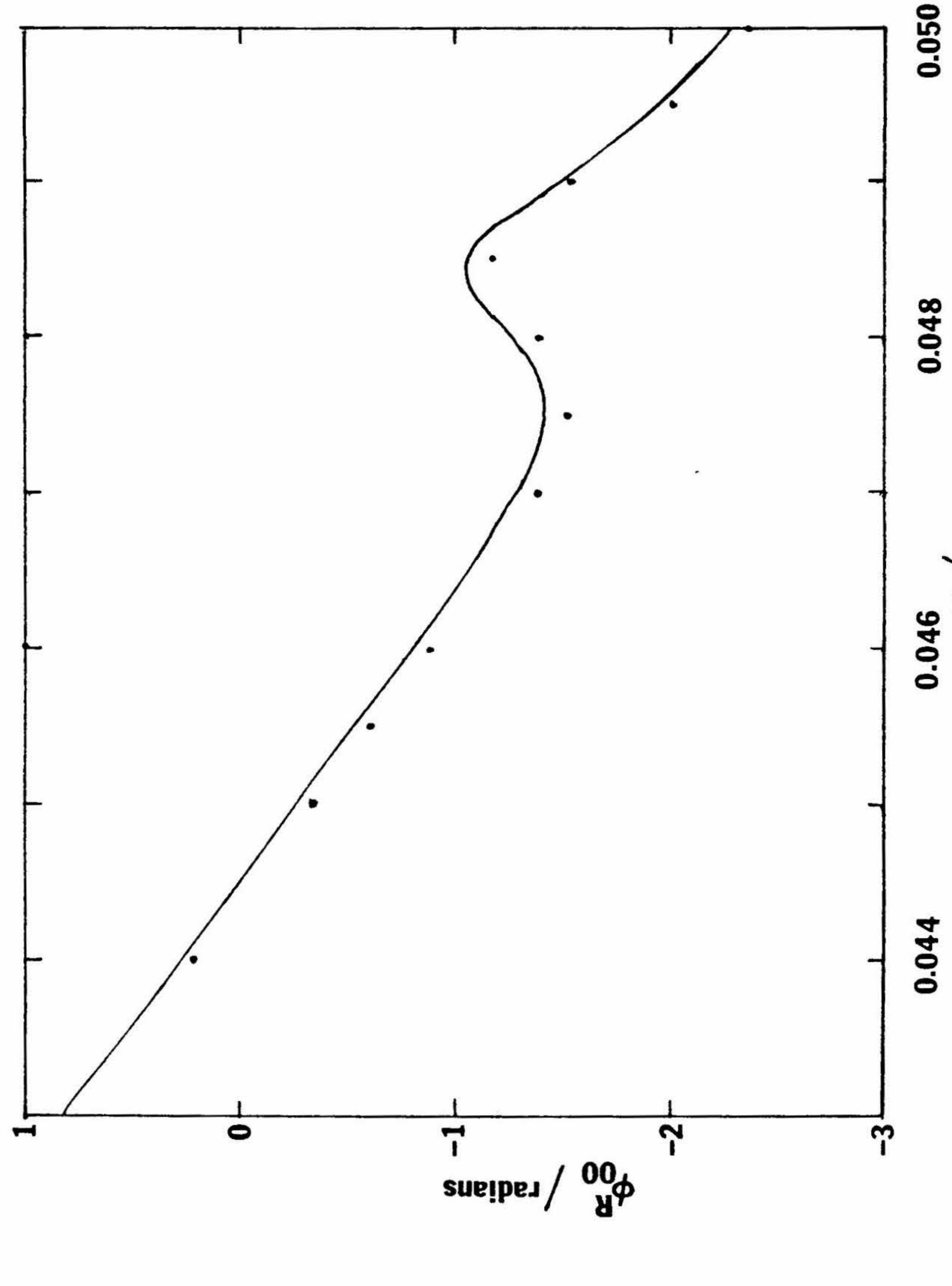

Figure 3